



The
University
Of
Sheffield.

The Influence of Groundwater on the Mineralogy of Cement for Nuclear Waste Disposal

Rita Vasconcelos

A thesis submitted in partial fulfilment of the requirements for the
degree of Doctor of Philosophy

The University of Sheffield
Faculty of Engineering
Department of Materials Science and Engineering

June 2019

Abstract

Geological disposal is the main preferable option for the long-term management of radioactive waste by many countries, including the United Kingdom (UK). A Geological Disposal Facility (GDF) is based on a multi-barrier concept, which utilises a series of engineered barriers that provide physical and chemical containment for radioactive waste, mitigating the potential for radionuclide release to the geo- and bio-spheres. Cementitious materials are used for many different parts of the multi-barrier GDF, having a wide range of purposes, for example as waste encapsulate, as backfill or as a sealant. Therefore, understanding the mineralogical evolutions of these cementitious materials, especially when in contact with groundwater, is key for the development of a robust safety case.

In this Thesis, investigation of the main mineralogical and microstructure characteristics of two different cementitious materials, a high-pH cement considered to be used as a backfill material in one of the UK GDF conceptual scenarios for the disposal of intermediate level waste (Nirex Reference Vault Backfill, NRVB), and a low-pH cement considered to use by many European countries (called Cebama reference cement), was performed. Extended experiments were also carried out to help develop a detailed understanding of the interactions of these cements with three different groundwater compositions (granitic, saline and clay).

Long-term evolution of the phase assemblage of both cements showed that hydration of NRVB was completed within 2 months, whereas for the Cebama reference cement paste, hydration was incomplete even after 1.5 years of curing. Differences between the two cementitious materials were also observed in terms of phase assemblage. Additionally, NRVB presented a higher porosity when compared to the Cebama reference cement paste, which was found to be a very dense material with very low porosity.

The work presented in this Thesis demonstrates key differences between the two cementitious materials when in contact with groundwater. In the case of NRVB, the pH of the solutions was mainly buffered through the dissolution of portlandite, C-S-H and ettringite. Moreover, precipitation of secondary phases was observed due to interactions with the different groundwaters, affecting the overall porosity of NRVB. In the Cebama reference cement paste, the edge of the sample was the main area affected by the groundwater interactions. In this degraded area, decalcification of C-S-H and ettringite was observed, being these hydrate phases the main responsible for the buffering of the solutions. In addition, the formation of a protective layer was observed when carbonates were present in the groundwater composition, reducing in this way further groundwater interactions.

Acknowledgements

It has been a great adventure doing my PhD in Sheffield and there are a number of people which I need to thank for their support and for making Sheffield feel like home.

First of all, I would like to thank my supervisors Dr. Claire Corkhill and Prof. John Provis for giving me the opportunity of doing this PhD (even though I did not know anything about cement) and for their support and encouragement throughout these 4 years. And an extra special thanks to Claire for her dedication over the last 6 months in helping me achieve my aim of submitting my thesis by my birthday.

I would like to express my gratitude to everyone, especially in Immobilisation Science Laboratory (ISL), that helped me in any way with my laboratory work. A special thanks to Oday Hussein for his endless patience and assistance with my work in the Cement lab, without him this PhD would have been much more difficult to finish. Thank you to Colleen and Sam Walling for the helping me a lot with Geoff when he was not behaving, and also to Brant Walkley for sharing his expertise with NMR experiments.

Sheffield has felt like home mainly due to the people that I met in ISL. I am deeply thankful for the countless experiences and fun moments provided throughout my four years here. All the after work pubs and all the socials made my time here a pleasure. For all the chats and coffee breaks, thank you to Toni. To my desk mates: Seb – thanks for the sweets, music and ‘Pub?’; Hannah – thank you for all the chocolates that helped me during my writing up period; and Sam Waters – thank you for all the chats and for showing me how to swear at a computer. Thank you to Sarah Kearney for all the GEMS sessions and discussions. Thank you to James Vigor for helping me a lot with XRD and Rietveld refinement. Thank you to everyone that in one way or another made my time here so enjoyable.

A special thanks to Mafalda, who through many phone calls kept my spirits up. Also, to my Nabiças (Shorty, Sara and Ines), for the laughs shared.

My greatest thanks will go to Rob. His unconditional love, support and patience, especially in the past 6 months, have been invaluable. Thank you so much for always being there to make me laugh and to calm me down in the more stressful moments. Thank you for always believing in me – Também posso?

And finally, an enormous thank you to my family – Pai, Mi, Xano and Gonçalo – for their endless love and support, even though most of the time we have been in different countries. Muito obrigada!!!

Publications

Journal publications:

1. R.G.W. Vasconcelos, N. Beaudoin, A. Hamilton, N.C. Hyatt, J.L. Provis and C.L. Corkhill, Characterisation of a high pH cement backfill for the geological disposal of nuclear waste: The Nirex Reference Vault Backfill, *Applied Geochemistry* 89 (2018) 180-189. doi:10.1016/j.apgeochem.2017.11.007.
2. R.G.W. Vasconcelos, A. Idiart, N.C. Hyatt, J.L. Provis and C.L. Corkhill, Preliminary groundwater leaching experiments with Nirex Reference Vault Backfill, *MRS Advances* 3 (2018), 1175-1180. doi:10.1557/adv.2018.248.

Conference publications and presentations:

1. R.G.W. Vasconcelos, N.C. Hyatt, J.L. Provis and C.L. Corkhill, Characterisation of NRVB, a high-pH backfill material, 1st Annual Workshop Proceedings Cebama, Barcelona, Spain, 11th – 13th May 2016. (*S+T proceedings and poster presentation*)
2. R.G.W. Vasconcelos, N.C. Hyatt, J.L. Provis and C.L. Corkhill, Characterisation of UK and French geological disposal cement materials prior to groundwater leaching, Environmental Mineralogy Group, Research in progress Meeting, Bristol, UK, 9th June 2016. (*Poster presentation*)
3. R.G.W. Vasconcelos, N.C. Hyatt, J.L. Provis and C.L. Corkhill, Characterisation of the UK NRVB prior to groundwater leaching, 36th Cement and Concrete Science Conference, Cardiff, UK, 5th – 6th September 2016. (*Extended abstract and oral presentation*)
4. R.G.W. Vasconcelos, A. Idiart, N.C. Hyatt, J.L. Provis and C.L. Corkhill, Preliminary assessment of interaction between UK backfill cement material and groundwater, 2nd Annual Workshop Proceedings Cebama, Helsinki, Finland, 16th – 19th May 2017. (*S+T proceedings and oral and poster presentation*)
5. R.G.W. Vasconcelos, J.L. Provis and C.L. Corkhill, Characterisation of UK cement backfill material pre- and post-groundwater leaching experiments, Scientific Basis for Nuclear Waste Management Symposium, Sydney, Australia, 29th October – 3rd November 2017. (*Oral presentation*)
6. R.G.W. Vasconcelos, B. Walkley, N.C. Hyatt, J.L. Provis and C.L. Corkhill, The physico-chemical evolution of a low-pH cement in contact with groundwater, 3rd Annual Workshop Proceedings Cebama, Nantes, France, 17th – 18th April 2018. (*S+T proceedings and oral and poster presentation*)

7. R.G.W. Vasconcelos, N.C. Hyatt, J.L. Provis and C.L. Corkhill, Long-duration leaching experiments using high- and low-pH cements, NUWCEM, Avignon, France, 24th – 26th October 2018. (*Extended abstract and oral presentation*)

Other publications:

1. R.G.W. Vasconcelos, J.L. Provis and C.L. Corkhill, State of the art review of the NRVB: A UK high-pH backfill material, Cebama project State-of-the-art Review (D1.03), KIT-INE publication, 2016. Report-Nr. KIT-SR 7734; ISBN 978-3-7351-0660-7.
2. M. Hayes, G. Cann, E. Butcher, A. Qaisar, S.A. Walling, R.G.W. Vasconcelos, C.L. Corkhill and J.L. Provis, Evaluation of the effects of an organic superplasticiser on the microstructure of blended blast furnace slag: Portland cement grouts for nuclear waste treatment, NUWCEM, Avignon, France, 24th – 26th October 2018.

List of Abbreviations

AFm	Alumina ferric oxide monosulphate; in this thesis referred to monocarboaluminate, hemicarboaluminate and monosulphoaluminate
AFt	Ettringite
BET	Brunauer-Emmett-Teller
BFS	Blast furnace slag
BJH	Barrett-Joyner-Halenda
C-S-H	Calcium silicate hydrate
EDX	Energy dispersive X-ray spectroscopy
GDF	Geological disposal facility
HLW	High level waste
IC	Ion chromatography
ICP-OES	Inductively coupled plasma - optical emission spectrometry
ILW	Intermediate level waste
LLW	Low level waste
LDE	Long-duration experiment
MAS	Magic angle spinning
MIP	Mercury intrusion porosimetry
NMR	Nuclear magnetic resonance
NRVB	Nirex Reference Vault Backfill
PC	Portland cement
PSD	Position sensitive detectors
SCM	Supplementary cementitious materials
SEM	Scanning electron microscopy
SNF	Spent Nuclear Fuel
TGA	Thermogravimetric analysis
VOI	Volume-of-interest
w/s	Water-to-solids ratio
XCT	X-ray computed tomography
XRD	X-ray diffraction

XRF

X-ray fluorescence

Cement Chemical Nomenclature

A = Al_2O_3

C = CaO

F = Fe_2O_3

H = H_2O

M = MgO

S = SiO_2

Mineral Name	Chemical Formula	Cement Formula
Alite	Ca_3SiO_5	C_3S
Belite	Ca_2SiO_5	C_2S
Tricalcium aluminate	$\text{Ca}_3\text{Al}_2\text{O}_6$	C_3A
Ferrite	$\text{Ca}_2\text{AlFeO}_5$	C_4AF
Calcium Silicate Hydrate	$\text{CaO}_x \cdot \text{SiO}_2 \cdot x\text{H}_2\text{O}$	C-S-H
Magnesium Silicate Hydrate	$\text{MgO}_x \cdot \text{SiO}_2 \cdot x\text{H}_2\text{O}$	M-S-H
Portlandite	$\text{Ca}(\text{OH})_2$	CH
Ettringite	$\text{Ca}_6\text{Al}_2(\text{OH})_{12}(\text{SO}_4)_3 \cdot 26\text{H}_2\text{O}$	AFt
Hemicarboaluminate	$\text{Ca}_4\text{Al}_2(\text{OH})_{12}(\text{CO}_3)_{0.5} \cdot 5.5\text{H}_2\text{O}$	AFm
Monocarboaluminate	$\text{Ca}_4\text{Al}_2(\text{OH})_{12}(\text{CO}_3)_3 \cdot 5\text{H}_2\text{O}$	AFm

Table of Contents:

Chapter 1: Introduction	1
Chapter 2: Literature Review	5
2.1: Introduction to Radioactive Waste	5
2.2: Geological Disposal of Radioactive Waste	7
2.3: Nirex Reference Vault Backfill (NRVB).....	9
2.3.1: Composition and Chemical Analysis.....	9
2.3.2: Properties	12
2.3.3: Strength (compressive strength)	13
2.3.4: Porosity	14
2.3.5: Permeability	14
2.3.6: Gas Permeability.....	15
2.3.7: Cracking.....	15
2.3.8: Buffering Capacity.....	16
2.3.9: NRVB Carbonation	18
2.4: Low-pH cement	20
2.4.1: Cebama Reference Cement Mix	23
2.5: Groundwater Interactions with Cement.....	24
2.5.1: Leaching experiments	26
2.6: Concluding remarks.....	29
Chapter 3: Experimental Methods	31
3.1: Materials and solutions	31
3.1.1: Nirex Reference Vault Backfill (NRVB) cement	31
3.1.2: Cebama Reference Cement.....	32
3.1.3: Synthetic Groundwater Compositions	32
3.2: Cement – Groundwater Contact Methodology	34
3.2.1: Semi-dynamic cement-groundwater contact experiment.....	35
3.2.2: Static cement-groundwater contact experiment.....	36
3.2.3: pH measurements.....	36

3.3: Analytical Methods.....	37
3.3.1: Particle Size Distribution	37
3.3.2: Isothermal Calorimetry	37
3.3.3: X-Ray Diffraction (XRD)	38
3.3.4: Synchrotron X-Ray Diffraction.....	42
3.3.5: Thermogravimetric Analysis – Mass Spectrometry (TG-MS).....	46
3.3.6: Scanning Electron Microscopy (SEM) and Energy Dispersive Spectroscopy (EDX).....	46
3.3.7: Solid-State Nuclear Magnetic Resonance (NMR) Spectroscopy.....	48
3.3.8: Mercury Intrusion Porosimetry (MIP)	50
3.3.9: Nitrogen sorption porosity analysis	51
3.3.10: X-Ray Computed Tomography (XCT)	53
3.3.11: Inductively Coupled Plasma Spectroscopy (ICP-OES)	54
3.3.12: Ion Chromatography (IC).....	55
Chapter 4: Characterisation of NRVB and Cebama reference cement paste	57
4.1: Introduction.....	57
4.2: NRVB Characterisation	58
4.2.1: Precursor materials.....	58
4.2.2: NRVB (20 °C).....	61
4.2.3: NRVB (40 °C).....	71
4.3: Cebama Reference Cement Characterisation.....	78
4.3.1: Precursor materials.....	78
4.3.2: Cebama Reference Cement (20 °C)	82
4.3.3: Cebama Reference Cement (40 °C)	88
4.4: Conclusions.....	93
Chapter 5: In-situ Synchrotron X-ray Diffraction Study of High- and Low-pH Cement Hydration	95
5.1: Introduction.....	95
5.2: NRVB Hydration	96
5.2.1: Synchrotron X-ray diffraction.....	96
5.2.2: Ex-situ ²⁹ Si MAS NMR	104
5.3: Cebama Reference Cement Hydration.....	110

5.3.1: Synchrotron X-ray Diffraction.....	111
5.3.2: Ex-situ ²⁹ Si MAS NMR	114
5.4: Conclusions.....	118
Chapter 6: Mineralogical and porosity assessment of NRVB in contact with simulated groundwater solutions	121
6.1: Introduction.....	121
6.2: Mineralogical and microstructural evolution of NRVB without groundwater	123
6.3: Mineralogical and microstructural evolution of NRVB with Granitic Groundwater (Semi-Dynamic Experiment).....	129
6.3.1: Mineralogical evolution of NRVB	129
6.3.2: Nano- and micro-structural evolution of NRVB	142
6.3.3: Solution chemistry	143
6.4: Mineralogical and microstructural evolution of NRVB with Saline Groundwater (semi-dynamic experiment).....	146
6.4.1: Mineralogical evolution of NRVB	146
6.4.2: Nano- and micro-structural evolution of NRVB	156
6.4.3: Solution chemistry	158
6.5: Mineralogical and microstructural evolution of NRVB with Clay groundwater (semi-dynamic experiment).....	161
6.5.1: Mineralogical evolution of NRVB	161
6.5.2: Nano- and micro-structural evolution of NRVB	173
6.5.3: Solution chemistry	175
6.6: Discussion.....	178
6.6.1: Comparison with control samples not in contact with groundwater.....	178
6.6.2: Comparison between different groundwater compositions	178
6.6.3: Comparison between semi-dynamic and static experiment.....	186
6.7: Conclusions.....	186
Chapter 7: Mineralogical and porosity assessment of the Cebama Reference Cement in contact with simulated groundwater solutions	189
7.1: Introduction.....	189
7.2: Mineralogical and microstructural evolution of Cebama reference cement paste without groundwater	190

7.3: Mineralogical and microstructural evolution of NRVB with Granitic Groundwater (semi-dynamic experiment).....	196
7.3.1: Mineralogical evolution of Cebama reference cement paste	196
7.3.2: Nano- and micro-structural evolution of Cebama reference cement paste	206
7.3.3: Solution chemistry	207
7.4: Mineralogical and microstructural evolution of NRVB with Saline Groundwater (semi-dynamic experiment)	210
7.4.1: Mineralogical evolution of Cebama reference cement paste	210
7.4.2: Nano- and micro-structural evolution of Cebama reference cement paste	219
7.4.3: Solution chemistry	220
7.5: Mineralogical and microstructural evolution of NRVB with Clay groundwater (semi-dynamic experiment)	222
7.5.1: Mineralogical evolution of Cebama reference cement paste	222
7.5.2: Nano- and micro-structural evolution of Cebama reference cement paste	231
7.5.3: Solution chemistry	232
7.6: Discussion.....	234
7.6.1: Comparison with control samples not in contact with groundwater	234
7.6.2: General comparison between different groundwater compositions	235
7.6.3: Comparison between semi-dynamic and static experiments.....	239
7.7: Conclusions.....	241
Chapter 8: Conclusions and Future work	245
8.1: Summary and Conclusions.....	245
8.2: Future Work	248
Appendix I	251
Appendix II.....	275
Static experiments performed with NRVB in contact with groundwater	275
Appendix III	279
Static experiment performed with Cebama Reference Cement paste in contact with groundwater.....	279
References	283

Chapter 1: Introduction

For the long-term management of radioactive waste, geological disposal has been selected as the most suitable solution, not only for the United Kingdom (UK), but also for many European countries. The Geological Disposal Facility (GDF) design is based on a multi-barrier concept, where natural and engineered barriers will be used together to contain and mitigate the release of radionuclides from the waste to the environment, allowing radioactive decay to occur without exposing the biosphere to radioactive elements.

Cementitious materials feature in all current concepts for geological disposal as, for example, waste encapsulation grouts, waste containers and backfills, seals and fracture grouts, tunnel/vault linings and supporting structures including floors, roadways, bulkheads and buttresses. Their use confers a number of advantages, including low cost, ease of use/emplacement, provision of radiation shielding, high surface area for sorption of radionuclides and provision of an alkaline environment, which decreases the solubility of many cationic radionuclides.

In this Thesis, two different cements were investigated: (1) a high-pH backfill cement that has been investigated within the context of a conceptual UK disposal facility for intermediate level waste (ILW) in a hard-rock environment (e.g. granite), called Nirex Reference Vault Backfill (NRVB); and (2) a low-pH cement that has been investigated as a likely plug/seal cement material in disposal concepts that include a bentonite clay buffer. This cement is based on the Finnish low-pH GDF cement material that has been adapted by the European research consortium, called Cebama (of which this project is a part), as a baseline reference material for a number of research groups investigating the interfacial reactions that occur between low-pH cement and bentonite.

As part of the GDF engineered barrier, the lifetime performance of cementitious materials is required to be extremely long, as many long-lived radionuclides are present in the radioactive waste. This Thesis, therefore, has two key objectives:

- 1) To develop a detailed, long-term understanding of the hydration reaction of NRVB and Cebama cements, including a detailed assessment of the mineralogy as a function of curing time and temperature, and a high-resolution synchrotron study of the kinetics of mineral formation; and
- 2) To evaluate how the microstructure (porosity) and chemical conditioning capacity of the NRVB and Cebama cements is altered when in contact with groundwater.

With respect to the first objective, the hydration behaviour of these two cements is expected to be significantly different since they differ greatly in their composition. Since the NRVB is a unique material, patented in 1994 for use in a UK GDF constructed in hard-rock, there has been relatively little investigation of the mineralogy or hydration kinetics, particularly over extended timescales. The

Cebama cement is somewhat better understood in this respect, however the slow nature of the hydration reaction (due to the presence of supplementary cementitious materials) has not been studied at high resolution over long-time scales.

With respect to the second objective, there are relatively few investigations of how hardened cement paste will change when in contact with groundwater. Since the chemical conditioning capability (i.e. the ability to generate alkaline conditions for radionuclide sorption) and porosity (important for egress of gas and ingress of water) are dependent on the mineralogy of the cement matrix, it is important to understand how inorganic solution species (e.g. CO_3^{2-} , SO_4^{2-} etc.) and pH may alter the phase assemblage.

This Thesis comprises four experimental Chapters that aim to address these objectives, and is organised as follows:

Chapter 2 contains an introduction to radioactive waste and the concept of geological disposal, followed by a review of the relevant literature pertaining to the mineralogy and microstructure of the two different cements studied, including an assessment of the limited studies on their leaching performance in groundwater. Part of this review was published in Cebama project state-of-the-art Review (KIT-INE publication), as Vasconcelos et al., (2016). The experimental methodology for all of the results Chapters is described in **Chapter 3**.

Chapter 4 describes the characterisation of different precursor materials that can be used to synthesise the NRVB cement and an assessment of how these alter the hydration behaviour and properties of the final product after 28 days of curing. This has particular importance to “security of supply” for NRVB powder precursors, should this material be utilised in a future UK GDF. This Chapter also evaluates the hydration behaviour, over a 28 day period, of NRVB and Cebama cements as a function of two different curing temperatures, at 20 °C and 40 °C. The room temperature was used as a standard curing condition to correlate with the data obtained in the long-duration synchrotron XRD experiment performed at Diamond Light Source (results in **Chapter 5**). For the extended experiments with groundwater, 40 °C was used, as advised by the UK waste management organisation, Radioactive Waste Management (RWM), to be representative of the peak of a 50 year thermal transient after backfilling of the disposal area [1]. Part of this Chapter is also published in Applied Geochemistry, as Vasconcelos et al., (2018).

The hydration behaviour of the two cement materials, over a 4 year period at room temperature, is described in **Chapter 5**, which details the results of the world’s first long duration synchrotron experiment at Diamond Light Source. In these results, the rate of change of the mineralogical constituents of the cements as a function of hydration time, is quantified by Rietveld refinement of synchrotron X-ray diffraction data, and is complimented by nuclear magnetic resonance spectroscopy analysis of the non-crystalline hydration phases. Some repetition between Chapters 4 and 5 was

unavoidable; the unique nature of the experiments performed in Chapter 5, and the high level of detail acquired, required a stand-alone chapter. This will be submitted for publication later in 2019.

Chapters 6 and 7 detail the results of extended contact experiments between NRVB (**Chapter 6**) and Cebama (**Chapter 7**) cements with groundwater. Since the geology of the UK disposal facility is not yet known, it was decided to investigate the behaviour of cements in contact with groundwaters representative of the GDF concepts of other European countries. These include: a synthetic granite groundwater solution, based on that from the Swedish bedrock; a clay groundwater based on the Callovo-Oxfordian clay of the French GDF concept at Meuse/Haute-Marne underground rock laboratory; and a saline solution representative of deep groundwaters in the Earth's crust.

Finally, **Chapter 8** comprises a summary and the overall conclusions of the work performed, with recommendations of possible future work to be performed.

Chapter 2: Literature Review

Part of this Chapter is published as “State of the art review of the NRVB: A UK high-pH backfill material” in Cebama project State-of-the-art Review (D1.03), KIT-INE publication, 2016, by Vasconcelos et al. (Report-Nr. KIT-SR 7734; ISBN 978-3-7351-0660-7)

2.1: Introduction to Radioactive Waste

Radioactive waste is a term that applies to all the radioactive material arising from nuclear power (to produce electricity), from the use of isotopes in medicine (for health purposes), from research, and from military nuclear operations. A significant amount of radioactive waste has been produced worldwide, and the classification of these wastes varies according to the regulatory policies applied in each country, being generally dependent on the radionuclide inventory and half-life. In the UK, radioactive waste can be generically divided, according to the quantity of radioactivity the waste contains and the generated heat, into High Level Waste (HLW), Intermediate Level Waste (ILW) and Low Level Waste (LLW) [1–3]. HLW includes waste where the temperature rises significantly as a result of its radioactivity (radioactive decay), and so requires substantial radiation shielding and remote handling [3]. This type of waste includes spent nuclear fuel (SNF) and some reprocessing wastes (e.g. vitrified fission, actinide and activation products) from the nuclear fuel cycle [4]. ILW comprises waste that does not generate a significant amount of heat, but exceeds the upper boundaries of radioactivity for LLW. Examples of these type of wastes are: steel, graphite, concrete, fuel cladding, reactor components and sludges [5]. In the case of LLW, this comprises the waste with the lowest radioactivity. Typical examples of LLW are disposed paper, metal and protective clothing from nuclear operations and medical research facilities [3,5].

Since radioactive wastes have a great variety regarding their physical (solid, liquid or gas), chemical (volatile, organic, non-organic, etc.) and radiological (heat-generation, half-life) characteristics, and to reduce their intrinsic risks (e.g. radiological release), immobilisation of the waste into a more stable wasteform is required [4]. Wasteform materials should follow certain requirements, like [4]: be a solid material to help with transport and storage; be stable at specific temperatures according to the radioactive decay heat released; and be durable, to ensure long-term storage and disposal, without the risk of radionuclide release to the environment. A type of immobilisation is chemical containment, which is used to immobilise HLW in order to reduce the mobility and toxicity of the radionuclides.

Vitrification is a technique widely used for the treatment of HLW, and consists of the immobilisation of highly active liquor or solids into a glass matrix, and in this way, radionuclides are chemically immobilised within the atomic structure of the glass.

In the case of immobilisation of ILW, physical containment of the waste is more usually performed, where cement grout is frequently used [6]. Portland cement (PC) is the most common type of cement used, and is frequently blended with supplementary cementitious materials (SCMs) such as blast furnace slag (BFS), fly ash and silica fume [6–8].

The use of cement as an encapsulation matrix has many advantages, including [3,9]:

- Low cost and simpler processing route
- Conversion of fluid or granular wastes into a solid form
- Provide radiation shielding
- Alkaline environment, which decreases the solubility of many cationic radionuclides
- Provide sorption and reaction sites for some radionuclides

However, there are also a number of disadvantages of using cement. One of them is the volume increase associated with cementation. This gives rise to a significantly larger volume of conditioned waste, contributing to an increase of the cost and size of the final repository [4,10].

Another disadvantage is the interaction between cement and some metallic wastes. The continuous corrosion of reactive metals in the alkaline and free water-containing environment within the cement matrix may cause the formation of corrosion products and the generation of hydrogen, that can result in expansion/cracking of the waste package [9,11].

Other problems might also arise from the security of powder supply [12]. External factors can influence the production and availability of PC and SCMs, and so these materials need to be produced with tight guidelines, so future properties can be accurately predicted [12].

Latest numbers estimate that the worldwide inventory of nuclear waste generated from nuclear power production (taken from the International Atomic Energy Agency, 2007) is 2.2 million m³ of ILW and LLW, 34 000 m³ vitrified HLW and 180 000 metric tonnes heavy metal of spent nuclear fuel (SNF) [4]. In the UK, ILW comprises a significant proportion of the UK's projected inventory of radioactive waste, approximately 450 000 m³ [5]. A number of options have been proposed for the safe disposal of this waste, and some of those options are discussed in the next section.

2.2: Geological Disposal of Radioactive Waste

The safe disposal of radioactive wastes is of extreme importance. Due to the long-lived nature of many radionuclides present in the radioactive waste, the requirement of some long-term storage options is needed. Disposal above ground, sea disposal, disposal in space and deep borehole disposal are some of the options that have been investigated worldwide [13–15]. However, most of these options are considered nowadays unfeasible [16]. The disposal of the waste deep underground (several hundred of metres or more) in a geological disposal facility (GDF), is the preferred option and has international consensus as being the safest route [1,2,7,16].

A GDF design is based on a multi-barrier concept, where natural and engineered barriers are used together to contain and prevent the release of the radionuclides to the environment, allowing safe radioactive decay to occur [1]. Different GDF design concepts are being considered for the disposal of ILW and HLW.

In the UK, for example, one of the concepts under consideration for the geological disposal of ILW/HLW in a hard crystalline rock is shown in Figure 2.1. In this concept, after the wastefrom has been conditioned (e.g. encapsulated in a cement grout), the wastefrom will be packaged in stainless steel to provide a primary structural and mechanical barrier, and then placed deep underground, at depths between 200-1000 metres [2]. Then, a buffer/backfill material will be used to surround the packaged wastefrom, filling the gap between the waste package and the host rock. This barrier can be composed of clay/bentonite (specifically for HLW disposal) or cement (specifically for ILW disposal), and has the aim to control the movement of groundwater and to provide sorption capacity for radionuclides. An example of a buffer is bentonite, which has been considered for use in many European countries (e.g. Switzerland, France and Sweden) for the disposal of HLW, due to its low hydraulic permeability and swelling pressure, which allows a self-sealing capacity and closes gaps around the emplacement tunnels [17]. Another example of a backfill material is a high-pH cement, called Nirex Reference Vault Backfill (NRVB), considered for use in one of the GDF scenarios in the UK for the disposal of ILW, and this cementitious material is one of the main focus of this Thesis.

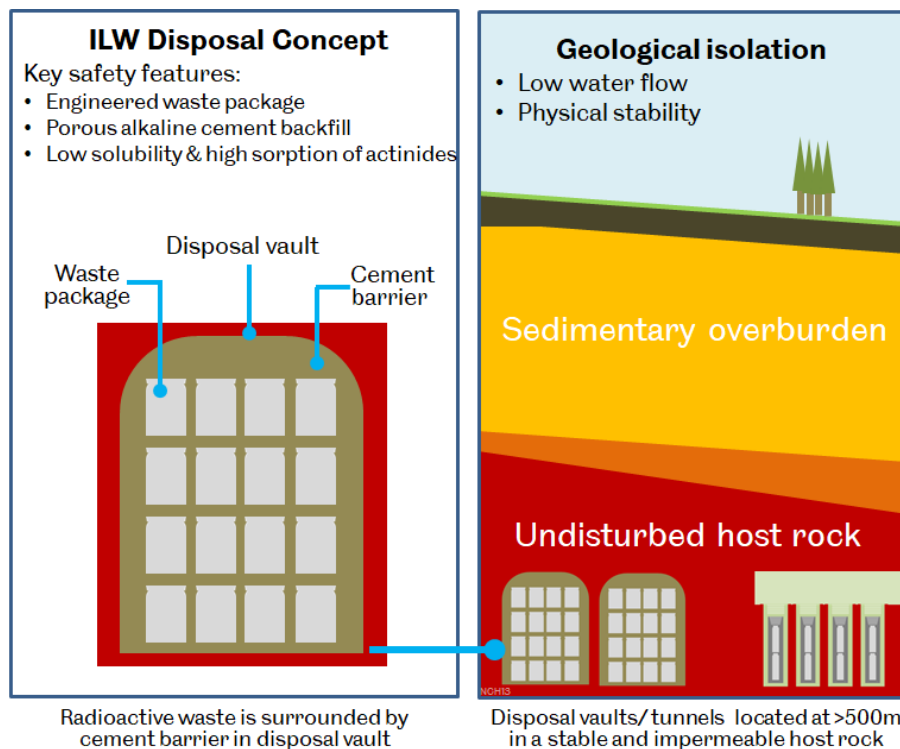


Figure 2.1. UK conceptual GDF scenario in a high-strength crystalline rock, for the disposal of ILW (from [4]).

The last barrier is the host rock itself, which should be stable against ground movement and have a slow moving hydrogeology in order to minimise the movement of radionuclides to the surface. Several rock types are being considered for hosting a GDF [1,4,18]:

- High strength crystalline rock (e.g. granite), is characterised by a pattern of fracture, and any fluid movement occurs predominantly through these fractures, also called discontinuities. It is also characterised by a low porosity and permeability. Likely to have groundwater with low to moderate salinity.
- Lower strength sedimentary rock (e.g. clay), comprises geologically younger sedimentary rocks, which have low permeability, are plastic and can form a tight seal around the engineered barrier. Groundwater movements occur mainly by diffusion.
- Evaporites (salt), can comprise anhydrite (anhydrous calcium sulphate), halite (rock salt) or other minerals that result from the evaporation of salt water. It has very extremely low permeability, and movement of the groundwater is absent.

Cementitious materials are being considered for all current concepts for geological disposal, and some of their applications are [7]: as mentioned before, waste encapsulation grouts; waste containers and overpacks, buffers and backfills; seals and fracture grouts; tunnel plugs; tunnel/vaults linings; and supporting structures including floors, roadways, bulkheads and buttresses. It should be noted that cement is usually not used as a backfill/buffer material for HLW disposal, due to the detrimental effects

that high temperature (characteristic of HLW waste) have in the cementitious materials. Therefore, clay/bentonite buffers are used as an alternative. However, cementitious materials are still considered to use in this context for the construction of supporting structures including floors, roadways, bulkheads and buttresses. In this project, a high-pH cement (Nirex Reference Vault Backfill, NRVB) considered to use as a backfill material in the context of ILW disposal, and low-pH cement (PC, BFS and silica fume blend) considered to use in supporting structures in the context of HLW disposal are being studied, and to follow is a brief literature review related to the two cements.

2.3: Nirex Reference Vault Backfill (NRVB)

NRVB has an important role as an engineered barrier to achieve the necessary degree of long-term waste isolation and containment for the UK's GDF. This cementitious backfill material has been specified to fulfill a number of benefits [19]:

- Long-term maintenance of alkaline porewater chemistry to suppress dissolved concentrations of many important radionuclides. NRVB can chemically condition the groundwater to high pH for long-time scales, due to dissolution of the cement hydrate phases;
- Long-term maintenance of a high active-surface-area for sorption of key radionuclides, mainly due to the calcium silicate hydrate (C-S-H) formed during the hydration of cement. This disordered cement hydrate mineral can provide a very large surface area onto which many key radionuclides would sorb;
- Relatively high permeability and porosity to ensure homogeneous chemical conditions and to allow the escape of gas generated by chemical reactions within the repository;
- Possibility for reversibility/retrievability due to the low strength of NRVB, which facilitates the possibility of re-excavation of the vault to gain access to or remove waste packages [20,21].

2.3.1: Composition and Chemical Analysis

NRVB is a high porosity cement composed of Portland cement (CEM I 52.5N), hydrated lime (calcium hydroxide, $\text{Ca}(\text{OH})_2$) and limestone flour (calcium carbonate, CaCO_3). The target formulation for this material is : 450 kg m^{-3} Portland Cement (PC), 170 kg m^{-3} hydrated lime, 495 kg m^{-3} limestone flour and 615 kg m^{-3} water; water/cement ratio of 1.37 and a water/solids ratio (w/s) of 0.55, by mass [19].

When in contact with water, the hydration of PC occurs, forming a mixture of mineral phases that provide the main properties of this cementitious backfill. The products from this reaction in NRVB are calcium silicate hydrate ($\text{CaO}\cdot\text{SiO}_2\cdot x\text{H}_2\text{O}$; C-S-H), calcium hydroxide (also known as portlandite,

Ca(OH)₂, ettringite (Ca₆Al₂(SO₄)₃(OH)₁₂·26H₂O) and calcium monocarboaluminate hydrate (Ca₄Al₂(OH)₁₂(CO₃)₃·5H₂O) [1, 2, 5, 6]. C-S-H and CH are considered to be the most significant cement hydrate phases, because they are expected to provide the majority of the buffering capacity [19]. According to a model (database not specified) based on the mineral assemblages (at early age) and high temperature (80 °C) studied by [24], the initial mineralogy (28 days of curing) of NRVB can be presented as (Table 2.1):

Table 2.1. Short-term high temperature model (80 °C) (adapted from [24])

Component	Abbreviation	Content in dry NRVB (mol m ⁻³)
Portlandite	CH	3704
Calcium silicate hydrate	C-S-H	758
Hydrogarnet	C ₃ AH ₆	311
Calcite	CaCO ₃	4950

The formation of hydrogarnet-type phases was predicted in this model, although more recent advances in cement chemistry and phase assemblage prediction models indicate that this may be less likely due to the high quantity of carbonate present in this cement formulation [25].

Figure 2.2 shows X-ray diffraction (XRD) patterns from fresh NRVB, and NRVB cured for 4 months and 3 years [26]. The fresh NRVB is dominated by calcite, whereas in cured NRVB (both 4 months and 3 years) the phase assemblage is dominated by portlandite, with also a significant calcite contribution. Moreover, in fresh NRVB it seems that the authors observed the presence of hatrurite, which is a PC clinker phase, showing the presence of unreacted PC. These analyses do not identify C-S-H, because C-S-H, and possibly other hydrated products, may exist in the form of amorphous rather crystalline structures [27], hence no crystalline diffraction peak is observed.

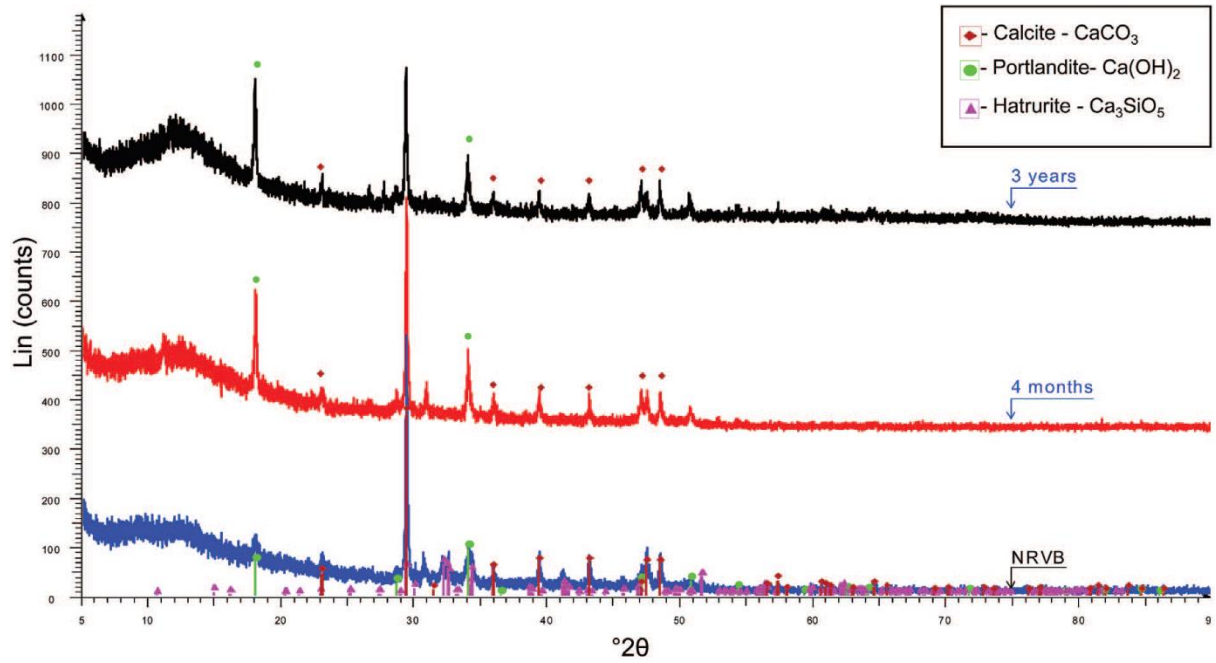


Figure 2.2. XRD spectra of fresh NRVB powder, NRVB after 4-months curing and NRVB after 3-years curing (from [26])

Figure 2.3 shows the relationship between the temperature and weight loss of the NRVB when heated to 1000 °C, using differential thermal analysis (TGA) and derivative thermogravimetric analysis [27]. The peak identified at 130 °C is attributed to the loss of chemically bound water in C-S-H. Between 400 to 460 °C, a peak related to the dehydration of calcium hydroxide is observed [27]. A third peak, at 650 to 770 °C, is attributed to the weight loss due to the decomposition of CaCO₃ and the consequent release of CO₂ [27].

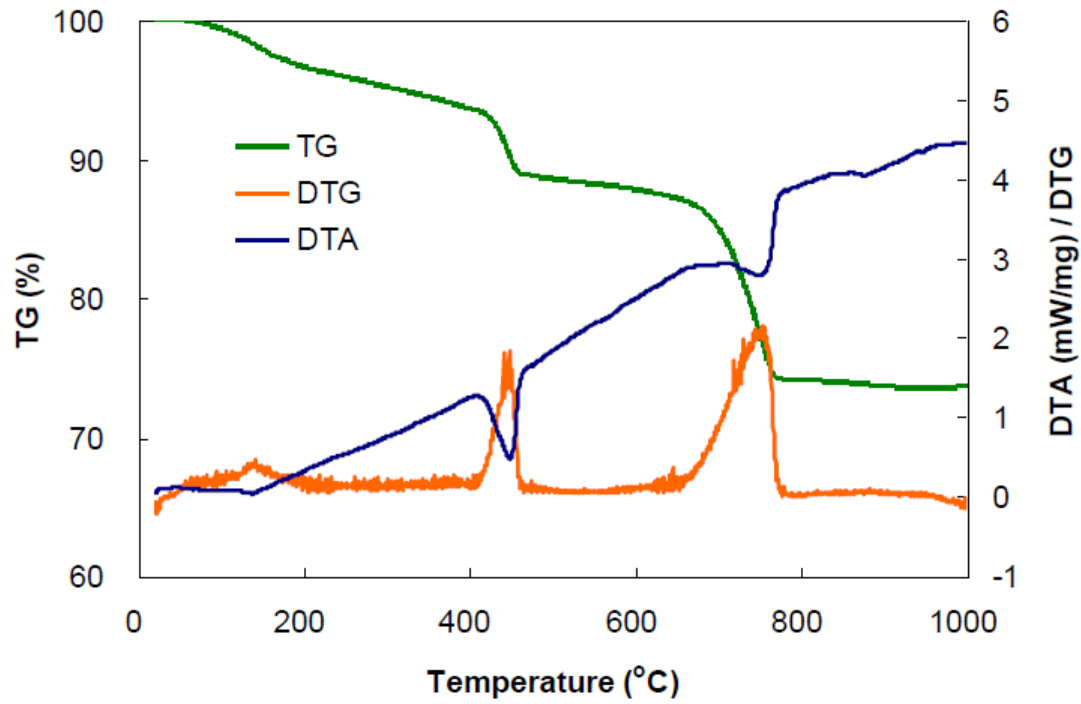


Figure 2.3. TG/DTA/DTG curves of fresh NRVB (from [27])

2.3.2: Properties

The general properties of NRVB, summarized by [7,19] are detailed in Table 2.2.

Table 2.2. NRVB properties (adapted from [7,19])

Property	Measured value
Bleed (100 mm high column and a large column 900 mm)	1.7%
Adiabatic temperature rise (do not specify sample size)	~ 40 °C
Setting time (Vicat)	Initial - 4 hours Final - 4 hours 50 minutes
Density (100 mm cubes)	Saturated - 1731 kg m ⁻³ Oven dried - 1095 kg m ⁻³
Compressive strength (100 mm cubes)	7 days - 4.95 MPa 28 days - 5.95 MPa 90 days - 6.26 MPa
Flow time (flow cone test)	Initial - 12.0 seconds At 1 hour - 14.0 seconds
Gas permeability (test described below)	Dry - 2 x 10 ⁻¹⁵ m ² Saturated - 5 x 10 ⁻¹⁷ m ²
Water permeability (test not specified)	1 x 10 ⁻¹⁶ m ²

It is clear that NRVB is a very porous cement that allows: gas migration; high alkalinity for chemical conditioning; low bleed and high fluidity for good void filling; and relatively low strength to facilitate the possibility of re-excavation of the vault to gain access to or remove waste packages, if required [19]. The literature pertaining to the key physico-mechanical properties of NRVB is detailed in the following section.

2.3.3: Strength (compressive strength)

The compressive strength of NRVB is gained mostly in the first 7 days of curing, with a reported 7-day value of about 4.95 MPa [19]. After this time, the compressive strength increases a small amount from ~ 5.95 MPa to 6.26 MPa from 28 to 90 days. When comparing with compressive strength values obtained for a conventional Portland cement (w/s = 0.50), (e.g. 31 MPa, 45 MPa and 46 MPa after 7, 28 and 90 days, respectively, from [28]), the values obtained for NRVB are very low. This relatively low strength thus allows retrievability of waste packages from within NRVB-backfilled vaults [20,21,29].

Since the repository operating temperatures will be higher than the 20 °C used for standard cement curing, studies have been performed to assess the effect of curing temperature (30 °C, 60 °C and 90 °C, cured in moist or excess volume of water) on the strength of NRVB [19]. Results showed that increasing the temperature of curing corresponds to a reduction in the strength, for example after 28 days of curing at 90 °C, the compressive strength was halved when compared to curing at 30 °C [19]. Similar results have been obtained with Portland-limestone cement, where a temperature increase negatively influenced compressive strength, due to the observed enhanced hydration rates and formation of denser

hydration products, which led to a coarser porosity and an increase of the pore radii [30]. It should be noted, however, that such high curing temperatures (90 °C) are not expected within a GDF vault for ILW (maximum temperature expected is 40 °C [1]).

2.3.4: Porosity

NRVB was developed to be highly porous. High porosity is advantageous for the following purposes [19]:

- Allows the diffusion of any gaseous discharge from the waste packages (e.g. H₂, CO₂ or CH₄ gas), that would otherwise build up and pressurise the geological disposal facility vault;
- Allows the ingress of groundwater, leading to rapid saturation. Under these conditions, the chemical buffering capacity of the backfill will be initiated due to dissolution of the cement phases by groundwater.
- The high surface area afforded by such high porosity gives rise to a large surface area capable of sorbing radionuclide species.

NRVB is relatively porous; the total porosity of NRVB (w/s = 0.55; w/c ratio 1.367), including a high quantity of unreacted material, was reported to be 50 % using mercury intrusion porosity and nitrogen desorption methods, at an unspecified curing age [19]. However, comparing the density obtained in the dry state and in water (Table 2.2) we can calculate the porosity to be 35%. X-ray computed tomography (XCT) gave a segmented porosity of ~ 40 % for large scale samples in the non-carbonated region of an NRVB-carbonation trial [31].

2.3.5: Permeability

The NRVB permeability coefficient is approximately $1 \times 10^{-16} \text{ m}^2$ [19]. This value was obtained in uncracked backfill by monitoring inflow and outflow rates until they reached a steady state (reported on the basis of an unspecified testing method). Because cracks may develop as a result of plastic settlement, early-age thermal contraction and expansion of the waste packages (corrosion), and they contribute to the effective permeability, a value for cracked NRVB of about $4 \times 10^{-13} \text{ m}^2$ has been estimated [7]. Consequently, groundwater may flow through the cracks. This is expected as the ingress of water will allow NRVB to provide homogeneous chemical condition, as mention previously.

2.3.6: Gas Permeability

After closure, the formation of gases is expected to occur in the GDF, e.g. from corrosion of Magnox cladding, fuel fragments, uranium and steel under anaerobic conditions; microbial degradation of organic compounds and; radiolysis of water [32]. As a result, the permeability of NRVB should be sufficient to allow gas movement without significant over-pressurisation and cracking [19]. The gas permeability coefficient for argon and helium in NRVB at 28 days of curing (in a membrane of NRVB 20 mm thick, average pressure of 100 kPa) was found to be approximately $2 \times 10^{-15} \text{ m}^2$ in dry conditions and $5 \times 10^{-17} \text{ m}^2$ in saturated grout [19,32]. The average pore radius was determined to be 0.45 μm , with a pore size distribution ranging from 5 nm to $> 1 \mu\text{m}$ [32]. Harris and colleagues [32] concluded, using the premise that a material is considered to crack if the calculated stress exceeds the tensile strength, that NRVB is able to release gas at a sufficient rate without generating cracks.

2.3.7: Cracking

The formation of cracks in the backfill material could influence the post-closure performance, since they can influence the flow of groundwater through the repository (as stated above), affect the chemistry of the pore water in the cracks, and impact upon the transport of radionuclides in solution and the migration of gases [33].

When the tensile strain exceeds the tensile strain capacity of the material, cracking occurs [19]. The cracking of NRVB may occur soon after backfill placement and as the backfill ages. The processes by which the cracks are formed include:

- Differential movement between backfill and waste packages or vault walls, where backfill strains would arise from changes in temperature, moisture content, etc;
- Internal pressures from the expansive corrosion of waste and containers or from gas generated by metal corrosion or organic waste decomposition;
- The precipitation of minerals such as magnesium hydroxide (or brucite) (formed by interactions between groundwater or other components of the repository and the NRVB), within the backfill porosity and the dissolution of calcium hydroxide and C-S-H minerals (although this may also block cracks).

The mechanisms of crack formation include plastic shrinkage cracking, plastic (differential) settlement cracking, and thermal cracking [34]. The former occurs when the water is evaporated from the surface more quickly than the rate of bleed water arrival. When there are different depths of backfill adjacent to each other at the top of a waste package, this produces a plastic settlement cracking. Also, when there

are changes in temperature this can create thermal expansion and contraction and, potentially, strain that could cause thermal cracking. These changes in temperature may be caused by the heat generated by the cement hydration reaction in the NRVB and by the radiogenic heat produced by radioactive decay of the radionuclides in the waste packages [34].

Backfill separation from the vault walls may be a consequence of the chemical and thermal shrinkage. This gap may provide a flow-path for the groundwater to bypass the waste, and reduce the likely transport of radionuclides out of the waste [34].

2.3.8: Buffering Capacity

To achieve chemical containment of long-lived radionuclides in the waste, NRVB has the capacity to buffer repository porewater at high alkalinity for a long period of time [19]. In the beginning, the main components of NRVB are expected to be portlandite; C-S-H gels; calcium carbonate; and hydrated calcium aluminates [1,19,22–24]. The initial porewater pH will be about 13.5, caused by the dissolution of the more soluble sodium and potassium hydroxides, present in the PC. After the dissolution of the alkali metal salts, buffering of the porewater will continue by the dissolution of portlandite. A solution saturated with respect to portlandite is formed with a pH of about 12.5 at 25 °C, equivalent to a hydroxyl molality of 0.03 mol kg⁻¹ water and a total calcium concentration of about 0.02 mol kg⁻¹ [19]. After the calcium hydroxide has been exhausted, pH buffering will occur by the incongruent dissolution of C-S-H phases with relatively high calcium/silicon molar ratios (Ca / Si) of ~1.5. From this, dissolution will result in the release of calcium and hydroxide ions, thus lowering the Ca/Si ratio and reducing the pH value at which the water is buffered [23,35].

The timescale and capacity for buffering by portlandite is dependent on the initial quantity of NRVB in a vault, the amount of the calcium hydroxide content of the NRVB that is consumed by reaction with wasteforms, and the rate of groundwater leaching [19].

Influence of groundwater on buffering capacity

High pH cementitious backfill materials are expected to strongly influence the chemistry of the near field. The evolution of the chemistry of these materials in a GDF is mainly dependent on the geochemistry and flow rate of the groundwater [7,36].

Groundwater is expected to react with NRVB and the intermediate level wastes it encapsulates, which contain magnesium, sulphur and aluminum, among other important elements. These interactions may result in the formation of some secondary minerals, such as calcite, brucite, ettringite, hydrogarnet,

CO₃-hydrotalcite and Al-monocarbonate [1,23]. Such secondary minerals could continue to buffer the porewater at pH values of pH 10 to pH 12 [23], and are expected to precipitate in the NRVB porosity and subsequently become mineralised or re-dissolved [19]. The main consequence of the precipitation of secondary phases is a potential reduction in the NRVB porosity in the region where groundwater flows into a vault. This is particularly the case for high carbonate-containing ground waters, due to the precipitation of calcite and other Mg/Ca bearing phases. The result is that subsequent inflow, and gas migration pathways, will be reduced [19]. It is important to emphasize that these precipitation reactions will depend on the composition and concentration of the groundwater solutes [36], which will depend on the specific location of the GDF (e.g. in a clay, granite or evaporite host rock).

Numerous modeling studies have been performed to understand the pH evolution on leaching NRVB [1]. Figure 2.4 describes one such study [1], which gives the four sequential stages of cement dissolution.

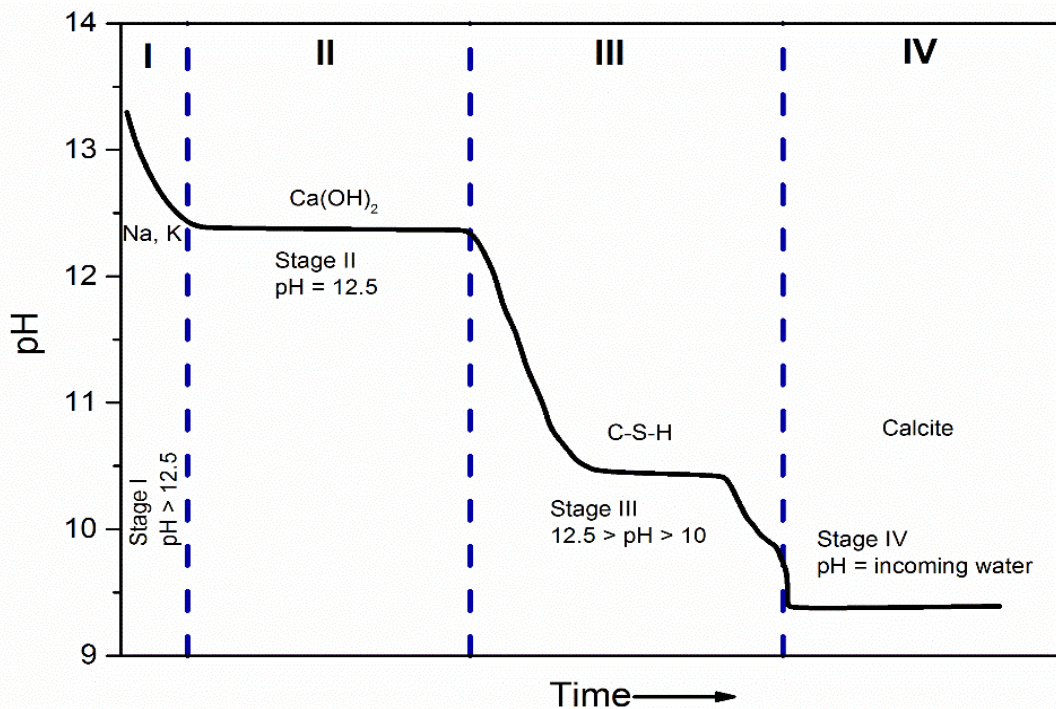


Figure 2.4. Schematic representation of the evolution of pH at 25 °C in cement pore fluid as a result of groundwater leaching (from [1]).

A series of accelerated leach testing experiments have been performed to demonstrate the ability of NRVB to buffer simulated groundwater [37]. In these experiments, it was possible to observe the removal of all calcium hydroxide, and consequent buffering controlled by the dissolution of the C-S-H gel, at a pH of about 11. During the test, the porosity was measured and an increase of about 20% was observed, but the sample remained intact. A surface coating of brucite (magnesium hydroxide) was formed at the region of inflow, which reduced the permeability coefficient by about an order of magnitude [19].

A long-term leaching study (run for up to two years) was carried out to provide data on the evolution of pH during extensive leaching of the NRVB [22]. Three different leachant compositions were used (deionized water, 0.1 M and 1 M NaCl solutions). In this study it was found that there is sufficient alkaline buffering capacity present to maintain the leachate above pH 10 for 1000 cumulative specimen volumes for all three leachants. It was also observed that the trend of reduction in pH from the pH 12.5 - 12.6 plateau was in the order of 1 M NaCl > 0.1 M NaCl > deionized water. This indicates that chloride will increase the rate of leaching of the calcium from within cementitious materials.

2.3.9: NRVB Carbonation

In GDF conditions, carbonation of the NRVB may occur at several stages: during backfilling at the end of the operational phase of a repository (NRVB could react with carbon dioxide in the air of the vaults); during the post-closure phase when the repository has re-saturated and alkaline degradation of organic material in the waste could produce carbon dioxide; and also during this last phase when carbon dioxide or carbonate species could be introduced in inflowing groundwater [19,34].

For cement carbonation to occur, carbon dioxide must be dissolved in water and react with high alkalinity components present in NRVB, i.e. products of cement hydration (for example, calcium hydroxide, calcium silicate hydrate and various calcium aluminate hydrate or ferro-aluminate hydrates). From this reaction, the products formed will be calcium carbonate, silica gel and hydrated aluminium and iron oxides, while sulphate will convert to gypsum after complete carbonation [27,31]. The main effects of the carbonation are: the reduction in the buffering capacity (i.e. in the pH) due to the consumption of calcium hydroxide, and alterations to the physical properties by decreasing the pore volume and permeability [27,38]. Because there is precipitation of the CaCO₃ in the pore structure, this will increase in volume and lead to structural changes, including changes to the density and porosity [27,31]. In Figure 2.5, VOI (Volume-of-Interest) images from samples of NRVB that are carbonated and non-carbonated are shown, with the respective differences in the fraction of pores. It can be observed that the carbonated samples presented a reduced porosity compared to the non-carbonated samples, associated with the precipitation of calcium carbonates [31].

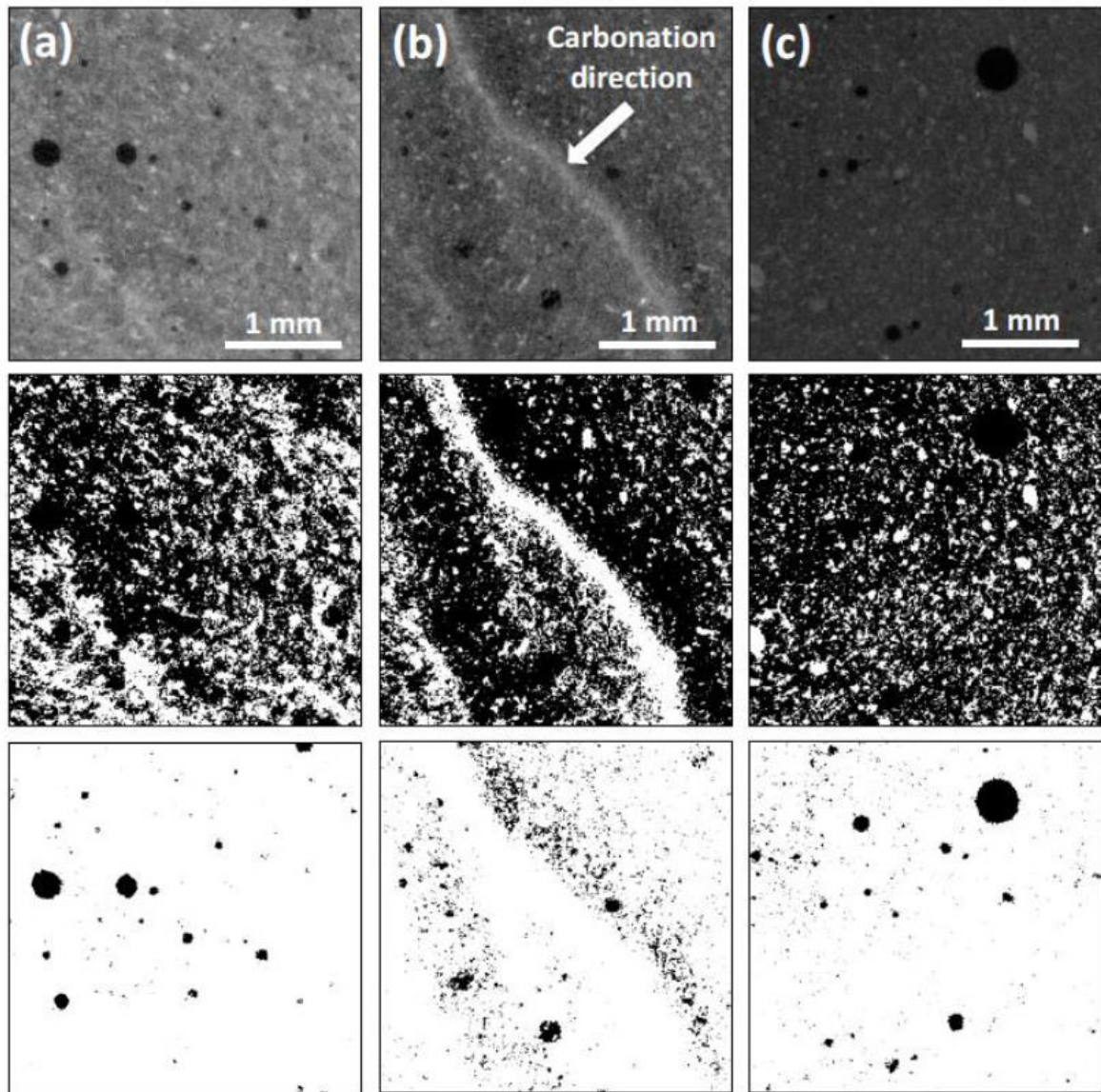


Figure 2.5. Selected VOI (a) carbonated sample, (b) partially carbonated sample, and (c) non-carbonated sample. Top image: grey scale image, centre image: segmented into solid (white) and pore (black) regions, and bottom image: segmented into large pores (black) (from [31]).

Some authors have observed that carbonation can also be associated with crack sealing, due to the precipitation of CaCO_3 [19]. It was also found that the gas permeability is reduced by half on carbonation, but it was concluded that this might not adversely affect the transport of gases and fluids through NRVB, however further work is needed to understand this [38]. One advantage of carbonation is that the $^{14}\text{CO}_2$ (g) generated will be absorbed by the calcium component of the cement, thereby preventing the release of $^{14}\text{CO}_2$ as a gas phase to the far field or the biosphere [27].

Because of the changes in the physical and chemical properties of the cementitious backfill, some studies have been carried out to understand the extent of carbonation in NRVB. The main conclusions were: NRVB retards the migration of any released CO_2 ; carbonation resulted in consumption of portlandite; and XRD results showed that the hydrated cement phases were completely replaced by

calcium carbonate within the main region of carbonation [27,31], as can be seen in Figure 2.6. When carbonation occurs, the peaks corresponding to calcium hydroxide are no longer visible and the intensity of the peaks corresponding to calcium carbonate increase [27].

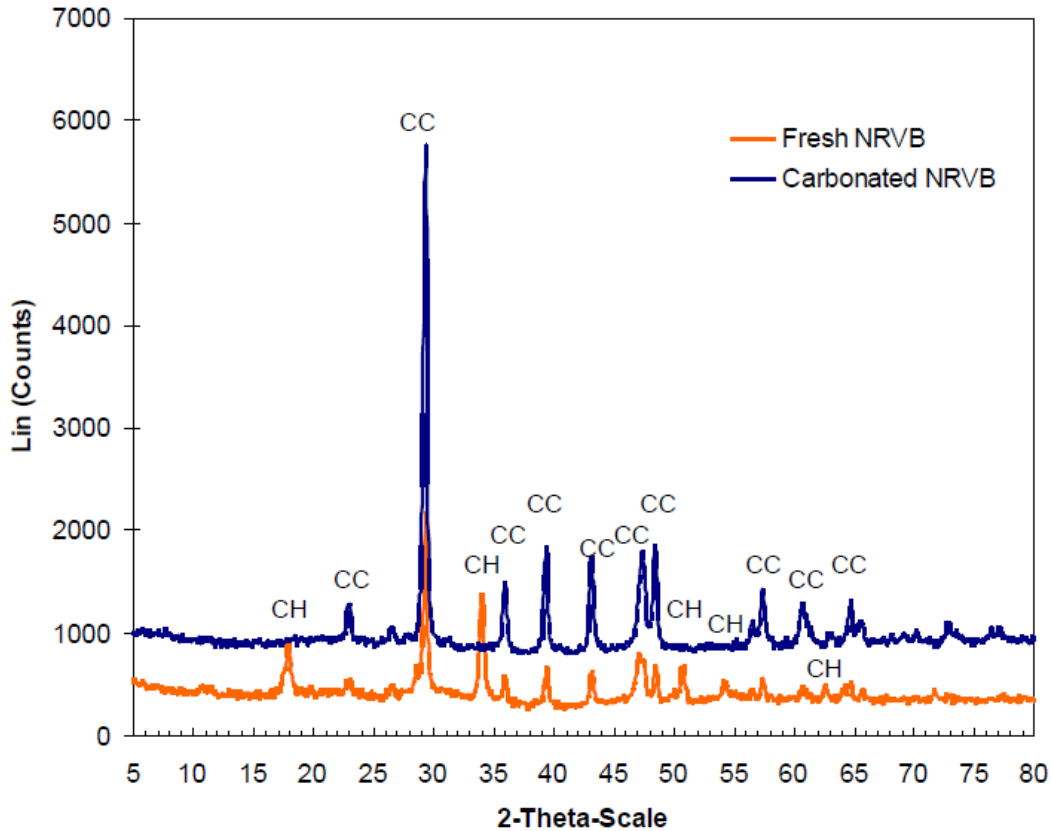


Figure 2.6. XRD diffractograms of fresh NRVB and carbonated NRVB; CC represents calcium carbonated, and CH represents calcium hydroxide (from [27]).

C-S-H can also be affected during carbonation. Morandea et al. [39] show that a decalcification of C-S-H occurs in the presence of CO_2 . This will consequently lead to a smaller molar volume and smaller Ca / Si ratio of C-S-H when compared to non-carbonated C-S-H. Moreover, C-S-H does not release physical water during carbonation, unlike portlandite. This will result in a highly hydrated silica gel [39].

2.4: Low-pH cement

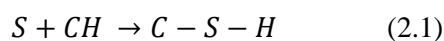
The use of Portland cement in a GDF concept provides a highly alkaline environment (pH above 12), which reduces the solubility of many radionuclides [7,9,40]. However, this characteristic can be problematic when other barriers are being considered in the GDF [41], and safety of the repository is determined by the stability of these barriers. Bentonite is an example of a material that has been

considered to use in repositories in many European countries (like Switzerland, France, Spain, etc) for the disposal of HLW, and its stability is influenced by the pore water pH [17]. It was previously observed that the alkaline environment provided by cementitious materials cause dissolution-precipitation reactions in bentonite, and consequently the loss of its swelling capacity (the main characteristic for the use of this sealing material in the GDF) [42–45]. It was also observed that these alterations are significantly reduced when the pH is below 11 [43]. Another consequence of using pure PC is the characteristic high temperature rise from the cement hydration [46], which have negative effects for the long-term durability of the material, by causing for example the formation of cracks in the materials [44,45]. Therefore, a potential solution is the formulation of a low-pH and low-heat cement, which would improve the compatibility of the different materials in the repository environment.

To formulate this low-pH cement, a set of criteria was defined [44,45]:

- Chemical compatibility with clay
 - Pore solution with low alkalinity (achieved through reduction of formation of portlandite)
 - pH ideally below 11
- Low heat of hydration (lower than PC, < 250 J/g)
- Easy supply
- Chemical resistance to geological environment (e.g. sulphate and chloride attack)

To achieve these characteristics, the high-percentage replacement of PC by SCMs is an attractive option. Supplementary cementitious materials are by-products or natural materials that can either show hydraulic or pozzolanic behavior. As a brief explanation, a hydraulic binder is a material that when in contact with water forms cementitious products, in a so-called hydration reaction. Some of these materials are considered to have a latent hydraulicity, meaning that their hydraulic activity is relatively low, when compared to PC, and needs a chemical or physical activation for the hydration to happen [47]. A pozzolan is a siliceous or a siliceous and aluminous material, which in the presence of moisture will react chemically with calcium hydroxide to form compounds that possess cementitious properties (like C-S-H) [47]. This process is also known as pozzolanic activity, i.e. is the degree of reaction between a pozzolan and Ca^{2+} or $\text{Ca}(\text{OH})_2$ in the presence of water [47–49]. Equation 2.1 shows the pozzolanic reaction using cement chemist’s notation ($\text{C}=\text{CaO}$; $\text{H}=\text{H}_2\text{O}$, $\text{S}=\text{SiO}_2$).



Three of the most common SCMs studied worldwide are fly ash, blast furnace slag and silica fume.

Blast furnace slag (BFS) is an example of a latent hydraulic material, being a by-product in the extraction of pig iron in blast furnaces. The chemical composition of BFS can vary significantly depending on the composition of the raw materials in the iron production process. When cooled

sufficiently, it rapidly forms a glassy material (almost fully noncrystalline) [50–52]. The main oxide constituents of BFS are CaO, SiO₂, Al₂O₃ and MgO [53]. It is very common, nowadays, to use BFS in combination with Portland cement. In systems with high replacement levels of BFS, it was possible to observe the absence of portlandite, the formation of C-S-H with low Ca/Si ratio, the presence of hydrotalcite-like phase and AFm phases (alumina, ferrite, monosulphate or monocarbonate) [49,50]. Due to the higher content of Al₂O₃ in the BFS than in PC, C-S-H shows the incorporation of more Al into its structure [54,55]. However, studies showed the very slow hydration of this material, for example residual BFS was found in cements with 20 years old [54]. Some benefits of using PC-BFS blends are the lower heat of hydration observed, lower porosity and higher strength [56].

Silica fume, also known as ‘microsilica’ or ‘condensed silica fume’, is a very fine amorphous powder resulting from the production of alloys of silicon or ferrosilicon [57–59]. It is considered a very good pozzolanic material, due to the high content of amorphous silica and very fine particle size distribution (average diameter of 0.15 μm) [56,59]. When silica fume is added to PC systems, consumption of portlandite is observed, a progressively more low Ca/Si ratio C-S-H is formed [49,60,61]. Furthermore, with C-S-H with low Ca/Si ratio and with Al incorporated, there is an increase of alkali uptake, which in turn leads to a reduction of the pH in the pore solution (due to the reduction of alkali concentration in solution) [44,45]. Some of the microstructural advantages of using silica fume are related to the high increase of the strength of the cement (including compressive strength), and chemical attack resistance (e.g. to sulphate and chloride), due to the decrease in permeability [57,59]. One of the consequences of using silica fume is the poor workability observed [62]. This happens due to the easy agglomeration and very high surface area of the particles, which leads to the need of more water to maintain the workability. To overcome this, the use of superplasticisers and/or ultrasonication is necessary [56,62].

Fly ash, also known as ‘coal fly ash’ or ‘pulverised fuel ash’, is a by-product from the combustion of coal and lignite [47]. The main composition of fly ash is SiO₂ and Al₂O₃, and the amount of CaO is often limited, but can vary depending on the origin of the fly ash [49]. As observed with silica fume, when fly ash is mixed with PC, a reduction of the amount of portlandite present is observed. This reduction, though, is less pronounced than for silica fume, due to the limited early reactivity of fly ash and the presence of CaO in the composition [49]. Benefits of using this PC blend can include an increase of the strength, reduced heat of hydration, reduced permeability, resistance to chemical attack (e.g. sulphate attack), and improved workability, mainly at later curing times [56].

To obtain a low-pH cement, one of the important factors to consider is the reduction of the presence of portlandite, since this phase is the main responsible for buffering the pore solution to a high pH (as observed in Section 2.3.7). Therefore, the use of pozzolanic materials with Portland cement is essential. A number of advantages can be found when using pozzolanic materials with Portland cement, like [44,45]: the conversion of portlandite (formed during PC hydration) into C-S-H; reduction of PC used,

which decreases the heat output during hydration; and the Ca/Si ratio of C-S-H is lower, which benefits the sorption of alkalis into C-S-H structure, reducing their availability in solution, and so reduction of the pH. The absence or low presence of portlandite means that the buffering capacity is mainly provided by the low Ca/Si ratio C-S-H, characteristic of this type of cements. The dissolution of this low Ca/Si ratio C-S-H will be preferentially through the leaching of SiO₂ [7,41].

Cau-Dit-Coumes and colleagues [44] presented a paper that discussed the design of a low-heat, low-pH and high strength cement to be used in a GDF. From that study, it was concluded that low-pH cements could be designed using either binary blends (e.g. PC with silica fume) or ternary blends (e.g. PC with silica fume and fly ash or BFS). Pore water pH was found to be below 11 for the formulations with higher silica content (Figure 2.7).

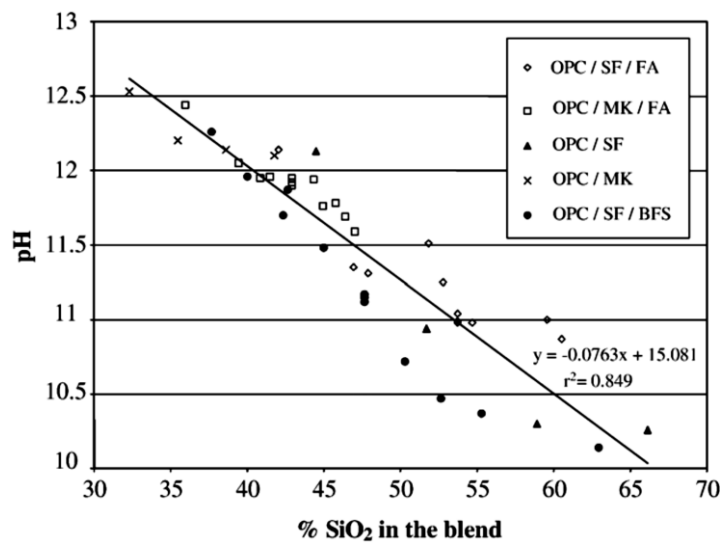


Figure 2.7. Correlation between solution pH and silica content in the binder (from [44]).

A study performed later by the same group [45], showed that all PC blends containing high replacement values of silica fume, fly ash and BFS had a reduced heat of hydration, refined porosity and pH values below 12.

2.4.1: Cebama Reference Cement Mix

Within the European Cebama research consortium, a low-pH cement was formulated as reference mix. This mix design will allow data comparison between various studies from the different groups that belong to the Cebama project.

The Cebama reference mix has a ternary binder composition with CEM I, silica fume and BFS (developed by VTT, Technical Research Centre of Finland). This composition was based on the ternary mix design of Posiva (Finnish Nuclear Waste Management Organisation), which has been previously

studied for nuclear waste repository deposition tunnel end plugs [63]. The aim was to have identical total binder content, CEM I content and Ca/Si ratio, but using BFS instead of fly ash, as agreed during a Cebama meeting. Since fly ash-based low-pH cements are more widely studied than BFS-based low-pH cements, the Cebama project saw an opportunity to increase the knowledge of the latter cements [64]. Also, BFS is considered to be a more homogeneous material and have longer availability than fly ash from the perspective of security of supply [64]. Table 2.3 shows the composition of both Posiva's and Cebama's low pH cement formulations.

Table 2.3. Composition of the ternary mix design from Posiva and the Cebama consortium.

Posiva mix composition		Cebama reference mix composition	
<i>Total binder content</i>	280 kg/m ³	<i>Total binder content</i>	280 kg/m ³
<i>CEM I</i>	105 kg/m ³	<i>CEM I</i>	105 kg/m ³
<i>Silica fume</i>	91 kg/m ³	<i>Silica fume</i>	110 kg/m ³
<i>Fly ash</i>	84 kg/m ³	<i>Blast furnace slag</i>	65 kg/m ³
<i>CaO/SiO₂ ratio</i>	0.61	<i>CaO/SiO₂ ratio</i>	0.61

Due to the high content of silica fume used in the Cebama reference mix, a superplasticiser was used. Pantarhit LK (FM) is the naphthalene-based superplasticiser chosen, since polycarboxylate-based superplasticisers are not allowed in Finland's nuclear waste repository [63,64].

Characterisation of Cebama reference cement paste is shown in Chapter 4.

2.5: Groundwater Interactions with Cement

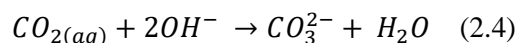
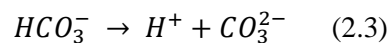
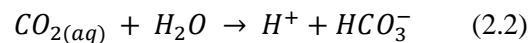
Cementitious materials are considered to be used in all current concepts for geological disposal, as described above. The presence of these materials is expected to strongly influence the chemistry of the near field environment, including groundwater [1,7]. The composition of the groundwater will depend on the geology where the GDF is constructed, which can be in a granitic, clay or saline environment. The interactions between the cementitious materials and the groundwater have significant effects on each other, leading to chemical conditioning of the groundwater due to the higher pH characteristic of the porewater of the cements (described in the previous sections), and to changes in the microstructure and mineralogy of the cement. The composition of both groundwater and cementitious materials is expected to evolve with the continuous flow of the groundwater, which may alter, for example, the rate of radionuclide release and the groundwater flow rates and paths, due to possible changes in the porosity and permeability of the host rock. The focus of this section is to review the understanding, so far, of how groundwater interactions affect the microstructure of cementitious materials in a geological disposal facility context.

In the literature, studies have been performed to understand how individual chemical components of groundwater can react with cementitious phases, as a way of trying to understand such complex interactions. Some of the major species that are present in the groundwater and have been studied are chloride, sulphate and carbon dioxide.

Interactions with chloride in solution usually result in reactions with aluminate phases to form an AFm phase called Friedel's salt ($\text{Ca}_4\text{Al}_2(\text{OH})_{12}\text{Cl}_2 \cdot 4\text{H}_2\text{O}$), which is stable at chloride concentrations between a few mmol/L to over 3 mol/L [65–67]. The formation of this phase can be through dissolution/precipitation and ion exchange [66]. The latter happens when the positive layer of monosulphate or monocarboaluminate, AFm phases, releases an OH^- ion and exchange with a free Cl^- . The other interaction that occurs is with C-S-H, where surface complexation and electrostatic interaction of ions happens with the surface of C-S-H [68].

Another common component in groundwaters is sulphate, which has a detrimental impact when interacting with cement phases. This type of interaction is called external sulphate attack and usually results in a physical expansion, often followed by cracking and spalling. When the alterations in the hydrate phases occur due to the action of sulphates present in the original mix, this is called internal sulphate attack [52]. Focusing on external sulphate attack, the penetration of sulphate ions in cementitious materials from sulphate-bearing solutions results in the formation of gypsum ($\text{CaSO}_4 \cdot 2\text{H}_2\text{O}$), ettringite ($\text{Ca}_6\text{Al}_2(\text{OH})_{12}(\text{SO}_4)_3 \cdot 26\text{H}_2\text{O}$) or thaumasite ($\text{Ca}_3[\text{Si}(\text{OH})_6 \cdot 12\text{H}_2\text{O}] \cdot (\text{CO}_3) \cdot \text{SO}_4$) [52]. Usually this attack occurs coupled with calcium leaching (decalcification). One of the consequences of the formation of gypsum and ettringite is the localised expansion that might occur, and ultimately cause cracking [66,69].

Carbonation can result when cementitious materials are in contact with groundwater; when gaseous carbon dioxide first interacts with cement pore water (or groundwater), it starts to dissolve as HCO_3^- and CO_3^{2-} (see Equations 2.2 and 2.3). Then CO_3^{2-} reacts with dissolved calcium to form (and precipitate) calcite. These reactions lead to a decrease of the pH in solution (Equation 2.4) [7,66].



As described in Section 2.3.8, the formation of calcite can result in a reduction of the porosity of the material, and consequently the formation of a protective layer at the surface. Thus, the formation of a calcite layer is desirable in bicarbonate-dominated waters [7].

Decalcification, which is defined as the dissolution of portlandite and C-S-H when exposed to water with lower Ca concentration than the cement system, can occur upon contact of cement with

groundwater. The leaching of calcium is a combination of dissolution and diffusion processes, and results in an increase of the porosity and permeability, and consequently loss of mechanical strength [66].

2.5.1: Leaching experiments

Leaching experiments have been performed to try to understand how groundwater interactions with cementitious materials considered for use in GDFs may affect their long-term performance. Section 2.3.7 showed several examples of those experiments performed specifically with NRVB.

Some studies have been conducted using demineralised water as an aggressive solution as a worst leaching case scenario. Faucon and colleagues [70] have studied the leaching behavior of two mineralogically distinct cement pastes: Portland cement and Portland cement (30 %) with BFS (70 %) when in contact with demineralised water. After 6 months of leaching, in an inert gas environment (N_2), they observed the formation of a degraded layer in both cements. This layer was composed of residual anhydrites, hydrogarnet, iron-substituted C-S-H, and hydrotalcite. They also observed that there was dissolution of portlandite, AFm and AFt phases, when compared to the non-degraded zone. A consequence of this dissolution was the observed concentration gradient between the surface (i.e. degraded zone) and the core of the sample (i.e. non-degraded zone). This led to the migration of magnesium and iron ions to the surface, and consequent formation of hydrotalcite, in the case of magnesium, and C-S-H with iron incorporated (iron replaces calcium).

Later, the same group [71] made a review of the physico-chemical mechanisms of demineralised water degradation of cement pastes used for nuclear waste disposal. A degraded and a non-degraded zone are observed, the former being characterised by decalcification of the cement, mainly via the dissolution of portlandite and calcium from C-S-H. This decalcification results in a decrease of the Ca/Si ratio from the intact part of the cement to the degraded zone. The incorporation of iron and aluminium in the C-S-H with lower Ca/Si ratio seems to enhance the stability of this phase in the degraded zone.

While formulating a low-pH cement, Codina et al [45] performed a 4 month leaching experiment where five different cement blends (binary or ternary mixes) (Table 2.4) were placed in contact with pure water, for calcium leaching tests.

Table 2.4. Composition of the different cement blends investigated in [45] (weight %).

	PC	CEM V	Silica fume	Fly ash	BFS
B	60 %	-	40 %	-	-
T1	37.5 %	-	32.5 %	30 %	-
T2	37.5 %	-	32.5 %	-	30 %
T3	20 %	-	32.5 %	-	47.5 %
Q	-	60 %	40%	-	-

Similar results were observed to the ones discussed above, where there is a clear degraded zone and a non-degraded zone in the core of the sample (Figure 2.8). In the degraded zone, decalcification of the cements pastes was observed, with a decrease of the Ca/Si ratio of the C-S-H. However, this decalcification zone was 4 times smaller when compared to Portland cement. The degradation depth ranged between 700 μm to 1 mm. They also observed, through XRD analyses, the disappearance of portlandite (for the samples that contained this phase in their initial mineralogy), disappearance of ettringite and formation of hydrotalcite-like phase for the samples that contained BFS.

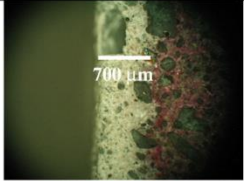
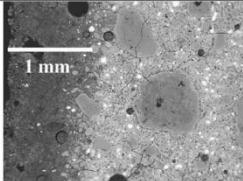
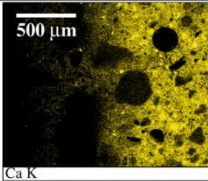
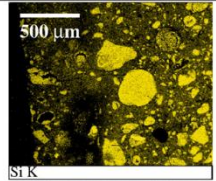
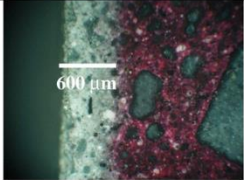
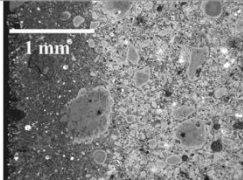
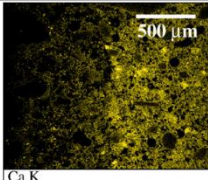
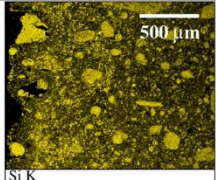
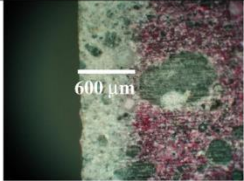
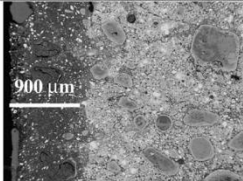
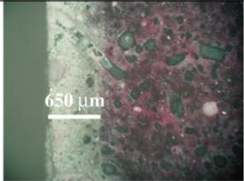
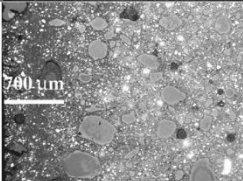
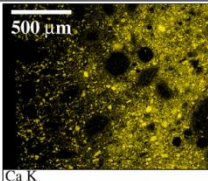
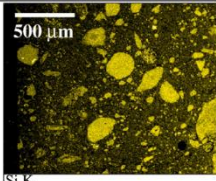
Blend	Optical microscopy observations	SEM observations (BSE)	SEM with X-ray microanalysis (Map of Ca)	SEM with X-ray microanalysis (Map of Si)
B				
T1				
T2				
T3				

Figure 2.8. Images from the samples (B, T1, T2 and T3) after 4 months of leaching with pure water, obtained by optical microscopy and SEM (from[45]).

In the same subject of formulating a low-pH cement, Calvo et al [42] discussed the results of a low-pH cement (60 % PC and 40 % silica fume) in contact with granitic groundwater. In this study, flow-through groundwater leaching was performed, for a duration between 14 months and 2 years. Also in this study, a degraded zone was observed (between 700 μm and 1600 μm). In this zone was observed decalcification of C-S-H, followed by the inclusion of Mg and also Cl^- in the C-S-H structure and other phases. This inclusion is believed to be due to a “charge defect” caused by the leaching of calcium, which is being compensated by the progressive inclusion of Mg, observed also in other studies (e.g. [72]). However, regarding Cl^- inclusion, the authors did not mention any conclusions. In this paper, the authors concluded that the low-pH cement had good resistance against granitic groundwater interactions.

However, a different result was obtained when a low-pH cement (37 % CEM I cement, 30 % fly ash and 33 % silica fume) and a conventional Portland cement sample were placed in contact with synthetic clayey solution [73]. In this study, an original experimental setup was used to reproduce the geological conditions observed in a Callovo-Oxfordian rock, using a specific CO_2 partial pressure. After 5 months of leaching, where the groundwater was replaced at specific intervals, both cements presented similar alteration mechanisms, but totally different intensities and extension of the degradation zone. Decalcification was observed for both cements, being stronger in the low-pH cement paste (> 1.5 mm) than in the CEM I cement paste (<100 μm). The authors of [73] proposed two parameters to explain these differences:

1. In low-pH cement, due to the absence of portlandite, the decalcification will occur directly in the C-S-H phase. Since the Ca/Si ratio of the C-S-H of the low-pH cement is originally lower than that of the CEM I (Ca/Si ratio of 1 for the former and 1.65 for the latter), and considering that a similar decalcification occurs for both cements, the amorphous silica stage is reached in the low-pH cement, which is associated with increase of the macroporosity (Figure 2.9).

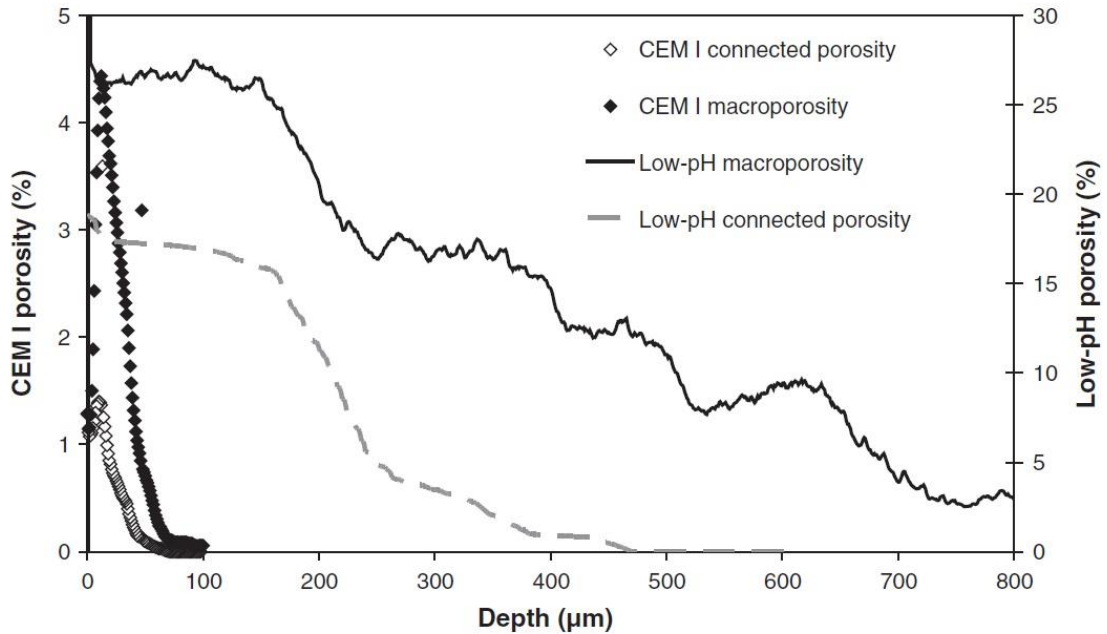


Figure 2.9. Porosity comparison between CEM I and low-pH cement pastes, after 1 month in contact with clayey solution (from [73]).

2. Due to carbonation, CEM I cement paste developed a carbonate crust in the surface, being a protective barrier to the exchange of soluble species with the groundwater. On the other hand, no crust was formed in the low-pH cement.

Sulphate and magnesium action are observed in CEM I cement paste, with the formation of ettringite in the macroporosity openings from the portlandite dissolution, and with magnesium precipitation in the carbonate crust in the degraded zone. For the low-pH cement, the authors [73] believed that the magnesium has incorporated in the C-S-H structure or formed M-S-H, but no proof was shown in the paper. This information led to the conclusion that the degradation of clay groundwater was higher for the low-pH cement than for the Portland cement sample [73].

Different modelling studies have been developed and performed to understand the long-term behaviour of cements when in contact with the groundwater under GDF conditions (some examples, [23,74–78]). Although modelling is important to comprehend what happens in a long time scale (most of the times difficult to replicate in a laboratory scale), more experiments are needed to obtain more precise and confident data that can support the modelling findings.

2.6: Concluding remarks

Geological disposal is the preferred option for the disposal of radioactive waste in many countries. Cementitious materials will be ubiquitous within such facilities, being used in a variety of applications,

including: waste encapsulation grouts; waste containers and overpacks; buffers and backfills; seals and fracture grouts; tunnel/vaults linings; etc. This Thesis considers two types of cement, used in two different scenarios:

(1) in one of the UK conceptual scenarios for the disposal of cementitious ILW it is proposed to use a high-pH backfill material, called NRVB, to encapsulate the waste packages. The benefits of using this material (e.g. capacity to buffer groundwater chemistry at a high pH, high porosity for gas migration etc.) may be detrimentally affected by the interaction of the material with groundwater;

(2) in the case of many European countries, to prevent issues associated with cement/bentonite clay interaction, a low-pH cement is considered for use as plugs and seals. These cements provide a pore solution with low alkalinity ($\text{pH} < 11$) which does not degrade clay. However, it is not well-understood how interaction with groundwater will influence the properties of such cements; as such, the European research consortium, Cebama, are investigating low pH cement-clay-water interactions.

Such interactions, between the cementitious materials used in the geological disposal and groundwater, are expected to occur during the long period of time which the GDF is expected to last. Leaching studies have been performed to understand how these interactions may affect the physical and chemical structure of the cementitious materials. Most of the studies described previously used aggressive solutions (e.g. deionised water, NaCl solutions, etc) as accelerated leaching tests. A few studies were described where groundwater was used, however the number of these studies performed in a geological disposal context is very limited. Moreover, most of the studies carried out were based on geochemical/transport models.

The research presented in this Thesis aims to improve and further develop understanding of the long-term performance of relevant cementitious materials in a geological disposal facility context.

Chapter 3: Experimental Methods

3.1: Materials and solutions

3.1.1: Nirex Reference Vault Backfill (NRVB) cement

Batches of Nirex Reference Vault Backfill (NRVB) cement paste were prepared according to the formulation presented in Table 3.1, with a water/solid ratio (where solid includes all the powder materials used) of 0.55. In Chapter 4, a comparison between NRVB formulated using laboratory (pure) materials and using industrial materials (used, for example, by the National Nuclear Laboratory in their studies of NRVB [22]) is performed. It is possible to find in the literature data pertaining to NRVB prepared with both types of precursor (e.g. [22,79]). To verify the consistency between the cement formed using these two types of starting materials, two different batches of NRVB were studied. For the NRVB formulated using laboratory chemicals, denoted NRVB (Lab), the starting materials were: CEM I 52.5 N sourced from Hanson Cement Ltd, Ribblesdale works (i.e. Sellafield specification; BS EN 197-1:2011); $\text{Ca}(\text{OH})_2$ ($\geq 95.0\%$) and CaCO_3 ($\geq 99.0\%$) were sourced from Sigma-Aldrich. In the case of NRVB formulated using industrial materials, denoted NRVB (Ind), the following products were used: CEM I 52.5 N (as above); hydrated lime sourced from Tarmac Cement & Lime (Tunstead Quarry, Buxton, UK); and limestone flour sourced from National Nuclear Laboratory (Tendley Quarry, Cumbria, UK; BS EN 13043:2002). Characterisation of the different raw materials is shown in Chapter 4.

NRVB formulated with laboratory materials was used in Chapter 5 and NRVB formulated with industrial materials was used in Chapter 6 for the experiment with contact with different groundwater compositions.

Table 3.1. NRVB formulation [19,80].

Material	Content (kg m^{-3})
CEM I 52.5 N	450
$\text{Ca}(\text{OH})_2$ / Hydrated lime	170
CaCO_3 / Limestone flour	495
Water	615

Cement batches were mixed using a Kenwood mixer for 5 minutes. Subsequently, the cement pastes were placed in centrifuge tubes and cured at 20 °C (for Chapter 4 and 5) and at 40 °C (for Chapter 4 and 6) and 95 % relative humidity, for specific time points (from 1 day to 2 years). For the samples where hydration was stopped for characterisation purposes, cement monoliths were placed in acetone for 3 days, and then vacuum dried to allow all the acetone to evaporate.

3.1.2: *Cebama Reference Cement*

Batches of Cebama reference cement paste were prepared using the formulation shown in Table 3.2, with a water/solid ratio (w/s) of 0.25. All materials were provided by VTT (Technical Research Centre of Finland). The cement paste was mixed by first adding the silica fume with 15% of the CEM I and BFS to the mixing bowl and slowly adding the water and superplasticiser, and hand mixing for 3 minutes. A high shear mixer was used until the paste turned to a liquid and the remainder of the CEM I was added and shear mixed. The cement paste was placed in centrifuge tubes and cured at 20 °C (for Chapter 4 and 5) and at 40 °C (for Chapter 4 and 6) and 95 % relative humidity, for specific time points (from 1 day to 1.5 years). For the samples where hydration was stopped for characterisation purposes, acetone was used to stop the hydration.

Table 3.2. Cebama reference cement paste formulation [64].

Material	Content (kg m⁻³)
CEM I 42.5 MH/SR/LA	1050
Silica fume	1100
BFS	650
Plasticizer pantarhit LK (FM)	12.6

3.1.3: *Synthetic Groundwater Compositions*

For the experiments where cement samples were placed in contact with groundwater, three different groundwater compositions were used, representative of the different generic geological environments (granitic, saline and clay groundwater) considered for geological disposal of radioactive waste. The granitic groundwater used was that developed in [81], which simulates groundwater in granitic terrain (Allard water). The composition represents groundwater between 100-500 m in Swedish bedrock [82].

The saline groundwater was also developed in [81] and simulates deep saline groundwater (NASK water). The composition represents groundwater found at 500 m depth below Äspö, the likely site for the Swedish geological disposal facility [82]. Finally, the composition of the clay groundwater utilised is detailed in [83], and simulates groundwater in the Callovo-Oxfordian formation. This composition represents groundwater between 460-505 m in the Meuse/Haute-Marne underground rock laboratory in France. It is important to note that, although it is known that clay groundwater contains carbonates [73,84], the use of this particular composition *without* bicarbonate added was a decision from the UK Radioactive Waste Management organisation (RWM), a funding body in this project, to see possible effects that the absence of carbonates might have in the groundwater interaction with the cementitious materials.

The composition of the different groundwaters is detailed in Table 3.3 and 3.4. The different chemicals were weighed and dissolved in 2 L of distilled water and stirred. Then the groundwaters were transferred to the anaerobic chamber to equilibrate for 1 week prior to use. Due to the long-duration of the experiments (up to 18 months), the total volume of groundwater needed would be around tens of litres. Therefore, it was necessary to prepare new solutions at each time point of replacement (mentioned below). Consequently, each solution was not always exactly the same due to minor errors in weighing chemicals. Nevertheless, these minor discrepancies were accounted in the analysis of the results obtained, as it will be shown in Chapters 6 and 7. Table 3.5 shows the measured composition of each groundwater determined by ICP-OES. The minor amounts observed of Al and Si are due to impurities in some of the chemicals used. The chemicals used were: CaCl₂ (99+ %, Acros); KCl, MgCl₂, NaHCO₃ (≥ 98 %, Sigma); NaCl (≥ 99 %, VWR); and Na₂SO₄ (99 %, Alfa Aesar).

The pH obtained for each of the solutions was: 8.5, 8.2 and 7.5 for granitic, saline and clay groundwater, respectively.

Table 3.3. Composition of synthetic groundwaters, with components listed in amount (mg) required to make 1 L of solution

Chemicals	Granitic Groundwater (mg)	Saline Groundwater (mg)	Clay Groundwater (mg)
KCl	7.45	156.45	81.95
CaCl₂	55.49	2208.50	832.35
MgCl₂.6H₂O	40.66	81.32	1158.81
NaCl	35.06	7597.2	1461.00
Na₂SO₄	14.20	568.16	2130.6
NaHCO₃	168.00	168.00	-

Table 3.4. Elemental composition of synthetic groundwaters, with components listed in millimoles per 1 L of solution.

Chemical Element	Granitic Groundwater (mmol)	Saline Groundwater (mmol)	Clay Groundwater (mmol)
K	0.1	2.1	1.1
Ca	0.5	19.9	7.5
Mg	0.2	0.4	5.7
Na	2.8	140	55
SO₄	0.1	4	15
Cl	2.1	172.7	52.5
HCO₃	2	2	-

Table 3.5. Synthetic groundwater composition, as analysed by ICP-OES and IC in mg/L. Errors are the standard deviation of triplicate measurements.

Element	Granitic Groundwater (mg/L)	Saline Groundwater (mg/L)	Clay Groundwater (mg/L)
Ca	22.07 ± 0.04	764.8 ± 9.62	307.5 ± 6.6
Mg	5.09 ± 0.34	11.55 ± 0.28	143.4 ± 0.8
S	2.90 ± 0.46	130.4 ± 2.4	511.8 ± 10.5
Na	64.15 ± 0.99	3018.5 ± 64.3	1215 ± 12.0
K	5.80 ± 0.47	85.09 ± 0.45	42.73 ± 1.06
Si	0.59 ± 0.53	0.66 ± 0.28	0.35 ± 0.29
Al	0.78 ± 0.12	1.73 ± 0.27	1.07 ± 0.06
Cl	73.19 ± 0.41	7023.71 ± 2.64	1818.15 ± 3.45

3.2: Cement – Groundwater Contact Methodology

To understand the mineralogy and microstructure evolution of the cementitious materials being studied in this project when in contact with three different types of groundwater, two types of long-duration experiments were performed: semi-dynamic and static. The set-up of these experiments was agreed between University of Sheffield and two collaborator groups from the EU project Cebama consortium (Amphos 21 and Forschungszentrum Juelich), who performed transport modelling experiments in parallel to this Thesis, using the results obtained (presented in [85]) (results not shown as it is not in the scope of this Thesis).

For the contact experiments, cylindrical monoliths of 15 mm height x 15 mm diameter were prepared (Figure 3.1a). To allow only radial diffusion of the groundwater, the end of the cylinders was sealed with epoxy resin. Both experiments were carried out in an inert environment (inside of a stainless steel

“bean tin”, CO₂-free; Figure 3.1b) at 40 °C, which is considered to be the maximum temperature 50 years after backfilling the GDF [1], for a given time period. Post-experiment characterisation included: analysis of the solutions for pH and elemental concentration through Inductively Coupled Plasma-Optical Emission Spectroscopy (ICP-OES) and Ion Chromatography (IC); and analysis of the cements through X-ray Diffraction (XRD), Thermogravimetric analysis-Mass Spectroscopy (TGA-MS), Scanning Electron Microscopy coupled with Energy Dispersive Spectroscopy (SEM-EDX), Solid-State Nuclear Magnetic Resonance (NMR) Spectroscopy, Mercury Intrusion Porosimetry, Nitrogen Sorption and X-ray Computed Tomography (XCT).

3.2.1: Semi-dynamic cement-groundwater contact experiment

A semi-dynamic experiment was performed to allow investigation of the mineralogical alterations of the cements when in contact with the different groundwater compositions in a relatively aggressive environment, where replacement of the entire volume of groundwater was performed every 2 months.

Monolith samples were placed in 60 mL Teflon vessels (placed in Teflon baskets to allow contact of the solution with the whole monolith) in contact with 50 mL (solid/liquid ratio of 10 m⁻¹) of each of the three groundwater compositions (Table 3.3). Duplicates of samples and blanks were used. Sampling and replacement of the groundwater was performed every 2 months for a total time of 18 months for NRVB and 12 months for the Cebama reference cement (this shorter experiment was due to the late arrival of Cebama precursor materials from VTT). At each sampling time point, duplicate vessels were sacrificed, with aliquots of solution taken for analysis (pH, ICP-OES and IC), and the monoliths were placed in contact with acetone to stop the hydration, for post-characterisation. For the vessels that were not sacrificed, complete replacement of the groundwater was performed (to simulate fast groundwater flow in a GDF). The sampling and replacement of the groundwater was performed in a controlled environment (CO_{2(g)} and O_{2(g)}-free). Cement control samples were cured (without groundwater, at 40 °C) alongside this experiment, and were sampled (and hydration stopped) at the same time points for comparison.



Figure 3.1. (a) Cylindrical monolith placed inside a 60 mL Teflon vessels; (b) Stainless steel “bean tin” being purged continuously with nitrogen gas.

3.2.2: Static cement-groundwater contact experiment

The second long-duration experiment performed was static, where two monoliths (NRVB and Cebama reference cement) were placed in individual 2 L Teflon vessels, also using Teflon baskets, in contact with 2 L (s/l ratio of 0.7 m^{-1}) of each of the groundwater compositions. Sampling was performed every month (for 18 months), where aliquots of solutions (4 mL) were removed for analysis (pH, ICP-OES and IC). This volume was not replaced, in an attempt to replicate extremely low (or no) groundwater flow in a GDF. At the end of the experiment, the volume of solution removed for analysis did not exceed 10 % of the total volume. The cement monoliths were studied at the end of the experiment, being placed in contact with acetone to stop the hydration for post-characterisation.

3.2.3: pH measurements

At each time point of sampling, the pH of the solutions was measured at room temperature ($\sim 25 \text{ }^\circ\text{C}$) inside the anaerobic chamber. Calibration of the pH probe was performed before using to pH 4, 7 and 10. It is important to note that these values were not corrected to the high ionic strength of the leachates, and so the pH measurements presented in this Thesis are indicative rather than absolute [86]. As pH is non-linear, the pH values are presented as a range taking into account the measurements performed.

3.3: Analytical Methods

3.3.1: Particle Size Distribution

The particle size distribution of the raw materials used in the different cement formulations may influence a number of cement properties, such as reactivity, strength development, heat release, porosity and microstructure [87,88]. The dry dispersed state method was used for the analysis of the particle size of the raw materials used in this project. The advantage of using dry dispersion is the possibility of measuring the particle size in the same state as that in which the material is processed, without the need of using a dispersant. With this method, the samples were dispersed using a venturi controlled by compressed air.

In the case of, for example, silica fume, it was necessary to use a liquid dispersion method, to avoid agglomeration of the particles. Therefore, isopropanol ($\geq 99.8\%$, Sigma) was the dispersant chosen in this project, as it does not react with the material.

Experimental Particle size analysis used in this Thesis:

Chapter 4: Particle size distribution measurements were carried out using Mastersizer 3000 PSA, and the results were analysed using Malvern Instruments software. The refractive index used for calcium carbonate and limestone flour was 1.57; for calcium hydroxide and hydrated lime was 1.53; for Portland cement was 1.3; for silica fume was 1.54; and for BFS was 1.63. The absorption index was the same for any material, 0.1, and the weighted residual was less than 1 for each sample analysed.

3.3.2: Isothermal Calorimetry

To study the hydration reaction of cementitious materials, isothermal calorimetry analysis is generally used. The principle of this technique is to study the heat of hydration of cement over a long period of time, by recording chemical reactions undergoing either exothermic or endothermic events. In the case of hydration of cements, different exothermic reactions occur, which can be correlated to the formation of different hydrate phases [89,90].

With this method, a cement paste sample is placed in an ampoule inside of the calorimeter, where a heat flow sensor is connected to a heat sink, keeping the chamber at a constant temperature. The heat produced from the sample is measured, and it is compared to a reference sample (usually water), so any external heat can be subtracted [90,91].

Experimental isothermal calorimetry parameters used in this Thesis:

Chapter 4 and 5: Isothermal calorimetry was performed on cement paste samples using a TA Instruments TAM Air calorimeter, at both 20 °C and 40 °C. In the case of the samples that were analysed at 40 °C, prior to mixing, the raw materials and water were kept at this temperature. The materials were then mixed externally (for similar times used in the original mix described in Section 3.1), and 20 g of sample was placed in a plastic ampoule and then into the calorimeter for 7 days. Water was used as a reference calculated to match the total water content of each of the formulations.

3.3.3: X-Ray Diffraction (XRD)

X-ray diffraction (XRD) is an analytical technique used for the identification of crystalline phases present in a sample [90]. X-rays (or monochromatic X-rays) are generated when an electron beam hits a metal target (anode), e.g. Cu. This incident electron beam will excite an inner shell electron, which will induce the movement of an electron from higher atomic shell to fill this inner shell. The energy difference produced by this movement will emit characteristic X-rays (Figure 3.2).

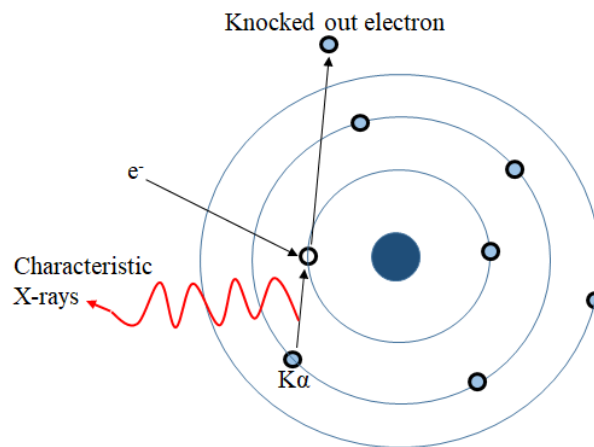


Figure 3.2. Generation of characteristic X-rays.

These X-rays can interact with a sample, which will result in incident X-rays being scattered by the atoms present in the lattice planes (described by Miller indices, hkl), which will then diffract either constructively or destructively, according to Bragg's Law (Equation 3.1) [92]:

$$n\lambda = 2d \sin \theta \quad (3.1)$$

where λ represents the X-rays wavelength, θ is the angle of incidence and d the spacing between two planes (Figure 3.3). From this interference, a characteristic diffraction intensity is produced, allowing the identification of the phases. In the present work, each of the phases were identified by comparing the peaks in a XRD pattern to a database containing peak patterns of known phases. The Inorganic Crystal Structure Database (ICSD) and the Powder Diffraction File (PDF) were used to perform phase identification.

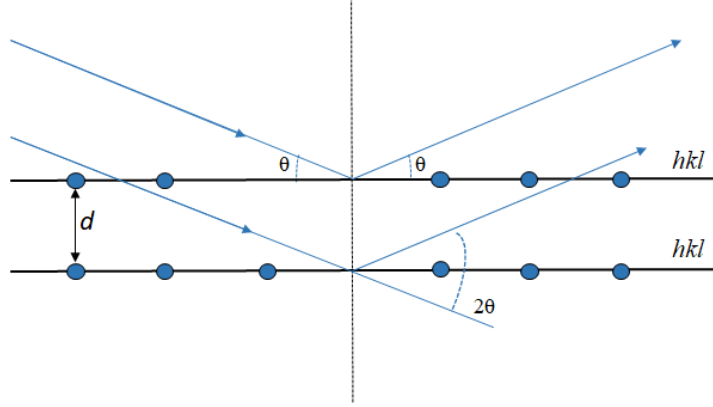


Figure 3.3. Derivation of Bragg's Law, $n\lambda = 2d \sin\theta$

Rietveld Refinement

To quantify the crystalline phases present in the cement samples, Rietveld refinement was performed. In the Rietveld method, minimisation of the difference between the measured and calculated patterns is achieved by using a non-linear least square approach [93]. The peak intensities are calculated using the following Equation 3.2:

$$I^{Calc} = s \sum_i L_k |F_k|^2 \varphi(2\theta_i - \theta_k) P_k A + B_i, \quad (3.2)$$

where I^{Calc} is the calculated intensity at a given data point, s is the scale factor, L_k is the Lorentz-polarisation factor, F_k is the structure factor, φ is the reflection profile function, θ is the Bragg angle, P_k is the preferred orientation, A is the absorption factor, B_i is the background intensity and k is the miller indices of a specific Bragg reflection [90,93]. The non-linear least squares method is performed using the following algorithm (Equation 3.3):

$$M = \sum_i W_i (I_i^{exp} - I_i^{calc})^2, \text{ where } W_i = I_i^{exp \frac{1}{2}} \quad (3.3)$$

where I_i^{exp} is the experimentally determined intensity for a given data point [93]. This will allow the refinement of lattice parameters, crystalline strain, atomic coordinates, experimental factors and grain size [93].

In the present work, only *relative* proportions of weight fractions were obtained since it is not possible to quantify the amorphous fraction using this method with the available data. Alternatively, the amorphous content was studied using Nuclear Magnetic Resonance (NMR) (Section 3.3.7).

Table 3.6. Sources of structural information for different cement phases identified in this Thesis.

Phase	Notation/ Crystal System	PDF codes	Reference
Alite (Ca ₃ SiO ₅)	Triclinic/T1	01-070-1846	[94]
Belite (Ca ₂ SiO ₅)	Monoclinic/β	01-086-0398	[95]
Tricalcium aluminate (Ca ₃ Al ₂ O ₆)	Cubic	01-070-0839	[96]
Ferrite (Ca ₂ AlFeO ₅)	Orthorhombic	01-071-0667	[97]
Gypsum (CaSO ₄ ·2H ₂ O)	Monoclinic	33-0311	[98]
Calcite (CaCO ₃)	Rhombohedral	01-086-0174	[99]
Portlandite (Ca(OH) ₂)	Rhombohedral	01-072-0156	[98]
Ettringite (Ca ₆ Al ₂ (OH) ₁₂ (SO ₄) ₃ ·26H ₂ O)	Rhombohedral	00-041-1451	[100]
Hemicarboaluminate (Ca ₄ Al ₂ (OH) ₁₂ (CO ₃) _{0.5} ·5.5H ₂ O)	Rhombohedral	00-041-0221	[101]
Monocarboaluminate (Ca ₄ Al ₂ (OH) ₁₂ (CO ₃) ₃ ·5H ₂ O)	Triclinic	01-087-0493	[102]
Hydrotalcite-like phase (meixnerite) (Mg ₄ Al ₂ (OH) ₁₄ ·3H ₂ O)	Rhombohedral	00-014-0191	[103]

Experimental XRD parameters used in this Thesis:

Chapter 4: For XRD analysis, samples were crushed to a powder and sieved to a size fraction of < 63 μm. A Bruker D2 Phaser diffractometer utilising a Cu Kα source and Ni filter was used and measurements were taken from 5° to 70° 2θ with a step size of 0.02° and 2 s counting time per step.

Chapter 5: See Section 3.3.4 (Synchrotron X-ray Diffraction)

Chapter 6 and 7: XRD analysis was performed on powder (< 63 μm, prepared as described above) using a PANalytical X'Pert3 Powder diffractometer utilising a Cu Kα source. Measurements were taken from

5° to 70° 2θ with a step size of 0.02° and 2 s counting time per step. Rietveld analysis was performed only for the NRVB samples, using Bruker AXS Topas 4.2 software [104], and the crystal structure information used for each phase is identified in Table 3.6. Errors associated with this quantification were obtained through Rietveld refinement software, Topas.

3.3.4: Synchrotron X-Ray Diffraction

With the same principle of the powder XRD, synchrotron X-ray diffraction provides high resolution diffraction patterns by using synchrotron radiation. In a synchrotron facility, electrons are generated and accelerated into the storage ring by the linear accelerator and the booster synchrotron [105]. When the path of the electrons in the large storage ring is changed, the electrons will emit energy, which will be directed into the beamlines. The alternating magnetic fields present in the straight sections (in the storage ring) will allow the electrons to oscillate producing more synchrotron radiation [105].

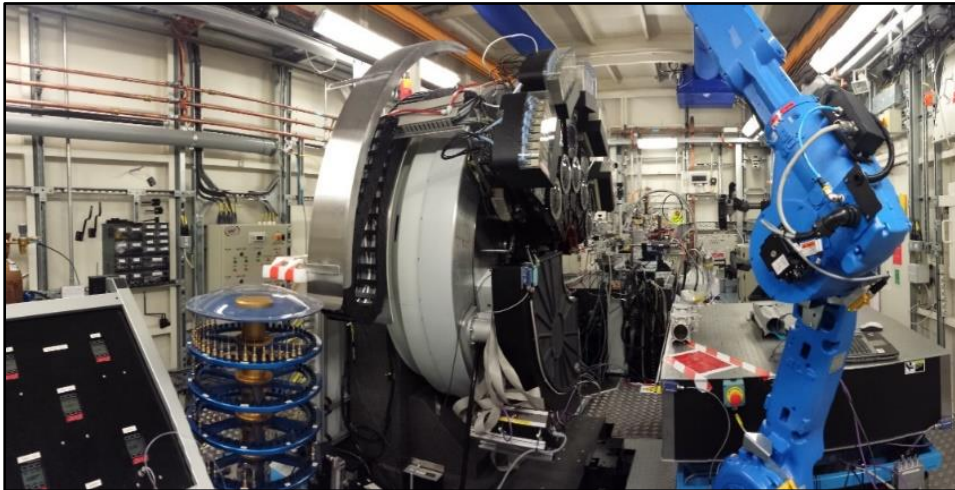


Figure 3.4. Beamline I11 from Diamond Light Source, showing the Mythen Position Sensitive Detector (PSD) (bottom part of the circle) and samples (left side).

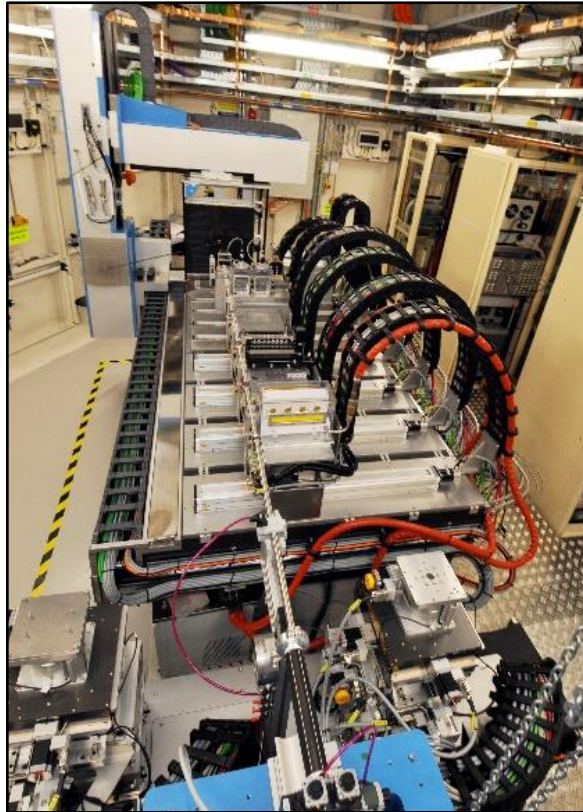


Figure 3.5. Beamline I11 from Diamond Light Source, showing the Long-duration experiment set-up (LDE). X-ray beam at the bottom, detector at the top, and samples in the middle.

Experimental synchrotron XRD parameters used in this Thesis:

Chapter 5: This experiment was initiated in October 2014 by Dr. Claire Corkhill, Prof. Neil Hyatt, Dr. Laura Gardner and James Vigor, at beamline I11 of Diamond Light Source. Technical descriptions of the beamline are given by Thompson et al [106,107] and Murray et al [108]. This experiment was divided in two parts: (I) frequent scans were taken to study the beginning of the hydration reaction (only studied with NRVB for 44 hours); (II) a long-duration experiment was performed where scans were taken at specific time points, to understand the evolution of the hydrate phases at later curing times (performed with NRVB for 4 years, and Cebama reference cement for 1.5 years).

Table 3.7. Synchrotron XRD scan times for the NRVB formulation.

NRVB (scan times)	
<i>First 44 hours</i>	First scan – 4 min after mixing
	Every 10 min until 30 min
	Every hour until 44 h
<i>3 days to 4 years</i>	3 days until 1 year – once/week
	Except between 17 days and 59 days
	1 year until 3 years – once/month
	Last scan taken at 4 years

Table 3.8. Synchrotron XRD scan times for the Cebama reference cement formulation.

Cebama (scan times)	
<i>90 min to 1.5 years</i>	First scan – 90 min after mixing
	Every week until 7 months
	Every month until 1 year
	Last scan taken at 1.5 years

The first part of the experiment was performed using an array of Mythen position sensitive detectors (PSD, Figure 3.4) with a 90° aperture for very rapid acquisition (subseconds/pattern), which allows sufficient temporal resolution to observe the first few hours of the hydration reaction [106,107]. A monochromatic beam with a wavelength of 0.82570(1) Å was used for the experiment. NRVB samples were mixed with the same procedure as described in Section 3.1, and transferred into a Kapton tube using an electric toothbrush. Then, the filled Kapton tube was placed inside a 0.7 mm glass capillary, which was sealed at the end with superglue (to mitigate against carbonation of the cement) and transferred immediately into the experimental hutch. The time taken between cement mixing and the first scan was approximately 8 minutes. A PSD detector was used to scan the samples, with an angular range between 2° and 92° 2θ with a step size of 0.004° 2θ. Each scan took approximately 15 seconds. The duration of this part of the experiment was 44 hours (Table 3.7).



Figure 3.6. Long-duration experiment (LDE) sample stage set-up. Numbers indicate the different cement samples being analysed.

The second part of the experiment was performed to study the long-duration evolution of the hydrate phases present in the NRVB and in the Cebama reference cement. For NRVB, the samples from the previous experiment (PSD detector) were transferred to beamline I11 LDE (Long-duration experiment, Figure 3.5) 3 days after mixing, and the experiment was carried out for 4 years (Table 3.6). In the case of Cebama reference cement, the sample was mixed using the same procedure described in Section 3.1.2 and transferred to a Kapton tube, and then to the 0.7 mm glass capillary, which was sealed with superglue (Figure 3.6). The scans were taken at specific intervals (Table 3.8) until 1.5 years. A monochromatic beam with varying wavelength (0.41 - 0.62 Å) was used. The LDE detector was used to scan the samples, and a CeO₂ standard, with an angular range between 2° and 36° 2θ with a varying step size ≤ 0.05°. Each scan took several minutes.

Because it was decided not to add an internal standard to the cement samples (since this could interfere with the hydration reaction by dissolving or providing nucleation sites for hydration products to form [90]), Rietveld analysis was performed only for the NRVB sample since this was highly crystalline and contained only one amorphous phase. In contrast, since the Cebama cement contained at least three different amorphous phases, it was not possible to quantify the amount of crystalline phases present without an internal standard or a more complex analysis process (partial or no known crystal structure – PONKCS [109]). Ongoing collaboration with the BRGM (France) is currently underway in support of phase quantification.

Rietveld analysis was performed using Bruker AXS Topas 4.2 software [104] in conjunction with J-Edit, and the crystal structure information used for each phase is identified in Table 3.5. Batch analysis was performed, where results from the previous scan determined the initial values and constraints applied in the next scan. The lattice parameters were constrained to refine within 2.5 % of their

published value. Errors associated with this quantification (in weight %) were obtained through Rietveld refinement software, Topas. For any further processing of the data, i.e. conversion to mol% to allow comparison with NMR data, the errors were calculated through propagation using standard formulae.

3.3.5: Thermogravimetric Analysis – Mass Spectrometry (TG-MS)

Thermogravimetric analysis (TGA) is an analytical technique used to identify hydrate phases present in cementitious materials through the mass loss of a sample when heated to controlled temperatures under controlled atmosphere (usually N₂). Differential thermogravimetric analysis (DTG) corresponds to the derivative of the TGA data, which allows the extraction of extra information from the TGA and so distinguish the thermal events that might overlap [90,110]. Mass spectrometry (MS) was coupled to analyse the evolved gases from the TGA instrument. This consists in the gas particles present in the furnace being ionised, which results in charged particles. The MS will then separate and measure the mass of each ion. Through the charge to mass ratio, where the charge is usually 1, it is possible to identify each species [90]. The identification of these gases will then help with the final identification of the cement phases.

The use of TG-MS is usually as a complementary technique to other analysis, like XRD, since it allows the identification of amorphous phases.

Experimental TGA-MS parameters used in this Thesis:

Chapters 4, 6 and 7: A PerkinElmer Pyris 1 thermogravimetric analyser was utilised. Approximately 40 mg of cement powder was used. The temperature ranged from room temperature to 1000 °C with a heating rate of 10 °C/minute under N₂ (nitrogen) atmosphere. Derivatives of TG (DTG) curves were calculated. A Hiden Analytical mass spectrometer (HPR-20 GIC EGA) was used to record the mass spectrometer signals for H₂O and CO₂.

3.3.6: Scanning Electron Microscopy (SEM) and Energy Dispersive Spectroscopy (EDX)

Scanning electron microscopy (SEM) has been widely used to study the microstructure and composition of polished surfaces of cement samples [90,111]. This technique consists of an electron source that emits a collimated beam of electrons, which are accelerated to pass a set of lenses to condense the stream of monochromatic electron to focus the beam to a small point. Subsequently, the electron beam passes through a series of coils directing the beam to the surface of the sample [111]. When in contact with the sample, a number of interactions between electrons and the material occur. From this interaction can result two types of emission (Figure 3.7): 1) secondary electrons which are generated

due to inelastic scattering of electrons in the sample, producing a low energy electrons useful for topographic information; 2) and backscattered electrons (BSE), which result from elastic scattering, meaning that the electrons have similar energies as the incident electrons. This elastic scattering strength is dependent of the atomic number of the elements present in the sample, allowing the analysis of the different phases over a wide range of magnification [90,112].

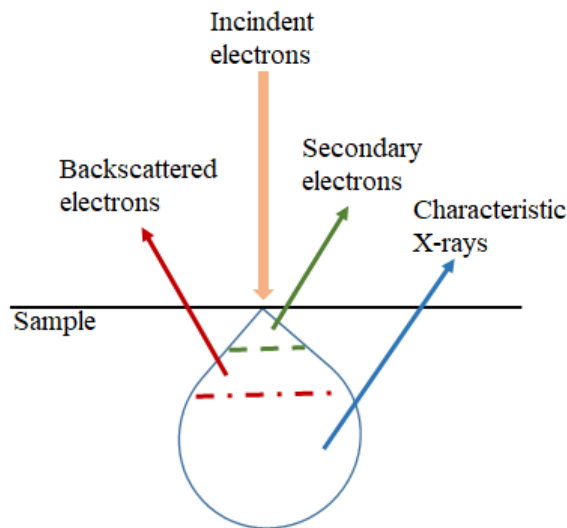


Figure 3.7. Signal generation in SEM: Secondary electrons; Backscattered electrons; and Characteristic X-rays.

Energy dispersive X-ray (EDX) is usually coupled to SEM for analysis of the chemistry of the samples. An incident electron interacts with the inner shell electrons knocking an electron out of the atom. An electron from the upper shell (higher energy) fills the place of the ejected electron, and the energy difference between the two shells results in the emission of a characteristic X-ray of the element. These X-rays are detected and quantified, allowing the identification of the different elements present in the sample (Figure 3.7) [90].

Experimental SEM-EDX parameters used in this Thesis:

Sample preparation: Samples were sectioned using an Isomet saw and mounted in epoxy resin. After leaving for 24 hours to harden, the samples were ground using grit paper from size 400, 600, 800 and 1200 until the cement surface was exposed. The samples were then polished using 6, 3, 1 and 0.25 μm diamond paste and isopropyl alcohol. The samples were carbon coated and painted with silver paint to make them electrically conductive.

Chapter 4: BSE images were recorded using a Hitachi TM3030 scanning electron microscope operating with an accelerating voltage of 15 kV. EDX analysis was performed using a Quantax 70 software and elemental maps were collected for between 15 to 20 minutes. Imaging and compositional analysis was undertaken between 1000x to 1500x magnification.

Chapters 6 and 7: An Inspect F50 FE-SEM was used for the analysis of cement samples after contact with the different groundwater compositions for 12 and 18 months. The accelerating voltage was 15kV, the spot size was 3 (unknown beam diameter) and the working distance did not require adjustment for EDS measurements.

For the samples that were in contact with groundwater for 6 months, analysis was performed at University of Manchester, by Dr. Heath Bagshaw. The instrument is a FEI Quanta 650, running at 15kV equipped with a Bruker Quantax EDS system with an Xflash6/30 detector running Esprit V2.0 analysis software. The analysis was carried out under variable pressure conditions (0.6mbar) to minimise charging in the sample - images were captured using Secondary Electrons (LFD detector (large field detector) and Backscattered Electrons (CBS detector - Concentric BackScattered detector). The maps were collected as 12 x 1 fields stitched together (XY), each field was collected for 10 frames. EDS spectra were also obtained at the centre and edge on the sample. Errors associated with the data were obtained through the software used to process the data.

3.3.7: Solid-State Nuclear Magnetic Resonance (NMR) Spectroscopy

Nuclear Magnetic Resonance (NMR) is a technique commonly used in cementitious systems to study structural characteristics of poorly crystalline or amorphous materials, which are difficult to identify through XRD or other techniques [113]. In NMR spectroscopy, the interactions between the magnetic momentum of a certain nuclei (with non-zero spin) and the applied magnetic fields will allow to obtain more information about the local chemical environment of the active nuclei, and possible effects of near-neighbour nuclei [113,114]. During an NMR experiment, a sample will be exposed to external magnetic field, after which it is irradiated with pulses of radiofrequency radiation, which will allow the ground energy state to split into various energy levels [114]. In turn, the lower energy states will become excited through the absorption of energy, moving to higher energy state. However, when the pulse of radiofrequency radiation is removed, relaxation of the nuclei occurs, through the return of the excited energy state to lower energy state, emitting an electromagnetic response, which is measured as free induction decay [114]. Then to obtain a NMR spectrum (resonance frequency), this free induction decay is converted using a Fourier transform [113,114]. The resonance frequency obtained is recorded as a chemical shift relative to a known standard, and it will be dependent on the local environment around the studied nuclei [114].

As NMR experiments are being performed in solids, the resulting NMR spectra will often appear broadened, due to dipole-dipole interactions, chemical shift anisotropy and quadrupolar interactions [113,114]. Magic angle spinning (MAS) is often used to reduce or eliminate these interactions, by spinning a sample at an angle of 54.74° to the static magnetic field, suppressing in this way the dipolar interactions and removing the chemical shielding anisotropy and first-order quadrupolar interactions (spins = $\frac{1}{2}$, without second-order quadrupolar interactions) which will result in a narrowing spectral lineshapes [113,114]. However, MAS NMR experiments can not remove the second-order interactions for quadrupolar nuclei with spins $> \frac{1}{2}$. Spinning at multiple angles, either simultaneously in double rotation spinning or sequentially in double angle spinning, it is one of the possible ways of improving the signal of the second-order interactions [114].

In the present study, ^{29}Si MAS NMR and ^{27}Al MAS NMR were used to study the C-(A)-S-H structure, the silicon-containing clinker phases, silica fume and BFS and also the aluminium-containing hydrate phases.

Experimental MAS NMR parameters used in this Thesis:

Chapter 4, 5, 6 and 7: In Chapter 4, the ^{29}Si MAS NMR and ^{27}Al MAS NMR spectra for the NRVB 28 days cured at 20°C were collected at the EPSRC National Solid-state NMR Service. ^{29}Si NMR were collected on a Varian VNMRS 400 (9.4 T) spectrometer at 79.435 MHz using a probe for 6 mm o.d. zirconia rotors and a spinning speed of 6 kHz, a pulse width of $4\ \mu\text{s}$ (90°), a relaxation delay of 2.0 s, and with a minimum of 30000 scans. ^{27}Al NMR spectra were collected on the same instrument at 104.198 MHz using a probe for 4 mm o.d. zirconia rotors and a spinning speed of 12 kHz, a pulse width of $1\ \mu\text{s}$ (25°), a relaxation delay of 0.2 s, and a minimum of 7000 scans. ^{29}Si and ^{27}Al spectra were referenced to pure tetramethylsilane (TMS) and 1.0 M aqueous $\text{Al}(\text{NO}_3)_3$, respectively.

The remaining data was collected in the Chemistry Department at University of Sheffield, by Dr. Sandra van Meurs, with help of Dr. Brant Walkley. Solid state single pulse ^{29}Si and ^{27}Al magic angle spinning (MAS) NMR spectra were acquired on a Bruker Avance III HD 500 spectrometer at 11.7 T (B_0) using a 4.0 mm dual resonance CP/MAS probe, yielding a Larmor frequency of 99.35 MHz for ^{29}Si and 130.32 MHz for ^{27}Al . ^{29}Si MAS NMR spectra were acquired using a $4\ \mu\text{s}$ non-selective ($\pi/2$) excitation pulse, a measured 15 s relaxation delay, a total of 512 scans and spinning at 12.5 kHz. ^{27}Al MAS NMR spectra were acquired using a $1.7\ \mu\text{s}$ non-selective ($\pi/2$) excitation pulse, a measured 5 s relaxation delay, a total of 512 scans and spinning at 12.5 kHz. All ^{29}Si and ^{27}Al spectra were referenced to pure tetramethylsilane (TMS), 1.0 M aqueous $\text{Al}(\text{NO}_3)_3$ and 1.0 M aqueous $\text{NaCl}_{(\text{aq})}$, respectively, at 0 ppm.

Deconvolutions of the ^{29}Si MAS NMR were performed using non-linear minimisation of the sum of squared errors using Gaussian curves [115–118]. A minimum number of peaks possible were fitted. Q^n

(mAl) classification were used in the analysis, where a Si tetrahedron is connected to nSi tetrahedral ($0 > n > 4$), and m is the number of neighbouring AlO_4 tetrahedra [119]. To help to fit the PC, BFS and silica fume, deconvolution of the raw materials was performed. Estimated uncertainty in site percentages was based on the influence of the signal/noise ratio of the spectra on the deconvolution procedures. Calcium/silicon (Ca/Si) ratio, aluminium/silicon (Al/Si) ratio and the mean chain length (MCL) were calculated using the following equations (3.4, 3.5 and 3.6) from Richardson et al. [120]:

$$\frac{Ca}{Si} = \frac{\frac{3}{2}Q^1 + \frac{2}{3}Q^2}{Q^1 + Q^2} \quad (3.4)$$

$$\frac{Al}{Si} = \frac{\frac{1}{2}Q^2(1Al)}{Q^1 + Q^2 + Q^2(1Al) + Q^3 + Q^3(1Al)} \quad (3.5)$$

$$MCL = \frac{2}{\left(\frac{Q^1}{Q^1 + Q^2 + Q^2(1Al) + Q^3 + Q^3(1Al)}\right)} \quad (3.6)$$

Errors associated with these calculations were obtained through combination and propagation of the errors using standard formulae.

3.3.8: Mercury Intrusion Porosimetry (MIP)

With mercury intrusion porosimetry (MIP), the pore size distribution, and consequently the porosity, of cementitious materials can be studied. This technique is based on the assumption that the pores are cylindrical and connected to allow the penetration of mercury. Washburn's law was used to determine the pore diameter, by applying the following (Equation 3.7):

$$D = - \frac{4\gamma\cos(\theta)}{P} \quad (3.7)$$

where D is the pore diameter (μm), θ the contact angle between the fluid and the pore mouth ($^\circ$) ($\theta = 130^\circ$), γ the surface tension of the fluid (N/m), and P the applied pressure to fill the pore with mercury (MPa). It should be noted that MIP experiments measure the pore entry size and not the real pore sizes of the sample [90]. Therefore, if a narrow entry pore is the only path for the wider size pore, the volume of the latter pore will be evaluated as being of a smaller diameter [90,121]. This is called the ink-bottle effect, which will lead to an underestimation of the larger pores [90,122]. MIP results are generally plotted as cumulative pore volume vs pore entry radius.

Experimental MIP parameters used in this Thesis:

Chapters 4, 6 and 7: Small pieces of NRVB¹ and Cebama reference cement paste were placed into the sample holder of an Autopore V 9600 (Micromeritics Instruments). The maximum pressure applied was 208 MPa, the surface tension was 485 mN/m and the contact angle was 130°. Smallest pore entry size detected by the equipment is approximately 0.003 µm. These measurements were performed by Dr. Oday Hussein. Errors are representative of the intrinsic instrument error.

3.3.9: Nitrogen sorption porosity analysis

Gas adsorption is a technique that can be used to study micropores and mesopores in a porous material. The principle of this technique is that gas molecules (adsorbate) will physically adsorb onto the surface of the solid sample (adsorbent), due to van der Waals forces between the adsorbate and the adsorbent [90]. For this to occur, very low temperatures are required, and are usually obtained by using liquid nitrogen. Nitrogen is a common adsorbate gas used in cementitious materials, as it is an inert gas that has low reactivity with these materials. The resulting data, adsorbed gas amount and corresponding relative pressure, will allow to obtain information about specific surface area, pore volume, and pore size distributions by applying different methods (e.g. Brunauer-Emmett-Teller (BET) and Barret-Joyner-Halenda (BJH) [123,124]).

The BET theory was used in this project to determine the specific surface area of two of the raw materials. The BET method is based on the multilayer adsorption of gas molecules onto the adsorbent and can be expressed by the following Equation 3.8 [123]:

$$\frac{P}{V_a(P_0-P)} = \frac{1}{V_m C} + \frac{C-1}{V_m C} \left(\frac{P}{P_0}\right) \quad (3.8)$$

where P_0 is the saturation pressure of the gas, P is the pressure of the gas in equilibrium with the sample, V_a is the amount of gas adsorbed, C is a constant and V_m is the amount of gas needed to cover the surface with a monolayer. V_m can then be obtained by plotting the first fraction of the equation versus P/P_0 , through the slope and intercept of the obtained line. Once V_m is known, the specific surface area can be determined using (Equation 3.9):

$$S_{BET} = \frac{N_A V_m A_N}{V_o} \quad (3.9)$$

being N_A the Avogadro constant, A_N the area of the surface occupied by a single adsorbed gas molecule (for nitrogen is assumed $16.2 \times 10^{-20} \text{ m}^2$) and V_o the molar volume of gas.

¹ Note: Due to the very low compressive strength presented by NRVB (around 8 MPa), this technique, which reaches pressures of 208 MPa, was found not suitable (after using in Chapter 4) to quantify the finer pores due to the potential for collapse of pores during analysis.

The volume pore size distribution was obtained using the BJH model [124], which considers that when a critical relative pressure is reached, condensation occurs in the pores (Kelvin Equation, 3.10):

$$\ln\left(\frac{P}{P_0}\right) = \frac{-2\gamma V_0 \cos \theta}{RT(r_p - t_c)} \quad (3.10)$$

where γ is the surface tension at the liquid-vapour interface, V_0 is the molar volume of the liquid, θ is the contact angle between liquid and pore (which will be zero for N_2), R is the gas constant, r_p is the pore radius and t_c is the thickness of the adsorbed layer during adsorption. However, some assumptions need to be made to use this equation: (1) before condensation, a pre-adsorbed film on to the pore wall has occurred; (2) and like with MIP, the pores are considered to have a cylindrical shape [90]. Another condition that needs to be satisfied before determining the pore size distribution is that all pores need to be considered filled. In that way, the pore size diameter (d) can be calculated using the following Equation 3.11:

$$d = \frac{4V}{A} \quad (3.11)$$

where A is the surface area obtained through BET and V is the pore volume determined from the adsorption/desorption isotherm. The pore size distribution can be obtained by either the adsorption or desorption curves. In the current study, desorption curves were chosen as it is the most common used and comparison with other data can be made [90]. The range of pore sizes studied was between 2 – 40 nm.

Experimental Nitrogen Sorption parameters used in this Thesis:

Chapters 4 and 6: To determine the BET surface area (Chapter 4) and the pore size distribution (BJH, Chapter 6), nitrogen adsorption-desorption measurements were studied at 77 K on a Micromeritics 3 Flex apparatus. Powder samples of raw material (Chapter 4) and of NRVB (Chapter 6) were weighed to around 0.5 g and degassed under vacuum at 40 °C for 24 hours, to reduce interferences during measurements. Then, these samples were cooled with liquid nitrogen and analysed by measuring the volume of gas (N_2) adsorbed at specific pressures. The pore volume was taken from the desorption branch of the isotherm at $P/P_0 = 0.3$.

Since MIP was used to study the porosity of Cebama reference cement paste, it was decided that due to cost limitations it was unnecessary to use nitrogen sorption for the same purpose.

3.3.10: X-Ray Computed Tomography (XCT)

X-ray Computed Tomography (XCT) is a non-destructive technique commonly used to observe and study the interior features of a solid object, by producing 3D image stacks from 2D projections (by applying mathematical reconstructions from slice-series). In cementitious materials, this technique has been used to analyse the pore structure and network [125–131].

In this technique, X-ray radiation is directed to the sample (continuously), and due to mainly the density (but also atomic number) of the material, the incident X-rays will be attenuated (Figure 3.8). These X-rays can be either from a collimated beam or from a divergent beam. The sample, which is positioned in a rotational stage, is rotated through 360° and images are acquired at constant time steps. The diffracted X-rays will pass through a scintillator to the detector. From a series of 2D radiographs obtained, 3D reconstructions can be performed by applying different mathematical algorithms, which will not be discussed here (as data processing was performed externally).

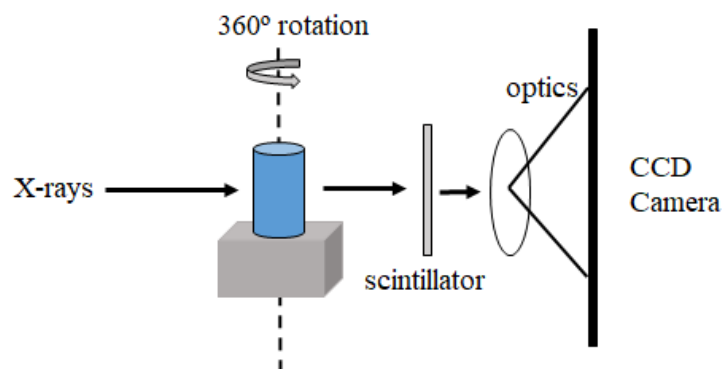


Figure 3.8. Schematic of XCT equipment (simplified).

From the obtained data, quantitative analysis in terms of porosity, for example, can be obtained by performing segmentation of the images. The histograms of the images will show peaks with higher or lower absorption voxels, where the lower absorption voxels correspond to surrounding air and internal void space, which will allow discrimination between pore space and binder phases (solid) [130]. One of the main disadvantages of XCT is the fact that to obtain high resolution, and so be possible to observe the smaller pores (micron to nanoporosity), very small samples (micrometre size) and long-time scans are required.

Experimental XCT parameters used in this Thesis:

Chapters 4, 6 and 7: The XCT experimental procedure and most of the data processing was performed externally.

In Chapter 4, part of the samples (NRVB 20 °C) were analysed at the University of Strathclyde by Dr. Nicolas Beaudoin, using a Nikon XTH 320/225 system. The rotation stage position was set so the X-ray source-to sample distance was minimal and allowed a minimum voxel size of 3 micrometres. Scanning conditions were an accelerating voltage of 100 keV, 28 μ A current (corresponding to power 2.8 W) using a silver target. The exposure time for each projection was 2.829 seconds, lasting 3141 projections (1 frame per projection) and leading to a scan-time of 2.5 hours. Once reconstructed, a software built-in algorithmic correction was applied to correct for artefacts related to beam-hardening [132]. All volumes were reconstructed in 16 bit greyscale, and converted to a .tif stack. This data processing was performed by the author of this Thesis: A volume of interest (VOI) was selected for each sample, using standards previously reported in the literature, i.e. the VOI should be at least 100 μm^3 , or higher than 3 to 5 times the size of the largest distinct feature, to minimise finite size error. In this study, the VOI size chosen was 0.42 mm^3 (250 x 250 x 250 voxels at 3 μm resolution).

For the rest of the samples (in Chapters 4, 6 and 7), the analysis and data processing was performed by Dr. Haris Paraskevoulakos from University of Bristol. A Zeiss Xradia 520 Versa S-ray microscope was used. The rotation stage position was set so the X-ray source-to sample distance was minimal and allowed a minimum voxel size of 1.5 micrometres. The exposure time for each projection was 2.0 seconds, leading to a scan-time of ~2 hours. Reconstruction and data processing was not performed by the author of this Thesis, but a brief summary of the procedure is given as followed: threshold segmentation was performed using Avizo software, through the identification of different intensity values; the lower intensity regions were identified as voids and used as the threshold value to distinguish the pores/voids from the matrix of the sample. Porosity values were obtained through this analysis. Errors were calculated from standard deviation of triplicate thresholding.

3.3.11: *Inductively Coupled Plasma Spectroscopy (ICP-OES)*

This technique is used to identify and quantify different elements present in a solution. In the equipment, the sample (a liquid) is first vaporised by a nebuliser, and will then pass through a plasma torch, which will atomize and ionise the sample. Also due to the plasma, which is generated when argon gas is ionised at high frequency electricity, the atoms will be excited by two processes: inelastic scattering of an electron from an atom and the radiative-recombination of an ion with an electron, which will lead to the emission of photons [133]. Due to the presence of optical and radial windows in the equipment, a range of wavelengths can be collected, and identification of the elements is performed by comparing

with characteristic emission peaks for each element. Direct relation between the intensity of the emission peak and quantity is performed.

Experimental ICP-OES parameters used in this Thesis:

Chapters 6 and 7: Analysis of the major elements present in the solutions prior to, and after, the experiment was performed using a Thermofisher Scientific iCAP Duo6300 Inductively Coupled Plasma-Optical Emission Spectrometer. Multi-element calibration standards were prepared using high quality Fluka elemental standards of known concentration diluted in a nitric acid solution. The standards contained Ca, Mg, Na, Al, S, Si and K diluted with 10% ultra-pure nitric acid at a maximum concentration of 100 mg/L. The actual samples were filtered (0.22 μm), diluted (1:20 dilutions) and acidified with 20 μL of concentrated HNO_3 (99.999% purity) prior to analysis. A ceramic torch and an internal standard of 5 mg/L Au solution were used to help analyse these complex samples (high ionic strength). The use of an internal standard helps to improve the accuracy and precision of the results, as Au emission intensities are measured and ratioed to the initial internal standard and then the values obtained for the samples can be corrected by this same ratio, compensating for sample matrix effects [134]. Errors were calculated using the standard deviation of duplicate measurements.

3.3.12: Ion Chromatography (IC)

Ion Chromatography (IC) is an analytical technique that separates ions based on their affinity to the ion exchanger [135]. Two types of IC can be used: anion-exchange and cation-exchange. In the current project, anion-exchange was used to quantify chloride ions present in the different solutions.

To help separate the ions present in a sample, an eluent is usually used. So, in an IC equipment, a sample is loaded and injected into the eluent stream (composition and concentration of the eluent remain constant). With the help of a pump, the eluent and the sample will pass through first a guard column, which will remove contaminants that might affect the analysis, and then through the separator column. It is in this column that the ions of the sample will be separated, on the basis that different ions will migrate through the column at different rates, depending on their interactions with the ion exchange sites [135,136]. After, a suppressor will suppress the conductivity of the eluent and enhance the detection of selected ions. The ions will then be identified based on their retention time and quantified by integrating the peak area or peak height. The use of standard solutions will help with this identification and quantification.

Experimental IC parameters used in this Thesis:

Chapters 6 and 7: Analysis of the solutions for Cl concentration was performed using a Thermofisher Scientific Dionex ICS-1100 Ion Chromatography System. Calibration standards were prepared using high quality Merck elemental standards of known concentration. The standards contained Cl diluted with UHQ water at a maximum concentration of 100 mg/L. The samples were filtered (0.22 μm) and diluted (1:20 dilutions) prior to analysis. The eluent used was composed of 4.5 mM Na_2CO_3 and 1.4 mM NaHCO_3 . Errors were calculated using the standard deviation of duplicate measurements.

Chapter 4: Characterisation of NRVB and Cebama reference cement paste

Part of this Chapter is published as “Characterisation of a high pH cement backfill for the geological disposal of nuclear waste: The Nirex Reference Vault Backfill” in *Applied Geochemistry* (vol. 89, pp. 180 – 189, 2018) by Vasconcelos et al. [137] (Appendix I).

4.1: Introduction

Understanding the initial chemistry and microstructure of cement pastes, before experiments with different groundwater compositions, is essential so that differences can be identified in the samples pre- and post-contact with groundwater. For this purpose, in this Chapter a detailed characterisation of NRVB and Cebama reference cement pastes, cured for 28 days, is presented. In the case of NRVB, and since more than one formulation can be found in the literature and in this Thesis (as mentioned in Chapter 3), a comparison between NRVB formulated using laboratory materials [79] and using industrial materials [22] is performed. Moreover, two different curing temperatures, room temperature (20 °C), and 40 °C, were used. The room temperature was used as a standard curing condition to correlate with the data obtained in the long-duration synchrotron XRD experiment performed at Diamond Light Source (results in Chapter 5). For the extended experiments with groundwater, 40 °C was used, as advised by the UK waste management organisation, Radioactive Waste Management (RWM), to be representative of the peak of a 50 year thermal transient after backfilling of the disposal area [1].

For this characterisation, a wide variety of techniques were used, to better understand the complex matrix characteristics of the cementitious materials. Techniques used in this Chapter are: particle size distribution, X-ray Fluorescence (XRF), X-ray Diffraction (XRD), Scanning Electron Microscopy / Energy Dispersive Spectroscopy (SEM/EDS), Thermogravimetry-Mass Spectrometry (TG-MS), X-ray Computed Tomography (XCT), Mercury Intrusion Porosimetry (MIP) and Nuclear Magnetic Resonance spectroscopy (NMR).

4.2: NRVB Characterisation

As mentioned in Chapter 2, NRVB was designed and characterised in the 1990s [19]. However, there has not been a comprehensive characterisation of this material, where all tests are performed on a consistent batch. Additionally, some of the raw materials used in the early development of this cement are no longer available due to changes in the powder suppliers [12], therefore, the materials to be used when a GDF is in operation may differ in composition and other key characteristics. As such, it is important to understand how the chemical composition and physical properties of the backfill raw materials may affect the short- and long-term performance of the NRVB. The results presented in this section were published as a peer-reviewed paper in the journal *Applied Geochemistry* [137] and pertain to two mixtures of precursor materials: (1) “laboratory” NRVB (NRVB (Lab)), composed of reagent grade $\text{Ca}(\text{OH})_2$ and CaCO_3 added to CEM I; and (2) “industrial” NRVB (NRVB (Ind)), composed of precursors used by the National Nuclear Laboratory in their formulation of NRVB, including hydrated lime and limestone flour, mixed with CEM I.

4.2.1: Precursor materials

The chemical composition of the starting materials, as calculated using XRF of powdered materials, is shown in Table 4.1. The composition was very similar for both $\text{Ca}(\text{OH})_2$ and hydrated lime. However, a slight difference was observed between CaCO_3 and limestone flour. For example, CaCO_3 contained more CaO than the limestone flour (57 wt% and 48 wt%, respectively). On the other hand, limestone flour presented a higher concentration (between 1.6 and 5.4 wt%) of SiO_2 , Fe_2O_3 , MgO and Al_2O_3 than reagent grade CaCO_3 , which contained below 0.5 wt% of these elements (Table 4.1).

Table 4.1. Composition of precursor materials, as determined by XRF analysis (precision ± 0.1 wt%)

Compound (wt. %)	CEM I 52.5 N	Limestone Flour (Ind)	CaCO_3 (Lab)	Hydrated Lime (Ind)	$\text{Ca}(\text{OH})_2$ (Lab)
Na_2O	0.3	0.2	< 0.1	< 0.1	< 0.1
MgO	1.2	1.6	< 0.1	0.5	0.5
Al_2O_3	5.2	1.9	< 0.1	< 0.1	0.1
SiO_2	19.7	5.4	< 0.1	0.5	0.7
P_2O_5	0.2	0.1	< 0.1	< 0.1	< 0.1
K_2O	0.5	0.3	< 0.1	< 0.1	< 0.1
CaO	64.1	48.1	57.0	73.9	74.5
Fe_2O_3	2.1	1.7	< 0.1	< 0.1	< 0.1

SO ₃	-	893 ppm	37 ppm	-	-
LOI	3.5	39.6	43.3	23.2	24.4

Differences in the particle size distribution between CaCO₃ and limestone flour were also observed in Figure 4.1a, where 50 % of the particles were smaller than 19.7 μm for CaCO₃ and 11.5 μm for limestone flour. In the case of the industrial and laboratory grade Ca(OH)₂ (Figure 4.1b), the particle size distributions were found to be very similar.

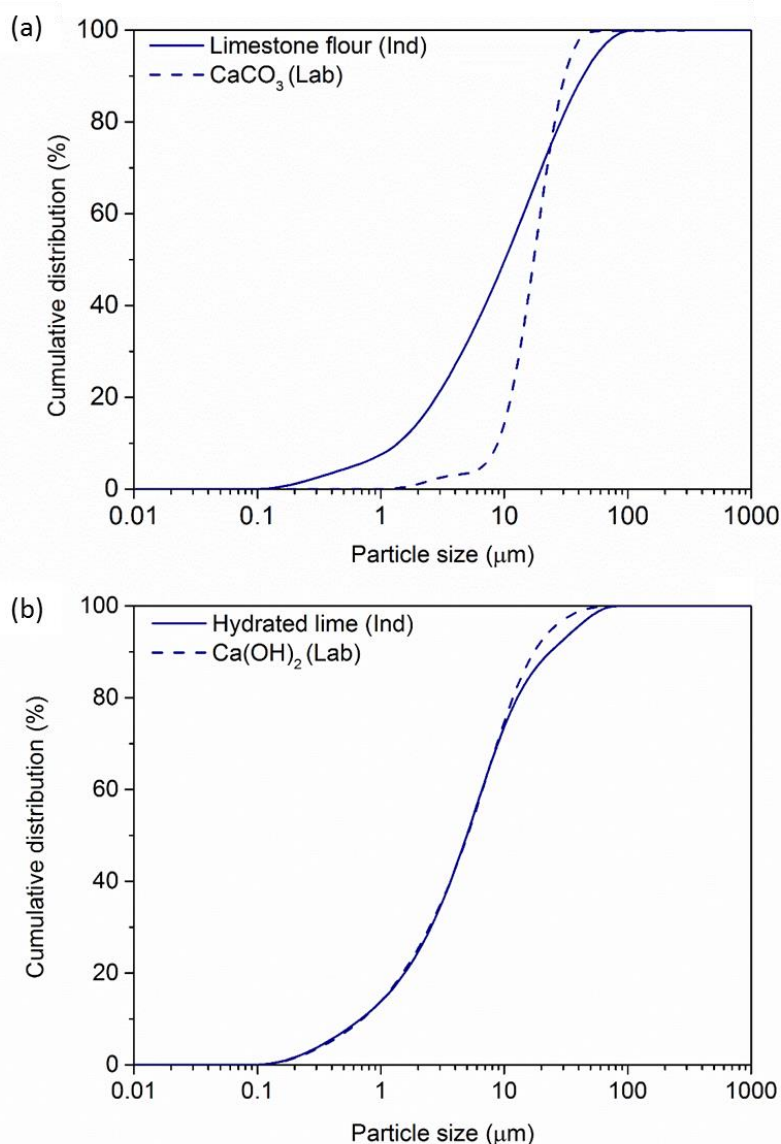


Figure 4.1. Particle size distributions of (a) CaCO₃ and limestone flour and; (b) Ca(OH)₂ and hydrated lime.

The fact that there was only a small difference between CaCO₃ and limestone flour is also observed in the XRD pattern of these two precursor materials (Figure 4.2a). These differences are related to the

presence of aragonite in the limestone flour and the reflections of calcite being slightly more intense in the CaCO_3 . In the case of Ca(OH)_2 and hydrated lime (Figure 4.2b), the presence of the same peaks was observed.

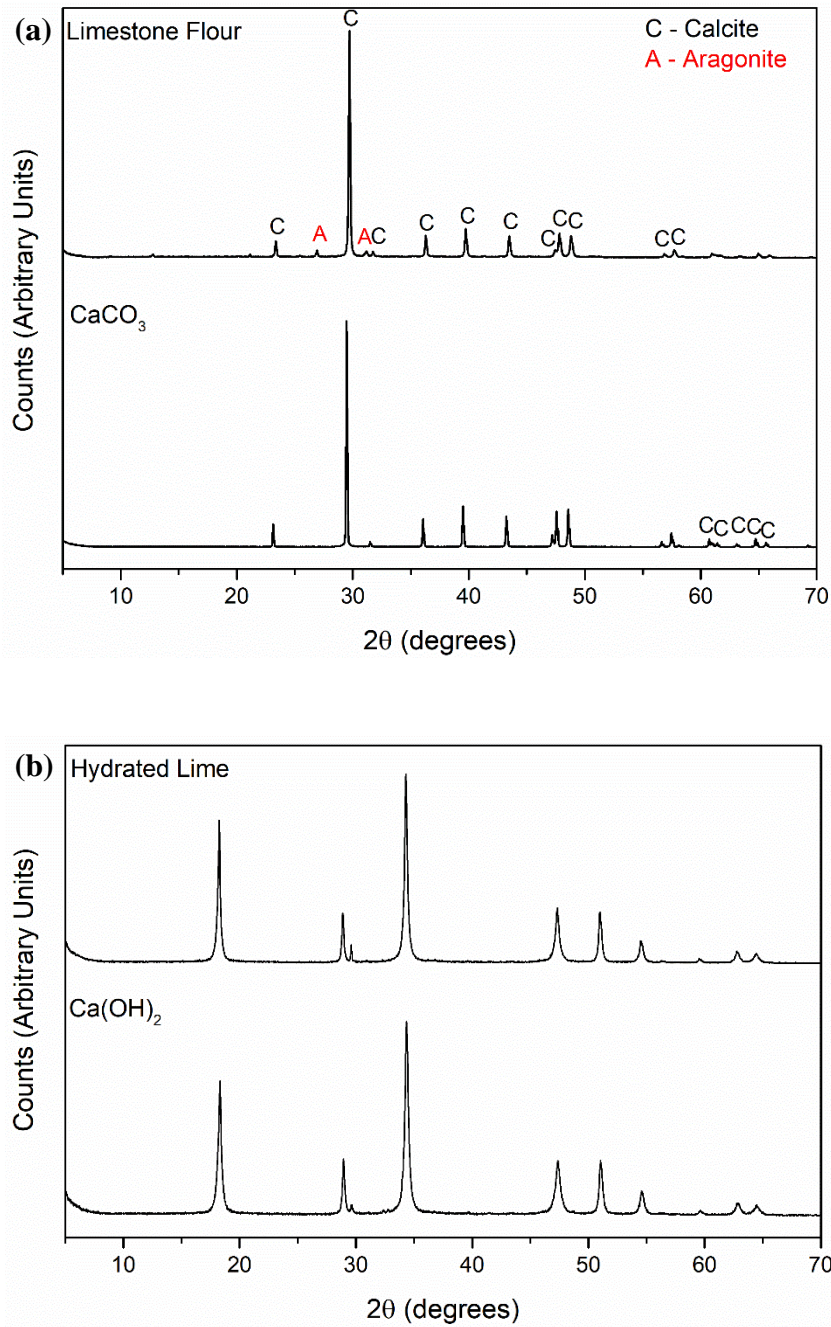


Figure 4.2. XRD patterns of (a) CaCO₃ and limestone flour, and (b) Ca(OH)₂ and hydrated lime.

4.2.2: NRVB (20 °C)

Figure 4.3a shows the isothermal calorimetric measurements of the heat generated by both NRVB formulations during hydration. It is possible to identify the four main hydration stages, as observed in a plain Portland cement (PC). In comparison to PC, the heat flow was lower (Figure 4.3b) by a factor of ~2 [46]. This is related to the much lower fraction of material undergoing hydration in the NRVB

formulation (due to the high proportion of supplementary cementitious materials). Comparing the two formulations of NRVB, it can be observed that the heat flow was very similar, however one subtle difference was observed: the curve corresponding to the sulphate depletion period (labelled 4, Figure 3a) of NRVB (Ind) evidenced a more intense reaction than NRVB (Lab). One possible explanation is the formation of additional calcium monocarboaluminate hydrate in NRVB (Ind) as observed in XRD and NMR data (discussed below). In accordance with the particle size analysis (Figure 4.1a), the limestone flour used in NRVB (Ind) demonstrated a significantly higher surface area than CaCO_3 used in NRVB (Lab), with values of $5.2 \pm 0.2 \text{ m}^2/\text{g}$ and $3.7 \pm 0.2 \text{ m}^2/\text{g}$, respectively. The higher surface area was responsible for a higher rate of calcite dissolution and also the availability of more nucleation sites, resulting in the formation of more hydration products [138]. Another factor to consider is the higher content of sulphate present in the industrial raw material, which may have contributed to the observed differences; the limestone flour of NRVB (Ind) had 893 ppm sulphur, compared with 37 ppm in the hydrated lime of NRVB (Lab) (Table 4.1).

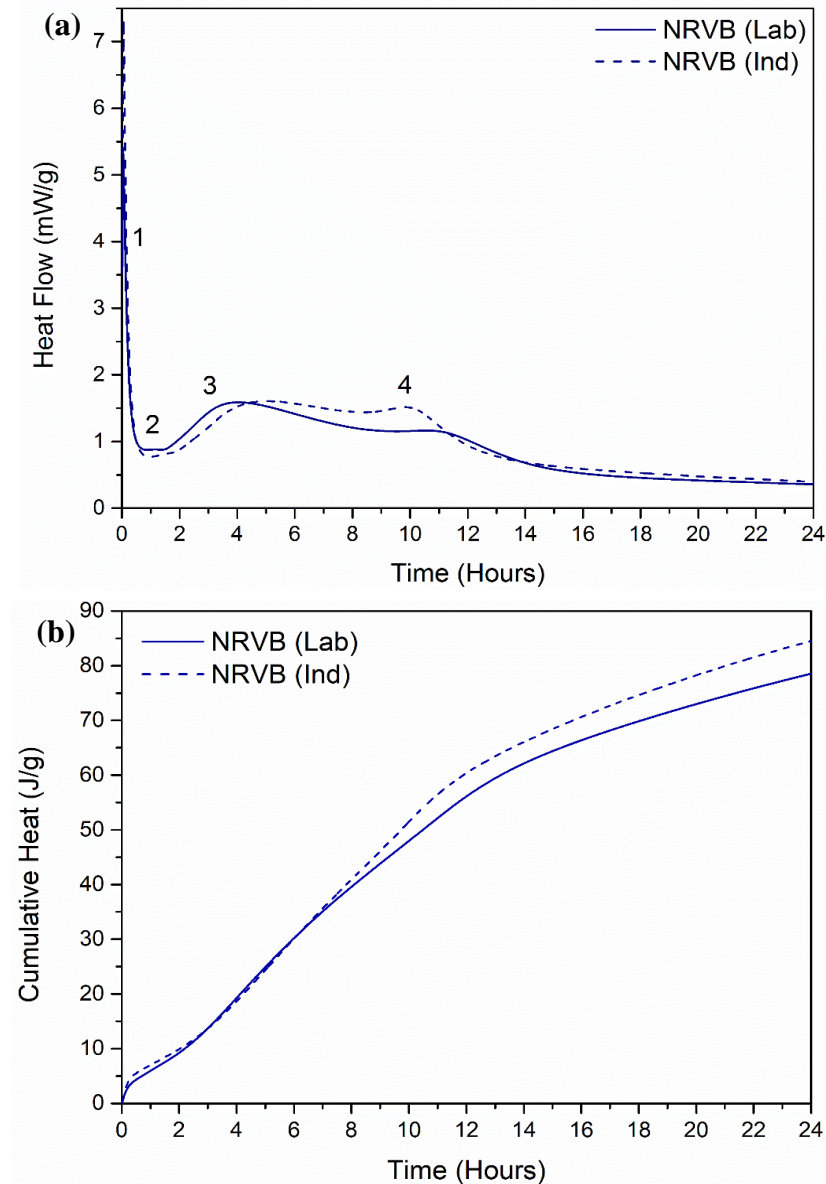


Figure 4.3. (a) Isothermal calorimetry data for NRVB (Lab) and NRVB (Ind) at 20 °C. Thermal features identified are: (1) dissolution and aluminate reaction; (2) induction period; (3) reaction of alite and formation of calcium silicate hydrate; (4) sulphate depletion. (b) Cumulative heat of NRVB (Lab) and NRVB (Ind).

The main phases identified in the NRVB formulations by XRD were calcite (CaCO_3 ; PDF 01-086-0174) and portlandite ($\text{Ca}(\text{OH})_2$; PDF 01-072-0156) (Figure 4.4). Ettringite ($\text{Ca}_6\text{Al}_2(\text{OH})_{12}(\text{SO}_4)_3 \cdot 26\text{H}_2\text{O}$; PDF 00-041-1451), calcium monocarboaluminate hydrate ($\text{Ca}_4\text{Al}_2(\text{OH})_{12}(\text{CO}_3)_3 \cdot 5\text{H}_2\text{O}$; PDF 01-087-0493) and calcium hemicarboaluminate hydrate ($\text{Ca}_4\text{Al}_2(\text{OH})_{12}[\text{OH}(\text{CO}_3)_{0.5}] \cdot 5.5\text{H}_2\text{O}$; PDF 00-041-0221) were also identified. These results are in agreement with those identified previously in NRVB cured at ambient temperature [26]. While the phase assemblage for each formulation was similar, subtle differences were observed in the peak

intensities of several reflections; monocarboaluminate reflections were more intense in NRVB (Ind) than NRVB (Lab), while reflections of calcite were more intense in NRVB (Lab). These differences may be attributed to the chemical composition, particle size distribution and surface area of the CaCO₃ and limestone flour. However, preferential orientation cannot be ruled out, especially for layered or platy phases such as monocarboaluminate and portlandite.

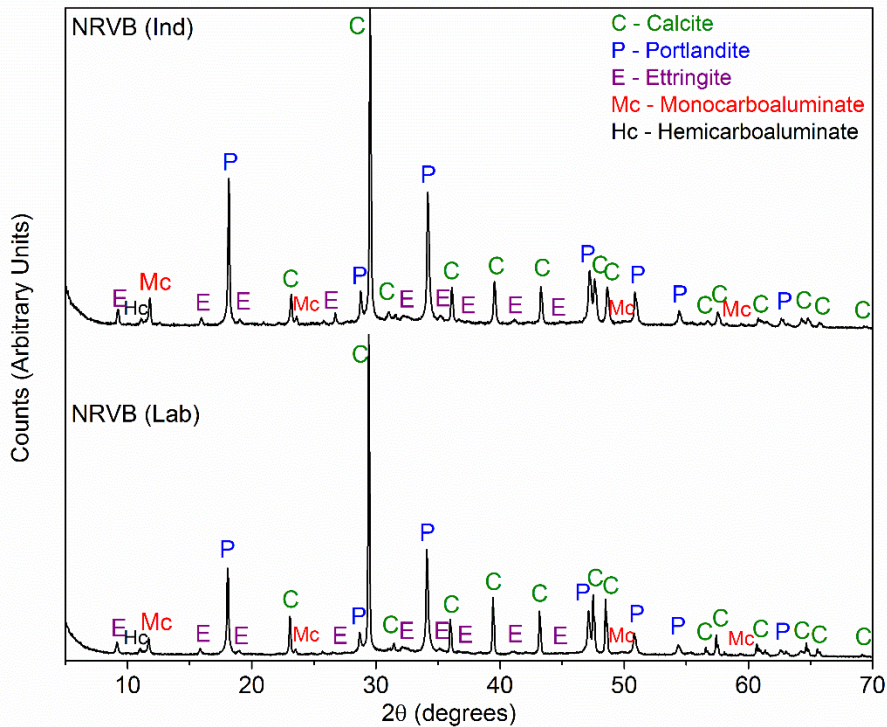


Figure 4.4. X-ray diffraction patterns for (bottom) NRVB (Lab) and (top) NRVB (Ind) after 28 days of curing at 20 °C.

TG-MS analysis confirmed the presence of these phases (Figure 4.5). The two peaks between 100 and 200 °C can be attributed to the presence of ettringite and monocarboaluminate, while the peaks between 400 to 500 °C, and 650 to 800 °C correspond to portlandite and calcite, respectively [27,30]. The same peaks were observed for both formulations, however for the NRVB (Ind) (Figure 4.5b) an additional peak was observed at ~ 650 °C, corresponding to the presence of magnesian calcite (Ca_xMg_(1-x)CO₃) and supported by the presence of more Mg in NRVB (Ind) than in NRVB (Lab) (Table 4.1).

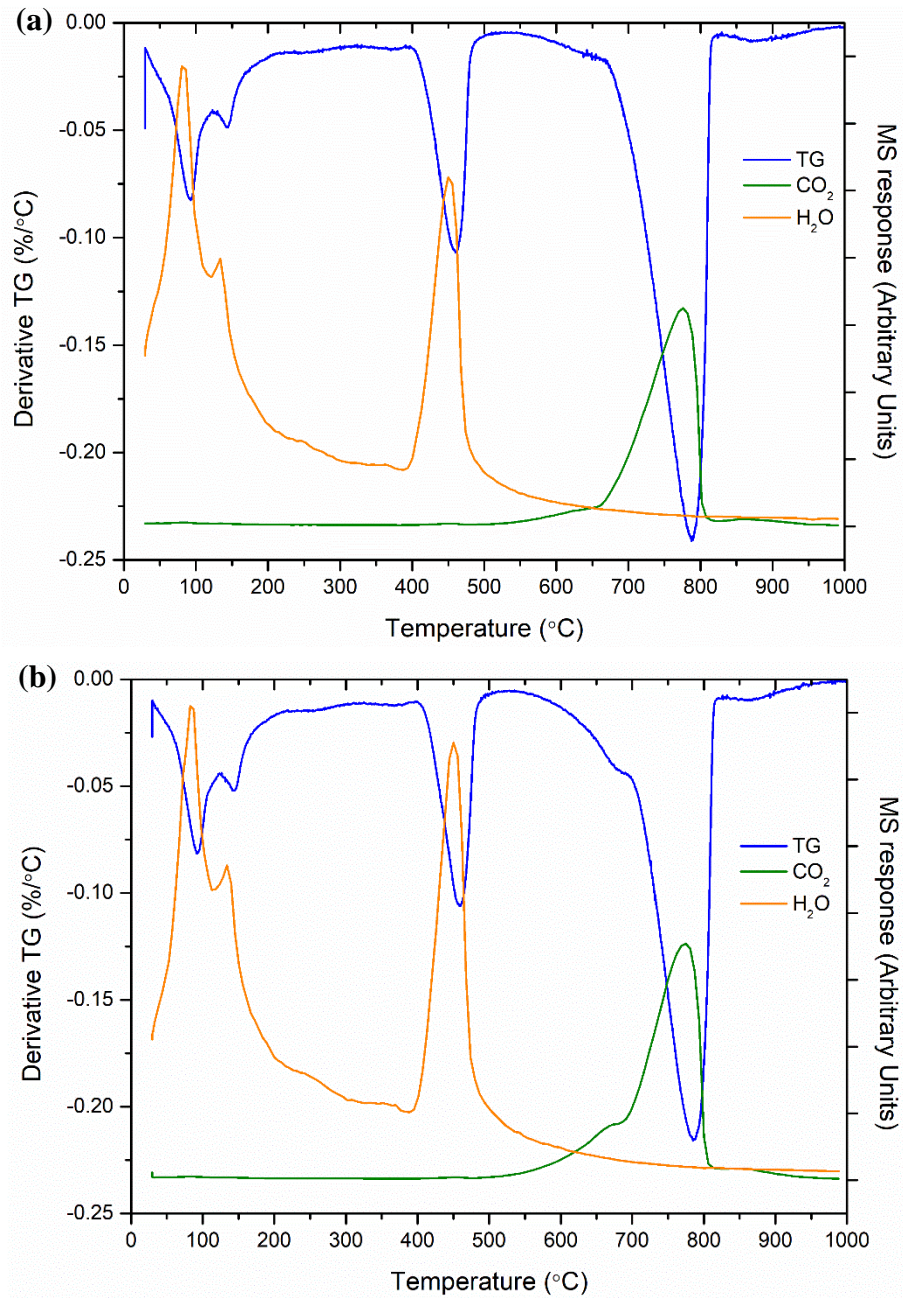


Figure 4.5. TGA-MS data for (a) NRVB (Lab); and (b) NRVB (Ind) after 28 days of curing at 20 °C.

Through SEM imaging and EDX analysis it was possible to identify the microstructure of the different hydrate phases, as shown in Figure 4.6. The large Ca-containing rhombohedral crystals (labelled A, Figure 4.6) are portlandite. The Ca and Si-rich phase surrounding portlandite crystals (labelled B, Figure 4.6) is likely to be C-S-H. The areas containing higher concentrations of aluminium (labelled C, Figure 4.6) suggest the presence of AFm phases. The areas labelled D are indicative of the presence of sulphate-containing AFm phases and/or ettringite, due to the higher concentration of both aluminium and

sulphate. Comparing the SEM images of the two formulations, it is possible to identify the same hydrate phases, however the matrix of NRVB formulated with industrial materials had a more fine-grained morphology, consistent with the analysis of limestone flour by particle size analysis (Figure 4.1a).

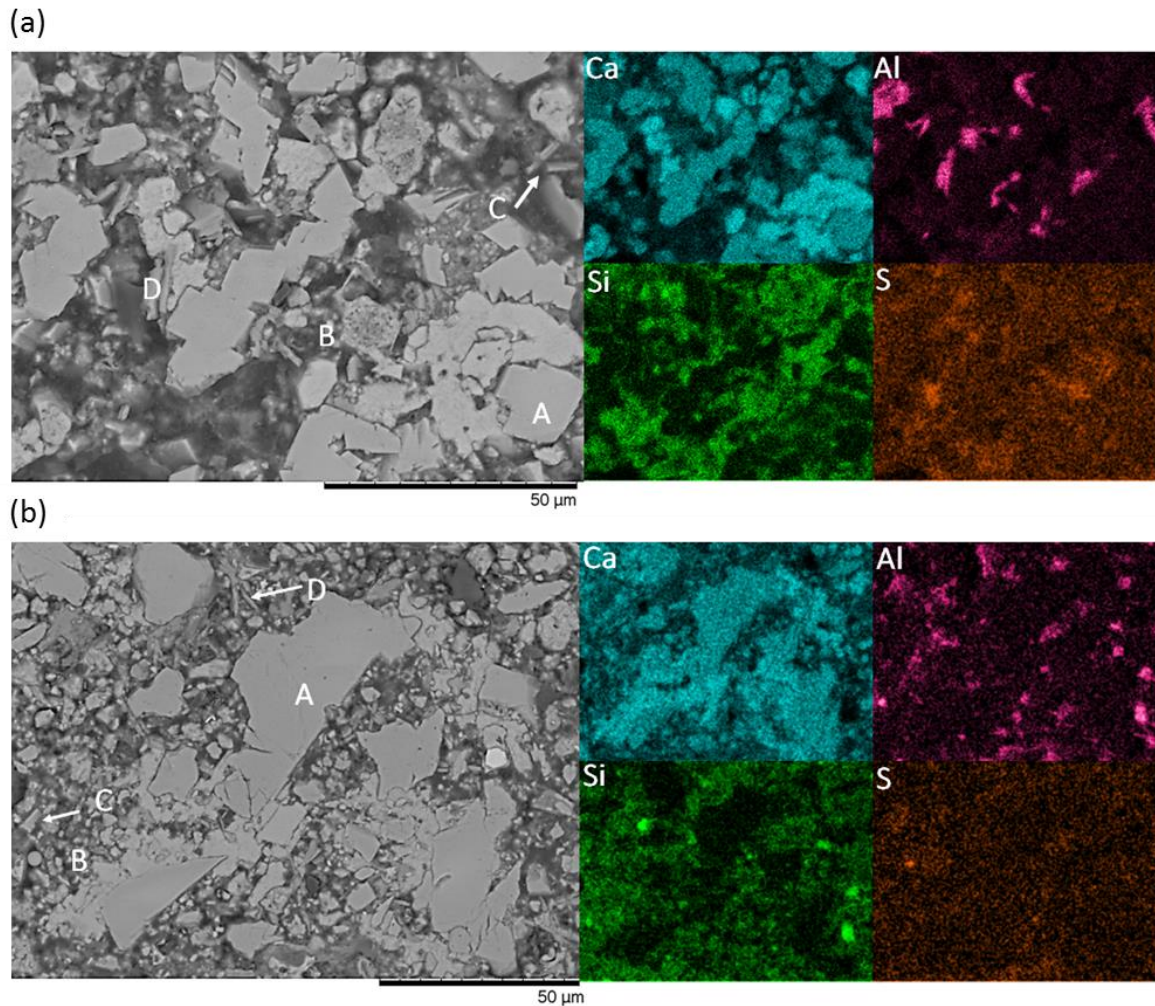


Figure 4.6. BSE SEM micrographs of (a) NRVB (Lab) and (b) NRVB (Ind) at 28 days of curing at 20 °C, with the corresponding EDX maps.

In the ^{29}Si MAS NMR spectra (Figure 4.7) it was possible to identify some unreacted Portland cement through the presence of alite (chemical shifts -69 and -73.9 ppm) and belite (-71.2 ppm) [90] in both NRVB formulations (cured for 28 days). Contributions from Q^1 (-79 ppm), $\text{Q}^2(1\text{Al})$ (-83 ppm) and Q^2 (-84 ppm) silicate environments were also observed in both formulations; these chemical shifts are characteristic of C-S-H [139,140]. A small resonance was also observed at -90 ppm corresponding to $\text{Q}^3(1\text{Al})$. The presence of Al shows the incorporation of this element in the C-(A)-S-H [140]. Comparison of the two formulations reveals a small difference in the spectra (Figures 4.7) between NRVB (Lab) and NRVB (Ind); this is related to the intensity of the resonances of Q^2 (-84 ppm), $\text{Q}^2(1\text{Al})$

(-83 ppm) and $Q^3(1Al)$ (-90 ppm) sites. A possible reason is the difference observed in the reactivity of the raw materials used in the two formulations, specifically the higher surface area of the limestone flour.

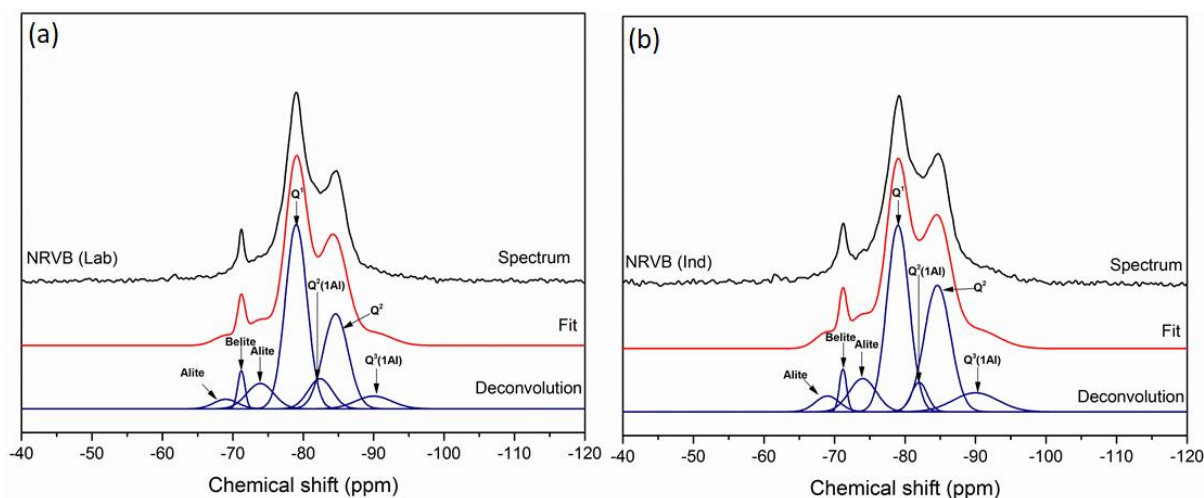


Figure 4.7. ^{29}Si MAS NMR spectra, and deconvolution results, for (a) NRVB (Lab) and; (b) NRVB (Ind) after 28 days of curing at 20 °C.

Figure 4.8 shows the ^{27}Al NMR spectra of NRVB (Lab) and NRVB (Ind). The small peak observed at approximately -69 ppm (more evident for NRVB Ind) is attributed to the substitution of Al for Si in C-S-H [141], in agreement with the observation of small peaks corresponding to $Q^2(1Al)$ and $Q^3(1Al)$ in the ^{29}Si MAS NMR spectra (Figure 4.7). The peaks visible at approximately +13 and +9 ppm indicate the presence of octahedrally coordinated Al in ettringite and AFm phases. As stated previously in the literature [141], it is not possible to distinguish between the different AFm phases due to the similar chemical shifts of their Al sites. Comparing the two formulations, it is possible to see a difference in the proportion of ettringite and AFm phases present; the presence of more AFm in NRVB (Ind) is related to the higher availability of dissolved carbonate (higher surface area) and consequent formation of monocarboaluminate, in accordance with the results observed by isothermal calorimetry (Figure 4.3a) and XRD (Figure 4.4).

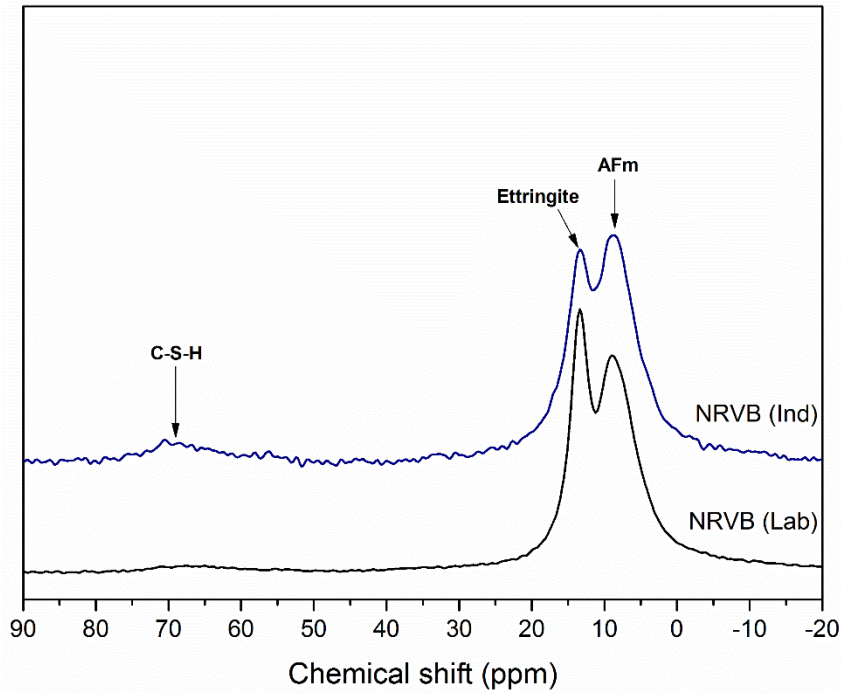


Figure 4.8. ^{27}Al MAS NMR spectra of NRVB (Lab) and NRVB (Ind) after 28 days of curing at 20 °C.

A two-fold approach was applied to determine the porosity of the two NRVB formulations, to ensure all pore sizes were considered in the analysis. Mercury Intrusion Porosimetry (MIP), where it is understood that the pore diameters obtained correspond to the pore entry size and not the real size of the pore [90], was performed to compare the trend and changes in the pore size distribution between the two NRVB formulations [122]. Figure 4.9 shows the cumulative intrusion as a function of the pore entry size diameter for NRVB (Lab) and NRVB (Ind). The curve for NRVB (Lab) allocates essentially all of the pores to threshold pore entry radii below 0.8 μm , whereas for NRVB (Ind) the curve allocates all of the pores to sizes below 0.5 μm . This small difference was also evident in the total porosity obtained, where for NRVB (Lab) the percentage of total porosity obtained was $38 \pm 1\%$ and for NRVB (Ind) was $32 \pm 1\%$. It is important to note that, due to the low compressive strength of NRVB (around 8 MPa [137]), this technique (which reaches pressures of 208 MPa in the instrument used in this study) might not be suitable for quantifying the finer pores due to the potential for collapse of pores during analysis. This is expected to occur at ~ 0.14 mL/g of intrusion for NRVB (Lab) and at ~ 0.15 mL/g for NRVB (Ind) based on the respective compressive strengths of these two formulations.

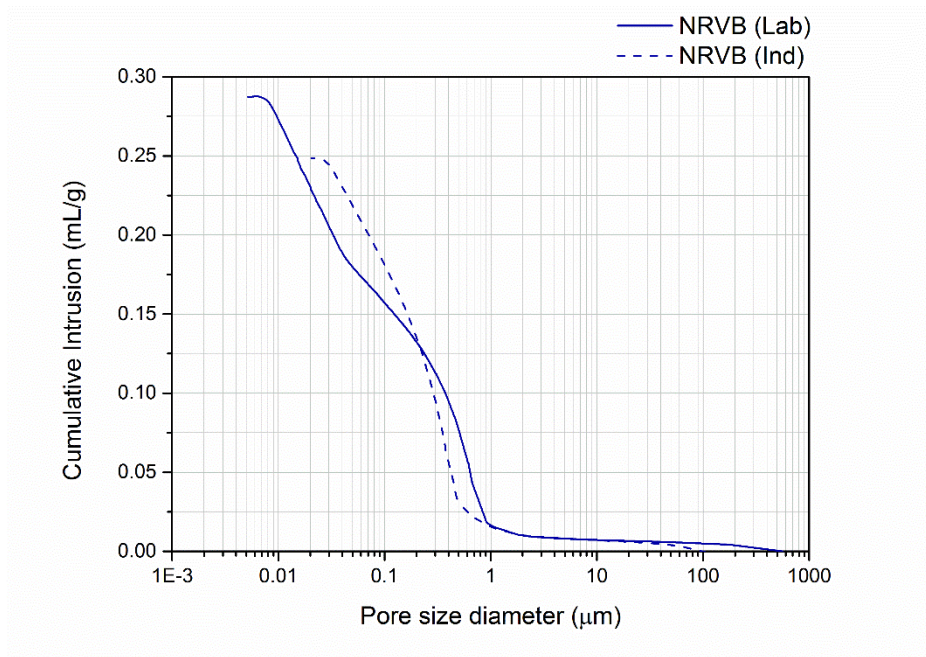


Figure 4.9. Pore entry size distribution of NRVB (Lab) and NRVB (Ind) after 28 days of curing at 20 °C, measured using MIP.

X-ray Computed Tomography (XCT) was also used to study the porosity of NRVB. This technique has the advantage of being non-invasive and allowing three-dimensional reconstructions, but has limitations in spatial resolution. Figure 4.10 shows selected slices of the volume-of-interest (VOI) for the two samples analysed. Quantitative analysis was performed using segmentation of the VOI. A threshold value was chosen based on the line shape of the image histograms, which show peaks of higher and lower absorption voxels, where the lower absorption voxels correspond to surrounding air and internal void space [130], allowing discrimination between pore space and binder phases (solid). The MIP results were used to guide the thresholding process, so the comparison between the results obtained by the two techniques is to some degree influenced by this.

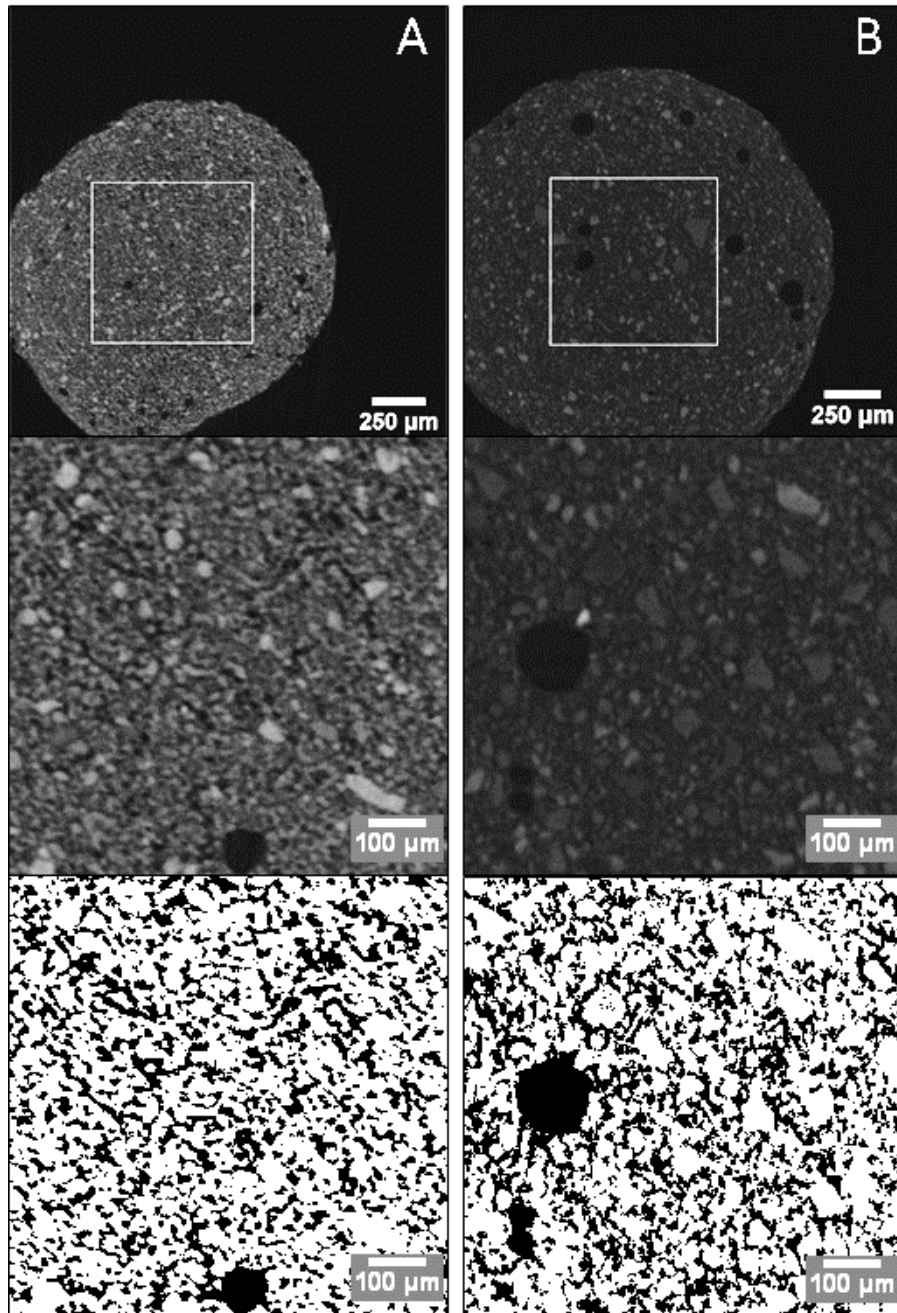


Figure 4.10. XCT data for (a) NRVB (Lab) and (b) NRVB (Ind) cured at 20 °C. Top: Slices through the tomographic reconstruction, showing the selected VOI (square); centre: selected slices through the VOI in each sample; and bottom: segmented into solid (white) and pore (black) regions.

No cracks were observed in the samples at this early age (28 days of hydration). The porosities obtained from tomographic data were $39 \pm 2 \%$ for NRVB (Lab) and $35 \pm 2 \%$ for NRVB (Ind). This difference is related, once more, to the difference observed in the hydration reaction of both cements, due to the smaller particle size and higher surface area of limestone flour.

The porosity results are in the same range as that presented by Heyes et al. [31] ($\sim 40 \%$), however they are lower than those reported by Francis et al. [19], where the porosity measured using MIP and nitrogen

desorption was around 50 %. It is important to note, however, using the density values presented in the work of Francis et al. [19], one can calculate the porosity value as being ~35 %, which brings into question the higher porosity value reported (50 %); the results obtained in this work, therefore, are not dissimilar to those previously reported. Differences in the characteristics between the raw materials used in the 1990's and those used in the present study could give rise to differences in measured porosity, and in the earlier characterisation, there may have been more air bubbles, acquired during the mixing of the cement, that influenced the total porosity detected.

4.2.3: NRVB (40 °C)

In this Section, NRVB samples (made with laboratory and industrial precursors) were synthesised and cured for 28 days (as described above), but with a curing temperature of 40 °C.

Figure 4.11 shows the results of isothermal calorimetry over a 24 hour period. Due to the sensitivity of the equipment, it was impossible to keep the material at 40 °C between the time of the mixture and the actual measurement. Therefore, the first 30 minutes are not considered in this data set. When comparing the heat flow of the two samples analysed, it was possible to observe an increase of the heat flow (almost 3 mW/g) in the stages labelled as 2, 3 and 4 of the hydration process, when compared with the results observed at 20 °C (~ 1.5 mW/g, Figure 4.3). The reaction rate also increased for both samples, for example, the stages labelled 3 and 4 finished after 5 hours at 40 °C, whereas in the samples that were cured in 20 °C, those two hydration stages lasted around 12 hours. This is due to the curing temperature, which leads to an overall increase of the heat flow and an increase of the reaction rate, as observed previously in the literature [142–144].

When comparing the two formulations, the same trend was observed as the samples cured at 20 °C (Figure 4.3), i.e. the heat flow observed for both formulations at 40°C was very similar, and the curve corresponding to the sulphate depletion (labelled 4, Figure 4.11a) showed a more intense reaction in the NRVB (Ind) in comparison to NRVB (Lab). As stated before, this is due to the difference observed in the particle size distribution and surface area, and also the difference of the sulphate content observed between CaCO₃ and limestone flour. Figure 4.11b, shows that the cumulative heat output for both samples was similar and comparable with the results obtained at 20 °C.

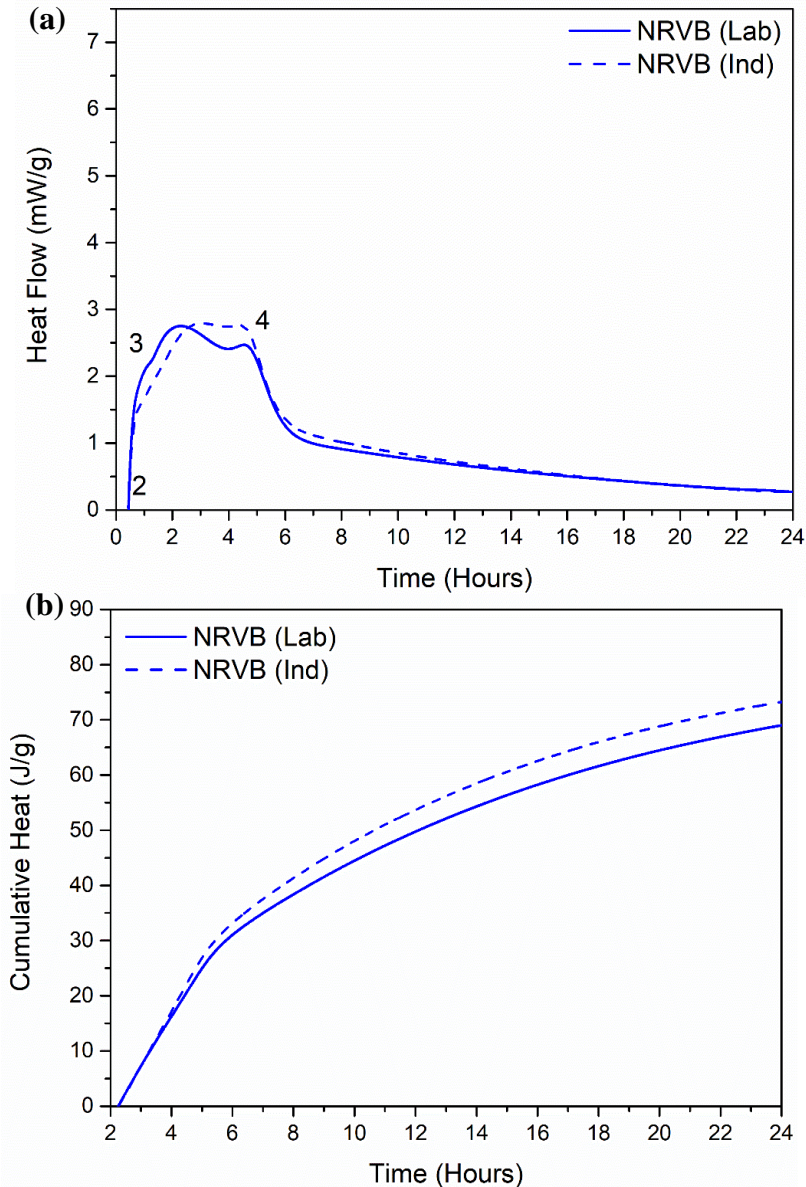


Figure 4.11. (a) Isothermal calorimetry data for NRVB (Lab) and NRVB (Ind) cured at 40 °C. Thermal features identified are: (2) induction period, (3) reaction of alite and formation of calcium silicate hydrate, (4) sulphate depletion; (b) Cumulative heat of NRVB (Lab) and NRVB (Ind).

From the XRD patterns obtained for both samples (Figure 4.12), the same hydrate phases were observed as at 20 °C, being calcite, portlandite, ettringite and calcium monocarboaluminate hydrate. However, no hemicarboaluminate hydrate was present in these samples. The slow transformation of hemicarboaluminate to monocarboaluminate at later curing times has been observed in cementitious materials containing limestone flour [141,145–147]. The observed absence of hemicarboaluminate might indicate that the faster hydration reaction observed at 40 °C led to a faster transformation into monocarboaluminate. No other significant differences were observed between the two formulations.

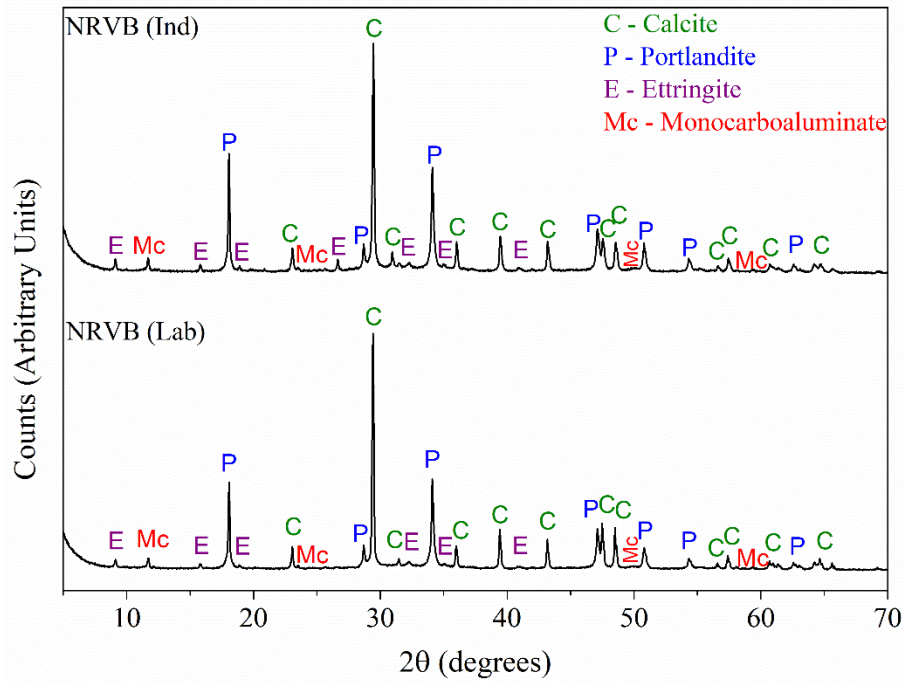


Figure 4.12. X-ray diffraction patterns for (bottom) NRVB (Lab) and (top) NRVB (Ind) after 28 days of curing at 40°C.

TG-MS analysis (Figure 4.13) shows agreement with the previous results. Therefore, as observed in the NRVB samples that were cured at 20 °C, the two peaks between 100 and 200 °C are attributed to the presence of ettringite and AFm phases, while the peaks between 400 to 500 °C, and 650 to 800 °C correspond to portlandite and calcite, respectively. This was observed for both samples, where the same peaks were detected for both formulations. However, for the NRVB (Ind) (Figure 4.13b) an additional peak was observed at ~ 650 °C, corresponding to the presence of magnesian calcite ($\text{Ca}_x\text{Mg}_{(1-x)}\text{CO}_3$), observed also in the NRVB (Ind) sample cured at 20 °C.

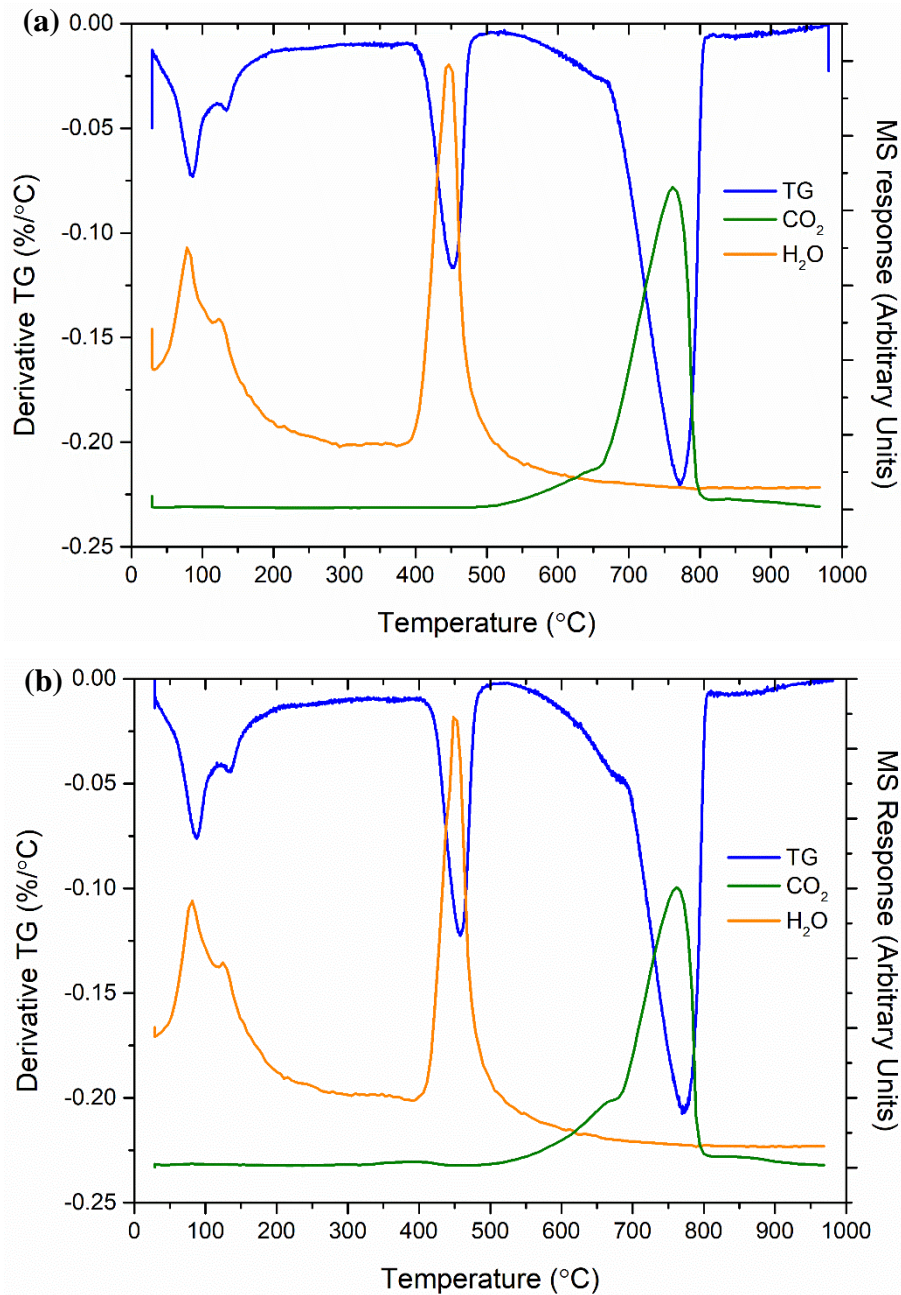


Figure 4.13. TGA-MS data for (a) NRVB (Lab) and (b) NRVB (Ind) after 28 days of curing at 40 °C.

The different hydrate phases identified through XRD and TGA-MS were observed in the SEM-EDX analysis, as shown in Figure 4.14. Portlandite crystals were observed in both samples (labelled A, Figure 4.14), which are surrounded by the Ca and Si-rich area that might once more correspond to the C-S-H gel (labelled B, Figure 4.14). The areas containing high concentrations of mainly aluminium are suggestive of the presence of AFm phases, in this case monocarboaluminate. The needle-shape phases rich in aluminium and sulphur are indicative of the presence of ettringite and/or sulphate-containing AFm phases. Comparing the SEM images of the two formulations, it was possible to observe similar

microstructures, consistent with the identification of the same hydrate phases. However, as observed for the samples at 20 °C, the matrix of the NRVB formulated using industrial materials showed a more fine grained morphology, which is in agreement with the observed smaller particle size of the limestone flour (Figure 4.1a).

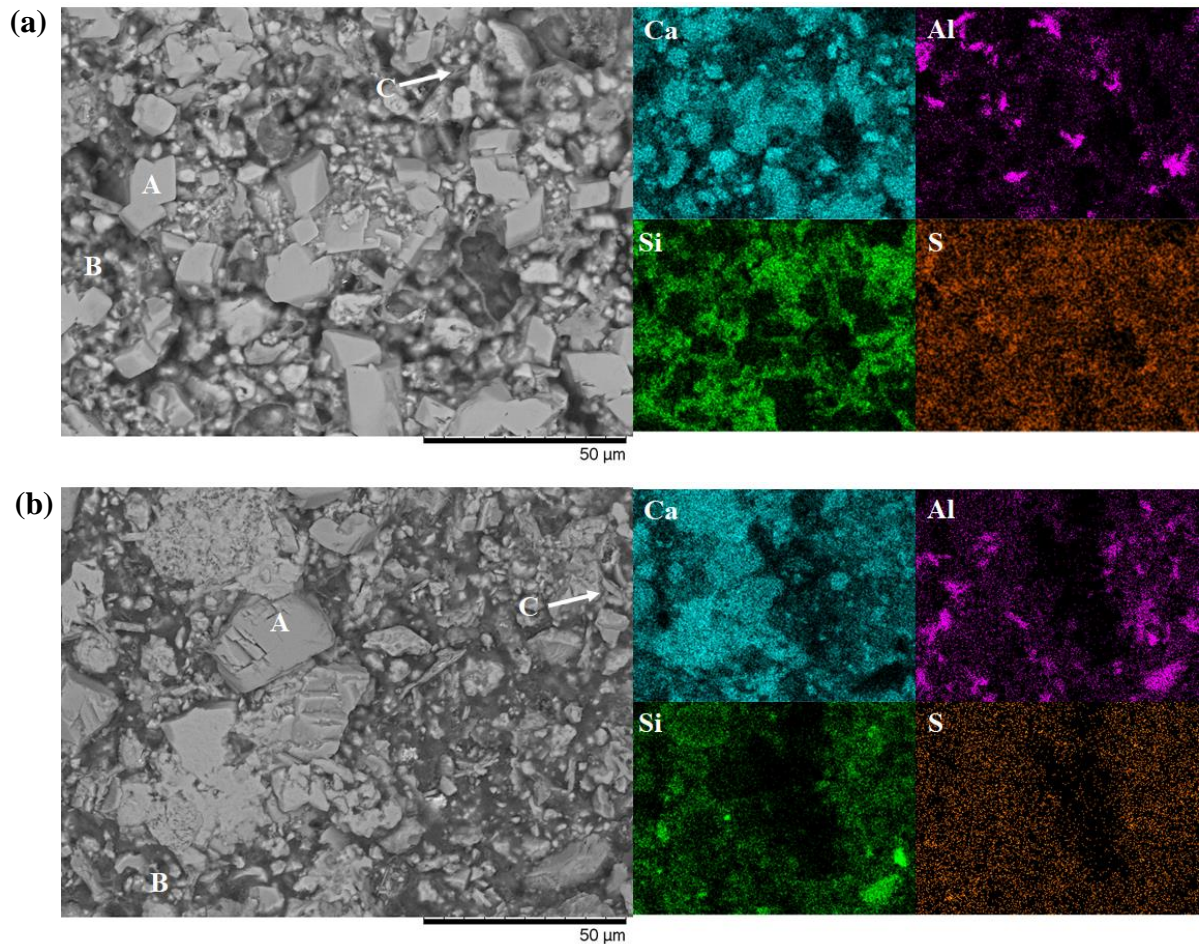


Figure 4.14. BSE SEM micrographs of (a) NRVB (Lab) and (b) NRVB (Ind) at 28 days of curing at 40 °C, with the corresponding EDX maps.

²⁹Si MAS NMR analysis was performed on both NRVB formulations, and slight differences were observed when comparing to the results obtained for the samples cured at 20 °C. From Figure 4.15, it was observed that the peaks that were attributed to alite and belite in Figure 4.7 were not present. A possible explanation is the more rapid hydration reaction observed at 40 °C (Figure 4.11) led to the full reaction of Portland cement. In Figure 4.15b, a peak at around -70 ppm is present, which could be attributed to the presence of belite. However, taking into account the results obtained through XRD (Figure 4.12) and SEM-EDX (Figure 4.14), where no belite was detected, it is considered that if belite is present it will be below the signal to noise obtained in the measurements.

In terms of C-S-H structure, contributions from Q¹ (Q¹(I) -79 ppm; Q¹(II) -82 ppm), Q²(1Al), Q², Q³ and Q³(1Al) silicate environments were observed in both formulations. The presence of the Q²(1Al)

and $Q^3(1Al)$ resonances show the incorporation of aluminium in the C-(A)-S-H structure, also visible in the ^{27}Al MAS NMR spectra shown in Figure 4.16. It seems that more aluminium is being incorporated in the C-S-H in the NRVB samples cured at 40 °C, when comparing to the samples cured at 20 °C. Previous studies showed that with increasing temperatures, an increase of the incorporation of this element into the bridging sites of C-(A)-S-H phase is observed [148,149].

Comparison between the two NRVB formulations showed slight differences in the intensities of different peaks, for example in Q^3 and $Q^3(1Al)$. The slightly higher reactivity of the raw materials used in the NRVB (Ind), due to the higher surface area of the limestone flour, might be the reason for the observed differences.

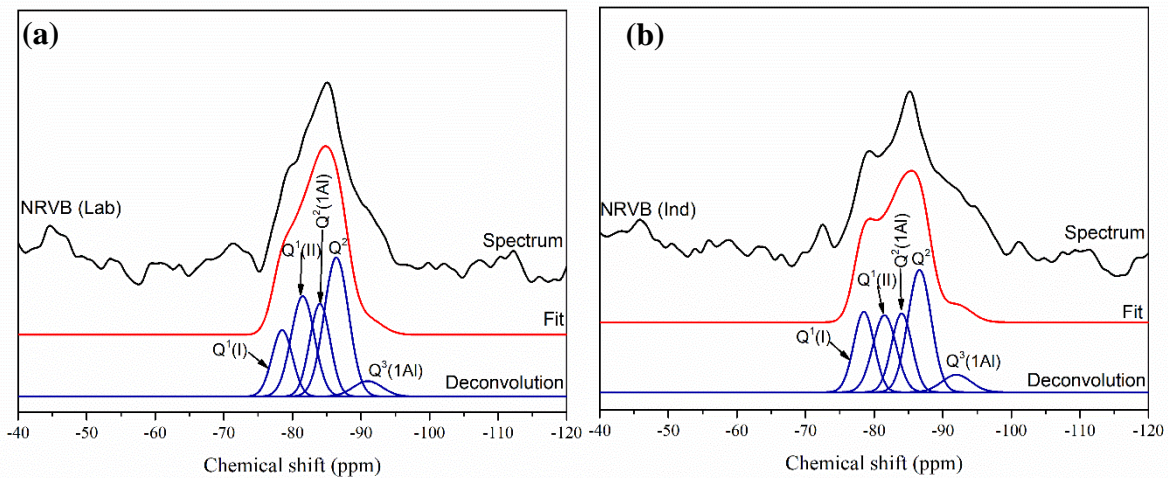


Figure 4.15. ^{29}Si MAS NMR spectra, and deconvolution results, for (a) NRVB (Lab) and; (b) NRVB (Ind) after 28 days of curing at 40 °C.

From the ^{27}Al MAS NMR spectra (Figure 4.16) it was possible to identify similar peaks to those observed in the NRVB samples that were cured at 20 °C. The peaks visible at approximately 14 and 9 ppm correspond to the octahedrally coordinated Al in ettringite and AFm phases. The broad peak observed at around -67 ppm is attributed to the incorporation of aluminium in C-S-H, in agreement with the observed peaks corresponding to $Q^2(1Al)$ and $Q^3(1Al)$ in the ^{29}Si MAS NMR spectra (Figure 4.15). This broad peak was observed in both samples at 40 °C, unlike the samples that were cured at 20 °C (Figure 4.8), where this peak was only evident in the NRVB sample formulated with industrial materials. Moreover, the peaks corresponding to ettringite and AFm phases show different intensities between the NRVB (Lab) that was cured at 20 °C and 40 °C. In this sample, the peak intensity of AFm phases is slightly higher than the peak intensity of ettringite, whereas for the same sample cured at 20 °C the opposite occurred. A possible explanation is again related to the higher degree of reaction observed for the samples that were cured at 40 °C, where the hydration of more calcium carbonate led to the formation of more AFm phases, like monocarboaluminate [141,147]. For the samples that were

formulated with industrial materials, no significant differences were observed between the two curing temperatures.

Regarding differences between the two formulations cured at 40 °C, a slightly higher intensity of the peak corresponding to ettringite was observed for the sample that was formulated with industrial materials, which might be due to the slightly higher sulphur content observed in these samples (Table 4.1), i.e. more sulphate is available for the formation of this AFt phase [150].

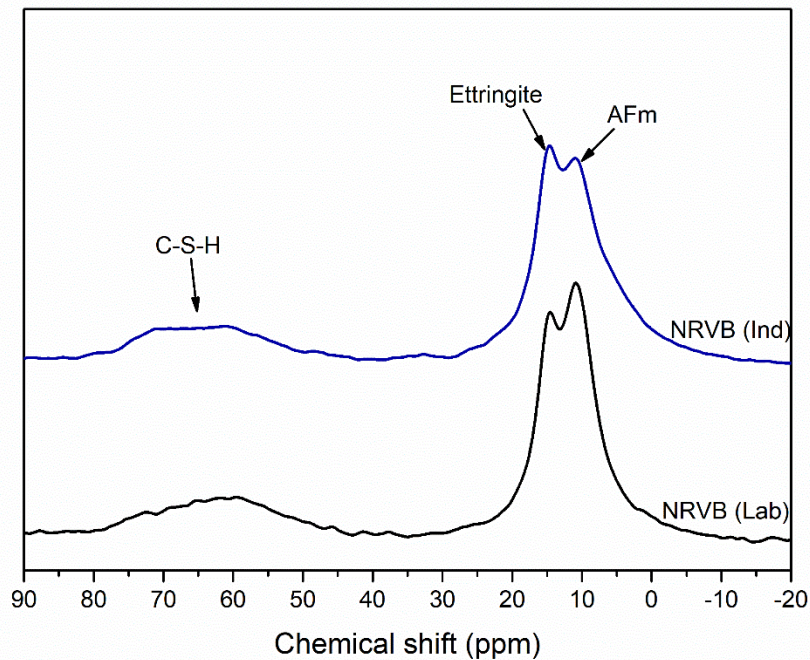


Figure 4.16. ^{27}Al MAS NMR spectra of NRVB (Lab) and NRVB (Ind) after 28 days of curing at 40 °C.

To study the porosity of both NRVB formulations cured at 40 °C, only MIP was used due to the unavailability of the XCT equipment for these specific samples. Nonetheless, from Figure 4.17 it is possible to observe similarities in terms of porosity with the samples that were cured at 20 °C. A smaller pore entry size was observed for the sample that was formulated with industrial materials (below 0.9 μm) when comparing to the NRVB (Lab) (below 1.5 μm). These values were slightly higher than the ones obtained in the samples cured at 20 °C, which might be due to a slight coarsening of the microstructure with higher temperature curing [151,152]. However, the overall total porosity measured for the NRVB samples cured at 40 °C was lower than for the samples cured at 20 °C, being around $28 \pm 3 \%$ for NRVB (Lab) and $30 \pm 3 \%$ for NRVB (Ind). Once again, the higher degree of hydration observed for the samples that were cured at 40 °C, and consequently the formation of more hydrated phases, might be the reason for the observed difference [153]. No significant differences were observed between the total porosities of the two formulations cured at 40 °C.

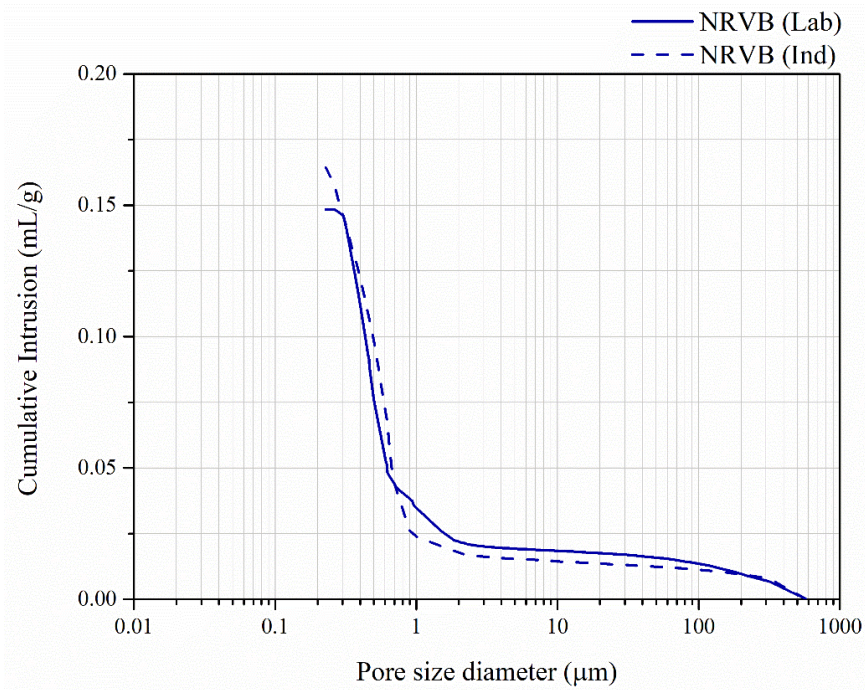


Figure 4.17. Pore entry size distribution of NRVB (Lab) and NRVB (Ind) after 28 days of curing at 40 °C, measured using MIP.

4.3: Cebama Reference Cement Characterisation

4.3.1: Precursor materials

XRF analysis of the Cebama reference cement raw materials (PC, BFS and silica fume) is shown in Table 4.2.

Table 4.2. Major constituents of raw materials, as determined by XRF and represented as oxides
(precision $\pm 0.1\%$)

Compound (wt.%)	CEM I 42.5 N	Blastfurnace slag	Silica fume
Na₂O	0.1	0.6	0.3
MgO	0.9	8.2	0.8
Al₂O₃	3.8	10.1	0.4
SiO₂	21.9	34.8	95.5
P₂O₅	0.1	<0.05	<0.05
K₂O	0.6	0.6	1.0
CaO	65.5	39.8	0.8
TiO₂	0.2	1.9	<0.05
Mn₃O₄	0.3	0.4	<0.05
Fe₂O₃	4.8	1.0	0.8
BaO	0.05	0.06	<0.05
Loss Free Total	98.2	97.5	99.6

Particle size analysis was also performed on these powders, and the results presented in Figure 4.18 show that in the case of PC and BFS, 50 % of the particles were less than 14.4 μm and 11.4 μm , respectively. The wider particle size distribution presented by silica fume shows the agglomerative nature of this material. From Figure 4.18, where ultrasonic bath and dispersant were applied, 50 % of the particles were less than 18.2 μm and 90 % were less than 52.2 μm . The use of ultrasonic treatment (and/or high-shear mixer) and dispersants in the form of superplasticizers is very common in cements that have silica fume in their formulations, as a way of improving the performance of this material [62,154]. However, it seems that even with this pre-treatment, agglomeration occurred, as silica fume particle size should be smaller than Portland cement. Arvaniti et al. [155], observed the same problem; they rationalised that when particles of silica fume are smaller than 1 μm , it is difficult to separate them due to the Van der Waals forces, even after 55 min of sonication.

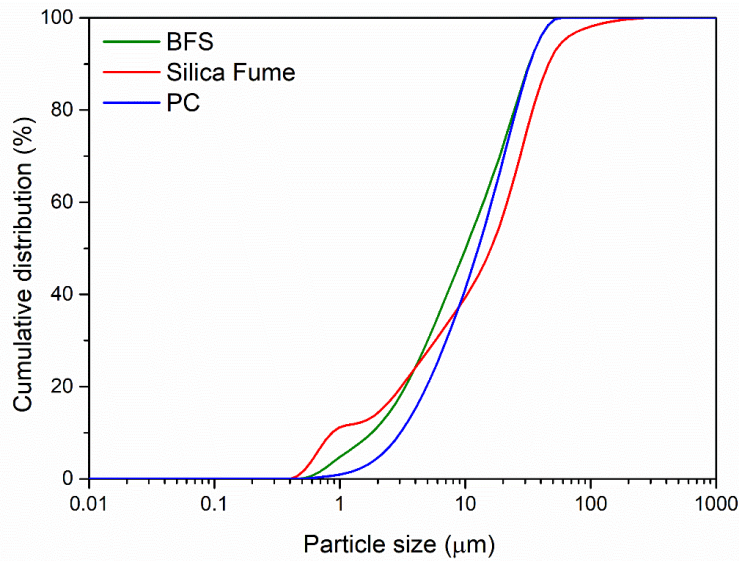


Figure 4.18. Particle size distribution of Portland cement (PC), blast furnace slag (BFS) and silica fume.

Through XRD analysis (Figure 4.19), it was possible to identify the mineralogy of the different raw materials. The CEM I 42.5N spectrum (Figure 4.19a) shows the expected clinker composition: alite (Ca_3SiO_5 ; PDF 01-070-1846), belite (Ca_2SiO_4 ; PDF 01-086-0398), aluminat ($\text{Ca}_3\text{Al}_2\text{O}_6$; PDF 01-070-0839), ferrite ($\text{Ca}_2\text{AlFeO}_5$; PDF 01-071-0667), gypsum ($\text{CaSO}_4 \cdot 2\text{H}_2\text{O}$; PDF 33-0311) and calcite. The Portland cement used in this formulation is slightly different from the one used in the NRVB formulation, varying only the standard strength class, which here is 42.5 and for the NRVB is 52.5. The presence of significant diffuse scattering features in the BFS and silica fume diffractograms (Figure 4.19b,c) shows the amorphous nature of these cementitious materials. In the silica fume diffractogram (Figure 4.19c), it was possible to identify peaks corresponding to quartz, the main component of this precursor material.

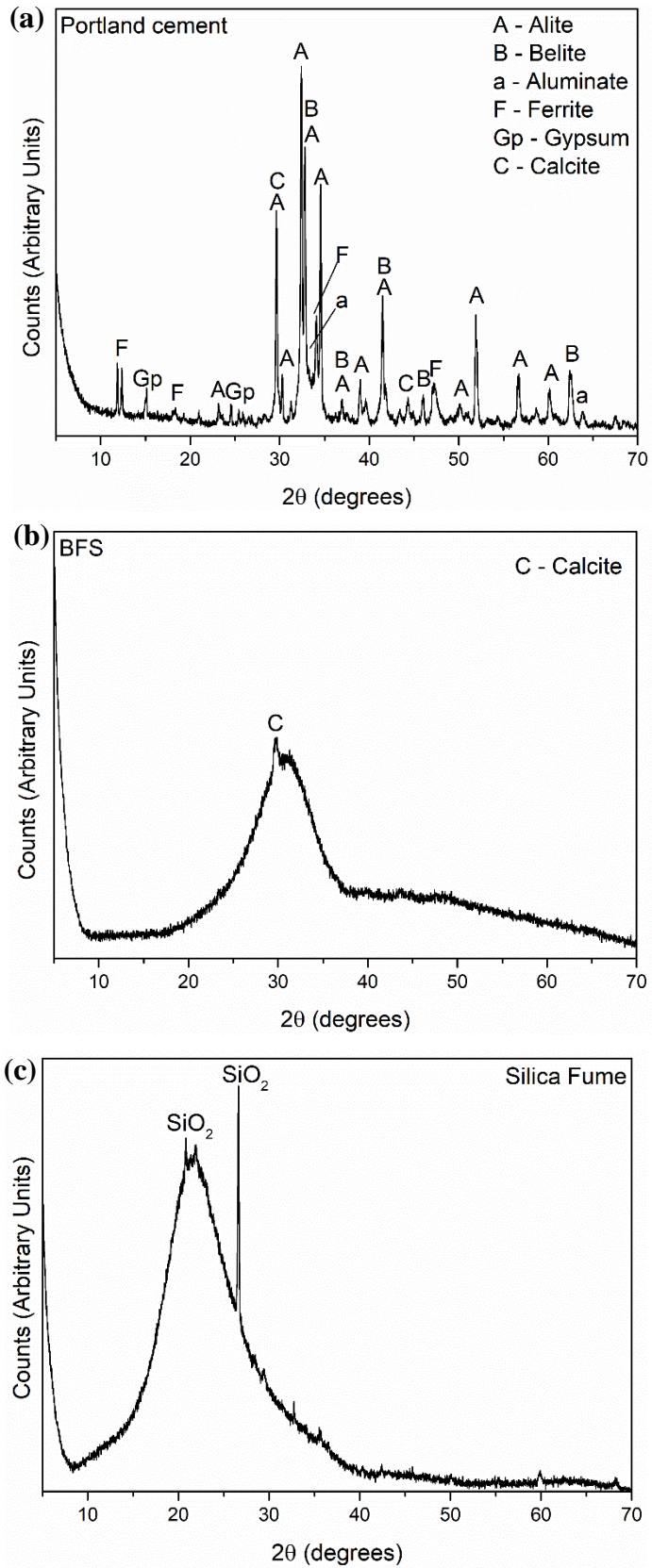


Figure 4.19. X-ray diffraction patterns of (a) CEM I 42.5N, (b) BFS and (c) silica fume.

4.3.2: Cebama Reference Cement (20 °C)

Through isothermal calorimetry, performed at 20 °C for 72 hours (Figure 4.20), it was observed that the peak heat release of the Cebama reference cement was low when compared to normal Portland cement formulations, being less than 1 mW/g and above 5 mW/g respectively [46]. This is expected due to the high replacement of PC with supplementary cementitious materials (SCM) [46]. This low heat of hydration is one of the main desired characteristics for this type of cement, to minimise, for example, the formation of micro-cracks in the material [44,45]. In Figure 4.20, it can be observed that the induction period (labelled 2) was longer than for the normal PC cements (between 1 to 2 hours usually); this is also due to the high replacement of PC with SCMs in this cement [49,156,157]. BFS is a latent hydraulic material which starts reacting at later ages, and silica fume retards hydration as its reactivity increases only after the pore solution pH is above 10.7 [47,49,158]. The addition of superplasticiser can be also a contributor to this retardation of the acceleration stage (labelled 3) [159]. Another interesting observation is the continuous slow release of heat after period 4, which evidences the continuous hydration of the Cebama reference cement paste, especially the reaction of BFS and silica fume at later ages.

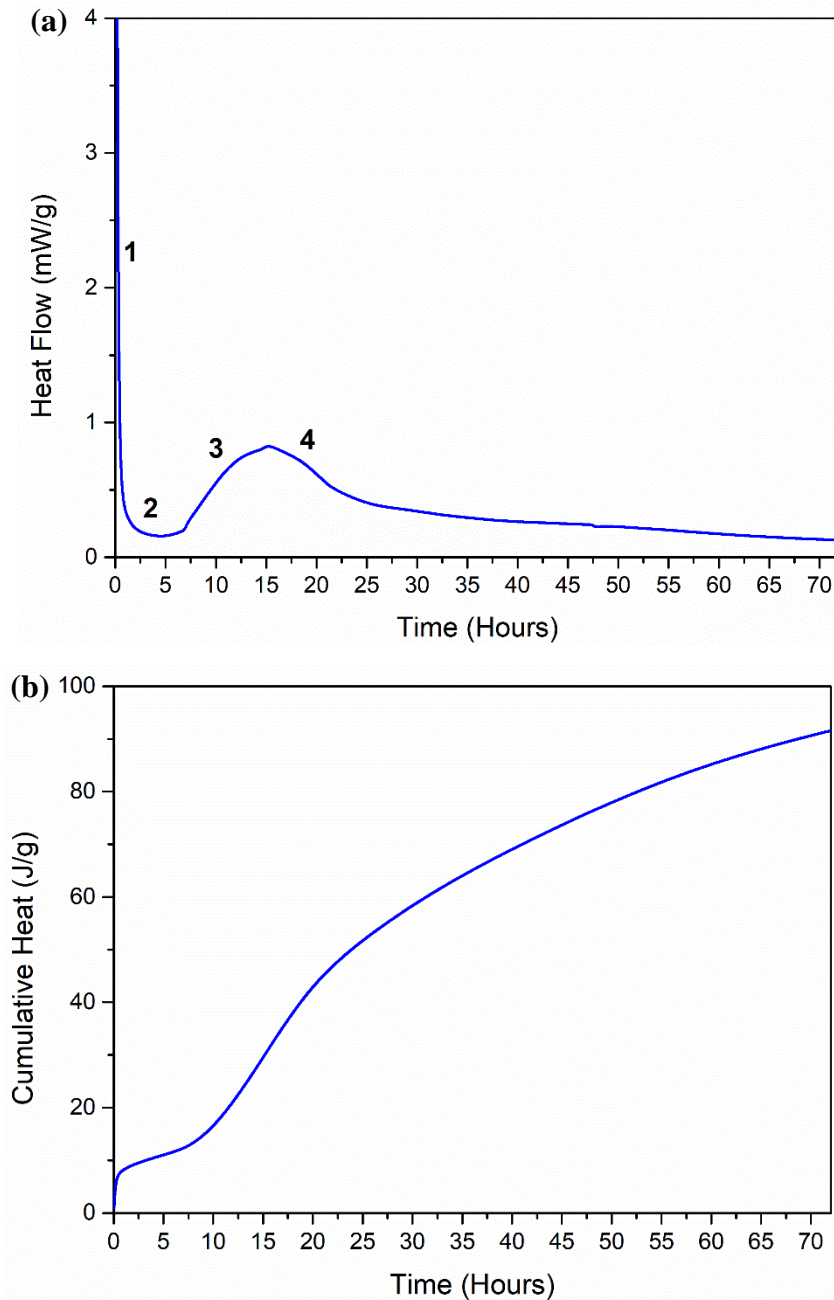


Figure 4.20. (a) Isothermal calorimetry data for Cebama reference cement paste cured at 20 °C. Thermal features identified are: (1) dissolution and aluminite reaction (2) induction period, (3) reaction of alite and formation of calcium silicate hydrate, (4) sulphate depletion; (b) Cumulative heat of Cebama reference cement paste.

After 28 days of curing at 20 °C, the main hydrate phases identified by XRD (Figure 4.21) were calcite, ettringite, a hydrotalcite-like phase (meixnerite, $Mg_4Al_2(OH)_{14} \cdot 3H_2O$; PDF 00-014-0191) and the AFm phase monocarboaluminate. Some unreacted PC was observable as peaks of alite and belite, and it is very likely that unreacted BFS and silica fume are also present, although their glassy nature makes their identification by XRD challenging in the presence of C-S-H. The presence of low quantities of

portlandite may be indicative of limited reactivity of the silica fume at early curing time; either kinetic (due to the pH not be high enough for the silica fume to react quickly) or mass transport limitations mean that the portlandite has not yet been fully consumed by the pozzolanic reaction. Previous studies observed the same hydrate phase composition for similar cement blends [42,45].

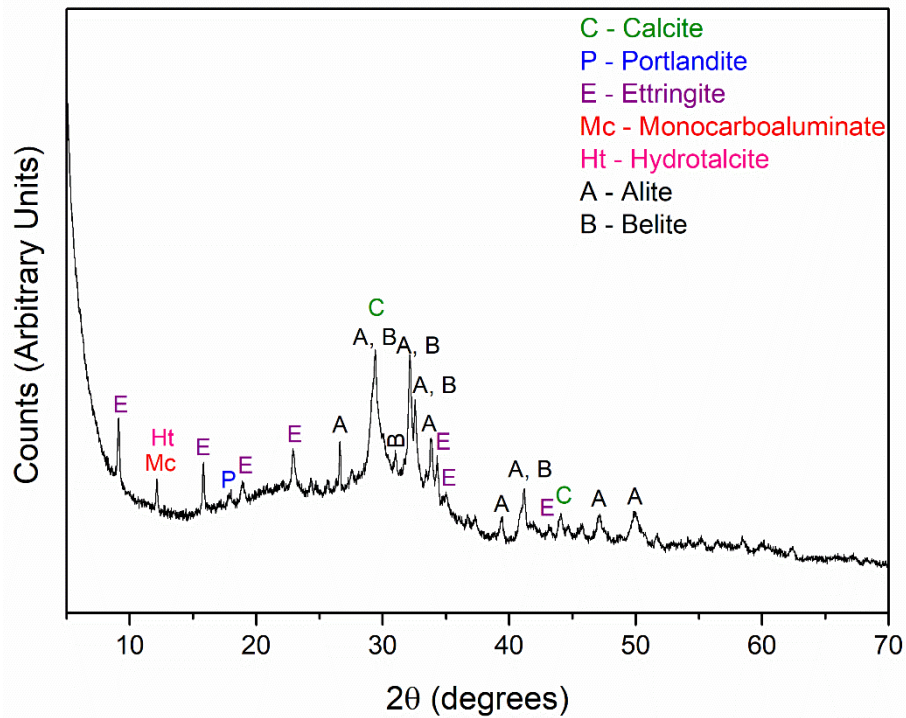


Figure 4.21. X-ray diffraction pattern of Cebama reference cement paste after 28 days of curing at 20 °C.

The results of TG-MS analysis of this paste are shown in Figure 4.22. It was possible to identify a broad peak corresponding to ettringite and AFm phases between 100 °C and 200 °C [52,90]. Some C-S-H was also observed via the mass loss between 50 °C and 100 °C [52,90]. In agreement with its low quantity observed in XRD, from the TG-MS data the presence of portlandite was not observed. The peak at around 800 °C corresponds to the presence of calcite.

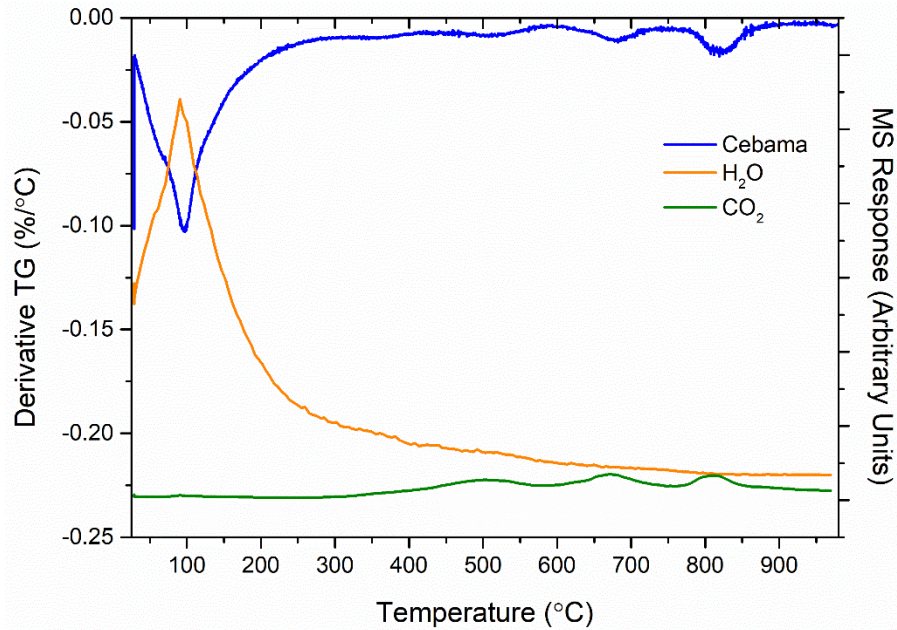


Figure 4.22. TGA-MS data for Cebama reference cement paste after 28 days of curing at 20 °C.

From Figure 4.23 (SEM-EDX analysis), the presence of unreacted agglomerates of silica fume, and BFS (labelled A and B respectively in Figure 4.23), is visible. The presence of the former component can be explained by the inclusion of this raw material in excess when compared to the amount of portlandite present in this system [160], and the evidently agglomerated nature of the silica fume particles. Also, the low w/s ratio used in the formulation, and consequent difficulty in dispersing the silica fume, can be a possible explanation. In the case of BFS, it is well known that this material reacts very slowly, being still present even after almost 20 years when used at high volume in cements [161]. In terms of hydrate phases, C-S-H gel was identified as the matrix area (labelled C, Figure 4.23), rich in silica and calcium, around the silica fume and BFS particles.

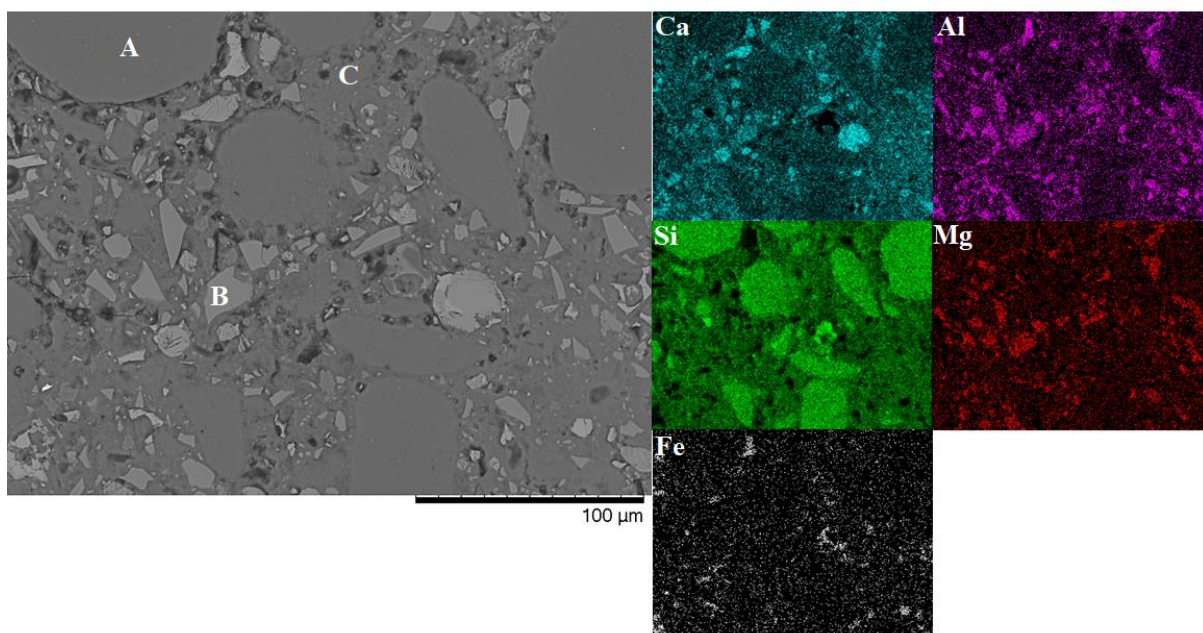


Figure 4.23. BSE SEM micrograph of Cebama reference cement paste after 28 days of curing at 20 °C, with the corresponding EDX maps.

The unreacted Portland cement was visible in the ^{29}Si MAS NMR spectra (Figure 4.24a), which shows the presence of alite (chemical shift at -69 and -73 ppm) and belite (-70.8 ppm) [90]. The peaks from these phases, alongside the $\text{Q}^1(\text{I})$, $\text{Q}^1(\text{II})$ and $\text{Q}^2(1\text{Al})$ sites from the C-A-S-H gel phase, are overlapped by the broad BFS peaks, which might affect the quantification of the Ca/Si ratio within the C-A-S-H gel [162]. The two Q^1 environments are separated by the nature of the charge-balancing cations, monovalent and divalent, which are due to the different field strengths leading to separate resonances [117,162,163]. Resonances exhibiting chemical shifts corresponding to the presence of Q^1 ($\text{Q}^1(\text{I})$ - 73.9 ppm and $\text{Q}^1(\text{II})$ - 78.9 ppm), $\text{Q}^2(1\text{Al})$ (-81.6 ppm), Q^2 (-84.5 ppm), Q^3 (-96.1 ppm) and $\text{Q}^3(1\text{Al})$ (-89.8 ppm) silicon environments in C-A-S-H were also identified [61,139,140]. The existence of Al within the first coordination sphere of Q^n silicon sites demonstrates the incorporation of this element in an Al-substituted calcium silicate hydrate (C-A-S-H) binder phase. This was also visible in the ^{27}Al NMR spectrum (Figure 4.24b), from the presence of a broad tetrahedral Al peak (between 80 and 50 ppm) that contains contributions from Al^{IV} in C-A-S-H, and also from unreacted BFS [164]. In the octahedral Al region of Figure 4.24b, a peak corresponding to ettringite (14 ppm) and a small shoulder at the chemical shift around 9 ppm, corresponding to the presence of AFm and hydrotalcite-like phases, was also identified. These results are in agreement with the XRD and TG-MS data shown above.

To obtain the total porosity of the Cebama reference cement paste cured at 20 °C for 28 days, MIP was performed. XCT analysis was not performed for this sample due to unavailability of the equipment.

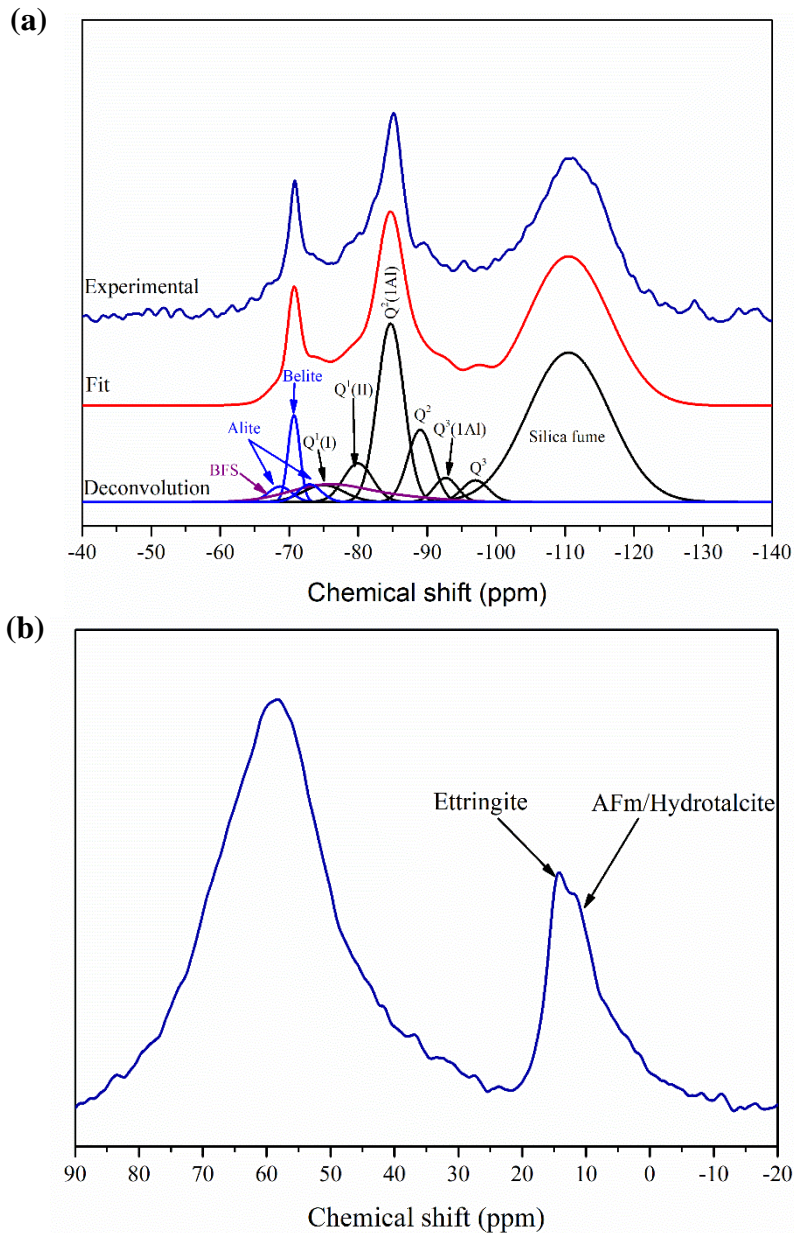


Figure 4.24. (a) ^{29}Si MAS NMR spectra and deconvolution results, and (b) ^{27}Al MAS NMR spectra, of Cebama reference cement paste after 28 days of curing at 20 °C.

From Figure 4.25, it is evident that the bulk of pores had entry sizes below 0.02 μm . The corresponding total porosity obtained from this measurement was around $16 \pm 3 \%$. This low value of total porosity shows the high density of this material after 28 days of curing.

The total porosity value obtained in this study is lower than that reported by Codina et al. for a blended cement of similar SCM content [45], where the porosity measured through MIP was around 34.9 %

after 1 month and 32.6 % after 3 months. However, the w/s ratio used in that study was around 0.5, which is much higher than the w/s ratio used in the present work (0.25), which likely led to the obtained higher porosity. In another study, the porosity measured through MIP, in a mortar sample composed of PC, silica fume and fly ash (w/s ratio of 0.5) was around 23 % after 3 months, being around the same range as observed here [44].

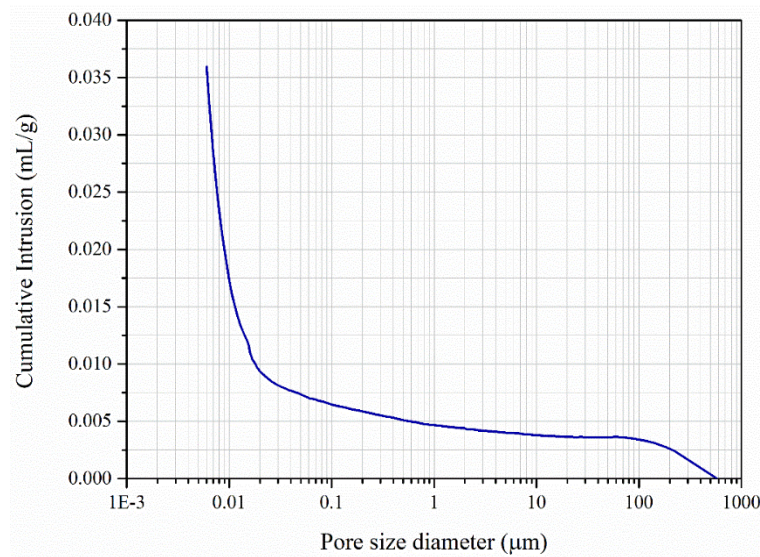


Figure 4.25. Pore entry size distribution of Cebama reference cement paste after 28 days of curing at 20 °C, determined using MIP.

4.3.3: Cebama Reference Cement (40 °C)

Isothermal calorimetry was performed under the same conditions as described in Section 4.2.3 for the NRVB cement at 40 °C, with the same limitation of keeping the material at 40 °C at the time of the mixing, and so the first 30 minutes are not considered in this data set, and the initial peak (labelled 1 in Figure 4.20) is not observable. From Figure 4.26 it was possible to observe that the hydration reaction occurs more quickly than in the sample that was cured at 20 °C (Figure 4.20). For example, the hydration stages labelled as 3 and 4 occurred between 5 and 15 hours at 40 °C (Figure 4.26), compared to between 10 and 25 hours at 20 °C (Figure 4.20). Further, the cumulative heat was higher at 40 °C of curing (around 120 J/g) when compared to 90 J/g at 20 °C. This is expected and has been observed in previous studies [165,166].

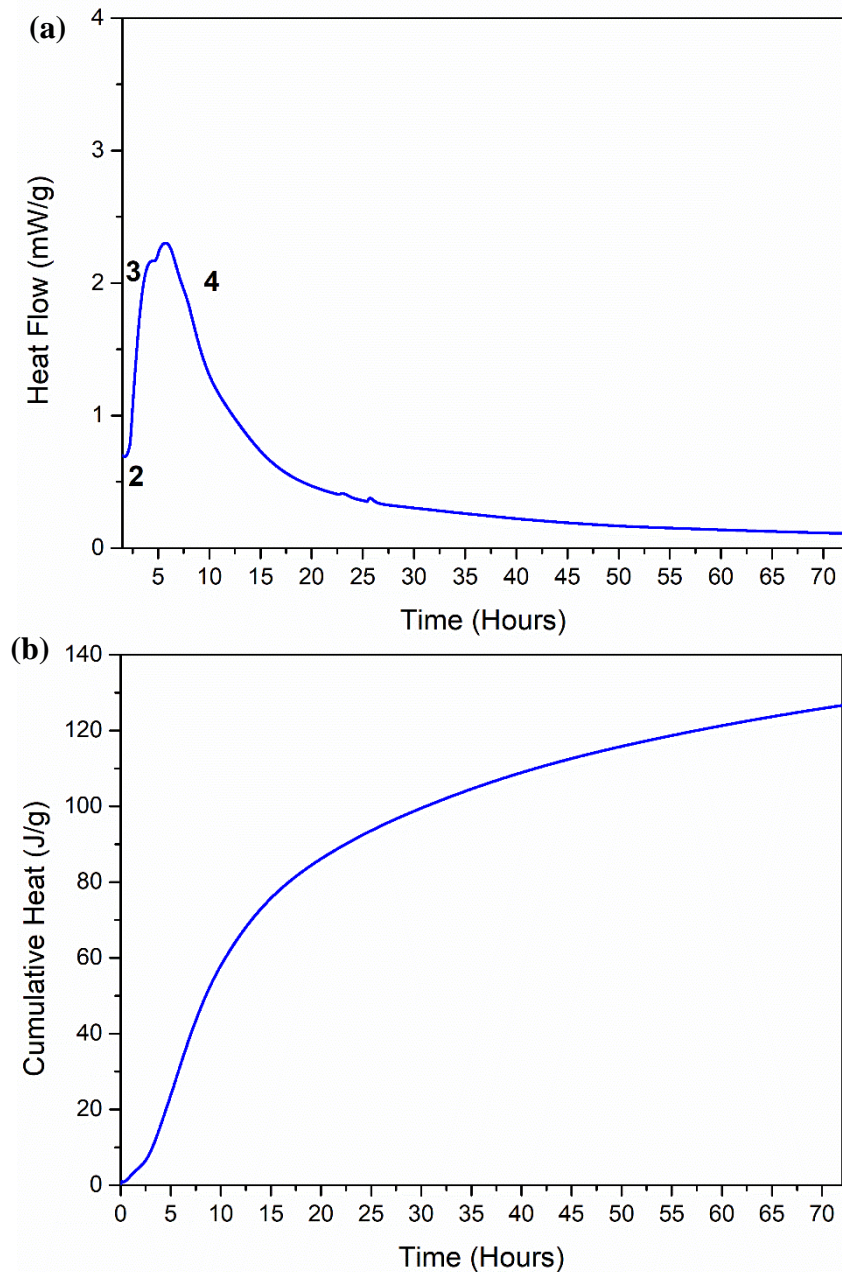


Figure 4.26. (a) Isothermal calorimetry data for Cebama reference cement paste cured at 40 °C. Thermal features identified are: (2) induction period, (3) reaction of alite and formation of calcium silicate hydrate, (4) sulphate depletion; (b) Cumulative heat of Cebama reference cement paste.

Regarding the hydrate phases present after 28 days of curing at 40°C, a similar composition to the one observed at 20 °C was determined by XRD, as shown in Figure 4.27. Unreacted Portland cement was observed through the presence of alite and belite, whereas the broad scattering between 15° and 35° (2θ) is indicative of the presence of unreacted silica fume and BFS. The main hydrate phases present were calcite, ettringite, AFm phases and hydrotalcite.

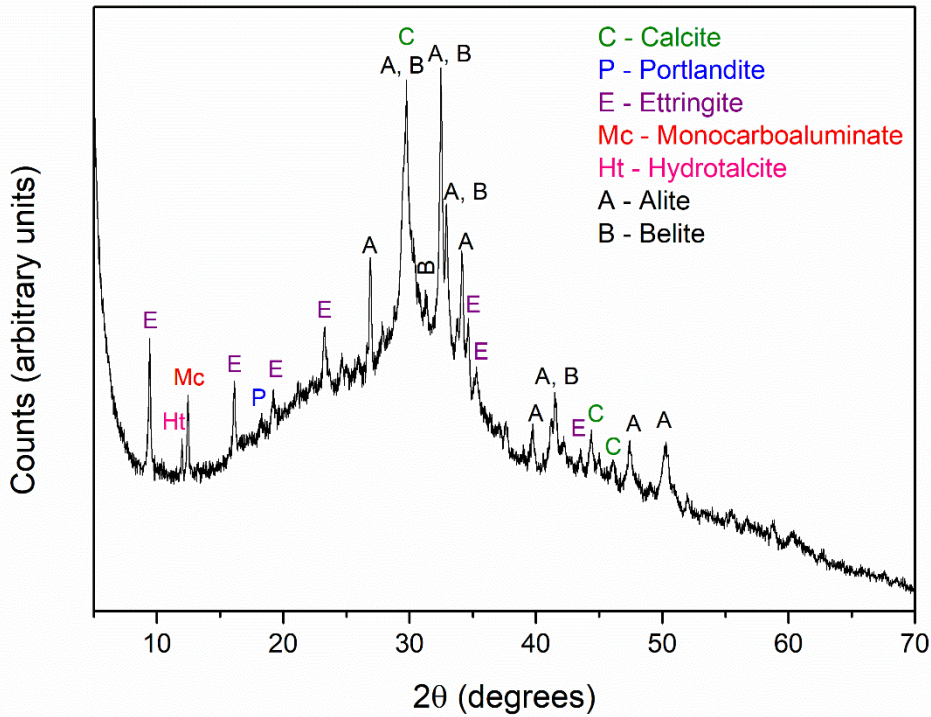


Figure 4.27. X-ray diffraction pattern of Cebama reference cement paste after 28 days of curing at 40 °C.

From TG-MS analysis (Figure 4.28), a slight increase in the width of the peak before 100 °C might indicate that more C-S-H is being formed in the cement cured at 40 °C than at 20 °C. The faster hydration reaction observed in the calorimetry results (Figure 4.26) correlates well with the reaction happening faster and therefore more C-S-H being formed.

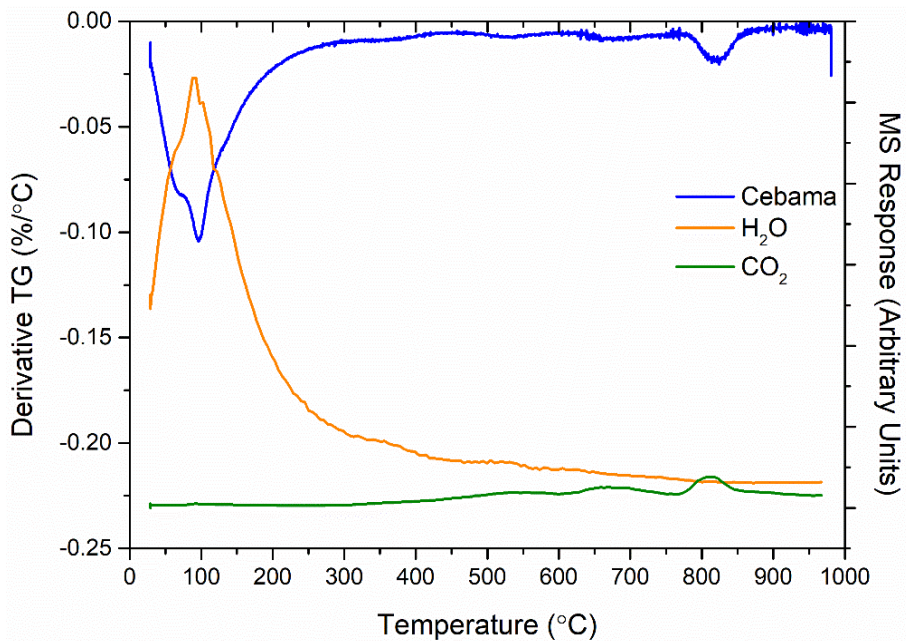


Figure 4.28. TGA-MS data for Cebama reference cement paste after 28 days of curing at 40 °C.

From the SEM-EDX images (Figure 4.29), a similar microstructure was observed at 40 °C when compared to the same sample cured at 20 °C. In Figure 4.29, it is possible to identify a combination of unhydrated material as silica fume (labelled A) and BFS (labelled B), and hydrated phases (labelled C).

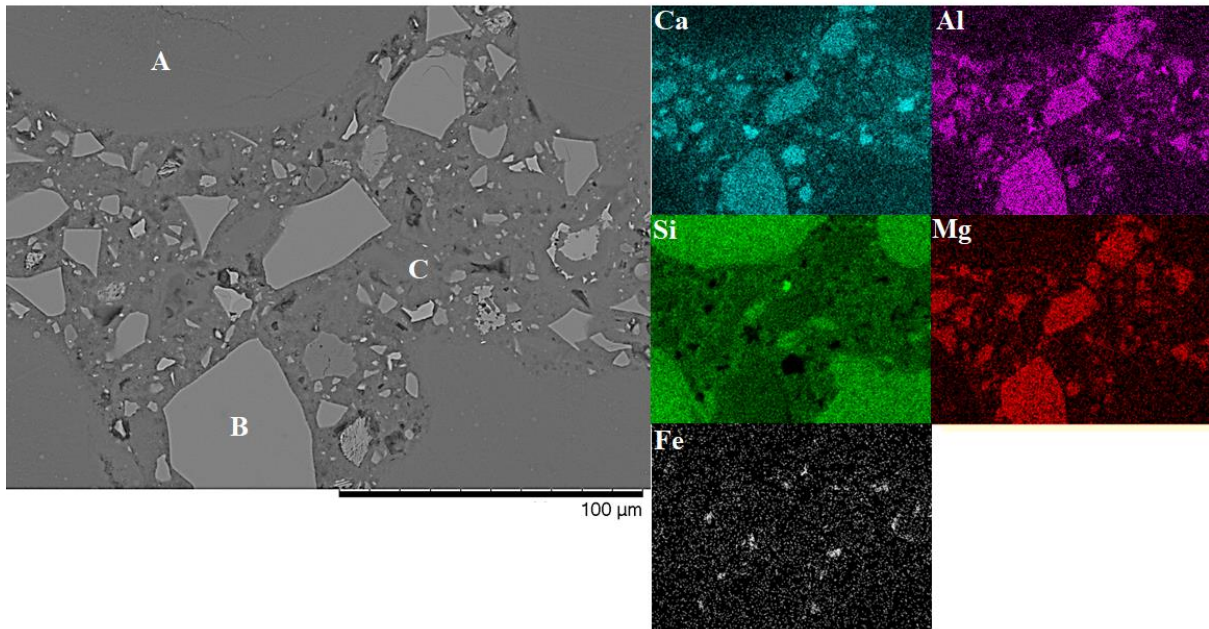


Figure 4.29. BSE SEM micrograph of Cebama reference cement paste after 28 days of curing at 40 °C, with the corresponding EDX maps.

Similar results were obtained through ^{29}Si MAS NMR analysis when comparing to the samples that were cured at 20 °C. In Figure 4.30a, the same deconvolution was performed, with the unreacted material identified through the presence of alite, belite, BFS and silica fume. The C-S-H structure is mainly identified through the presence of Q^1 ($\text{Q}^1(\text{I})$ and $\text{Q}^1(\text{II})$), $\text{Q}^2(1\text{Al})$, Q^2 , Q^3 and $\text{Q}^3(1\text{Al})$ silicon environments. The presence of $\text{Q}^2(1\text{Al})$ and $\text{Q}^3(1\text{Al})$ confirms the incorporation of aluminium in the C-S-H, as was observed in the sample that was cured at 20 °C. This is also visible in the ^{27}Al MAS NMR spectrum (Figure 4.30b), through the presence of the broad peak between 80 and 50 ppm, which corresponds to Al^{IV} in C-S-H, and also to unreacted BFS. The presence of ettringite and AFm/hydrotoalcite-like phases is identified through the peak at 14 ppm and the shoulder at 9 ppm, respectively. The intensity of the peak corresponding to ettringite is higher when comparing to the sample that was cured at 20 °C, which might be related to the slightly higher rate of hydration observed due to the increased curing temperature used.

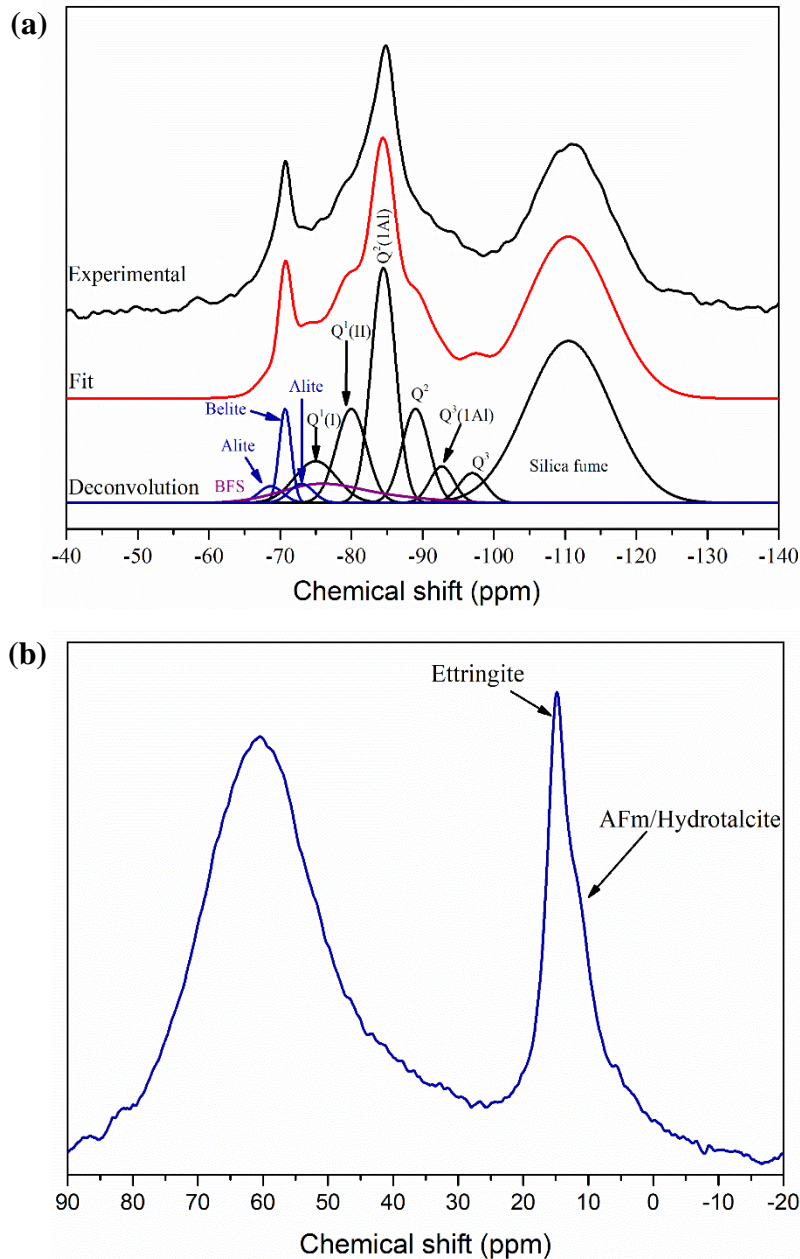


Figure 4.30. (a) ^{29}Si MAS NMR spectra and deconvolution results, and (b) ^{27}Al MAS NMR spectra, of Cebama reference cement paste after 28 days of curing at 40 °C.

Figure 4.31 shows the pore entry size diameter in relation to the cumulative intrusion, as measured by MIP. The curve allocates the bulk of pores to pore entry sizes below 0.1 μm , and the total porosity was measured as around $19 \pm 3 \%$. This porosity is very similar, within the error, to the porosity obtained for the sample that was cured at 20 °C.

For this sample, XCT analysis was also performed. The data obtained through this technique were analysed by Dr. Haris Paraskevoulakos, from University of Bristol, and due to the method of analysis used (MIP results were not used to guide the threshold position, as was the case for NRVB) and the

resolution of the equipment (1.5 microns), only the macroporosity was identified (pores > 1.5 μm). In this way, the macroporosity obtained was around $3.8 \pm 1.4 \%$. This demonstrates the dense nature of this material, with the porosity mainly composed of small pores (i.e. nanoporosity).

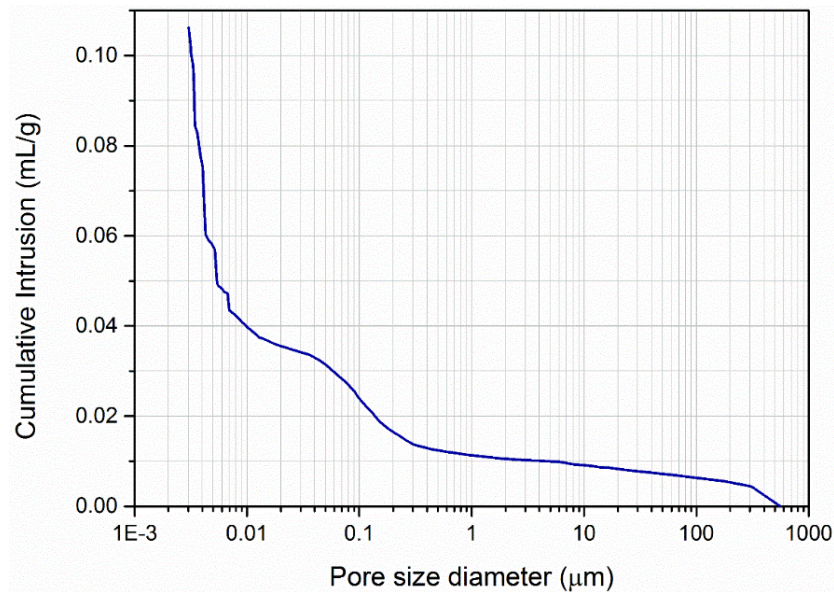


Figure 4.31. Pore entry size distribution of Cebama reference cement paste after 28 days of curing at 40 °C, determined using MIP.

4.4: Conclusions

It is well known that changes in temperature can alter the mineralogy of the hydrate phases formed in Portland cement based systems, which can include destabilisation of certain phases at high temperature, for example ettringite [25,30,144,149,165,167]. However, most of these alterations occur when temperatures rise above 50 °C.

In this Chapter, characterisation of NRVB formulated with two different sources of raw material (laboratory and industrial materials) and characterisation of the Cebama reference cement paste was performed. Two different curing temperatures were used, 20 °C and 40 °C, to match the extended experiment conditions used in the subsequent Chapters of this Thesis.

NRVB samples synthesised with industrial materials showed a slightly higher rate of hydration than the NRVB samples that were formulated with laboratory materials, independent of the temperature of curing used. This was caused by the differences observed in the surface area and chemical composition of the raw materials, particularly CaCO_3 and limestone flour. The higher rate of hydration also resulted in a slight increase of the relative quantity of monocarboaluminate formed, an increase of ettringite formed (potentially due to differences in the sulphur concentration, which was more evident at 40 °C) and also differences in the porosity (mainly at 20 °C).

When comparing the different curing temperatures, the main difference observed was in the rate of hydration; as the temperature was doubled, the rate of hydration was almost twice as fast, as identified by isothermal calorimetry (Figure 4.3 and 4.11). Minor differences in mineralogy were also observed, which were related to the extent of hydration, for example, hemicarboaluminate was present in the samples that were cured at 20 °C, but not in the samples that were at 40 °C. The quicker rate of conversion of hemicarboaluminate into monocarboaluminate at 40 °C is a possible explanation [147]. Another difference observed between the two curing temperatures was the apparent total reaction of Portland cement in the NRVB samples cured at 40 °C, as observed through ²⁹Si MAS NMR. Furthermore, an increase of the incorporation of aluminium into the bridging sites of C-A-S-H was visible. The higher hydration reaction obtained at a curing temperature of 40 °C, led to a slight decrease of the porosity, due to the consequent formation of more hydration products. Nevertheless, the overall phase assemblage of NRVB was similar at both temperatures. The main hydrate phases present after 28 days of curing were: calcite, portlandite, ettringite and monocarboaluminate.

As a low-pH cement with high percentages of replacement of Portland cement with supplementary cementitious materials, Cebama reference cement paste showed a high amorphous component. Through XRD and ²⁹Si MAS NMR analysis, unreacted Portland cement, BFS and silica fume were present at 28 days of curing, for both curing temperatures. The main hydrate phases present in the Cebama reference cement paste were calcite, C-A-S-H, ettringite, AFm phases and hydrotalcite-like phases, and this was observed independently of the curing temperature used. In terms of C-S-H structure, incorporation of aluminium is visible and was expected, due to the presence of BFS in the formulation [140,161,162].

In respect to the different curing temperatures used, no significant differences were observed in the final phase assemblage and porosity (after 28 days). As observed with NRVB, only a slight increase of the hydration reaction was visible, mainly observed through isothermal calorimetry (Figure 4.20 and 4.26).

This slight increase of the hydration reaction rate observed for both cement formulations when cured at 40 °C when in comparison with 20 °C is in accordance with the Arrhenius law, where reaction rates are dependent on the temperature. In this case, the increase in temperature led to an observed slight increase of the hydration reaction.

Nevertheless, it is important to note that no significant differences were observed in the overall phase assemblage and porosity of both cementitious materials, when the two different temperatures were used.

It is of importance to understand how the phase assemblage of the different cementitious materials considered for use in a geological disposal facility will evolve with time, as their performance is required to last long periods of time. In the long-term, interaction with groundwater will likely occur, so having an initial thorough knowledge of the microstructure of these cements will allow a better understanding of the possible changes that will arise from those interactions. The long-term evolution of the mineralogy of these cementitious materials is discussed in detailed in the following Chapter.

Chapter 5: In-situ Synchrotron X-ray Diffraction Study of High- and Low-pH Cement Hydration

5.1: Introduction

Cementitious materials will be widely used in geological disposal facilities (GDFs) for radioactive waste (as waste forms, as backfill materials, for sealing and structural components), and so it is important to understand how the mineralogy of the cement evolves with time. Cement hydration is a complex process, where a sequence of overlapping chemical reactions occur, and the time taken for this process to be completed can vary between a few months to hundreds of years, depending on the cement composition [52,54,119,168–170]. One advantage of using cementitious materials in the context of geological disposal is their capability for radionuclide sorption [9,40], since many of the hydrate phases can incorporate these elements through ion exchange [171–173], or provide high surface areas for ionic sorption [173]. Therefore, knowing accurately which hydrate phases are present, and how they evolve with time, will allow the development of more precise models to predict radionuclide sorption, porosity evolution and pH buffering capacities, which is necessary for the development of a robust post closure safety case for the GDF.

A combination of techniques are typically used to study the hydration of cementitious materials, which include, for example, isothermal calorimetry, ex-situ X-ray diffraction (XRD), thermogravimetric analysis (TGA) and nuclear magnetic resonance spectroscopy (NMR) [119,141,145,168,169,174].

In this project, a world first, fully in-situ synchrotron XRD experiment has been performed, where cement samples were mixed and analysed at specific intervals (as described in Chapter 3) for 4 years in the case of NRVB, and 1.5 years in the case of Cebama reference cement. This high-resolution synchrotron instrument allows the provision of highly detailed and accurate data obtained during a long period of time [108]. One of the exciting novelties of this study was the possibility of studying the initial hydration reaction of a blended cement (the first few hours, only studied previously through isothermal calorimetry and ex-situ techniques), where most of the main hydrate phases are formed, at the high resolution only obtained in an X-ray synchrotron instrument.

In this Chapter, the results obtained from this experiment are shown, including semi-quantification of the different crystalline phases using Rietveld refinement. Ex-situ ^{29}Si MAS NMR analysis of the samples at specific time points was also performed to provide structural information for poorly crystalline phases such as C-S-H.

5.2: NRVB Hydration

5.2.1: Synchrotron X-ray diffraction

It is well known from the literature that the first few days are important for cement hydration. As soon as dry cement powders are brought into contact with water, a series of different chemical reactions occur, leading to the formation of different cement hydrate phases. The formation of these hydrate phases will be responsible for the setting and hardening of the cement, and also for its microstructural properties. The main reactions (chemical equations shown below) responsible for the setting of the mineralogical and microstructural properties of the cementitious materials are related to the clinker phases present in the Portland cement (PC). The reactions of alite (Ca_3SiO_5) and tricalcium aluminate ($\text{Ca}_3\text{Al}_2\text{O}_6$) begin within the first few minutes/hours and will lead to the formation of portlandite ($\text{Ca}(\text{OH})_2$) and C-S-H, in the case of alite (Equation 5.2), and ettringite (AFt phase, $\text{Ca}_6\text{Al}_2(\text{OH})_{12}(\text{SO}_4)_3 \cdot 26\text{H}_2\text{O}$), in the case of tricalcium aluminate (Equation 5.1) [52,169,175]. These phases are responsible for the observed initial setting and the early development of strength in the cementitious materials. These reactions will be followed by further hydration of the aluminate phases for the formation of AFm phases, like monosulphate ($\text{Ca}_4\text{Al}_2\text{O}_6(\text{SO}_4) \cdot 12\text{H}_2\text{O}$), monocarboaluminate ($\text{Ca}_4\text{Al}_2(\text{OH})_{12}(\text{CO}_3) \cdot 5\text{H}_2\text{O}$), or hemicarboaluminate ($\text{Ca}_4\text{Al}_2(\text{OH})_{12}(\text{CO}_3)_{0.5} \cdot 5.5\text{H}_2\text{O}$). The reaction of belite (Ca_2SiO_4) is expected to occur mainly at later ages, contributing to the strength development in mature cements, through the formation of further portlandite and C-S-H (Equation 5.4) [52,169,175]. Most of these reactions occur within the first 24 hours of curing, and a detailed description is performed below, where semi-quantitative XRD data and isothermal calorimetry will be compared.

Table 5.1. Synchrotron XRD scan times for the NRVB formulation.

NRVB (scan times)	
<i>First 44 hours</i>	First scan – 4 min after mixing
	Every 10 min until 30 min
	Every hour until 44 h
<i>3 days to 4 years</i>	3 days until 1 year – once/week
	Except between 17 days and 59 days
	1 year until 3 years – once/month
	Last scan taken at 4 years

To better understand these initial reactions, XRD scans were taken more frequently for the first 44 hours (Table 5.1), and the patterns are shown in Figure 5.1. In this Figure, it is possible to observe the evolution of the intensity of the peaks of certain phases as a function of time. In the first scan, taken around 4 minutes after mixing, it is possible to observe the presence of the clinker phases (alite, belite, tricalcium aluminate and ferrite), and of the initial raw materials portlandite and calcite. Over the first 44 hours of hydration, an increase of the formation of portlandite, ettringite and hemicarboaluminate was observed. Also observed was a decrease of the intensity of the peaks corresponding to alite, belite, aluminate and gypsum. These variations are expected to occur in the first few days of hydration and have been previously observed in similar cement formulations [141,146,168,170].

To understand the evolution of the different cement hydrate phases with curing time, semi-quantification of the XRD data was performed through Rietveld analysis of the crystalline phases present in the NRVB. In this analysis, no amorphous content was accounted, as no internal or external standards were measured during this experiment. Therefore, it is important to point out that the relative concentrations obtained for the crystalline phases through Rietveld refinement will be slightly higher than the true amounts present when an amorphous phase is also considered. Nevertheless, for the purpose of observing the hydration trend, these values are considered as semi-quantitative concentrations. Rietveld analysis was performed using the Bruker AXS Topas 4.2 software, and the crystal structure information used for each phase is identified in Chapter 3, Section 3.3.3. Batch analysis was performed, where results from the previous scan determined the initial values and constraints applied in the next scan. The lattice parameters were constrained to refine within 2.5 % of their published value.

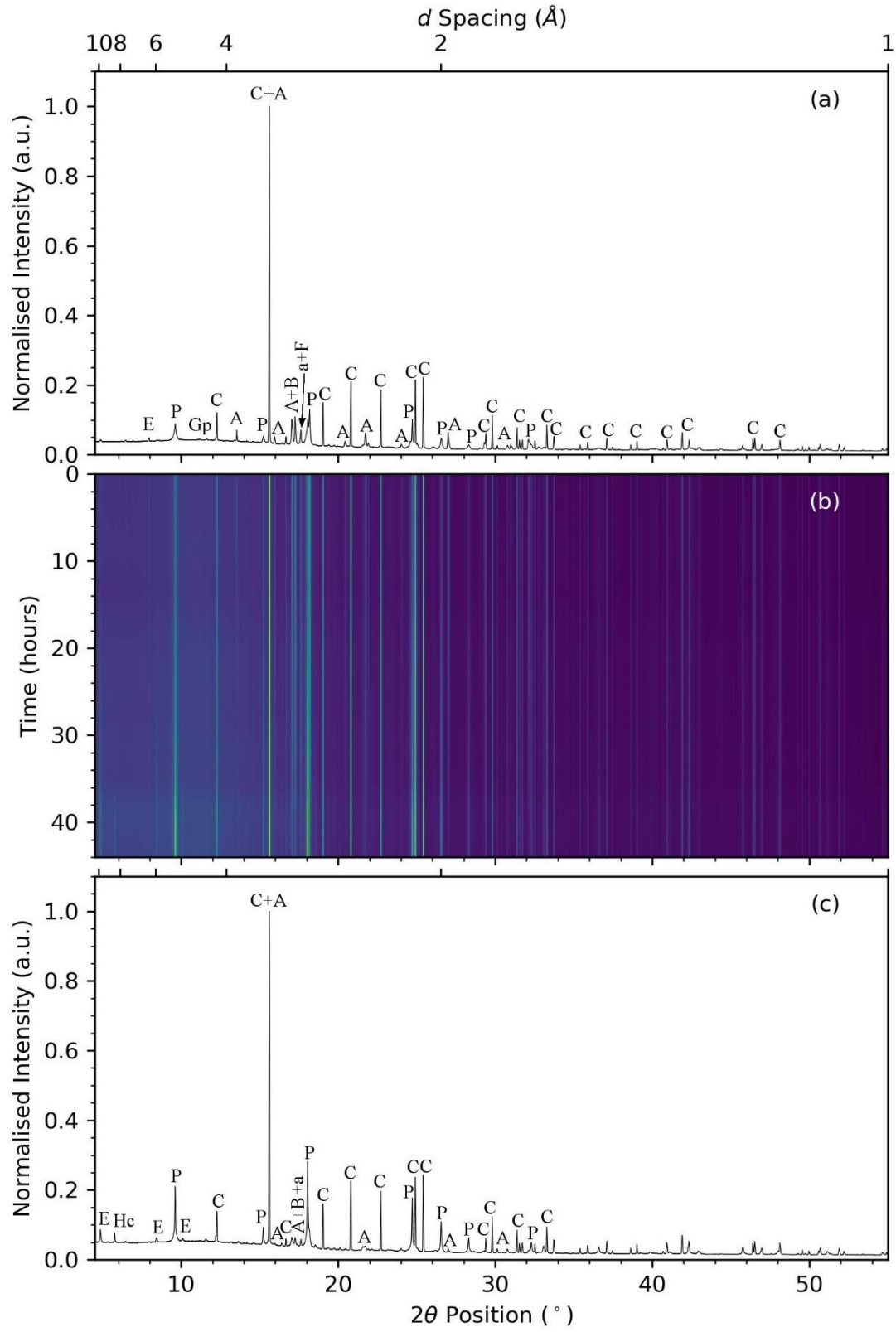


Figure 5.1. (a) X-ray diffraction pattern for NRVB at 8 minutes after mixing; (b) NRVB peak intensity variation as a function of curing time; (c) X-ray diffraction pattern for NRVB at 44 hours. Phases are labelled as: A – alite; B – belite; a – aluminat; F – ferrite; Gp – gypsum; P – portlandite; E – ettringite; Hc – hemicarboaluminate.

Figure 5.2. details the semi-quantitative evaluation of the different crystalline phases performed with the XRD data for the first 44 hours of the experiment (not including C-S-H), compared with the isothermal calorimetry performed for the same time period. From these results it is possible to observe the initial presence of ettringite, showing the characteristic early reaction of tricalcium aluminate with gypsum ($\text{CaSO}_4 \cdot 2\text{H}_2\text{O}$) (Equation 5.1). Indeed, it is well known that aluminate phases react very rapidly, within the first few minutes of hydration, which leads to the observed initial increase of temperature (the reaction is exothermic) visible in the isothermal calorimetry shown in Figure 5.2 (labelled 1) [52,169,170,175,176].

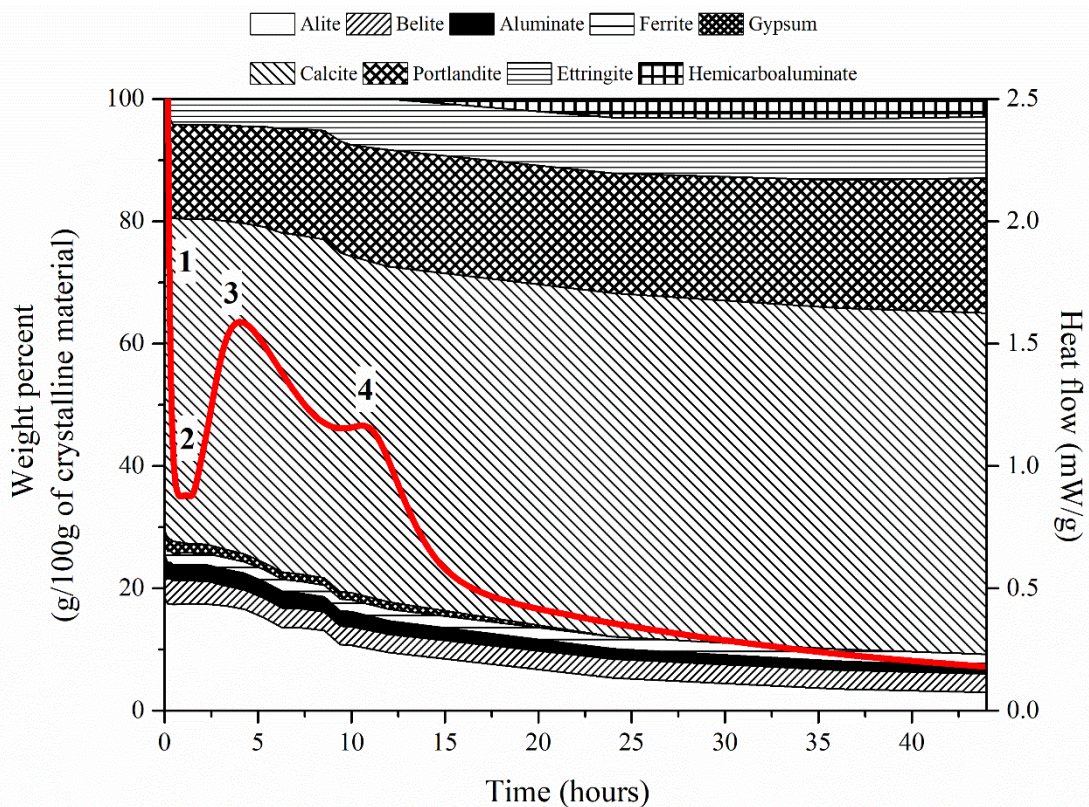
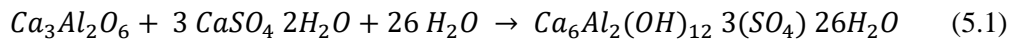
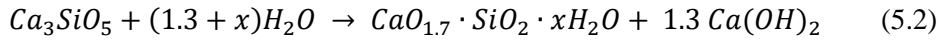


Figure 5.2. Semi-quantitative evaluation of XRD patterns of NRVB at curing times between 5 minutes after mixing and 44 hours compared with the isothermal calorimetry performed during 44 hours (red line; right-hand y axis). Thermal features identified are: (1) dissolution and aluminate reaction; (2) induction period; (3) acceleration period; (4) sulphate depletion.

During this period (labelled 1, Figure 5.2), the initial reaction of alite is also observed, which results in the initial formation and precipitation of portlandite and C-S-H (Equation 5.2, where x represents the amount of water associated with C-S-H) [175].



From Figure 5.2, it is also possible to identify the induction period (labelled 2), where a slowdown of the hydration reaction was observed. A number of reasons have been attributed to the occurrence of this slow period of reaction, most notably the formation of a metastable layer of a calcium silicate hydrate phase that covers the alite particles, reducing their dissolution and, therefore, slowing the hydration reaction [169,170]. Careful microscopic analysis would be required to confirm this. A more recent theory has been also proposed, called “geochemical” theory of dissolution, which advocates that the rate of dissolution is dependent on the undersaturation conditions of the solution in respect to the dissolving phase [138]. In this theory, it has been claimed that high degrees of undersaturation lead to rapid dissolution, as it is considered energetically favourable to etch pits to form [138]. However, there is still no consensus within the scientific community regarding the occurrence of this slow period of reaction [138]. The induction period was around 1 hour. Similar results were obtained by Lothenbach et al [141] for a similar formulation (PC with limestone), where the end of the induction period was at around 3 hours.

The next stage of hydration observed for NRVB was the acceleration period (labelled 3, Figure 5.2), where further reaction of alite occurred to form portlandite and C-S-H (not shown in Figure 5.2). This is visible through the decrease of the relative concentration of alite after 4 hours and the consequent increase of the relative concentration of portlandite (Figures 5.3b and c). The increase of the formation of C-S-H will be later explained through ^{29}Si MAS NMR data.

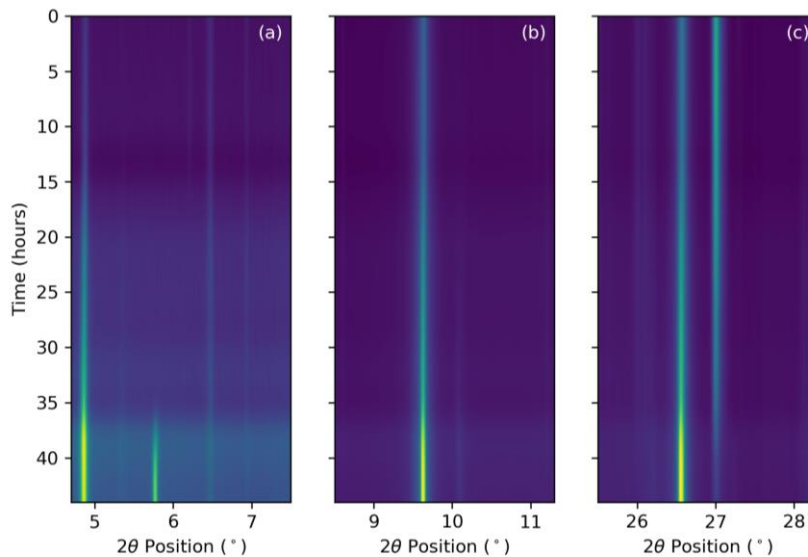
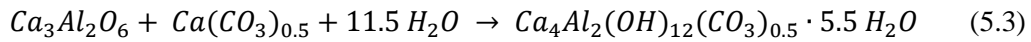
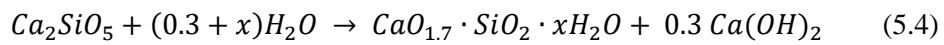


Figure 5.3. Extracts from Figure 5.1 to highlight specific regions; a) increase of the intensity of ettringite ($4.9^\circ 2\theta$) and hemicarboaluminate ($5.9^\circ 2\theta$); b) increase of the intensity of portlandite ($9.7^\circ 2\theta$); and c) decrease of the intensity of alite ($27^\circ 2\theta$) and increase of the intensity of portlandite ($26.6^\circ 2\theta$).

The formation of ettringite during the acceleration period increased (Figure 5.3a), agreeing with the decrease of aluminate, i.e., further reaction of aluminate with gypsum (Equation 5.1). At around 11 hours of hydration, the sulphate depletion period commenced (labelled 4, Figure 5.2), where the formation of hemicarboaluminate hydrate occurred (Figure 5.3a). The formation of this AFm phase occurs once all of the gypsum has reacted; the unreacted aluminate reacts with calcite [52,141,145,147] to form hemicarboaluminate, according to Equation 5.3.



Belite (Ca_2SiO_4) reaction is known to be relatively slow for the first 28 days of hydration [52], which is the reason why not much variation occurred during the first 44 hours (Equation 5.4).



After the initial hydration period of 44 hours, XRD measurements were taken between 3 days and 4 years, with the analysis times set out in Table 5.1. The resulting diffraction patterns, and consequent variations in the intensities of the peaks as function of time, are shown in Figure 5.4. The main difference observed during this period was related to the visible decrease in the intensity of the peaks corresponding to hemicarboaluminate (8.1 Å) and the concurrent increase in the intensity of the peaks corresponding to monocarboaluminate (7.5 Å) (shown by the red arrow in Figure 5.4b). The reason for this transformation is described in detail below. Moreover, no clinker phases were observed in the Figure 5.4c, after 4 years of curing.

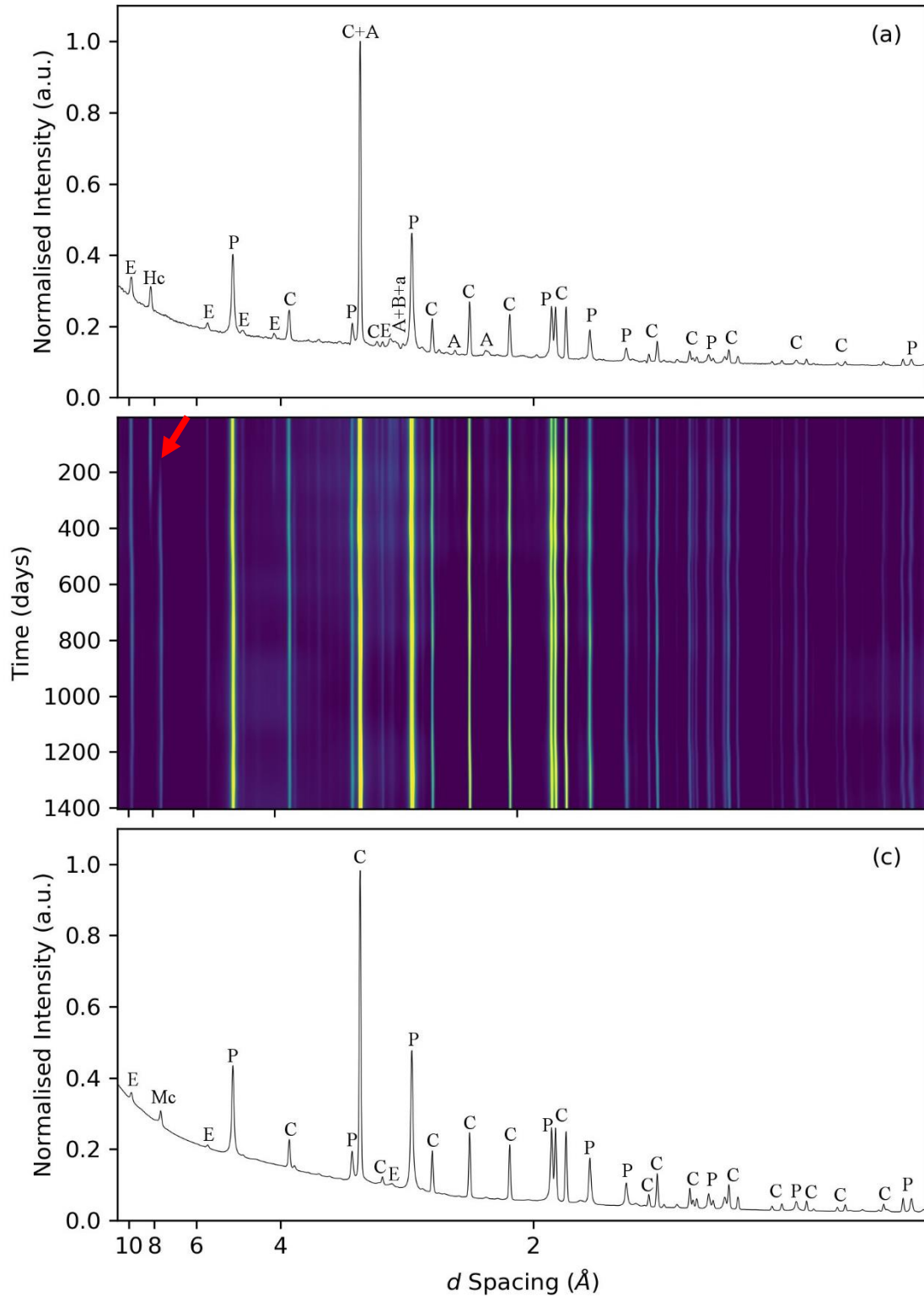


Figure 5.4. (a) X-ray diffraction pattern for NRVB at 3 days; (b) NRVB peak intensity variation as a function of curing time; (c) X-ray diffraction pattern for NRVB at 4 years. Phases are labelled as: A – alite; B – belite; a – aluminat; Gp – gypsum; P – portlandite; E – ettringite; Hc – hemicarboaluminate; and Mc – monocarboaluminate.

To further understand these results, semi-quantification of the different crystalline phases was performed by the Rietveld method, excluding C-S-H, as shown in Figure 5.5.

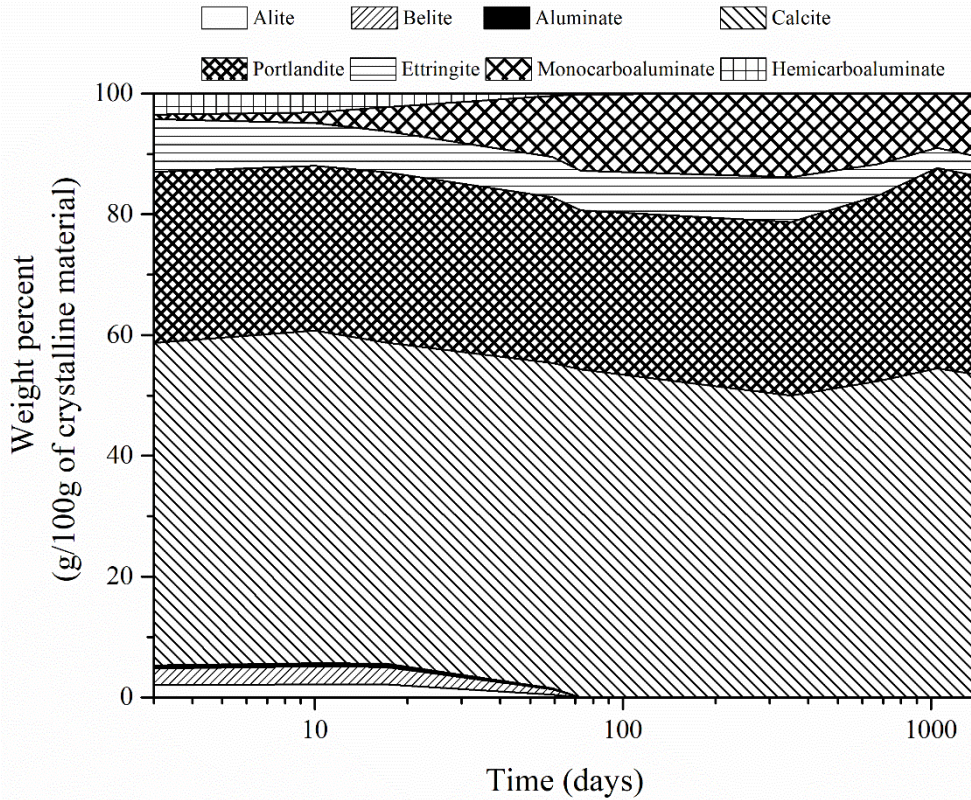
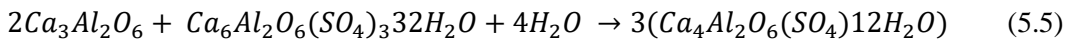
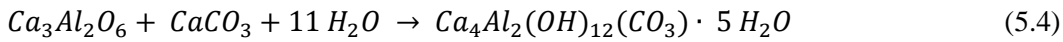


Figure 5.5. Semi-quantitative evaluation of XRD patterns of NRVB at curing times between 3 days and 4 years.

The initial formation of hemicarboaluminate, within the first day of hydration, has been reported in similar cement formulations containing high content of limestone (CaCO_3) [141,145,177,178]. It has been proposed that in limestone-rich cements, that hemicarboaluminate ($\text{Ca}_4\text{Al}_2(\text{OH})_{12}(\text{CO}_3)_{0.5} \cdot 5.5\text{H}_2\text{O}$) is kinetically more favourable to form than monocarboaluminate ($\text{Ca}_4\text{Al}_2(\text{OH})_{12}(\text{CO}_3) \cdot 5\text{H}_2\text{O}$) [145]. In other words, taking into account that calcite needs to be available for the formation of both phases, in the case of hemicarboaluminate, only 0.5 mol of CO_3 is needed for each $[\text{Ca}_4\text{Al}_2(\text{OH})_{12}]$ unit, whereas for monocarboaluminate, 1.0 mol is required for its formation. Therefore, in the beginning of the hydration period, because only a small amount of calcite had been dissolved by the porewater [145], hemicarboaluminate was more favourable to form, whereas with further dissolution of calcite over time (Figure 5.4), hemicarboaluminate was replaced by monocarboaluminate [52,145]. This conversion is visible in the semi-quantitative data presented in Figure 5.4, where the maximum rate of formation of monocarboaluminate (0.2 g/100 g crystalline/d) is concurrent with the maximum rate of dissolution of hemicarboaluminate (0.1 g/100 g crystalline/d). The slightly higher rate of formation of monocarboaluminate when compared to the rate of dissolution of hemicarboaluminate might be due to further reaction of tricalcium aluminate with calcite to form additional monocarboaluminate (Equation

5.4). The total depletion of hemicarboaluminate and the maximum relative concentration of monocarboaluminate occur at around 2 months of curing (59 days).

Ettringite (AFt) was present throughout the experiment, with a slight decrease of its relative concentration observed towards 4 years. In Portland cement it is expected that once all the gypsum has been reacted and, if tricalcium aluminate is still present, ettringite should begin to convert to monosulphate (AFm-SO₄) (Equation 5.5). The stability of ettringite as a function of curing time, observed here for NRVB, is a consequence of the use of CaCO₃ as a precursor material in the NRVB formulation. Because tricalcium aluminate reacts with CaCO₃ to form hemi/monocarboaluminate (AFm-CO₃), and sulphate ions can be easily interchanged by carbonate ions during this reaction [179], the formation of AFm-CO₃, rather than AFm-SO₄, stabilises SO₄²⁻ in ettringite, as tricalcium aluminate dissolution is balanced by CO₃²⁻ ions instead. This has the effect of delaying the destabilisation of ettringite and its conversion to monosulphate [141,177,179].



All of the clinker phases from the Portland cement included in NRVB had reacted at around 2 months. Due to the timescales of the measurements (shown in Table 5.1), where one measurement was taken after 17 days and the following time point after was after 59 days (due to the beamline shutdown in this period), no certainty is possible about the precise time when all of the clinker phases had reacted. However, taking into account the ²⁹Si MAS NMR data presented below, it is believed to occur between 28 days (where clinker phases were still present) and 2 months. The extra nucleation sites provided by the addition of CaCO₃ and Ca(OH)₂ as precursor materials and the high w/s ratio used in the formulation (0.55) might have accelerated this clinker reaction, as has been observed in previous work where limestone was used in the formulation [141,145].

The observed slight increase of the relative concentration of calcite at later ages might be related to the partial carbonation of portlandite or C-S-H, as the nature of the experiment set up was not to completely isolate the cement from air. Nevertheless, these values are within the quantification error attributed to this Rietveld analysis, of around 3 %.

5.2.2: *Ex-situ* ²⁹Si MAS NMR

The results observed from analysis by ²⁹Si MAS NMR investigation of duplicate samples (i.e. the same batch as those samples on the beamline, but kept separate for additional analysis) are in accordance with those results obtained in the XRD experiment. In Figure 5.6b the ²⁹Si MAS NMR spectra of NRVB

at different times of hydration between 1 day and 2 years are shown. The deconvolution performed for these data is shown in Figure 5.6a, and explained below.

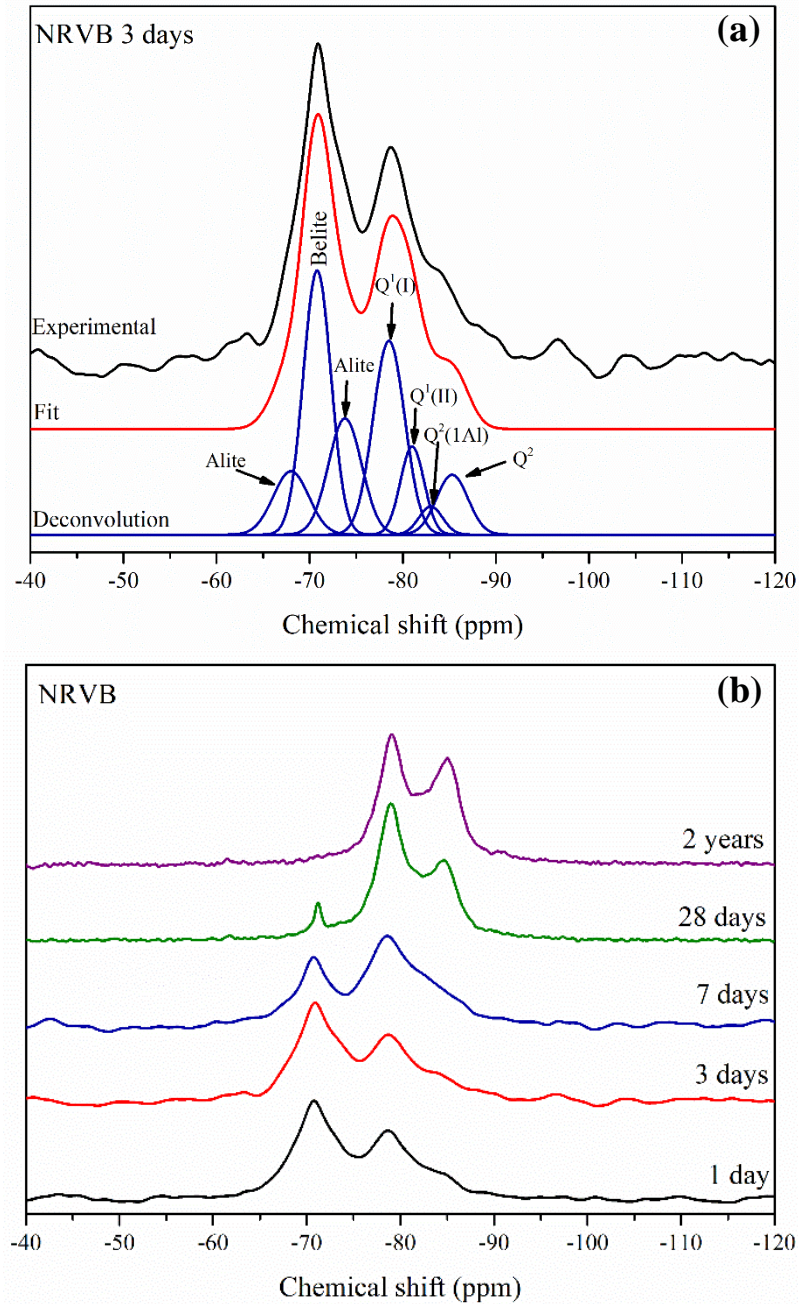


Figure 5.6. (a) Deconvoluted ^{29}Si MAS NMR spectrum of NRVB cured for 3 days; (b) ^{29}Si MAS NMR spectra of NRVB as a function of curing time.

For the Portland cement contribution, three resonances were assigned, two corresponding to alite (at -68 ppm and -74 ppm), and one corresponding to belite at -71 ppm [90]. For the C-S-H gel structure deconvolution, different Q^n sites were assigned. The first contribution is attributed to the Q^1 site, which at 1 day, is considered as a single Gaussian peak (at -78.7 ppm), but at later ages, two non-equivalent Q^1 environments were assigned. This identification is attributed to differences between the shielding

behaviour, i.e. chemical shifts, of Q¹ sites charge-balanced by Ca²⁺ or H⁺ [115,116]. The attribution of two Gaussian peaks, as Q¹(I) at -78.7 ppm and Q¹(II) at -82.3 ppm, was carried out as the smallest number of peaks that could adequately represent this region of the spectra. Q² and Q²(1Al) were identified in the chemical shift at -87 ppm and -83.5 ppm, respectively [139]. At around 28 days of curing, an extra Gaussian peak appeared corresponding to Q³(1Al) at -89 ppm, evidencing the occurrence of cross-linking. The presence of Q²(1Al) and Q³(1Al) shows the incorporation of Al in the C-S-H structure [140], not previously identified in NRVB.

Table 5.2. Results of deconvolution of ²⁹Si MAS NMR spectra of NRVB as a function of curing time. The estimated uncertainty in absolute site percentages is ± 2%.

Days	Belite	Alite	Q¹	Q²(1Al)	Q²	Q³(1Al)
1	27%	29%	29%	0	7%	0
3	29%	23%	28%	3%	9%	0
7	17%	17%	43%	8%	11%	0
28	4%	7%	57%	11%	21%	2%
702	0	0	52%	16%	29%	2%

Quantification of the deconvoluted ²⁹Si MAS NMR sites was performed through the integration of the area underneath each Gaussian peak, normalised to the total intensity of the sites to sum to 100 %. These data are shown in Table 5.2. and Figure 5.6. From Figure 5.6.a, a decrease in the relative concentration of alite and belite is observed, with a consequent increase in the relative concentration of C-S-H (i.e. the sum of Q¹, Q², Q²(1Al) and Q³(1Al)). After 1 day of curing, the relative concentration of C-S-H was 36 ± 1%, and between 3 days and 28 days the concentration increased gradually with the concurrent decrease in the relative concentration of alite and belite. To observe the consistency between XRD and ²⁹Si MAS NMR semi-quantification of alite and belite, the ratio between the two phases was calculated for each method and similar results, within error, were obtained (Table 5.3). The main difference that might occur is for the 28 days sample, since with XRD, the sample was analysed at 17 days, whereas with ²⁹Si MAS NMR it was analysed at 28 days.

Table 5.3. Alite/Belite ratio obtained through ^{29}Si MAS NMR and XRD at 1, 3, 7 and 17/28 days.

days	Alite/Belite ratio ^{29}Si MAS NMR	Alite/Belite ratio XRD
1	1.1 ± 0.1	1.2 ± 0.1
3	0.7 ± 0.1	0.6 ± 0.1
7	0.9 ± 0.1	0.7 ± 0.1
17 for XRD / 28 for NMR	0.8 ± 0.4	0.6 ± 0.1

Within the C-S-H Q^n sites (Figure 5.7b), the initial concentration of Q^1 species was higher relative to Q^2 and $\text{Q}^2(1\text{Al})$. The increase of the concentration of Q^1 species was gradual until 28 days, from where it was possible to observe a slow decrease of this site with time. Furthermore, a steady increase in the concentration of Q^2 was observed throughout 2 years. In the case of $\text{Q}^2(1\text{Al})$, an increase of the concentration is visible after 3 days of curing. An increase of the relative concentration of $\text{Q}^3(1\text{Al})$ is observed after 28 days of curing, evidencing the occurrence of cross-linking. The observed increase of the Q^2 , $\text{Q}^2(1\text{Al})$ site and $\text{Q}^3(1\text{Al})$ correlate well with the slow increase of the mean chain length (MCL) observed with time, i.e. at 1 day of curing the MCL of NRVB was 2.5 ± 0.4 and after 2 years was 4.3 ± 0.3 , as shown in Table 5.4.

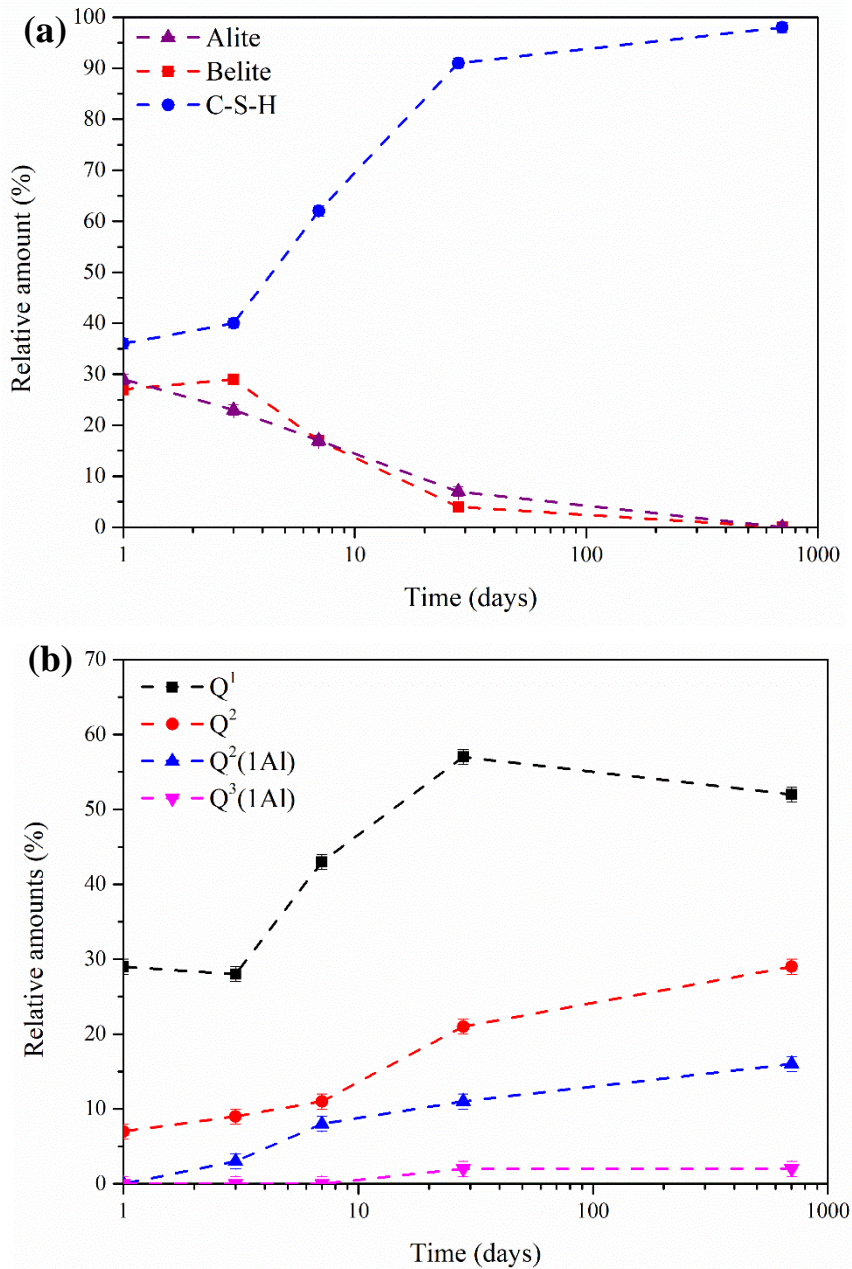


Figure 5.7. Deconvolution results of the ^{29}Si MAS NMR spectra, normalised to the total intensity of the reaction product; where (a) compares the relative amount of alite, belite and C-S-H with curing time, and (b) the evolution of the Q^n sites with curing time, in NRVB.

The Ca/Si ratio of C-S-H stayed relatively constant as a function of curing time (Table 5.4). It is important to note that the Ca/Si ratio obtained through this method is slightly lower than the values expected for this type of cement (CEM I found to be around 1.8 [73,180]). Previous studies have encountered similar results, where consistently lower Ca/Si values than expected were obtained when calculated from NMR spectra [120,162]. This is believed to be due to the process of deconvolution of NMR spectra based on the local environment of silicon, since a great variety of potential ion interactions may affect the chemical shift of each silicon species [162], and calcium environments are being inferred rather than probed directly.

In the case of the Al/Si ratio, a constant increase was observed with time (Table 5.4). This is related aluminium being available to incorporate in the C-S-H structure (from the clinker phases).

Table 5.4. Summary of structural evolution of C-(A)-S-H formed in NRVB as a function of curing time, based on the ^{29}Si MAS NMR deconvolutions.

Time (days)	Ca/Si Ratio	Al/Si Ratio	Mean Chain Length
1	1.43 ± 0.08	0	2.5 ± 0.4
3	1.39 ± 0.08	0.04 ± 0.01	2.9 ± 0.4
7	1.42 ± 0.05	0.06 ± 0.01	3.1 ± 0.3
28	1.27 ± 0.03	0.06 ± 0.01	3.5 ± 0.2
702	1.21 ± 0.03	0.08 ± 0.01	4.3 ± 0.3

For the data sets collected at 1, 3, 7 and 28 days, the quantitative data obtained through ^{29}Si MAS NMR was used to semi-quantify the amount of C-S-H present in NRVB. The ratio between the relative concentrations of belite and C-S-H was used to obtain the amount of this phase at each time point, as shown in Figure 5.8. The results obtained correlate well with those shown in Figure 5.7a, and show that the formation of C-S-H occurred within 1 day, being stable until 3 days, after which there was an increase in the rate of formation of this phase.

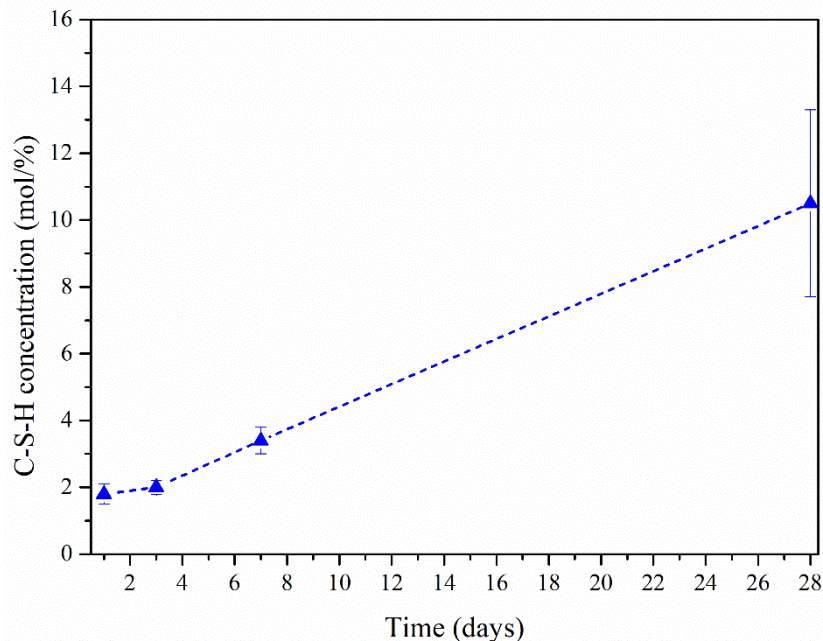


Figure 5.8. C-S-H concentration as a function of curing time. These values were based on the application of the quantitative data obtained through ^{29}Si MAS NMR spectroscopy to the quantitative values obtained in the in-situ synchrotron XRD experiment.

The limitation of using such a calculation for C-S-H quantification is that when all of the alite or belite have been consumed (since one of these phases is required for the analysis) there is no reference point for quantification. However, for this specific cement formulation, one can assume that once all of the alite and belite have reacted, and because these phases are the only source of Si in this system, no more C-S-H can be formed, reaching in this way, a maximum quantity when alite and belite have fully reacted. The only differences that might be observed are related with the C-S-H structure, i.e. with the relative concentrations of each Qⁿ sites, as shown in Figure 5.6b. Further analysis is required to observe if after 2 years of curing any changes in the C-S-H structure are observed. Analysis of a 4 year-old sample has been performed, however due to unexpected issues with the data, it has not been possible to analyse these results within the timeframe of this Thesis. Nevertheless, future analysis of a sample at cured for 4 years will be performed (when the sample matures to 4 years old in October 2019).

5.3: Cebama Reference Cement Hydration

This low-pH formulation will be used in the context of a geological disposal facility where a less alkaline environment (pH < 11) is required, for example, when in contact with the other natural or engineered barriers, especially those composed of clay [42,44,45]. The low pH nature of the cement is achieved by the replacement of Portland cement (PC) by supplementary cementitious materials (SCMs). The lower amount of PC present, combined with the slower rate of reaction afforded by the addition of SCMs that will largely hydrate only after the main clinker reaction has occurred [181], will significantly alter the overall hydration process compared to plain PC. In the Cebama reference cement paste it is therefore expected that the combination of BFS and silica fume will lead to a reduction of the amount of portlandite formed (due to the reaction of the clinker phases from PC) and an increase in the amount of C-S-H with low Ca/Si ratio formed, as a consequence of the pozzolanic reaction (Equation 5.6). This will consequently result in a pore solution with lower pH [42,44,45,182].



To help understand the hydration reaction of the Cebama reference cement paste, in-situ synchrotron XRD and ex-situ ²⁹Si MAS NMR data were obtained. For this cement paste, frequent scans were not able to be taken for the first few hours of hydration, due to access arrangements at the beamline (as explained in Chapter 3, Section 3.3.4). The scan times for this synchrotron XRD experiment are shown in Table 5.5. No XRD quantification by the Rietveld method was performed for this cement, as an external group from the Cebama European group is currently carrying out this analysis. Nevertheless, semi-quantification of the cement phases was performed by ex-situ ²⁹Si MAS NMR.

Table 5.5. Synchrotron XRD scan times for the Cebama reference cement formulation.

Cebama (scan times)	
<i>90 min to 1.5 years</i>	First scan – 90 min after mixing
	Every week until 7 months
	Every month until 1 year
	Last scan taken at 1.5 years

5.3.1: Synchrotron X-ray Diffraction

Figure 5.9 shows the differences in the XRD peak intensity of the different phases over the course of the 1.5 year investigation. The extremely high resolution obtained in this synchrotron data set is apparent, when compared to the XRD data shown in Chapter 4, and allows all peaks to be identified individually. Nevertheless, it is possible to observe the amorphous scattering between d spacings of 6 Å and 3 Å, which corresponds mainly to a combination of BFS, silica fume and C-(A)-S-H (Figure 5.9a,c).

From the first scan (Figure 5.9a), taken 90 min after mixing, it is possible to identify all of the clinker phases present in the PC, which include alite, belite, tricalcium aluminate, ferrite and gypsum. The intensities of the peaks corresponding to these phases decreased over time, even disappeared in the case of gypsum. However, for most of the phases it seems to be still present even after 1.5 years of curing (Figure 5.9c). This evidences the very slow ongoing hydration reaction of this material.

However, in the first scan, it is possible to identify some small peaks corresponding the hydrate phases portlandite and ettringite (e.g. for example at 9.5 Å, close-up in Figure 5.10). This demonstrates the initial rapid reaction of tricalcium aluminate to form ettringite, and also of alite to form portlandite and C-S-H, as observed above for NRVB (Equations 5.1 and 5.2). The extra nucleation sites available due to the presence of BFS and silica fume are the main reason that this initial reaction occurs more quickly than in NRVB [49,183]. The initial presence of these hydrate phases, especially portlandite, has been observed before, where similar low-pH formulations have been studied [42,119,182]. Indeed, Lothenbach et al [119] studied low-pH blends with PC and silica fume, and from 1 hour up to 7 days, and portlandite was detected in the XRD data. The high agglomeration of silica fume observed in Chapter 4 and its consequent low reactivity, and also BFS, at early curing ages is the main reason for this occurrence, as no consumption of portlandite to form C-S-H occurs [49,184].

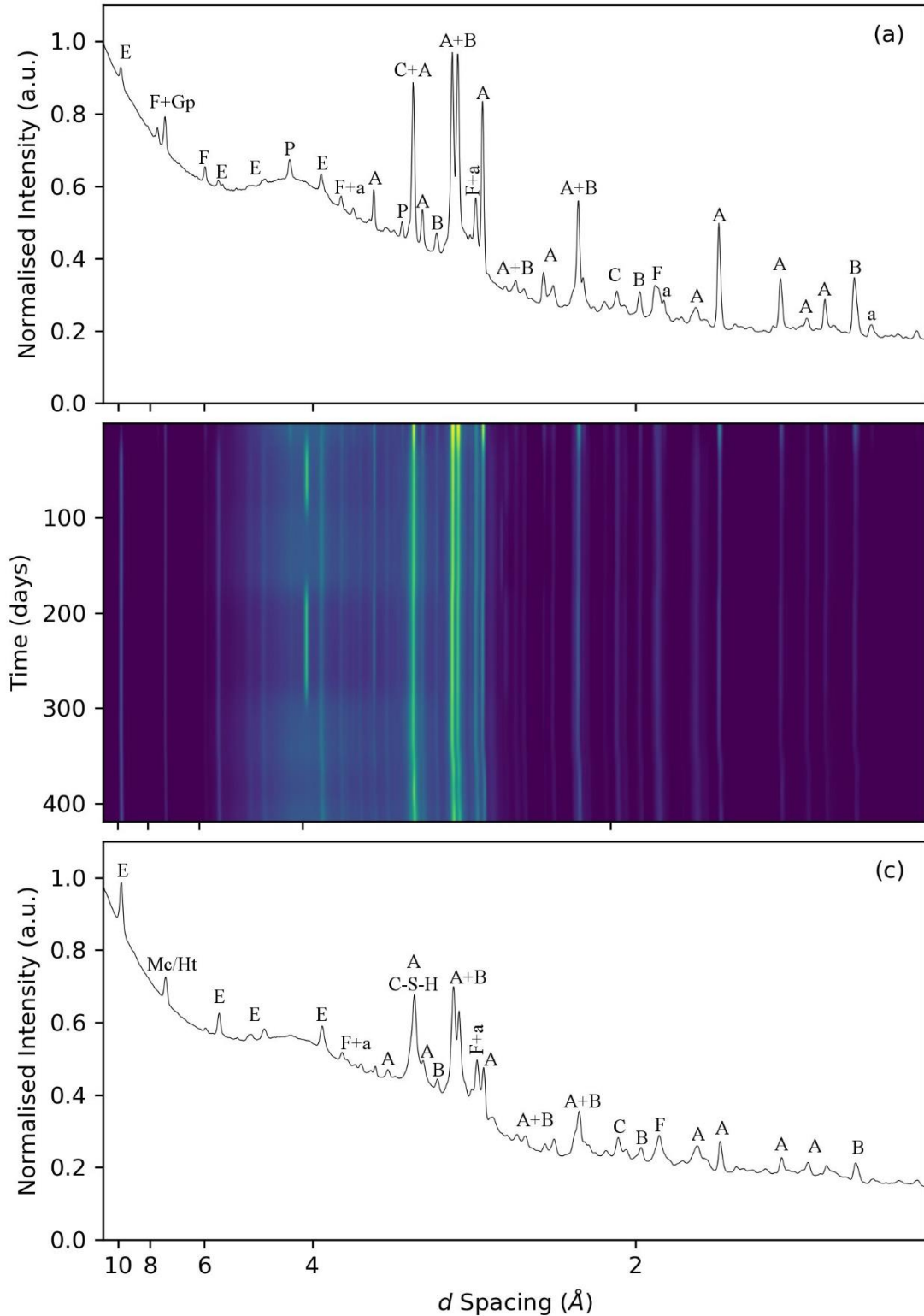


Figure 5.9. (a) X-ray diffraction pattern for Cebama reference cement at 90 min after mixing; (b) Cebama reference cement peak intensity variation as a function of curing time; (c) X-ray diffraction pattern for Cebama at 1.5 years. Phases are labelled as: A – alite; B – belite; a – aluminat; F – ferrite; Gp – gypsum; P – portlandite; E – ettringite; Mc – monocarboaluminate; Ht – hydrotalcite; C-S-H.

After 1.5 years (Figure 5.9c), the main changes that can be observed are related to the decrease of the intensity of the peaks corresponding to the clinker phases (close-up in Figure 5.10b), and also the slight decrease of the intensity of the broad scattering area observed, corresponding to the hydration of BFS and silica fume. The observed increase of the reaction of these phases results from an increase of the pore solution pH related with the dissolution of the clinker phases; the reactivity of SCMs depends on alkali activation [47,49,52,160,185,186]. With this increase of the hydration of the precursor materials, the formation of more hydrate phases occurred, which is apparent from the appearance of the peaks corresponding to hydrotalcite-like phase (meixnerite, $\text{Mg}_4\text{Al}_2(\text{OH})_{14}\cdot 3\text{H}_2\text{O}$), monocarboaluminate (close-up in Figure 5.10a) and C-S-H. The formation of AFm phase monocarboaluminate results from the reaction of tricalcium aluminate with calcite available in the cement clinker, as explained by Equation 5.3. The hydrotalcite-like phase is a hydrate phase formed due to the reaction of BFS, which contains MgO, and can have varying Mg/Al ratio depending on the degree of hydration of the BFS and availability of Al [187,188]. This will result in a slight variability on the position of the peak, with the incorporation of more Al responsible for a shift to lower angles [188].

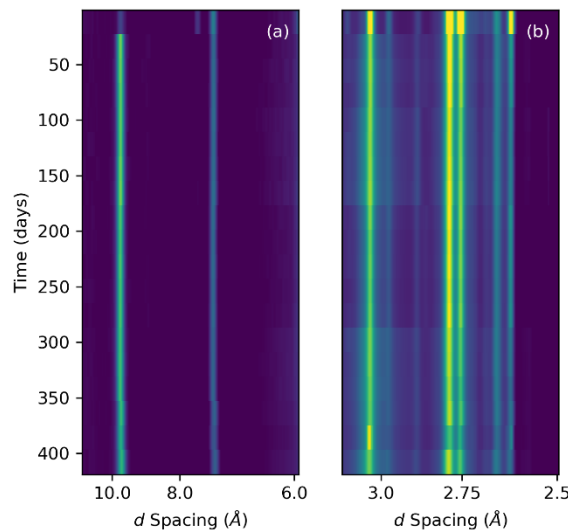


Figure 5.10. Extracts from Figure 5.9 to highlight specific regions; a) increase of the intensity of ettringite (9.5 Å) and AFm phases (7.3 Å); b) decrease of the intensity of the peaks corresponding to alite (around 2.97 and 2.77 Å) and belite (around 2.88 and 2.75 Å).

An increase of the intensity of the peak corresponding to ettringite was also observed, with the further hydration of tricalcium aluminate. The portlandite peak at ~ 4.7 Å, that was identified at early ages, was no longer present after 1.5 years of curing, indicating the increased reaction extent of the silica fume and BFS as a function of curing time [42,44,73,119,185].

5.3.2: *Ex-situ* ^{29}Si MAS NMR

For the Cebama reference cement paste, the deconvolution of ^{29}Si MAS NMR spectra consisted of first fitting the BFS contribution (purple line in Figure 5.11a) and then the silica fume at -111 ppm. For the contribution from PC, two Gaussian peaks were attributed to alite (at -68 ppm and -73 ppm) and a Gaussian peak to belite at -71 ppm. Q^1 species were divided in the same way as described before (Section 5.2.2), into $\text{Q}^1(\text{I})$ at -76.5 ppm and $\text{Q}^1(\text{II})$ at 78.8 ppm [115,116]. Contributions of Q^2 , $\text{Q}^2(1\text{Al})$, $\text{Q}^3(1\text{Al})$ and Q^3 were also observed at -84.6 ppm, -81.6 ppm, -89.8 ppm and 96.5 ppm [139,140], respectively. Figure 5.11b shows the ^{29}Si MAS NMR at different curing times.

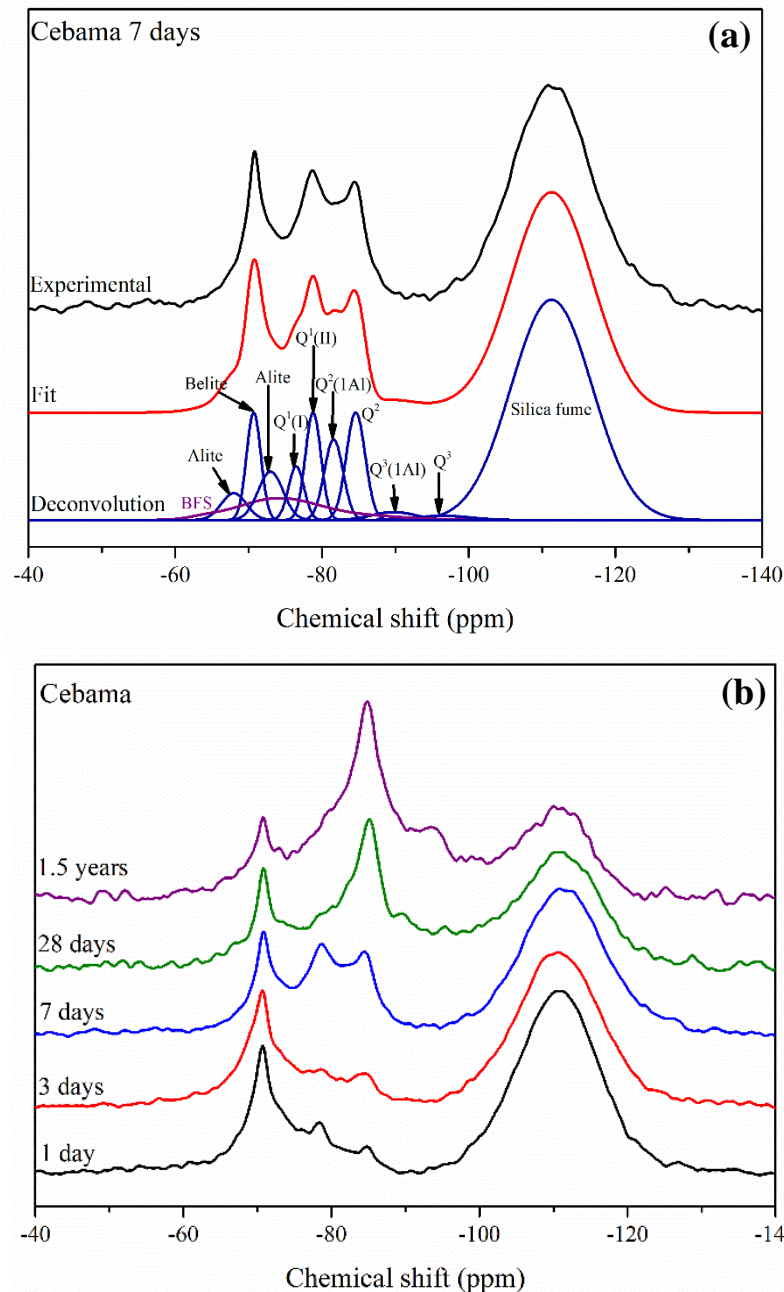


Figure 5.11. (a) Deconvoluted ^{29}Si MAS NMR spectrum of Cebama reference cement paste cured for 7 days; (b) ^{29}Si MAS NMR spectra of Cebama reference cement paste as a function of curing time.

Quantification of the deconvoluted ^{29}Si MAS NMR sites was performed through the integration of the area underneath each Gaussian peak, normalised to the total intensity of the sites to sum to 100 %. These results are shown in Figure 5.12 and Table 5.6. Until 3 days of curing, the hydration reaction was slow, as observed in Figure 5.12a. The reaction of alite and belite became more pronounced after 3 days, with a consequent gradual increase of the C-S-H. After 1.5 years of curing, the presence of alite and belite is still evident. A possible explanation for the observed slow reaction of the clinker phases is the low amount of water used in this formulation (w/s ratio of 0.25), which may affect the final extent of reaction

of the different anhydrous phases. Nevertheless, the presence of clinker phases at later curing times has been previously observed in blended cements [119,141,182].

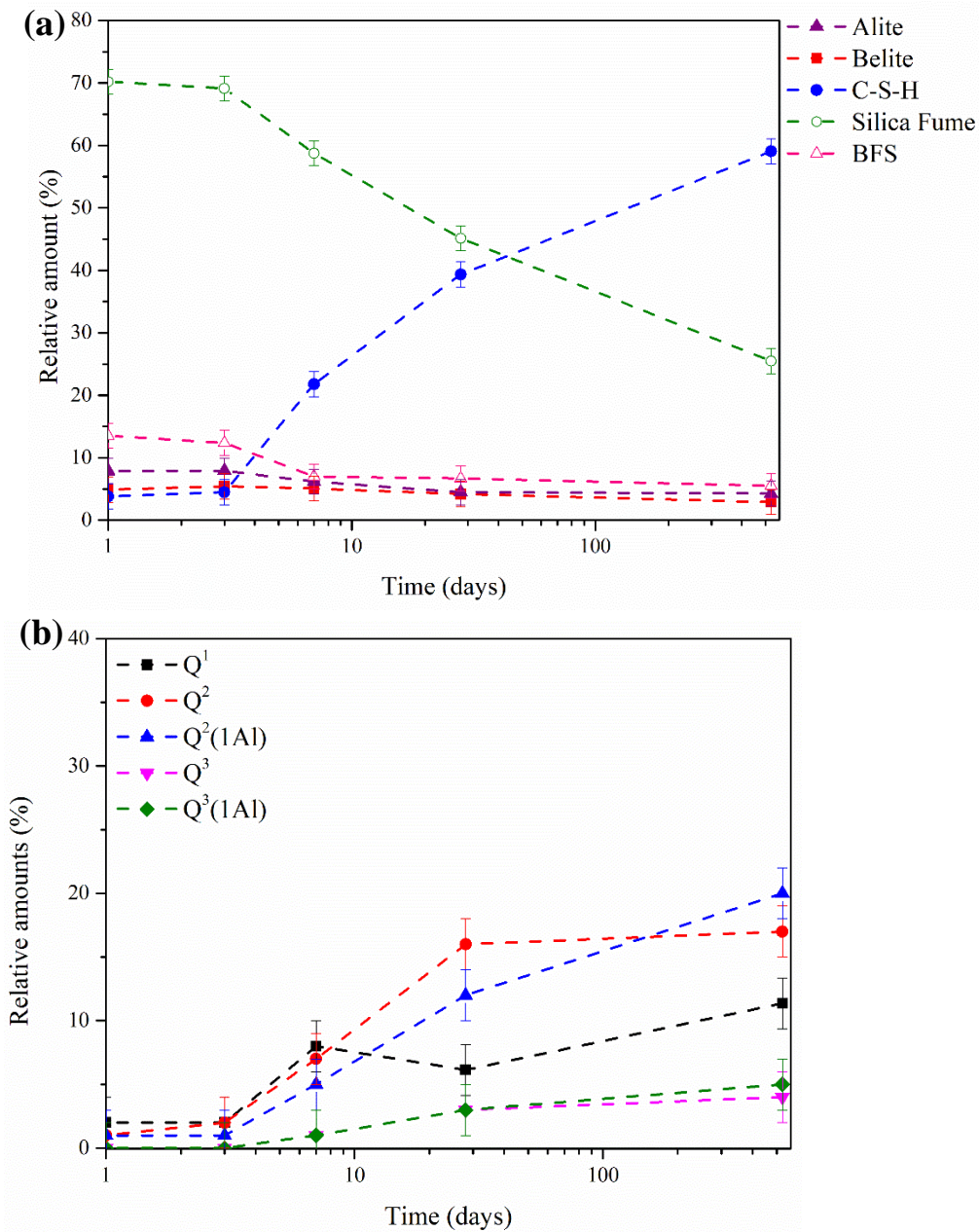


Figure 5.12. Deconvolution results of the ^{29}Si MAS NMR spectra, normalised to the total intensity of the reaction product; (a) compares the relative amount of alite, belite, silica fume, BFS and C-S-H with curing time, and (b) the evolution of the Q^n sites with curing time, in Cebama reference cement paste.

In the normalised ^{29}Si MAS NMR spectral deconvolutions (Figure 5.12b) it is possible to observe that the relative concentration of Q^1 species slightly decreased in the first 3 days of curing and the Q^2 sites increased. After this time, an increase in the relative concentration of both Q^1 and Q^2 sites was observed, as the reaction of the precursor materials increased (Figure 5.12). The appearance of $Q^3(1Al)$ and Q^3 at 7 days evidences the occurrence of some cross-linking of the C-S-H, and the consequent increase of the

MCL from 4.2 ± 2.5 at 1 day of curing, to 10.6 ± 3.3 after 1.5 years of curing (Table 5.6 and 5.7). The incorporation of Al into the C-S-H structure is verified with the increase of the relative concentration of $Q^2(1Al)$ and $Q^3(1Al)$. This correlates well with the observed increase of the Al/Si ratio (Table 5.7). This is related to the slow increase of the hydration of BFS and clinker phases, as more Al is available to incorporate into the C-S-H.

The slow reaction of BFS and silica fume is also visible in the ^{29}Si MAS NMR deconvolution. In the case of silica fume, until 3 days of curing, almost no reaction occurred (Table 5.6), likely as a consequence of the limited reactivity of these materials at early curing times [49]. However, after 7 days of curing, a gradual increase of the reaction of silica fume occurred, with the relative concentration of this material after 1.5 years being $25 \pm 2\%$. The presence of silica fume, even after 1.5 years of curing, is likely due to the high percentage used in this cement system (around 39%). Indeed, in a similar formulation where 40% of silica fume was used, the presence of this material was still visible at 3.5 years [119]. Having high amounts of silica fume increases the likelihood of agglomeration, which will decrease the reactivity of the silica fume by reducing its characteristic high surface area for reaction [49,119,154]. For the BFS, it is well known that the reaction of this material is very slow, with evidence of the presence of BFS even after 20 years of curing [54]. It has been suggested that the early hydration of BFS is due to reaction with alkali hydroxide, and subsequently reaction with portlandite [51,189]. Therefore, with the reduction of availability of portlandite, the reactivity of BFS decreases as well. Moreover, the lower w/s ratio used in the formulation will have an impact also in the BFS reactivity, as it is a hydraulic material [52]. However, it is interesting to see that $9 \pm 2\%$ of the BFS, between 1 day and 1.5 years, had reacted (Table 5.6).

Table 5.6. Results of deconvolution of ^{29}Si MAS NMR spectra of Cebama reference cement paste as a function of curing time. The estimated uncertainty in absolute site percentages is $\pm 2\%$.

Days	Belite	Alite	Q ¹	Q ² (1Al)	Q ²	Q ³ (1Al)	Q ³	Silica Fume	BFS
1	5%	8%	2%	1%	1%	0	0	70%	14%
3	5%	8%	2%	1%	2%	0	0	69%	12%
7	5%	6%	8%	5%	7%	1%	1%	59%	7%
28	4%	4%	6%	12%	16%	3%	3%	45%	6%
526	3%	4%	11%	20%	17%	4%	5%	25%	5%

From the deconvolution of the ^{29}Si MAS NMR spectra, it is possible to observe a decrease in the Ca/Si ratio as a function of time, however this seems to be within the error (Table 5.7). This is expected since the reaction of mainly silica fume, but also of BFS, leads to a decrease of the Ca/Si ratio [49,185,190]. The characteristic Ca/Si ratio of low-pH cements can vary between 1.2 and 0.8, needing to be lower than 1.1 to provide a low-pH pore solution [42,191]. It is important to note again that the values obtained

through this analysis for the Ca/Si ratio are expected to be slightly lower, as explained previously, due to deconvolution methodology.

Table 5.7. Summary of structural evolution of C-(A)-S-H formed in the Cebama reference cement paste as a function of curing time, based on the ^{29}Si MAS NMR deconvolutions.

Time (days)	Ca/Si Ratio	Al/Si Ratio	Mean Chain Length
1	1.2 ± 0.5	0.09 ± 0.02	4.2 ± 2.5
3	1.0 ± 0.5	0.10 ± 0.02	6.5 ± 3.1
7	1.1 ± 0.3	0.11 ± 0.02	5.9 ± 3.7
28	1.1 ± 0.1	0.20 ± 0.02	13.2 ± 3.2
527	1.0 ± 0.1	0.18 ± 0.02	10.6 ± 3.3

5.4: Conclusions

The aim of this Chapter was to show the results of the first fully in-situ X-ray diffraction study of the hydration of high- and low-pH cements being considered for use in a geological disposal facility for radioactive waste. These results were coupled with ex-situ ^{29}Si MAS NMR to observe the evolution of the amorphous phases present in the different cement systems, which are difficult to identify through XRD. Although no amorphous phases were considered in the Rietveld refinement, the evolution of the crystalline phases present in the cementitious materials was observed as a function of curing time.

In the case of NRVB, these experiments demonstrated the relatively rapid hydration reaction of this material, with a total reaction of the clinker phases occurring after two months of curing. The extra nucleation sites provided by the addition of CaCO_3 and $\text{Ca}(\text{OH})_2$ as precursor materials and the high w/s ratio used in the formulation (0.55) accelerated the clinker reaction. The early formation of hemicarboaluminate instead of monocarboaluminate was also observed, in agreement with a previous study performed by Zajac and colleagues [145], who demonstrated the faster initial formation kinetics of hemicarboaluminate when compared to monocarboaluminate. With further reaction of CaCO_3 , hemicarboaluminate started to convert into a slightly more stable monocarboaluminate. Since these two phases, hemicarboaluminate and monocarboaluminate, have preferential formation over monosulphoaluminate when in the presence of limestone flour [179], the stability of ettringite increases, i.e. it is possible to observe the presence of this phase even at later ages of curing (4 years).

In terms of C-S-H, ^{29}Si MAS NMR analysis was used to identify a gradual increase of the formation of this phase, which was coincident with the decrease of alite and belite, reaching a maximum point of formation once all the alite and belite had been consumed (after two months). With regards to the C-S-

H structure, incorporation of Al into the structure was observed after 1 day of curing. The appearance of a $Q^3(1Al)$ site after 28 days of curing indicates the occurrence of cross-linking, which indicated a slight increase of the mean chain length with time.

The hydration of the Cebama reference cement paste was shown to be slower when compared to NRVB. Due to the high replacement percentages of SCMs, and the low w/s ratio of this cement formulation, clinker phases, BFS and silica fume were still present after 1.5 years. Ettringite, monocarboaluminate, hydrotalcite-like phase and C-S-H were the main hydrate phases observed. Portlandite was present in the first XRD scan, demonstrating the slow initial reaction characteristic of the presence of agglomerated silica fume and of BFS. However, with time and with the increase of the reactivity of silica fume and BFS, the disappearance of portlandite was visible, being absent from the XRD pattern taken at 1.5 years of curing.

The formation of C-S-H was mainly observed after 3 days of curing. Al incorporation into the C-S-H structure was also observed, with an increase of the relative amount of the Q^3 sites, evidencing the occurrence of cross-linking and consequent increase of the mean chain length with time. With the increase of the reaction of silica fume and BFS, a decrease of the Ca/Si ratio was observed. This lower Ca/Si ratio is a requirement for this type of low-pH cementitious materials, since the lower amount of calcium ions will lead to an increase of the uptake of the alkaline elements present in solution, leading to a pore solution with lower pH [45,49,140,191].

These results are of key importance in the context of a GDF, as understanding how the different cement hydrate phases form and alter with time will enable the development of more precise models to predict radionuclide sorption, porosity evolution and pH buffering capacities, which are considered essential information for the development of a robust post closure safety case for the GDF. Moreover, the data presented in this chapter provide valuable baseline for experimental and modelling studies of groundwater – cement interactions, allowing phase stability, thermodynamic values and rate constants to be determined. This may be especially important due to the difference observed in the hydration kinetics between the two cementitious materials; hydration was observed to be completed for NRVB after around 2 months, whereas for cebama cement formulation clinker phases, BFS and silica fume were still present after 1.5 years. Therefore, different interactions might be observed when the different cementitious materials interact with groundwater.

With this deeper understanding of the microstructure and mineralogy evolution of these two cementitious materials, the next step is to observe how interactions with groundwater might affect these properties. This is the focus of the following two Chapters.

Chapter 6: Mineralogical and porosity assessment of NRVB in contact with simulated groundwater solutions

6.1: Introduction

As a backfill material considered for use in a geological disposal facility (GDF), NRVB is expected to interact with the geological environment, and specifically, with groundwater. As described in detail in Chapter 2, NRVB was designed to fulfil certain key characteristics for example to provide a high alkaline environment to promote radionuclide sorption, achieved through the dissolution of the cement hydrate phases. The conceptualised buffering behaviour of NRVB (Figure 6.1) when in contact with a neutral pH solution follows several stages: (I) the dissolution of the more soluble hydroxides (sodium and potassium) will increase the pH to about 13.5; (II) the dissolution of portlandite will buffer the porewater solution to a pH of around 12.5; (III) when all of the portlandite has been dissolved, the pH will be buffered through the dissolution of the high Ca/Si ratio C-S-H, which will slowly convert to a lower Ca/Si ratio C-S-H, due to the release of calcium and hydroxide ions. This is expected to buffer the pH to around 10.5 or lower; and (IV), the buffering will then occur due to the dissolution of the minerals with lower solubility, such as calcite.

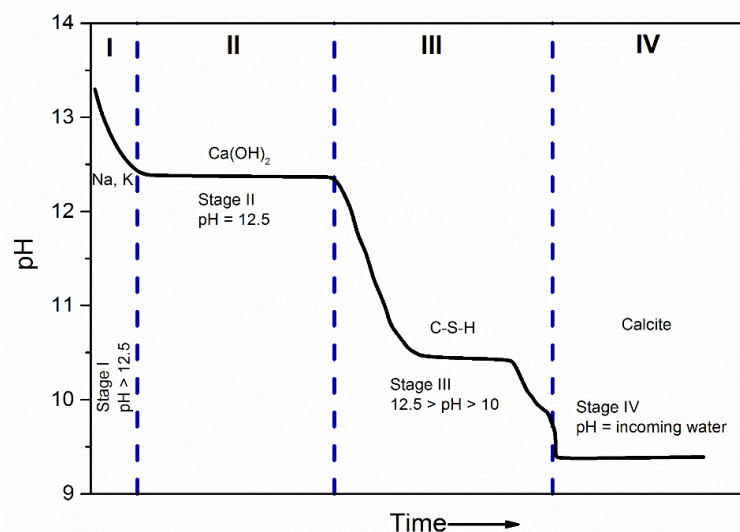


Figure 6.1. Schematic representation of the evolution of pH at 25 °C in cement pore fluid as a result of pure water leaching (from [1])

A small number of experiments can be found in the literature that have investigated the buffering behaviour of NRVB [22,37] in near-neutral solutions, using either deionised water, different

compositions of NaCl solutions, or simulated saline groundwater. However, there does not exist a comprehensive assessment of the evolution of the mineralogy and microstructure of NRVB as a function of groundwater contact, in the literature, and this is essential to support the development of a robust safety case for the disposal of radioactive waste in a GDF where NRVB is to be utilised as a backfill.

In this Chapter, results from an extended NRVB – groundwater contact experiment (carried out for 1.5 years) are presented. Full experimental details can be found in Chapter 3. Briefly, NRVB samples were placed in contact with three different types of synthetic groundwater (granitic, saline and clay) to represent the different possible geological environments for the GDF (Table 6.1). Experimental vessels were heated to 40 °C under exclusion of CO₂ and sampling was also performed under CO₂-exclusion. This was a semi-dynamic experiment, where sampling and replacement of the groundwater was performed every two months (to simulate the effects of the replenishment of groundwater solutes under conditions of flow, albeit at a greatly accelerated rate). Analysis of the cement samples was performed every 2 months by XRD and TGA, and the solution chemistry was measured at the same time periods by ICP-OES and IC. At selected time points (6, 12 and 18 months) further characterisation of the cement samples was performed by SEM, ²⁹Si MAS NMR, ²⁷Al MAS NMR and nitrogen sorption porosity analysis. XCT analysis was conducted on samples after 6 and 12 months. Parallel static experiments (to ascertain the behaviour when solution is not regularly replaced) were also performed, as detailed in Chapter 3.

Table 6.1. Composition (mg/L) of the synthetic groundwaters utilised in Chapters 6 and 7.

Element	Granitic Groundwater	Saline Groundwater	Clay Groundwater
Ca	20.0	796.0	300.0
Mg	4.9	9.7	138.5
S	3.2	128.2	480.9
Na	64.4	3218.6	1264.4
K	3.9	82.1	43.0
Cl	74.4	6122.2	1861.1
HCO₃	122.0	122.0	-

These experiments and methods aimed to determine the mineralogical and microstructural changes induced in NRVB by contact with groundwater as a function of time. This Chapter presents results first for the NRVB control samples that were cured for the same period of time without contact with

groundwater, then the samples that were in contact with synthetic granitic, saline and clay groundwaters.

6.2: Mineralogical and microstructural evolution of NRVB without groundwater

Figure 6.2 presents the X-ray diffraction results for the NRVB control samples cured for a total of 18 months. No changes were observed in the identified hydrate phases as a function of time, being the same as those identified in Chapter 4: calcite (CaCO_3), portlandite (Ca(OH)_2), ettringite ($\text{Ca}_6\text{Al}_2(\text{OH})_{12}(\text{SO}_4)_3 \cdot 26\text{H}_2\text{O}$) and monocarboaluminate ($\text{Ca}_4\text{Al}_2(\text{OH})_{12}(\text{CO}_3)_3 \cdot 5\text{H}_2\text{O}$). Semi-quantitative XRD Rietveld analysis was performed for the crystalline phases (Figure 6.3), and in the case of portlandite, monocarboaluminate and calcite, no major differences in the relative concentration were observed across this time period. In the case of ettringite a decrease of the relative concentration is visible as a function of curing time. A possible explanation is the decrease in the amount of sulphate ions available in the pore solution, which will lead to a destabilisation of ettringite, commonly observed in Portland cement formulations [138,147]. The quantity of C-S-H was expected to not vary, due to the fact that the maximum amount of C-S-H formation was achieved before the start of the experiment (no alite or belite observed at 28 days, Chapter 4). The evolution of the structure of this phase was studied through ^{29}Si MAS NMR.

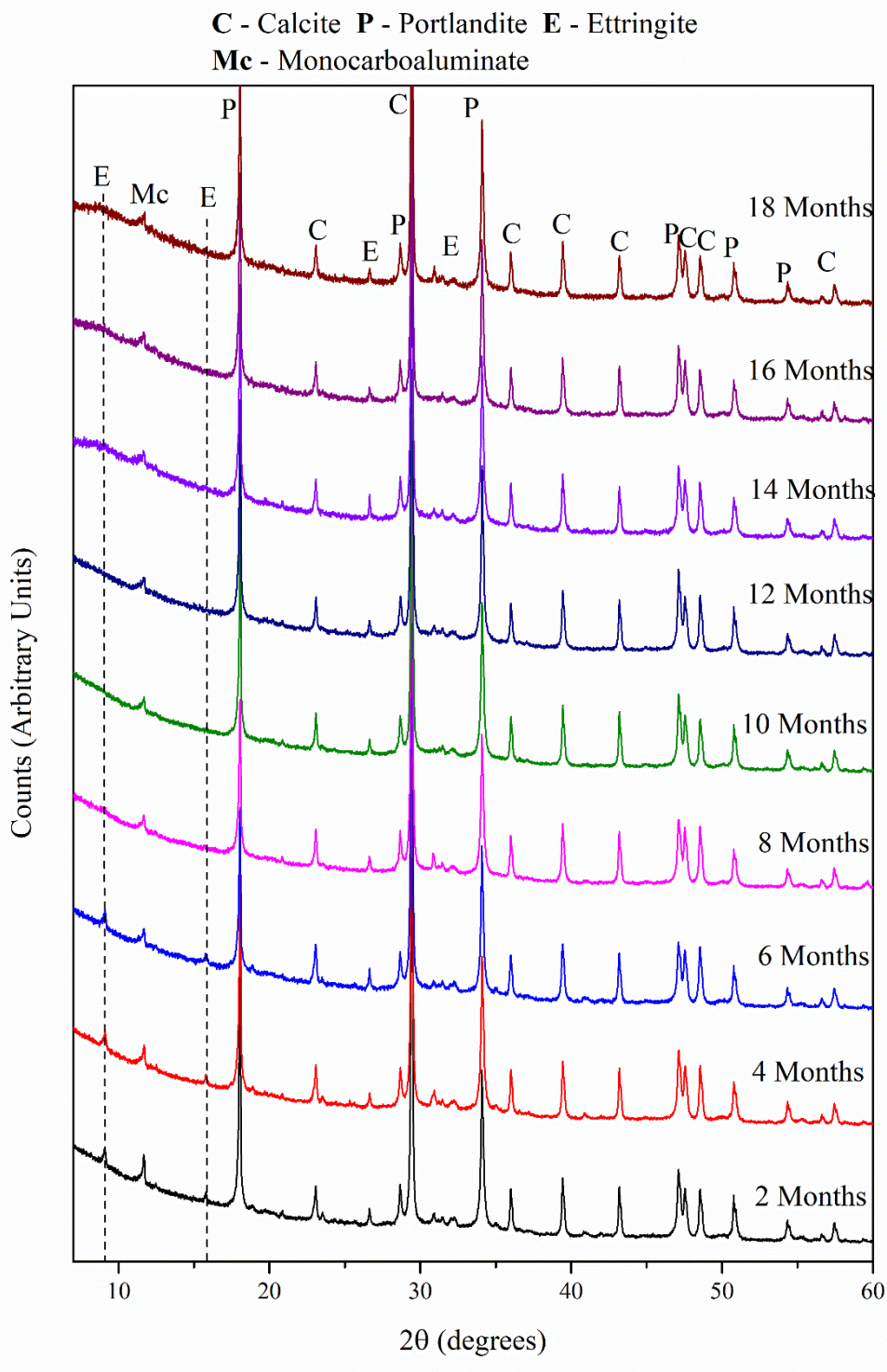


Figure 6.2. XRD patterns of NRVB control samples cured for 18 months.

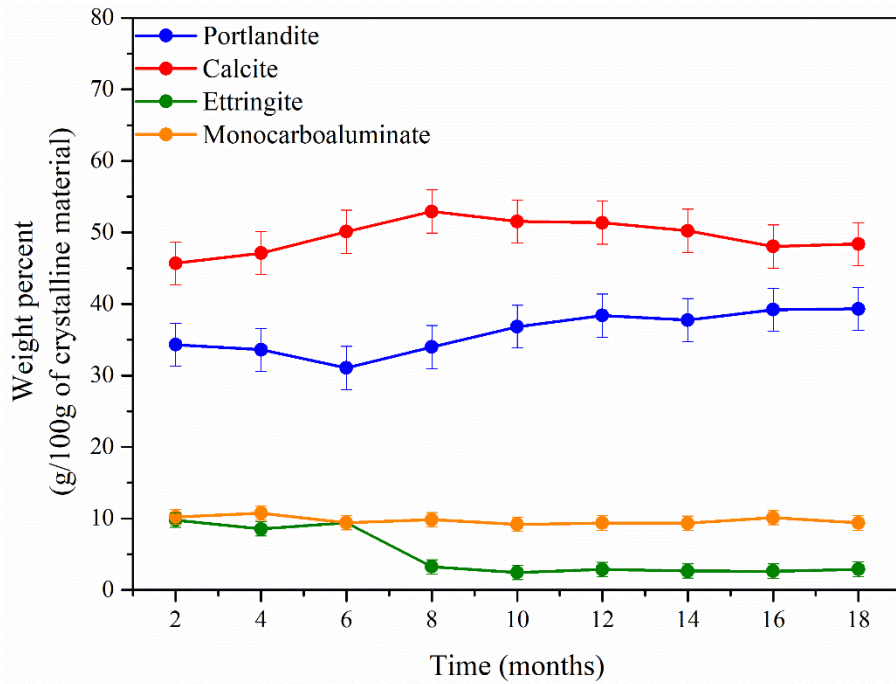


Figure 6.3. Semi-quantitative evaluation of the crystalline phases identified in XRD patterns of NRVB control samples cured for 18 months. Error bars obtained through Rietveld refinement software, Topas.

The observations made by XRD are in good agreement with TG analysis (Figure 6.4), where the presence of ettringite and monocarboaluminate (between the temperatures of 100 and 150 °C), portlandite (at around 450 °C), and calcite (between 750 and 800 °C) [192], was observed.

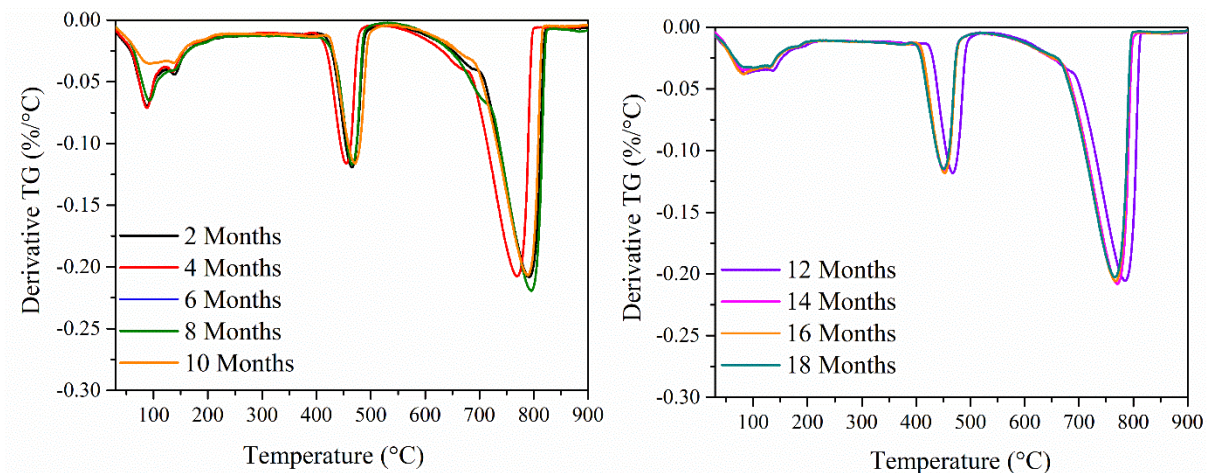


Figure 6.4. TGA data for NRVB control samples cured for 18 months.

To study the amorphous content, specifically the C-S-H structure, ^{29}Si MAS NMR was performed for the samples that were cured for 6, 12 and 18 months (Figure 6.5). Quantification of the Q-speciation of the C-S-H was performed by deconvolution of the ^{29}Si MAS NMR spectra (Figure 6.5a) with peaks

assigned to the main Q^n sites present in the NRVB samples (as described in Chapters 4 and 5) including: (1) two Q^1 environments, distinguishable by their difference in the charge-balancing cations (monovalent, $Q^1(I)$, and divalent, $Q^1(II)$) [116,117,162]; and (2) Q^2 , $Q^2(1Al)$, Q^3 and $Q^3(1Al)$ resonances assigned to the C-S-H structure. A peak at -74 ppm, representative of the hydrated silicon monomer, Q^0 , was also assigned, however, the precise structure of this species is argued in the literature [162,193]. This deconvolution approach was used for NRVB in all groundwater solutions described throughout the remainder of this Chapter.

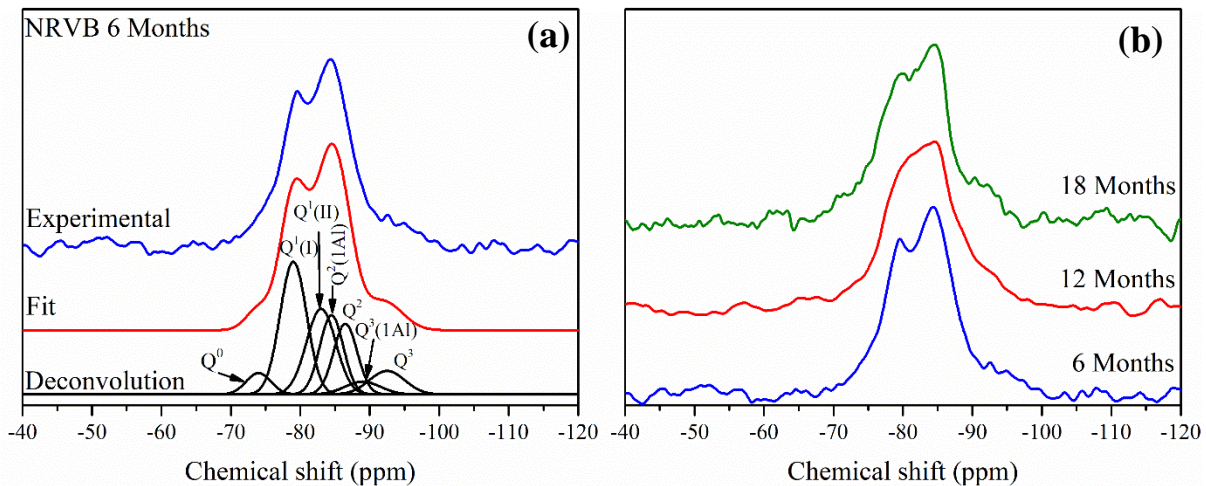


Figure 6.5. (a) Deconvoluted ^{29}Si MAS NMR spectrum of NRVB control sample cured for 6 months; (b) ^{29}Si MAS NMR spectra of NRVB control samples cured for 6, 12 and 18 months.

Between the different curing times, no significant differences were observed between the relative concentration of Q^1 , Q^2 and $Q^3(1Al)$ sites, being the slight variations within the error. A slight decrease of the relative concentration of $Q^2(1Al)$ and Q^3 was observed at later curing times. This resulted in no significant changes in the Ca/Si ratio and in the mean chain length (Table 6.3, which remained at $1.31 \pm 0.07\%$ and $3.6 \pm 0.4\%$, respectively). It is important to note that the Ca/Si ratio obtained through this method (using Richardson et al [120] equation) gives slightly lower values than those expected for this type of cement (CEM I found to be around 1.8 [180]). Previous studies have encountered similar results, where a consistent lower Ca/Si values were obtained [120,162]. This is believed to be due to the process of deconvolution of NMR spectra based on the local environment of silicon, since a great variety of potential ion interactions may affect the chemical shift of each silicon species [162].

Table 6.2. Results of deconvolution of ^{29}Si MAS NMR spectra of NRVB control samples. The estimated uncertainty in absolute site percentages is $\pm 2\%$.

	Q ¹	Q ² (1Al)	Q ²	Q ³ (1Al)	Q ³
6 Months	53 %	16 %	14 %	4 %	7 %
12 Months	51 %	11 %	19 %	3 %	8 %
18 Months	54 %	11 %	16 %	5 %	4 %

In the case of the Al/Si ratio, a slight decrease was observed, which agrees with the decrease in Q²(1Al). This means that a slight decrease of the incorporation of Al in the C-S-H structure occurred. However, the opposite seems to be apparent in the ^{27}Al MAS NMR spectra (Figure 6.6), where an increase of the intensity of the broad peak corresponding to Al in C-S-H, at around 70 ppm, is observed. This slight discrepancy might be attributed to the process of deconvolution performed in the ^{29}Si MAS NMR spectra, as the error for the attribution of the Gaussian peaks is 2%.

Table 6.3. Summary of structural evolution of C-S-H formed in NRVB control samples, based on the ^{29}Si MAS NMR deconvolutions.

	Ca/Si	Al/Si	MCL
6 Months	1.32 ± 0.07	0.08 ± 0.01	3.9 ± 0.5
12 Months	1.30 ± 0.07	0.06 ± 0.01	3.8 ± 0.5
18 Months	1.31 ± 0.07	0.06 ± 0.01	3.6 ± 0.4

From Figure 6.6, it is also possible to observe a decrease in the intensity of the peak attributed to ettringite (at around 14 ppm), which correlates well with the observed decrease of the relative concentration of this phase in XRD analysis (Figure 6.3). This destabilisation of ettringite, and consequent release of Al ions, might be responsible for the observed increase of the Al incorporation into the C-S-H structure. The peak intensity of the AFm phase (at around 9 ppm) seems to be more or less constant as a function of curing time, in good agreement with the XRD results.

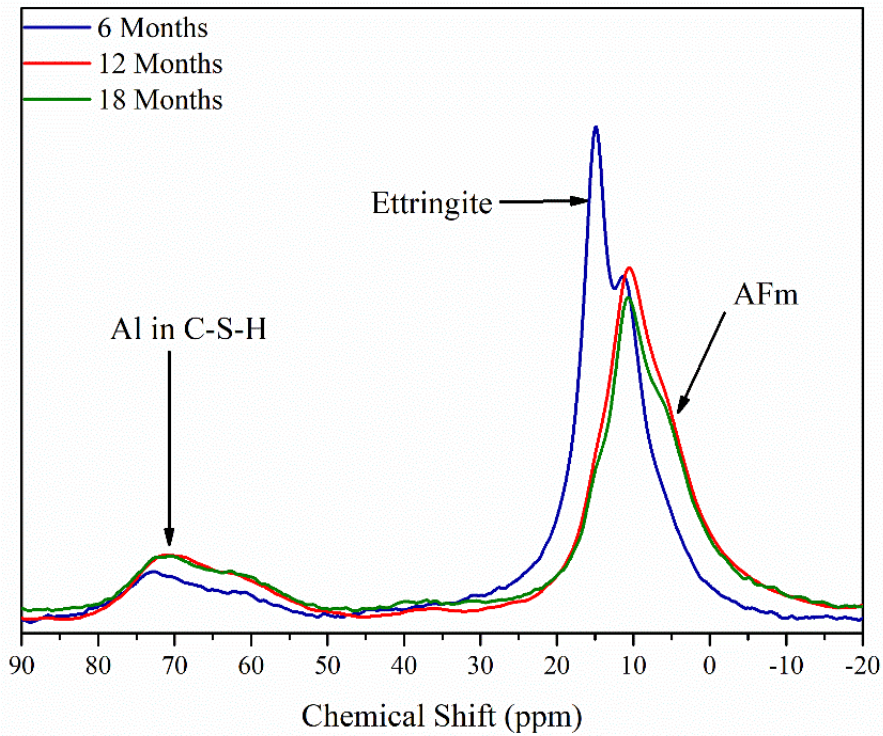


Figure 6.6. ^{27}Al MAS NMR spectra of NRVB control samples cured for 18 months.

To study the porosity of the NRVB, two different techniques were used: X-ray Computed Tomography analysis was used to determine the porosity of the larger sized pores ($> 1.5 \mu\text{m}$, termed herein as *macroporosity*), and nitrogen porosity analysis for the smaller sized pores ($< 50 \text{ nm}$, termed herein as *nanoporosity*). The latter is representative of the pores within C-S-H and interlayer spacings in layered minerals (such as monocarboaluminate and ettringite), while the former relates to porosity between different cement mineral phases.

In terms of macroporosity (Table 6.4), and taking into account the high errors attributed due to the high variability characteristic of processing this type of data (which is based in human error thresholding), no significant differences were observed between the samples that were cured for 6 months and for 12 months.

Table 6.4. *Macroporosity values of NRVB control samples cured for 6 and 12 months, obtained through XCT. Errors calculated from standard deviation of triplicate thresholding.*

	Macroporosity (%)
NRVB Control 6 Months	26.6 ± 8.2
NRVB Control 12 Months	19.1 ± 4.9

From Figure 6.7, a decrease in the volume of the pores $< 5 \text{ nm}$ in size was observed, and an increase of the volume of pores in the size range between 5 to 25 nm, occurred as a function of curing time. This

range of pore sizes is usually related to capillary porosity (space not occupied by hydration products, between 10 nm to a few μm) and C-S-H porosity (gel pores, < 12 nm) [194,195]. As no changes were observed in the C-S-H structure according to the ^{29}Si MAS NMR, this observed opening of the pores, i.e. shift of smaller pores to bigger pores, is likely due to the dissolution (destabilisation) of ettringite (pore sizes < 100 nm [196]), observed previously in the XRD and ^{27}Al MAS NMR.

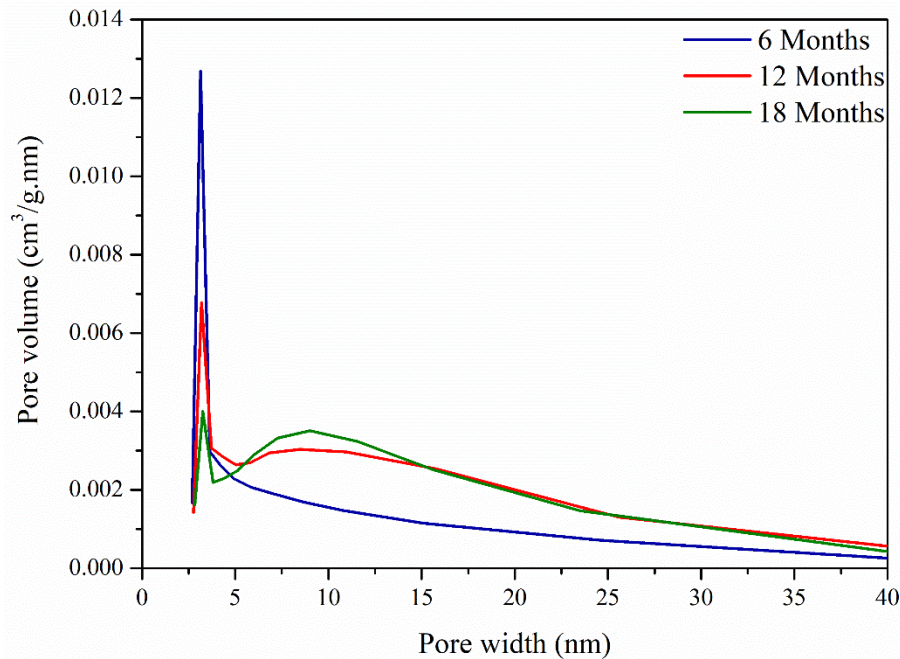


Figure 6.7. Pore size distribution curves for for NRVB control samples cured for 6, 12 and 18 months, determined using Barrett-Joyner-Halenda (BJH) desorption pore size and volume analysis.

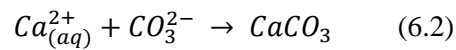
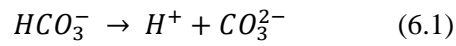
6.3: Mineralogical and microstructural evolution of NRVB with Granitic Groundwater (Semi-Dynamic Experiment)

6.3.1: Mineralogical evolution of NRVB

X-ray diffraction analysis of NRVB (Figure 6.8) in contact with granitic groundwater for 18 months showed a decrease in the intensity of the Bragg reflection corresponding to portlandite, which is different from the behaviour of the NRVB control sample (Figure 6.2 and 6.3), where no significant changes in the peak intensity were observed. From the semi-quantitative XRD Rietveld analysis (Figure 6.9), a quasi-linear decrease of the concentration of portlandite was observed over time, with almost none of this phase detected after 18 months. This observation is in agreement with TG analysis (Figure 6.10), which shows that the peak at around 450 °C corresponding to portlandite decreased with time, disappearing after 18 months of contact with granitic groundwater.

Ettringite and monocarboaluminate were two other hydrate phases identified in the XRD patterns, however no major differences in these were observed to occur as a function of time, in either the XRD or TG analysis.

An increase of the relative concentration of calcite was observed over time (Figure 6.9). This is visible in the TG graph (Figure 6.10) with the increase of the intensity of the peak at around 800 °C. This is a consequence of the presence of bicarbonate (HCO_3^-) in the groundwater composition (Table 6.1), rather than a consequence of the ageing of NRVB (as observed in Section 6.2 where no significant changes in the calcite concentration were visible); when dissolved bicarbonate reacts with free calcium ions, either from the groundwater or from the dissolution of the different hydrate phases in the cement (mainly portlandite), the formation/precipitation of carbonate phases occurs according to Equations 6.1 and 6.2 [66].



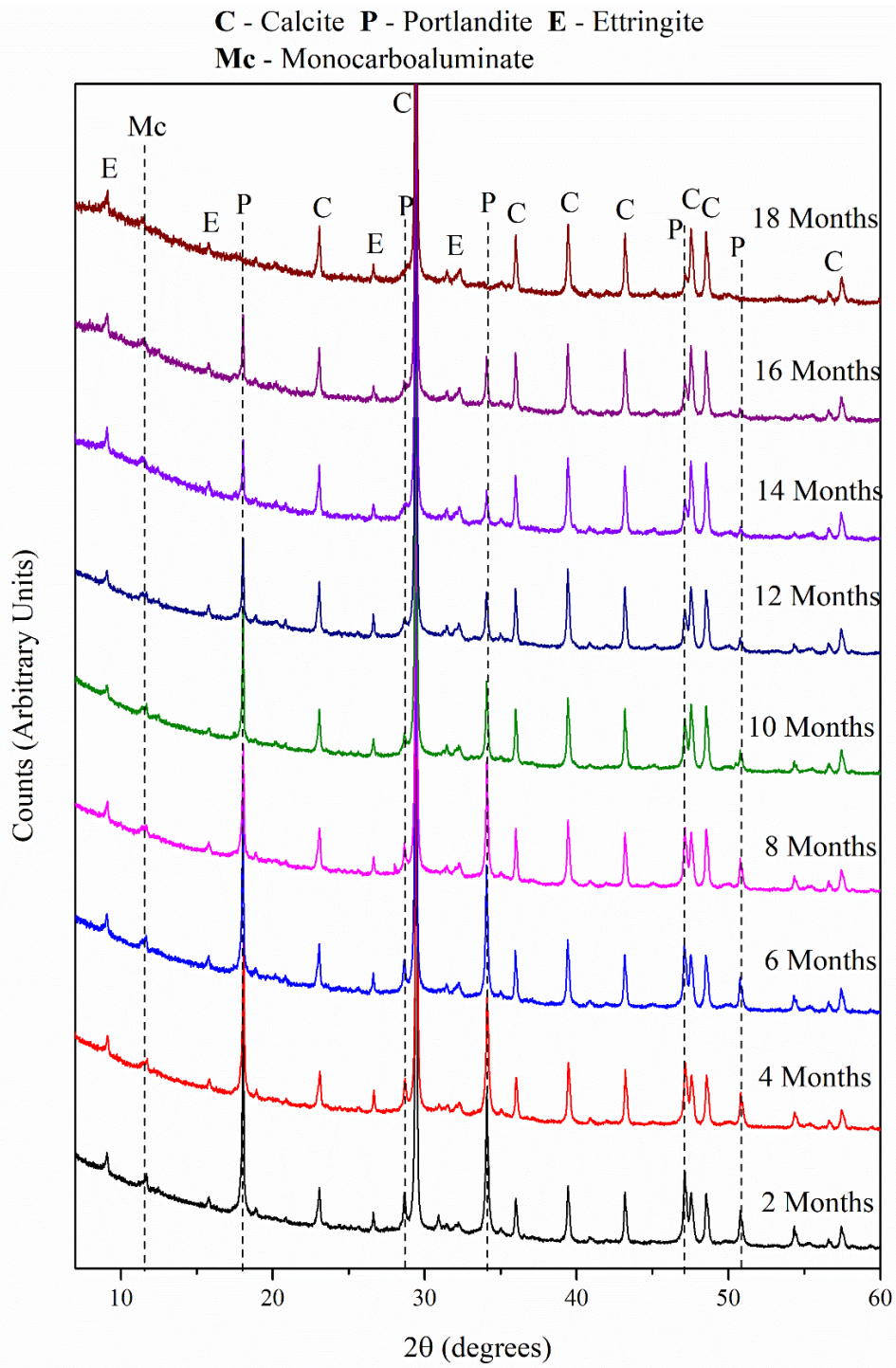


Figure 6.8. XRD patterns of NRVB samples that were placed in contact with granitic groundwater for 18 months.

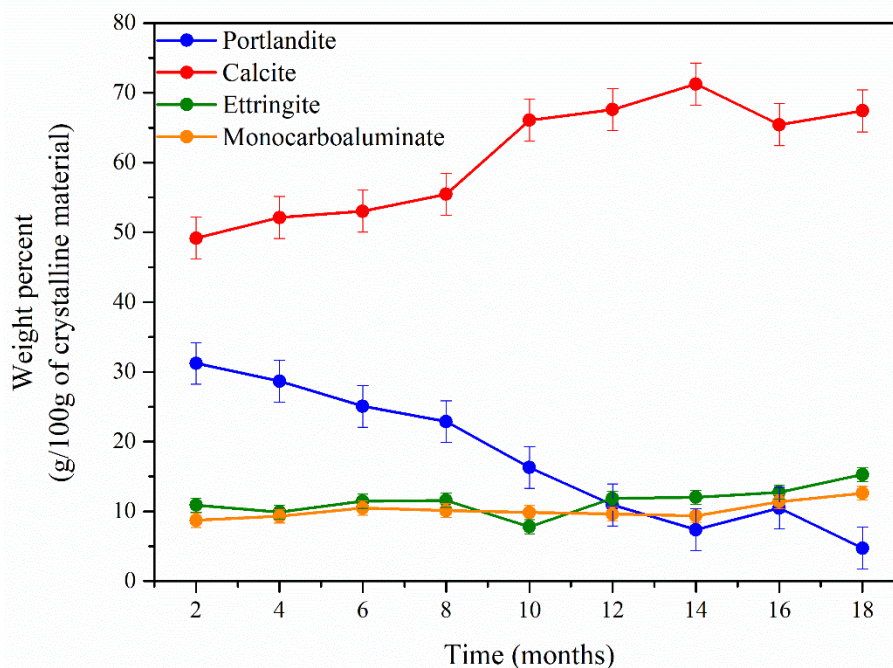


Figure 6.9. Semi-quantitative evaluation of the crystalline phases identified in XRD patterns of NRVB that was in contact with granitic groundwater for 18 months. Error bars obtained through Rietveld refinement software, Topas.

From the TG analysis, it was also possible to observe a broad shoulder between 250 and 400 °C, being more evident in the samples after 2 and 4 months of contact with granitic groundwater (Figure 6.10). The lower temperature region of this shoulder can be attributed to Friedel's or Kuzel's salt ($\text{Ca}_4\text{Al}_2(\text{OH})_{12}\text{Cl}_2 \cdot 4\text{H}_2\text{O}$; $\text{Ca}_4\text{Al}_2(\text{OH})_{12}\text{Cl}(\text{SO}_4)_{0.5} \cdot 5\text{H}_2\text{O}$, respectively), indicating the uptake of Cl from solution, and the higher temperature region (around 400 °C) to brucite ($\text{Mg}(\text{OH})_2$) [192]. Also observed in these samples, especially after 2 and 4 months, was a peak at around 500 °C, which is attributed to the presence of magnesium carbonate (MgCO_3) [192]. The disappearance of this peak after 4 months of contact with groundwater might be related to the preferable formation of CaCO_3 , as more Ca ions are available than Mg ions. This is visible through the increase of the peak intensity of calcite (Figure 6.10).

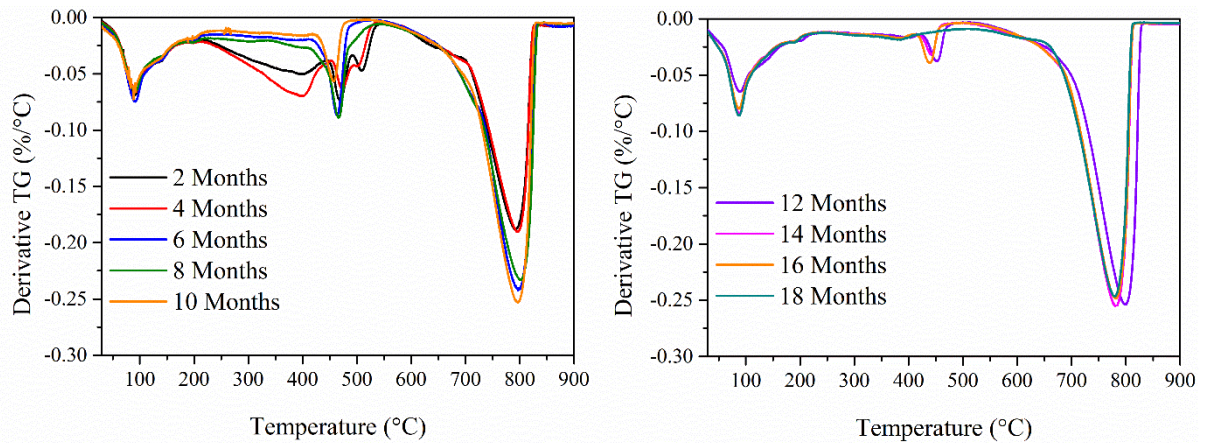


Figure 6.10. TGA data for NRVB samples that were in contact with granitic groundwater for 18 months.

To better understand the evolution of the C-S-H structure as a function of time in contact with granite groundwater, ^{29}Si MAS NMR spectroscopy was performed on NRVB samples after 6, 12 and 18 months of contact with groundwater (Figure 6.11). Clear differences were observed between the different time points of sampling, as shown in Figure 6.11b. It can be agreed that the differences observed are related to the sample being in contact with granitic groundwater, as no significant changes were observed in the control sample cured for 18 months (Section 6.2).

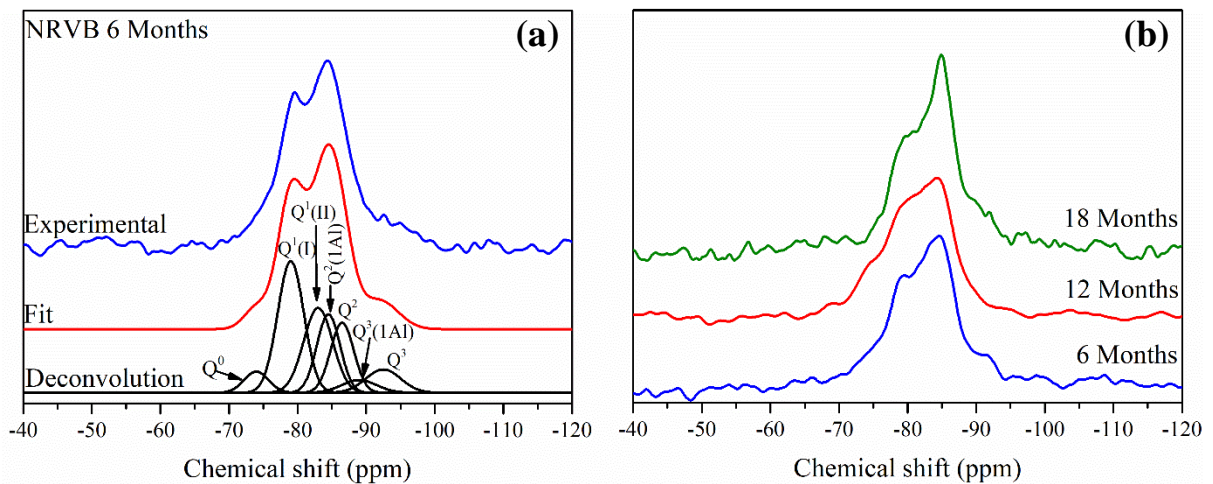


Figure 6.11. (a) Deconvoluted ^{29}Si MAS NMR spectrum of NRVB cured for 6 months; (b) ^{29}Si MAS NMR spectra of NRVB that were in contact with granitic groundwater for 6, 12 and 18 months.

Between 6 and 12 months of contact with groundwater, no differences were observed in the different Q^n sites (Table 6.5), with the values very similar to those obtained for the NRVB control sample at similar curing times (Table 6.2). However, between 12 and 18 months, a decrease in the relative concentration of Q^1 sites was observed, from $54 \pm 2\%$ at 12 months to $46 \pm 2\%$ at 18 months (Table 6.5). This resulted in an increase of the Q^2 and $Q^3(1Al)$ sites, which is indicative of the occurrence of

cross-linking and the incorporation of more Al into the C-S-H structure, possibly due to the destabilisation of ettringite (due to leaching of S observed in the ICP-OES results, Figure 6.19c) and the consequent extra free Al ions (as observed in the ^{27}Al MAS NMR, below). Accordingly, an increase of the mean chain length (MCL) occurred, from 3.5 ± 0.4 at 12 months to 4.7 ± 0.6 after 18 months of the experiment (Table 6.6). Once more, this was apparent only in the samples that were in contact with groundwater, and not in the control samples, demonstrating that these differences are related to the groundwater contact and not ageing of the cement.

Table 6.5. Results of deconvolution of ^{29}Si MAS NMR spectra of NRVB samples that were in contact with granitic groundwater. The estimated uncertainty in absolute site percentages is $\pm 2\%$.

	Q ¹	Q ² (1Al)	Q ²	Q ³ (1Al)	Q ³
6 Months	52 %	13 %	19 %	3 %	3 %
12 Months	54 %	11 %	19 %	1 %	3 %
18 Months	46 %	12 %	28 %	9 %	2 %

The Ca/Si ratio and Al/Si ratio were obtained using the equations of Richardson et al [120] (as described in Chapter 3), and differences were observed with time (Table 6.6). The Ca/Si ratio decreased from 1.28 ± 0.07 at 6 and 12 months to 1.18 ± 0.06 at the end of the experiment. With the observed reduction of portlandite, almost not detected in the XRD and TG analysis, it is believed that this decrease in the Ca/Si ratio is related to decalcification of C-S-H, as continuous leaching of Ca into solution was also observed (Figure 6.19a). Indeed, this has been observed in previous work [197], where the Q¹/Q² ratio was used to show that decalcification of C-S-H was occurring in CEM I samples in contact with clay groundwater, i.e. a reduction of this ratio was attributed to the decalcification of C-S-H.

Table 6.6. Summary of structural evolution of C-S-H formed in NRVB samples that were in contact with granitic groundwater, based on the ^{29}Si MAS NMR deconvolutions.

	Ca/Si	Al/Si	MCL
6 Months	1.28 ± 0.07	0.07 ± 0.01	3.7 ± 0.5
12 Months	1.28 ± 0.07	0.06 ± 0.01	3.5 ± 0.4
18 Months	1.18 ± 0.06	0.06 ± 0.01	4.7 ± 0.6

The results from ^{27}Al MAS NMR correlate well with these results. In Figure 6.12, comparison between NRVB samples that were in contact with granitic groundwater for 6, 12 and 18 months is made, and four peaks are distinguished: the broad peak with a centre at around 70 ppm is attributed to the incorporation of Al in the C-S-H structure; the peaks at around 14 ppm and 9 ppm indicate the presence of octahedrally coordinated Al in ettringite and AFm phases, respectively; and the peak at around 5 ppm is attributed to the third aluminate hydrate (TAH) [198]. TAH is an amorphous/disordered phase,

which is formed in minor amounts in Portland cements and blended Portland cements, in addition to AFt and AFm phases [162,198].

A gradual increase in the intensity of the peak corresponding to Al in C-S-H was observed as a function of time, in agreement with the ^{29}Si MAS NMR data, that showed an increase in the relative concentration of $\text{Q}^2(1\text{Al})$ and $\text{Q}^3(1\text{Al})$ sites. The intensity of the peak corresponding to ettringite decreased between 6 and 12 months. This is due to the leaching of sulphate from NRVB, as discussed later in this Section. However, a slight increase in the intensity of the same peak was observed to occur between 12 months and 18 months, demonstrating the increase of the formation of this phase at later ages of contact with groundwater. These differences were not visible in the previous XRD and TGA results, which might be indicative that this variability, if it occurred, was not significant.

Considering the AFm phases, a slight decrease in the intensity of the peak was observed with time (Figure 6.12), which might suggest that monocarboaluminate (AFm) was converted to ettringite (AFt) [147]. However, this change was not evident through XRD and TG data. The observed decrease allows the observation of the peak attributed to Third Aluminate Hydrate (TAH), which otherwise overlaps with the peak attributed to AFm phases.

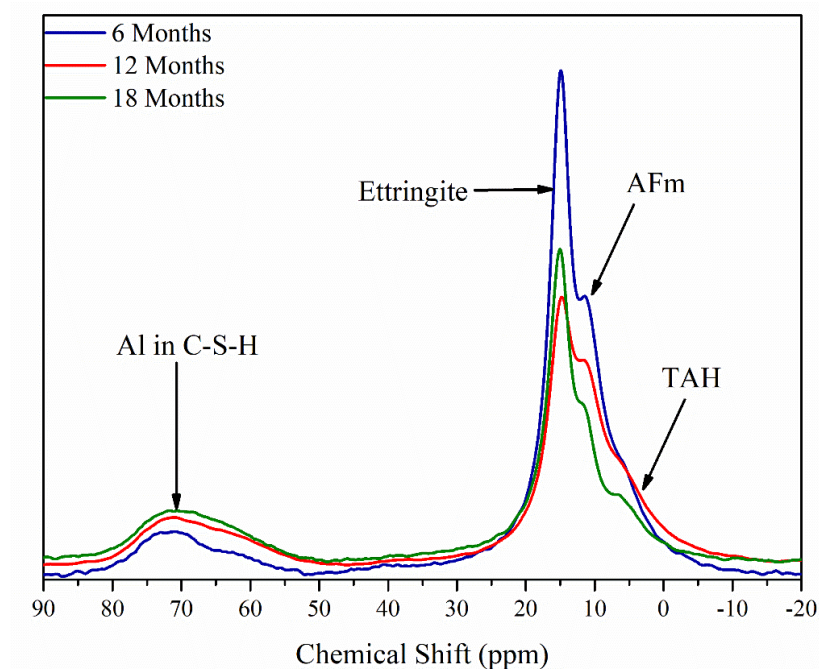
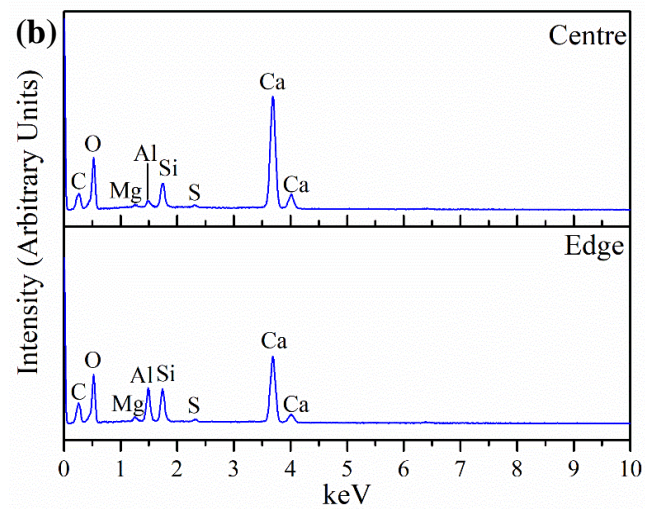
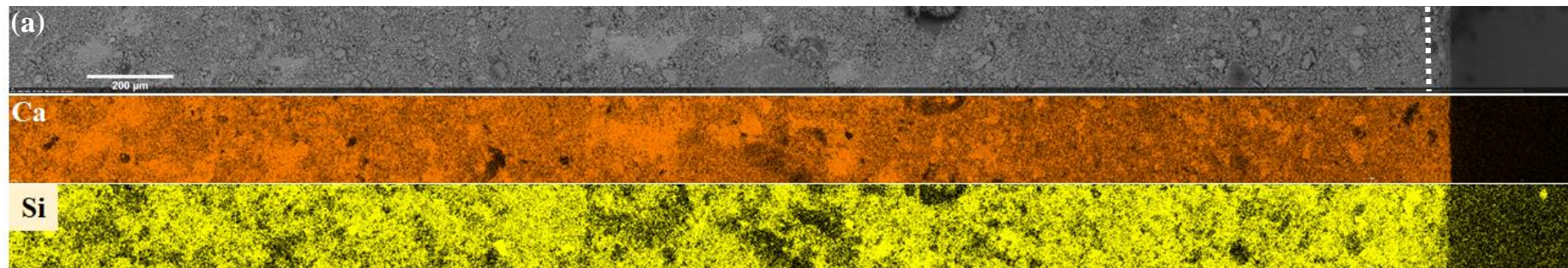


Figure 6.12. ^{27}Al MAS NMR spectra of NRVB samples that were placed in contact with granitic groundwater for 18 months.

Since the top and bottom of the NRVB samples were sealed, to encourage radial diffusion of groundwater into cement (for transport modelling performed by EU project partners, performed externally to this Thesis), it was possible to ascertain whether there was an element / mineral phase assemblage gradient, from the outside of the NRVB pellet (in contact with solution), to the centre. SEM – EDX analysis across the entire radius of the samples was performed. The results for NRVB in contact with granitic groundwater for 6 months are shown in Figure 6.13, which includes the BSE image, elemental maps and elemental spectra from points collected at the edge (to the right of the white dashed line in Figure 6.13) and the centre of the sample (towards the left hand side of the image), and gives the atomic percentage of each element at those points. A depletion in Ca was observed at the edge of the sample (19.60 ± 0.99 at.%) when compared to the centre of the sample (26.91 ± 1.45 at.%) (Figure 6.13, Table). Furthermore, a slight increase of the Al concentration at the edge of the sample was also observed. However, no other differences were visible.



	Edge (at %)	Centre (at %)
Ca	19.60 ± 0.99	26.91 ± 1.45
Mg	0.78 ± 0.08	0.31 ± 0.05
Al	5.65 ± 0.33	0.79 ± 0.08
Si	5.67 ± 0.31	3.13 ± 0.20
S	0.39 ± 0.06	0.31 ± 0.05

Figure 6.13. SEM-EDX analysis of NRVB sample that was in contact with granitic groundwater for 6 months; (a) BSE image and elemental maps; (b) spectra associated with point analysis; Table: point analysis in atomic %, with absolute error from the measurement.

After 12 months of contact with granitic groundwater, similar analysis was performed but at a higher magnification (Figure 6.14a). At this magnification it was possible to observe a layer at the edge of the sample, composed mainly of Ca with some incorporation of Mg. The linescan indicates that there is a slight increase of the magnesium concentration at the edge of the NRVB sample (Figure 6.14b), which is consistent with the precipitation of brucite observed in TGA data (Figures 6.10). However, it should be noted that this slight increase might be due to the position of the linescan, which might have sampled a Mg-rich particle.

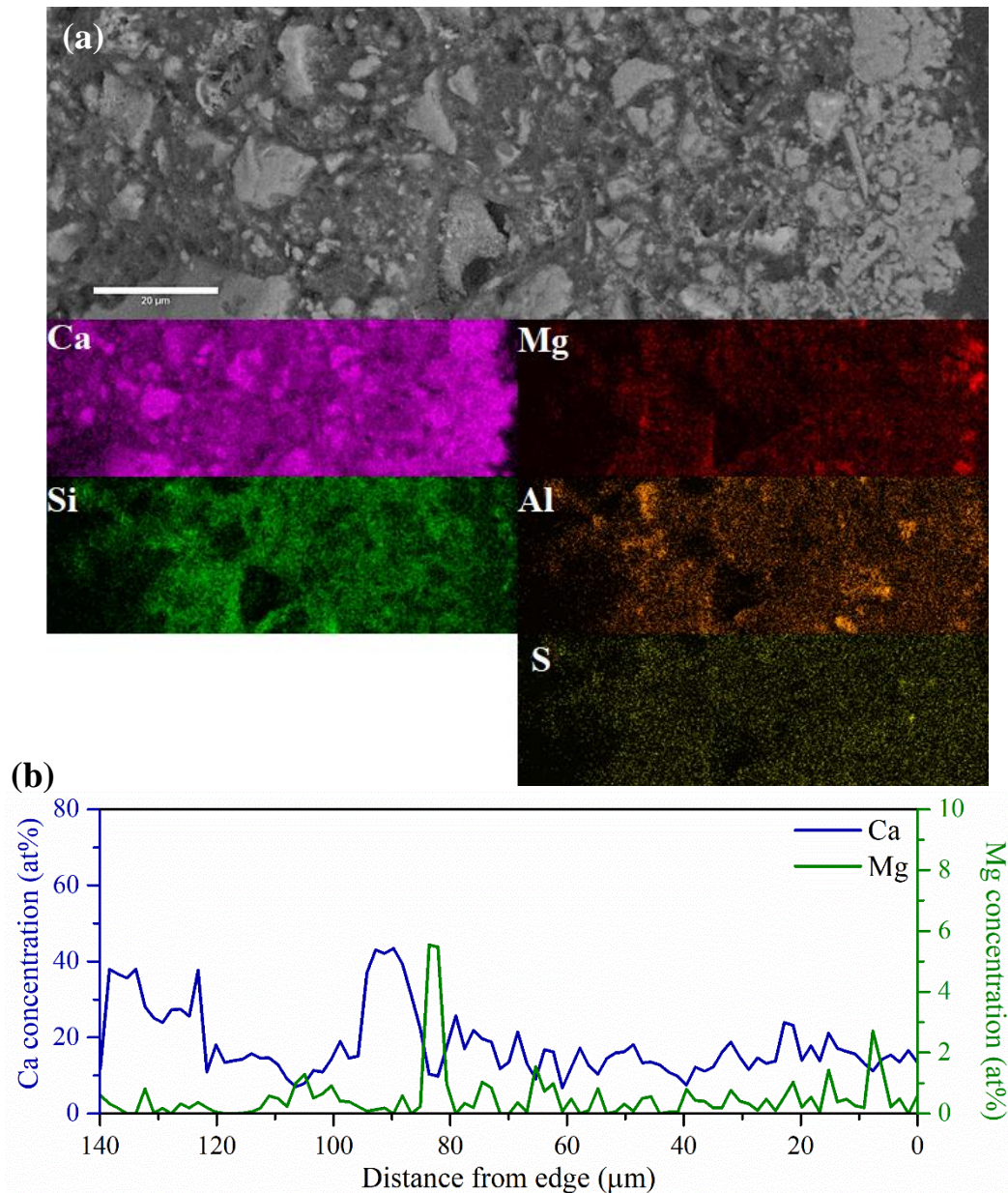


Figure 6.14. SEM-EDX analysis of NRVB sample that was in contact with granitic groundwater for 12 months; (a) BSE image and elemental maps; (b) Linescan of magnesium and calcium in atomic %.

To distinguish whether different mineral phases were present at the edge and the centre of the NRVB in contact with granitic groundwater for 12 months, 100 to 150 EDX point spectra were acquired, per region in the edge or centre, and the molar ratios were plotted, as shown in Figure 6.15. The EDX data were then compared with the ideal composition of each hydrate phase and the compositional trend lines connecting C-S-H and portlandite/calcite with the other hydrate phases. The red points in Figure 6.15 relate to the EDX data acquired in the centre of the pellet after 12 months of contact time with groundwater; a mixture of portlandite, monocarboaluminate and brucite was observed. In the Al/Ca vs Cl/Ca plot (Figure 6.15d), it is possible to observe that a small number of data points collected from the centre of the sample are located along the indicative lines corresponding to Friedel's and Kuzel's salt compositions, suggesting that Cl⁻ may be incorporated in the NRVB, in agreement with TG analysis (Figure 6.10) of these samples. It is clear that there are no major differences between the phase assemblage at the edge and the centre of the pellet in contact with granitic groundwater for 12 months. This may be due to the high porosity of NRVB, allowing penetration of groundwater solutes throughout the entire pellet.

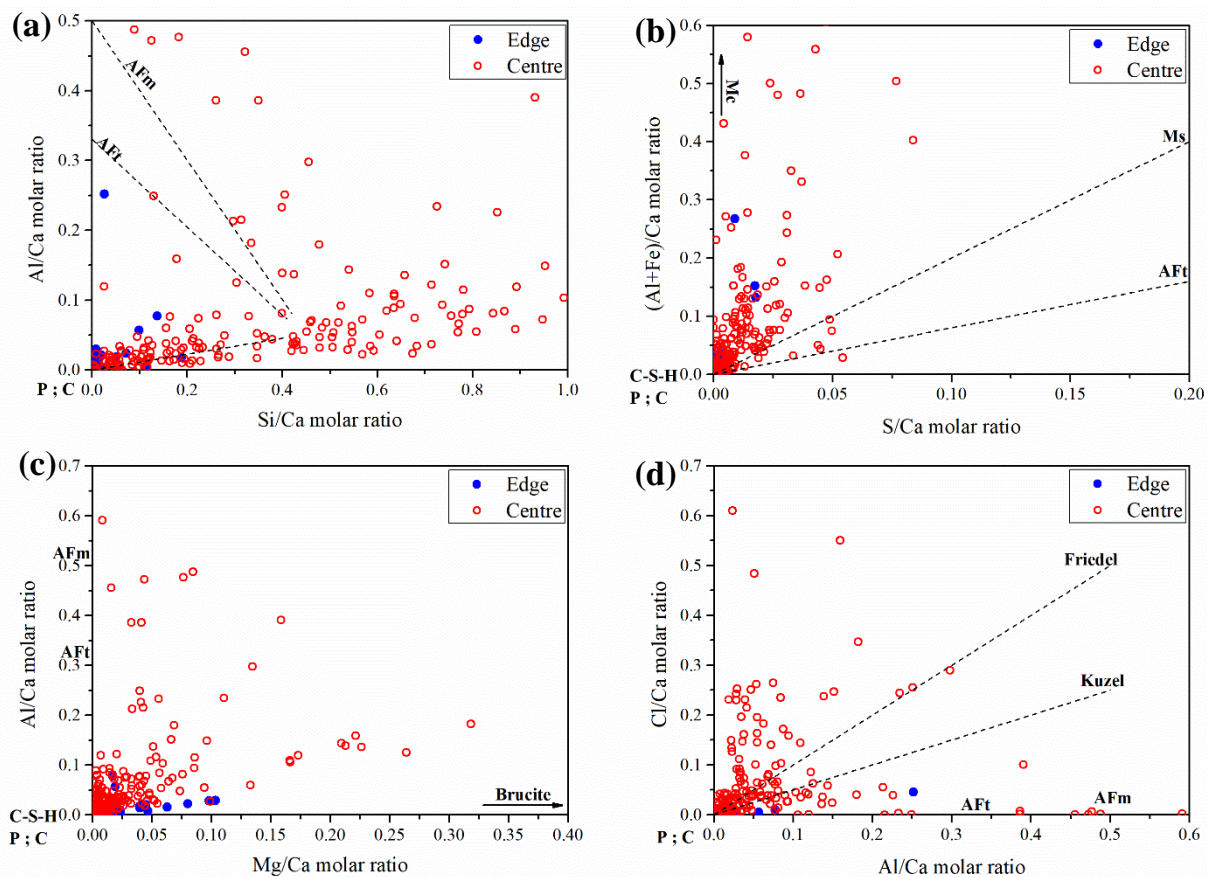


Figure 6.15. Elemental molar ratio plots of SEM-EDX point analysis in NRVB sample that was in contact with granitic groundwater for 12 months: (a) Si/Ca vs Al/Ca; (b) S/Ca vs (Al+Fe)/Ca; (c) Mg/Ca vs Al/Ca; (d) Al/Ca vs Cl/Ca. The dashed lines are compositional trend lines connecting C-S-H or portlandite/calcite with other hydrate phases. P – portlandite; C – calcite; Mc – monocarboaluminate; Ms – monosulphoaluminate; AFm – Ms and Mc; AFt – ettringite.

At 18 months of contact with groundwater, the NRVB sample presented similar findings to those described above for 12 months of contact time, with a visible Ca- (and possibly Mg-) rich outside layer observed (Figure 6.16). The linescan shows that the at% of Mg present in the outside layer was slightly higher (around 7 at%, Figure 6.16b) than that observed at 12 months (around 3 at%, Figure 6.14b), evidencing a possible increase in the precipitation of brucite into the outside layer of the sample. The constant replenishment of Mg (in the granitic groundwater solution every 2 months) is likely to be the reason for the observed overall increase.

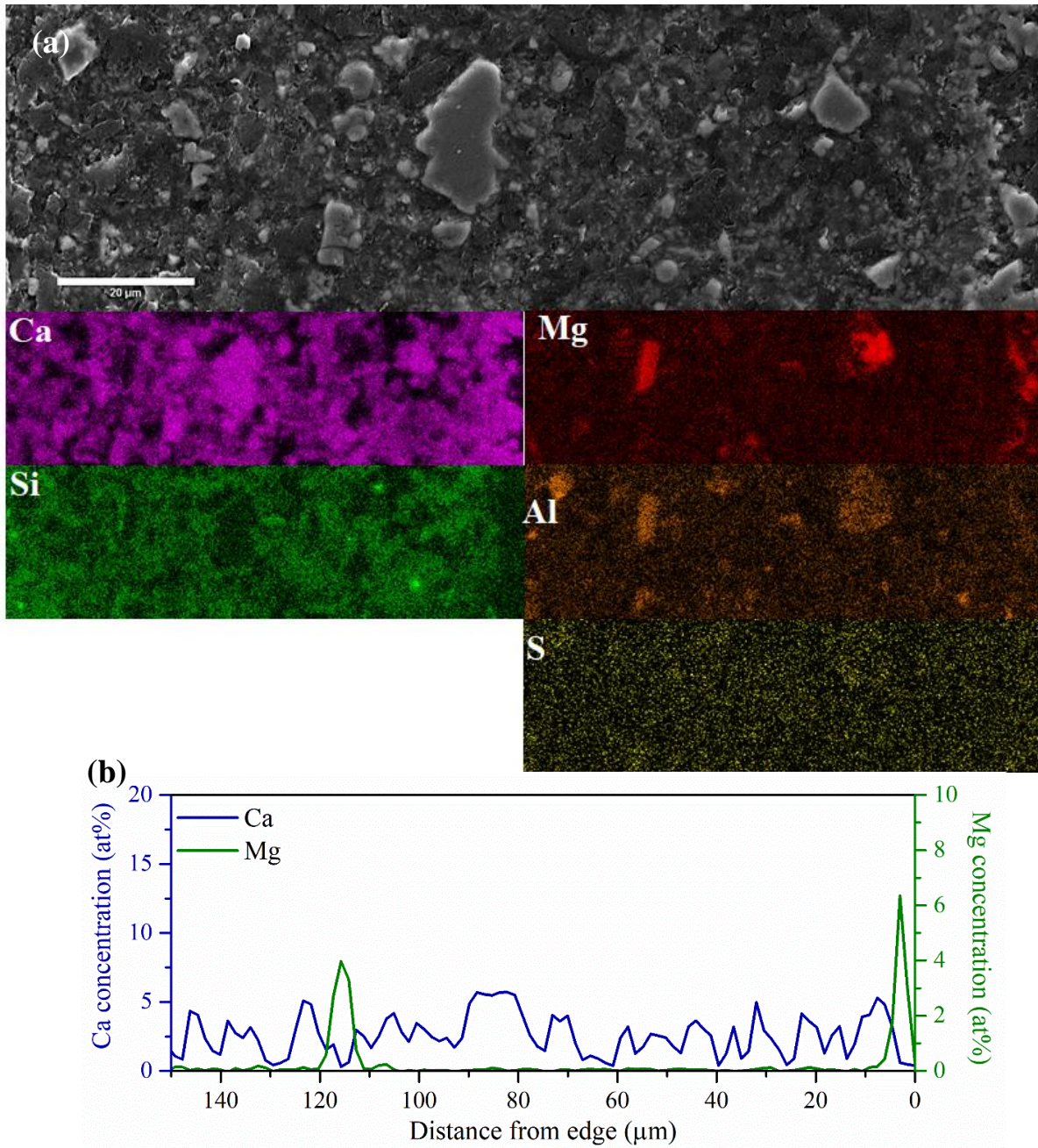


Figure 6.16. SEM-EDX analysis of NRVB sample that was in contact with granitic groundwater for 18 months; (a) BSE image and elemental maps; (b) Linescan of magnesium and calcium in atomic %.

From the molar ratio plots for NRVB in contact with granite groundwater for 18 months (Figure 6.17), it is possible to conclude that the edge area is rich in mainly Ca-containing phases, e.g. calcite. In the centre area of the NRVB pellet, the results indicate the main hydrate phases present are C-S-H, portlandite and AFm phases (Figure 6.17a,b,c). In terms of Cl⁻ uptake, it seems that no further incorporation of this element into the NRVB was observed with time, with the plot at 18 months (Figure 6.17d) being similar to the one observed at 12 months (Figure 6.15d). Some brucite may have precipitated at the edge of the sample, as some of the blue points present in the Mg/Ca vs Al/Ca plot are situated towards this phase.

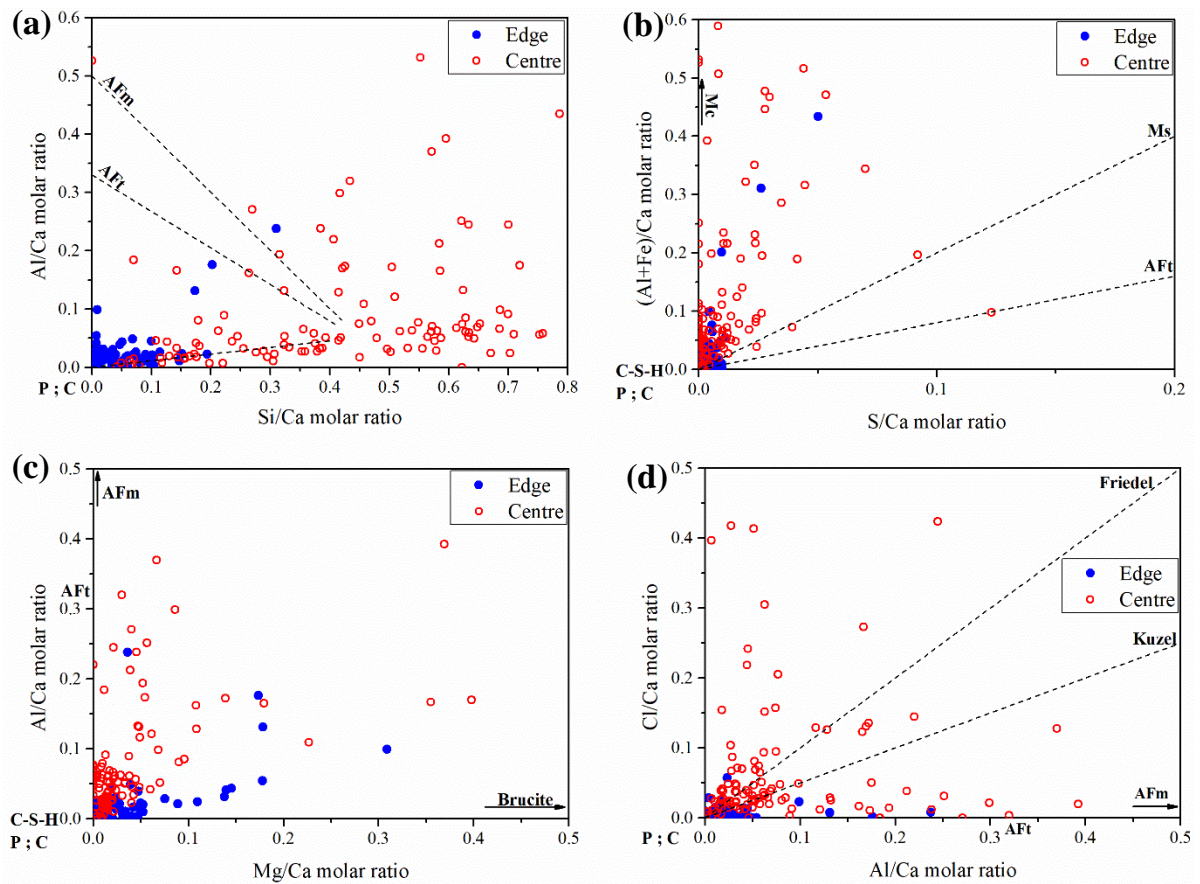


Figure 6.17. Elemental molar ratio plots of SEM-EDX point analysis in NRVB sample that was in contact with granitic groundwater for 18 months: (a) Si/Ca vs Al/Ca; (b) S/Ca vs (Al+Fe)/Ca; (c) Mg/Ca vs Al/Ca; (d) Al/Ca vs Cl/Ca. The dashed lines are compositional trend lines connecting C-S-H or portlandite/calcite with other hydrate phases. P – portlandite; C – calcite; Mc – monocarboaluminate; Ms – monosulphoaluminate; AFm – Ms and Mc; AFt – ettringite.

6.3.2: Nano- and micro-structural evolution of NRVB

Since a number of mineralogical changes were observed when NRVB was in contact with granitic groundwater, porosity analysis was undertaken to determine whether these changes influenced the overall structure of the samples.

The macroporosity results of NRVB contacted with groundwater for 6 months gave lower values than NRVB that was of the same age, but not contacted with groundwater (~12% porosity compared with 26%, respectively). This indicates a significant reduction in porosity when NRVB is in contact with granitic groundwater (Table 6.7). After 12 months, the porosity reduced a little, but values were close to those measured at 6 months of experiment. Dissolution of portlandite, apparent from the XRD data, should lead to an overall increase in macroporosity. However, precipitation of both calcite and brucite was observed, which, according to these results, blocks the pores of NRVB quite significantly. Indeed, the precipitation of these phases has previously shown in the literature to have a “healing” effect in terms of reducing the porosity [180,197,199,200].

Table 6.7. Macroporosity values of NRVB samples that were in contact with granitic groundwater for 6 and 12 months, obtained through XCT. Errors calculated from standard deviation of triplicate thresholding.

	Macroporosity (%)
NRVB Granitic 6 Months	12.3 ± 3.0
NRVB Granitic 12 Months	9.3 ± 1.7

Figure 6.18 shows the results of nanopore width as a function of pore volume at 6, 12 and 18 months of contact time with granitic groundwater. There was an increase in the volume of the pores < 5 nm in size with increasing groundwater contact time, and also an increase of the volume of pores in the size range of 5 to 25 nm, especially at 18 months. This is likely due to a combination of an increase in the capillary porosity due to dissolution of hydrate phases (portlandite and ettringite), and also due to the observed slight decalcification of C-S-H at 18 months, which leads to an increase in the volume of gel pores (< 12 nm) [194,201]. These results, especially for pores < 5 nm at 18 months, were different when compared to the control samples, therefore, the observed changes are related to the contact with groundwater, and the consequent decalcification of C-S-H (not simply ageing). The increase of the nanoporosity due to dissolution of hydrate phases, mainly C-S-H, has been previously observed when

cement samples were placed in contact with ammonium nitrate solution to study the decalcification processes [194].

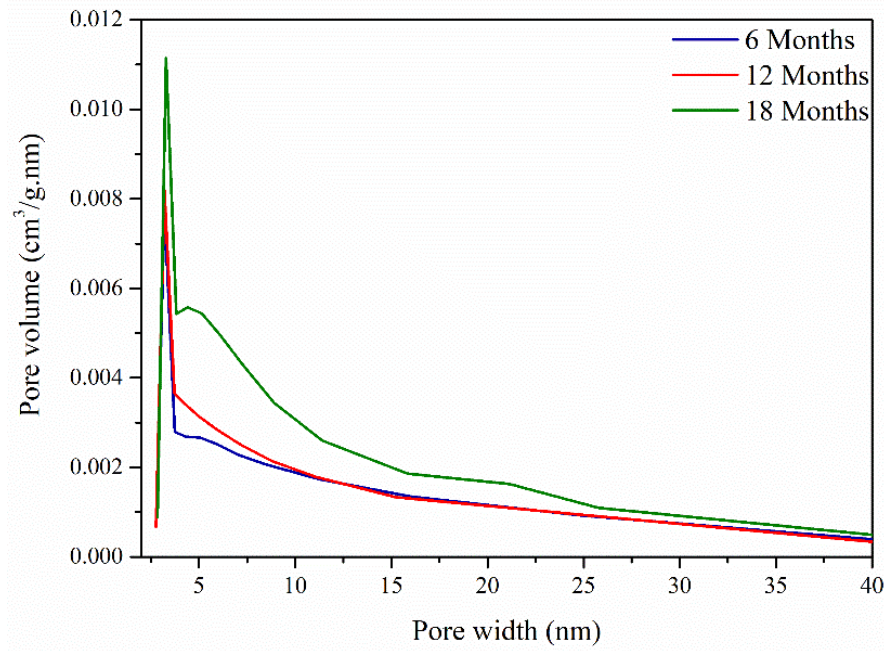


Figure 6.18. Pore size distribution curves for NRVB samples that were in contact with granitic groundwater for 6, 12 and 18 months, determined using Barrett-Joyner-Halenda (BJH) desorption pore size and volume analysis.

6.3.3: Solution chemistry

At each time point of sampling, the pH of the solutions was measured (at room temperature) and an increase in pH relative to the blank solution (pH 8.5 for granitic groundwater) was always observed, as intended in the design of the NRVB material. After 2 months of contact with groundwater (i.e. the first time point of measurement) the pH was 11.7 – 12.3. An increase of the pH was observed until 8 months, where it reached a maximum of 12.9 – 13.3. For the following time points, a small decrease of the pH was observed, being around 12.1 – 12.4 after 18 months. Although a decrease was observed, the pH was $\text{pH} > 12$ throughout the experiment.

ICP-OES and IC analysis of the solutions was performed, and the results are shown in Figure 6.19. The data are presented as “difference in measured concentration relative to the blank”, with the blank being the groundwater solution used to replace the solution every two months (measured prior to addition to NRVB). The blank value is equal to zero in every graph. In presenting the results in this format, it is possible to observe where concentrations of elements were higher than in the blank groundwater solution (i.e. elements leached out of the cement), or lower, indicating that they had been incorporated as a mineral phase within the cement. This also allows accountancy of minor discrepancies in the

composition of the groundwater added at each time point (the total volume used over the 18 months duration of the experiment was several tens of litres, so it was necessary to prepare new solution at each time point, and each solution was not always exactly identical due to minor errors in weighing chemicals).

Significant concentrations of Ca were leached from the cement throughout the duration of the experiment (Figure 6.19a). A slight decrease in the concentration of Ca leached after 6 months was observed, which may be related to the formation of a Ca and Mg-rich outer layer (e.g. Figure 6.16), which might act as a protective layer, slightly reducing the amount of Ca leached. At pH values of >10 , Mg precipitation as brucite is thermodynamically favoured, as previously observed in the solid state analysis of NRVB samples (Section 6.3.1). Accordingly, the concentration of Mg was found to always be lower than that in the granitic groundwater.

In terms of S, an initial leaching of this element from the NRVB to the solution was observed (Figure 6.19c). This is in agreement with the previous observations made on the cement samples, where an initial reduction of the quantity of the sulphur-bearing phase ettringite, was observed (e.g. Figure 6.10). Thus, ettringite was leached from NRVB. With continued replacement of leachate, and hence S, over the 18 month duration of the experiment, the amount of S leached reduced (with values at 18 months being similar to the blank, i.e. no leaching or precipitation). This is concurrent with the observed increase in ettringite formation between 12 and 18 months, as observed in the ^{27}Al MAS NMR. It is clear that the S concentrations in solution are linked to the ettringite content of the NRVB, and the reason for the fluctuation in content is thought to be due to the fact that granitic groundwater has a low concentration of S (around 3 mg/L), which will possibly destabilise the AFt phase through leaching of S. However, these fluctuations occur at very small scale, i.e. the variations in the concentration are very small, being detectable neither by XRD nor TGA (solid-state techniques).

Initial leaching of the Si was observed, followed by a rapid reduction in leaching until 6 months when the concentration was similar to that in the original granite groundwater solution. The initial release may result from the dissolution of free silicon. In terms of chloride, an initial uptake of this element was observed for the first 4 months, being followed by a combination of leaching and uptake. The observed appearance of Cl-rich phases, like Friedel's/Kuzel's salts, mainly in the samples that were in contact with the groundwater for 2 and 4 months (Figure 6.10), correlate well with this behaviour.

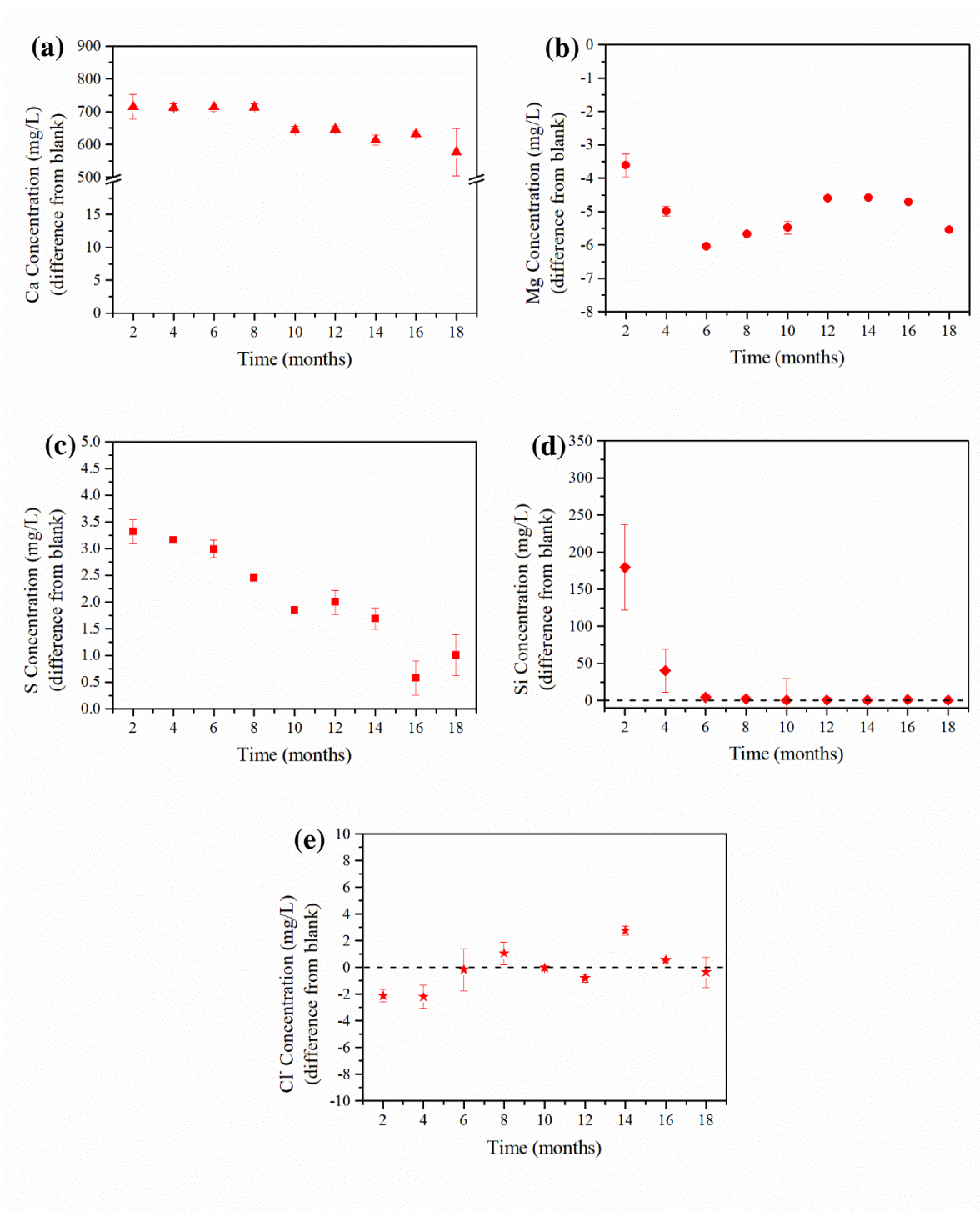


Figure 6.19. Elemental concentrations in solution (mg/L) obtained through the difference from blank for NRVB samples that were in contact with granitic groundwater for 18 months: (a) Ca concentration; (b) Mg concentration; (c) S concentration; (d) Si concentration; (e) Cl concentration. Errors were calculated using the standard deviation of duplicate ICP-OES and IC measurements.

6.4: Mineralogical and microstructural evolution of NRVB with Saline Groundwater (semi-dynamic experiment)

6.4.1: *Mineralogical evolution of NRVB*

As observed for the NRVB samples in contact with granitic groundwater, there were distinct differences between NRVB in contact with saline groundwater when compared to the non-groundwater contacted NRVB (Section 6.2). There was a quasi-linear decrease in the intensity of the XRD peak corresponding to portlandite (Figures 6.20 and 6.21), as was observed for samples in contact with granitic groundwater. However, in this case, portlandite seemed to disappear after 16 months. The disappearance of the peak corresponding to monocarboaluminate was observed after 6 months and, at the same time, the intensity of the peaks related to ettringite increased. This is due to the presence in the saline groundwater composition of high amounts of sulfate (S) (Table 6.1), which will favour the conversion of monocarboaluminate into ettringite, a more stable phase in high S environments [52,147]. However, from the semi-quantitative results it is apparent that the formation of ettringite reached a plateau after 14 months (Figure 6.21). A possible slight decrease was observed after 18 months, but this variation seems to be very small.

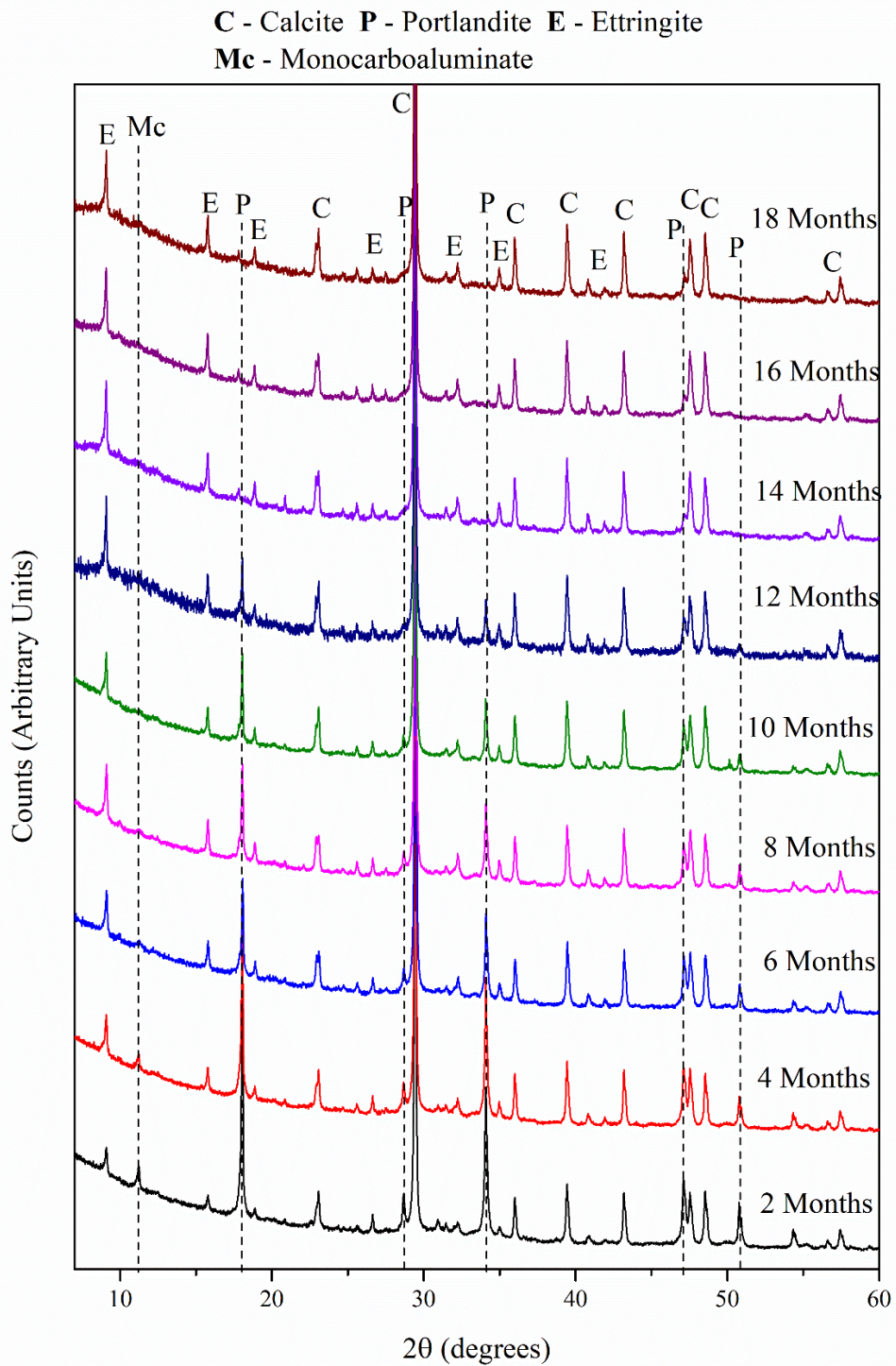


Figure 6.20. XRD patterns of NRVB samples that were placed in contact with saline groundwater for 18 months.

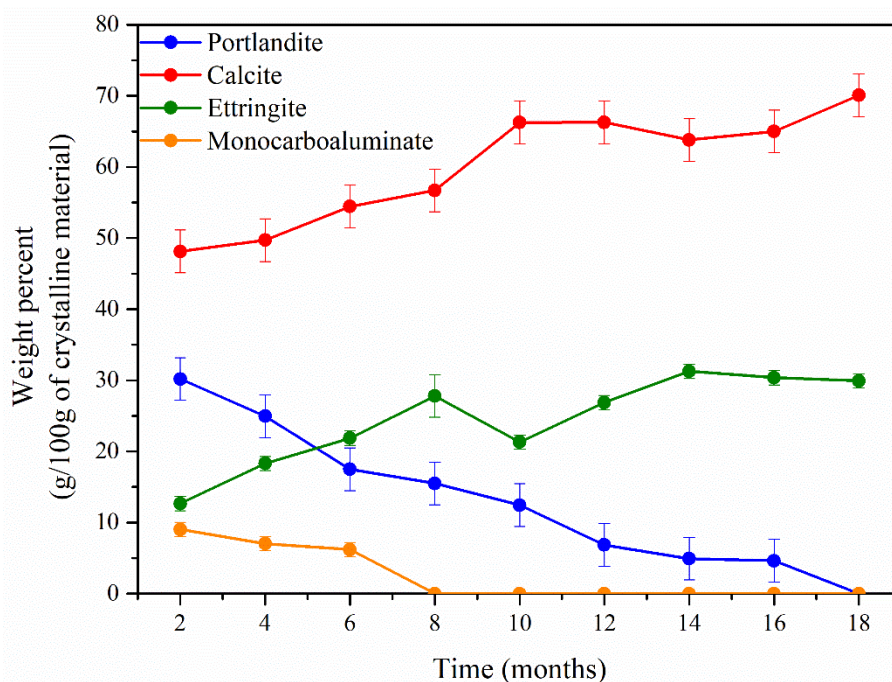


Figure 6.21. Semi-quantitative evaluation of the crystalline phases identified in XRD patterns of NRVB that was in contact with saline groundwater for 18 months. Error bars obtained through Rietveld refinement software, Topas.

These findings agree well with the results obtained in the TG analysis, shown in Figure 6.22, where an increase in the intensity of the peak at 100 °C, related to ettringite, was observed as a function of time, reaching a maximum intensity at 14 months. The shoulder corresponding to monocarboaluminate, at 150 °C, disappeared after 6 months of the experiment, as also observed in the XRD patterns. The portlandite peak at around 450 °C decreased with time until it was no longer evident after 14 months (in contrast to 16 months in the XRD data). The NRVB samples from 2 to 8 months of contact with saline groundwater exhibited a broad peak at lower temperature values than portlandite, which is indicative of the presence of brucite (at around 350 °C) and possibly some Cl⁻ containing phases (Friedel or Kuzel's salt). After 8 months, only the peak related to brucite was visible.

In terms of carbonates, it was possible to observe an increase in the intensity of the peak between 750 and 800 °C, which is due to the presence of HCO₃⁻ in the saline groundwater composition (Equations 6.1 and 6.2). This was also observed in the semi-quantitative XRD analysis, where an increase in the relative concentration of calcite as a function of time was apparent (Figure 6.21). It is interesting to note a slight shoulder at around 600 °C, which corresponds to CaCO₃ polymorphs that contain some magnesium [192], since in this groundwater, the Mg content is high (Table 6.1).

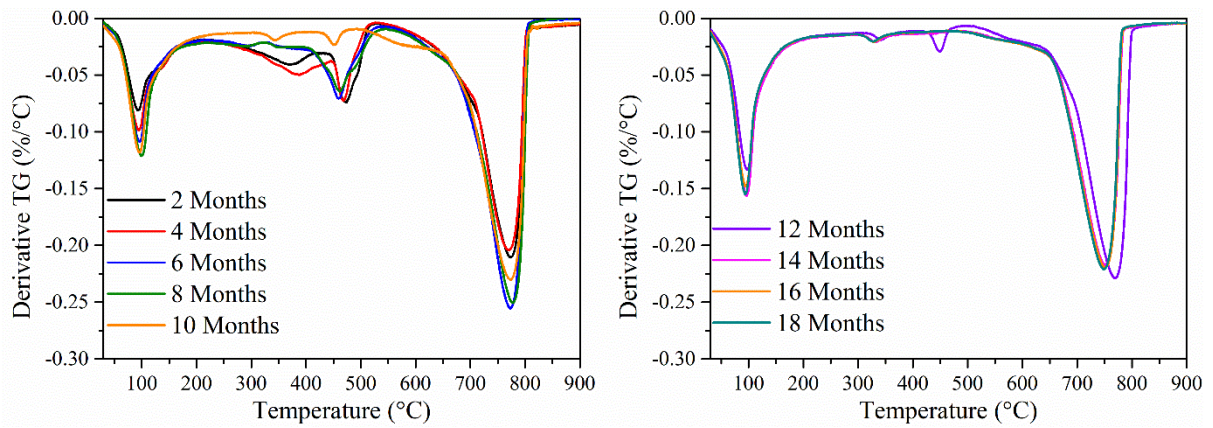


Figure 6.22. TGA data for NRVB samples that were in contact with saline groundwater for 18 months.

In the ^{29}Si MAS NMR spectra (Figure 6.23b), clear differences were observed when comparing the samples at 6, 12 and 18 months of contact with saline solution. From the quantification obtained through the deconvolution of the ^{29}Si MAS NMR spectra (Figure 6.23a), a decrease in the relative concentration of the Q^1 sites is observed as a function of time, from $56 \pm 2\%$ at 6 months to $34 \pm 2\%$ at 18 months (Table 6.8). This was concurrent with an increase of the Q^2 site relative concentration (Table 6.8), indicating an increase of the MCL (Table 6.9).

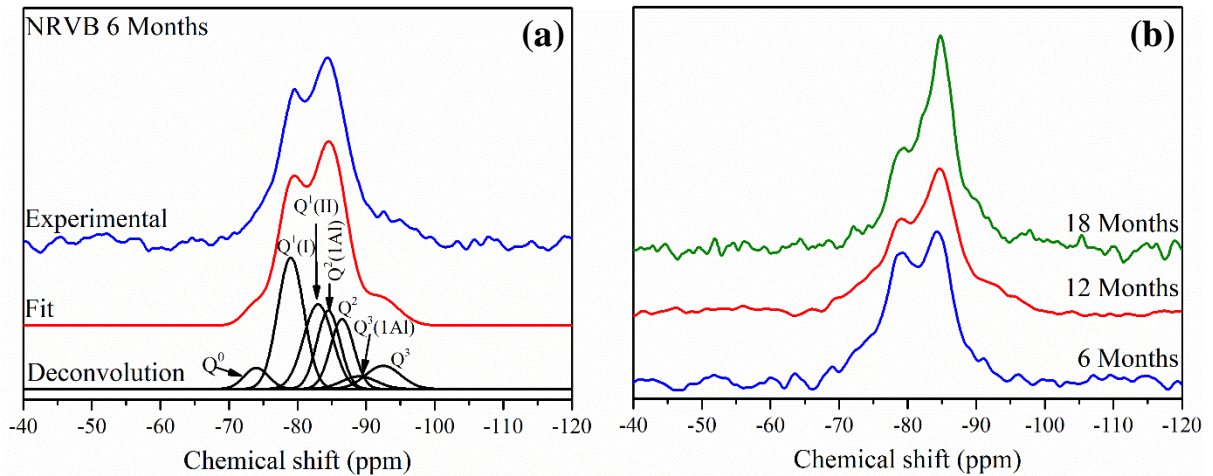


Figure 6.23. (a) Deconvoluted ^{29}Si MAS NMR spectrum of NRVB cured for 6 months; (b) ^{29}Si MAS NMR spectra of NRVB that were in contact with saline groundwater for 6, 12 and 18 months.

The slight decrease of the $\text{Q}^2(1\text{Al})$ and $\text{Q}^3(1\text{Al})$ from 6 to 12 months of contact with saline groundwater is indicative of the reduction of Al incorporation in the C-S-H structure, which is also visible in the ^{27}Al MAS NMR spectra (Figure 6.24). This is linked to the formation of ettringite (as observed in XRD and TGA data): the high concentration of S in solution sequesters Al to form ettringite, rather than incorporating it in C-S-H. However, an increase in the relative concentration of these same sites, $\text{Q}^2(1\text{Al})$ and $\text{Q}^3(1\text{Al})$, occurs for the 18 month exposed sample, showing an increase of the Al

incorporation into the C-S-H. The ^{27}Al MAS NMR spectra (Figure 6.24) confirms this behaviour, and shows that the peak corresponding to Al in C-S-H increased after 18 months. These data also show that the peak corresponding to ettringite (at 14 ppm, Figure 6.24) had decreased at 18 months. Combined, these data indicate that some ettringite destabilisation occurred at this time, possibly related to the observed total consumption of portlandite (Figures 6.21 and 6.22) and consequent dissolution of ettringite, which led to Al being incorporated back to the C-S-H structure. It has been shown before in leaching experiments with demineralised water [66,71,202] that after all portlandite has been dissolved, secondary phases start to dissolve: first the AFm phases, followed by AFt phases and calcite. The observed constant leaching of Ca (see Figure 6.31a), even after all portlandite has been consumed, might be indicative of the dissolution of ettringite. However, this effect is thought to be small, since a decrease in the ettringite content was not evident in the XRD and TG data.

Table 6.8. Results of deconvolution of ^{29}Si MAS NMR spectra of NRVB samples that were in contact with saline groundwater. The estimated uncertainty in absolute site percentages is $\pm 2\%$.

	Q ¹	Q ² (1Al)	Q ²	Q ³ (1Al)	Q ³
6 Months	56 %	9 %	23 %	4 %	1 %
12 Months	42 %	7 %	30 %	3 %	5 %
18 Months	34 %	14 %	37 %	10 %	0 %

In terms of the changes in Ca/Si and Al/Si ratio as a function of time, slight differences were observed (Table 6.9). A decrease of the Ca/Si ratio was observed to occur with time, with values of 1.15 ± 0.06 and 1.07 ± 0.06 , for 12 and 18 months, respectively. This slight decrease may be attributed to decalcification of C-S-H, as a continuous Ca leaching is evident from the ICP-OES results (Figure 6.31a). Once more, this apparent decalcification of C-S-H happens when almost all the portlandite has been dissolved (between 14 and 18 months).

A slight decrease of the Al/Si ratio was observed when comparing the control sample cured for 6 months and the sample that was in contact with saline solution for 6 months (0.08 ± 0.01 and 0.05 ± 0.01 , respectively). This correlates well with the observed increase of the formation of ettringite, meaning that the Al that was incorporated into the C-S-H structure is being used for the formation of this phase. However, after 18 months of contact with groundwater an increase of the Al/Si ratio is observed, as a consequence of the destabilisation of ettringite, as mentioned before. An increase in the MCL (Table 6.9) was observed with time, agreeing well with the observed increase of the relative concentration of Q², Q²(1Al) and Q³(1Al) sites, with the latter site indicative of the occurrence of some cross-linking.

Table 6.9. Summary of structural evolution of C-S-H formed in NRVB samples that were in contact with saline groundwater, based on the ^{29}Si MAS NMR deconvolutions.

	Ca/Si	Al/Si	MCL
6 Months	1.26 ± 0.06	0.05 ± 0.01	3.5 ± 0.4
12 Months	1.15 ± 0.06	0.04 ± 0.01	4.5 ± 0.6
18 Months	1.07 ± 0.06	0.07 ± 0.01	6.1 ± 0.8

From the ^{27}Al MAS NMR spectra (Figure 6.24), no AFm phases were present in the samples at 6 months of contact with saline groundwater, in accordance with the results observed by XRD. However, the appearance of the TAH at a chemical shift of around 5 ppm is visible, as it was observed in the samples that were in contact with granitic groundwater.

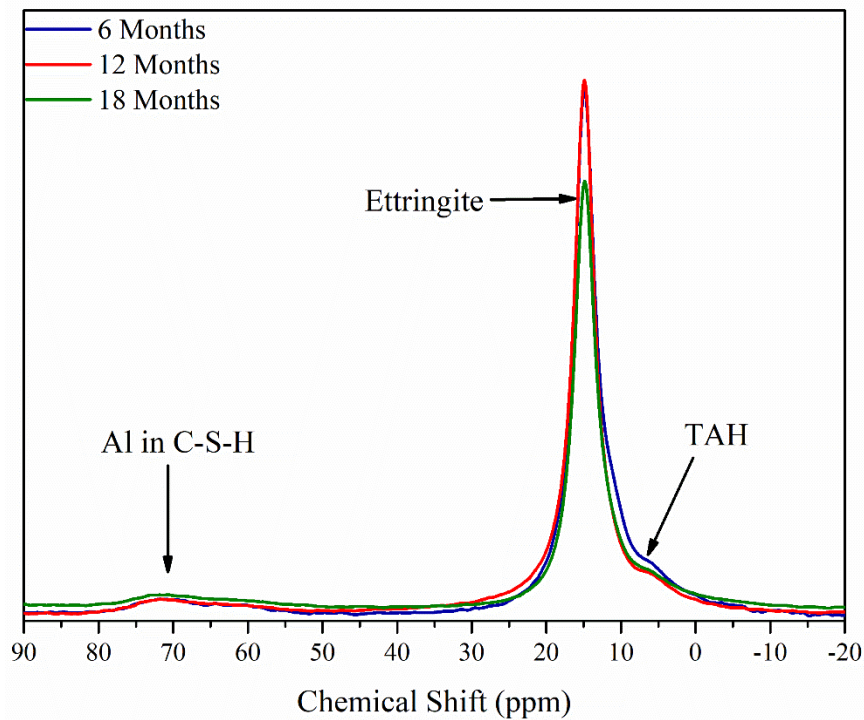
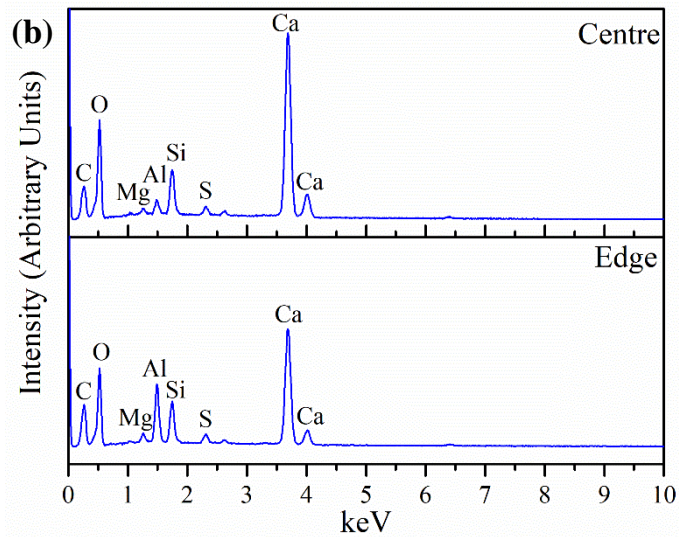
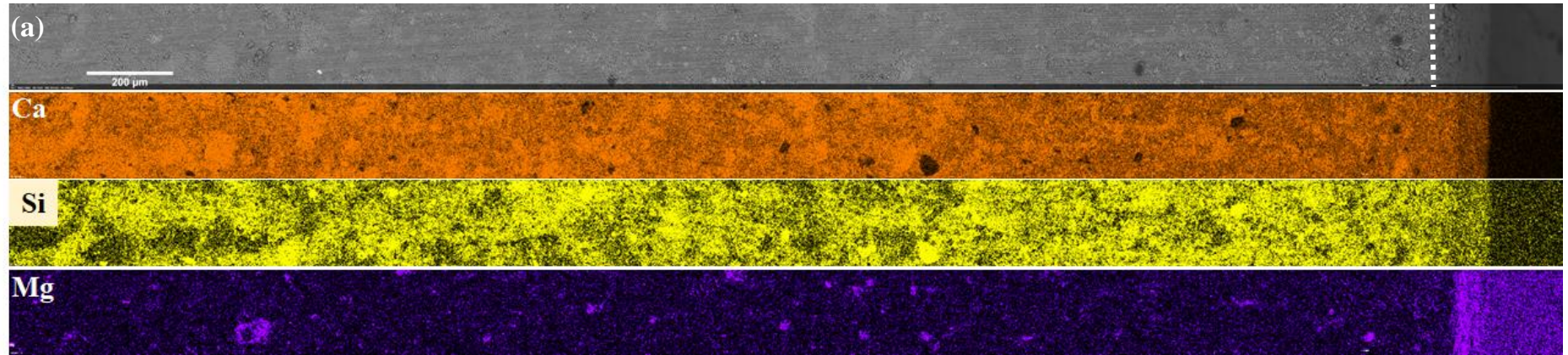


Figure 6.24. ^{27}Al MAS NMR spectra of NRVB samples that were placed in contact with saline groundwater for 18 months.

SEM-EDX analysis was performed at the edge and the centre of the NRVB samples (Figure 6.25). After 6 months of contact with saline groundwater, there was depletion of Ca at the edge of the sample and a layer enriched in Mg and possibly Al at the outer edge. Moreover, from the Mg elemental map, it was possible to observe the precipitation of this element throughout the entire sample.



	Edge (at %)	Centre (at %)
Ca	19.08 ± 1.02	24.54 ± 1.26
Mg	0.89 ± 0.09	0.50 ± 0.06
Al	5.47 ± 0.33	1.03 ± 0.09
Si	3.95 ± 0.23	3.47 ± 0.20
S	0.84 ± 0.08	0.62 ± 0.06

Figure 6.25. SEM-EDX analysis of NRVB sample that was in contact with saline groundwater for 6 months; (a) BSE image and elemental maps; (b) spectra associated with point analysis; Table: point analysis in atomic %, with absolute error from the measurement.

After 12 months of contact with saline groundwater, similar results were observed, with a thin outside Mg-rich layer (Figure 6.26a). At higher magnification, and from the linescan obtained (Figure 6.26b), it is noticeable that the thickness of this Mg-rich outside layer is no more than 5 to 10 μm . The elemental maps also show a number of areas with high quantities of Al and S, which are indicative of the presence of ettringite needles (in the BSE image, these are the areas where the sample charges more).

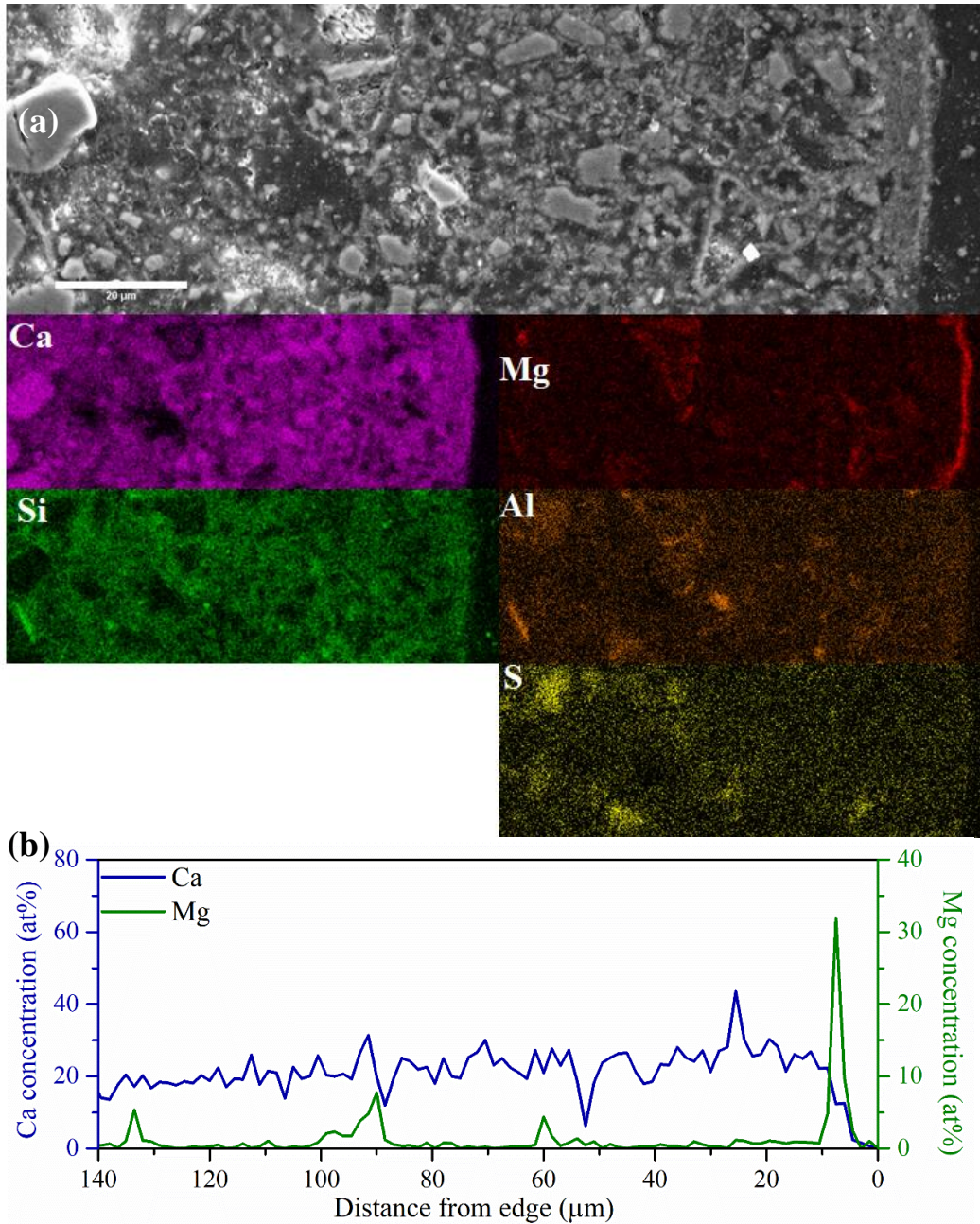


Figure 6.26. SEM-EDX analysis of NRVB sample that was in contact with saline groundwater for 12 months; (a) BSE image and elemental maps; (b) Linescan of magnesium and calcium in atomic %.

Through a range of molar ratio plots obtained from EDX point analysis, it is clear that ettringite was present throughout the entire sample, not being restricted to the edge or the centre (Figure 6.27a,b). Some of the points also plot around the line indicative of AFm phases (Figure 6.27a), which might be related to the presence of Friedel's/Kuzel's salts rather than monocarboaluminate, as in the other plots the points do not seem plot towards that phase (e.g. Figure 6.27b). The differences between the edge and the centre area of the sample were mainly related to the presence of Mg; Figure 6.27c shows that the concentration of brucite was greater in the edge than the centre. In terms of Cl⁻ uptake, it is possible to observe from the Al/Ca vs Cl/Ca diagram (Figure 6.27d) that there was more formation of Kuzel's salt ($\text{Ca}_4\text{Al}_2(\text{OH})_{12}\text{Cl}(\text{SO}_4)_{0.5}\cdot 5\text{H}_2\text{O}$) than in the granitic groundwater samples, due to the presence of high amounts of S in the saline groundwater.

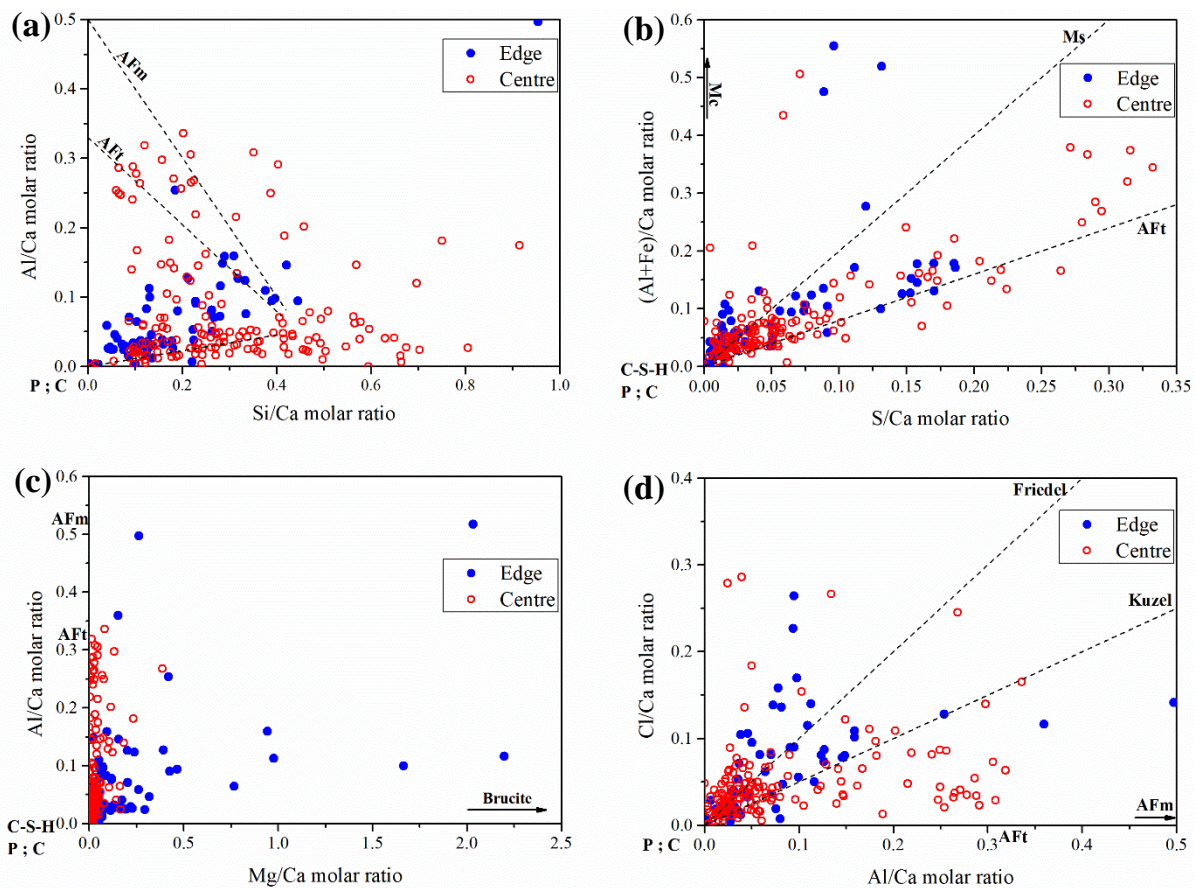


Figure 6.27. Elemental molar ratio plots of SEM-EDX point analysis in NRVB sample that was in contact with saline groundwater for 12 months: (a) Si/Ca vs Al/Ca; (b) S/Ca vs (Al+Fe)/Ca; (c) Mg/Ca vs Al/Ca; (d) Al/Ca vs Cl/Ca. The dashed lines are compositional trend lines connecting C-S-H or portlandite/calcite with other hydrate phases. P – portlandite; C – calcite; Mc – monocarboaluminate; Ms – monosulphoaluminate; AFm – Ms and Mc; AFt – ettringite.

In the sample of NRVB exposed to saline groundwater for 18 months (Figure 6.28), the same features were observed; the Mg-rich outer layer was not any thicker (Figure 6.28b). Additionally, the

precipitation of Ca in the outer layer was apparent. Areas with high concentrations of Al and S were evident, indicating the presence of AFt phase ettringite (red arrow in Figure 6.28a).

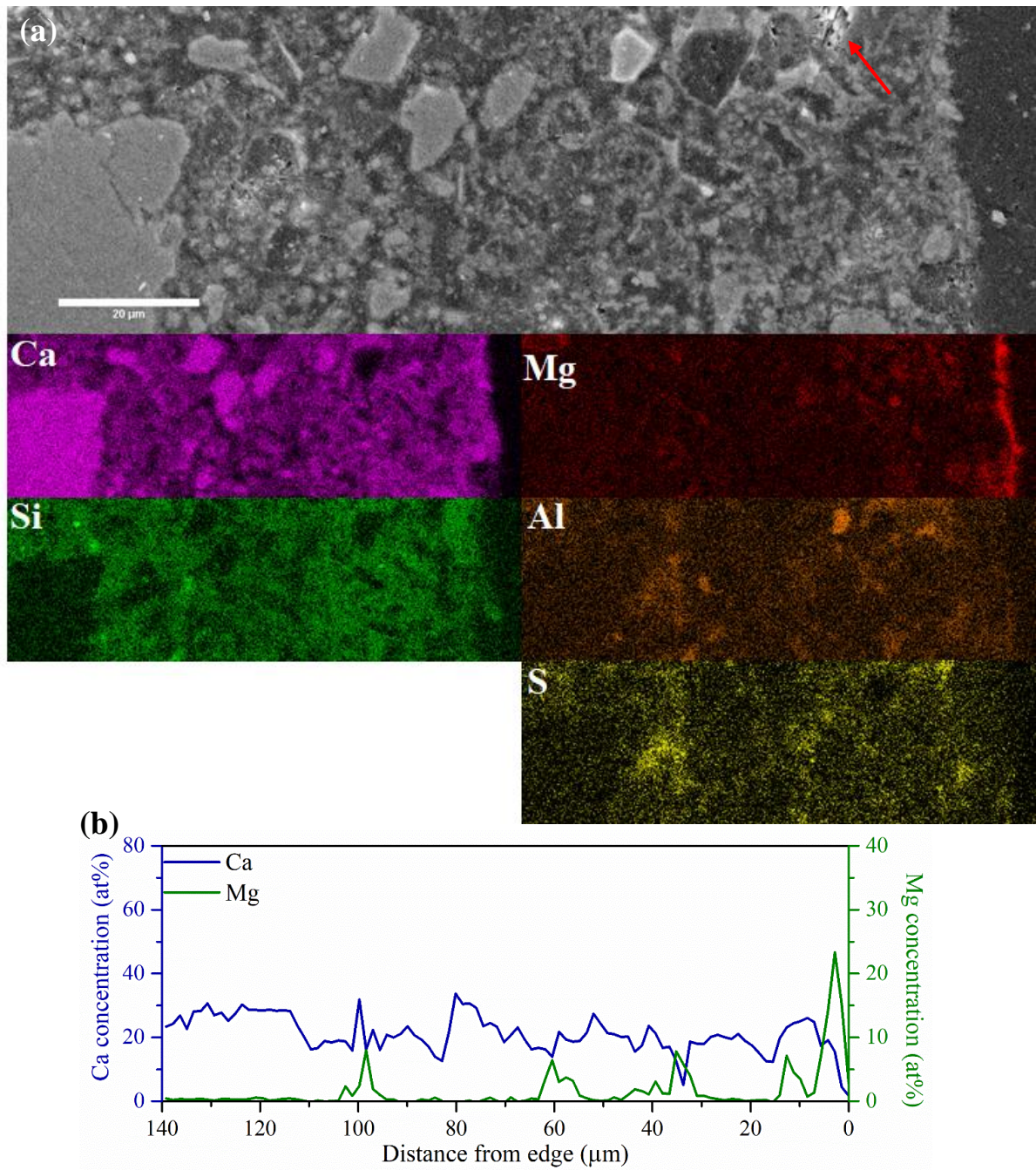


Figure 6.28. SEM-EDX analysis of NRVB sample that was in contact with saline groundwater for 18 months; (a) BSE image and elemental maps; (b) Linescan of magnesium and calcium in atomic %.

The presence of ettringite was confirmed in the Si/Ca vs Al/Ca and S/Ca vs (Al+Fe)/Ca plots, and its presence was noticeable throughout the sample (Figure 6.29). Once more, Mg-rich phases, like brucite, were more evident in the edge area of the sample (Figure 6.29c), agreeing well with the Mg-rich outside

layer observed in Figure 6.28. The preferential formation of Kuzel's salt was again observed, and possibly more evident in the edge area of the sample. In the case of the points collected from the centre area, an intermixing of Kuzel's salt and ettringite was observed.

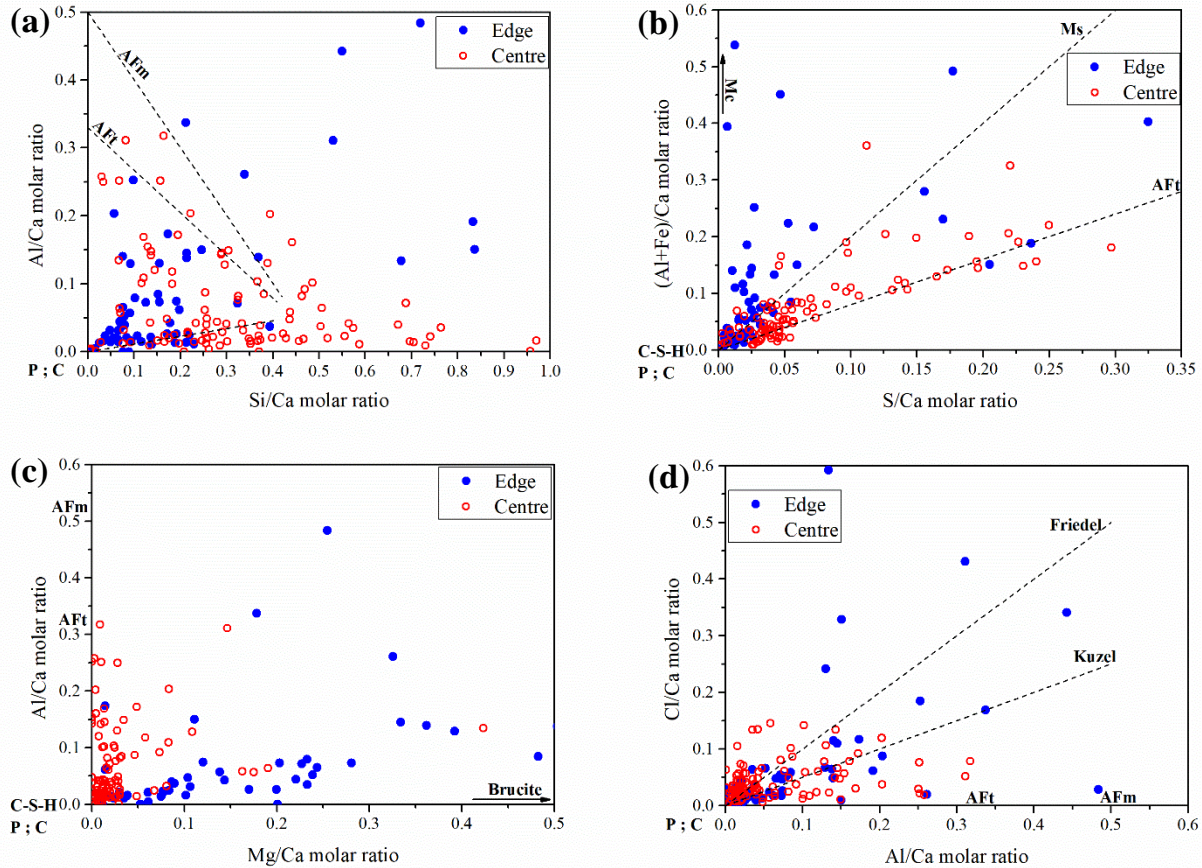


Figure 6.29. Elemental molar ratio plots of SEM-EDX point analysis in NRVB sample that was in contact with saline groundwater for 18 months: (a) Si/Ca vs Al/Ca; (b) S/Ca vs (Al+Fe)/Ca; (c) Mg/Ca vs Al/Ca; (d) Al/Ca vs Cl/Ca. The dashed lines are compositional trend lines connecting C-S-H or portlandite/calcite with other hydrate phases. P – portlandite; C – calcite; Mc – monocarboaluminate; Ms – monosulphoaluminate; AFm – Ms and Mc; AFt – ettringite.

6.4.2: Nano- and micro-structural evolution of NRVB

Changes in the macroporosity of the NRVB samples after contact with saline groundwater, as analysed by XCT, are summarised in Table 6.10. A decrease of the macroporosity was observed for the sample that was in contact with saline groundwater for 6 months when compared with the control sample at the same age (~ 19 % porosity compared to 26 %, respectively), which might be a result of the formation of secondary phases, like brucite, calcite and ettringite. However, due to the high variability characteristic of processing of this type of data (which is mainly based in human error thresholding), the errors are quite large, so these values are essentially the same. If one does not consider the error, a slight increase of the macroporosity could be interpreted, between 6 and 12 months, which could be

related to the dissolution of portlandite (crystal sizes might vary between 1 to 100 μm [201]). Once again, should be noted that these values are within error, even when comparing to the control samples at the same age ($26.6 \pm 8.2\%$ at 6 months and $19.1 \pm 4.9\%$ at 12 months).

Table 6.10. Macroporosity values of NRVB samples that were in contact with saline groundwater for 6 and 12 months, obtained through XCT. Errors calculated from standard deviation of triplicate thresholding.

Macroporosity (%)	
NRVB Saline 6 Months	18.6 ± 6.9
NRVB Saline 12 Months	23.4 ± 8.1

Figure 6.30 shows the results of the nanoporosity analysis, as obtained by nitrogen sorption. An overall increase in the volume of the nanopores was observed as a function of time, especially in the size range from ~ 4 to 25 nm. For pores < 5 nm, a small increase in the intensity was observed. The 12 month sample did not have that range of pores (i.e. the observed sharp peak), this might be due to sample preparation (e.g. the procedure of stopping the hydration). For the range of pores between 5 to 20 nm it is clear that an increase of volume was observed between 6 and 12 months. The increase of the capillary porosity (between 10 nm to 40 nm) is due to a combination of the dissolution of portlandite, the initial conversion of monocarboaluminate into ettringite, and possibly at later ages (18 months), due to dissolution of ettringite observed through XRD, TG and ^{27}Al MAS NMR, leading to the opening of small pores. The observed increase of the gel pores (< 5 nm) is possibly related to the slight decalcification of C-S-H observed in the ^{29}Si MAS NMR spectra. This observed increase of the volume of small pores, due to decalcification of C-S-H and other hydrate phases, has been previously observed in similar studies using ammonium nitrate solution to accelerate decalcification in cements, as mentioned above [194,201].

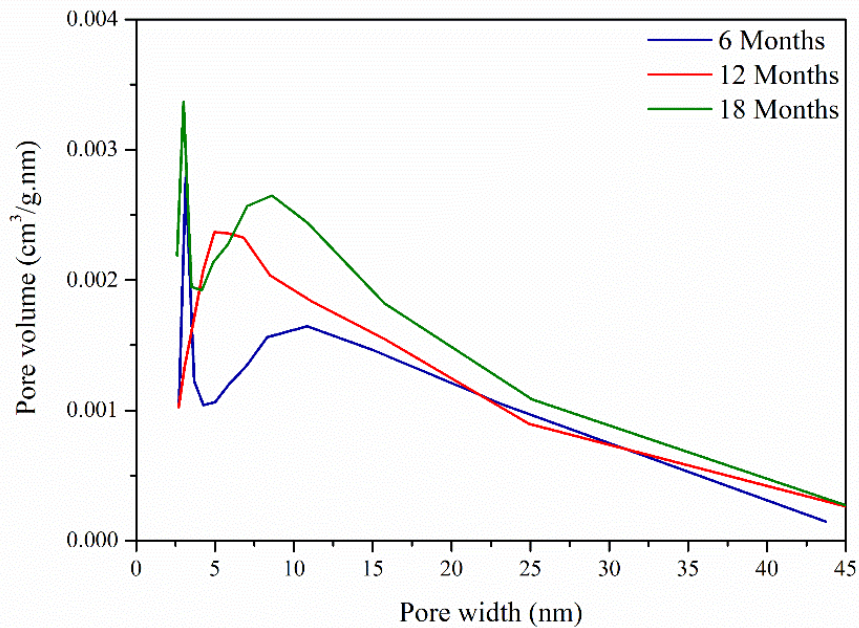


Figure 6.30. Pore size distribution curves for NRVB samples that were in contact with saline groundwater for 6, 12 and 18 months, determined using Barrett-Joyner-Halenda (BJH) desorption pore size and volume analysis.

6.4.3: Solution chemistry

An increase of the pH of the solution was observed compared with the original saline groundwater (pH 8.2), reaching a maximum pH of 12.9 – 13.3 after 8 months of the experiment. As observed for the granitic groundwater, after a rapid early increase, the pH decreased, reaching pH 12.0 – 12.3 after 18 months. Again, the pH of the solution was > pH 12 during the entire experiment, evidencing the capacity of NRVB to buffer the pH to alkaline values, even in aggressive environments (high replacement rate of groundwater).

Constant leaching of Ca was observed from the ICP-OES analysis of the solutions (Figure 6.31a). Slight variability was observed, with a decrease of the leaching of Ca after 14 months. This correlates well with the observed total dissolution of portlandite by this time point, evident in XRD and TG data. Taking into account the observations relating to ettringite destabilisation at this time, from 14 months, the continued leaching of Ca is associated with this, and possibly from the slight decalcification of C-S-H. The removal of Mg from solution was observed to occur (Figure 6.31b), in agreement with evidence presented that shows the precipitation of Mg-phases such as brucite. Because the pH of the solution remains > pH 12, brucite is thermodynamically stable throughout the experiment. Uptake of S from the groundwater to the cement was observed for the duration of the experiment (Figure 6.31c). As time progressed, the concentration of S being removed from the solution by the cement decreased, until at 14 months, the concentration of S in solution in the presence of NRVB had plateaued and was almost

the same as in the blank. At this time point, the NRVB could be considered to be in equilibrium with respect to S, achieved by reaching a maximum capacity for the incorporation of sulphur. This correlates well with the observed maximum ettringite formation obtained at 14 months of the experiment according to the results from XRD and TG analysis.

Leaching of Si was observed for the first 2 months of contact time, but thereafter, the concentration was the same as in the blank solution. The initial release may result from the dissolution of free silicon from the cement clinker. With regards to Cl, which was present at approximately 6122 mg/L in the blank saline groundwater solution, an initial high uptake of this element by the cement was observed. From 4 months onwards, the concentration of Cl in the presence of NRVB was greater than that in the blank, suggesting that the retained Cl was slowly released back to the solution. This is in agreement with solid state analysis of the NRVB samples, which identified Friedel's and Kuzel's salts.

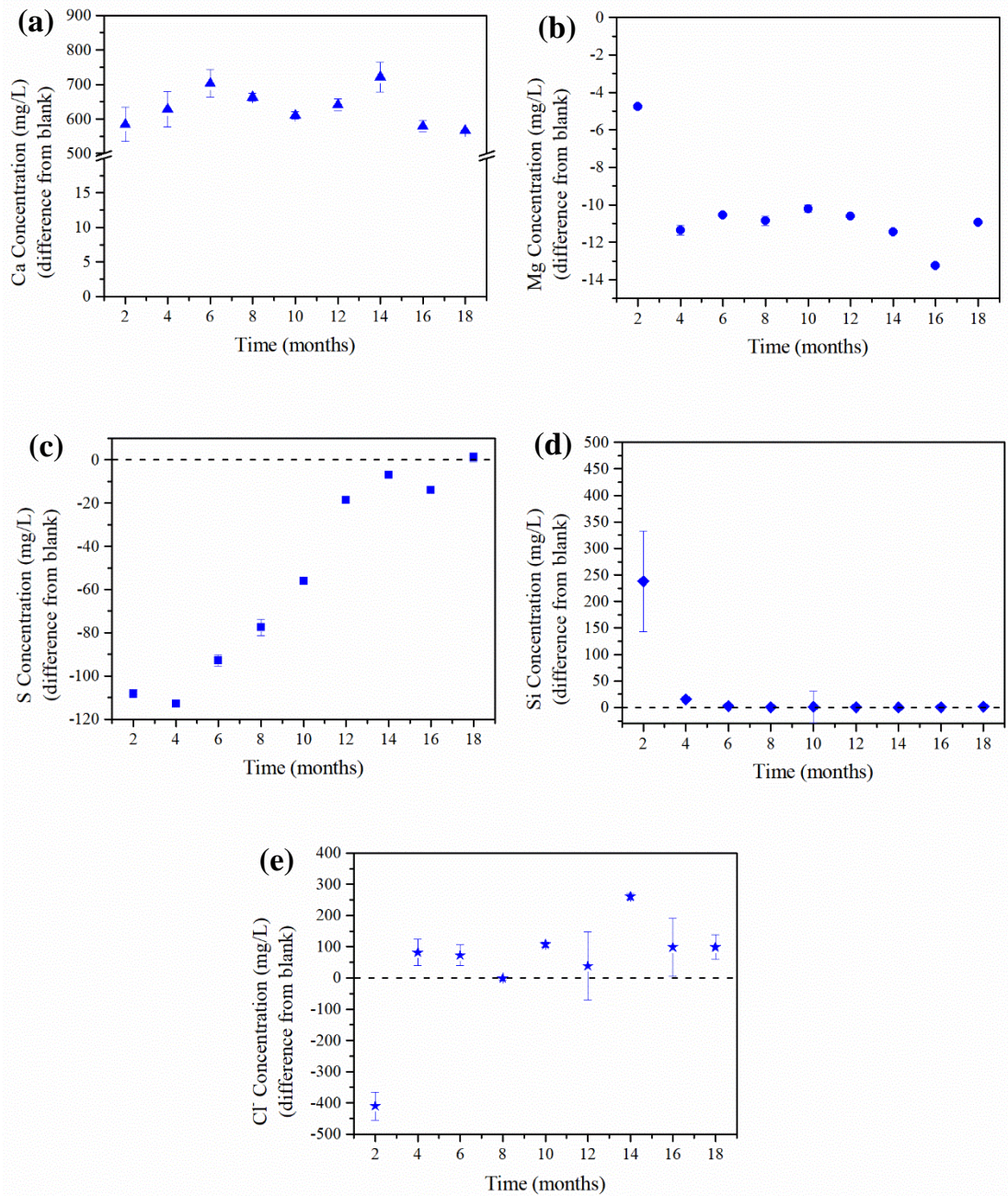


Figure 6.31. Elemental concentrations in solution (mg/L) obtained through the difference from blank for NRVB samples that were in contact with saline groundwater for 18 months: (a) Ca concentration; (b) Mg concentration; (c) S concentration; (d) Si concentration; (e) Cl concentration. Errors were calculated using the standard deviation of duplicate ICP-OES and IC measurements.

6.5: Mineralogical and microstructural evolution of NRVB with Clay groundwater (semi-dynamic experiment)

6.5.1: Mineralogical evolution of NRVB

As previously observed, when NRVB samples are in contact with groundwater, portlandite dissolution occurred. Figure 6.32 shows XRD patterns for NRVB samples that were in contact with clay groundwater for 18 months. A decrease of the peak intensity for portlandite was observed and after only 12 months it was not possible to detect portlandite by XRD (Figure 6.33). The early total consumption of portlandite (at 12 months) when compared to NRVB samples that were in contact with granitic (at 18 months) and saline groundwater (at 16 months) might be due to the lower pH observed in the blank clay groundwater (pH around 7.5, compared with 8.5 and 8.2 for granite and saline solutions, respectively), which might promote the dissolution of portlandite. The peak for monocarboaluminate also reduced until it was no longer visible in the XRD trace, after 4 months of contact with the groundwater (Figure 6.33).

A clear increase of the intensity of the Bragg reflections corresponding to ettringite was observed as a function of time, which is to be expected from the presence of high concentrations of S in the clay groundwater (Table 6.1). The increased concentration of ettringite is also evident in the TGA data, where the ettringite peak (detected at a temperature of 100 °C) increased with time (Figure 6.34). From the semi-quantitative XRD data (Figure 6.33), a slight decrease of the ettringite content was observed after 14 months.

A small peak corresponding to brucite, at $\sim 18^\circ 2\theta$, was observed in the XRD dataset (Figure 6.32). In the TGA (Figure 6.34), the broad peak at around 350 and 400 °C became sharper at later time points and also corresponds to brucite.

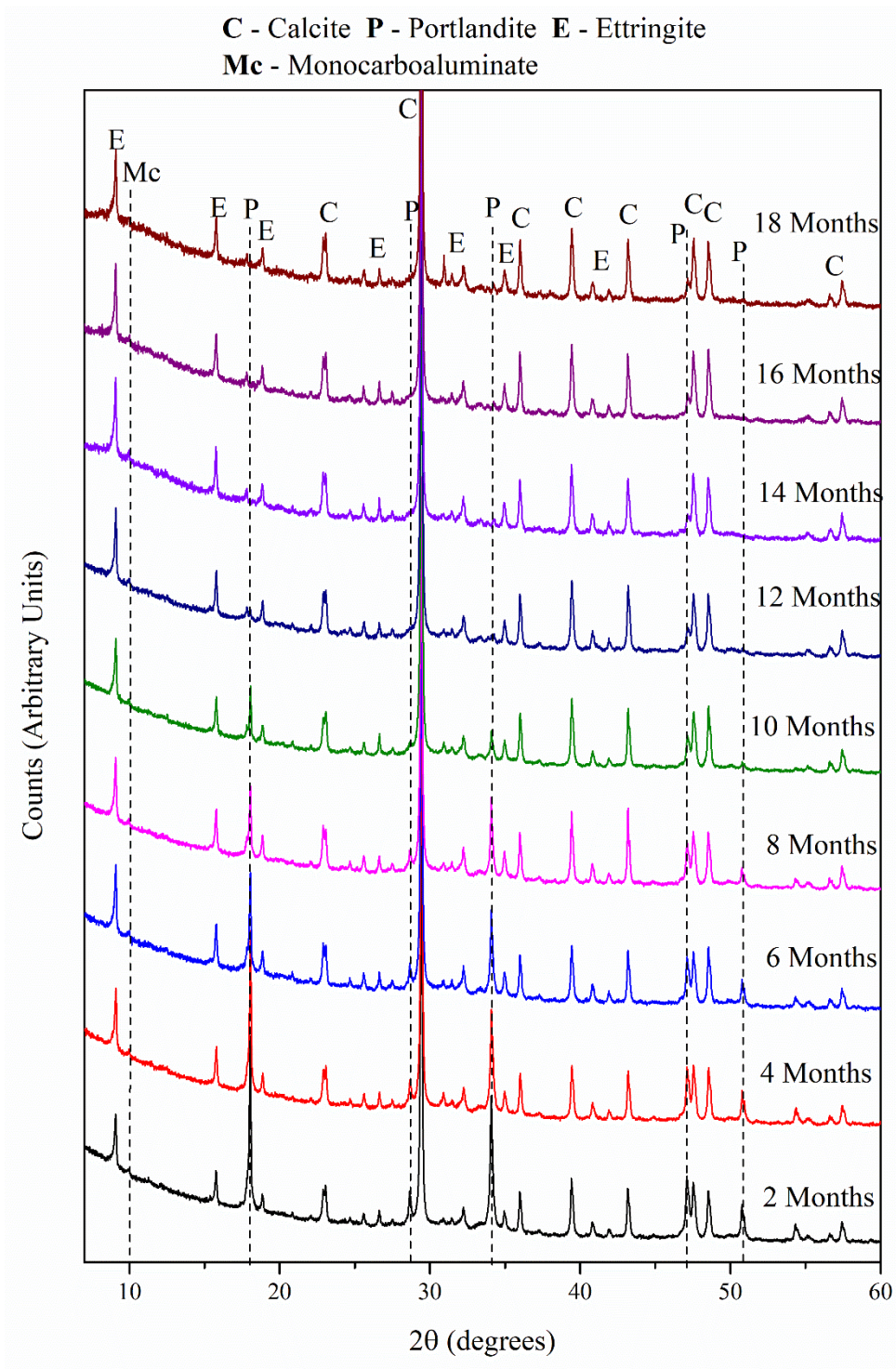


Figure 6.32. XRD patterns of NRVB samples that were placed in contact with clay groundwater for 18 months.

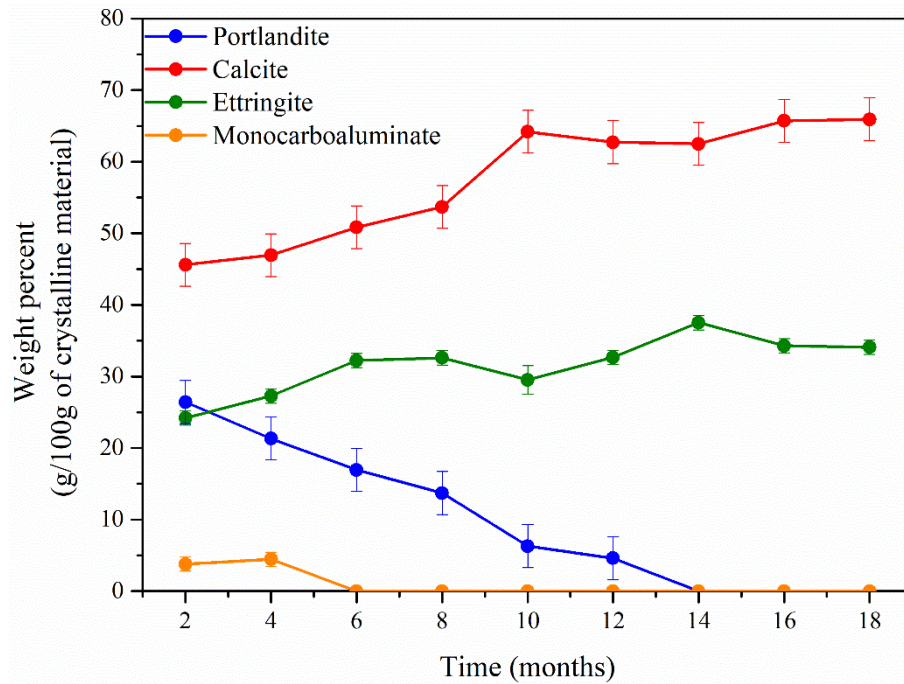


Figure 6.33. Semi-quantitative evaluation of the crystalline phases identified in XRD patterns of NRVB that was in contact with clay groundwater for 18 months. Error bars obtained through Rietveld refinement software, Topas.

Chloride-containing salts (Friedel’s and Kuzel’s salts) were observed in the TGA data for NRVB samples exposed to clay solution for 2 to 8 months (Figure 6.34, ~300 °C). After 8 months, the presence of these phases was not visible through this technique. Concerning the carbonates, a slight increase of the intensity of the peak at around 800 °C was observed from 4 months to 6 months, when it did not change any further, showing that little carbonation occurred in these samples (Figure 6.34). These results correlate well with the XRD data (Figure 6.33).

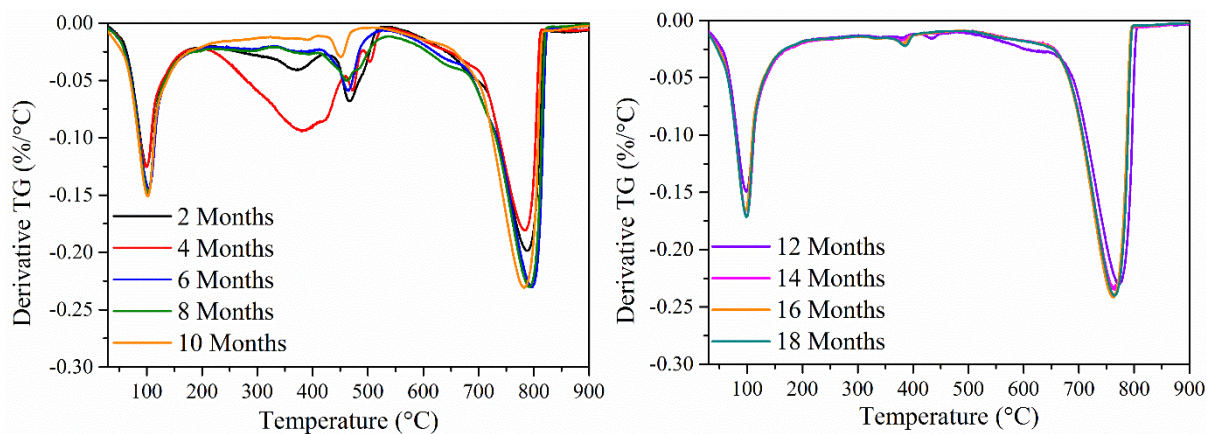


Figure 6.34. TGA data for NRVB samples that were in contact with clay groundwater for 18 months.

Figure 6.35b compares the ^{29}Si MAS NMR spectra for the NRVB samples that were in contact with clay groundwater for 6, 12 and 18 months, and differences can be clearly observed. From the deconvolution of the different ^{29}Si MAS NMR spectra (example of the deconvolution shown in Figure 6.35a), it was possible to observe that the relative intensity of Q^1 sites decreased from $54 \pm 2\%$ at 6 months to $32 \pm 2\%$ at 18 months (Table 6.11). This decrease is correlated with an increase in the relative concentration of Q^2 sites. An increase of the Q^3 and $\text{Q}^3(1\text{Al})$ is indicative of the occurrence of cross-linking, which, when linked with the increase of Q^2 sites, indicates an increase of the MCL with increasing time of exposure to the clay solution, increasing from 3.5 ± 0.4 at 6 months to 6.2 ± 0.9 after 18 months of contact with groundwater (Table 6.12).

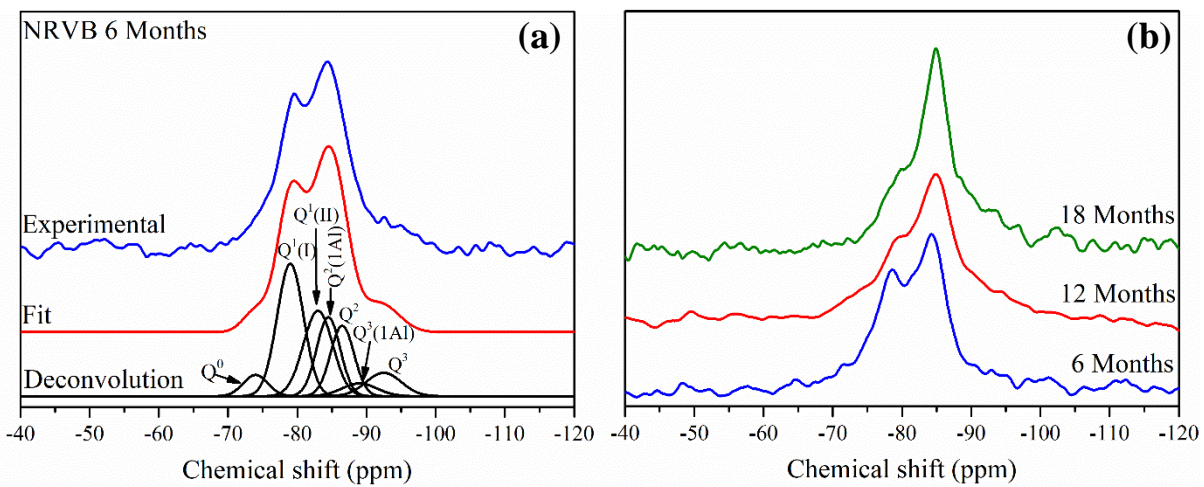


Figure 6.35. (a) Deconvoluted ^{29}Si MAS NMR spectrum of NRVB cured for 6 months; (b) ^{29}Si MAS NMR spectra of NRVB that were in contact with clay groundwater for 6, 12 and 18 months.

Table 6.11. Results of deconvolution of ^{29}Si MAS NMR spectra of NRVB samples that were in contact with clay groundwater. The estimated uncertainty in absolute site percentages is $\pm 2\%$.

	Q^1	$\text{Q}^2(1\text{Al})$	Q^2	$\text{Q}^3(1\text{Al})$	Q^3
6 Months	54 %	7 %	24 %	3 %	4 %
12 Months	39 %	7 %	28 %	5 %	9 %
18 Months	32 %	8 %	33 %	13 %	10 %

In terms of the Ca/Si ratio of the C-S-H, a slight decrease was observed after 12 months of contact with clay groundwater (Table 6.12). This again might be related to the observed total dissolution of portlandite after 12 months (XRD and TG data), meaning that a possible decalcification of C-S-H might be occurring as part of the buffering process. An initial decrease of the Al/Si ratio is observed on the NRVB sample that was in contact with groundwater for 6 months (0.04 ± 0.01) when comparing to the

control sample that was cured for the same amount of time (0.08 ± 0.01). As for the explanation given for saline groundwater, the Al from the C-S-H is possibly being used for the formation of ettringite.

Table 6.12. Summary of structural evolution of C-S-H formed in NRVB samples that were in contact with clay groundwater, based on the ^{29}Si MAS NMR deconvolutions.

	Ca/Si	Al/Si	MCL
6 Months	1.24 ± 0.07	0.04 ± 0.01	3.5 ± 0.4
12 Months	1.15 ± 0.07	0.04 ± 0.01	4.9 ± 0.7
18 Months	1.07 ± 0.07	0.04 ± 0.01	6.2 ± 0.9

In terms of ^{27}Al MAS NMR results (Figure 6.36), a decrease in the intensity of the peak corresponding to ettringite (14 ppm) was observed to occur over time. This decrease was only evident in the XRD after 14 months, when no portlandite was detected. As observed before, after dissolution of all portlandite has occurred, a possible dissolution of ettringite may happen [71,202]. This is evidenced by the continuous leaching of Ca, observed through ICP-OES (Figure 6.43a). This slight decrease of ettringite concentration, led to the available free Al being incorporated back into C-S-H, as a slight increase of the peak at around 70 ppm is visible (Figure 6.36).

There were no peaks corresponding to AFm (at around 9 ppm, Figure 6.36) present in any of the samples, which correlates well with XRD and TG analysis results, where no monocarboaluminate was observed in NRVB after 6 months of contact with clay solution. It was therefore possible to observe the peak at 5 ppm corresponding to TAH, which did not change in intensity during the experiment.

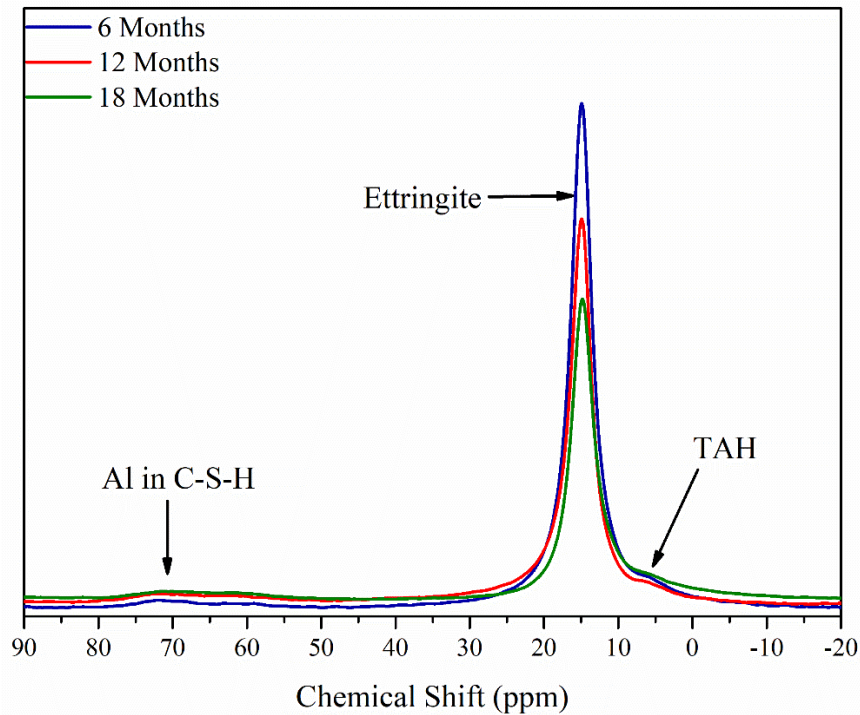
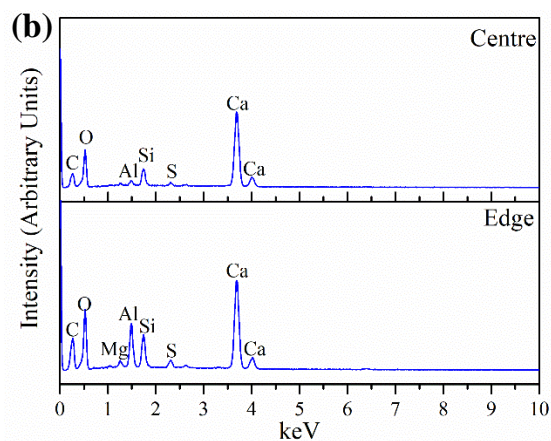
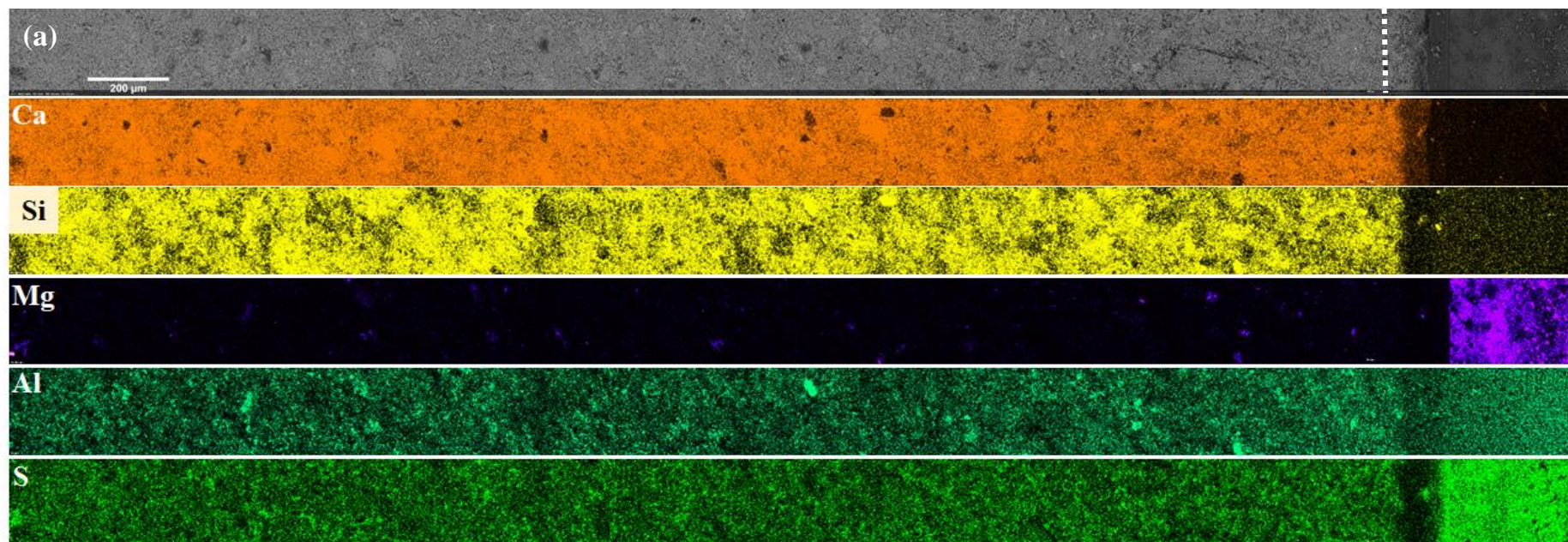


Figure 6.36. ^{27}Al MAS NMR spectra of NRVB samples that were placed in contact with clay groundwater for 18 months.

After 6 months of contact with clay groundwater, NRVB exhibited some depletion of Ca at the edge of the sample (Figure 6.37). Differences between the edge and the centre of the sample were not evident at this time point in samples contacted with granitic or saline groundwater. From the elemental mapping shown in Figure 6.37, it is noticeable that the presence of high amounts of Al and S were distributed throughout the entire sample. Together with the other solid state analysis results, this evidences the existence of ettringite. No significant concentration gradient was evident between the edge of the sample and the centre, besides a higher amount of Al at the edge when comparing to the centre. A possible explanation is that an initial destabilisation of ettringite is starting to occur at the edge of the sample, leading to the availability of Al. Unlike the other samples, no outer layer of Mg was visible after 6 months.



	Edge (at %)	Centre (at %)
Ca	18.84 ± 1.04	25.15 ± 1.32
Mg	0.75 ± 0.08	0.39 ± 0.06
Al	5.02 ± 0.31	0.87 ± 0.09
Si	3.74 ± 0.23	3.21 ± 0.20
S	0.87 ± 0.08	0.51 ± 0.06

Figure 6.37. SEM-EDX analysis of NRVB sample that was in contact with clay groundwater for 6 months; (a) BSE image and elemental maps; (b) spectra associated with point analysis; Table: point analysis in atomic %, with absolute error from the measurement.

Using elemental mapping at higher magnification for the NRVB sample in contact with clay groundwater for 12 months, it was possible to observe a thin (<10 μm) layer rich in Mg (Figure 6.38). The presence of ettringite needles was distinguishable as areas of high surface charging that were rich in Al and S.

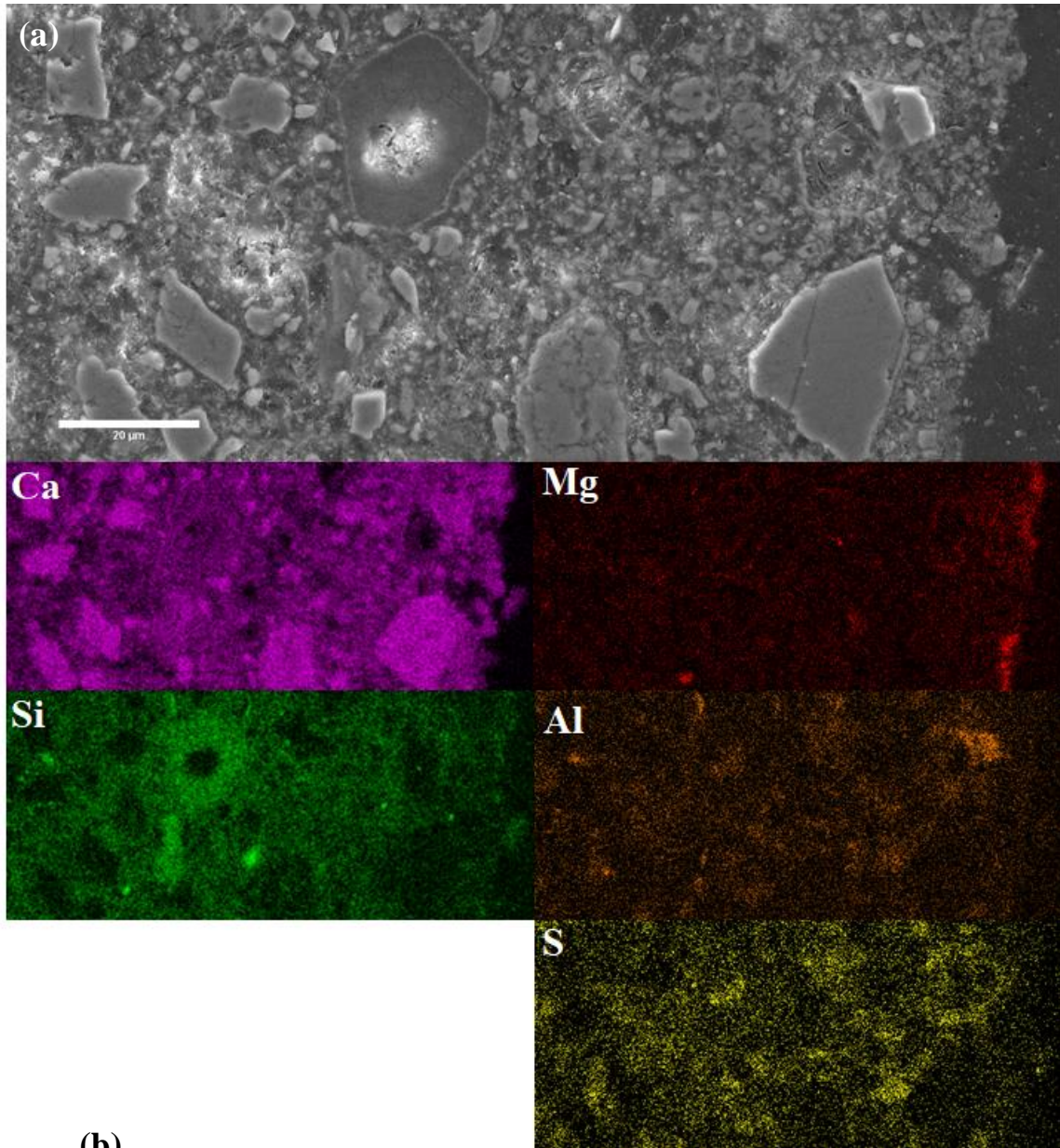


Figure 6.38. SEM-EDX analysis of NRVB sample that was in contact with clay groundwater for 12 months; (a) BSE image and elemental maps; (b) Linescan of magnesium and calcium in atomic %.

The Si/Ca vs Al/Ca and the S/Ca vs (Al+Fe)/Ca plots constructed from EDX point spectra taken on NRVB contacted with clay groundwater for 12 months are shown in Figure 6.39. There were no significant differences between the edge and the centre of the sample with the exception of phases containing Mg or S. The main hydrate phases present were a mixture of ettringite and C-A-S-H with a high Ca/Si ratio. The formation of brucite was favoured at the edge of the sample (Fig. 6.39c), while ettringite formation occurred more in the centre of the sample. In terms of chloride uptake, once again no considerable differences were observed between the points collected at the edge and the centre of the sample. A combination of Friedel's salt and mainly Kuzel's salt were observed, with possibly some incorporation of chloride in the C-S-H structure (points with low Al/Ca ratio but slightly high Cl/Al ratio, Figure 6.39d).

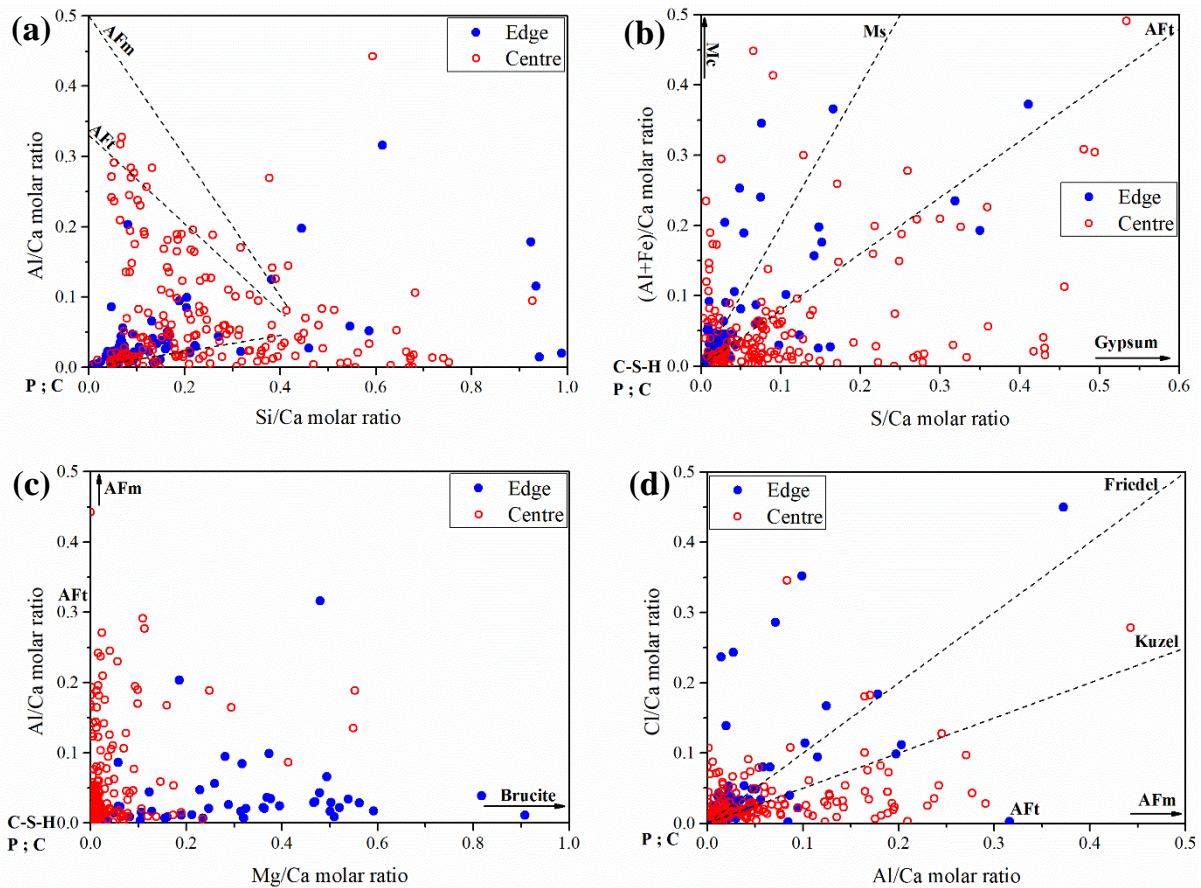


Figure 6.39. Elemental molar ratio plots of SEM-EDX point analysis in NRVB sample that was in contact with clay groundwater for 12 months: (a) Si/Ca vs Al/Ca; (b) S/Ca vs (Al+Fe)/Ca; (c) Mg/Ca vs Al/Ca; (d) Al/Ca vs Cl/Ca. The dashed lines are compositional trend lines connecting C-S-H or portlandite/calcite with other hydrate phases. P – portlandite; C – calcite; Mc – monocarboaluminat; Ms – monosulphoaluminat; AFm – Ms and Mc; AFt – ettringite.

After 18 months of contact with clay groundwater, an increase in the thickness of the Mg-rich outer layer was observed (Figure 6.40). This layer, according to the linescan (Figure 6.40b), had a thickness of ~18 μm , and only contained Mg among the elements mapped here. In the area preceding the outer

layer, a Ca-rich area was observed. Areas with high quantities of ettringite were visible throughout the sample, due to the high Al and S concentration.

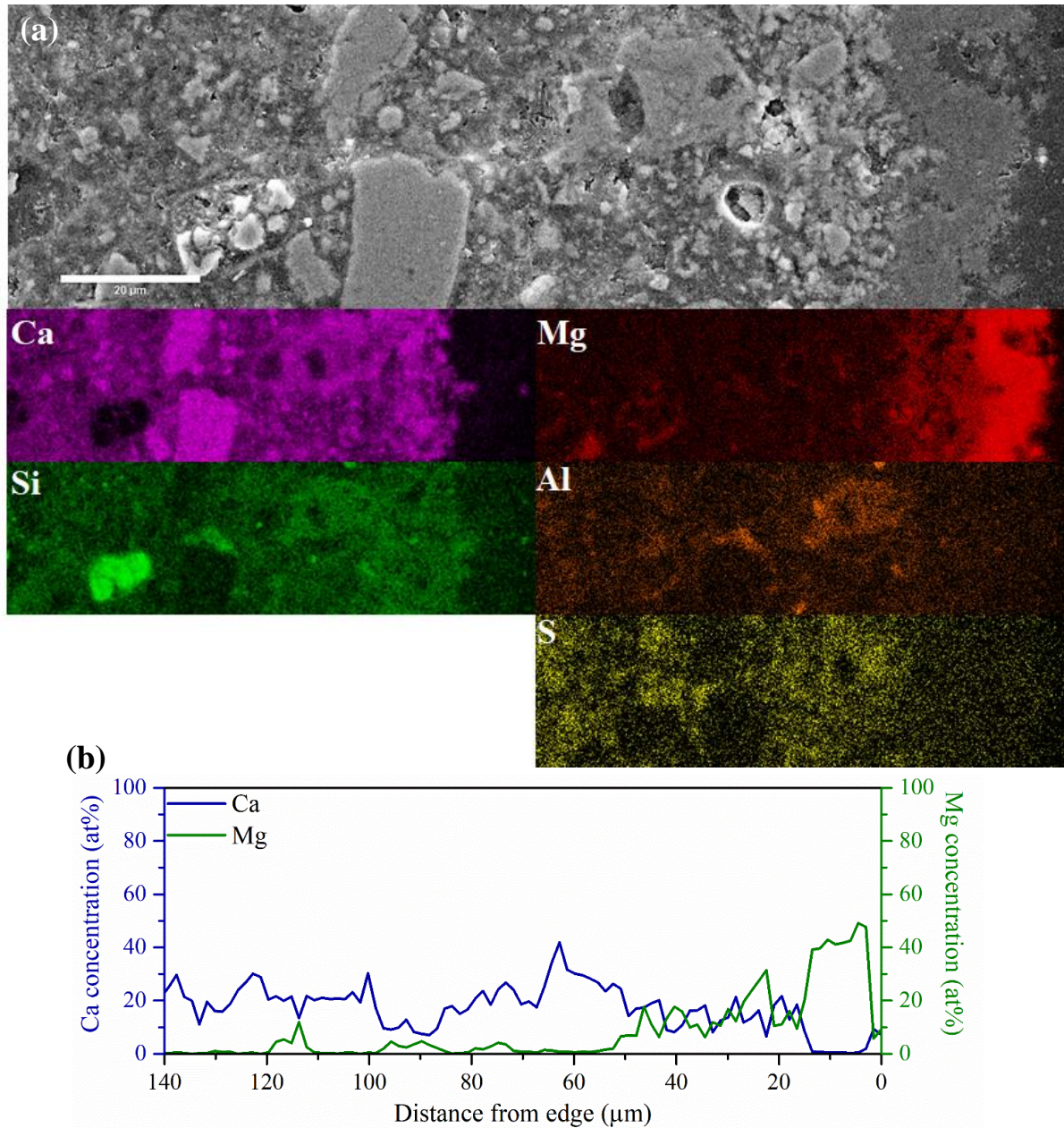


Figure 6.40. SEM-EDX analysis of NRVB sample that was in contact with clay groundwater for 18 months; (a) BSE image and elemental maps; (b) Linescan of magnesium and calcium in atomic %.

After 18 months, according to the different molar ratio plots (Figure 6.41), the main hydrate phase present throughout the sample was ettringite. One difference that was observed from the ratio plots that was not noticeable in the elemental mapping (Figure 6.40) was the higher amount of S observed in the points acquired at the edge. This could be explained by the precipitation of gypsum (CaSO_4) only at the edge. However, the formation of gypsum was not detected using the range of other techniques applied

to these samples, meaning that if gypsum were present at the edge of the sample, it was in small quantities that were not detected when bulk analysis was performed. Another interesting observation is the higher concentration of Cl observed in the points collected at the edge of the sample. According to Figure 6.41e, Friedel's salt and Kuzel's salt were formed predominantly at the edge of the sample, and Cl was also possibly incorporated into the C-S-H structure at the edge only, as identified by the points on the left side of Figure 6.41e with high Cl/Ca ratio and low Al/Ca ratio.

In terms of Mg concentration, it is clear that the edge of the sample was composed of Mg-rich phases such as brucite (Figure 6.41c,d). However, it is interesting to see that some points collected from the centre of the sample also have a high Mg/Ca ratio, indicating that precipitation of brucite also occurred in the centre of the NRVB sample.

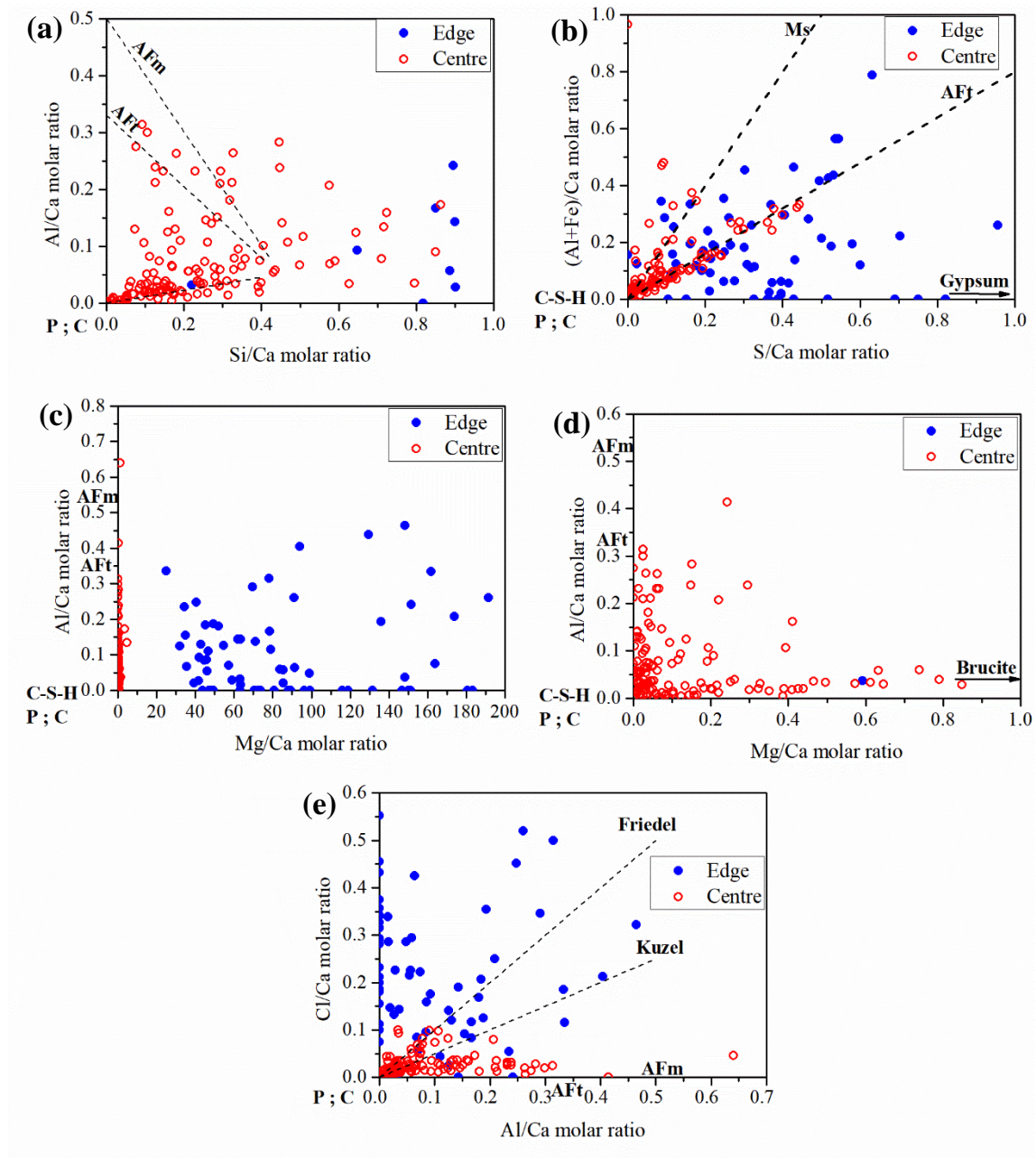


Figure 6.41. Elemental molar ratio plots of SEM-EDX point analysis in NRVB sample that was in contact with clay groundwater for 18 months: (a) Si/Ca vs Al/Ca; (b) S/Ca vs (Al+Fe)/Ca; (c) Mg/Ca vs Al/Ca; (d) Mg/Ca vs Al/Ca; (e) Al/Ca vs Cl/Ca. The dashed lines are compositional trend lines connecting C-S-H or portlandite/calcite with other hydrate phases. P – portlandite; C – calcite; Mc – monocarboaluminat; Ms – monosulphoaluminat; AFm – Ms and Mc; AFt – ettringite.

6.5.2: Nano- and micro-structural evolution of NRVB

No significant differences were observed in the macroporosity of NRVB samples that were in contact with clay groundwater as a function of time (Table 6.13). However, a decrease of the macroporosity was observed when compared to the NRVB control samples. The observed increase of the formation of

brucite and ettringite might be responsible for this behaviour, resulting in some healing of the pores formed during portlandite dissolution. This change in porosity for the 6 month control vs 6 month groundwater-contacted samples is greater than that observed for the saline groundwater, but similar to that for granitic groundwater. The reason for these differences is not totally clear, as similar dissolution and precipitation of secondary phases is occurring due to contact with groundwater, however it should be highlighted once again the high errors attributed to this technique.

Table 6.13. Macroporosity values of NRVB samples that were in contact with clay groundwater for 6 and 12 months, obtained through XCT. Errors calculated from standard deviation of triplicate thresholding.

	Macroporosity (%)
NRVB Clay 6 Months	13.5 ± 6.2
NRVB Clay 12 Months	12.2 ± 4.9

Nanoporosity analysis (Figure 6.42) showed that there was a decrease in the volume of the smallest pores (< 5 nm) as a function of time. A possible explanation is that a widening of the pores is occurring, as indicated by the observed increase of the volume of the pores ranging in size from 5 to 25 nm. This might be related to a combination of factors, which were possible to observe through the previous techniques: (1) the observed initial destabilisation of monocarboaluminate, which converted to ettringite needles, observed in the XRD and TG data; (2) the observed destabilisation of ettringite at the end of the experiment; and (3) possibly due to decalcification of this phase (observed in the XRD and ²⁷Al MAS NMR). The observed slight decalcification of C-S-H did not seem to have the same effect on the porosity (especially <5 nm) as observed in the previous groundwaters. The reason for these results are not clear from the data obtained, but it should be considered that method of hydration cessation might influence the results, especially for small pores (nanoporosity) [90], although care was taken by using the same procedure in all samples.

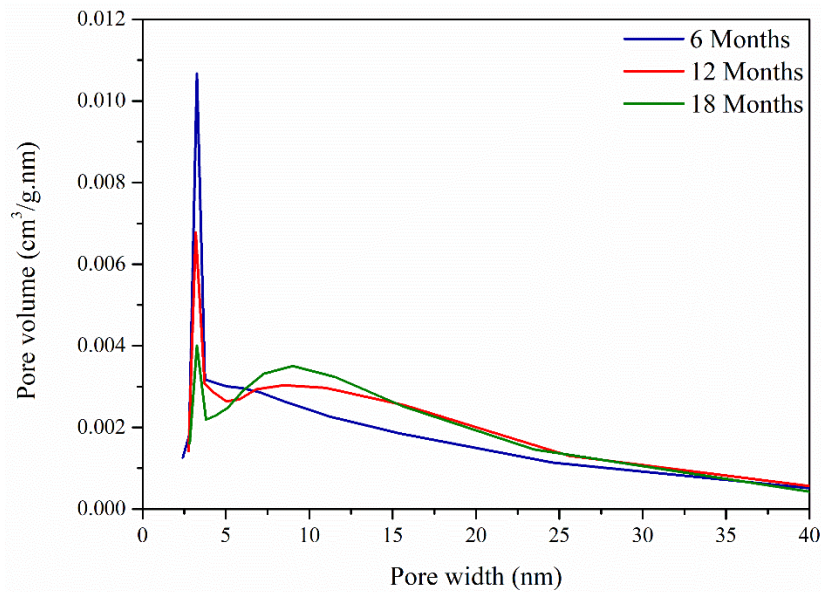


Figure 6.42. Pore size distribution curves for NRVB samples that were in contact with clay groundwater for 6, 12 and 18 months, determined using Barrett-Joyner-Halenda (BJH) desorption pore size and volume analysis.

6.5.3: Solution chemistry

The starting pH of the clay groundwater solution was pH 7.5, which increased to a maximum of pH 12.9 – 13.2 after 8 months of contact with NRVB. After this time, the pH decreased to a value of 11.5 – 11.8 after 18 months. The pH at the end of the experiment was lower than for the other groundwater solutions, which is likely due to (a) the lower original starting pH; and (b) the buffering be mainly due to the dissolution of C-S-H and ettringite.

From the ICP-OES analysis of the solutions (Figure 6.43), the continuous leaching of Ca was observed throughout the experiment. For the first 8 months, the leaching of Ca increased gradually, after which time the amount of Ca leached reduced (Figure 6.43a). This is likely related to the fact that no more portlandite was available to leach after 12 months (from XRD and TG results). When comparing the total concentration of Ca leached into the granitic and saline groundwater, it is possible to observe that more of this element is leached out from the samples that were in contact with clay groundwater (maximum leaching of around 700, 750 and 900 mg/L, for granitic, saline and clay, respectively). This agrees well with the observed earlier consumption of portlandite for the samples in contact with clay solution (Figure 6.32 and 6.34). Further leaching of Ca after this time indicates that dissolution of ettringite, and possibly some decalcification of C-S-H, is occurring.

As observed previously with NRVB samples that were placed in contact with granitic and saline groundwater, the high pH of these solutions leads to the precipitation of Mg-bearing phases. In

agreement, despite the lower pH of this solution compared to the others (but still around 12), the concentration of Mg in solution was always lower than that in the blank (Figure 6.43b), suggesting that brucite precipitation occurred in clay groundwater.

Concerning the concentration of S, it was possible to observe an initial uptake of this element by NRVB samples (Figure 6.43c). However, after 4 months of contact time, the cement system appeared to reach a maximum capacity for S uptake (as was also observed in the sample that was in contact with saline groundwater), and so the concentration of this element appeared to be similar to that in the blank clay solution. After 14, 16 and 18 months, a small amount of leaching of S was observed. This again might be related to the possible dissolution of ettringite occurring, after all portlandite has been consumed.

As observed with the other groundwater compositions, an initial leaching of Si occurred, after which time the amount of Si present in solution was similar to that obtained in the blank (Figure 6.43d). In agreement with EDX point analysis, XRD and TGA data, an initial uptake of chloride by the NRVB was observed (Figure 6.43e), and as a function of time the uptake converted into leaching, especially at 16 and 18 months of contact time.

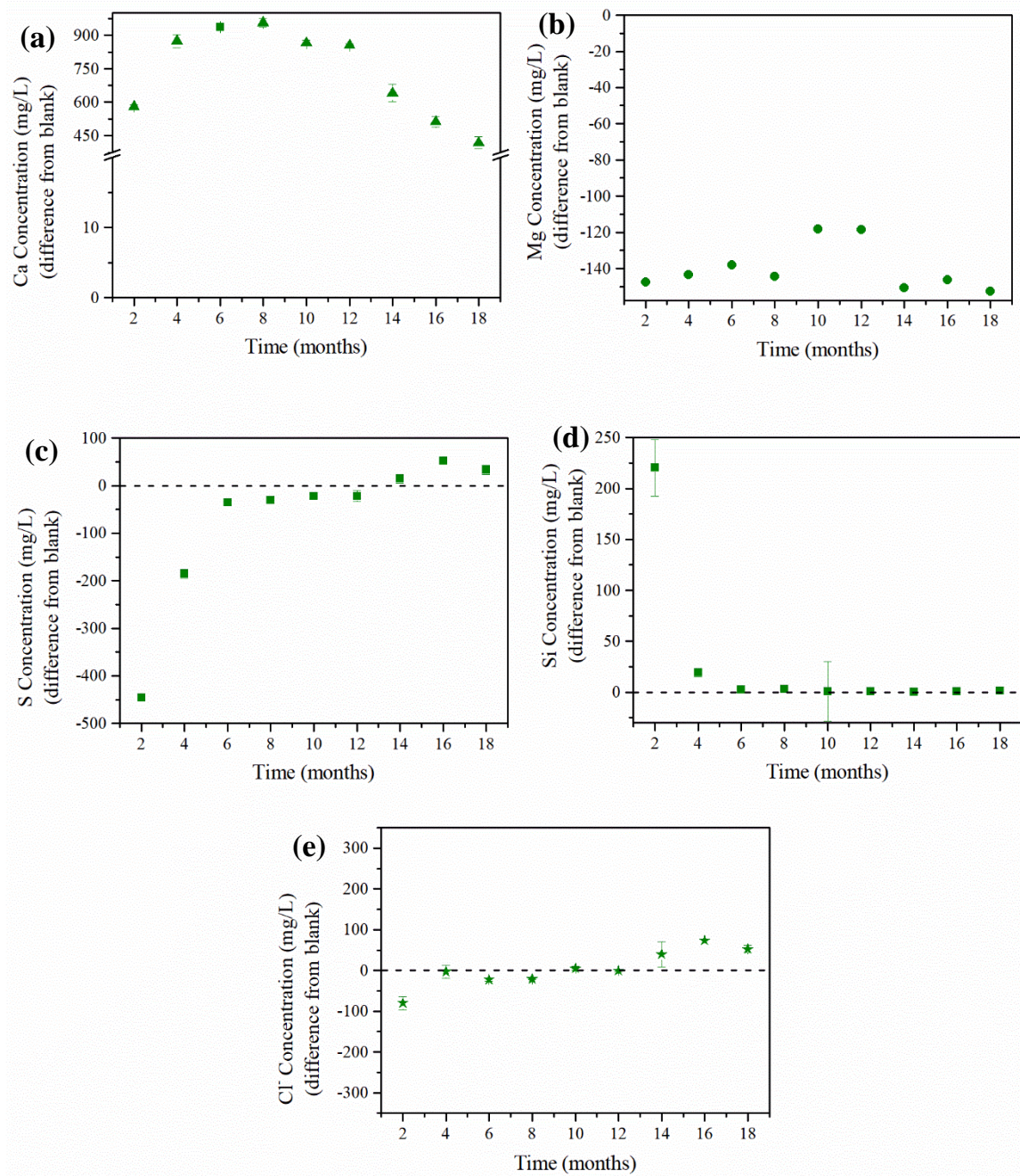


Figure 6.43. Elemental concentrations in solution (mg/L) obtained through the difference from blank for NRVB samples that were in contact with granitic groundwater for 18 months: (a) Ca concentration; (b) Mg concentration; (c) S concentration; (d) Si concentration; (e) Cl concentration. Errors were calculated using the standard deviation of duplicate ICP-OES and IC measurements.

6.6: Discussion

6.6.1: *Comparison with control samples not in contact with groundwater*

For all the samples that were in contact with the different groundwater compositions, it can be concluded, by reference to the control samples not in contact with groundwater, that the observed differences in the microstructure and porosity were due to the contact with the solutions and not due to ageing of the NRVB. In terms of evolution of the main hydrate phases in the control samples, portlandite was present for the duration of the experiment (18 months). Likewise, the presence of monocarboaluminate and calcite was identified and there were no significant changes in their relative concentration in the absence of groundwater. Ettringite was also present in the control samples, however a decrease of the relative concentration of this phase was observed with time (Figures 6.2, 6.4 and 6.6); destabilisation of ettringite is expected at later ages, due to the absence of S in the pore solution [141,150,178]. With all the alite and belite reacted after 28 days of curing (Chapters 4 and 5), a maximum amount of C-S-H formation was achieved before the start of the experiment. In this way, evolution of the structure of C-S-H was studied instead, through ^{29}Si MAS NMR. After 6, 12 and 18 months of curing in the absence of groundwater, no significant differences were observed, with the relative concentration of the different Q^n sites similar for the different time points.

In terms of porosity, a distinction between macroporosity and nanoporosity was designated. No significant differences were observed in the macroporosity of the NRVB control samples at 6 and 12 months. Whereas for the nanoporosity a slight decrease of the volume of pores <5 nm in size, and an increase of the volume of pores in the size range between 5 and 25 nm was observed. This is attributed to the opening of the pores due to destabilisation of ettringite. It should be noted that this decrease in the nanoporosity is very small as the pore volume values obtained for these samples were small.

The differences observed in the samples that were in contact with the different groundwater compositions is discussed below.

6.6.2: *Comparison between different groundwater compositions*

One of the main characteristics of NRVB is to provide an alkaline environment in the geological disposal facility [19,137]. So the aim of this study was to investigate how the mineralogy and consequent porosity, would evolve with time when in contact with groundwater, since these factors will influence the pH buffering capacity of NRVB. As an accelerated test, a semi-dynamic experiment was

performed where replacement of each type of groundwater (granitic, saline and clay groundwater) occurred every 2 months for 18 months.

pH buffering and portlandite

Once NRVB samples were placed in contact with any of the groundwater compositions, an instant increase of the pH was observed, reaching a maximum pH of around 13 for all of the samples. This initial increase of the pH to values above 12 was expected, since the major hydrate phase of the NRVB is portlandite; its dissolution results in the presence of Ca and OH⁻ ions in solution, which will consequently increase the pH [19,22,137,203]. In this experiment it was interesting to observe that, depending on the groundwater used, the rate of dissolution of portlandite varied (Figure 6.44). For example, in the case of the samples that were in contact with granitic groundwater, portlandite was no longer apparent in the XRD or TGA data after 18 months (Figures 6.9 and 6.10), whereas for the samples that were in contact with saline and clay groundwater, this occurred sooner, after around 16 and 12 months (Figures 6.21 and 6.33), respectively. A difference in the initial pH of the blank solutions for each groundwater is likely to be an important factor, i.e. since the clay groundwater presented the lower initial pH (around 7.5), a higher amount of portlandite dissolution occurred when buffering the pH to values near pH 13. The total dissolution of portlandite was observed in a previous study, where NRVB samples were placed in contact with deionised water and different concentrations of NaCl [22]. However, no indication of the time taken for the total dissolution of this phase was mentioned, but high fluxes of water were used [22]. Furthermore, in studies where CEM I was placed in contact with different solutions (granitic and clay groundwater, demineralised water and sea water), a similar behaviour was observed, where portlandite was depleted over time [71,81,180,197]. It is important to note that portlandite consumption was observed throughout the entire sample (as evidenced in XRD and TG analysis in bulk samples, and in cross-sectional EDX mapping) and not specifically in a degradation zone, as was observed by Dauzeres and colleagues, when CEM I samples were placed in contact with clay groundwater [73]. The high porosity observed in the NRVB, as compared with CEM I, is a possible explanation for this difference.

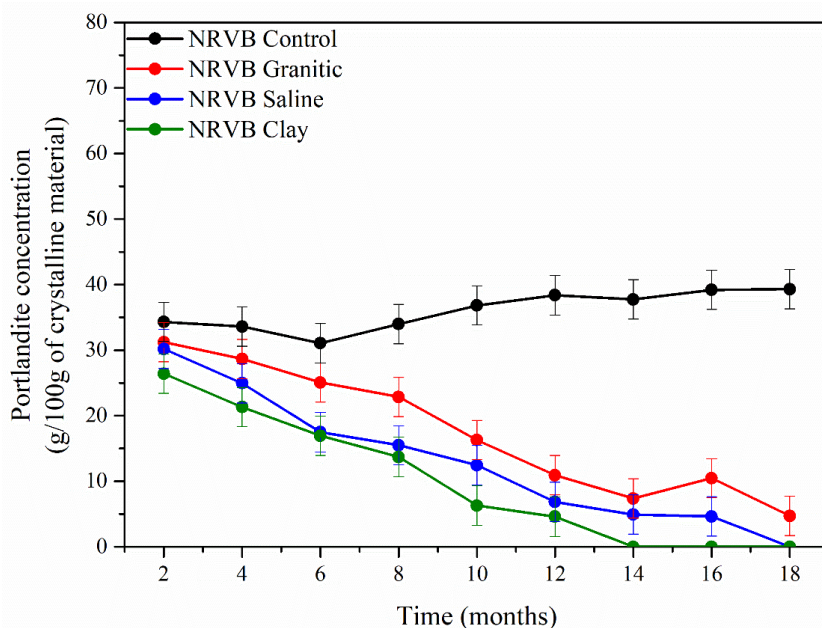


Figure 6.44. Semi-quantitative evaluation of Portlandite concentration from XRD patterns of NRVB control samples cured for 18 months and NRVB samples that were in contact with granitic, saline and clay groundwater for 18 months. Error bars obtained through Rietveld refinement software, Topas.

NRVB mineralogy and porosity as a function of groundwater composition

Granitic groundwater. In comparison to the control NRVB sample, several changes were observed when NRVB was contacted with granitic groundwater. In addition to the decrease of portlandite content mentioned above, there was increase in the calcite content. This is believed to be due to the presence of bicarbonates, HCO_3^- , in the groundwater composition, which led to the formation of CaCO_3 (Equations 6.1 and 6.2). A layer, rich in Ca and a small amount of Mg, was formed on the outer edge of the samples. The data available suggest that these elements were present as precipitates of calcite (CaCO_3) and brucite (Mg(OH)_2) [197,204], although further analysis e.g. by micro-focus XRD is required to confirm this. A small quantity of chloride-rich phases, mainly Friedel's salt, was also observed (Figure 6.15), due to the presence of around 75 mg/L Cl in the granitic solution. From the beginning of the experiment until around 12 months, the content of ettringite decreased (Figure 6.12) and S was leached to solution (Figure 6.19c). This initial leaching of S is a consequence of the small amount of this element in the granitic groundwater (around 3 mg/L), resulting in a destabilisation of AFt phases.

After 18 months of contact with granitic groundwater, further changes were observed. Analysis of ^{29}Si MAS NMR indicated that a slight decalcification of the C-S-H occurred and the mean chain length of the C-S-H increased from 3.5 at 12 months to 4.7 at 18 months. As a consequence of the decalcification, a slight decrease of the pH was observed, reaching around 12.3 ± 0.2 after 18 months.

As expected, these mineralogical alterations influenced the porosity of the NRVB samples. There was an apparent decrease of the macroporosity (from $12.3 \pm 3.0\%$ at 6 months to $9.3 \pm 1.7\%$ at 12 months), which is attributed to the precipitation of calcite and brucite. This is in good agreement with a reactive-transport modelling study of NRVB in contact with groundwater relevant to a crystalline rock disposal scenario [205], which predicted that the formation of ettringite, carbonates, and Cl- and Mg-rich phases led to the decrease of the porosity, through pore clogging, resulting in a reduction in capacity for solute transport [205]. Conversely, an increase of the nanoporosity was observed, which might be related to the destabilisation of the ettringite needles, which might have led to an increase of the capillary porosity (5 to 40 nm). Moreover, the slight decalcification of C-S-H might be responsible to the observed increase of the gel pores (pores < 5 nm). Although an increase of the nanoporosity is occurring, this variation is minor as the values obtained for the pore volume are small (in the range of $0.011 \text{ cm}^3/\text{g}\cdot\text{nm}$). On the other hand, the reduction observed in the macroporosity when comparing to the control sample ($26.6 \pm 8.2\%$ at 6 months in control sample to $12.3 \pm 3.0\%$), will possibly affect the permeability of this cementitious material. Further work, and transport modelling, are required to understand how this evolution of the porosity might affect the transport properties of the NRVB.

Clay and saline groundwaters. Since the changes in NRVB mineralogy and porosity were similar in the clay and saline groundwater, these are considered here together.

The presence of sulphur in the groundwater (128.2 and 480.9 mg/L for saline and clay groundwaters, respectively) had a significant impact in the phase assemblage of the samples that were in contact with these two groundwaters. A high uptake of S was observed, in the beginning of the experiment (Figures 6.31 and 6.43), which led to the increase of the formation of ettringite (Figure 6.21 and 6.33). Consequently, due to the presence of S in the pore solution, monocarboaluminate became unstable, leading to the disappearance of this phase over time, as conversion to ettringite occurs [147]. This is visible through XRD, TG and ^{27}Al MAS NMR results, where an increase of the peaks corresponding to ettringite and a decrease of the peaks (or absence in the case of ^{27}Al MAS NMR) corresponding to monocarboaluminate is observed. Additionally, the results show a decrease in the uptake of S over time, which indicates that the NRVB had a threshold capacity for S uptake; for saline groundwater this occurred after 16 months, and for clay groundwater at 12 months. This was concurrent with the consumption of portlandite (which was no longer apparent in XRD and TGA data at these time points), suggesting that the Ca used to form ettringite was possibly sourced from portlandite within the NRVB. Upon the consumption of portlandite (at 16 and 12 months for saline and clay groundwaters, respectively), dissolution of ettringite began to occur. This was evidenced by the leaching of S and by the continuous leaching of Ca, even after all the portlandite had been dissolved. Indeed, dissolution of ettringite is expected to happen after portlandite dissolution has occurred, as observed in previous studies where cementitious materials were placed in contact with demineralised water [71,202].

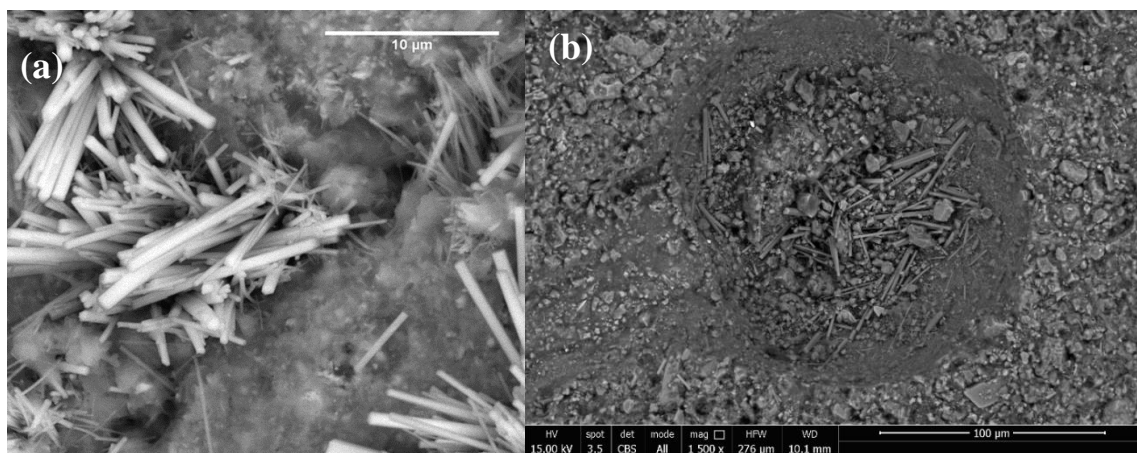


Figure 6.45. BSE images of ettringite needles (a) in NRVB sample that was in contact with clay groundwater for 6 months (high magnification); (b) in NRVB sample that was in contact with saline groundwater 6 months.

As observed for the granitic groundwater, Mg- and Ca-bearing precipitates were observed in samples of NRVB exposed to clay and saline groundwaters (Figures 6.27, 6.29, 6.39 and 6.41). The Mg-bearing precipitate is likely brucite, which formed a crust-like outer layer on the samples; this was greater in thickness for samples in clay groundwater than saline (~18 µm compared with ~10 µm, respectively), which is associated with the greater concentration of Mg in the clay groundwater (~9 mg/L compared with ~138 mg/L for saline). The Ca-bearing precipitates were present mainly in saline groundwater: HCO_3^- was present in the saline groundwater, therefore, it is possible that the precipitates are composed of calcite [66]. However, the clay groundwater did not contain HCO_3^- (as requested by Radioactive Waste Management), so the Ca-related phases visible in the sample might be mainly due to the limestone flour present in the initial NRVB composition.

Chloride was present in high concentrations in both groundwaters (~6122 and ~1861 mg/L, for clay and saline solutions, respectively). The uptake of this element was mainly observed at the beginning of the experiment when Friedel's and Kuzel's salts were identified in the TG and SEM-EDX data (Figures 6.22, 6.29d, 6.34 and 6.41e). The formation of the mixed chloride-sulphate AFm phase Kuzel's salt, not very evident in the granitic groundwater, was promoted by the presence of S in the groundwater solutions [204,206]. In NRVB contacted with clay groundwater for 18 months, Cl was incorporated in C-S-H at the edge of the sample (Figure 6.41e). This edge region also showed an elevation in Mg. This is in agreement with the work of de Weerd et al. [207], who showed that an increase of the chloride binding in the C-S-H occurs when there is a decrease of the pH, and that this decrease of the pH can be due to the local formation of hydroxide consuming phases such as brucite. Those authors also found that when SO_4^{2-} is present in the solution, there is a reduction of the Cl binding, since SO_4^{2-} will more

readily be incorporated by the C-S-H. However, in the case of the clay groundwater an increase of the leaching of S was observed at later ages, which might have promoted the Cl binding into the C-S-H.

The C-S-H structure of the NRVB in contact with saline and clay groundwaters was found to be different from that of the control NRVB samples, as determined by NMR. As observed for samples contacted with granitic groundwater, there was a slight decalcification of the C-S-H and the mean chain length increased (from 3.5 at 6 months to ~6 at 18 months for both saline and clay solutions). This increase of the mean chain length was higher than observed in the granitic groundwater (4.7 at 18 months, for both groundwaters). Different factors might be responsible for this difference, for example the higher availability of different elements, like S and Cl, present in the saline and clay groundwater (Table 6.1) to incorporate in the structure, or due to destabilisation of ettringite, which will lead to a higher availability of Al. Aluminium incorporation in the C-S-H structure varied during the experiment; at earlier contact times the incorporation was relatively low (Figures 6.12 and 6.24), which is attributed to the inclusion of Al in ettringite. At later contact times, a reduction of the Al NMR peak corresponding to ettringite was observed, and a consequent increase of the peak corresponding to aluminium in C-S-H occurred. This is concurrent with the destabilisation of ettringite (described above).

In terms of porosity, as observed for the samples that were in contact with granitic groundwater, a decrease of the macroporosity was observed with time. This might be due, once again, to the precipitation of calcite and brucite in the areas where portlandite had been dissolved. The precipitation of ettringite needles in these areas might also contribute for this reduction (Figure 6.45). This healing effect, due to the precipitation of secondary phases, has been previously observed [180,197,200]. However, it seems that this decrease in the macroporosity was more evident for the granitic and clay groundwater when comparing to the saline (~12 %, ~14 % and ~19 %, respectively). No clear justification was found for these results, however it should be highlighted the high errors obtained through this technique.

Regarding the nanoporosity, an increase of the volume of the smaller pores was observed (< 25 nm), being this range of pores sizes related to the capillary porosity (space not occupied by hydrate phases). A combination of the dissolution of ettringite and the observed slight decalcification of C-S-H, might be responsible for this increase [201]. Nevertheless, it should be noted that the pore volume obtained in the current measurements was very small, which might mean that these alterations occurred in a small scale.

In previous work, where CEM I was placed in contact with either sea water or clay groundwater, a zonation in porosity was observed, with the outermost layer presenting a lower porosity, which was attributed to the precipitation of secondary phases such as calcite, brucite and ettringite [197,200]. A second zone, inside this outer layer, showed an increased porosity [197,200]. In the current study, since porosity analysis was performed on bulk samples, it was not possible to establish such differences,

however, from the SEM-EDX analysis it seems that the precipitation of secondary phases was generally observed throughout the sample, with the exception of Mg-rich phases, which were more evident at the edge of the sample. The high porosity presented by the NRVB (when compared with CEM I materials) is likely to be the reason for this observation, since the well connected pores present a route for groundwater saturation for the entire sample.

pH vs time

Taking into account all the observed alterations in the microstructure and mineralogy, a comparison is made with the buffering behaviour of NRVB that was proposed in [1], and shown in Figure 6.1. For all groundwaters it was possible to observe the occurrence of the portlandite dependent buffering stage (stage II in Figure 6.1). In the case of granitic groundwater this lasted until the end of the experiment, where almost no portlandite was detected. For the saline and clay groundwater, portlandite dissolution occurred until 14 and 12 months, respectively. During this period, the pH was kept at around 13 for all groundwaters (Figure 6.46).

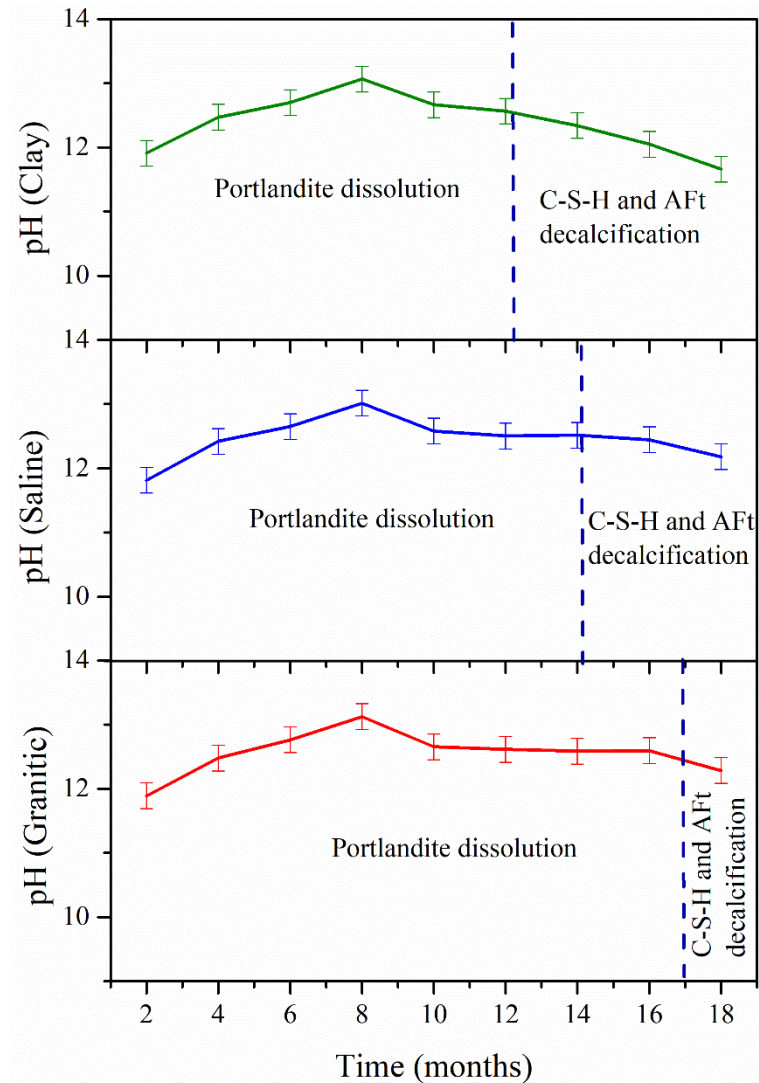


Figure 6.46. pH evolution of granitic, saline and clay groundwater over 18 months of contact with NRVB.

With all of the portlandite consumed (or almost all consumed), destabilisation/dissolution of ettringite and slight decalcification of C-S-H are the main factors that influence the buffering of the pH. This stage (III stage in the original schematic, Figure 6.1) was mainly achieved by the samples that were in contact with saline and clay solutions, but the onset of this behaviour was also observed (mainly through decalcification of C-S-H) in the granitic groundwater also. A decrease of the pH was then observed, being at around pH 12 after 18 months. It seems that the start of the decalcification of C-S-H and dissolution of ettringite occur once only a small amount of portlandite remains. Moreover, a continuous leaching of Ca is occurred (ICP-OES results) after the portlandite had been consumed, being indicative that a combination of decalcification of C-S-H and ettringite destabilisation/dissolution are responsible for the buffering capacity in stage III of Figure 6.1.

6.6.3: Comparison between semi-dynamic and static experiment

To establish whether the accelerated nature of the semi-dynamic experiments influenced the changes observed, a second experiment was performed, where NRVB samples were placed in contact with the same groundwaters, but no replacement was performed, i.e. it was a static experiment. The data are described in full in Appendix II. A brief summary is as follows:

- The pH was kept constant throughout the experiment, being \sim pH 12.3 ± 0.2 , 12.1 ± 0.2 and 12.0 ± 0.3 , for the samples that were in contact with granitic, saline and clay groundwater, respectively;
- Total consumption of portlandite occurred in all groundwaters by 18 months;
- An increase in the formation of ettringite and brucite for the NRVB samples that were in contact with saline and clay solutions was observed throughout the experiment; and
- An equilibrium was reached between the cement system and the solution.

In summary, the static experiments largely gave the same results as the semi-dynamic experiments, in terms of the phases formed. The main difference was the higher pH observed in the static experiments, which is a result of not replenishing the groundwater solution at regular intervals.

6.7: Conclusions

A semi-dynamic experiment has been performed using three different types of groundwater, and alterations in the mineralogy and microstructure were studied. When comparing to the NRVB control samples (cured without contact with groundwater), it was visible that the alterations observed were due to contact with groundwater and not due to ageing.

Once NRVB was placed in contact with the different groundwater compositions, an instant increase of the pH was observed, reaching around pH 12 at the end of the experiment. In the case of the granitic groundwater the pH buffering was controlled mainly by the dissolution of portlandite, whereas for the saline and clay groundwater a combination of portlandite, C-S-H and ettringite dissolution were the main phases responsible for maintaining alkaline pH values.

Although all of the groundwaters had similar chemical elements in their composition, the concentration at which each element was present was different, and this significantly influenced the degree of mineralogical alterations that occurred in the NRVB samples. It was visible that the samples that were in contact with granitic groundwater seemed to be affected by the contact at a slower rate than the samples that were in contact with saline and clay groundwater.

The main differences were related with the concentration of S and Mg present in the groundwaters. In the case of S, this element was present in very low quantities in the granitic groundwater, which led to a destabilisation of ettringite. While, in the case of the saline and clay groundwater a higher content of S was present, leading to an uptake of this element by the NRVB samples, which resulted in the destabilisation of monocarboaluminate and the formation of more ettringite. However, once all of the portlandite had been consumed, a destabilisation of ettringite was observed.

Moreover, the high concentration of Mg in the saline and clay groundwater resulted in a higher precipitation of Mg-rich phases, for example brucite, than observed in the samples that were in contact with granitic groundwater. An interesting observation was that for the groundwaters that contained carbonates in their composition (granitic and saline), the precipitation of brucite was coupled with the precipitation of calcite, which formed an outside layer. In the case of the clay groundwater, since no carbonates were present in the composition, the precipitation of an outside layer rich in only magnesium was instead observed.

It is important to point out that all the differences observed due to the contact with the different groundwaters, were visible throughout the entire sample, highlighting the characteristic high porosity of NRVB. However, a general decrease of the macroporosity was observed due to the precipitation of secondary phases, like calcite, brucite and ettringite. In the case of ettringite, the formation of cracks might be observed, due to the expansion behaviour that generally the formation of this phase can provide [66,150,208]. On the other hand, there is not enough understanding of how crack formation will behave under confining pressure in a geological disposal facility. Since one of the major requirements of NRVB as a cement backfill is to maintain a high porosity, these results are potentially of significance to the safety case. Further modelling work should be performed to try to understand if these differences observed in the microstructure will affect the overall purpose of the NRVB, which is to provide an alkaline environment for radionuclide uptake.

The main purpose of NRVB in a GDF context is to provide a high-pH environment when in contact with groundwater. This was observed in the present study, regardless of the groundwater composition. Moreover, when NRVB samples were in contact with granitic groundwater the mineralogical alterations seem to have occurred at a lower rate when comparing to the saline and clay groundwater. These results are of significance to the UK GDF concept where this backfill material is considered to be used, in a crystalline rock [19,137].

Chapter 7: Mineralogical and porosity assessment of the Cebama Reference Cement in contact with simulated groundwater solutions

7.1: Introduction

Low-pH cements were formulated in the context of geological disposal facilities to minimise detrimental effects that high-pH cements, such as Portland cement, can have on the surrounding environment, particularly on clay buffers. The pore solution of this type of cement is expected to be around pH 11, and so the buffering capacity will be mainly due to the dissolution of C-S-H (low Ca/Si ratio), the main hydrate phase present.

Taking this into account, it is expected that the microstructural evolution of the Cebama reference cement paste when in contact with the different groundwater compositions will be different from that observed with NRVB in Chapter 6.

Recent studies have been performed using different formulations of low-pH cement in contact with granitic and clay groundwater [42,73,84,209]. A comparison of these data with those from the current study will be performed later in this Chapter.

In this Chapter, results from an extended experiment (carried out for 1 year) where Cebama reference cement paste (cured for 28 days) was placed in contact with three different types of simulant groundwater (granitic, saline and clay, Table 7.1) in the conditions described in the previous chapter and shown in Chapter 3, will be presented. Analysis of the cement samples was performed every 2 months by XRD and TGA, and the solution chemistry was measured at the same time points by ICP-OES and IC. At selected time points (6 and 12 months) further characterisation of the cement samples was performed by SEM, ^{29}Si MAS NMR, ^{27}Al MAS NMR, XCT and MIP analysis. Parallel static experiments (to ascertain the behaviour when solution is not regularly replaced) were also performed (as detailed in Chapter 3).

Table 7.1. Composition (mg/L) of the synthetic groundwaters utilised in Chapters 6 and 7.

Element	Granitic Groundwater	Saline Groundwater	Clay Groundwater
Ca	20.0	796.0	300.0
Mg	4.9	9.7	138.5
S	3.2	128.2	480.9
Na	64.4	3218.6	1264.4
K	3.9	82.1	43.0
Cl	74.4	6122.2	1861.1
HCO ₃	122.0	122.0	-

These experiments aimed to determine the mineralogical and microstructural changes induced in Cebama reference cement by contact with groundwater, as a function of time. This Chapter presents results first for the Cebama control samples that were cured for the same period of time without contact with groundwater, then data from the samples that were in contact with granitic, saline and clay groundwaters are described.

7.2: Mineralogical and microstructural evolution of Cebama reference cement paste without groundwater

Figure 7.1 shows the XRD data for the Cebama control sample that was cured for 12 months. No significant differences were observed between the different XRD spectra at the different time points. A possible slight reduction of the intensity of the peaks corresponding to the clinker phases, alite (Ca_3SiO_5) and belite (Ca_2SiO_4), occurred. In turn, a slight increase of the intensity of the hydrate phases was observed. However, these differences are very small. Nevertheless, the main hydrate phases present after 12 months are: ettringite ($\text{Ca}_6\text{Al}_2(\text{OH})_{12}(\text{SO}_4)_3 \cdot 26\text{H}_2\text{O}$), monocarboaluminate ($\text{Ca}_4\text{Al}_2(\text{OH})_{12}(\text{CO}_3)_3 \cdot 5\text{H}_2\text{O}$), a hydrotalcite-like phase ($\text{Mg}_4\text{Al}_2(\text{OH})_{14} \cdot 3\text{H}_2\text{O}$, meixnerite), calcite (CaCO_3), and C-S-H.

E - Ettringite **Mc** - Monocarboaluminate
Ht - Hydrotalcite **A** - Alite **B** - Belite
C - Calcite **Si** - SiO₂

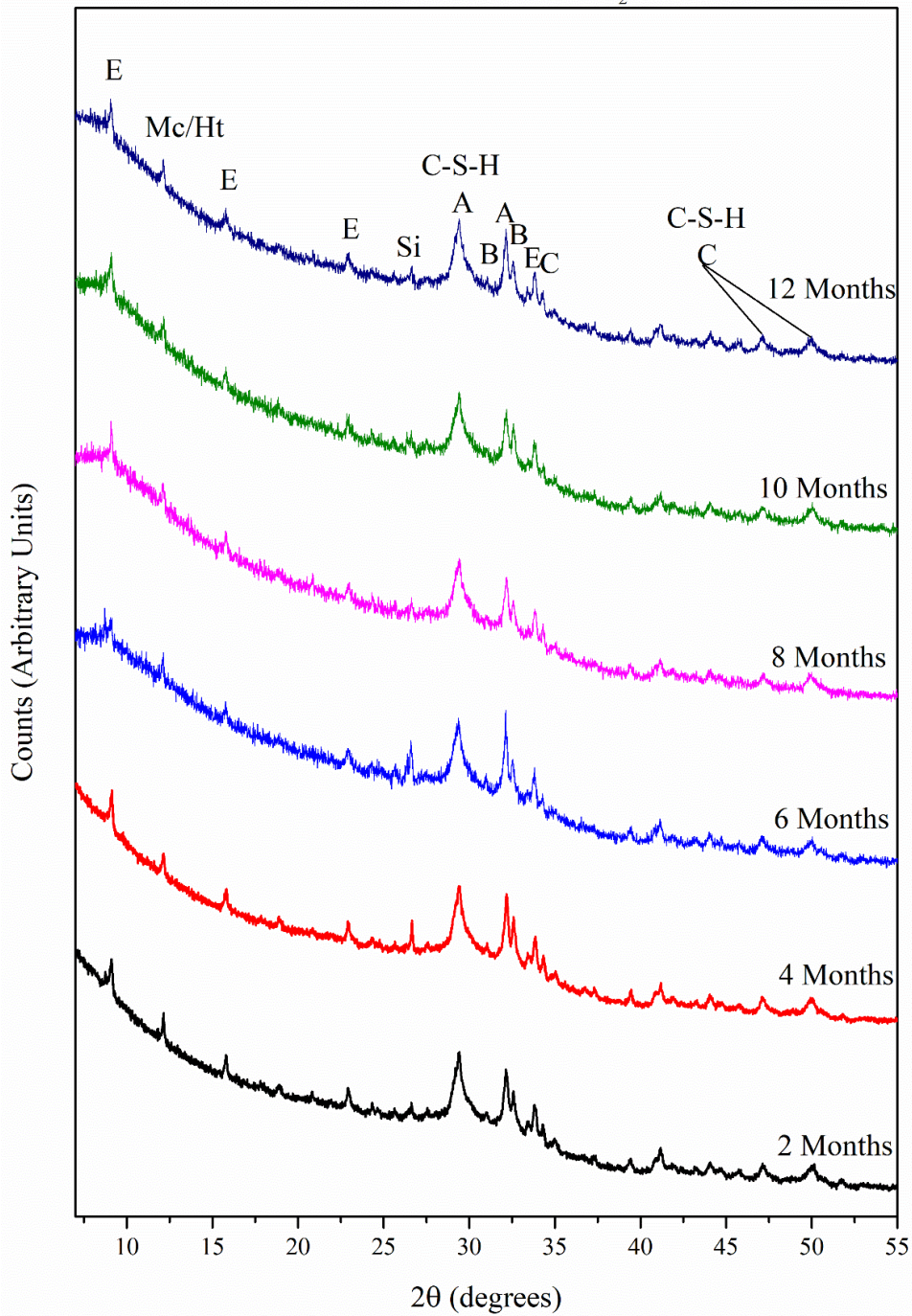


Figure 7.1. XRD patterns of Cebama reference cement control samples cured for 12 months.

The same phases were identified through TG analysis (Figure 7.2), and no significant changes were observed to occur with curing time. A slight increase of the peak between 50 and 100 °C [52,192] was observed, and corresponds to the mass loss from loosely bound water within C-S-H. This is likely

indicative of slow cement hydration with time. However, in terms of other hydrate phases, no significant differences were observed, with the peaks corresponding to AFt and AFm phases (between 100 and 150 °C) very similar in intensity in all of the samples. The peak at around 800 °C corresponds to the presence of calcite, in accordance with the XRD analysis.

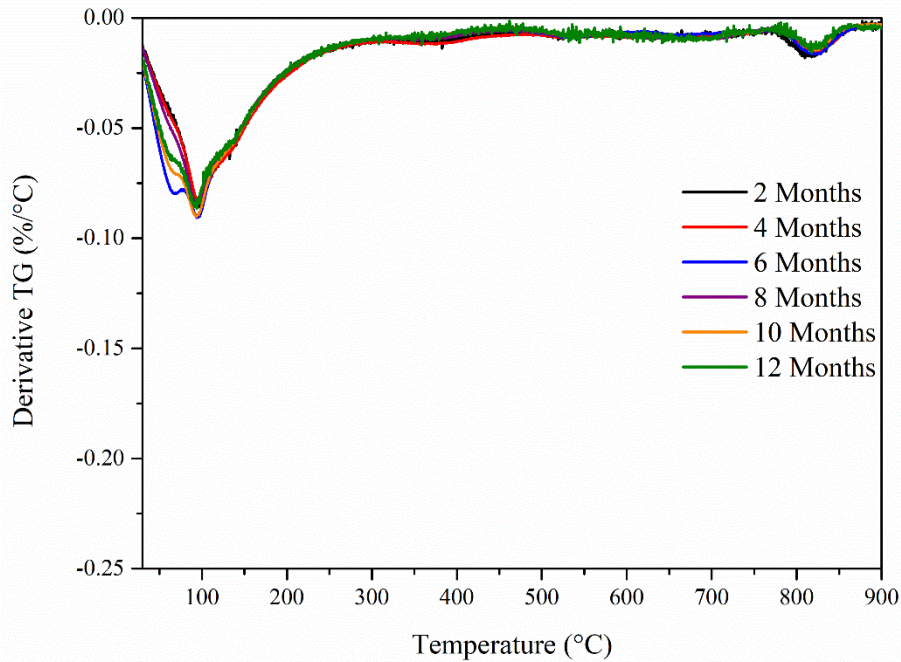


Figure 7.2. TG data for Cebama reference cement control samples cured for 12 months.

Due to the highly amorphous nature of this low-pH cement, further analysis by ^{29}Si MAS NMR and ^{27}Al MAS NMR was performed to better understand the evolution, with time, of the amorphous components, e.g. blast furnace slag (BFS), silica fume, and C-S-H.

Once again, no significant differences were observed in the ^{29}Si MAS NMR spectra of the samples that were cured for 6 and 12 months (Figure 7.3b). However, for a more detailed analysis of these results, - quantification of the different sites (deconvolution shown in Figure 7.3a) was performed. The deconvolution performed with these samples was very similar to that previously made in Chapters 4 and 5, and is as follows: (1) a broad peak was assigned to the glassy BFS component of the sample; (2) unreacted alite and belite were identified, with the signal attributed to the former being composed of two peaks; (3) silica fume has a very distinct peak at around -111 ppm; (3) for the C-S-H structure two Q^1 environments were distinguished by the nature of the charge-balancing cations which, due to their differing extent of shielding, resulted in separate resonances [116,117,162]; and lastly, Q^2 , $\text{Q}^2(1\text{Al})$, Q^3 and $\text{Q}^3(1\text{Al})$ were also identified as part of the C-S-H structure. It should be noted that the overlap of the BFS peak with many other peaks will influence the quantification performed, but for comparison

purposes, these results were considered. This deconvolution approach was used for the Cebama reference cement in all groundwater solutions described throughout the remainder of this Chapter.

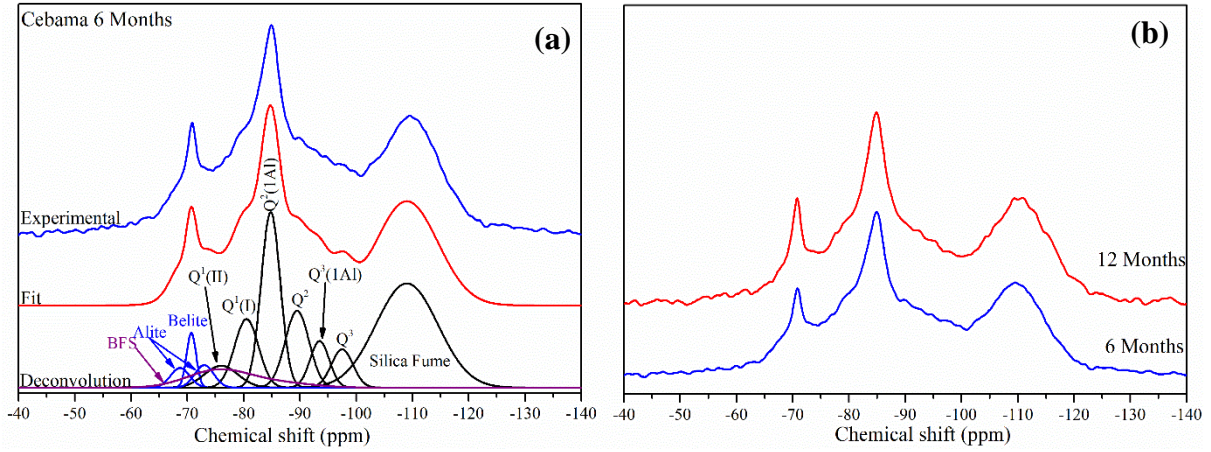


Figure 7.3. (a) Deconvoluted ^{29}Si MAS NMR spectrum of Cebama reference cement cured for 6 months; (b) ^{29}Si MAS NMR spectra of Cebama reference cement control samples cured for 6 and 12 months.

Quantification of the different sites (Table 7.2) confirms the very slow hydration reaction of this cementitious material (as also seen in Chapter 5), as no significant differences were observed between the relative concentrations of components at 6 and 12 months of curing. Likewise, from the calculated Ca/Si ratio, Al/Si ratio and mean chain length (MCL) (Table 7.3), no differences were observed between the different curing times.

Table 7.2. Results of deconvolution of ^{29}Si MAS NMR spectra of Cebama reference cement control samples. The estimated uncertainty in absolute site percentages is $\pm 2\%$.

	Belite	Alite	Silica fume	BFS	Q ¹	Q ² (1A1)	Q ²	Q ³ (1A1)	Q ³
6 Months	3 %	4 %	34 %	7 %	12%	18 %	10 %	5 %	4 %
12 Months	3 %	4 %	33 %	6 %	11 %	18 %	10 %	4 %	4 %

Table 7.3. Summary of structural evolution of C-S-H formed in Cebama reference cement control samples, based on the ^{29}Si MAS NMR deconvolutions.

	Ca/Si	Al/Si	MCL
6 Months	1.1 ± 0.2	0.18 ± 0.02	9.2 ± 3.3
12 Months	1.1 ± 0.2	0.19 ± 0.02	10.4 ± 4.2

In the ^{27}Al MAS NMR spectra (Figure 7.4), it is possible to observe an increase of a broad tetrahedral Al peak, between 80 and 50 ppm, which corresponds to Al^{IV} in C-S-H and also unreacted BFS. This is not observed in the ^{29}Si MAS NMR spectra, where no significant changes in the relative concentration of C-S-H were observed. The reason for this discrepancy is not clear, but might be due to errors occurred during the deconvolution process in the ^{29}Si MAS NMR. A slight increase of the intensity of the peak corresponding to ettringite (at 14 ppm) was also observed to occur with time. This slight increase is not so evident in the XRD and TGA, which might be indicative that this increase, if it is truly occurring, is very small.

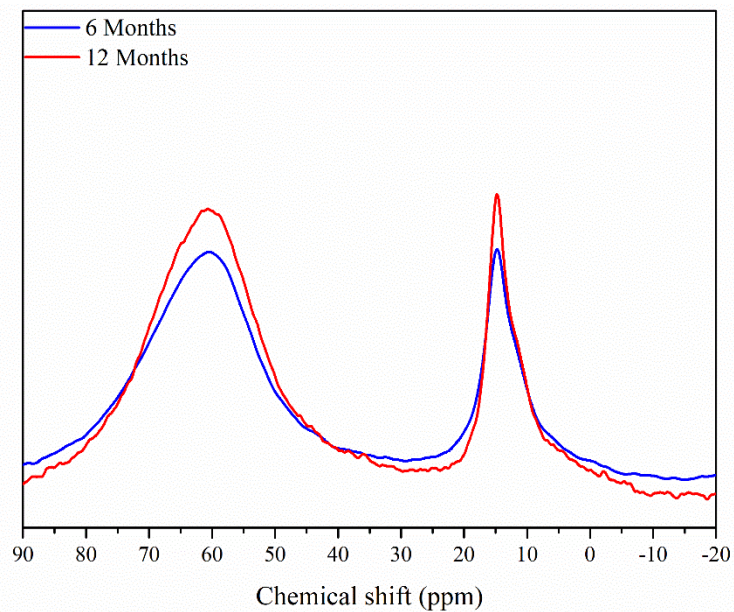


Figure 7.4. ^{27}Al MAS NMR spectra of Cebama reference cement control samples cured for 6 and 12 months.

To study the porosity of the Cebama reference cement paste, two different techniques were used: X-ray Computed Tomography analysis was used to determine the porosity of the larger sized pores ($> 1.5 \mu\text{m}$, termed herein as macroporosity), and mercury intrusion porosimetry (MIP) for a wide range of pore sizes, including smaller pores (smallest pore entry size detected of around $0.003 \mu\text{m}$).

Through XCT analysis (Table 7.4), a slight decrease of the macroporosity between the sample cured for 6 months and the sample cured for 12 months was observed. This decrease might indicate that more hydrate phases (for example hydrotalcite-like phase, maximum particle size $4.5 \mu\text{m}$ [210]) formed, which filled the bigger pores. However, it should be noted that the values are within the error (relatively high uncertainty is attributed to this technique, due to human error in thresholding), so the observed decrease is not significant.

Table 7.4. Porosity measurements obtained by XCT and MIP for Cebama reference cement control samples. XCT errors calculated from standard deviation of triplicate thresholding. MIP errors represent the intrinsic instrument error.

	Macroporosity through XCT (%)	Porosity through MIP (%)
NRVB Control 6 Months	4.5 ± 0.9	9 ± 2
NRVB Control 12 Months	2.8 ± 0.9	10 ± 2

Figure 7.5 shows the pore entry size diameter relative to the cumulative intrusion for the Cebama samples after 6 and 12 months of curing. For both samples, the curve allocates the bulk of the pores to pore entry sizes below 0.15 μm. However, it seems that for the 12 month cured sample the cumulative intrusion was higher than for the 6 months sample, which means that more small pores were detected in the former sample. However, the total porosity obtained through this technique was the same for both samples, at around 9 ± 2 %.

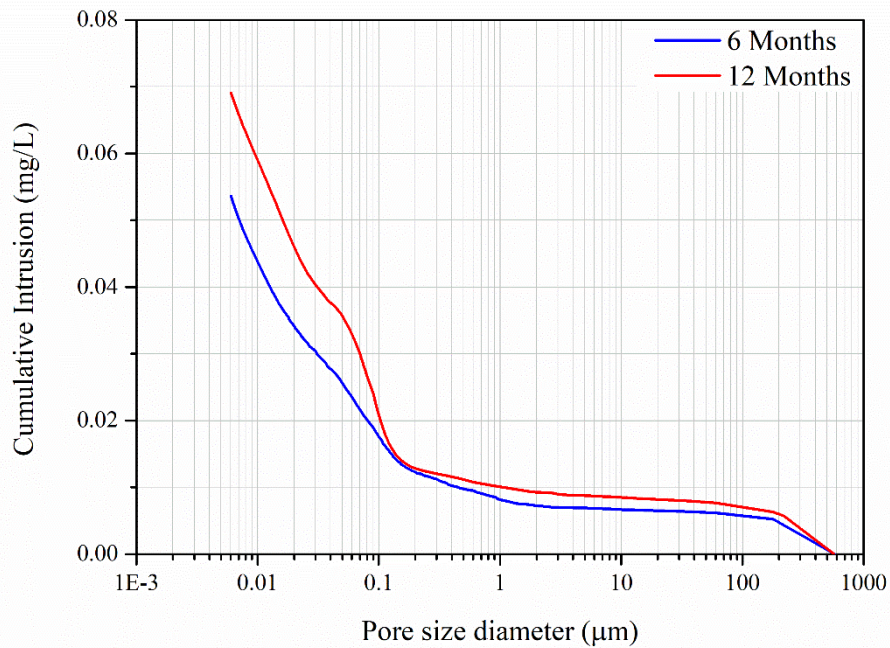


Figure 7.5. Pore entry size distribution of Cebama reference cement control samples cured for 6 and 12 months, determined by MIP.

7.3: Mineralogical and microstructural evolution of NRVB with Granitic Groundwater (semi-dynamic experiment)

7.3.1: Mineralogical evolution of Cebama reference cement paste

After 12 months of contact with granitic groundwater, the XRD results (Figure 7.6) show slight differences in the peak intensities of some of the phases as a function of time. A decrease of the intensity of the peaks corresponding to the clinker phases, e.g. alite and belite, was observed. Although the peak of alite overlaps with C-S-H (at $29^\circ 2\theta$), making it difficult to observe the decrease here, the ^{29}Si MAS NMR spectra (results shown below, Table 7.5) show that a decrease in alite is apparent, indicating that cement hydration had occurred. This decrease is in contrast to the control sample at the same age (Section 7.2), where no significant changes were observed.

In terms of hydrate phases, a slight increase in the intensity of the peaks corresponding to ettringite was observed with time. However, no other differences were visible, with the main hydrate phases present after 12 months of contact with granitic groundwater similar to those in the control sample of the same age: ettringite, monocarboaluminate, hydrotalcite-like phase (meixnerite), C-S-H and calcite. It is interesting to note that no portlandite was observed in any of the XRD patterns at each sampling time point, similar to the control sample. The absence of portlandite is expected in these cement systems due to the presence of silica fume and BFS, which will convert this phase into C-S-H through pozzolanic reactions.

E - Ettringite **Mc** - Monocarboaluminate
Ht - Hydrotalcite **A** - Alite **B** - Belite
C - Calcite **Si** - SiO₂

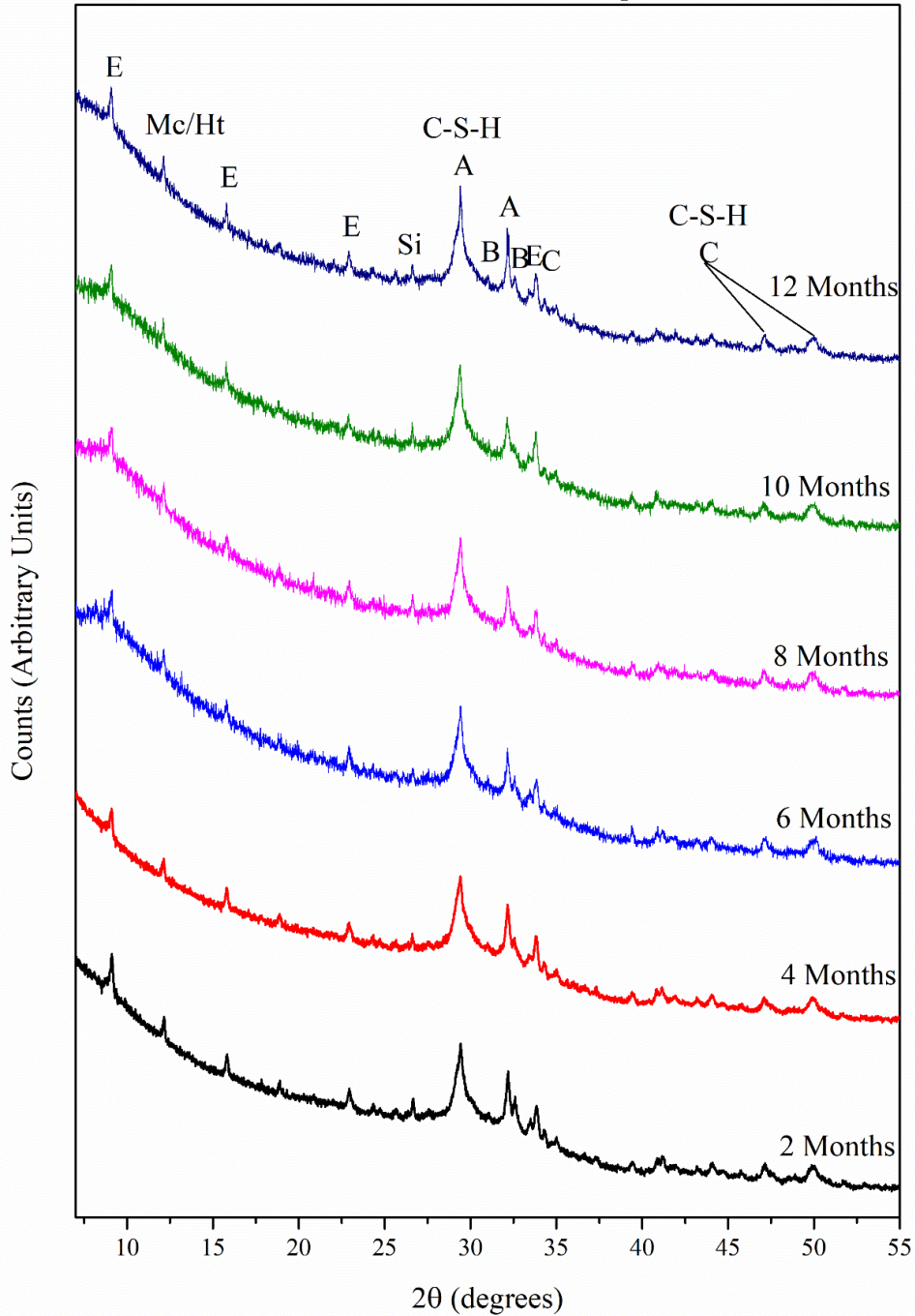


Figure 7.6. XRD patterns of Cebama reference cement samples that were placed in contact with granitic groundwater for 12 months.

The results obtained through TGA agree well with the XRD data. In Figure 7.7, the peak between 50 and 100 °C correspond to the mass loss due to release of loosely bound water from within C-S-H, and the peak around 100 °C corresponds to AFt and AFm phases [52,90,192]. An increase in the intensity of these peaks was observed over time, even when compared to the control samples, indicating the

enhanced hydration of Cebama reference cement paste when in contact with granitic groundwater. The rate of increase in cement hydration seems higher when comparing 4 months to 6 months, whereas for longer times the rate of increase of these peaks is less pronounced. The observed decrease of intensity of the same peaks solely in the 8 months sample might be related to the procedure of stopping the hydration, which potentially affected the results, although care was taken to minimise those effects.

The peaks observed at 680 and 840 °C correspond to CaCO_3 polymorphs [52,90,192], and no clear differences were observed in the intensity of these peaks with time, showing that no increase of carbonation of the sample was observed throughout the experiment.

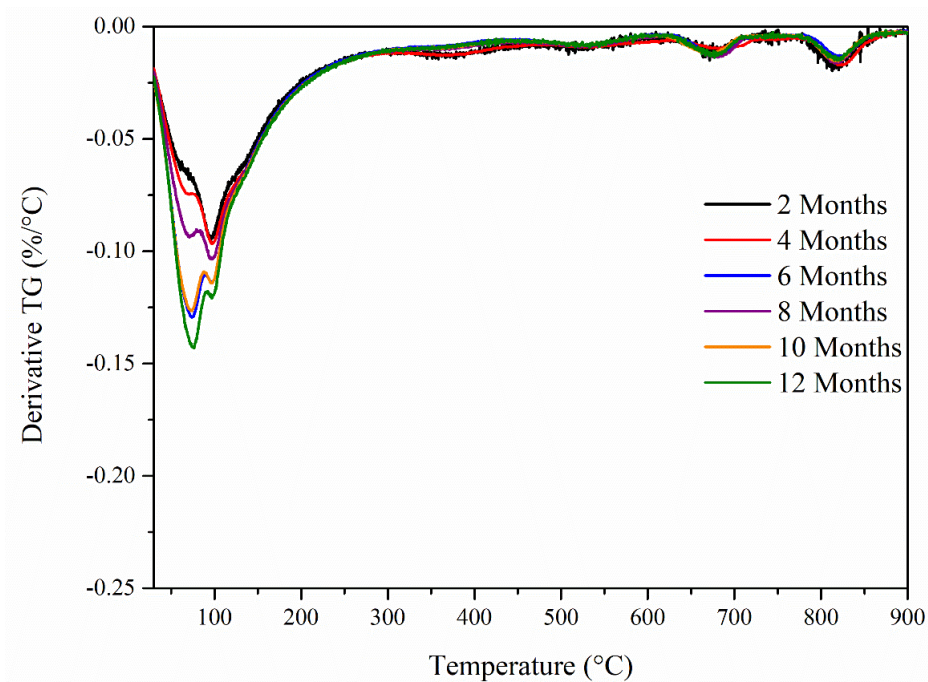


Figure 7.7. TG data for Cebama reference cement samples that were in contact with granitic groundwater for 12 months.

Figure 7.8b shows the ^{29}Si MAS NMR results for Cebama reference cement paste after 6 and 12 months of contact with granitic groundwater. From this Figure, a decrease of the peak intensity corresponding to belite, at -71 ppm, was observed. Moreover, a decrease of the silica fume peak at -111 ppm is visible, indicating that more hydration or dissolution of this material was occurring with time. This decrease was not observed in the control sample, highlighting that these differences were due to the contact with the simulant groundwater solution.

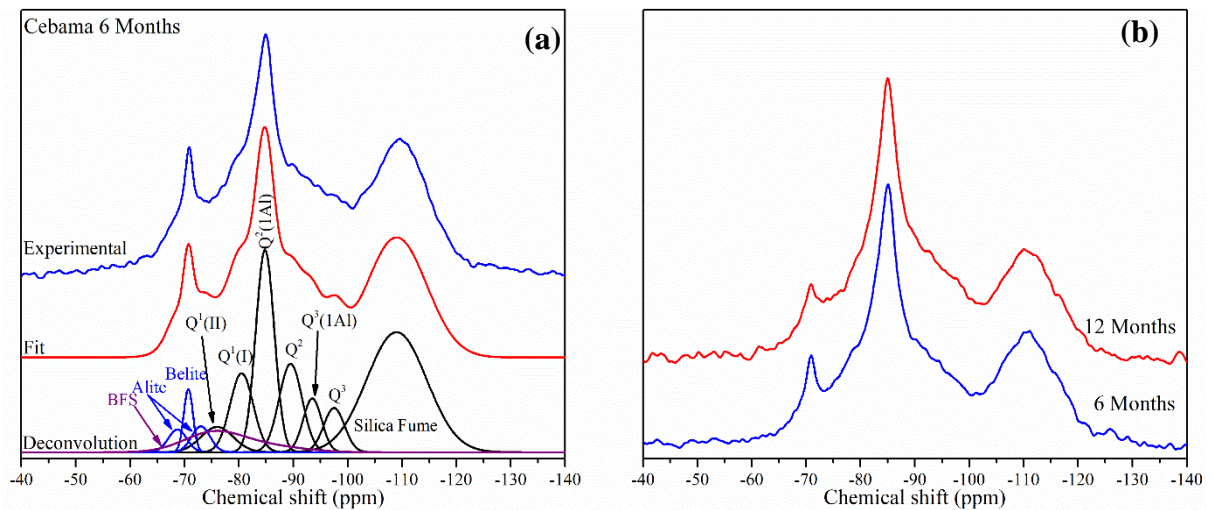


Figure 7.8. (a) Deconvoluted ^{29}Si MAS NMR spectrum of Cebama reference cement cured for 6 months; (b) ^{29}Si MAS NMR spectra of Cebama reference cement that were in contact with granitic groundwater for 6 and 12 months.

An increase of the hydration of this low-pH cement was confirmed through the slight decrease of the relative concentration of belite, alite, silica fume and BFS (Table 7.5), when compared to the Cebama reference cement paste control samples, being more evident for the 12 month-old samples.

An increase of the relative concentration of C-S-H with time was also observed, with the relative concentration of C-S-H after 6 months of contact at $56 \pm 2\%$ and after 12 months $60 \pm 2\%$, compared with $\sim 49 \pm 2\%$ in the control sample (Table 7.2 and 7.5). The relative concentrations of Q^2 slightly increased, as hydration of BFS and silica fume occurs. The presence of Q^3 and $\text{Q}^3(1\text{Al})$ are indicative of cross-linking silicon (Q^3) and aluminium substitution within a cross-linking site in the C-S-H gel ($\text{Q}^3(1\text{Al})$).

Table 7.5. Results of deconvolution of ^{29}Si MAS NMR spectra of Cebama reference cement samples that were in contact with granitic groundwater. The estimated uncertainty in absolute site percentages is $\pm 2\%$.

	Belite	Alite	Silica fume	BFS	Q^1	$\text{Q}^2(1\text{Al})$	Q^2	$\text{Q}^3(1\text{Al})$	Q^3
6 Months	2 %	4 %	32 %	5 %	11 %	24 %	10 %	6 %	5 %
12 Months	2 %	2 %	30 %	4 %	14 %	22 %	14 %	5 %	5 %

From the deconvolution of the ^{29}Si MAS NMR spectra, it was observed that the Ca/Si ratio, the Al/Si ratio and MCL did not significantly change as a function of time when this cement was in contact with granitic groundwater, being 1.1 ± 0.16 , 0.19 ± 0.02 and 10.0 ± 3.2 , respectively, after 12 months of the experiment (Table 7.6). A slight increase in the Al/Si ratio was observed when comparing to the control sample, evidencing the reaction of the BFS in the samples that were in contact with granitic solution.

Table 7.6. Summary of structural evolution of C-S-H formed in Cebama reference cement samples that were in contact with granitic groundwater, based on the ^{29}Si MAS NMR deconvolutions.

	Ca/Si	Al/Si	MCL
6 Months	1.1 ± 0.21	0.21 ± 0.02	12.0 ± 4.6
12 Months	1.1 ± 0.16	0.19 ± 0.02	10.0 ± 3.2

In the ^{27}Al MAS NMR spectra (Figure 7.9), differences were observed between the samples after 6 and 12 months of contact with granitic groundwater. The slight shift and increase observed in the broad tetrahedral Al peak, between 80 and 50 ppm (which contains contributions from Al^{IV} in C-S-H and unreacted BFS), for the sample at 12 months shows again the increase of hydration of this low-pH cement as a function of leaching time. A slight increase of the intensity of the peak corresponding to ettringite (at 14 ppm) was also observed with time. These results are in agreement with previously observed XRD and TG data.

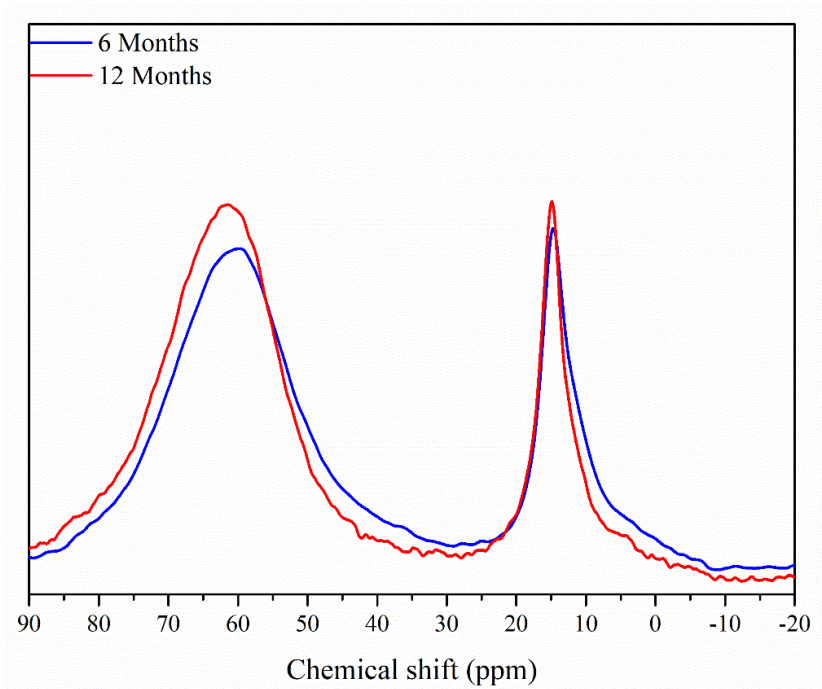
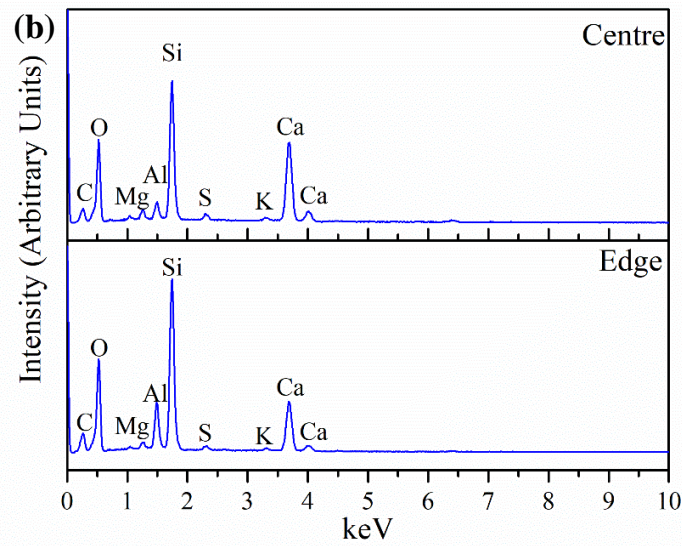
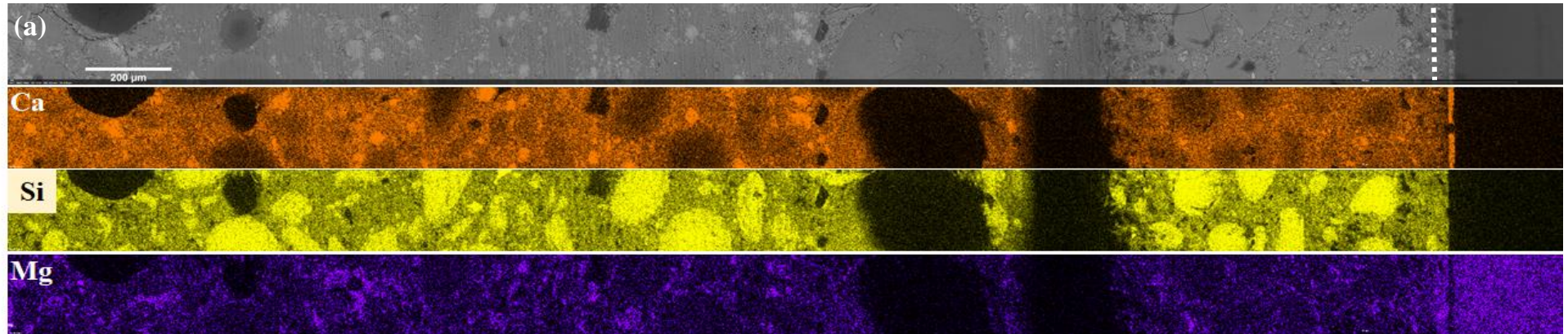


Figure 7.9. ^{27}Al MAS NMR spectra of Cebama reference cement samples that were placed in contact with granitic groundwater for 6 and 12 months.

In this experiment, epoxy was used to seal the ends of the cylinder monolith and so provide unidirectional contact of groundwater. To help understand if an element / mineral phase assemblage gradient is observed from the edge (area in direct contact with groundwater) to the centre of the sample (area not in direct contact with groundwater), SEM-EDX analysis was performed.

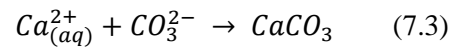
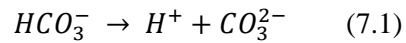
Figure 7.10a shows a BSE image and elemental maps (for Ca, Si and Mg) of Cebama reference cement paste after 6 months of contact with granitic groundwater. Due to insufficient image quality of sulphur and aluminium elemental mappings, these were not shown in Figure 7.10a. A small outside layer composed mainly of calcium was observed. In the area before this layer, a decrease of the concentration of Ca and an increase of the concentration of Mg is apparent. Elemental spot analysis was performed in the edge (to the right of the white dashed line, Figure 7.10a) and centre of the sample (in the centre of the sample, LHS of the image), and the spectra associated with each area are shown in Figure 7.10b, with the corresponding atomic percentages of major elements shown in the Table. A visible difference was observed in the atomic percentages of Ca and Mg between the edge and the centre of the sample, demonstrating the formation of an outside Ca-rich layer. Also, more Al was observed in the edge, which might be indicative of the slightly higher degree of hydration of BFS at the edge of the sample.



	Edge (at %)	Centre (at %)
Ca	9.58 ± 0.57	15.32 ± 0.80
Mg	0.71 ± 0.08	1.15 ± 0.10
Al	4.73 ± 0.31	1.77 ± 0.13
Si	18.14 ± 1.01	14.77 ± 0.75
S	0.50 ± 0.06	0.72 ± 0.07

Figure 7.10. SEM-EDX analysis of Cebama reference cement sample that was in contact with granitic groundwater for 6 months; (a) BSE image and elemental maps; (b) spectra associated with point analysis; Table: point analysis in atomic %, with absolute error from the measurement.

After 12 months of contact with granitic groundwater (observed at a higher magnification, Figure 7.11a), the same Ca-rich layer at the edge of the sample was observed, followed by a decrease of calcium concentration and an increase of magnesium concentration, as shown in Figure 7.11b. The thickness of this Ca-rich layer is around 15 μm after 12 months of contact with granitic groundwater. This outside layer is believed to be formed due to the precipitation of CaCO_3 , since HCO_3^- is one of the components present in the granitic groundwater. This carbonation reaction occurs as shown in Equations 7.1 and 7.2, and will lead to a decrease of the pH [66].



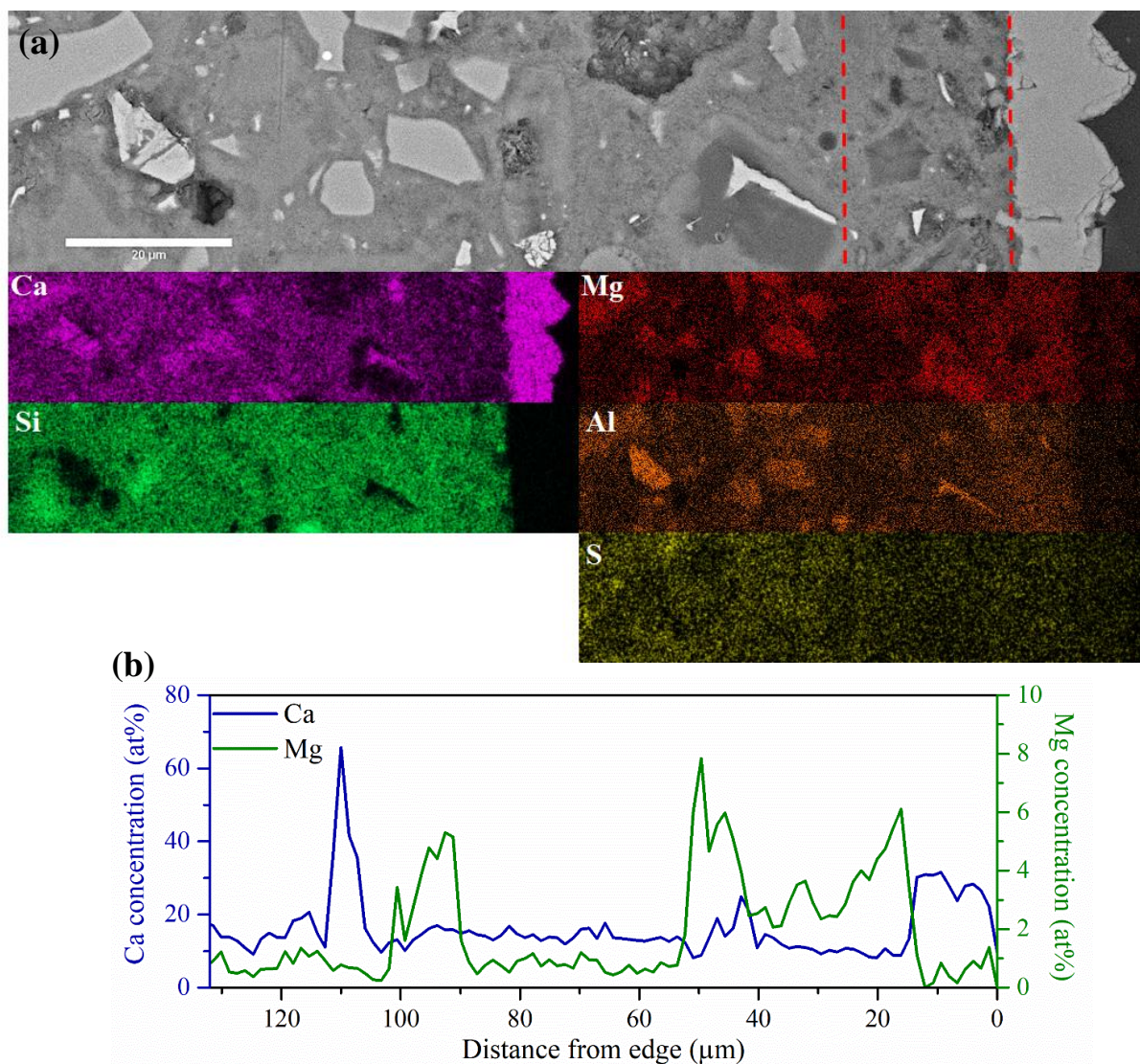


Figure 7.11. SEM-EDX analysis of Cebama reference cement sample that was in contact with granitic groundwater for 12 months; (a) BSE image and elemental maps; (b) Linescan of magnesium and calcium in atomic %.

To better understand the differences between the edge and the centre of the sample, SEM-EDX point analysis was performed, where between 100 to 150 points were manually placed in the edge and centre of the sample. Different elemental ratio plots (Figure 7.12) were in this way used to identify differences in the hydrate phase assemblage between the edge and centre of the sample. Compositional trend lines connecting C-S-H and portlandite/calcite with other hydrate phases are shown, based on the ideal compositions of the different hydrate phases. The edge region in this point analysis is the Mg-rich layer, just before the Ca-rich layer (indicated in the image by the red dashed lines, Figure 7.11a). This was chosen since the Ca-rich outside layer is mainly formed of calcium, which gives a Ca/Si molar ratio of average 580.8, and many of the ratios plotted give values near to zero (for example the S/Ca molar ratio of average 0.002). Moreover, it is believed that the main degradation process occurred before the

formation of the carbonate layer, i.e. the area just before this protective layer where there is observed a decrease of calcium (meaning decalcification of C-S-H might have happened).

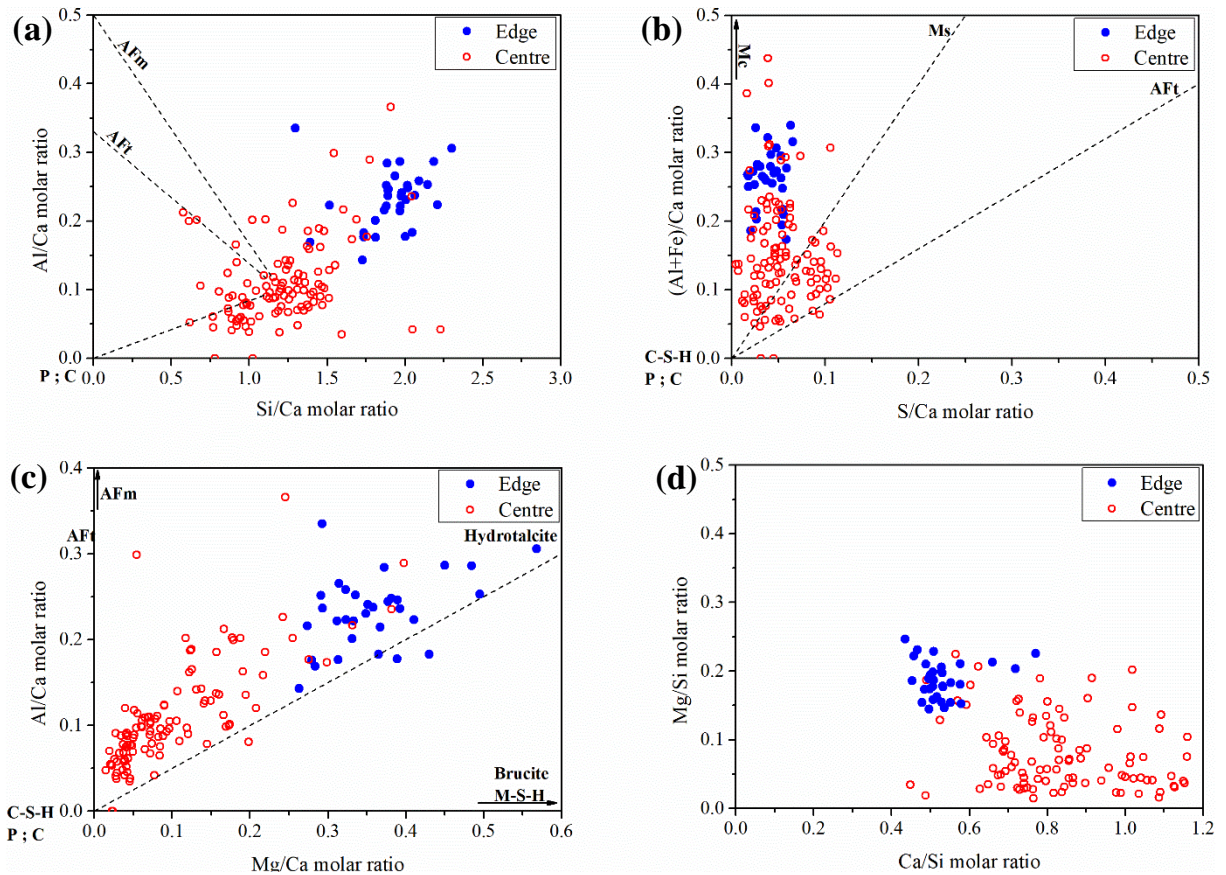


Figure 7.12. Elemental molar ratio plots of SEM-EDX point analysis in Cebama reference cement sample that was in contact with granitic groundwater for 12 months: (a) Si/Ca vs Al/Ca; (b) S/Ca vs (Al+Fe)/Ca; (c) Mg/Ca vs Al/Ca; (d) Ca/Si vs Mg/Si. The dashed lines are compositional trend lines connecting C-S-H or portlandite/calcite with other hydrate phases. P – portlandite; C – calcite; Mc – monocarboaluminat; Ms – monosulphoaluminat; AFt – ettringite; AFm – Ms and Mc.

From the plot of Si/Ca vs Al/Ca molar ratio (Figure 7.12a), it is possible to observe that the edge point analyses showed a higher Si/Ca ratio and Al/Ca ratio than the centre of the sample. This correlates well with the observed decrease of concentration of Ca in this region (in Figure 7.12b), which is indicative that some decalcification of C-S-H occurred in this area. Therefore, this area will have either C-S-H with higher Si content, or the presence of Si-rich phases, or even the presence of M-S-H. An interesting observation from the same plot is the observed higher Si/Ca ratio compared to the reference C-S-H, which is due to the higher content of silicon, resulting from the presence of silica fume particles [209] (i.e. the measured Si content also includes a contribution from silica fume, not only C-S-H).

The S/Ca vs (Al+Fe)/Ca diagram (Figure 7.12b), shows the presence of Al-rich phases low in S in the edge area, indicating a decrease in ettringite content in this region, whereas for the points collected in

the centre of the sample, an intermixing of ettringite and C-S-H (with possible incorporation of sulphur) was observed. This decrease of ettringite in the edge might be due to decalcification of this phase, and consequent dissolution [71,202]. This is visible through the leaching of S in the first 4 months of the experiment (ICP-OES data; Figure 7.14c). Additionally, the points corresponding to the edge of the sample have a higher concentration of aluminium, which was also observed in the Si/Ca vs Al/Ca plot.

In terms of Mg-rich phases, from the Mg/Ca vs Al/Ca plot (Figure 7.12c) it is possible to observe that the edge area was richer in hydrotalcite when compared to the centre area. This might indicate that more hydration of BFS occurs at the edge of the sample, since hydrotalcite is a product of BFS hydration [49,162,190]. Moreover, from the Ca/Si vs Mg/Si plot (Figure 7.12d) it is possible to observe possible presence of M-S-H with some amounts of Ca [211,212] is present in the edge area. It should be noted that the Mg/Si ratio is quite low, which is related to the small amount of Mg present in the granitic groundwater. It is interesting to note that in all plots, no portlandite was present, in agreement with XRD and TG analysis, which is expected in this type of cement formulation [44,45,49,182,197].

7.3.2: Nano- and micro-structural evolution of Cebama reference cement paste

Through XCT analysis, the macroporosity was studied, and no significant differences were observed between the control sample at similar age and the samples that were in contact with granitic groundwater, with the macroporosity around 4 % at 6 months and around 2 % at 12 months (Table 7.7). This slight decrease of the porosity observed for the samples at 12 months is indicative of the increase of the hydration, as mentioned before.

Table 7.7. Porosity measurements obtained by XCT and MIP for Cebama reference cement samples that were in contact with granitic groundwater. XCT errors calculated from standard deviation of triplicate thresholding. MIP errors represent the intrinsic instrument error.

	Macroporosity through XCT (%)	Porosity through MIP (%)
Cebama Granitic 6 Months	4.3 ± 0.4	5 ± 2
Cebama Granitic 12 Months	2.4 ± 0.9	5 ± 2

Figure 7.13 shows the pore entry size diameter in relation to the cumulative intrusion for the 6 and 12 month samples, and it is possible to observe that the curve allocates the bulk of pores to pore entry sizes below 0.2 µm, for both samples. However, it seems that for the 6 months sample, the cumulative

intrusion is slightly higher than observed for 12 months sample, which means that fewer small pores were detected in the sample after 12 months of contact with groundwater. A combination of the formation of more C-S-H, as observed in the ^{29}Si MAS NMR, and the occurrence of some carbonation (observed in the SEM-EDX analysis outer layer), might be the reasons for the filling of the pores. The total porosity obtained from this measurement was around $5 \pm 2\%$ for both samples, which is somewhat smaller than the total porosity obtained for the control samples, $\sim 9 \pm 2\%$ (Table 7.3). This initial decrease of the porosity might be due to the increase of hydration observed for the samples that were in contact with groundwater, and so more hydrate phases precipitated into the pores. However, with the observed formation of a carbonate outside layer after 6 months of experiment, no changes of porosity were further observed. This might mean that this carbonate layer might be acting as a protective layer for further contact of groundwater with the cement.

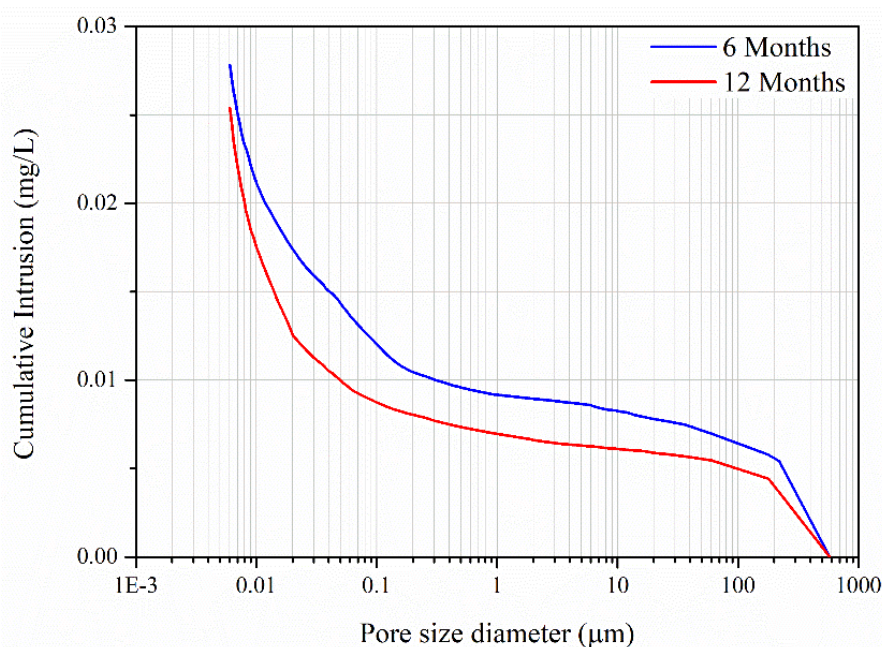


Figure 7.13. Pore entry size distribution of Cebama reference cement samples that were in contact with granitic groundwater for 6 and 12 months, determined by MIP.

7.3.3: Solution chemistry

The pH (obtained at room temperature) of the solutions varied as a function of leaching time. For the first 2 and 4 months, the pH of the solution increased to values of around 11.0 – 11.3 (pH of the blank was 8.5). Subsequently, a decrease of the pH occurred, being 9.2 – 9.5 at 6 months and reaching similar values to the blank after 12 months, of around 8.3 – 8.6. This decrease of the pH after 4 months might be related to the formation of the protective Ca-rich layer observed in the SEM-EDX images. The

formation of this outside layer, which increased in thickness with time, might have led to less interaction of the groundwater with the cement, and consequently a reduction in the leaching of alkaline portions of the cement.

Figure 7.14 describes the concentration of each element present in solution, obtained through ICP-OES and IC. The data are presented as “difference in measured concentration relative to the blank”, with the blank being the groundwater solution used to replace the solution every two months (measured prior to addition to Cebama reference cement). The blank value is equal to zero in every graph. In presenting the results in this format, it is possible to observe where concentrations of elements were higher than in the blank groundwater solution (i.e. elements leached out of the cement), or lower, indicating they had been incorporated as a mineral phase within the cement. This also allows accountancy of minor discrepancies in the composition of the groundwater added at each time point (the total volume used over the 12 months duration of the experiment was several tens of litres, so it was necessary to prepare new solution at each time point, and each solution was not always exactly identical due to minor errors in weighing chemicals).

The Ca concentration in solution shows that this element leached from the cement to the solution during the first 4 months of contact with groundwater (Figure 7.14a). However, from 6 months onwards, it was possible to observe that an uptake of this element into the cement occurred. This correlates well with the formation of the Ca-rich layer at the edge of the sample, observed through SEM-EDX analysis after 6 months.

Due to the high pH observed for the first 4 months (above pH 12), an initial precipitation/uptake of Mg is visible, followed by a gradual dissolution of this element with the decrease of the pH as a function of time, with the concentration of this element similar to that of the blank after 12 months (Figure 7.14b).

In respect to S and Si concentration, an initial leaching from the cement to the solution was observed for both elements (Figure 7.14c and d). This leaching might be related to the dissolution of ettringite observed at the edge of the sample (Figure 7.12b) and the dissolution of silica fume. From 6 months onwards, the concentration of these elements was similar to the blank, which indicate that no further leaching or uptake of S and Si occurred. This might be again a consequence of the formation of the Ca-rich outside layer, which might prevent further leaching.

A very small uptake of chloride was observed for the first 2 months of contact with granitic groundwater, which was followed by a combination of leaching and uptake until 8 months into the experiment, from when the concentration of this element in solution was similar to that which was present in the blank (Figure 7.14e). In EDX measurements it was not possible to detect this element due to the extremely low concentrations present.

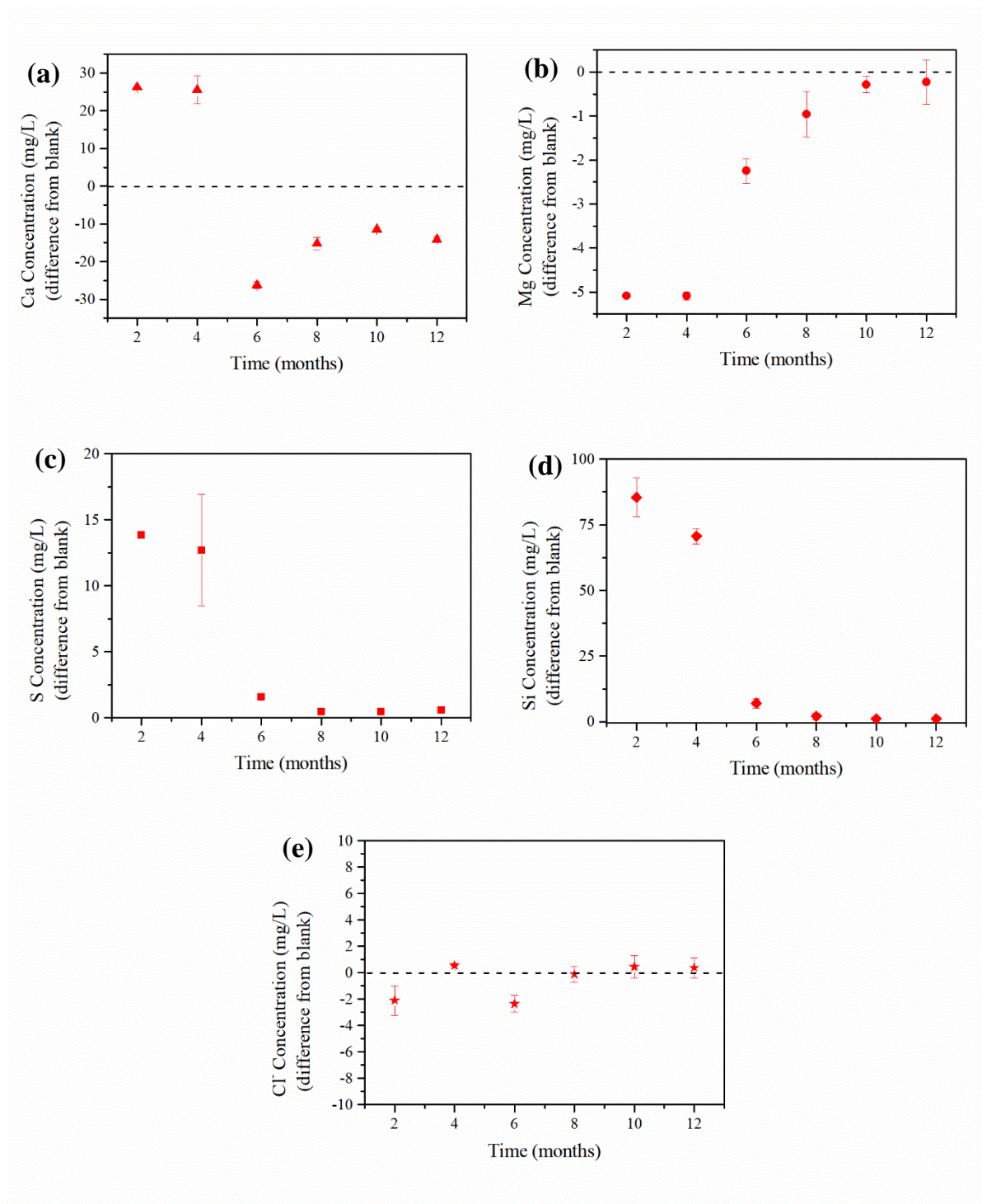


Figure 7.14. Elemental concentrations in solution (mg/L) obtained through the difference from blank for Cebama reference cement samples that were in contact with granitic groundwater for 12 months: (a) Ca concentration; (b) Mg concentration; (c) S concentration; (d) Si concentration; (e) Cl concentration. Errors were calculated using the standard deviation of duplicate ICP-OES and IC measurements.

7.4: Mineralogical and microstructural evolution of NRVB with Saline Groundwater (semi-dynamic experiment)

7.4.1: Mineralogical evolution of Cebama reference cement paste

XRD patterns obtained every two months for Cebama reference cement paste in contact with saline groundwater are displayed in Figure 7.15, and showed similar results to those previously observed with granitic groundwater.

The main differences observed were related to the decrease in the intensity of the peaks corresponding to belite and alite. A slight increase of the intensity of the peaks corresponding to the hydrate phases AFt (ettringite), AFm (monocarboaluminate) and hydrotalcite-like phase (meixnerite) was also observed. The peak corresponding to SiO₂ in the sample at 12 months had higher intensity than observed in the other samples, which might be due to some contamination of quartz when the sample was being prepared.

E - Ettringite **Mc** - Monocarboaluminate
Ht - Hydrotalcite **A** - Alite **B** - Belite
C - Calcite **Si** - SiO₂

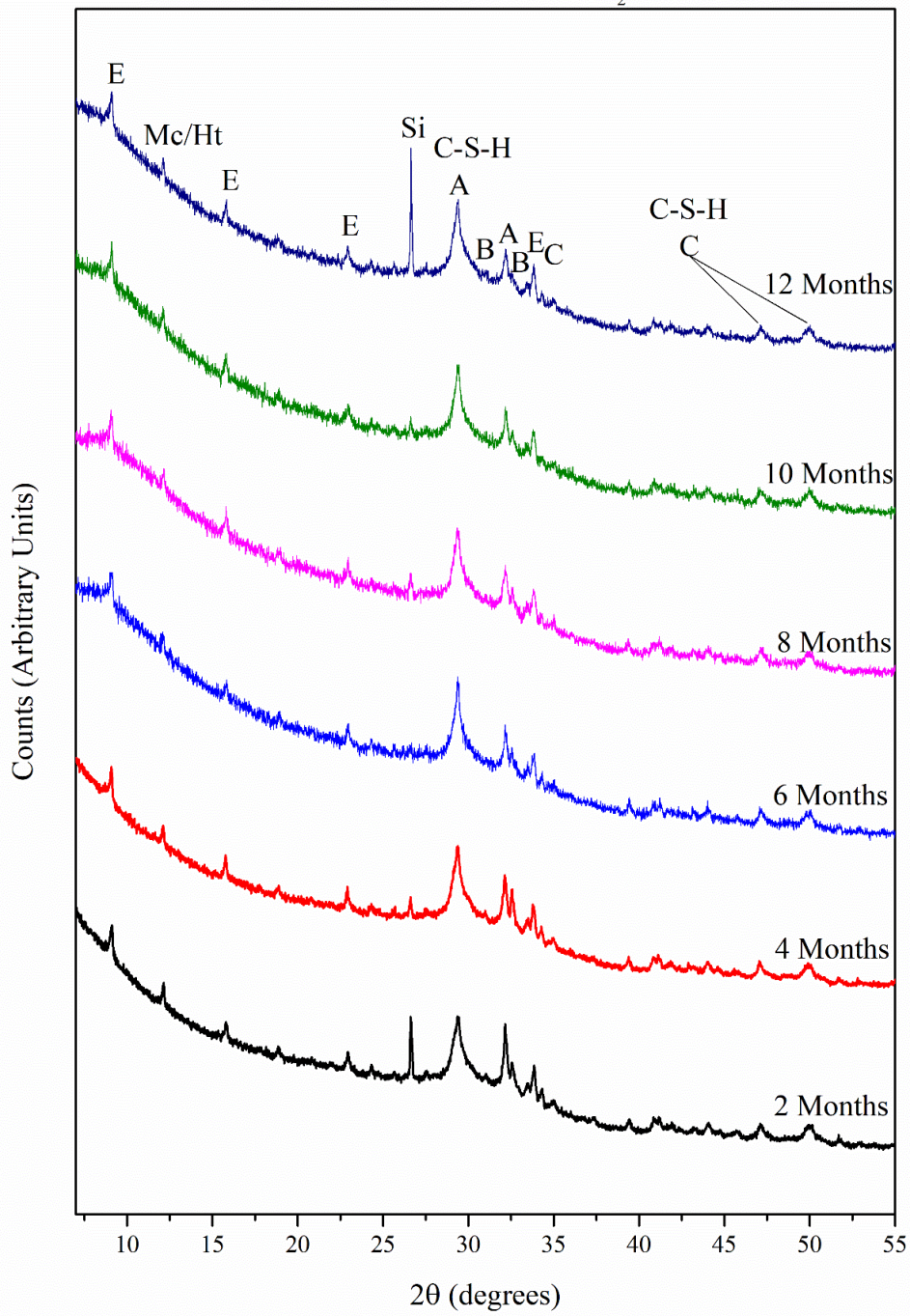


Figure 7.15. XRD patterns of Cebama reference cement samples that were placed in contact with saline groundwater for 12 months.

In the TG analysis (Figure 7.16), the peaks corresponding to the loss of water from C-S-H (between 50 to 100 °C) and to the formation of ettringite (around 100 °C) increased as a function of time. This rate of increase was higher for the samples at 6 months when compared to longer contact times. The peaks

corresponding to carbonates (between 600 and 800 °C) show that no increase of carbonation occurs over time.

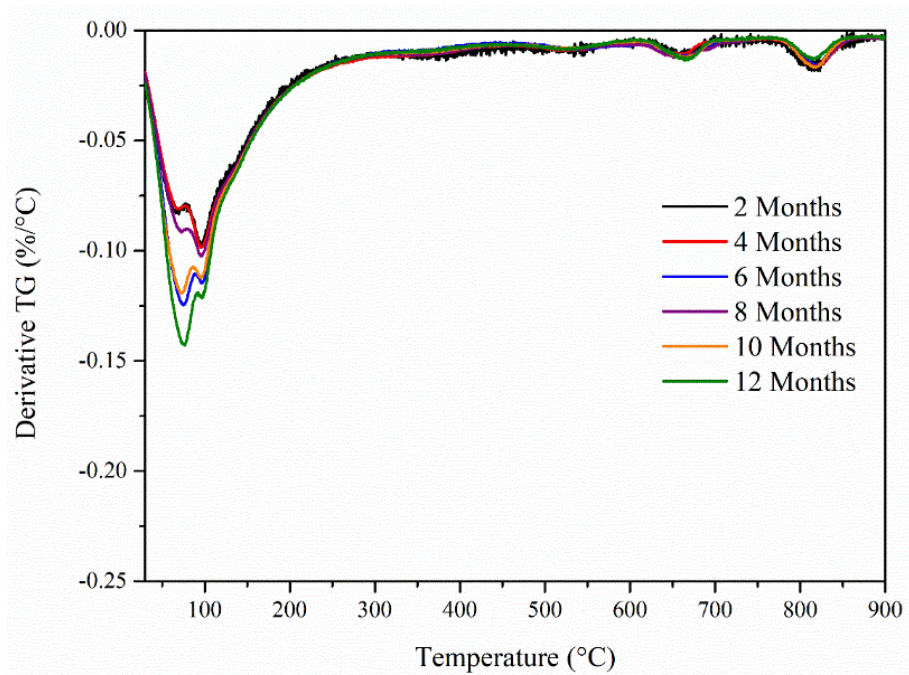


Figure 7.16. TG data for Cebama reference cement samples that were in contact with saline groundwater for 12 months.

The ^{29}Si MAS NMR spectra of the samples that were in contact with saline groundwater for 6 and 12 months, and the corresponding deconvolutions (described previously in Section 7.2.1), are shown in Figure 7.17. A similar trend was observed when comparing to the samples that were in contact with granitic groundwater, where a decrease in the intensity of the peak corresponding to silica fume is visible. The relative concentration of silica fume after 6 months was around $33 \pm 2\%$, and $28 \pm 2\%$ after 12 months (Table 7.8). This is significantly less than the control sample after 12 months ($33 \pm 2\%$), suggesting that silica fume had either been leached, or consumed in hydration reactions.

Between 6 and 12 months of contact with saline groundwater, no significant differences were observed in the relative concentration of alite, belite and BFS (Table 7.8). This indicates that no further increase of the reaction of these components occurred after 6 months. When comparing to the control sample, it is evident that more hydration occurred as a consequence of the contact with the saline solution (Section 7.2, Table 7.2).

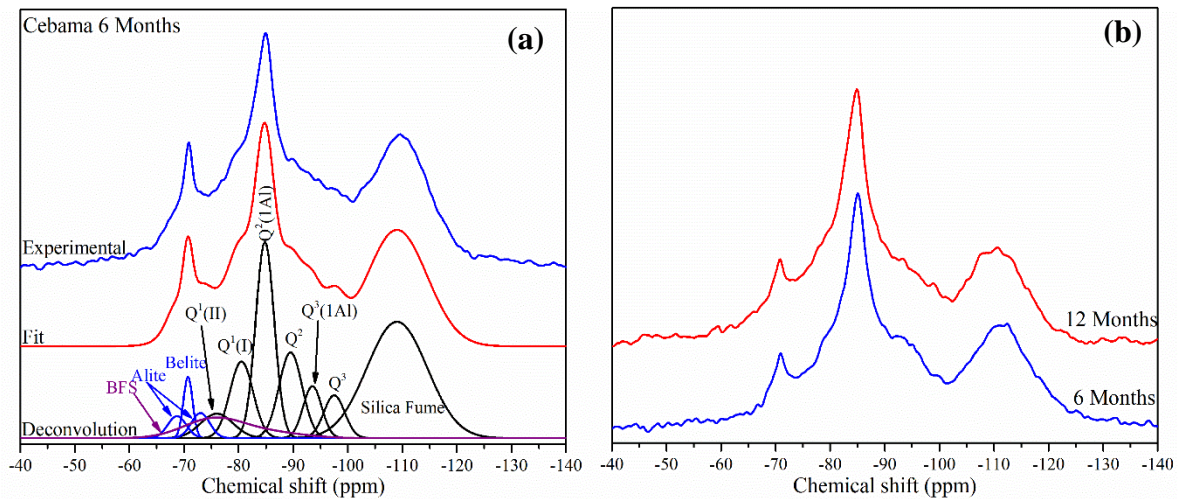


Figure 7.17. (a) Deconvoluted ^{29}Si MAS NMR spectrum of Cebama reference cement cured for 6 months; (b) ^{29}Si MAS NMR spectra of Cebama reference cement that were in contact with saline groundwater for 6 and 12 months.

Table 7.8. Results of deconvolution of ^{29}Si MAS NMR spectra of Cebama reference cement samples that were in contact with saline groundwater. The estimated uncertainty in absolute site percentages is $\pm 2\%$.

	Belite	Alite	Silica fume	BFS	Q ¹	Q ² (1Al)	Q ²	Q ³ (1Al)	Q ³
6 Months	2 %	4 %	33 %	4 %	10 %	25 %	11 %	5 %	5 %
12 Months	2 %	3 %	28 %	4 %	15 %	22 %	12 %	4 %	4 %

Table 7.9 details the Ca/Si ratio, Al/Si ratio and MCL obtained in the different samples, and no significant differences were visible between the samples. However, an increase of the Al/Si ratio when comparing to the control samples occurred, as a consequence of the increase of BFS reaction.

Table 7.9. Summary of structural evolution of C-S-H formed in Cebama reference cement samples that were in contact with saline groundwater, based on the ^{29}Si MAS NMR deconvolutions.

	Ca/Si	Al/Si	MCL
6 Months	1.1 ± 0.2	0.22 ± 0.02	13.7 ± 5.8
12 Months	1.1 ± 0.2	0.19 ± 0.02	8.3 ± 3.7

Figure 7.18 shows the ^{27}Al MAS NMR spectra, and after 12 months of contact with saline groundwater an increase of the intensity of the peak corresponding to AFt phases (at 14 ppm), in this case ettringite, was observed. A slight increase of the broad resonance attributed to both Al^{IV} in C-S-H and unreacted

BFS [164] was observed, indicating the formation of more C-S-H with time, in agreement with the previous data (TGA and ^{29}Si MAS NMR).

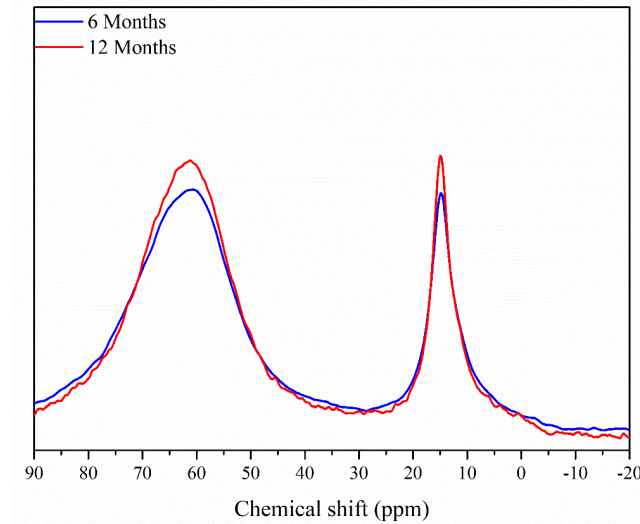
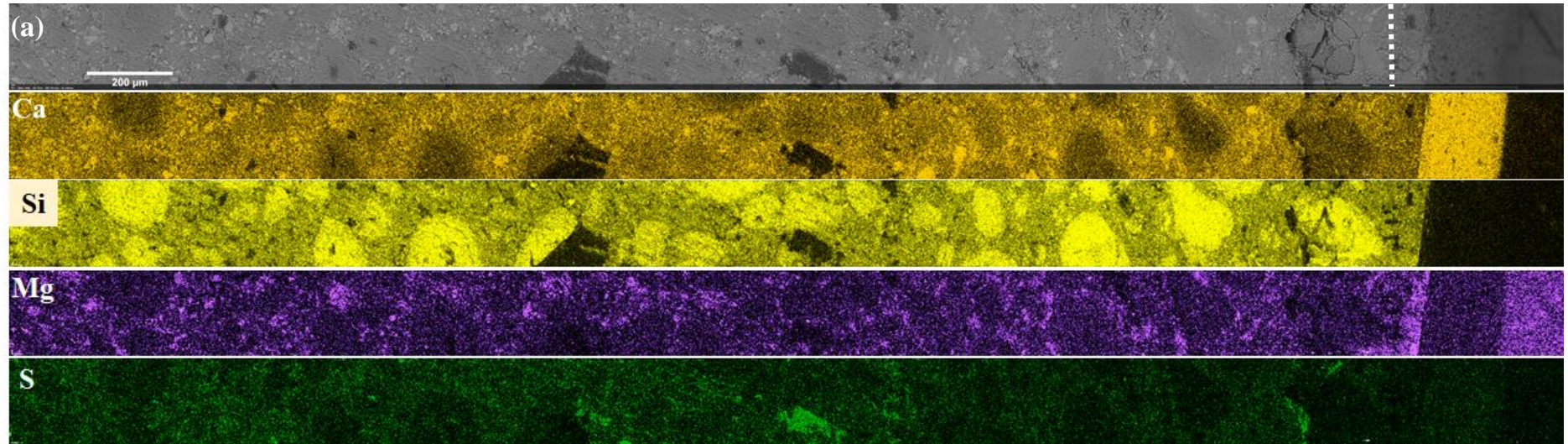


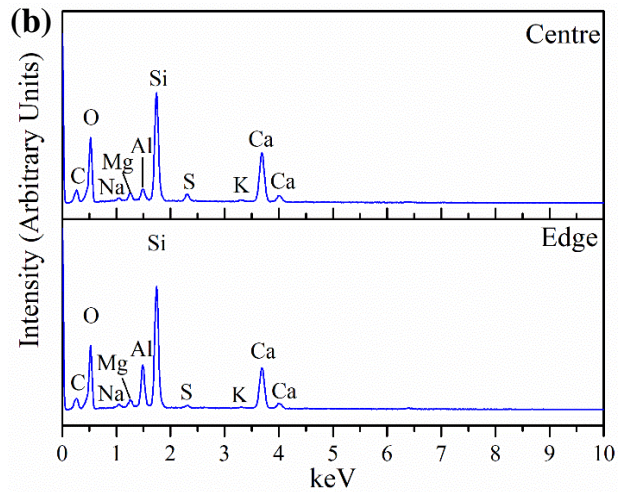
Figure 7.18. ^{27}Al MAS NMR spectra of Cebama reference cement samples that were placed in contact with saline groundwater for 6 and 12 months.

From the SEM image and elemental maps presented in Figure 7.19 for a sample that was in contact with saline groundwater for 6 months, it is possible to observe a layer forming on the edge of the sample. Due to the nature of the image obtained, it is quite difficult to understand if the Ca-rich layer at the edge area is part of the sample or not. Nevertheless, a Mg-rich layer near the outside of the sample was observed. It is interesting to note that S was observed throughout the sample, especially inside of the cracks/holes, which might be indicative of the formation of ettringite needles in these areas.

Point analysis was performed (Figure 7.19 and Table), and the main difference observed between the edge and the centre of the sample was a higher concentration of aluminium present at the edge (5.92 ± 0.35 at%). As mentioned in the discussion of exposure of this cement to granitic groundwater, this might be indicative of the higher degree of hydration of BFS in this area.



0



	Edge (at %)	Centre (at %)
Ca	10.87 ± 0.59	12.49 ± 0.68
Mg	1.04 ± 0.09	1.21 ± 0.10
Al	5.92 ± 0.35	1.57 ± 0.12
Si	17.97 ± 0.92	15.11 ± 0.78
S	0.42 ± 0.06	1.15 ± 0.09

Figure 7.19. SEM-EDX analysis of Cebama reference cement sample that was in contact with saline groundwater for 6 months; (a) BSE image and elemental maps; (b) spectra associated with point analysis; Table: point analysis in atomic %, with absolute error from the measurement.

For a better understanding of the evolution of these results with time, a higher magnification SEM-EDX analysis was performed on a sample after 12 months of contact with saline groundwater. From Figure 7.20a, the formation of a distinct layer at the edge of the sample can be observed. This layer, according to the elemental map, was rich mainly in Ca and some S, having a variable thickness with a maximum of 20 μm (Figure 7.20b). As for the sample that was in contact with granitic groundwater, the formation of this layer is related to the presence of HCO_3^- in the saline groundwater composition which, according to the reactions presented in the previous section (Section 7.3.1), will lead to the release of CO_3^{2-} , reacting afterwards with the free Ca present in the groundwater for the precipitation of CaCO_3 [66].

Just before this Ca-rich outside layer, there was an area depleted in Ca but rich in Mg, similar to the results observed in the samples that were in contact with granitic groundwater. The linescan results shown in Figure 7.20b, demonstrates these two layers.

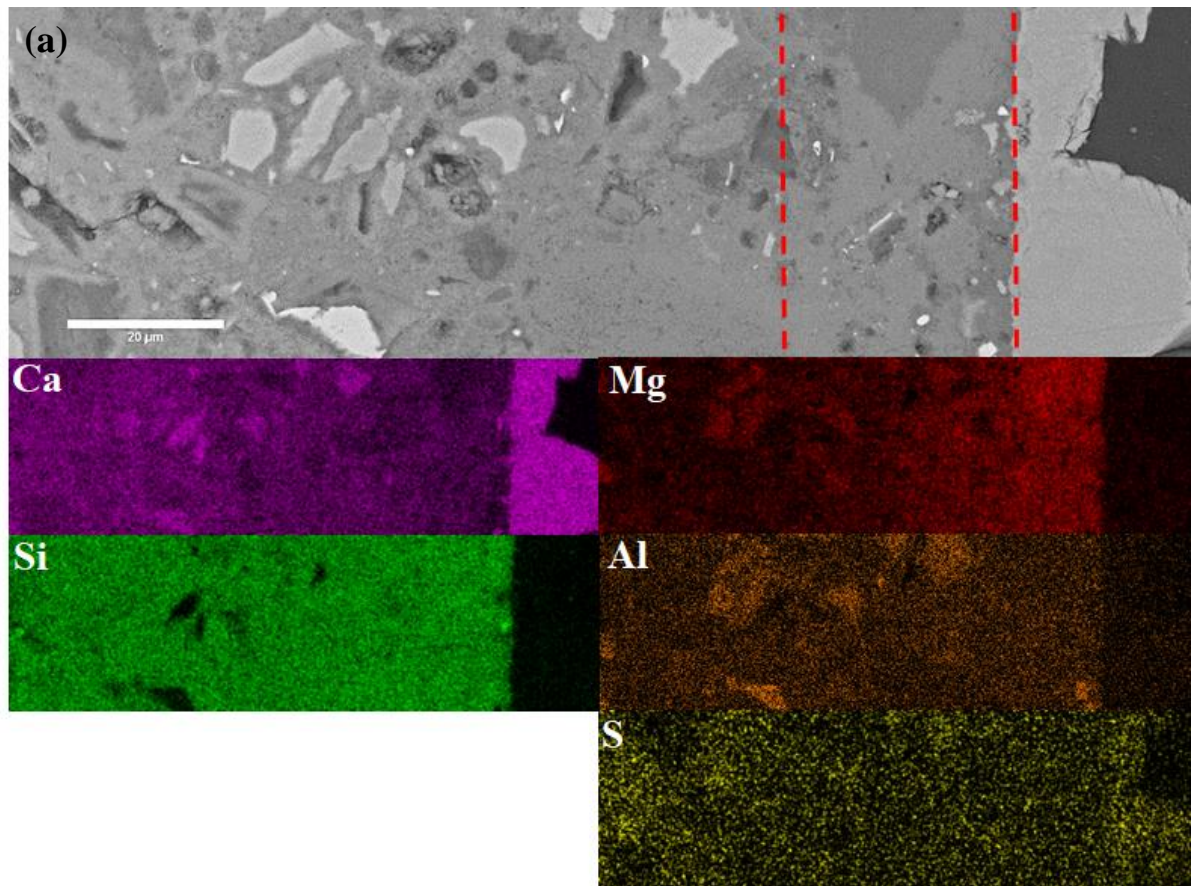


Figure 7.20. SEM-EDX analysis of Cebama reference cement sample that was in contact with saline groundwater for 12 months; (a) BSE image and elemental maps; (b) Linescan of magnesium and calcium in atomic %.

SEM-EDX point analysis was performed in the same way as described before, and molar ratio plots (Figure 7.21) were used to identify differences in the mineral assemblage between the edge (being the area just before the Ca-rich layer, indicated in the image by the red dashed lines, Figure 7.20a) and the centre of the Cebama reference cement sample. A similar justification as given with the Cebama sample that was in contact with granitic groundwater (Section 7.3.1) is given here for the chosen edge area to be presented (the Ca/Si molar ratio of this layer was around 415.9 average and the S/Ca molar ratio was

0.02 average), i.e, the edge corresponds to the area of the sample where more alteration occurred due to the interaction with the groundwater before the precipitation of the outside Ca-rich layer.

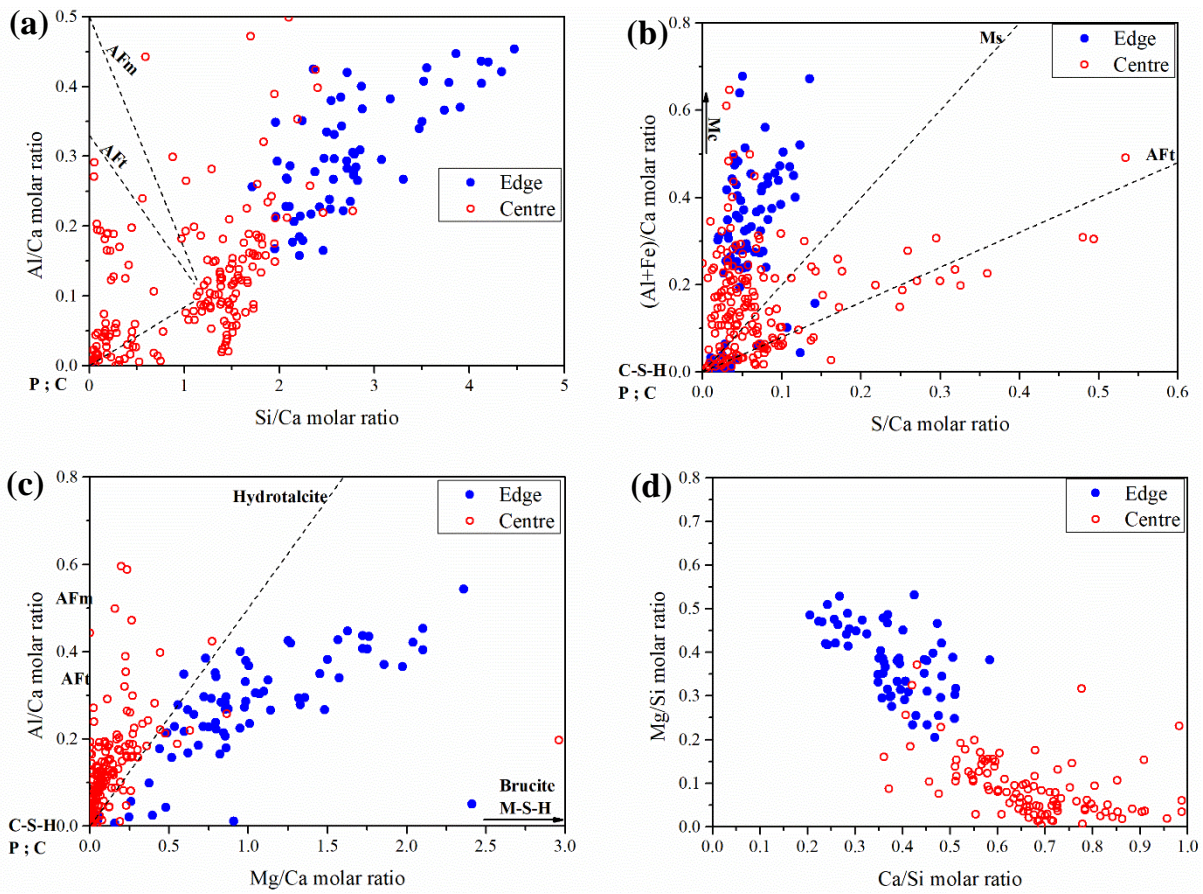


Figure 7.21. Elemental molar ratio plots of SEM-EDX point analysis in Cebama reference cement sample that was in contact with saline groundwater for 12 months: (a) Si/Ca vs Al/Ca; (b) S/Ca vs (Al+Fe)/Ca; (c) Mg/Ca vs Al/Ca; (d) Ca/Si vs Mg/Si. The dashed lines are compositional trend lines connecting C-S-H or portlandite/calcite with other hydrate phases. P – portlandite; C – calcite; Mc – monocarboaluminate; Ms – monosulphoaluminate; AFt – ettringite; AFm – Ms and Mc.

From the Si/Ca vs Al/Ca molar ratio diagram (Figure 7.21a), it is possible to observe that the points corresponding to the edge area have a higher Si/Ca molar ratio than the points corresponding to the centre, which agrees well with the depletion of Ca in this area. Consequently, in this area it is possible that some decalcification of C-S-H is occurring.

In terms of S incorporation (Figure 7.21b), it is possible to observe that the edge area has less S incorporation than the centre, where the presence of AFt phases is more evident. As observed for the granitic groundwater, it is believed that dissolution of ettringite is occurring in the edge region due to contact with the saline solution, leading to the leaching of Ca and S, confirmed by ICP-OES results (Figure 7.23a,c). It is also clear the presence of more Al in the edge when comparing to the points

collected in the centre of the sample. This might be a consequence of a higher degree of reaction of BFS at the edge of the sample, but further analysis is required to provide more evidence for this.

In the edge area, due to the higher concentration of Mg, it was possible to observe the formation of more Mg-phases (Figure 7.21c,d). In the Mg/Ca vs Al/Ca ratio diagram, the presence of more hydrotalcite intermixed with M-S-H is observed for the points collected at the edge of the sample when compared with the centre. Moreover, the presence of M-S-H intermixed with C-S-H in the edge area is confirmed in the Ca/Si vs Mg/Si molar ratio plot, where Mg/Si ratio of the points is between 0.25 and 0.55 [211,212].

7.4.2: Nano- and micro-structural evolution of Cebama reference cement paste

Through XCT and MIP it was not possible to observe any significant differences in the total porosity as a function of time in contact with saline groundwater (Table 7.10). However, when comparing to the control sample a decrease of the porosity was observed (from 4.5 and 2.8 ± 0.9 % in the control sample to 0.52 and 1.6 ± 0.4 % in the sample that was in contact with saline solution, at 6 and 12 months, respectively), evidencing the increase of the hydration observed in these samples when in contact with saline groundwater.

Table 7.10. Porosity measurements obtained by XCT and MIP for Cebama reference cement samples that were in contact with saline groundwater. XCT errors are calculated from standard deviation of triplicate thresholding. MIP errors represent the intrinsic instrument error.

	Macroporosity through XCT (%)	Porosity through MIP (%)
Cebama Saline 6 Months	0.52 ± 0.4	6 ± 2
Cebama Saline 12 Months	1.6 ± 0.4	4 ± 2

From Figure 7.22, it was possible to observe that for the 6 months sample, the bulk of the pores had pore entry sizes $< 0.6 \mu\text{m}$, whereas for the 12 months sample the pore entry size was $< 0.05 \mu\text{m}$, evidencing the smaller pore structure presented by the Cebama sample that was in contact with the saline groundwater for 12 months. However, no significant changes were observed in the total porosity obtained, which was around $6 \pm 2\%$ for the 6 months sample and $4 \pm 2\%$ for the 12 months (Table 7.10).

The observed reduction of the overall porosity of the Cebama reference cement paste as a function of leaching time might be an outcome of the increase of the hydration observed in these samples, which

led to the precipitation of more hydrate phases such as hydrotalcite, ettringite and C-S-H. Also, the precipitation of CaCO_3 mainly on the outside layer, observed through SEM-EDX analysis, but also possibly throughout the sample, might decrease the overall porosity of this cementitious material.

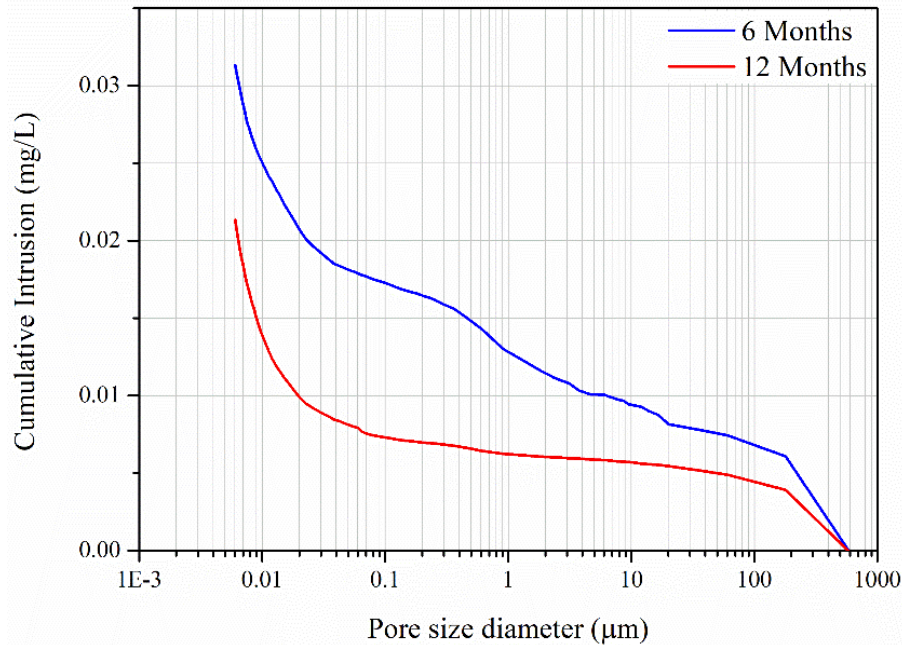


Figure 7.22. Pore entry size distribution of Cebama reference cement samples that were in contact with saline groundwater for 6 and 12 months, determined by MIP.

7.4.3: Solution chemistry

At each time point of sampling, the pH of the solution was measured (at room temperature), and for the first 6 months of the experiment, the pH increased to values of around 10.3 – 10.6 (pH of the blank was 8.2). After 8 months, a decrease of the pH was observed, from 9.4 – 9.7 at 8 months to 8.3 – 8.6 by the end of the experiment at 12 months. As observed in the samples that were in contact with granitic groundwater, this might be a consequence of the formation of the Ca-rich outside layer, which prevented any further leaching behaviour of the saline groundwater.

From the ICP-OES analysis of the solutions (Figure 7.23), it was possible to observe that the leaching of Ca occurred for the first 6 months, which was followed by a slow uptake of this element until the end of the experiment (Figure 7.23a), presumably to form the Ca-rich outside layer observed in the SEM-EDX results. Precipitation of Mg was observed for the first 6 months, correlating well with the higher pH observed during that period (Figure 7.23b). From 8 months until 12 months, the concentration of Mg is similar to the blank, evidencing the pH dependence of the stability of Mg in solution. Also,

the formation of a protective outside layer might have reduced the interaction of the groundwater with the cement sample.

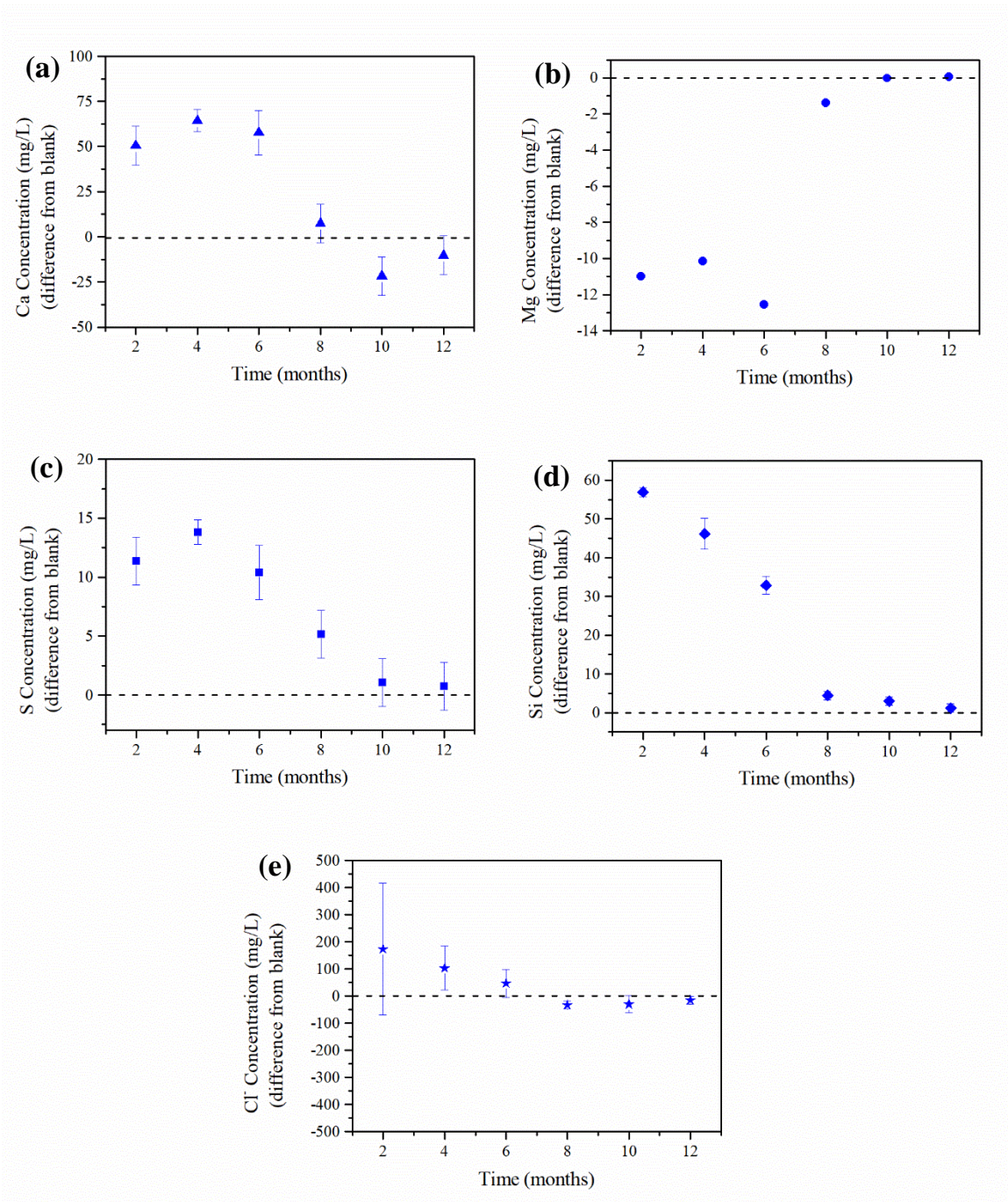


Figure 7.23. Elemental concentrations in solution (mg/L) obtained through the “difference from blank” for Cebama reference cement samples that were in contact with saline groundwater for 12 months: (a) Ca concentration; (b) Mg concentration; (c) S concentration; (d) Si concentration; (e) Cl⁻ concentration. Errors were calculated using the standard deviation of duplicate ICP-OES and IC measurements.

For S and Si, similar behaviours were observed (Figures 7.23c,d). At the start of the experiment, leaching of these elements into solution was visible, which might be due to the dissolution of ettringite

and silica fume. This was followed by a gradual slow decrease of the leaching, and after 12 months, for both elements, the concentration in solution had decreased to similar values to those observed in the blank. Once again, the observed formation of the outside Ca-rich layer might have led to a decrease of the interaction of the groundwater with the cement sample.

With regard to chloride concentration (Figure 7.23e), and taking into account the error bars obtained, no significant changes from the blank was observed for the duration of the experiment.

7.5: Mineralogical and microstructural evolution of NRVB with Clay groundwater (semi-dynamic experiment)

7.5.1: Mineralogical evolution of Cebama reference cement paste

From the XRD patterns of the Cebama reference cement paste in contact with clay groundwater for 12 months (Figure 7.24), the main differences observed were similar to those described in the previous groundwater compositions. A reduction of the peak intensity of belite and alite was observed over time. Also, a reduction of the intensity of the peak corresponding to SiO_2 was observed, corresponding to the hydration of silica fume. Increases of the peak intensities of ettringite, monocarboaluminate and hydrotalcite-like phase (meixnerite) occurred as a function of time.

E - Ettringite **Mc** - Monocarboaluminate
Ht - Hydrotalcite **A** - Alite **B** - Belite
C - Calcite **Si** - SiO₂

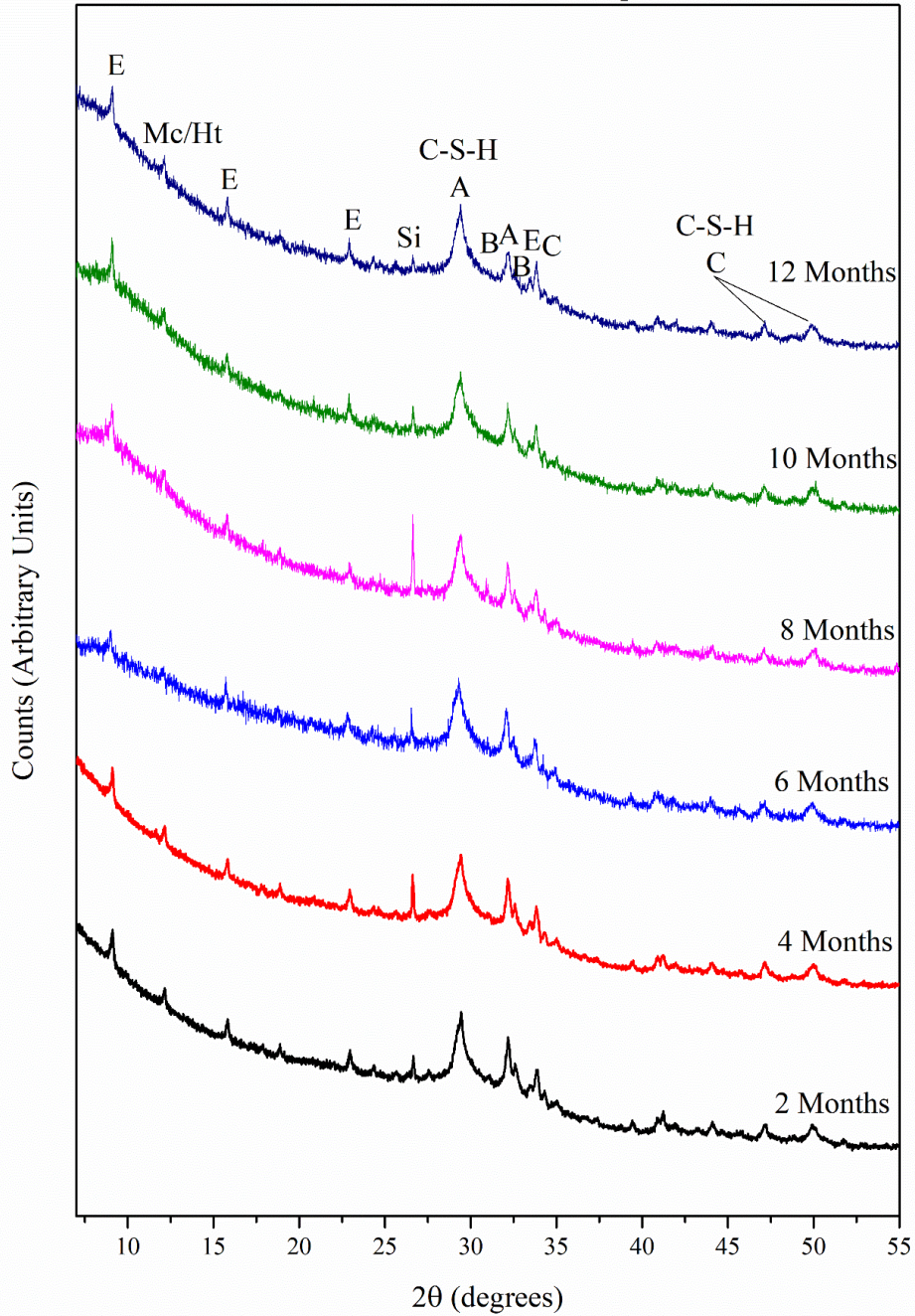


Figure 7.24. XRD patterns of Cebama reference cement samples that were placed in contact with clay groundwater for 12 months.

Through TG analysis (Figure 7.25), the increase of the hydration of the Cebama reference cement as a function of time in contact with clay groundwater was visible. From Figure 7.25, it is possible to identify the peak corresponding to the loosely bound water from within the C-S-H structure (between 50 and 100 °C) and the peaks related to AFt and AFm phases (between 100 and 150 °C), and an increase is

observed in the intensity of these peaks, mainly after 6 months and until the end of the experiment at 12 months.

As observed previously with the results from the other groundwater compositions, the presence of carbonates (from 650 °C onwards) seems not to change over time. Once again, and when comparing to the control samples (Section 7.2.1), it is evident that these differences are due to the contact with clay groundwater.

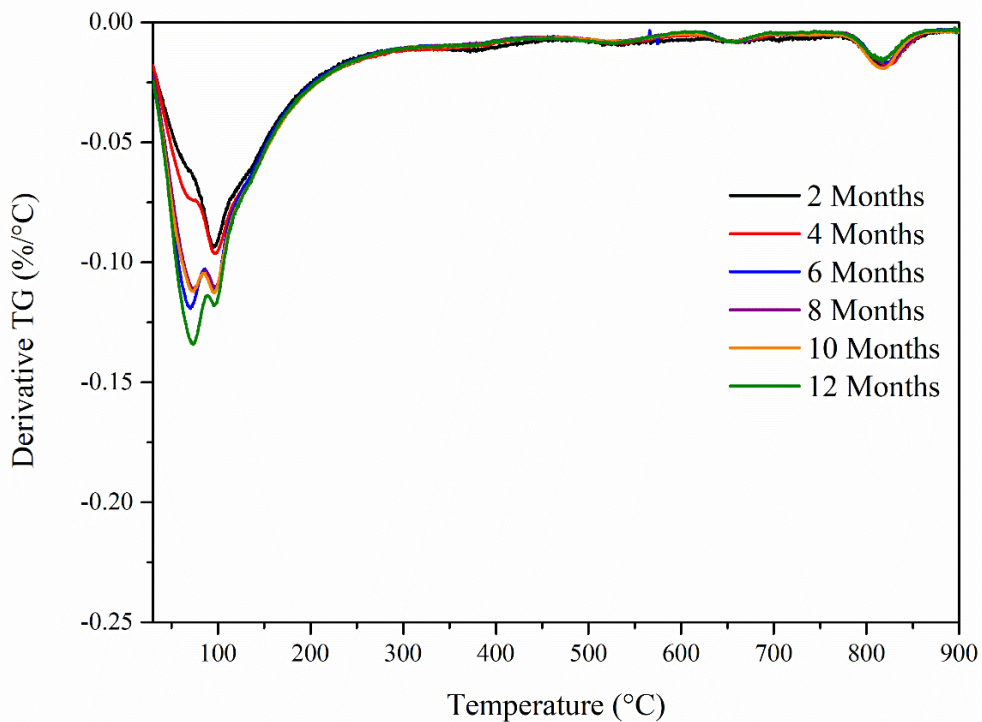


Figure 7.25. TG data for Cebama reference cement samples that were in contact with clay groundwater for 12 months.

In the ^{29}Si MAS NMR spectra of the samples at 6 and 12 months (Figure 7.26b), a decrease of the peak intensities for belite and silica fume was observed. When the deconvolution (Figure 7.26a) and semi-quantification (Table 7.11) of ^{29}Si MAS NMR spectra are performed, the increase of the hydration is more evident.

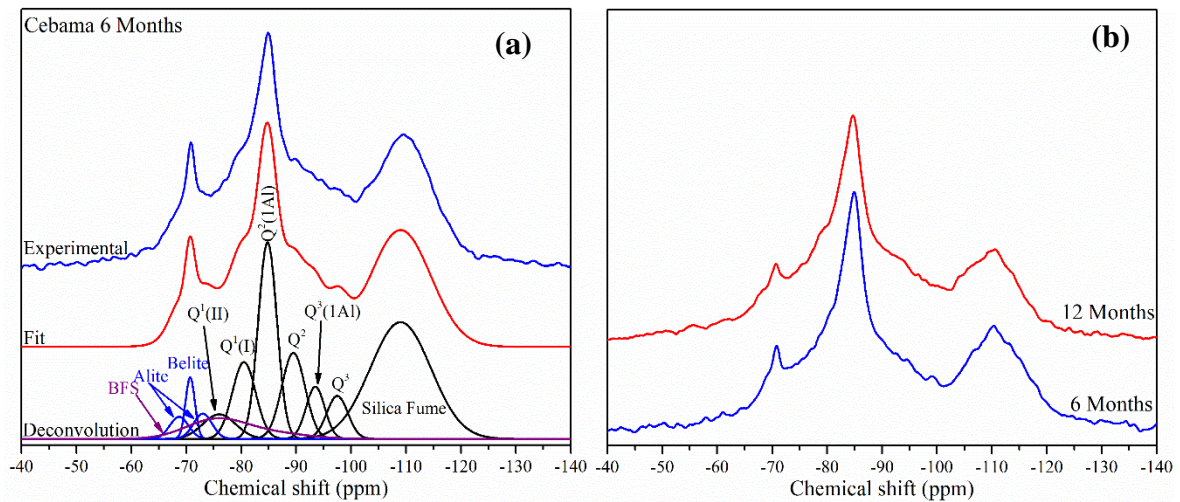


Figure 7.26. (a) Deconvoluted ^{29}Si MAS NMR spectrum of Cebama reference cement cured for 6 months; (b) ^{29}Si MAS NMR spectra of Cebama reference cement that were in contact with clay groundwater for 6 and 12 months.

A decrease of the relative concentration of belite, silica fume and BFS is observed with time (Table 7.11). An increase of the relative concentration of C-S-H is, consequently, visible from $55 \pm 2\%$ at 6 months to $60 \pm 2\%$ at 12 months (Table 7.11).

Table 7.11. Results of deconvolution of ^{29}Si MAS NMR spectra of Cebama reference cement samples that were in contact with clay groundwater. The estimated uncertainty in absolute site percentages is $\pm 2\%$.

	Belite	Alite	Silica fume	BFS	Q ¹	Q ² (1AI)	Q ²	Q ³ (1AI)	Q ³
6 Months	2 %	3 %	29 %	6 %	14 %	23 %	10 %	4 %	4 %
12 Months	1 %	3 %	27 %	4 %	18 %	21 %	11 %	5 %	5 %

With regard to the Ca/Si and Al/Si ratios and MCL, no significant differences were observed with time, with the Ca/Si ratio being around 1.2 ± 0.2 , the Al/Si ratio 0.19 ± 0.02 and the MCL around 7.7 ± 2.9 after 12 months of contact with clay groundwater (Table 7.12).

Table 7.12. Summary of structural evolution of C-S-H formed in Cebama reference cement samples that were in contact with clay groundwater, based on the ^{29}Si MAS NMR deconvolutions.

	Ca/Si	Al/Si	MCL
6 Months	1.2 ± 0.2	0.22 ± 0.02	9.8 ± 3.7
12 Months	1.2 ± 0.2	0.19 ± 0.02	7.7 ± 2.9

The ^{27}Al MAS NMR spectra (Figure 7.27) show similar results to those observed previously, with an increase of the peak intensity corresponding to the Al incorporated into the C-S-H as hydration of the BFS increased, and an increase of the peak intensity corresponding to AFt phases (at 14 ppm).

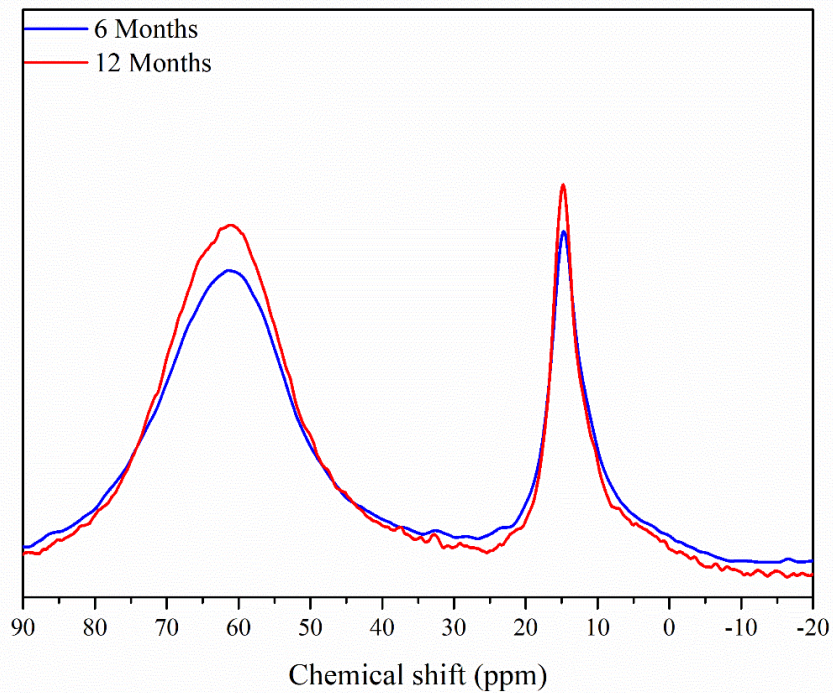
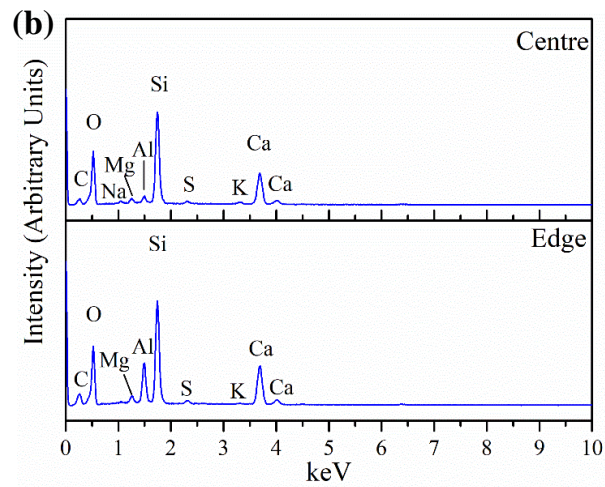
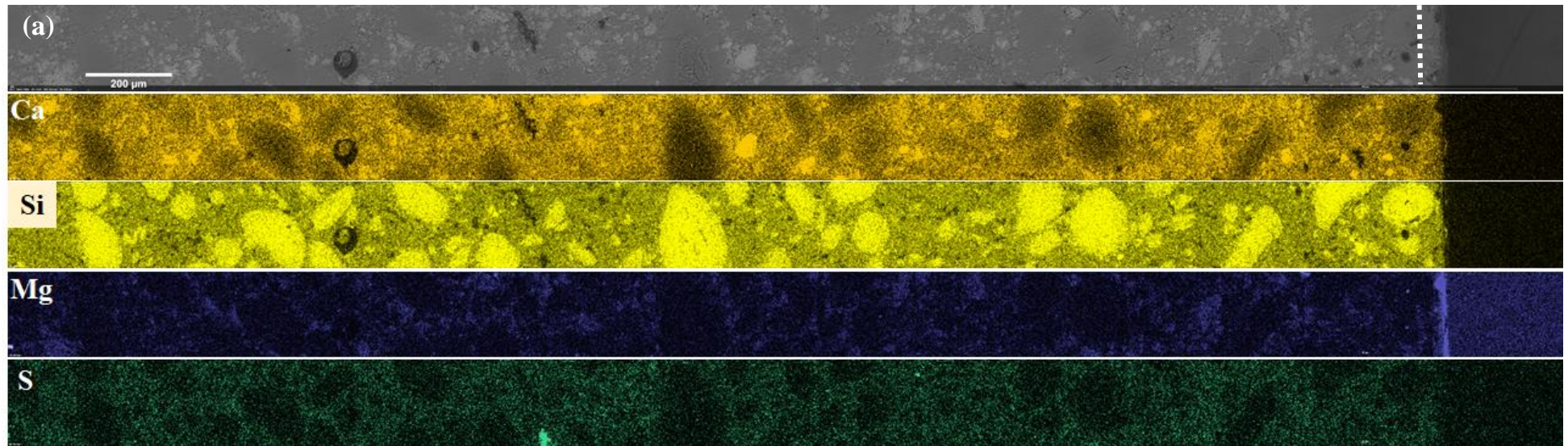


Figure 7.27. ^{27}Al MAS NMR spectra of Cebama reference cement samples that were placed in contact with clay groundwater for 6 and 12 months.

After 6 months of contact with clay groundwater, a layer at the edge of the sample composed mainly of Mg was observed in the SEM-EDX analysis, as shown in Figure 7.28a. Also, in the edge area it is possible to observe a higher amount of Al, around 6.27 ± 0.40 at%, when compared to the centre area where the Al atomic percentage was 1.22 ± 0.11 at% (Figure 7.28, Table). As mentioned in the discussion of previous groundwaters, this might be indicative of further hydration of BFS at the edge of the sample.

Regarding the overall sample, it was possible to observe, from the elemental maps, the presence of high concentrations of Mg and S. This is expected since the composition of this particular groundwater has high amounts of these two elements.



	Edge (at %)	Centre (at %)
Ca	11.24 ± 0.67	11.28 ± 0.66
Mg	1.16 ± 0.11	0.96 ± 0.10
Al	6.27 ± 0.40	1.22 ± 0.11
Si	16.71 ± 0.93	18.50 ± 1.00
S	0.60 ± 0.07	0.57 ± 0.07

Figure 7.28. SEM-EDX analysis of Cebama reference cement sample that was in contact with clay groundwater for 6 months; (a) BSE image and elemental maps; (b) spectra associated with point analysis; Table: point analysis in atomic %, with absolute error from the measurement.

Figure 7.29 shows SEM-EDX analysis, at a higher magnification, of a Cebama reference cement paste sample after 12 months of contact with clay groundwater. The Mg-rich layer at the edge of the sample was observed; this area was also depleted in Ca (Figure 7.29b). Unlike the samples contacted with the other groundwater solutions, which developed a protective Ca-rich outer layer, when in contact with clay groundwater, high concentrations of S and Al were identified throughout the entire sample (Figure 7.29a).

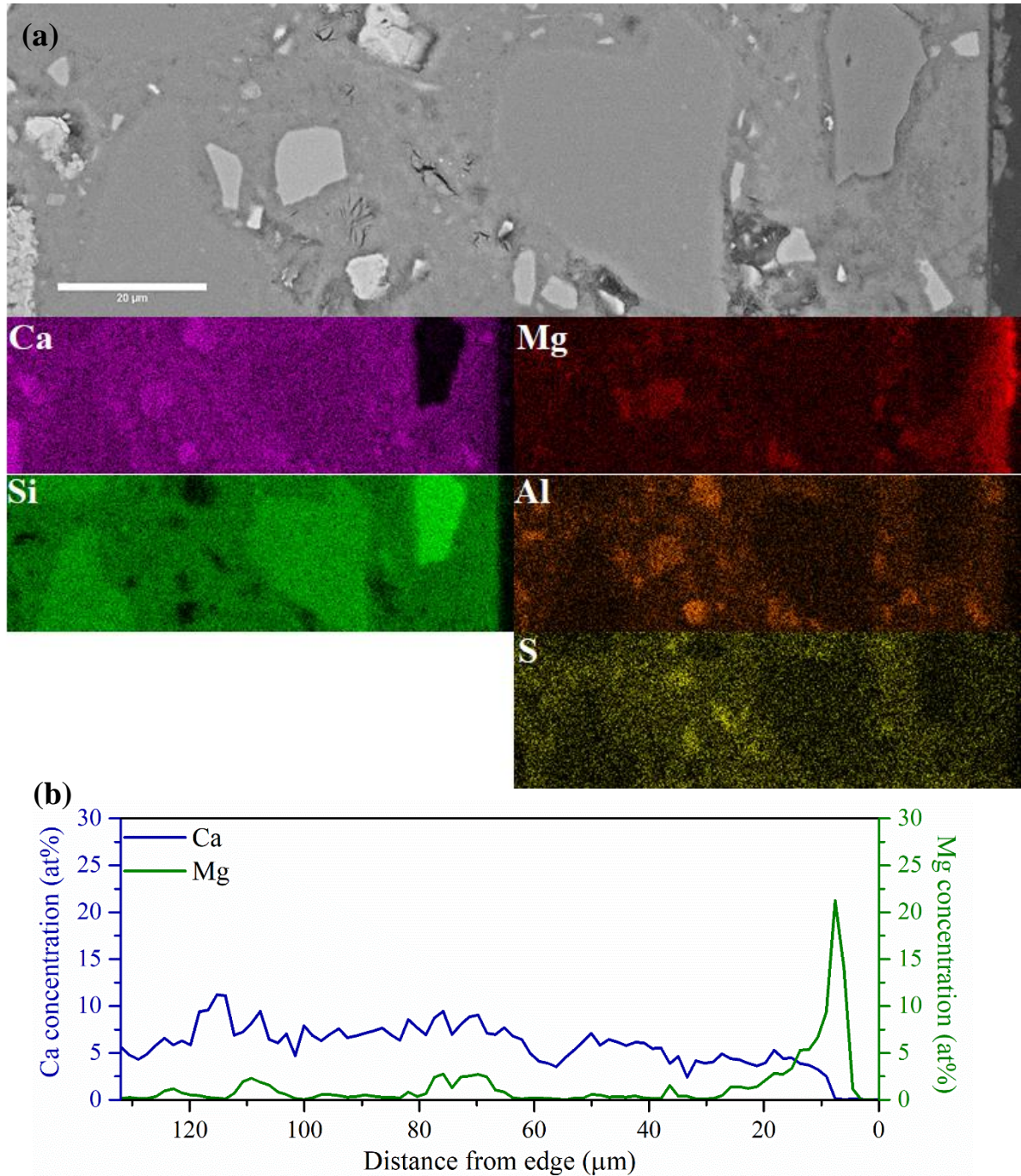


Figure 7.29. SEM-EDX analysis of Cebama reference cement sample that was in contact with clay groundwater for 12 months; (a) BSE image and elemental maps; (b) Linescan of magnesium and calcium in atomic %.

From the various point analysis plots (Figure 7.30), differences can be observed in the phase assemblage between the edge and the centre area of the sample. The Si/Ca vs Al/Ca plot clearly shows the Ca depletion observed in the edge area, with the higher Si/Ca ratio of the C-S-H when compared to the points collected in the centre.

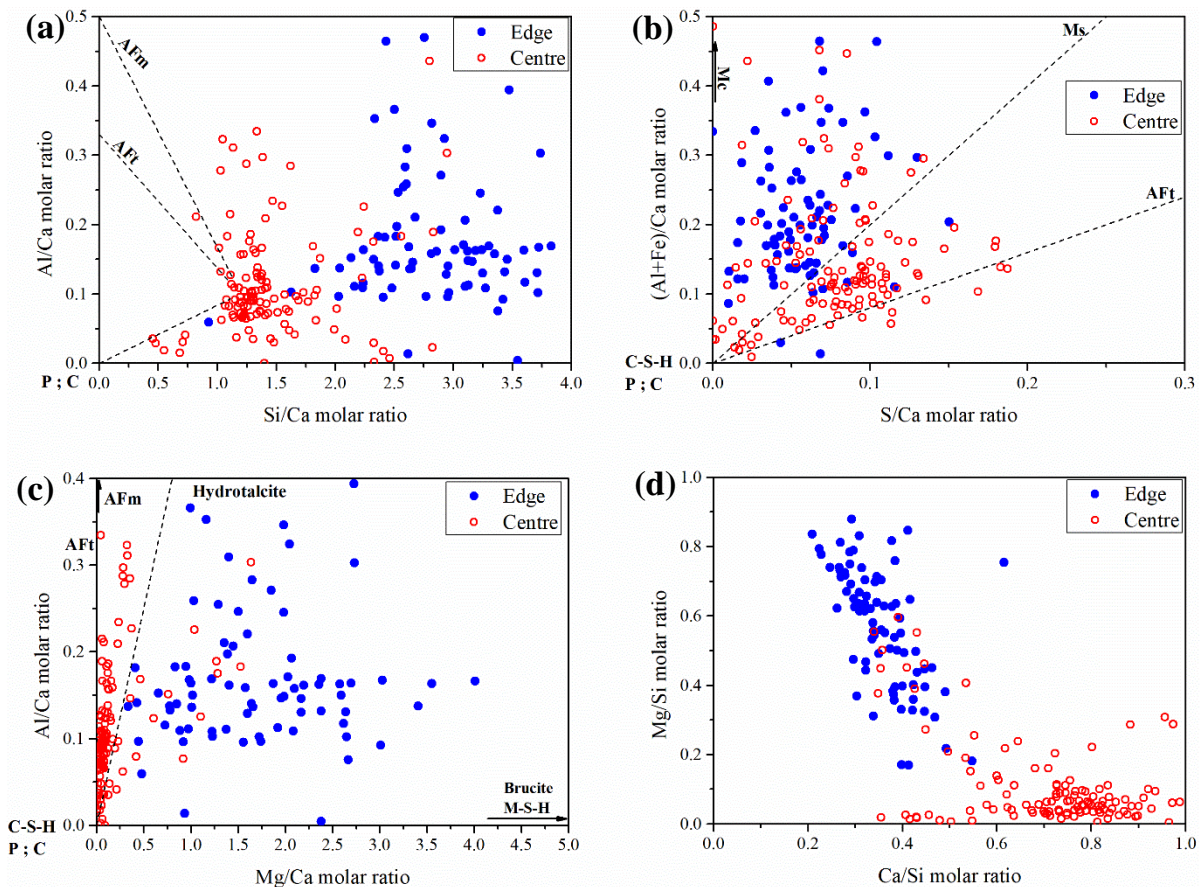


Figure 7.30. Elemental molar ratio plots of SEM-EDX point analysis in Cebama reference cement sample that was in contact with clay groundwater for 12 months: (a) Si/Ca vs Al/Ca; (b) S/Ca vs (Al+Fe)/Ca; (c) Mg/Ca vs Al/Ca; (d) Ca/Si vs Mg/Si. The dashed lines are compositional trend lines connecting C-S-H or portlandite/calcite with other hydrate phases. P – portlandite; C – calcite; Mc – monocarboaluminate; Ms – monosulphoaluminate; AFt – ettringite; AFm – Ms and Mc.

The high S content present in the clay groundwater had some effects on the overall phase assemblage of the sample, with the formation of more S-rich phases like ettringite (Figure 7.30b). It is also interesting to point out, in the same plot, the higher amount of Al present in the points collected at the edge, agreeing well with the results observed after 6 months of contact with clay groundwater (Figure 7.28, Table). This might be a consequence of a higher degree of reaction of BFS at the edge of the sample, but further analysis is required to provide more evidence for this. Moreover, the presence of ettringite seems to be more evident at the centre of the sample, which might be indicative of a possible dissolution of this phase at the edge of the sample.

In terms of Mg, since an outside layer rich in this element was found in EDX mapping, the formation of more Mg-like phases is expected in the edge area. The Mg/Ca vs Al/Ca plot shows exactly that, with the points collected at the edge present more at the right side of the diagram showing the presence of both hydrotalcite and M-S-H/brucite (Figure 7.30c). The points collected at the centre of the sample

plot towards the left side of Figure 7.30c, showing the intermixing of phases present, such as C-(A)-S-H, AFt and AFm phases. The presence of M-S-H intermixed with some C-S-H in the edge area is confirmed in Figure 7.30d, where points with high Mg/Si molar ratio are observed [211,212].

7.5.2: Nano- and micro-structural evolution of Cebama reference cement paste

No significant differences over time were observed in the porosity in the samples that were in contact with clay groundwater (Table 7.13). Nevertheless, when comparing to the control sample a decrease of the macroporosity obtained through XCT was observed, from $2.8 \pm 0.9\%$ for the control sample to $0.4 \pm 0.2\%$ for the sample in contact with clay solution, at 12 months. This is due to the increase of the formation of hydrate phases, as an increase of the hydration was observed (XRD, TG and NMR results).

Table 7.13. Porosity measurements obtained by XCT and MIP for Cebama reference cement samples that were in contact with clay groundwater. XCT errors calculated from standard deviation of triplicate thresholding. MIP errors represent the intrinsic instrument error.

	Macroporosity through XCT (%)	Porosity through MIP (%)
Cebama Clay 6 Months	1.4 ± 0.4	4 ± 2
Cebama Clay 12 Months	0.4 ± 0.2	5 ± 2

From Figure 7.31, it is apparent that the bulk of pores have pore entry sizes $<0.2 \mu\text{m}$, for both samples at 6 and 12 months. However, the volume of pores is somewhat higher for the sample at 12 months, meaning that an increase of porosity with leaching time. This is observed in the total porosity obtained from this measurement, being the total porosity for 6 months around $4 \pm 2\%$ and $5 \pm 2\%$ for the sample at 12 months (Table 7.13). Nevertheless, this increase in porosity is small (and possibly negligible) when the errors of the measurement are considered, so one can assume that no significant differences in the total porosity are observed between the sample at 6 months and 12 months of experiment. Once again, when comparing to the control samples, a decrease of the porosity was evident (from $10 \pm 2\%$ to $5 \pm 2\%$ at 12 months for control sample and sample in contact with clay solution), showing the effects of the contact with groundwater and the consequent increase of the hydration.

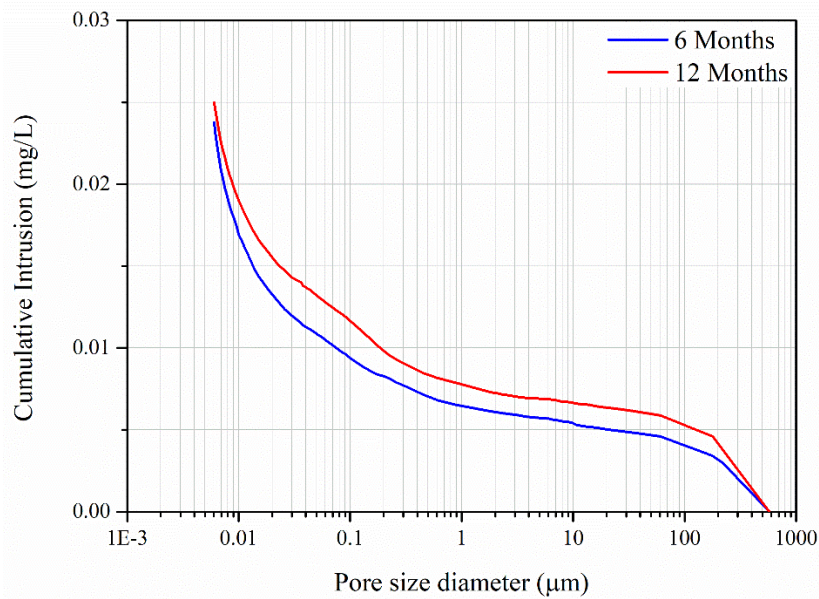


Figure 7.31. Pore entry size distributions of Cebama reference cement samples that were in contact with clay groundwater for 6 and 12 months, determined by MIP.

7.5.3: Solution chemistry

The solution pH for the samples that were in contact with clay groundwater (pH of the blank was 7.5) increased to around 9.6 – 9.9 for the first 6 months of experiment, staying more or less constant throughout the rest of the experiment (being around 9.2 – 9.5 after 12 months). From ICP-OES and IC analysis of the solutions, slightly different results were obtained for the experiment with clay groundwater (Figure 7.32) when compared with the previous experiments. Starting with the Ca concentration (Figure 7.32a), it is possible to observe that a continuous leaching of this element occurred with time, with an initially high concentration (at 2 months), and then lower concentrations for the remainder of the investigation.

With regard to Mg (Figure 7.32b), precipitation/uptake of this element was observed throughout the experiment, with the uptake of this element after 12 months being smaller compared with the first time point of sampling. This is related to the formation of the Mg-rich outside layer after 6 months of experiment; presumably, this region was then saturated with respect to Mg, which is why the uptake was lower at later time points.

It is interesting to observe that the S concentration varied between leaching and uptake as a function of time (Figure 7.32c). This might be occurring due to some destabilisation of ettringite at the edge of the sample (leaching of S is occurring), and the formation of this phase at the centre of the sample (uptake of S is happening), which was observed in the SEM-EDX spot analysis (Figure 7.30b).

In terms of Si concentration, the continuous leaching of this element was apparent, initially with a higher amount of leaching, then progressively less leaching, but never reaching the values of the blank (Figure 7.32d). These results are opposite to those observed with granitic and saline groundwater, where the leaching of Si stopped when the formation of the Ca-rich outside layer was observed, evidencing the possible protective nature of that layer for further groundwater interaction.

No changes were observed in the Cl concentration, with the values detected in solution similar to those observed in the blank (Figure 7.32e).

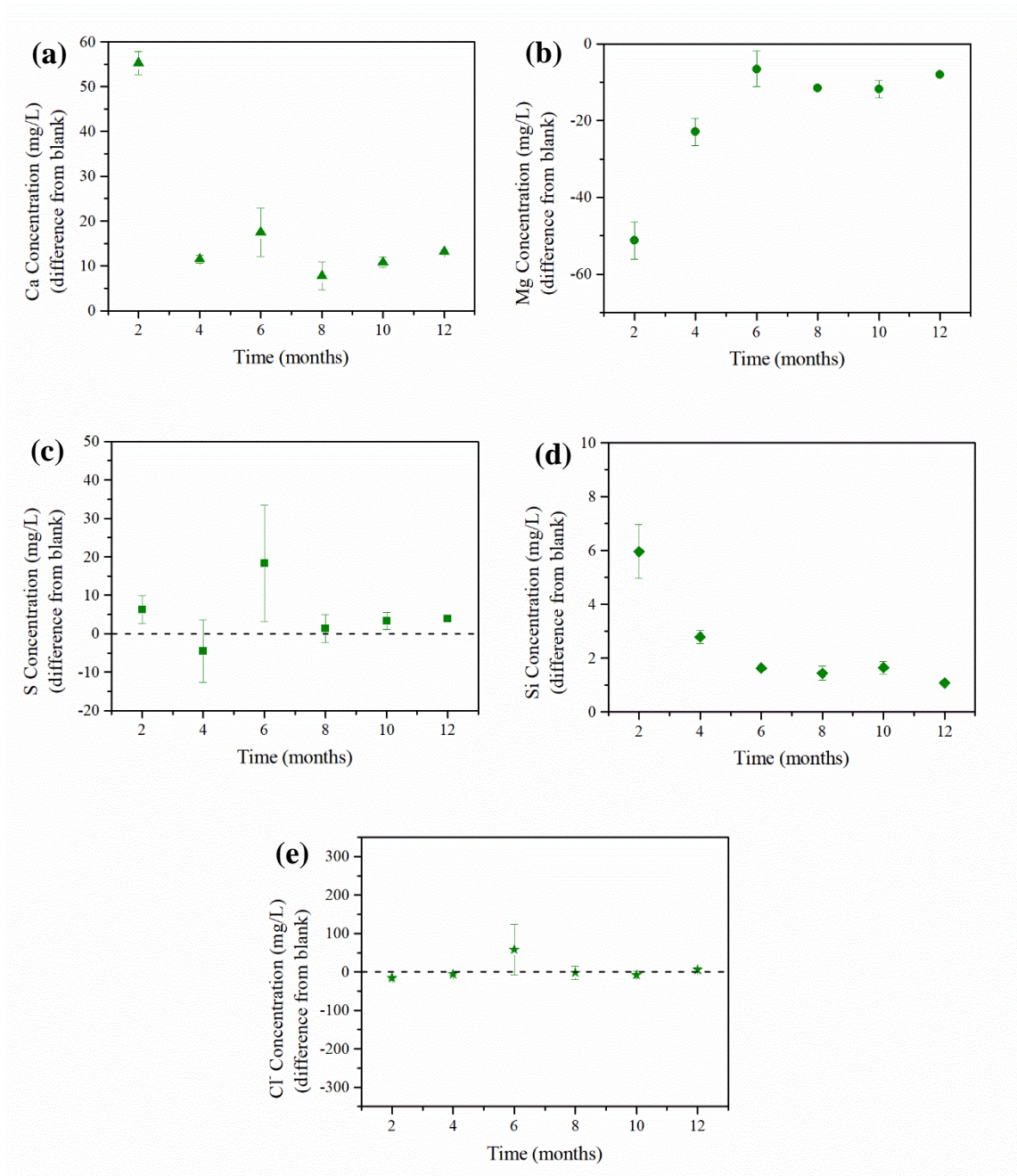


Figure 7.32. Elemental concentrations in solution (mg/L) obtained through the difference from blank for Cebama reference cement samples that were in contact with clay groundwater for 12 months: (a)

Ca concentration; (b) Mg concentration; (c) S concentration; (d) Si concentration; (e) Cl concentration. Errors were calculated using the standard deviation of duplicate ICP-OES and IC measurements.

7.6: Discussion

7.6.1: Comparison with control samples not in contact with groundwater

From the results presented, it was found, for all groundwater compositions, that there was an increase of the hydration reaction of the Cebama reference cement paste when comparing to the control samples (cured without contact with groundwater). As observed in the previous Chapters (Chapters 4 and 5), this low-pH cement is characterised by its slow hydration reaction, with the presence of clinker phases, BFS and silica fume even after 1.5 years of hydration (also observed in other studies, e.g. [119]). This is a consequence of both the presence of slow reacting BFS and silica fume, and the low amount of water used in this formulation (w/s ratio of 0.25, [64]). At the start of this experiment, the Cebama reference cement paste had been hydrated for 28 days, and so the hydration reaction was far from being completed (as observed in Chapter 4 and 5). From Section 7.2, showing the results for the control samples cured for 12 months, only a slight increase of the hydration was observed through XRD, TG and NMR. Therefore, when this cementitious material was placed in contact with the groundwater, the presence of extra water allowed the reaction to proceed. This increase of hydration was observed through XRD, which showed a decrease of the peak intensity of the clinker phases and an increase of the hydrated phases, and TG analysis, which showed an increase of the peak corresponding to the loosely bound water from within C-S-H. Through ^{29}Si and ^{27}Al MAS NMR results, the increase of hydration was also observed with a decrease in the relative concentrations of belite, alite, BFS and silica fume, and a consequent increase in the quantity of C-S-H and AFt phases. Moreover, in all samples placed in contact with the different groundwater compositions, the Ca/Si, Al/Si and MCL did not vary for the duration of the experiment (Tables 7.3, 7.6 and 7.9). However, there were slight variations observed especially in the Al/Si ratio when comparing to the control samples, which was due to the increase of the hydration of BFS. It is important to mention that these techniques were applied to bulk cement samples, meaning that any gradient (e.g. between the edge and the centre of the samples) was not visible in the results presented with these techniques.

In terms of porosity, an overall decrease of the porosity was observed when comparing the samples that were in contact with the different groundwaters and the control samples. That decrease was more evident in the saline and clay groundwater, which seem to be the samples that were more affected by the contact of the groundwater, as it will be explained below.

In previous studies [42,45,197,209,213], where interactions of low-pH cementitious materials with different geological environments were studied, there was no discussion of the increase of hydration. This might be due to possible differences in the curing ages (although not all of the studies reported the curing age of the cementitious materials at the start of the experiment), and different w/c ratios (the use of higher ratios increase the hydration reaction). However, in the Calvo et al. [42] investigation of low-pH cement samples in contact with granitic groundwater, it was mentioned that in the non-degraded zone of the cement, a decrease of anhydrous cement grains was observed, which could be interpreted as an increase of hydration observed in that area (although in the study, this conclusion was not drawn directly).

7.6.2: General comparison between different groundwater compositions

The aim of this semi-dynamic experiment was to elucidate the behaviour of the low-pH cement, Cebama reference cement paste, when in contact with three different types of groundwater, representative of the different geological environments. This Section discusses the differences in behaviour as a function of groundwater solution composition.

Cebama mineralogy and porosity as a function of groundwater composition

As mentioned above, when in contact with the different groundwater solutions, an increase of the Cebama reference paste hydration was observed through analysis of the bulk of the sample. However, to discern if any degradation zones were formed in the cement samples, since unidirectional flow was allowed in this semi-dynamic experiment, SEM-EDX analysis was performed.

In the case of the samples that were in contact with granitic and saline groundwater, it was possible to observe the formation of a Ca-rich outside layer. The formation of this layer is thought to have occurred due to the initial decalcification observed in the ICP results (Figure 7.14 and 7.23), and the presence of HCO_3^- in both groundwater compositions. As mentioned before, in the presence of dissolved Ca (from the decalcification of the C-S-H) and CO_3^{2-} (from the dissociation of HCO_3^-) in the pore solution, precipitation of carbonate phases is observed [66]. Previous studies [199,214] have found similar results when concrete samples were in contact with sea water for a long-period of time, with the formation of a calcite crust at the edge of the samples.

The type of decalcification mentioned was observed in the samples in contact with granitic and saline groundwater, in the area just before the Ca-rich outside layer. This layer is mainly characterised by a depletion of Ca and it is rich in Mg (Figures 7.11 and 7.20). It has been mentioned in previous studies that this observed decalcification may cause a “charge defect”, which is compensated by a progressive

inclusion of Mg [42]. This decalcified, Mg-rich layer appears to be two times thicker in the sample that was in contact with saline groundwater when compared to the sample that was in contact with granitic groundwater. ICP-OES results support this evidence, since it is possible to observe a longer leaching time of Ca in the saline groundwater (for 6 months of experiment), whereas the leaching of Ca in the granitic groundwater only occurred for 4 months. Moreover, the concentration of Mg present in the saline groundwater is higher (Table 7.1), thus more incorporation of Mg was observed. The main hydrate phases observed in this layer, as determined through spot analysis (Figures 7.12 and 7.21), were Mg-rich phases, like hydrotalcite and M-S-H. These results agree with those reported by Calvo et al. [42] when low-pH cement was in contact with granitic groundwater, where the inclusion of Mg was observed in the areas where decalcification occurred, leading to the formation of Mg-rich phases. Also with saline groundwater, similar results were observed where depletion of Ca combined with an increase of the concentration of magnesium led to the formation of M-S-H [199].

In the case of the samples that were in contact with clay groundwater, slightly different results were observed in terms of the degradation zones. In this experiment, a clay groundwater composition without any bicarbonate addition (HCO_3^-) was utilised, as requested by the project sponsors, Radioactive Waste Management (RWM, UK). Although it is known that this composition is not representative of the real conditions observed in a clayey environment [84,197,209,213,215], the RWM request for this groundwater composition was to see possible effects that the absence of carbonates might have in the groundwater interaction with cementitious materials.

The first main difference observed with clay groundwater was the absence of the formation of a Ca-rich outside layer throughout the experiment. This observation supports the statement that the formation of a carbonate layer in the granitic and saline groundwater is due to the presence of HCO_3^- in both groundwater compositions, and not due to atmospheric carbonation. Moreover, in terms of leached layers, a decalcified, Mg-rich zone was observed in the outside part of the sample at the interface with the solution (Figures 7.29 and 7.30). The formation of Mg-rich phases, especially M-S-H, was observed in all previous studies which involved low-pH cements in contact with clay groundwater or in a clayey environment [84,197,209,212,213,215].

The M-S-H phase observed in all groundwater compositions, being more evident in the clay groundwater due to the higher Mg/Si ratio (around 0.8, whereas for granitic and saline groundwaters Mg/Si ratio was around 0.2 and 0.5, respectively), was intermixed with C-S-H, showing the coexistence of both phases in the degraded area. The formation of this phase has been reported in many different studies where low-pH cement or concrete has been in contact with different types of groundwater (granitic and clay) or sea water [42,73,180,212,216].

In all of the groundwaters depletion of ettringite in the degraded zone (the Mg-rich layer) was observed when compared to the centre of the sample (where no clear alteration was observed due to interaction

with the groundwater). Similar results were observed in the study performed by Dauzeres et al. [197], where no ettringite was observed in the decalcified zone of the sample. They stated that this was due to the low pH observed, which led to the destabilisation of ettringite in this area [147,150,217]. In this study, it is also believed that dissolution of ettringite occurred, possibly contributing to the buffering of the pH (through the leaching of Ca), at the same time as decalcification of C-S-H. Indeed, it has been shown in previous studies that dissolution of AFt phases can be significant enough to buffer the pH [71,202].

Concerning Cl uptake, in this study and for all the groundwater compositions, no significant interaction was observed (IC results, Figures 7.14e, 7.23e and 7.32e). These results agree with those observed by Dauzeres et al. [197], but are opposite to the results observed by Calvo et al. [42], who observed a chloride-rich zone where decalcification occurs. A possible explanation for the low Cl uptake is the fact that the Cebama reference cement paste is composed of high replacements of supplementary cementitious materials, i.e. BFS and silica fume, which provides a dense structure with low porosity and so retards the chloride ingress [218,219].

With these mineralogical changes, the total porosity of the cementitious samples was affected. A slight decrease of the porosity was observed for all of the samples over the period of time of the experiment. As mentioned previously, this decrease, when comparing to the control samples, was mainly due to the observed increase of the hydration reaction, which meant the formation of more hydrate phases, like C-S-H, and consequent decrease of porosity. Another factor that influenced this decrease of the porosity, especially in the samples that were in contact with granitic and saline groundwater, was the carbonation which, besides forming an outside protective layer, might also have precipitated in some of the pores in the sample, reducing the porosity [66]. However, when comparing the two time points analysed for each sample (6 and 12 months), the variations in the porosity were within the error.

It is important to note that the porosity measurements were performed in the bulk sample, not being possible to differentiate the degraded zone (edge of the sample) from the centre of the sample (area not affected by the groundwater). However, from the SEM images shown in this Chapter, no evident differences were observed in terms of pores between the edge and the centre of the sample. In previous studies, an increase of the porosity was observed in the degraded zone when compared to the sound zone of the sample (area where solution does not interact with the cementitious material) [197,215].

Nevertheless, through these porosity measurements, and also through the SEM images, it was possible to observe how dense this cementitious material is, presenting a very low total porosity.

pH vs time

For all groundwater compositions, an initial increase of the pH was observed, varying between pH 10 and 11 depending on the groundwater being buffered (Figure 7.33). These pH values are in agreement with previous studies and are expected for this type of low-pH cement [42,44,45,49,197]. Buffering capacity is provided by decalcification of the C-S-H and also by the dissolution of ettringite for all of the samples; in the spot analysis plots it was observed that the edge points were higher in Si/Ca ratio and lower in S/Ca ratio than the centre points. However, in the case of the samples that were in contact with granitic and saline groundwater, a decrease of the pH was observed as a function of time, being after 12 months similar to the pH of the blank solutions. This decrease is thought to be related to the formation of the Ca-rich outside layer, which protected the cement from further interaction with groundwater, and so no additional buffering of the pH occurred [214]. For the granitic groundwater, the decrease of pH was observed after 4 months (Figure 7.33), correlating well with the uptake/precipitation of Ca observed in the ICP-OES results (Figure 7.14a). Whereas for the saline groundwater, it occurred after 6 months (Figures 7.33 and 7.23a). In the case of the clay groundwater, since no carbonate layer was formed, the pH values were kept more or less constant throughout the experiment (around 9.5).

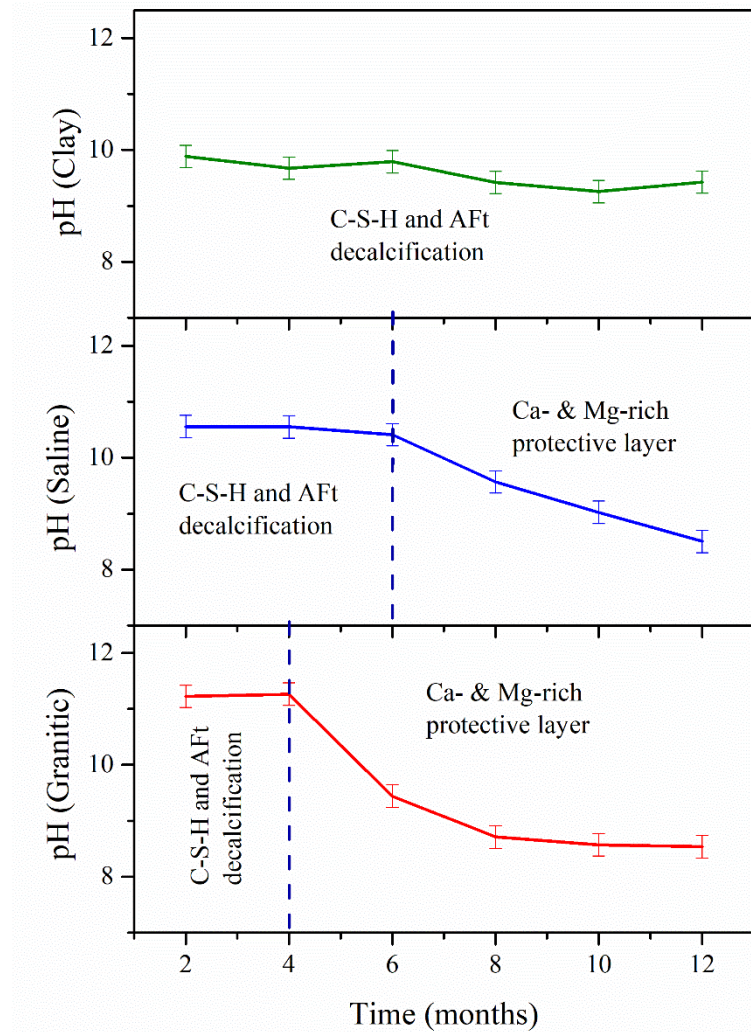


Figure 7.33. pH evolution of granitic, saline and clay groundwater over 18 months of contact with Cebama reference cement.

7.6.3: Comparison between semi-dynamic and static experiments

A static experiment was performed to help to establish, as mentioned in Chapter 6, if the accelerated nature of the semi-dynamic experiments influenced the changes observed. The data are fully described in Appendix III. A brief summary is given as follow:

- There was an increase of the hydration reaction of Cebama reference cement samples when compared to the control sample, with an observed decrease of the clinker phases and SCM (BFS and silica fume), and an increase of the hydrate phases, like hydrotalcite-like phase, monocarboaluminate, ettringite and C-S-H. This was the same as observed for the semi-dynamic experiments.
- The pH was kept constant throughout the experiment at around 9.5 ± 0.3 , 9 ± 0.3 and 10 ± 0.3 , for the granitic, saline and clay groundwater, respectively. This difference between the semi-

dynamic and static experiments might be due to a possible no formation of an outside protective layer. As it can be seen in Figure 7.34, mainly constant leaching of Ca, even though in small quantities, is observed throughout the experiment. It is also interesting to observe that Mg uptake is only occurring in the samples that were in contact with clay groundwater, a result similar to the semi-dynamic experiment.

- A chemical equilibrium was reached between the elements present in the groundwater and in the cementitious material (Figure 7.34).

In summary, an increase of the hydration was generally observed for the static experiment, being in agreement with the observed in the semi-dynamic experiment. However, some differences were observed between the two experiments, specifically related to the pH. In this experiment, the pH was constant throughout the 18 months, which was opposite to observed in the semi-dynamic experiment (mainly for granitic and saline groundwater). This might be a result of the no formation of an outside protective layer, as a lower groundwater interaction rate was obtained due to the no replacement of the groundwater.

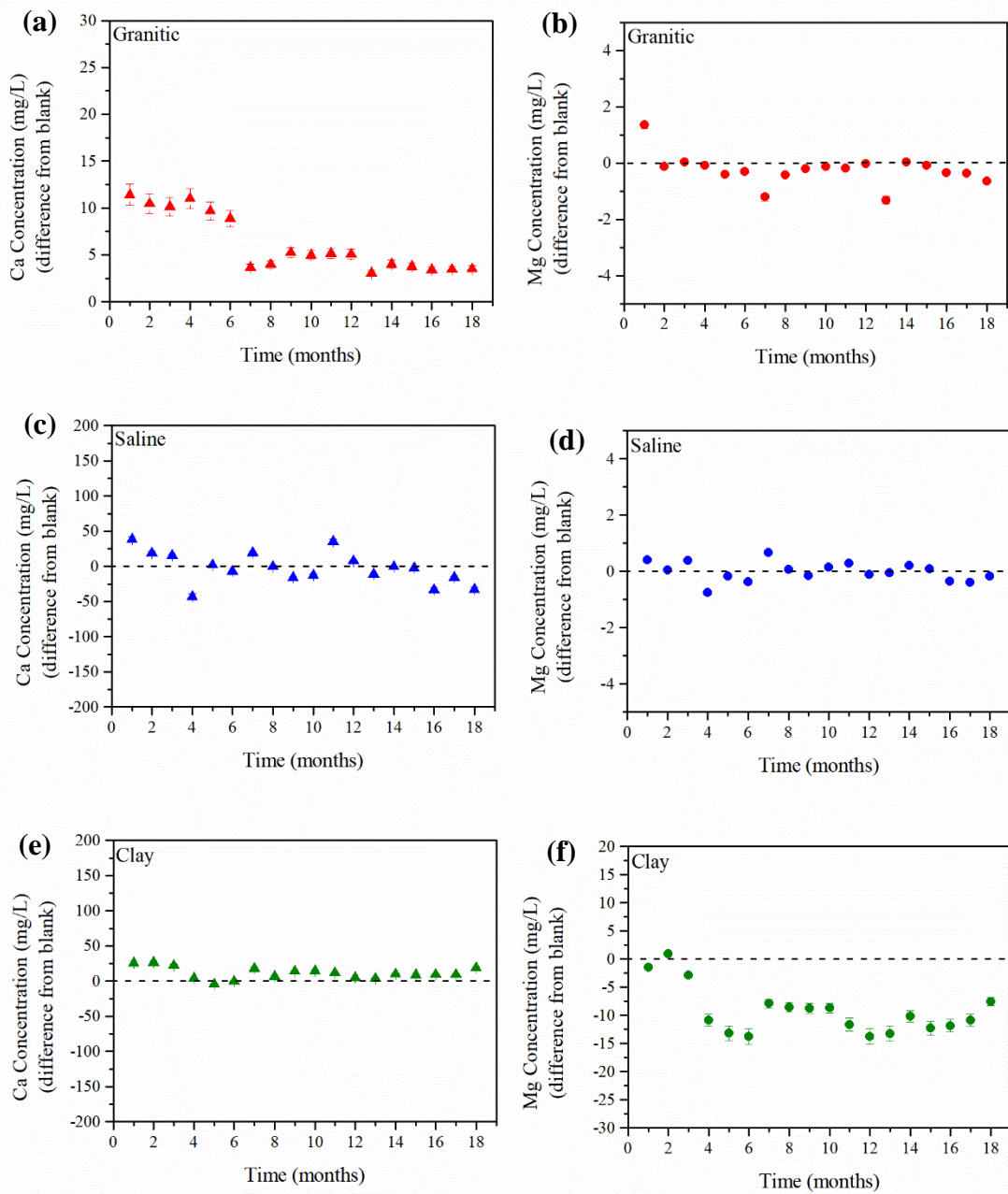


Figure 7.34. Ca and Mg concentrations in solution (mg/L) obtained through the difference from blank for Cebama reference cement paste samples that were in contact with granitic (a and b), saline (c and d) and clay (e and f) groundwater for 18 months. Errors were calculated using ICP-OES instrument error.

7.7: Conclusions

The Cebama reference cement paste, a low-pH cement, was placed in contact with three different types of groundwater (granitic, saline and clay groundwater) in a semi-dynamic experiment. This

cementitious material, when in contact with the different groundwater compositions, was observed to buffer the pH between 10 and 11, which are around the values expected for a low-pH cement. The buffering of the pH was mainly due to the decalcification of C-S-H and dissolution of ettringite.

In the cement samples, the main differences observed in the bulk of the sample were related with an increase of the hydration reaction. As was observed in the previous Chapters, the hydration process of this specific formulation is very slow, with the presence of clinker and supplementary cementitious materials present even after 18 months of curing. The combination of the use of very slow reacting raw materials (BFS and silica fume, when agglomerated) and the use of a low w/c ratio, are the main factors responsible for this slow hydration. In this way, once Cebama reference cement paste was placed in contact with any of the groundwater compositions, the extra available water was straight away used to increase the hydration reaction. Therefore, a decrease of the relative concentration of the clinker phases, like belite and alite, and of the silica fume and BFS was visible, with a consequent increase of the formation of hydrate phases like hydrotalcite and C-S-H. This increase in the hydration led to the observed decrease of the porosity.

However, the main differences observed due to the contact with the different groundwater compositions were visible when the centre and the edge of the sample were differentiated, since unidirectional flow of the groundwater was allowed in this experiment.

More alterations in the phase assemblage were observed at the edge of the sample than in the centre, and this was observed in all of the groundwater compositions. However, for the samples that were in contact with granitic and saline groundwater, the precipitation of a Ca-rich outside layer, with some incorporation of Mg, was observed after 6 and 10 months, respectively. This was due to the presence of carbonates in the groundwater compositions, which reacted with the free Ca from the observed initial decalcification of C-S-H and ettringite. The precipitation of the outside layer acted as a protective barrier for further contact of groundwater, which resulted in a decrease of the pH to values similar to the blanks.

In the case of the samples that were in contact with clay groundwater, since no carbonates were present in the composition, a continuous leaching was observed. However, the precipitation of more Mg-rich phases was visible at the edge of the sample. Nevertheless, the thickness of the degradation zone was quite small, in the range of a few microns, which might be due to the dense, low porosity nature of this low-pH cementitious material.

For all of the samples, the degradation zone was characterised mainly by decalcification of C-S-H, depletion of ettringite and the formation of Mg-rich phases like hydrotalcite and M-S-H.

The results presented in this chapter are of extreme importance for many European countries safety case, where clay/bentonite barriers are considered to use. Specifically, the importance of the

cementitious material to provide a low-pH environment when interactions with the geological environment occur, which was observed in the current work. Moreover, the observed formation of a protective layer when carbonates were present in the groundwater composition is a crucial result, as it shows that this protective layer reduced further interactions of the cementitious material with the groundwater.

Chapter 8: Conclusions and Future work

8.1: Summary and Conclusions

The aim of this Thesis was to evaluate the long-term performance of two different cementitious materials considered for use in a geological disposal facility context, when in contact with three different types of groundwater representative of the different geological environments. NRVB is a high-pH cement considered to be used in one of the UK disposal scenarios as a backfill material, whereas Cebama reference cement paste is a low-pH cement designed to be used in many European countries to prevent issues associated with bentonite clay interactions.

Through a detailed characterisation of both cementitious materials (Chapters 4 and 5), changes in the mineralogy and microstructure of these materials, as a function of curing time and temperature were ascertained. For NRVB it was observed that the main hydrate phases present after 28 days of curing were portlandite, calcite, ettringite, hemicarboaluminate, monocarboaluminate and C-S-H. With the long-duration synchrotron XRD experiment combined with ^{29}Si MAS NMR analysis (Chapter 5) it was visible that the total hydration of the clinker phases (Portland cement components) had occurred after 2 months of hydration. Moreover, with the total reaction of belite and alite, a maximum formation of C-S-H was obtained, as these phases are the only source of Si in this cementitious system. Porosity is one of the most important characteristics of NRVB, since it will allow interaction with the groundwater to provide a high-pH environment. The total porosity obtained in the present study was around 35 % after 28 days of curing, which is significantly lower than previously reported, despite using similar materials, identical synthesis methods and characterisation.

In the case of the Cebama reference cement paste, the main hydrate phases identified were: ettringite, monocarboaluminate, hydrotalcite and C-A-S-H. However, in this cementitious system the presence of unreacted material, including clinker phases, BFS and silica fume, was visible, even after 1.5 years of curing. A combination of the high replacement percentages of supplementary cementitious materials (SCMs), and their characteristic slow degree of reaction at low pH, and the low w/s ratio of this formulation, are responsible for this slow reaction. Moreover, agglomeration of silica fume was observed in these samples, which consequently reduced its reactive surface area, further reducing the pozzolanic reaction of the silica fume. This slow reaction of the SCMs was noticeable through the presence of portlandite at the early ages of curing. However, with further increase of the hydration and reaction of the BFS and silica fume, portlandite disappeared due to the pozzolanic reaction. In terms of

porosity, Cebama reference cement paste was found to be very dense and to have a low porosity, decreasing with increasing curing times (from ~19 % at 28 days to ~10 % after 1.5 years).

Different cementitious materials, with very different mineralogical and microstructural characteristics, are expected to behave differently when in contact with groundwater. To understand these differences, extended experiments were performed, where the cement samples were placed in contact with granitic, saline and clay groundwater.

Chapter 6 has shown that the mineralogy and microstructure of NRVB samples were strongly affected when in contact with the different groundwater compositions. Once NRVB samples were placed in contact with the different solutions, a rapid increase of the pH was observed, due to the initial dissolution of portlandite. Depending on the groundwater, the rate of dissolution of the different hydrate phases responsible for the pH buffering was different. In the case of the granitic groundwater, the pH was mainly buffered due to portlandite consumption and slight decalcification of C-S-H, whereas for the saline and clay groundwater a combination of dissolution of portlandite and the beginning of dissolution of C-S-H and ettringite were the main phases responsible for keeping the pH alkaline. Moreover, for the saline and clay groundwater, due to their higher concentration in S and Mg (S ~128 and 481 mg/L and Mg ~10 and 138 mg/L respectively) when compared to the granitic groundwater (S ~3 mg/L and Mg ~5 mg/L), further mineralogical alterations occurred with the formation of more ettringite and brucite, respectively. Likewise, in the groundwaters that contained carbonates in their composition (granitic and saline), precipitation of calcite was also observed, forming a protective outside layer. The precipitation of these secondary phases resulted in a general decrease of the porosity of NRVB. As having a high porosity is one of the requisites for NRVB as a backfill material, this observed decrease in the porosity is potentially significant to the UK safety case. Nevertheless, with this experiment it was evident that NRVB buffering capacity was fulfilled, as the pH was kept above 12 throughout the duration of the experiment.

In the Cebama reference cement paste, the alterations observed due to the contact with the groundwaters (Chapter 7) were different from those observed with the NRVB samples. As the hydration reaction was not completed before the experiment started, due to the very slow rate of hydration observed in Chapters 4 and 5, the main differences observed in the bulk of the sample were related to an increase of the extent of hydration once in contact with groundwater. This resulted in an overall decrease of the porosity. As a dense material, with very low porosity, the main alterations in terms of mineralogy were mainly observed at the edge of the sample. An overall decalcification of C-S-H and ettringite were observed, which were the main phases responsible for buffering the pH to values between 10 and 11. However, a decrease of the pH was observed, to values similar to those in the granitic and saline blanks, due to the formation of a protective outside layer, which formed as a result of a carbonation reaction with carbonate present in the groundwater solution. In the case of the clay groundwater, this was not observed

as no carbonates were present in the composition, and so the pH was kept more or less constant during the experiment. The high Mg content in the different groundwaters led to the formation of Mg-rich phases in the degraded zone, like hydrotalcite.

Figure 8.1 details the main differences in the pH buffering capacity between the two cementitious materials:

- In NRVB, portlandite content is high, being the main phase responsible for buffering; also high porosity leads to higher area for groundwater interaction.
- Cebama reference cement paste does not have any significant quantity of portlandite, thus, decalcification of C-S-H and AFt phases the main hydrates responsible for pH buffering; also, due to their very low porosity, the area of sample in contact with the groundwater was quite low, decreasing even more with the formation of the outside protective layer, when carbonates were present in the groundwater composition.

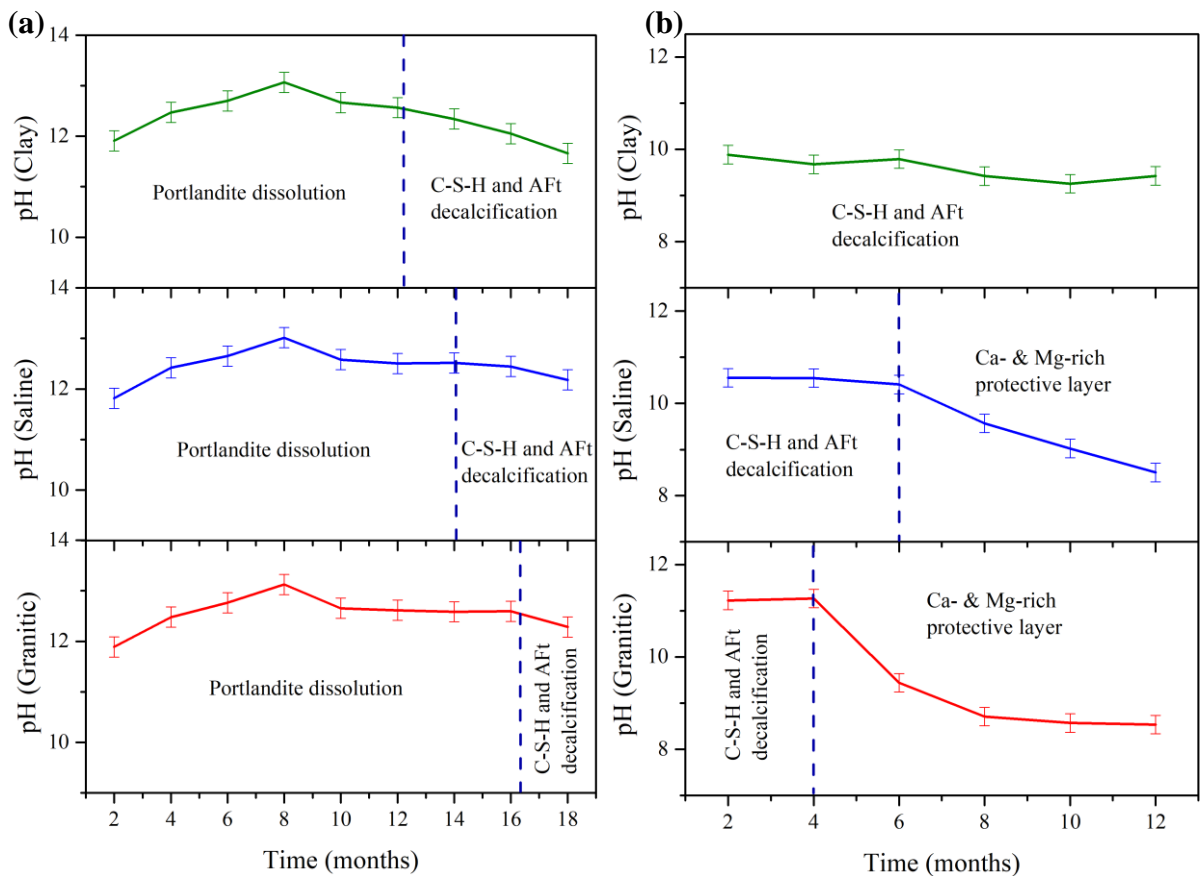


Figure 8.1. pH evolution of granitic, saline and clay groundwater when in contact with: a) NRVB for 18 months; b) Cebama reference cement paste for 12 months.

Ultimately, with the work presented in this Thesis, it was possible to demonstrate the feasibility of using the different cementitious materials in the GDF context when in contact with groundwater. In the case of NRVB, the main purpose of this cementitious material is to provide a high-pH environment when in contact with groundwater. Independently of the groundwater composition, this was observed in the present study. Moreover, when NRVB samples were in contact with granitic groundwater the mineralogical alterations seem to have occurred at a lower rate when comparing to the saline and clay groundwater. These results are of significance to the UK GDF concept where this backfill material is considered to be used, in a crystalline rock [19,137].

Regarding Cebama reference cement paste, this cementitious material was designed to provide a lowerpH environment when interactions with the geological environment/engineered barriers occur, especially in a clay context. The buffering of the solutions to a low-pH was obtained in the current work. Additionally, when carbonates were present, the formation of a protective layer was observed and resulted in a reduction of the interaction with the groundwaters. These results are of great importance for many European countries safety case, where clay/bentonite barriers are considered to use, as this protective layer will reduce possible interactions of the cementitious material with the groundwater. And therefore, this will reduce the probability of changes in the structure of the cement to occur that might affect the cement overall performance

Although this Thesis has added to the knowledge of cements interaction with groundwater and consequent mineralogical alterations, some questions remain that need to be answered, as it will be detailed below.

8.2: Future Work

The extended experiments were performed within the time-frame of a PhD. However, it is well known that for geological disposal of radioactive waste, timescales are on the order of 10,000's of years. For this reason, further work should include geochemical modelling, where the results obtained from these experiments can be used to predict the long-term mineralogical evolution of these cementitious materials, and consequent buffering capacity.

In Chapter 6 it was observed an overall decrease of the porosity of NRVB, due to contact with groundwater. High porosity is one of the main characteristics/requirements for this specific backfill material, and alterations in their porosity will possibly affect their permeability. Therefore, reactive transport modelling could be a way to better understand these alterations.

It was observed that one of the main alterations of Cebama reference cement paste when in contact with the different groundwater compositions was the increase of the hydration reaction. Greater information could be gained by performing a similar groundwater experiment, but with Cebama samples that were

cured for longer time periods, as different time scales for possible groundwater interaction may occur depending on the chosen geology.

Moreover, unlike the results observed in the NRVB static experiment, where similar results to the semi-dynamic experiment were obtained, with the Cebama reference cement slightly different results were observed in the static experiment. Therefore, additional work to understand how different groundwater flow rates would affect Cebama microstructure, would be of great interest.

Appendix I

Characterisation of a high pH cement backfill for the geological disposal of nuclear waste: The Nirex Reference Vault Backfill

Rita G. W. Vasconcelos¹, Nicolas Beaudoin^{2,3}, Andrea Hamilton², Neil C. Hyatt¹, John L. Provis¹, and Claire L. Corkhill^{1*}

¹NucleUS Immobilisation Science Laboratory, Department of Materials Science and Engineering, University of Sheffield, S1 3JD, UK

² Department of Civil and Environmental Engineering, University of Strathclyde, Glasgow, G1 1XJ, UK

³ School of Geographical and Earth Sciences, University of Glasgow, Glasgow G12 8QQ, UK

***corresponding author:** Claire Corkhill. email: c.corkhill@sheffield.ac.uk; tel: +44 (0) 1142223632

Abstract

In a conceptual UK geological disposal facility for nuclear waste within a high-strength, crystalline geology, a cement-based backfill material, known as Nirex Reference Vault Backfill (NRVB), will be used to provide a chemical barrier to radionuclide release. The NRVB is required to have specific properties to fulfil the operational requirements of the geological disposal facility (GDF); these are dependent on the chemical and physical properties of the cement constituent materials and also on the water content. With the passage of time, the raw materials eventually used to synthesise the backfill may not be the same as those used to formulate it. As such, there is a requirement to understand how NRVB performance may be affected by a change in raw material supply. In this paper, we present a review of the current knowledge of NRVB and results from a detailed characterisation of this material, comparing the differences in performance of the final product when different raw materials are used. Results showed that minor differences in the particle size, surface area and chemical composition of the raw material had an effect on the workability, compressive strength, the rate of hydration and the porosity, which may influence some of the design functions of NRVB. This study outlines the requirement to fully characterise cement backfill raw materials prior to use in a geological disposal facility and supports ongoing assessment of long-term post-closure safety.

Keywords: Geological disposal; Nuclear waste; Cement; Mineralogy; Microstructure

1. Introduction

Intermediate Level Waste (ILW) comprises a significant proportion, approximately 450 000 m³, of the UK's projected inventory of radioactive waste [5]. This includes waste arising from the reprocessing of spent nuclear fuel (e.g. spent fuel cladding) and from the operation, maintenance and decommissioning of nuclear facilities (e.g. sludges from the treatment of radioactive liquid effluents) [220]. This waste is destined for final disposal in a Geological Disposal Facility (GDF) [2], where the conditioned waste packages will be placed in vaults excavated in host rock, deep underground [1]. In a conceptual scenario where a high-strength crystalline rock will host the facility, the vaults will be backfilled with a cement-based material to provide a physical and chemical barrier to radionuclide release [1]. For this purpose, the Nirex Reference Vault Backfill (NRVB) has been considered [19].

NRVB was designed in the 1990s to fulfil a number of specific requirements for use in a UK geological disposal facility [19,80]. These include [20,21,29]:

- providing a high alkaline buffered environment, through the dissolution of the different cement hydrate phases by groundwater, to suppress dissolved concentrations of many radionuclides;

- possessing high permeability and porosity to ensure homogeneous chemical conditions, to allow the escape of the gases generated in the GDF and to provide a high surface area for radionuclide sorption; and
- exhibiting low strength to facilitate the possibility of re-excavation of the vaults, if required.

Despite an initial assessment of NRVB at the time of the design and patent [19], and subsequently, several assessments of various aspects of this material (e.g. mineralogy, strength, or porosity, as described below), there has not been a comprehensive characterisation of NRVB, where all tests are performed on a consistent batch. Additionally, some of the raw materials used in early development of NRVB are no longer available due to changes in the powder suppliers [12], therefore, materials to be used when a GDF is in operation may differ in composition and other key characteristics. It is important to understand how the chemical and physical properties of the backfill raw materials may affect the short- and long-term performance of the backfill, to support development of GDF engineering and post-closure safety assessment. We here present a literature review of the published data on NRVB, even where datasets are incomplete, or details pertinent to the analysis of the data are absent.

1.1. NRVB hydration

Portland cement (PC), calcium hydroxide [$\text{Ca}(\text{OH})_2$] and calcium carbonate (CaCO_3) are the main components of NRVB [80]. The original formulation used a water/solid ratio (w/s) of 0.55 and, according to this composition, Holland and Tearle [24] described the expected mineralogy of NRVB and the respective changes in relation with temperature. Theoretically, at ambient temperature, the phase assemblage of NRVB is expected to contain calcium hydroxide (also known as portlandite), calcite (CaCO_3), calcium silicate hydrate (C-S-H), AFt (ettringite) and AFm (monocarboaluminate) phases, and possibly hydrotalcite if magnesium carbonate is present in the limestone flour or in the Portland cement (Holland and Tearle, 2003). At high temperatures (80 °C), the formation of hydrogarnet-type phases was also predicted, according to the thermodynamic modelling (database not specified) performed by the same authors [24], although more recent advances in cement chemistry and phase assemblage prediction models indicate that this may be less likely due to the high quantity of carbonate present in this cement formulation. Experimental X-ray diffraction (XRD) performed on fresh (uncured) NRVB revealed that the main phase present was calcite, whereas for NRVB cured for 4 months and 3 years, the phase assemblage was dominated by portlandite [26].

Portlandite and C-S-H are expected to provide the high alkaline-buffering capacity of NRVB. It is proposed that when the backfill material is first in contact with groundwater, the pH will be buffered by the dissolution of the more soluble phases, alkali (i.e. Na, K) hydroxides and sulfates. After the removal of the alkali metal salts, buffering will continue through the dissolution of portlandite; a solution saturated with respect to portlandite is formed with a pH of about 12.5 at 25 °C [19]. After the portlandite has been exhausted, pH buffering will be maintained by the incongruent dissolution of C-S-

H phases with relatively high calcium/silicon molar ratios (Ca/Si), around 1.5. From this, dissolution will result in the release of calcium and hydroxide ions, thus lowering the Ca/Si ratio and reducing the pH value at which the water is buffered [23,35]. The buffering timescale and capacity of NRVB will depend mainly on the composition and rate of groundwater leaching [7,19]. According to a recent study regarding the leaching behaviour of C-S-H using demineralised water, even with a low Ca/Si ratio, the dissolution of C-S-H will buffer the pH to ~ 10 [221].

1.2. Physical properties of NRVB

The physical properties of NRVB were summarized by Francis et al. [19] and Bamforth et al. [7]. The compressive strength of the NRVB (w/s = 0.55) was found to be 4.9 MPa, 5.9 MPa and 6.3 MPa after 7, 28 and 90 days of curing respectively [19]. When comparing with compressive strength values obtained for Portland cement (w/s = 0.50), (e.g. 31 MPa, 45 MPa and 46 MPa after 7, 28 and 90 days, respectively, from Menéndez et al. (2003)), the values obtained for NRVB are very low. This relatively low strength thus allows retrievability of waste packages from within NRVB-backfilled vaults [20,21,29].

Since the repository operating temperatures will be higher than the 20 °C used for standard cement curing, studies have been performed to assess the effect of curing temperature (30 °C, 60 °C and 90 °C, cured in moist or excess volume of water) on the strength of NRVB [19]. Results showed that increasing the temperature of curing corresponds to a reduction in the strength, for example after 28 days of curing at 90 °C, the compressive strength was halved when compared to curing at 30 °C [19]. Similar results have been obtained with Portland-limestone cement, where a temperature increase negatively influenced compressive strength (Lothenbach et al., 2007). It should be noted, however, that such high curing temperatures (90 °C) are not expected within a GDF vault for ILW.

1.3. Microstructural properties of NRVB

Porosity and permeability must be carefully considered when designing a cementitious material for a GDF, since these properties will influence the transport characteristics of groundwater and radionuclide species through the cement. For example, having a high porosity (more than 30%) allows the ingress of groundwater, dissolution of the different hydrate phases, so providing a high alkaline environment. It also allows the diffusion of gases produced in the waste packages and gives rise to a high surface area, capable of sorbing radionuclide species.

NRVB is relatively porous; the total porosity of NRVB (w/s = 0.55; w/c ratio 1.367), includes a high quantity of unreacted material, was reported to be 50 % using mercury intrusion porosity and nitrogen desorption methods, at an unspecified curing age [19]. However, comparing the density obtained in dry and water we can calculate the porosity to be 35%. X-ray computed tomography (XCT) gave a

segmented porosity of ~ 40 % for large scale samples in the non-carbonated region of an NRVB-carbonation trial [31].

After closure, the formation of gases is expected to occur in the GDF, e.g. from corrosion of Magnox cladding, fuel fragments, uranium and steel under anaerobic conditions; microbial degradation of organic compounds and; radiolysis of water [32]. As a result, the permeability of NRVB should be sufficient to allow gas movement without significant over-pressurisation and cracking [19]. The gas permeability coefficient for argon and helium in NRVB at 28 days of curing (in a membrane of NRVB 20 mm thick, average pressure of 100 kPa) was found to be approximately $2 \times 10^{-15} \text{ m}^2$ in dry conditions and $5 \times 10^{-17} \text{ m}^2$ in saturated grout [19,32]. The average pore radius was determined to be $0.45 \text{ }\mu\text{m}$, with a pore size distribution ranging from 5 nm to $> 1 \text{ }\mu\text{m}$ [32]. Harris and colleagues concluded, using the premise that a material is considered to crack if the calculated stress exceeds the tensile strength, that NRVB is able to release gas at a sufficient rate without generating cracks [32].

Most of the results presented in the above summary were reported on the basis of unspecified testing methods and precursor materials, and little other detailed information is available about the cement hydration and microstructure of NRVB. Due to the importance of a backfill material in stabilising radioactive waste in a GDF, a thorough understanding of these properties of NRVB is crucial to build a robust post-closure safety case. In this paper, a full characterisation of NRVB is performed. The hydration reaction, the mineralogy and the mechanical properties are studied using two different types of raw materials to assess the implications of security of cement material supply on cement characteristics and performance. These results will have important implications regarding the applicability of older studies to present day materials in the disposal of nuclear wastes.

2. Materials and Methods

2.1. Materials

Batches of NRVB paste were prepared according to the formulation presented in Table 1, with a water/solid ratio (where solid includes all the powder materials used) of 0.55. It is possible to find in the literature data pertaining to NRVB prepared with laboratory (pure) materials (e.g. Corkhill et al., 2013) and also with industrial materials (e.g. Butcher et al., 2012). To verify the consistency between the cement formed using these two types of starting materials, two different batches of NRVB were studied. For the NRVB formulated using laboratory chemicals, denoted NRVB (Lab), the starting materials were: CEM I 52.5 N sourced from Hanson Cement Ltd, Ribblesdale works (i.e. Sellafield specification; BS EN 197-1:2011); $\text{Ca}(\text{OH})_2$ ($\geq 95.0 \%$) and CaCO_3 ($\geq 99.0 \%$) were sourced from Sigma-Aldrich. In the case of NRVB formulated using industrial materials, denoted NRVB (Ind), the following products were used: CEM I 52.5 N (as above); hydrated lime sourced from Tarmac Cement

& Lime (Tunstead Quarry, Buxton, UK); and limestone flour sourced from National Nuclear Laboratory (Tendley Quarry, Cumbria, UK; BS EN 13043:2002).

Table 1. NRVB formulation [19,80]

Material	Content (kg m ⁻³)
CEM I 52.5 N	450
Ca(OH) ₂ / Hydrated lime	170
CaCO ₃ / Limestone flour	495
Water	615

The particle size distribution was measured using a Mastersizer 3000 PSA, and the results analysed using Malvern Instruments software.

The chemical composition of the starting materials, as calculated using X-ray fluorescence (PANalytical Zetium XRF) of powdered materials, is shown in Table 2. The composition was very similar for both Ca(OH)₂ and hydrated lime. However, a slight difference was observed between CaCO₃ and limestone flour. For example, CaCO₃ contained more CaO than the limestone flour (57 wt% and 48 wt%, respectively). On the other hand, limestone flour presented a higher concentration (between 1.6 and 5.4 wt%) of SiO₂, Fe₂O₃, MgO and Al₂O₃ than reagent grade CaCO₃, which contained below 0.05 wt% of these elements (Table 2).

Table 2. Composition of raw materials, as determined by X-Ray Fluorescence analysis (precision ± 0.1 wt%).

Compound (wt. %)	CEM I 52.5 N	Limestone Flour (Ind)	CaCO ₃ (Lab)	Hydrated Lime (Ind)	Ca(OH) ₂ (Lab)
Na ₂ O	0.3	0.2	< 0.1	< 0.1	< 0.1
MgO	1.2	1.6	< 0.1	0.5	0.5
Al ₂ O ₃	5.2	1.9	< 0.1	< 0.1	0.1
SiO ₂	19.7	5.4	< 0.1	0.5	0.7
P ₂ O ₅	0.2	0.1	< 0.1	< 0.1	< 0.1
K ₂ O	0.5	0.3	< 0.1	< 0.1	< 0.1
CaO	64.1	48.1	57.0	73.9	74.5
Fe ₂ O ₃	2.1	1.7	< 0.1	< 0.1	< 0.1
SO ₃	-	893 ppm	37 ppm	-	-

Both cement batches were mixed using a Kenwood benchtop mixer for 5 minutes. Subsequently, the cement pastes were placed in centrifuge tubes or steel moulds (for compressive strength analysis) and cured at 20 °C and 95 % relative humidity, for 28 days.

2.2. Analytical Methods

Mechanical properties

The workability of both NRVB formulations was investigated using a mini-slump test [223]. The cement paste was placed in a cone (19 mm top opening x 38 mm bottom opening x 57 mm height) resting on a sheet of polymethyl-methacrylate. The cone was lifted vertically upwards and the resulting slump area measured using a scale. Each mini-slump test was repeated in triplicate.

The setting time was ascertained using a Vicatronic automatic recording apparatus (Vicat needle method) and 400 g of paste at 19-21 °C and 30-38 % relative humidity. The penetration of a needle (1.13 mm diameter) was monitored and the initial setting time was considered as the time when the needle penetration was 35 mm; the final setting time corresponded to less than 0.5 mm of penetration.

After 28 days of curing, compressive strength was measured on cubes with dimensions of 50 x 50 x 50 mm, in triplicate. Cubes were placed within a Controls Automax automatic compressive tester for analysis, with a loading rate of 0.25 MPa/s. The density of both formulations was measured using He pycnometry (Micromeritics AccuPyc II 1340) using approximately 0.40 g of powder (< 63 µm). A fill pressure of 82.7 kPa was purged 50 times over 20 cycles at 25 °C with an equilibration rate of 34.5 Pa/min.

Chemical analysis (hydration)

The heat flow resulting from the NRVB hydration reaction was studied using isothermal calorimetry analysis (TAM Air, TA Instruments) at 20 °C. Approximately 20 g of cement paste was mixed and the measurements were performed for 7 days. As reference sample, tap water was used.

For identification of the hydrate phases present in NRVB at an early age (28 days of curing), XRD and TGA-MS were performed on powder samples (< 63 µm). The former was carried out using a Bruker D2 Phaser diffractometer utilising a Cu K α source and Ni filter. Measurements were taken from 5° to 70° 2 θ with a step size of 0.02° and 2 s counting time per step. For TG-MS analysis, a PerkinElmer Pyris 1 thermogravimetric analyser was used. The temperature ranged from 20 °C to 1000 °C with a heating rate of 10 °C/minute under N₂ (nitrogen) atmosphere. A Hiden Analytical mass spectrometer (HPR-20 GIC EGA) was used to record the mass spectrometric signals for H₂O and CO₂.

Scanning Electron Microscopy (SEM) imaging and Energy Dispersive X-ray (EDX) analysis were performed on NRVB monolith samples mounted in epoxy resin and polished to a 0.25 μm finish using diamond paste. Backscattered electron (BSE) images were recorded using a Hitachi TM3030 scanning electron microscope operating with an accelerating voltage of 15 kV. EDX analysis was performed using Quantax 70 software and elemental maps were collected for 10 minutes.

Solid-state nuclear magnetic resonance (NMR) spectra for ^{29}Si were collected on a Varian VNMRS 400 (9.4 T) spectrometer at 79.435 MHz using a probe for 6 mm o.d. zirconia rotors and a spinning speed of 6 kHz, a pulse width of 4 μs (90°), a relaxation delay of 2.0 s, and with a minimum of 30000 scans. ^{27}Al NMR spectra were collected on the same instrument at 104.198 MHz using a probe for 4 mm o.d. zirconia rotors and a spinning speed of 12 kHz, a pulse width of 1 μs (25°), a relaxation delay of 0.2 s, and a minimum of 7000 scans.

Microstructure analysis (porosity)

To determine the Brunauer-Emmett-Teller (BET) surface area, nitrogen adsorption-desorption measurements were studied at 77 K on a Micromeritics 3 Flex apparatus. Powder samples of raw material were cooled with liquid nitrogen and analysed by measuring the volume of gas (N_2) adsorbed at specific pressures. The pore volume was taken from the adsorption branch of the isotherm at $P/P_0 = 0.3$. Mercury intrusion porosimetry (MIP) was used to study the total porosity and pore distribution of the samples. Small pieces of cement paste were placed into the sample holder of an Autopore V 9600 (Micromeritics Instruments). Washburn's law was used to determine the pore diameter, by applying the following equation: $D = (-4\cos\theta)\gamma/P$, where D is the pore diameter (μm), θ the contact angle between the fluid and the pore mouth ($^\circ$), γ the surface tension of the fluid (N/m), and P the applied pressure to fill the pore with mercury (MPa). The maximum pressure applied was 208 MPa, the surface tension was 485 mN/m and the contact angle was 130° .

The XCT scans were performed at the University of Strathclyde using a Nikon XTH 320/225 system, equipped with a 225 kV reflection gun, a microfocus multimetal target, and a 2000×2000 pixel flat panel photodetector (cell size 0.2×0.2 mm). The rotation stage position was set so the X-ray source-to-sample distance was minimal and allowed a minimum voxel size of 3 micrometres. Scanning conditions were an accelerating voltage of 100 keV, 28 μA current (corresponding to power 2.8 W) using a silver target. The exposure time for each projection was 2.829 seconds, lasting 3141 projections (1 frame per projection) and leading to a scan-time of 2.5 hours. Gun conditions would not saturate photodetector, consequently no metallic filter was required during the scans. Projections were overlapped in 3 different heights of the sample with CT Pro 3D software (© 2004-2016 Nikon Metrology) to reconstruct the centre of rotation of the 3D volumes. Once reconstructed, a software built-in algorithmic correction has been applied to correct for artifacts related to beam-hardening [132]. All volumes were reconstructed in 16 bit greyscale, and converted to a .tif stack. A volume of interest (VOI) was selected for each

sample, using standards previously reported in the literature, i.e. the VOI should be at least $100 \mu\text{m}^3$, or higher than 3 to 5 times the size of the largest distinct feature, to minimise finite size error. In this study, the VOI size chosen was 0.42 mm^3 (250 x 250 x 250 voxels at $3 \mu\text{m}$ resolution).

3. Results and Discussion

3.1. Mechanical Properties

The workability, determined by mini-slump testing, of NRVB (Lab) and NRVB (Ind) was found to be $56.5 \pm 0.8 \text{ mm}$ diameter and $68.4 \pm 1.7 \text{ mm}$ diameter, respectively. The higher fluidity of NRVB (Ind) is likely related to the difference observed in the particle size distribution between the sources of calcium carbonate (Figure 1a), where 50 % of the particles were smaller than $19.7 \mu\text{m}$ for CaCO_3 , and $11.5 \mu\text{m}$ for limestone flour. For laboratory and industrial grade Ca(OH)_2 (Figure 1b), the particle size distribution was found to be very similar.

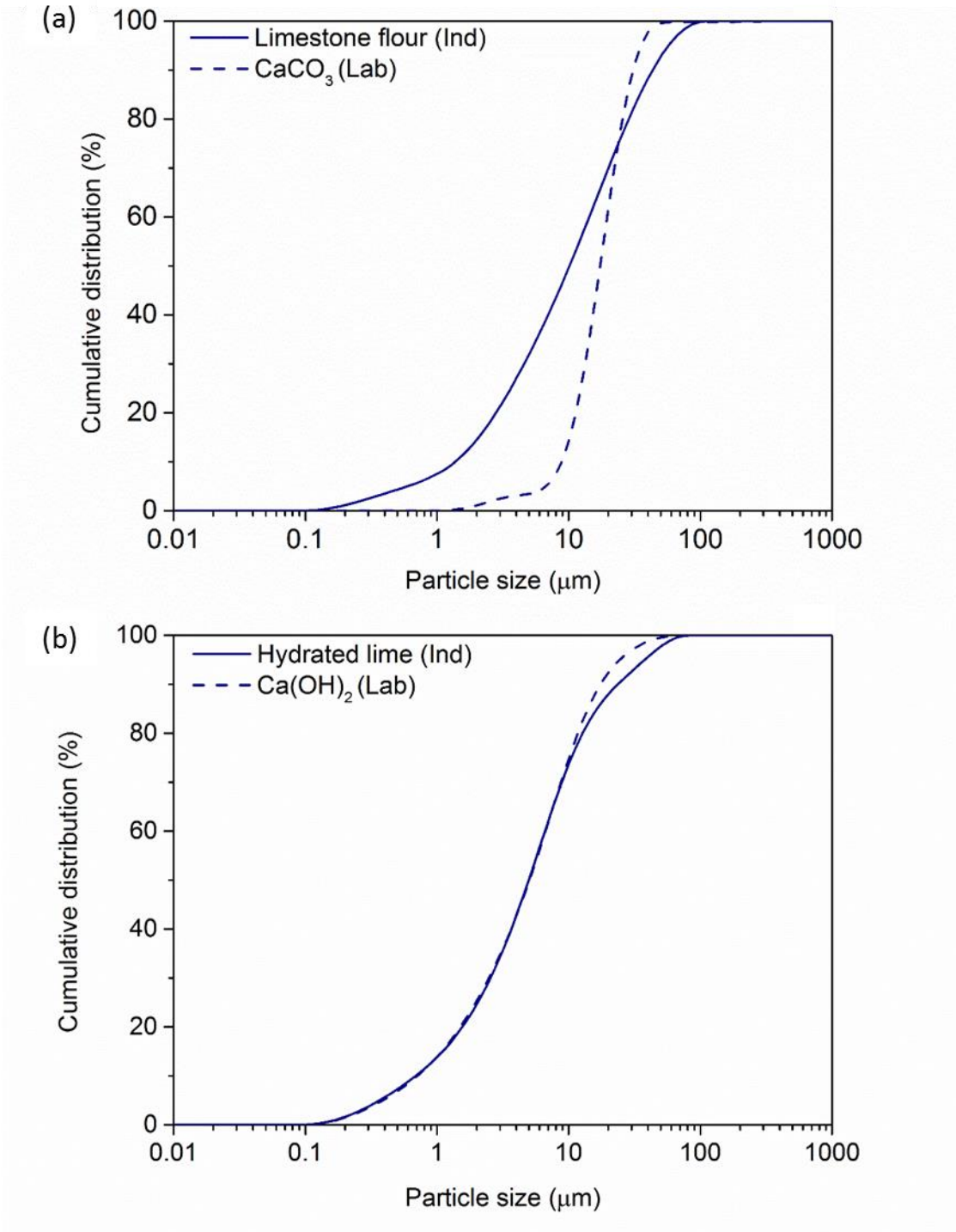


Fig 2. Particle size distribution of (a) CaCO₃ and limestone flour and; (b) Ca(OH)₂ and hydrated lime.

For general applications, the initial setting time of a cement should not be less than 45 min, and the final setting time should not be greater than 10 hours [52,56]. Using the Vicat method, it was possible to obtain an initial setting time of 5.3 hours, and a final setting time of 7.7 hours for NRVB (Lab). For NRVB (Ind) the values were very similar, with the initial and final setting times at 5.5 hours and 7.3

hours. This is in contrast to the initial NRVB formulation study, where an initial setting time of 4.05 hours and a final setting of 4.50 hours was observed [19]. Since the w/s ratio in the present study is the same as that used by Francis et al. [19], this difference is likely to be related to the use of different raw material, and a consequent difference in the reactivity of the materials.

After 28 days of curing, the compressive strength and density of the two materials were compared. The compressive strength was determined to be 8.2 ± 0.2 MPa for NRVB formulated using laboratory materials and 7.15 ± 0.04 MPa for NRVB formulated with industrial materials. This is somewhat greater than that measured by Francis et al. [19], who found a compressive strength of 5.9 MPa at 28 days for NRVB prepared using components available in the early 1990s. Since no characterisation of these starting materials was published, it is not possible to ascertain which component of this early NRVB formulation gave rise to the reduced strength, although it may be postulated that the 52.5 MPa grade cement used in our trials was of a higher strength grade than the materials used historically, as cement production at this high strength grade was much less common in the early 1990s. The density was determined by helium pycnometry to be 2.251 ± 0.001 g/cm³ for NRVB (Lab) and 2.328 ± 0.002 g/cm³ NRVB (Ind); previous measurements of NRVB density using the Archimedes method (100 mm cubes) gave a density of 1.7 g/cm³ in water-saturated NRVB samples and 1.1 g/cm³ in oven dried samples [19]. This lower value could reflect the difference in the methodology used; the Archimedes method determines bulk density, whereas pycnometry allows the determination of solid density as helium gas reaches all of the pores within the cement.

3.2. Chemical analysis (Hydration)

Figure 2a shows the isotherm generated for both NRVB formulations during hydration. It is possible to identify the four main hydration stages, as observed in a plain Portland cement. In comparison to Portland cement, the heat flow was lower (Figure 2b) by a factor of ~2 [46]. This is related to the much lower fraction of material undergoing hydration in the NRVB formulation. Comparing the two formulations of NRVB, it can be observed that the heat flow was very similar, however one subtle difference was observed: the curve corresponding to the sulfate depletion period (labelled 4, Figure 2a) of NRVB (Ind) indicates that it evidenced a more intense reaction than NRVB (Lab). One possible explanation is the formation of additional calcium monocarboaluminate hydrate in NRVB (Ind) as observed in XRD and NMR data (discussed below). In accordance with the particle size analysis (Figure 1a), determination of the surface area of the CaCO₃ sources indicated that the limestone flour used in NRVB (Ind) had a significantly higher surface area than CaCO₃ used in NRVB (Lab), with values of 5.2 ± 0.2 m²/g and 3.7 ± 0.2 m²/g, respectively. The higher surface area is responsible for a higher rate of calcite dissolution and also the availability of more nucleation sites, resulting in the formation of more hydration products [138]. Another factor to consider is the higher content of sulfate present in the

industrial raw material, which give rise to the observed differences; the limestone flour of NRVB (Ind) had 893 ppm sulfur, compared with 37 ppm in the hydrated lime of NRVB (Lab) (Table 2).

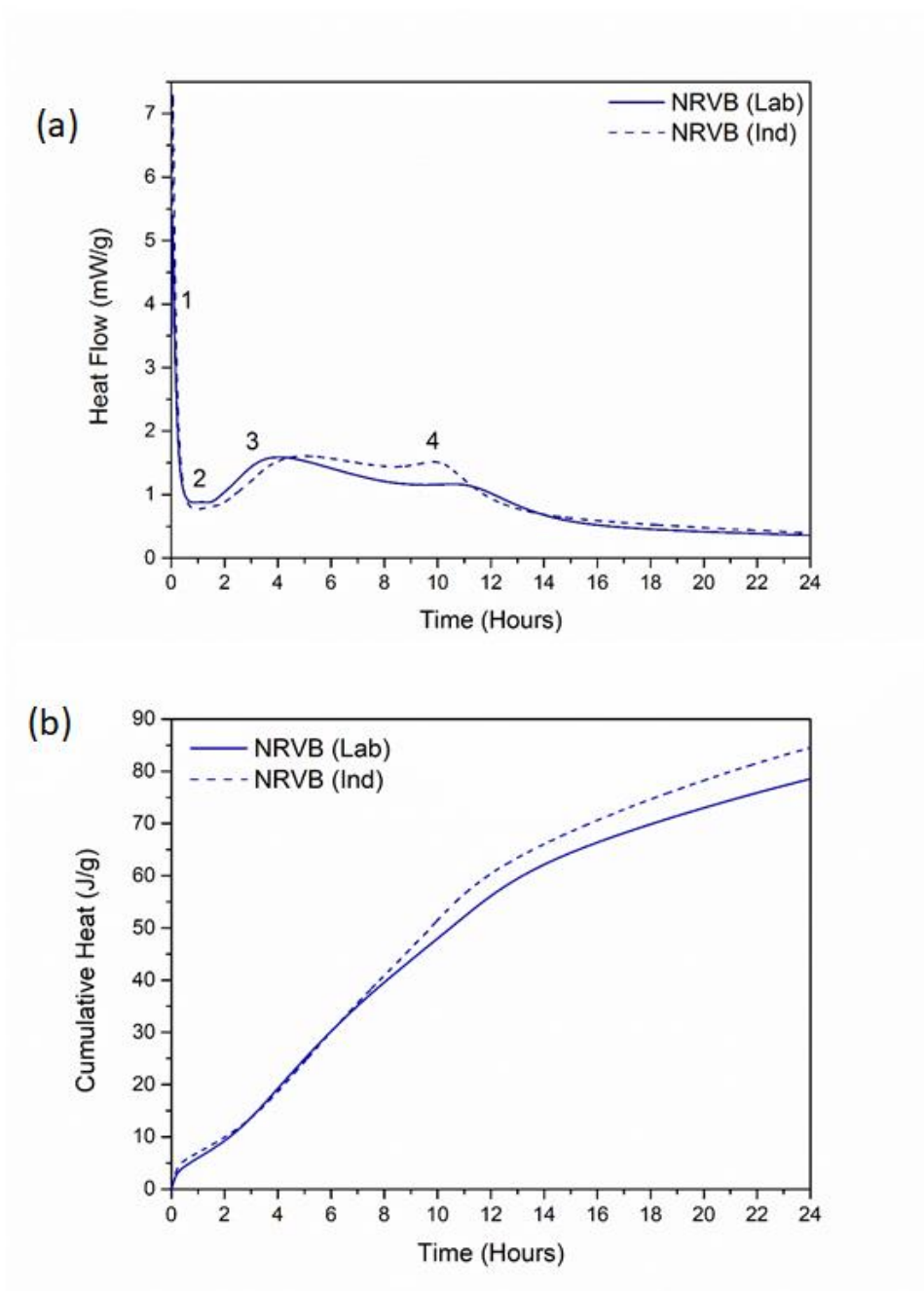
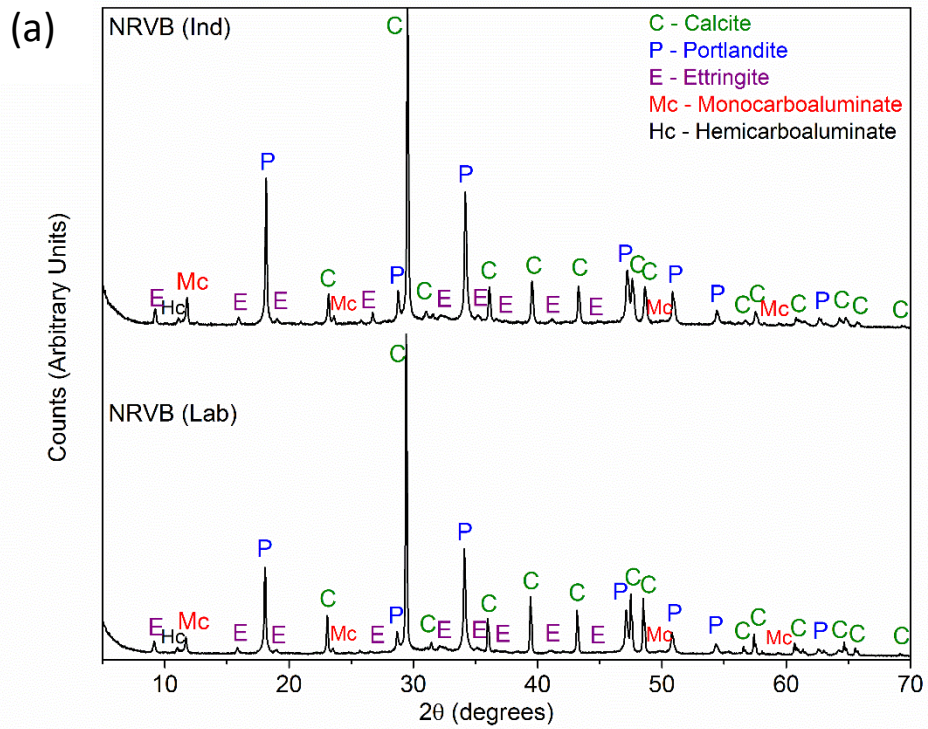


Fig. 3. (a) Isothermal calorimetry of NRVB (Lab) and NRVB (Ind). Thermal features identified are: (1) dissolution and C_3A reaction; (2) induction period; (3) reaction of alite and formation of calcium silicate hydrate; (4) sulfate depletion; (b) Cumulative heat of NRVB (Lab) and NRVB (Ind).

The main phases identified in the NRVB formulations by X-ray Diffraction (XRD) were calcite ($CaCO_3$; PDF 01-086-0174) and portlandite ($Ca(OH)_2$; PDF 01-072-0156) (Figure 3a). Ettringite

($\text{Ca}_6\text{Al}_2(\text{OH})_{12}(\text{SO}_4)_3 \cdot 26\text{H}_2\text{O}$; PDF 00-041-1451), calcium monocarboaluminate hydrate ($\text{Ca}_4\text{Al}_2(\text{OH})_{12}(\text{CO}_3)_3 \cdot 5\text{H}_2\text{O}$; PDF 01-087-0493) and calcium hemicarboaluminate hydrate ($\text{Ca}_4\text{Al}_2(\text{OH})_{12}[\text{OH}(\text{CO}_3)_{0.5}] \cdot 5.5\text{H}_2\text{O}$; PDF 00-041-0221) were also identified. These results are in agreement with those identified previously in NRVB cured at ambient temperature [26]. While the phase assemblage for each formulation was similar, subtle differences were observed in the peak intensities of several reflections; monocarboaluminate reflections were more intense in NRVB (Ind) than NRVB (Lab), while reflections of calcite were more intense in NRVB (Lab), which is also apparent in the XRD patterns corresponding to limestone flour and CaCO_3 (Figure 3b). These differences may be attributed to the chemical composition, particle size distribution and surface area of the CaCO_3 and limestone flour, however, preferential orientation cannot be ruled out, especially for layered or platy phases such as monocarboaluminate and portlandite.



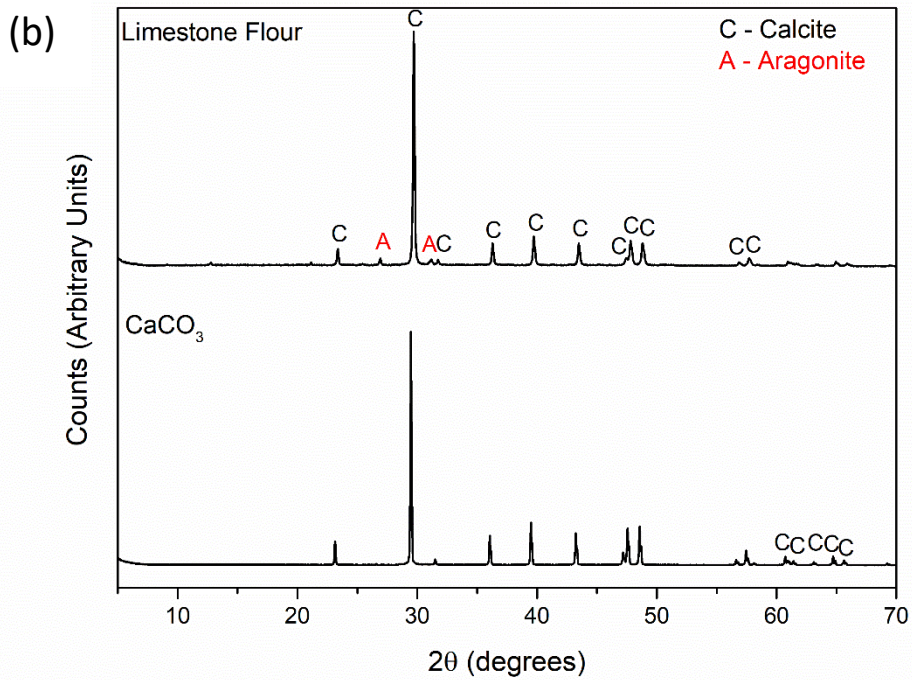


Fig 4. X-ray diffraction patterns for (a) NRVB (Lab) and NRVB (Ind) after 28 days of curing, and (b) Limestone Flour and CaCO₃. Crystalline phases are labelled.

TG-MS analysis confirmed the presence of these phases (Figure 4). The two peaks between 100 and 200 °C can be attributed to the presence of ettringite and monocarboaluminate, while the peaks between 400 to 500 °C, and 650 to 800 °C correspond to portlandite and calcite, respectively [27,30]. The same peaks were observed for both formulations, however for the NRVB (Ind) (Figure 4b) an additional peak was observed at ~ 650 °C, corresponding to the presence of magnesian calcite and supported by the presence of more Mg in NRVB (Ind) than NRVB (Lab) (Table 2).

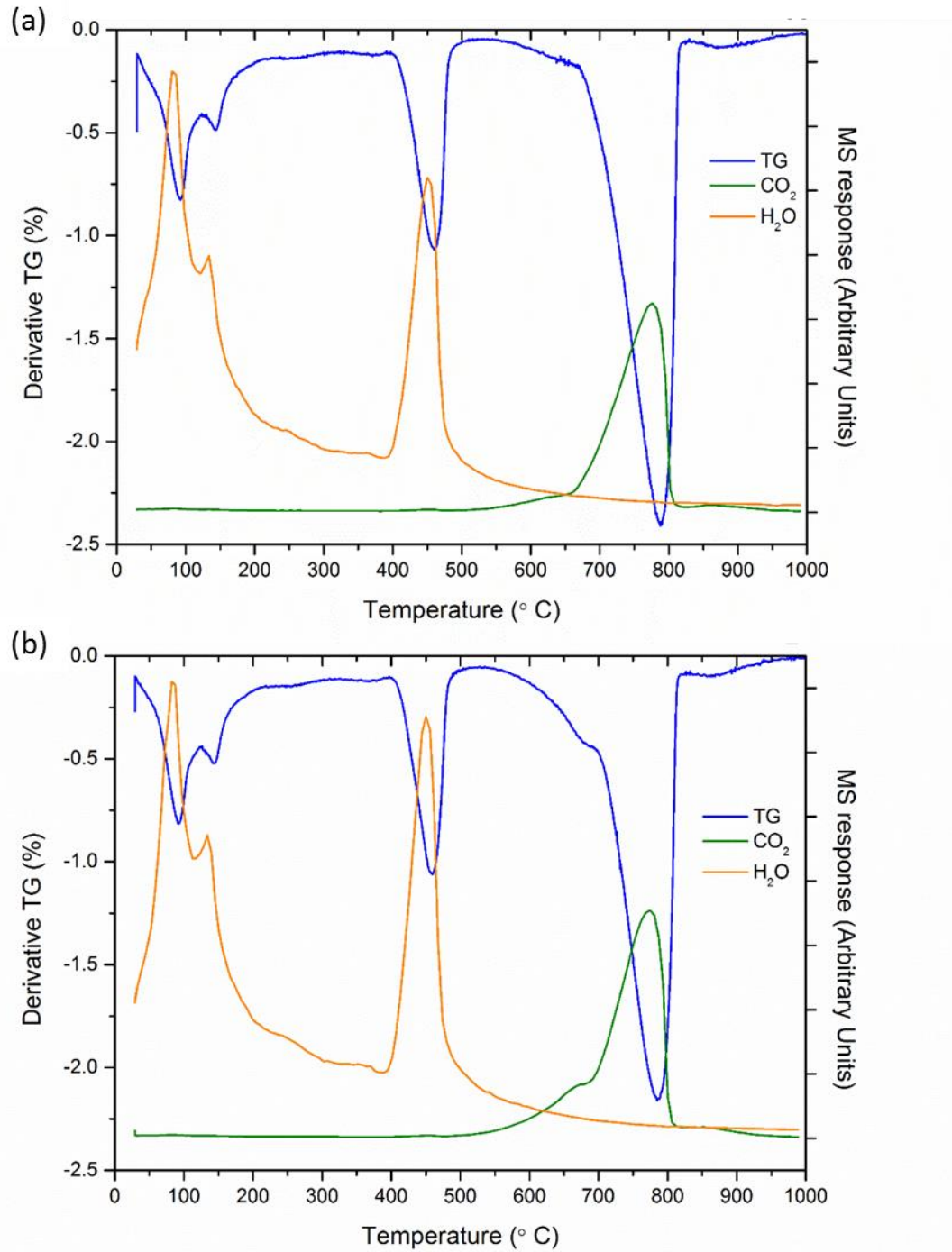


Fig. 5. TGA-MS for (a) NRVB (Lab); and (b) NRVB (Ind) after 28 days of curing.

Through SEM imaging and EDX analysis it was possible to identify the microstructure of the different hydrate phases, as shown in Figure 5. The large Ca-containing rhombohedral crystals (labelled A, Figure 5) are portlandite. The Ca and Si-rich phase surrounding portlandite crystals (labelled B, Figure 5) may be C-S-H. The areas containing higher concentrations of aluminium (labelled C, Figure 5)

suggest the presence of AFm phases. The areas labelled D are indicative of the presence of sulfate-containing AFm phases and/or ettringite, due to the higher concentration of both aluminium and sulfate. Comparing the SEM images of the two formulations, it is possible to identify the same hydrate phases, however the matrix of NRVB formulated with industrial materials has a more fine grained morphology, consistent with the analysis of limestone flour.

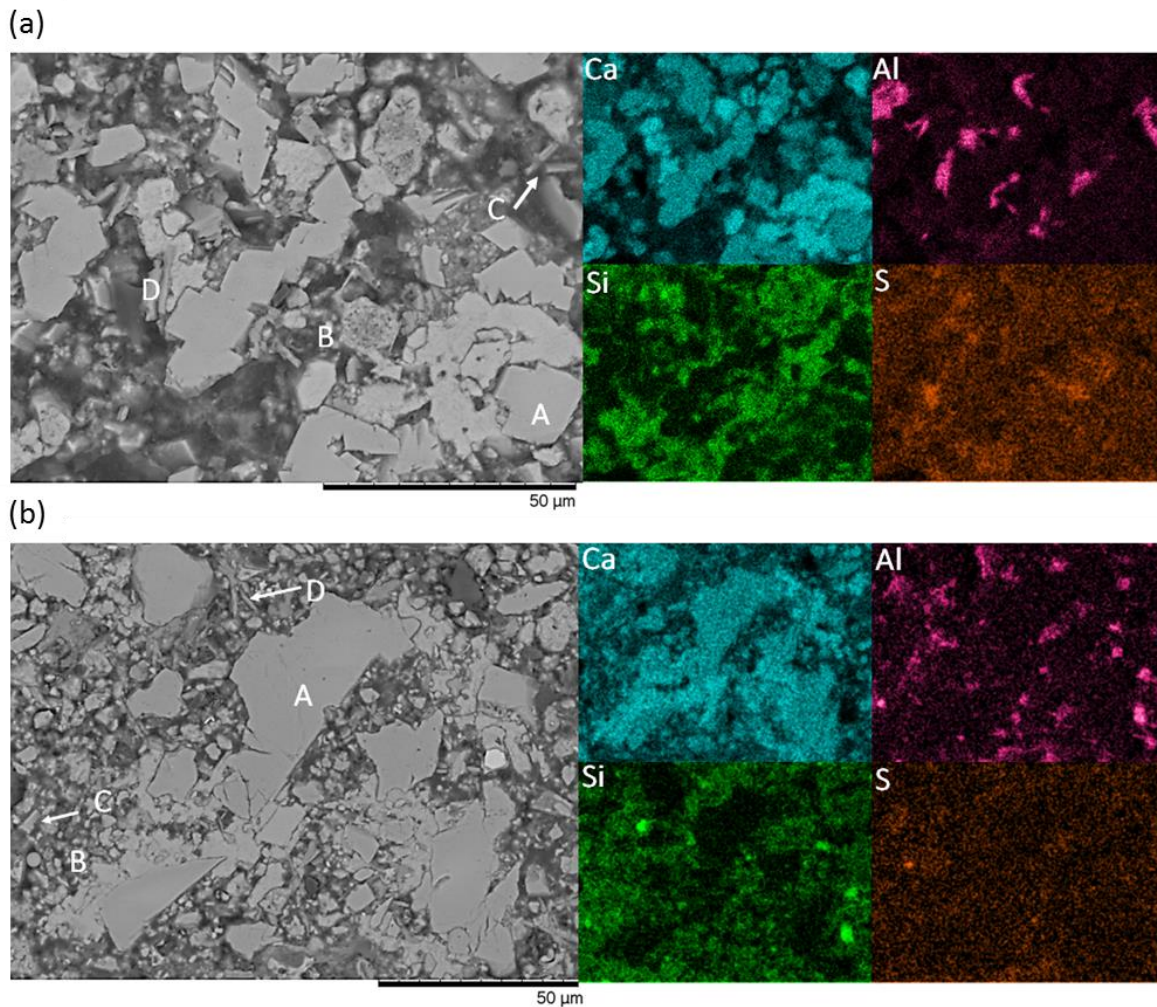


Fig. 6. BSE SEM micrograph of (a) NRVB (Lab) and (b) NRVB (Ind) at 28 days of curing, with the corresponding EDX maps.

In the ^{29}Si MAS NMR spectra (Figure 6) it was possible to identify some unreacted Portland cement through the presence of alite (chemical shifts -69 and -73.9 ppm) and belite (-71.2 ppm) [90] in both NRVB formulations. Contributions from Q^1 (-79 ppm), $\text{Q}^2(1\text{Al})$ (-83 ppm) and Q^2 (-84 ppm) silicate environments were also observed in both formulations; these chemical shifts are characteristic of C-S-H [139,140]. A small resonance was also observed at -90 ppm corresponding to $\text{Q}^3(1\text{Al})$. The presence of Al shows the incorporation of this element in the C-(A)-S-H [140]. Comparison of the two formulations reveals a small difference in the spectra (Figures 6a,b) between NRVB (Lab) and NRVB

(Ind); this is related to the intensity of Q^2 (-84 ppm), $Q^2(1Al)$ (-83 ppm) and Q^3 (1Al) (-90 ppm). A possible reason is the difference observed in the reactivity of the raw materials used in the two formulations, specifically the higher surface area of the limestone flour.

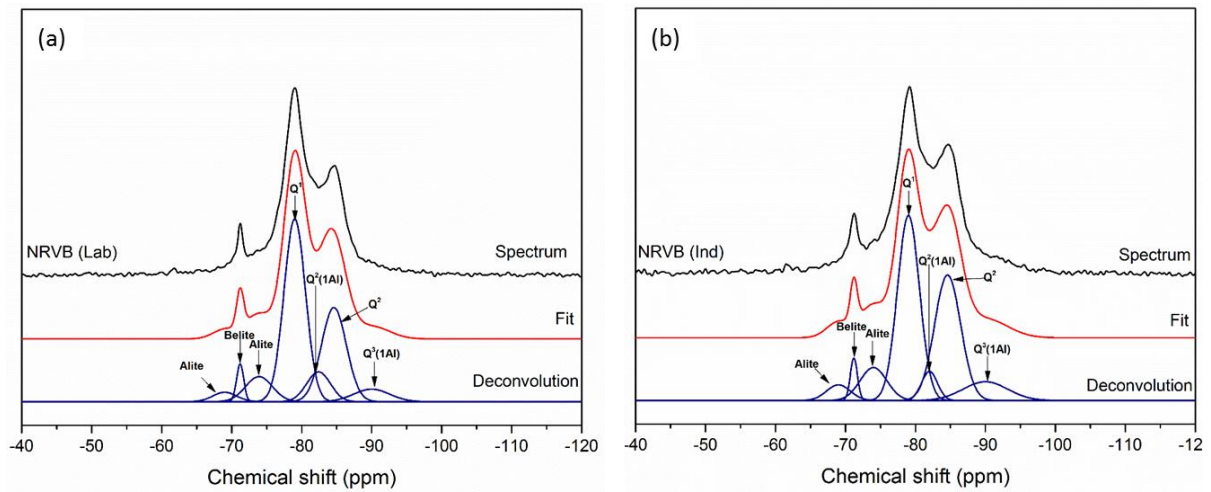


Fig. 7. ^{29}Si MAS NMR spectra, and deconvolution results, for (a) NRVB (Lab) and; (b) NRVB (Ind) after 28 days of curing.

Figure 7 shows the ^{27}Al NMR spectra of NRVB (Lab) and NRVB (Ind). The small peak observed at approximately -69 ppm (more evident for NRVB Ind) is attributed to the substitution of Al for Si in C-S-H (Lothenbach et al., 2008), in agreement with the observation of small peaks corresponding to $Q^2(1Al)$ and $Q^3(1Al)$ in the ^{29}Si MAS NMR spectra (Fig. 6). The peaks visible at approximately +13 and +9 ppm indicate the presence of octahedrally coordinated Al in ettringite and AFm phases. As stated previously in the literature (Lothenbach et al., 2008), it is not possible to distinguish between the different AFm phases due to the similar chemical shift. Comparing the two formulations, it is possible to see a difference in the proportion of ettringite and AFm phases present; the presence of more AFm in NRVB (Ind) is related to the higher availability of dissolved carbonate (higher surface area) and consequent formation of monocarboaluminate, in accordance with the results observed by isothermal calorimetry (Figure 2a) and XRD (Figure 3a).

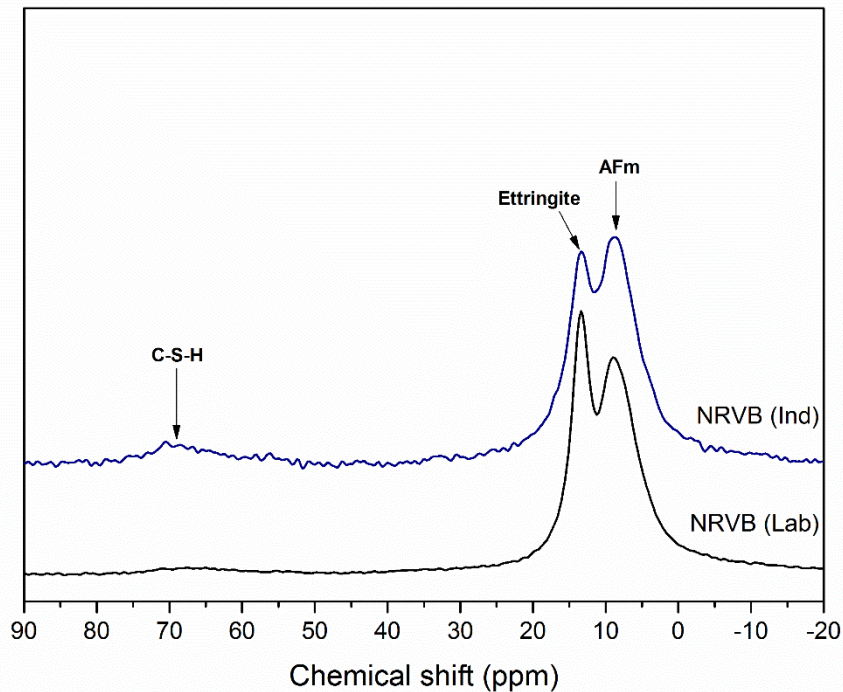


Fig. 8. ^{27}Al MAS NMR spectra of NRVB (Lab) and NRVB (Ind) after 28 days of curing.

3.3. Microstructure (Porosity)

A two-fold approach was applied to determine the porosity of the two NRVB formulations, to ensure all pore sizes were considered in the analysis. Mercury Intrusion Porosimetry, where it is understood that the pore diameters obtained correspond to the pore entry size and not the real size of the pore [90], was performed to compare the trend and changes in the pore size distribution between the two NRVB formulations [122]. Figure 8 shows the pore entry size diameter in relation to the cumulative intrusion for NRVB (Lab) and NRVB (Ind). The curve for NRVB (Lab) allocates essentially all of the pores to threshold pore entry radii below $0.8\ \mu\text{m}$, whereas for NRVB (Ind) the curve allocates all of the pores to sizes below $0.5\ \mu\text{m}$. This small difference is also evident in the total porosity obtained, where for NRVB (Lab) the percentage of total porosity obtained was $38 \pm 1\%$ and for NRVB (Ind) was $32 \pm 1\%$. It is important to note that, due to the low compressive strength of NRVB (around 8 MPa), this technique (which reaches pressures of 208 MPa in the instrument used in this study) might not be suitable to use to quantify the finer pores due to the potential for collapse of pores during analysis. This is expected to occur at $\sim 0.14\ \text{mL/g}$ of intrusion for NRVB (Lab) and at $\sim 0.15\ \text{mL/g}$ for NRVB (Ind) based on the strength data.

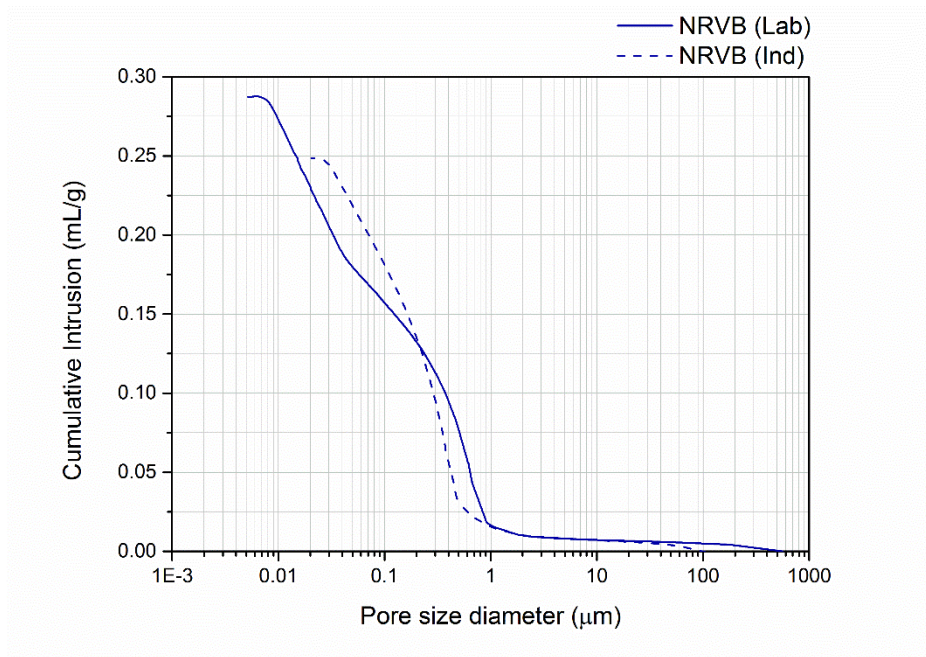


Fig. 9. Pore entry size distribution of NRVB (Lab) and NRVB (Ind) using MIP.

X-ray Computed Tomography was also used to study the porosity of NRVB. This technique has the advantage of being non-invasive and to allow three-dimensional reconstructions, but has limitations in spatial resolution. Figure 9 shows selected slices of the VOI for the two samples analysed. Quantitative analysis was performed using segmentation of the VOI. A threshold value was chosen based on the line shape of the image histograms, which show peaks of higher and lower absorption voxels, where the lower absorption voxels correspond to surrounding air and internal void space [130], allowing discrimination between pore space and binder phases (solid). The MIP results were used to guide the thresholding process, so the comparison between the results obtained by the two techniques is to some degree influenced by this.

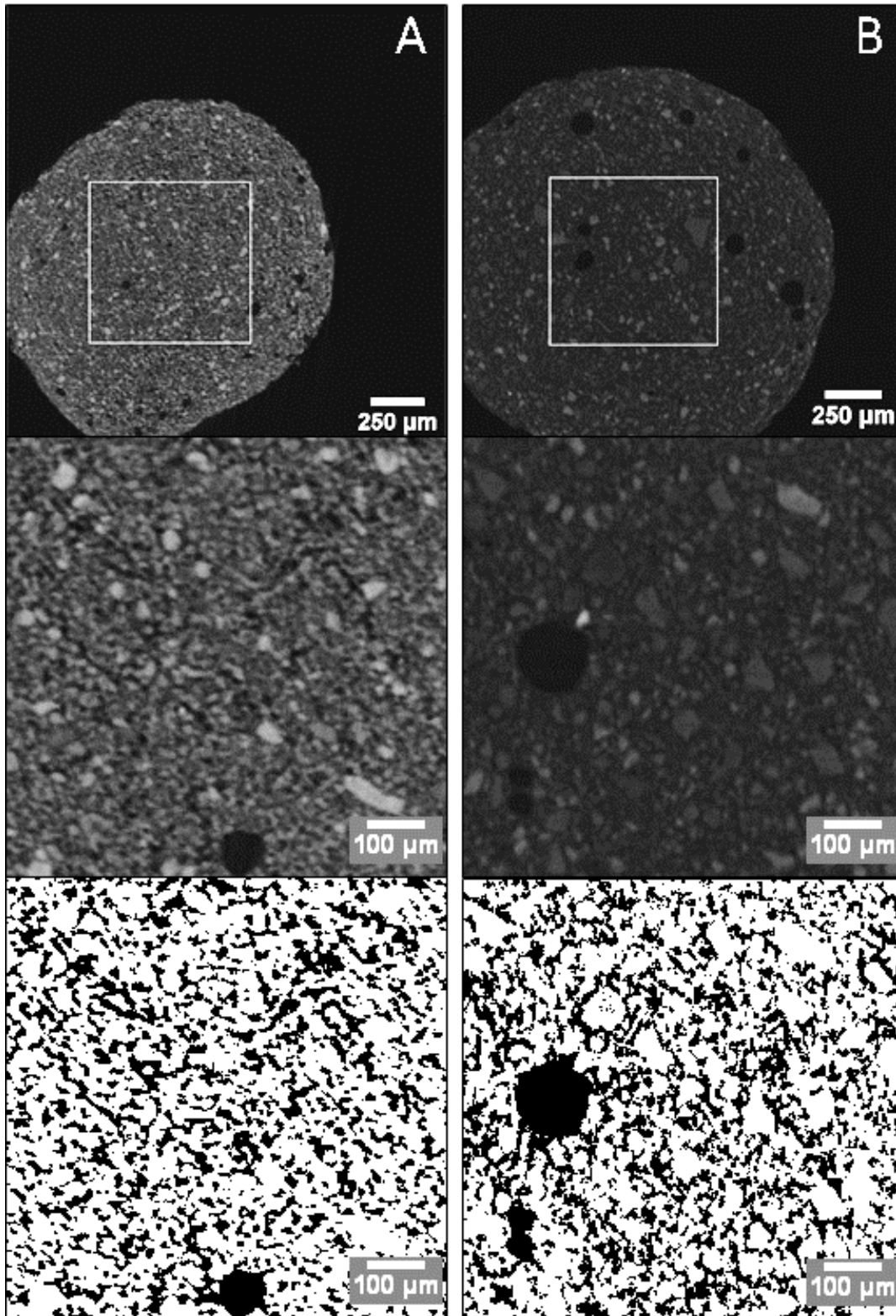


Fig. 9. XCT data of (a) NRVB (Lab) and (b) NRVB (Ind). Top: Slices through the tomographic reconstruction, showing the selected VOI (square); centre: selected slices through the VOI in each sample; and bottom: segmented into solid (white) and pore (black) regions.

No cracks were observed in the samples at this early age (28 days of hydration). The porosities obtained from tomographic data were 39 % for NRVB (Lab) and 35 % for NRVB (Ind). This difference is related, once more, to the difference observed in the hydration reaction of both cements, due to the smaller particle size and higher surface area of limestone flour.

The porosity results are in the same range presented by Heyes et al. [31] (~ 40 %), however they are lower than those reported by Francis et al. [19], where the porosity measured using MIP and nitrogen desorption was around 50 %. It is important to note, however, that by estimating the porosity using the density values measured in Francis et al. (~35 %), the results obtained in this paper are very similar. Differences in the characteristics between the raw materials used in the 1990's and those used in the present study are likely to be responsible for the differences observed. Also, in the early characterisation, there may have been more air bubbles that influenced the total porosity detected.

3.4. Influence of precursor materials on NRVB characteristics and properties

In summary, the differences in the surface area and chemical composition of the raw materials, particularly CaCO_3 and limestone flour, impacted the properties of the NRVB formulations. In addition to differences between the NRVB formulations investigated here, we also observed differences between the results obtained in this study when compared to the characterisation performed in the early 1990's, likely due to differences in the raw material and other unspecified properties. The impact of raw material selection on properties required for geological disposal are discussed below.

Workability, compressive strength and setting time were affected by the use of different raw materials. In the present study, the higher surface area of limestone flour resulted in a higher workability and lower compressive strength for NRVB formulated with industrial raw materials when compared to NRVB formulated with laboratory raw materials. When comparing our data with those from the early 1990's [19], the workability and setting time were a factor of ~ 1.5 lower in the present study, which we attribute to differences in fineness of the precursor materials used. The differences observed should not strongly influence the ability for the backfill to be poured within vaults, and the compressive strength values obtained are low enough to allow re-excavation of the vaults if necessary.

With regards to the long-term behaviour of NRVB, differences in the rate of hydration, the quantity of different hydrate phases, and the hydrate phase assemblage may influence the buffering capacity of the material. In the present study, the rate of hydration was faster in NRVB formulated with industrial raw materials due to the high surface area of limestone flour. The quantity of monocarboaluminate was also greater, which is a consequence of the higher availability and reactivity of dissolved carbonate in limestone flour. Furthermore, small differences in the chemical composition of limestone flour, for example, the presence of S (and, to a lesser extent, Mg) influenced the rate of hydration. This may have

implications for the hydrate phase assemblage at timescales longer than 28 days of curing; further work is required to investigate this.

Through ^{29}Si MAS NMR spectroscopy we have shown the incorporation of aluminium in the C-(A)-S-H of NRVB, and that the choice of raw material influences the quantity incorporated (Figs. 6 and 7). Previous studies have shown that aluminium incorporated into amorphous silica reduces significantly the dissolution rate, even in high alkaline environments [224–226]. Therefore, the buffering behaviour of the repository may not occur on the predicted time scale, or result in a pH comparable to that estimated when considering C-S-H dissolution only [1].

Finally, we observed that the choice of raw material also influences the 28-day porosity of the final NRVB, which is associated with the differences in hydration reaction outlined above; the formation of more hydrate products in NRVB formulated with industrial materials resulted in a slightly lower porosity. Significantly, the porosity measured in this study (~32 – 39%) was much lower than that reported by Francis et al. (1997), which was 50%. In a repository environment, such a difference may strongly influence the rate of groundwater ingress and the egress of gas, which are key design functions of NRVB.

4. Conclusion

The use of different raw materials in the synthesis of NRVB has been investigated, and the differences in workability, setting time, hydration and porosity analysed. These results are compared with those previously reported in the literature for this material, and the potential effects of differences in raw materials on the final use of NRVB have been explored. Surface area, fineness and chemical composition of the raw materials, particularly limestone flour, have been shown to influence, to a small extent, final backfill properties including setting time, compressive strength and buffering capacity. The effects on porosity seem to be significant, but this may also be due to differences in analysis techniques applied to investigate this property. This study highlights the importance of a detailed characterisation of raw materials used in the formulation of NRVB for use in a geological disposal facility, especially in light of concerns surrounding security of cement supply for future applications.

Acknowledgements

The authors wish to acknowledge funding for this research from Radioactive Waste Management and the European Commission Horizon 2020 Research and Training Programme, Cebama, of the European Atomic Energy Community (EURATOM), under grant agreement number 662147. CLC also wishes to acknowledge EPSRC for the award of an ECR Fellowship (EP/N017374/1). This research was

performed in part at the MIDAS Facility, at the University of Sheffield, which was established with support from the Department of Energy and Climate Change. Solid-state NMR spectra (^{27}Al , ^{29}Si) were obtained at the EPSRC UK National Solid-state NMR Service at Durham, and we thank Dr. David Apperley for his assistance in collection and interpretation of the results. X-ray microtomography is funded by the Scottish Funding Council's Oil and Gas Innovation Centre.

Appendix II

Static experiments performed with NRVB in contact with groundwater

From the analysis of the NRVB samples, it was possible to observe that similar results to the ones observed in the semi-dynamic experiment were obtained in this static experiment. In Figure AI.1a, XRD pattern of NRVB samples that were in contact with granitic, saline and clay groundwater for 18 months are compared to NRVB control sample that was cured for the same amount of time, but without contact with groundwater. The disappearance of the peak corresponding to portlandite is observed for all the samples, and correlates well with the results obtained through TGA (Figure AI.1b), where the disappearance of the peak at around 450 °C, corresponding to portlandite, is visible. In addition, it is possible to observe an increase of the peak intensity of ettringite for the samples that were in contact with saline and clay groundwater (Figure AI.1a). Semi-quantitative analysis of the XRD data showed an increase of the relative concentration from 9 ± 2 wt% for the control sample (cured for 18 months without contact with groundwater) to 28 ± 2 wt% for the sample that was in contact with saline groundwater and 35 ± 2 wt% for the sample that was in contact with clay groundwater. That increase is evident in the TG data, being the peak corresponding to ettringite at around 100 °C (Figure AI.1b). It is also evident that for the NRVB samples that were in contact with clay groundwater more ettringite was formed, which is due to the higher S content in this groundwater composition (480.9 mg/L) when compared to the saline (128.2 mg/L).

Additionally, in the XRD pattern it is possible to observe a decrease, in the case of the samples that were in contact with granitic groundwater, or the disappearance, in the case of the other samples, of the peak corresponding to monocarboaluminate (Figure AI.1a). As observed in the semi-dynamic experiment, the high content of sulphur in the saline and clay groundwater compositions led to the formation of more ettringite and consequently the destabilisation of monocarboaluminate [147].

In the Figure AI.1b, an extra small peak is observed at around 325 °C for both samples that were in contact with saline and clay groundwater, corresponding to the formation of brucite. The increase of the formation of carbonates in the samples that were in contact with the different groundwaters is observed between 550 and 800 °C, with the appearance of different polymorphs of calcite [192].

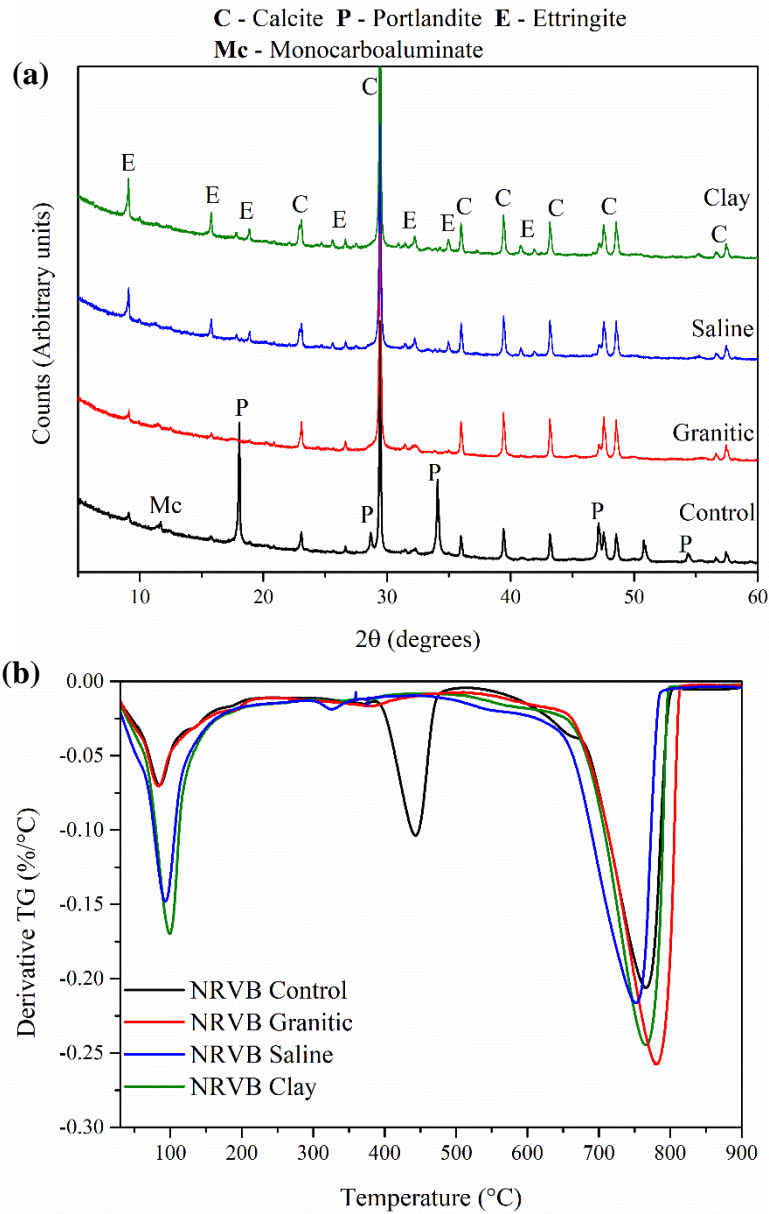


Figure AI.0.1. (a) XRD patterns and (b) TGA of NRVB samples that were placed in contact with granitic, saline and clay groundwater for 18 months.

As it was observed in the semi-dynamic experiment, once NRVB samples were placed in contact with the three groundwater compositions an increase of the pH was observed. No variation of the pH was observed throughout the experiment, being the pH around 12.3 ± 0.2 , 12.1 ± 0.2 and 12.0 ± 0.3 , for the samples that were in contact with granitic, saline and clay groundwater respectively. This stabilisation of the pH is indicative that a steady state has been reached in this experiment [74,227].

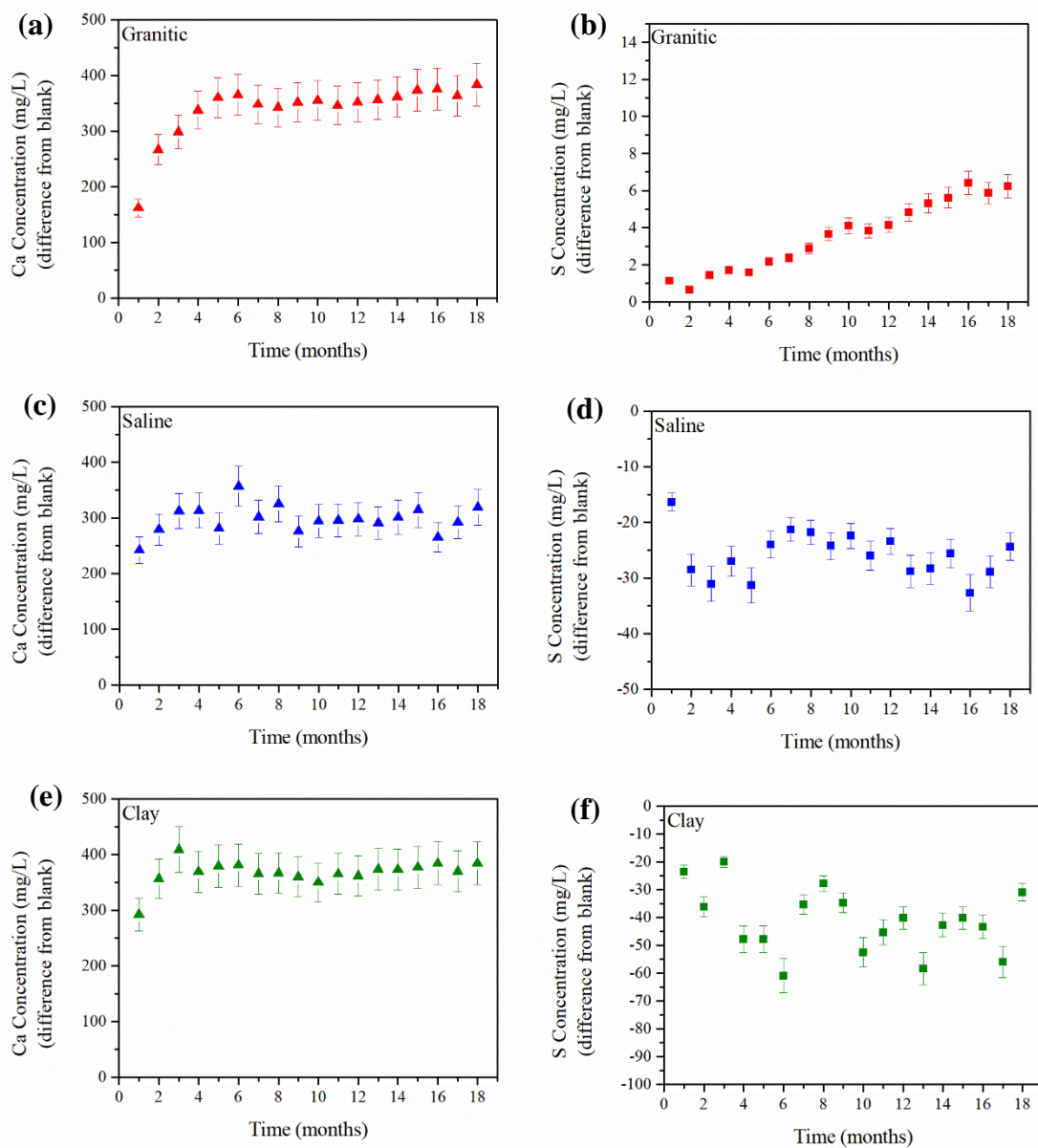


Figure AI.0.2. Ca and S concentrations in solution (mg/L) obtained through the difference from blank for NRVB samples that were in contact with granitic (a and b), saline (c and d) and clay (e and f) groundwater for 18 months. Errors were calculated using ICP-OES instrument error.

Figure AI.2 demonstrates ICP-OES analysis of the solutions performed every month for 18 months of experiment. In this figure, it is shown the results for the calcium and sulphur concentration present in the different groundwater compositions.

An initial increase of the calcium concentration is observed for all of the samples, reaching a plateau after around 3 months of the experiment, meaning that the calcium concentration becomes constant as

a function of time. The reaching of an equilibrium state in a static experiment is expected and has been previously observed in different studies, including some modelling results [37,72,74,227,228].

Differences are observed in the sulphur concentration in solution for the different groundwater compositions. In the case of the granitic groundwater, a linear leaching of the sulphur is observed over time, reaching an equilibrium after 14 months of experiment. On the other hand, an uptake of this element is observed in the case of saline and clay groundwater. These differences observed between the different solutions is due to the initial concentration of sulphur present in the blanks of the different groundwater compositions. In the case of granitic groundwater, the concentration of sulphur present in the blank is very small, about 0.1 mmol/L, therefore a leaching of this element is observed until a chemical equilibrium between the cement and the groundwater is reached. Whereas, in the case of the saline and clay groundwaters, the concentration of sulphur present in the blanks is much higher, around 4 and 15 mmol/L, respectively, as mentioned before. Consequently, an uptake of this element is observed throughout the experiment, hence the formation of more ettringite observed in these samples (Figure AI.1).

In the static experiment, the conditions of the system will approach inevitably an equilibrium between the mineral assemblage and the solution, whereas in the semi-dynamic experiment a constant change of the gradient will lead to a more aggressive reaction between the different elements. This key difference is what makes the results observed in the solution chemistry slightly different. However, the overall mineralogy results obtained for the NRVB samples in the different groundwater compositions is very similar to the results obtained in the semi-dynamic experiment. Meaning that, although the interaction will occur more slowly and an equilibrium is reached in a static experiment, a similar outcome is observed, with the main aim of buffering the pH to values of around 12 being reached in both experiment set-ups.

Appendix III

Static experiment performed with Cebama Reference Cement paste in contact with groundwater

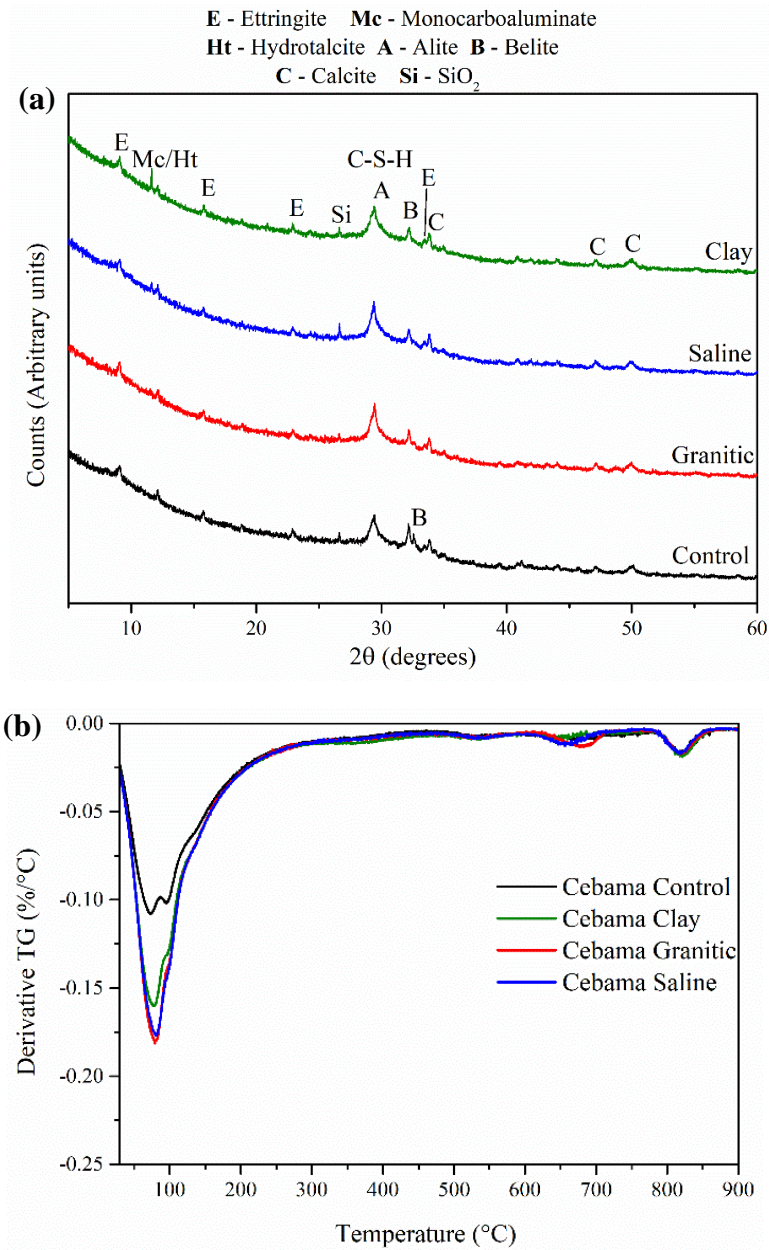


Figure AII.0.1. (a) XRD patterns and (b) TGA of Cebama reference cement paste samples that were placed in contact with granitic, saline and clay groundwater for 18 months.

Figure AII.1 display the XRD pattern and TG analysis of the Cebama reference cement paste samples after 18 months in contact with granitic, saline and clay groundwater compared with Cebama control sample after 18 months of curing. Similar results to the ones observed in the semi-dynamic experiment are obtained here, where it is possible to observe an increase of the hydration reaction for all of the samples. In the XRD pattern (Figure AII.1a), a decrease of the peak intensity corresponding to belite (at around 32° and 32.5° 2θ) is visible. In the case of the sample that was in contact with clay groundwater an increase of the peak corresponding to hydrotalcite is observed, which might be related with the higher amount of magnesium present in this groundwater composition when compared to the granitic and saline groundwater.

In the TG graph (Figure AII.1b), an increase of the intensity of the peak between 50 and 100 °C, corresponding to the loosely bound water within the C-S-H, and the peaks between 100 and 150 °C, corresponding to AFt and AFm phases, is observed. As observed in the semi-dynamic experiment, this increase is indicative of an increase of the hydration, which is expected once more water (in this case groundwater) is in contact with the Cebama reference cement paste samples.

At each time point of sampling, the pH of the different solutions was measured and an increase was observed for all the solutions. In the case of the samples that were in contact with granitic and clay groundwater the pH was kept constant throughout the experiment in around 9.5 ± 0.3 and 10 ± 0.3 , respectively. In the case of the samples that were in contact with saline groundwater the pH was kept around 9 ± 0.3 . It is interesting to point out that, no variation of the pH is observed during the experiment, which is opposite to the observed in the semi-dynamic experiment, where a reduction of the pH was observed over time. This is due to the fact that a lower chemical gradient is being used in this static experiment, and so a steady rate of dissolution is expected.

Since, for this static experiment, the solution chemistry was analysed every month, interesting results are expected, as no replacement of the groundwater was performed. ICP-OES results for Ca and Mg concentration for all groundwater compositions are shown in Figure AII.2.

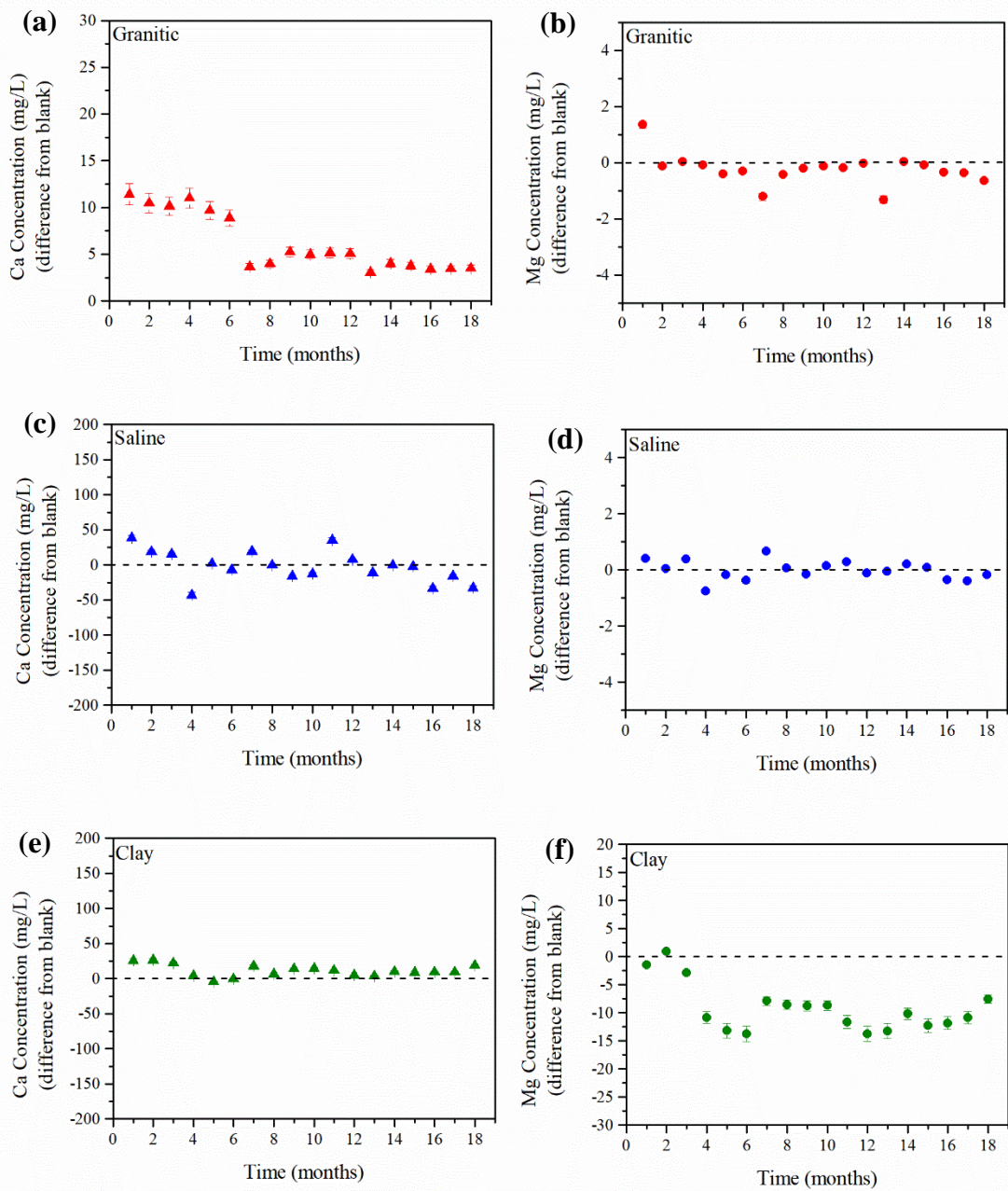


Figure AII.0.2. Ca and Mg concentrations in solution (mg/L) obtained through the difference from blank for Cebama reference cement paste samples that were in contact with granitic (a and b), saline (c and d) and clay (e and f) groundwater for 18 months. Errors were calculated using ICP-OES instrument error.

In terms of Ca concentration, a continuous leaching of this element is observed mainly in the granitic groundwater and in a small extent in the clay groundwater, whereas for saline groundwater a combination of leaching and uptake is observed. Concerning Mg concentration, and since the pH for all groundwater compositions was below 10, an uptake of this element was observed, mainly for the

clay groundwater. These results show that a chemical equilibrium is reached between the elements present in the groundwater and in the cementitious material, i.e. the system can be assumed to be at a steady state when the different element concentrations become constant as a function of time. With the Cebama reference cement paste, it seems that the steady state is reached in the first few months for all groundwater compositions, with just very small variabilities at certain time points. This might be related to the fact that this cementitious material is considered to be very dense and have low porosity, therefore interaction with the groundwater will be limited.

These results are slightly different from the ones observed in the semi-dynamic experiment. With continuous replacement of the groundwater, a constant change of the elemental gradient is observed, and with this a quicker reaction of the different chemical elements. Whereas, in the static experiment, the gradient between cement porewater and the groundwater will decrease, and so the leaching/uptake of the different elements will slow down.

A previous study, where Portland cement was placed in contact with NaCl and MgCl₂ rich solutions in a static experiment, observed that equilibrium conditions were reached [72]. Other studies, including modelling approaches, found the same conclusions, i.e. in the beginning of a static experiment the initial leaching/uptake rate will be high, and then these rates will slow down with time [37,74,227,228].

References

- [1] Nuclear Decommissioning Authority, Geological Disposal: Near-Field Evolution Status Report, 2010. Report no. NDA/RWMD/010.
- [2] Nuclear Decommissioning Authority, Geological Disposal: An overview of the generic Disposal System Safety Case, 2010. Report no. NDA/RWMD/033.
- [3] M.I. Ojovan, W.E. Lee, An Introduction to Nuclear Waste Immobilisation, Elsevier, Oxford, UK, 2005.
- [4] C.L. Corkhill, N.C. Hyatt, Nuclear Waste Management, IOP Publishing Ltd, 2018. doi:10.1088/978-0-7503-1638-5.
- [5] Nuclear Decommissioning Authority, Geological Disposal The 2013 Derived Inventory, 2015. Report no. NDA/RWM/120.
- [6] B. Batchelor, Overview of waste stabilization with cement, *Waste Manag.* 26 (2006) 689–698. doi:10.1016/j.wasman.2006.01.020.
- [7] P.B. Bamforth, G.M.N. Baston, J.A. Berry, F.P. Glasser, T.G. Heath, C.P. Jackson, D. Savage, S.W. Swanton, Cement materials for use as backfill , sealing and structural materials in geological disposal concepts . A review of current status, (2012) 1–235. SERCO/005125/001 Issue 3.
- [8] C.R. Wilding, The performance of cement based systems, *Cem. Concr. Res.* 22 (1992) 299–310. doi:10.1016/0008-8846(92)90069-8.
- [9] J.H. Sharp, J. Hill, N.B. Milestone, E.W. Miller, Cementitious Systems for Encapsulation of Intermediate Level Waste, in: 9th ASME Int. Conf. Radioact. Waste Manag. Environ. Remediat. Vol. 1, 2, 3, ASME, 2003: pp. 1425–1433. doi:10.1115/ICEM2003-4554.
- [10] Nuclear Decommissioning Authority, Plutonium credible options analysis, 2010. Report no. SMS/TS/B1-PLUT/002/A.
- [11] J. Cronin, N. Collier, Corrosion & Expansion of Grouted Magnox, 2011. NNL (11) 11524 Issue 3.
- [12] Radioactive Waste Management, RWM HAW Innovation and Delivery: A Review of Cement Powders Security of Supply, Specifications and Disposability Issues, 2016. Report no. NDA/RWM/144.
- [13] E.E. Rice, R.S. Denning, A.L. Friedlander, Preliminary Risk Assessment for Nuclear Waste Disposal in Space - Volume II, 1982.
- [14] International Atomic Energy Agency, The Long Term Storage of Radioactive Waste: Safety and Sustainability, 2003.
- [15] A.J. Beswick, F.G.F. Gibb, K.P. Travis, Deep borehole disposal of nuclear waste : engineering challenges, *Proc. Inst. Civ. Eng.* (2014) 1–20. doi:http://dx.doi.org/10.1680/ener.13.00016.
- [16] Nuclear Decommissioning Authority, Geological Disposal: How the world is dealing with its radioactive wastes, 2013.
- [17] P. Sellin, O.X. Leupin, The use of clay as an engineered barrier in radioactive-waste management - A review, *Clays Clay Miner.* 61 (2014) 477–498.

doi:10.1346/CCMN.2013.0610601.

- [18] Nuclear Decommissioning Authority, Geological Disposal: Geosphere status report, 2010. Report no. NDA/RWMD/037.
- [19] A.J. Francis, R. Cather, I.G. Crossland, Nirex Safety Assessment Research Programme: Development of the Nirex Reference Vault Backfill; Report on Current Status in 1994, 1997. Report no: S/97/014.
- [20] Nuclear Decommissioning Authority, Retrieval of Waste Emplaced in a Geological Disposal Facility, 2010. Doc no RWMDPP03 December.
- [21] United Kingdom Nirex Limited, Context Note 4.1: Retrieval, United Kingdom Nirex Ltd. (2005). Number: 484424 December.
- [22] E.J. Butcher, J. Borwick, N. Collier, S.J. Williams, Long term leachate evolution during flow-through leaching of a vault backfill (NRVB), *Mineral. Mag.* 76 (2012) 3023–3031. doi:10.1180/minmag.2012.076.8.18.
- [23] A.R. Hoch, G.M.N. Baston, F.P. Glasser, F.M.I. Hunter, V. Smith, Modelling evolution in the near field of a cementitious repository, *Mineral. Mag.* 76 (2012) 3055–3069. doi:10.1180/minmag.2012.076.8.21.
- [24] T.R. Holland, W.M. Tearle, Serco Assurance A Review of NRVB Mineralogy, Serco Assur. (2003).
- [25] T. Matschei, B. Lothenbach, F.P. Glasser, Thermodynamic properties of Portland cement hydrates in the system CaO-Al₂O₃-SiO₂-CaSO₄-CaCO₃-H₂O, *Cem. Concr. Res.* 37 (2007) 1379–1410. doi:10.1016/j.cemconres.2007.06.002.
- [26] M. Felipe-Sotelo, J. Hinchliff, N. Evans, P. Warwick, D. Read, Sorption of radionuclides to a cementitious backfill material under near-field conditions, *Mineral. Mag.* 76 (2012) 3401–3410. doi:10.1180/minmag.2012.076.8.53.
- [27] J. Sun, Carbonation kinetics of cementitious materials used in the geological disposal of radioactive waste, 2011. PhD thesis; <http://discovery.ucl.ac.uk/1306875/>.
- [28] G. Menéndez, V. Bonavetti, E.F. Irassar, Strength development of ternary blended cement with limestone filler and blast-furnace slag, *Cem. Concr. Compos.* 25 (2003) 61–67. doi:10.1016/S0958-9465(01)00056-7.
- [29] I.G. Crossland, S.P. Vines, Why a cementitious repository, 2001. Nirex Report N/034.
- [30] B. Lothenbach, F. Winnefeld, C. Alder, E. Wieland, P. Lunk, Effect of temperature on the pore solution, microstructure and hydration products of Portland cement pastes, *Cem. Concr. Res.* 37 (2007) 483–491. doi:10.1016/j.cemconres.2006.11.016.
- [31] D.W. Heyes, E.J. Butcher, J. Borwick, A.E. Milodowski, L.P. Field, S.J. Kemp, I. Mounteney, S.A. Bernal, C.L. Corkhill, N.C. Hyatt, J.L. Provis, L. Black, Demonstration of Carbonation of the NRVB, *Natl. Nucl. Lab.* 16 (2015).
- [32] A.W. Harris, A. Atkinson, P.A. Claisse, Transport of gases in concrete barriers, *Waste Manag.* 12 (1992) 155–178. doi:10.1016/0956-053X(92)90046-L.
- [33] B.T. Swift, P.B. Bamforth, A.R. Hoch, C.P. Jackson, D.A. Roberts, G.M.N. Baston, Cracking, Flow and Chemistry in NRVB, 2010. SERCO/TAS/000505/001.
- [34] I.G. Crossland, Cracking of the Nirex Reference Vault Backfill: A review of its Likely Occurrence and Significance, 2007. Crossland Report CCL/2007/1.
- [35] A.W. Harris, M.C. Manning, W.M. Tearle, C.J. Tweed, Testing of models of the dissolution of

- cements - Leaching of synthetic CSH gels, *Cem. Concr. Res.* 32 (2002) 731–746. doi:10.1016/S0008-8846(01)00748-7.
- [36] C.S. Walker, S. Sutou, C. Oda, M. Mihara, A. Honda, Calcium silicate hydrate (C-S-H) gel solubility data and a discrete solid phase model at 25 °C based on two binary non-ideal solid solutions, *Cem. Concr. Res.* 79 (2016) 1–30. doi:10.1016/j.cemconres.2015.07.006.
- [37] A.W. Harris, A. Atkinson, V. Balek, K. Brodersen, G.B. Cole, A. Haworth, Z. Malek, A.K. Nickerson, K. Nilsson, A.C. Smith, The Performance of Cementitious Barriers in Repositories, *Nucl. Sci. Technol.* (1994). EUR 17643.
- [38] G. Purser, A.E. Milodowski, J.F. Harrington, C.A. Rochelle, A. Butcher, D. Wagner, Modification to the flow properties of repository cement as a result of carbonation, *Procedia Earth Planet. Sci.* 7 (2013) 701–704. doi:http://dx.doi.org/10.1016/j.proeps.2013.03.102.
- [39] A. Morandea, M. Thiery, P. Dangla, Investigation of the carbonation mechanism of CH and C-S-H in terms of kinetics, microstructure changes and moisture properties, *Cem. Concr. Res.* 56 (2014) 153–170. doi:10.1016/j.cemconres.2013.11.015.
- [40] F.P. Glasser, Progress in the immobilization of radioactive wastes in cement, *Cem. Concr. Res.* 22 (1992) 201–216. doi:10.1016/0008-8846(92)90058-4.
- [41] U. Berner, D.A. Kulik, G. Kosakowski, Geochemical impact of a low-pH cement liner on the near field of a repository for spent fuel and high-level radioactive waste, *Phys. Chem. Earth.* 64 (2013) 46–56. doi:10.1016/j.pce.2013.03.007.
- [42] J.L.G. Calvo, A. Hidalgo, C. Alonso, L.F. Luco, Development of low-pH cementitious materials for HLRW repositories: Resistance against ground waters aggression, *Cem. Concr. Res.* 40 (2010) 1290–1297. doi:10.1016/j.cemconres.2009.11.008.
- [43] S. Ramírez, J. Cuevas, R. Vigil, S. Leguey, Hydrothermal alteration of “La Serrata” bentonite (Almeria, Spain) by alkaline solutions, *Appl. Clay Sci.* 21 (2002) 257–269. doi:10.1016/S0169-1317(02)00087-X.
- [44] C. Cau Dit Coumes, S. Courtois, D. Nectoux, S. Leclercq, X. Bourbon, Formulating a low-alkalinity, high-resistance and low-heat concrete for radioactive waste repositories, *Cem. Concr. Res.* 36 (2006) 2152–2163. doi:10.1016/j.cemconres.2006.10.005.
- [45] M. Codina, C. Cau-dit-Coumes, P. Le Bescop, J. Verdier, J.P. Ollivier, Design and characterization of low-heat and low-alkalinity cements, *Cem. Concr. Res.* 38 (2008) 437–448. doi:10.1016/j.cemconres.2007.12.002.
- [46] D. Jansen, F. Goetz-Neunhoeffler, B. Lothenbach, J. Neubauer, The early hydration of Ordinary Portland Cement (OPC): An approach comparing measured heat flow with calculated heat flow from QXRD, *Cem. Concr. Res.* 42 (2012) 134–138. doi:10.1016/j.cemconres.2011.09.001.
- [47] R. Snellings, G. Mertens, J. Elsen, Supplementary Cementitious Materials, *Rev. Mineral. Geochemistry.* 74 (2012) 211–278. doi:10.2138/rmg.2012.74.6.
- [48] K.L. Scrivener, B. Lothenbach, N. De Belie, E. Gruyaert, J. Skibsted, R. Snellings, A. Vollpracht, TC 238-SCM: hydration and microstructure of concrete with SCMs, *Mater. Struct.* 48 (2015) 835–862. doi:10.1617/s11527-015-0527-4.
- [49] B. Lothenbach, K. Scrivener, R.D. Hooton, Supplementary cementitious materials, *Cem. Concr. Res.* 41 (2011) 1244–1256. doi:10.1016/j.cemconres.2010.12.001.
- [50] I.G. Richardson, G.W. Groves, Microstructure and microanalysis of hardened cement pastes involving ground granulated blast-furnace slag, *J. Mater. Sci.* 28 (1993) 265–277. doi:10.1007/BF00349061.
- [51] S.C. Pal, A. Mukherjee, S.R. Pathak, Investigation of hydraulic activity of ground granulated

- blast furnace slag in concrete, *Cem. Concr. Res.* 33 (2003) 1481–1486. doi:10.1016/S0008-8846(03)00062-0.
- [52] H.F. Taylor, *Cement chemistry*, 2nd ed., Thomas Telford Publishing, 1997.
- [53] M. Moranville-Regourd, *Cements Made from Blastfurnace Slag*, in: P.C. Hewlett (Ed.), *Lea's Chem. Cem. Concr.*, 4th ed., Elsevier Science & Technology Books, 1998: pp. 637–678.
- [54] R. Taylor, I.G. Richardson, R.M.D. Brydson, Composition and microstructure of 20-year-old ordinary Portland cement-ground granulated blast-furnace slag blends containing 0 to 100% slag, *Cem. Concr. Res.* 40 (2010) 971–983. doi:10.1016/j.cemconres.2010.02.012.
- [55] I.G. Richardson, The nature of C-S-H in hardened cements, *Cem. Concr. Res.* 29 (1999) 1131–1147. doi:10.1016/S0008-8846(99)00168-4.
- [56] J. Bensted, P. Barnes, *Structure and Performance of Cements*, 2nd ed., Taylor & Francis e-Library, 2008.
- [57] D.D.L. Chung, Review - Improving cement-based materials by using silica fume, *J. Mater. Sci.* (2002) 673–682. doi:https://doi.org/10.1023/A:1013889725971.
- [58] Siddique, R, Khan, MI, Silica Fume, *Suppl. Cem. Mater.* 37 (2011) 54. doi:10.1007/978-3-642-17866-5.
- [59] P. Fidjestol, R. Lewis, *Microsilica as an Addition*, in: P.C. Hewlett (Ed.), *Lea's Chem. Cem. Concr.*, 4th ed., Elsevier Science & Technology Books, 1998: pp. 679–712.
- [60] X. Pardal, I. Pochard, A. Nonat, Experimental study of Si-Al substitution in calcium-silicate-hydrate (C-S-H) prepared under equilibrium conditions, *Cem. Concr. Res.* 39 (2009) 637–643. doi:10.1016/j.cemconres.2009.05.001.
- [61] I.G. Richardson, Tobermorite / jennite- and tobermorite / calcium hydroxide-based models for the structure of C-S-H: applicability to hardened pastes of tricalcium silicate, h-dicalcium silicate, Portland cement, and blends of Portland cement with blast-furnace slag, *Cem. Concr. Res.* 34 (2004) 1733–1777. doi:10.1016/j.cemconres.2004.05.034.
- [62] E.D. Rodríguez, L. Soriano, J. Payá, M.V. Borrachero, J.M. Monzó, Increase of the reactivity of densified silica fume by sonication treatment, *Ultrason. Sonochem.* 19 (2012) 1099–1107. doi:10.1016/j.ultsonch.2012.01.011.
- [63] E. Holt, M. Leivo, T. Vehmas, Low-pH concrete developed for tunnel end plugs used in nuclear waste containment, in: *Concr. Innov. Conf. 2014*, 2014: pp. 1–8.
- [64] T. Vehmas, A. Schnidler, M. Loiija, M. Leivo, E. Holt, Reference mix design and castings for low-pH concrete for nuclear waste repositories, in: *Proc. First Annu. Work. Horiz. 2020 Cebama Proj.*, 2016: pp. 101–111.
- [65] F. Barberon, V. Baroghel-Bouny, H. Zanni, B. Bresson, J.B. D'Espinose De La Caillerie, L. Malosse, Z. Gan, Interactions between chloride and cement-paste materials, *Magn. Reson. Imaging.* 23 (2005) 267–272. doi:10.1016/j.mri.2004.11.021.
- [66] F.P. Glasser, J. Marchand, E. Samson, Durability of concrete - Degradation phenomena involving detrimental chemical reactions, *Cem. Concr. Res.* 38 (2008) 226–246. doi:10.1016/j.cemconres.2007.09.015.
- [67] Z. Shi, M.R. Geiker, B. Lothenbach, K. De Weerd, S.F. Garzón, K. Enemark-Rasmussen, J. Skibsted, Friedel's salt profiles from thermogravimetric analysis and thermodynamic modelling of Portland cement-based mortars exposed to sodium chloride solution, *Cem. Concr. Compos.* 78 (2017) 73–83. doi:10.1016/j.cemconcomp.2017.01.002.
- [68] P. Henocq, J. Marchand, E. Samson, J.-A. Lavoie, J. Marchand, B. Bissonnette, R. Gagné, M.

Jolin, F. Paradis, Modeling of ionic interactions at the C–S–H surface—Application to CsCl and LiCl solutions in comparison with NaCl solutions, in: 2nd Int. Symp. Adv. Concr. through Sci. Eng. RILEM Proc., 2006. doi:10.1617/2351580028.023.

- [69] B. Tian, M.D. Cohen, Does gypsum formation during sulfate attack on concrete lead to expansion?, *Cem. Concr. Res.* 30 (2000) 117–123. doi:10.1016/S0008-8846(99)00211-2.
- [70] P. Faucon, P. Le Bescop, F. Adenot, P. Bonville, J.F. Jacquinot, F. Pineau, B. Felix, Leaching of cement: Study of the surface layer, *Cem. Concr. Res.* 26 (1996) 1707–1715. doi:10.1016/S0008-8846(96)00157-3.
- [71] P. Faucon, F. Adenot, J. Jacquinot, J.C. Petit, R. Cabrillac, M. Jorda, Long-term behaviour of cement pastes used for nuclear waste disposal: review of physico-chemical mechanisms of water degradation, *Cem. Concr. Res.* 28 (1998) 847–857. doi:10.1016/S0008-8846(98)00053-2.
- [72] C. Bube, V. Metz, E. Bohnert, K. Garbev, D. Schild, B. Kienzler, Long-term cement corrosion in chloride-rich solutions relevant to radioactive waste disposal in rock salt - Leaching experiments and thermodynamic simulations, *Phys. Chem. Earth.* 64 (2013) 87–94. doi:10.1016/j.pce.2012.11.001.
- [73] A. Dauzères, P. Le Bescop, C. Cau-dit-coumes, F. Brunet, X. Bourbon, On the physico-chemical evolution of low-pH and CEM I cement pastes interacting with Callovo-Oxfordian pore water under its in situ CO₂ partial pressure, *Cem. Concr. Res.* 58 (2014) 76–88. doi:10.1016/j.cemconres.2014.01.010.
- [74] P. Cote, T. Bridle, Long-term leaching scenarios for cement-based waste forms, *Waste Manag. Res.* 5 (1987) 55–66. doi:10.1016/0734-242X(87)90034-6.
- [75] Q.T. Phung, N. Maes, D. Jacques, J. Perko, G. De Schutter, G. Ye, Modelling the evolution of microstructure and transport properties of cement pastes under conditions of accelerated leaching, *Constr. Build. Mater.* 115 (2016) 179–192. doi:10.1016/j.conbuildmat.2016.04.049.
- [76] E. Stora, B. Bary, Q.C. He, E. Deville, P. Montarnal, Modelling and simulations of the chemo-mechanical behaviour of leached cement-based materials: Interactions between damage and leaching, *Cem. Concr. Res.* 40 (2010) 1226–1236. doi:10.1016/j.cemconres.2010.04.002.
- [77] J.M. Soler, M. Vuorio, A. Hautojärvi, Reactive transport modeling of the interaction between water and a cementitious grout in a fractured rock. Application to ONKALO (Finland), *Appl. Geochemistry.* 26 (2011) 1115–1129. doi:10.1016/j.apgeochem.2011.04.001.
- [78] F.P. Glasser, M. Tyrer, K. Quillin, D. Ross, J. Pedersen, K. Goldthorpe, D. Bennett, M. Atkins, The chemistry of blended cements and backfills intended for use in radioactive waste disposal, 1999.
- [79] C.L. Corkhill, J.W. Bridge, X.C. Chen, P. Hillel, S.F. Thornton, M.E. Romero-Gonzalez, S. a. Banwart, N.C. Hyatt, Real-time gamma imaging of technetium transport through natural and engineered porous materials for radioactive waste disposal, *Environ. Sci. Technol.* 47 (2013) 13857–13864. doi:10.1021/es402718j.
- [80] A.J. Hooper, Repository for radioactive waste-vault backfill, 1998. Patent number: 5,740,546.
- [81] M. Gascoyne, Influence of grout and cement on groundwater composition, 2002. Posiva Working Report 2002-07.
- [82] B. Lagerblad, J. Trägårdh, Conceptual model for concrete long time degradation in a deep nuclear waste repository, SKB, Tech. Rep. (1994).
- [83] A. Vinsot, S. Mettler, S. Wechner, In situ characterization of the Callovo-Oxfordian pore water composition, *Phys. Chem. Earth.* 33 (2008) S75–S86. doi:10.1016/j.pce.2008.10.048.
- [84] C. Lerouge, S. Gaboreau, S. Grangeon, F. Claret, F. Warmont, A. Jenni, V. Cloet, U. Mäder, In

- situ interactions between Opalinus Clay and Low Alkali Concrete, *Phys. Chem. Earth*. 99 (2017) 3–21. doi:10.1016/j.pce.2017.01.005.
- [85] M. Altmaier, V. Montoya, L. Duro, A. Valls, Proceedings of the Second Workshop of the HORIZON 2020 Cebama Project, in: 2018.
- [86] C.L. Corkhill, N.J. Cassingham, P.G. Heath, N.C. Hyatt, Dissolution of UK high-level waste glass under simulated hyperalkaline conditions of a collocated geological disposal facility, *Int. J. Appl. Glas. Sci.* 4 (2013) 341–356. doi:10.1111/ijag.12042.
- [87] Malvern Instruments Limited, *A Basic Guide to Particle Characterization*, (2012) 1–25.
- [88] Malvern Instruments Limited, *Dry powder method development for laser diffraction particle size distribution measurements*, (2014) 1–9.
- [89] L. Wadsö, M. Arndt, An international round robin test on isothermal (conduction) calorimetry for measurement of three-day heat of hydration of cement, *Cem. Concr. Res.* 79 (2016) 316–322. doi:10.1016/j.cemconres.2015.10.004.
- [90] K. Scrivener, R. Snellings, B. Lothenbach, *A Practical Guide to Microstructural Analysis of Cementitious Materials*, CRC Press, Taylor & Francis Group, 2016.
- [91] L. Wadsö, Operational issues in isothermal calorimetry, *Cem. Concr. Res.* 40 (2010) 1129–1137. doi:10.1016/j.cemconres.2010.03.017.
- [92] W.H. Bragg, W.L. Bragg, The Reflection of X-rays by Crystals, *Proc. R. Soc. A Math. Phys. Eng. Sci.* 88 (1913) 428–438. doi:10.1098/rspa.1913.0040.
- [93] H.M. Rietveld, A profile refinement method for nuclear and magnetic structures, *J. Appl. Crystallogr.* 2 (1969) 65–71. doi:10.1107/s0021889869006558.
- [94] N.I. Golovastikov, R.G. Matveeva, N.V. Belov, Crystal structure of the tricalcium silicate (CaO SiO_2)₃ = C3S, *Kristallografiya*. 20 (1975) 721–729.
- [95] W.G. Mumme, R.J. Hill, G. Bushnell-Wye, E.R. Segnit, Rietveld crystal structure refinements, crystal chemistry and calculated powder diffraction data for the polymorphs of dicalcium silicate and related phases, *Neues Jahrb Miner. Abh.* 169 (1995) 35–68.
- [96] P. Mondal, W. Jeffery, The Crystal Structure of Tricalcium Aluminate, $\text{Ca}_3\text{Al}_2\text{O}_6$, *Acta Crystallogr.* (1975).
- [97] A.A. Colville, S. Geller, The crystal structure of brownmillerite, $\text{Ca}_2\text{FeAlO}_5$, *Acta Crystallogr. Sect. B Struct. Crystallogr. Cryst. Chem.* 27 (2002) 2311–2315. doi:10.1107/s056774087100579x.
- [98] Á.G. De La Torre, S. Bruque, J. Campo, M.A.G. Aranda, The superstructure of C3S from synchrotron and neutron powder diffraction and its role in quantitative phase analyses, *Cem. Concr. Res.* 32 (2002) 1347–1356. doi:10.1016/S0008-8846(02)00796-2.
- [99] E.N. Maslen, V.A. Streltsov, N.R. Streltsova, N. Ishizawa, Electron density and optical anisotropy in rhombohedral carbonates. III. Synchrotron X-ray studies of CaCO_3 , MgCO_3 and MnCO_3 , *Acta Crystallogr. Sect. B*. 51 (1995) 929–939. doi:10.1107/S0108768195006434.
- [100] F. Goetz-Neunhoeffler, J. Neubauer, Refined ettringite ($\text{Ca}_6\text{Al}_2(\text{SO}_4)_3(\text{OH})_{12}\cdot 26\text{H}_2\text{O}$) structure for quantitative X-ray diffraction analysis, *Powder Diffr.* 21 (2006) 4–11. doi:10.1154/1.2146207.
- [101] T. Runčevski, R.E. Dinnebier, O. V. Magdysyuk, H. Pöllmann, Crystal structures of calcium hemicarboaluminate and carbonated calcium hemicarboaluminate from synchrotron powder diffraction data, *Acta Crystallogr. Sect. B Struct. Sci.* 68 (2012) 493–500. doi:10.1107/S010876811203042X.

- [102] G. Renaudin, M. François, The lamellar double-hydroxide (LDH) compound with composition $3\text{CaO}\cdot\text{Al}_2\text{O}_3\cdot\text{Ca}(\text{NO}_3)_2\cdot 10\text{H}_2\text{O}$, *Acta Crystallogr. Sect. C Cryst. Struct. Commun.* 55 (1999) 835–838. doi:10.1107/S0108270199003066.
- [103] S. Koritnig, P. Susse, Meixnerit, $\text{Mg}_6\text{Al}_2(\text{OH})_{18}\cdot 4\text{H}_2\text{O}$, ein neues Magnesium-Aluminium-Hydroxid-Mineral, *Tschermaks Min. Petr.Mitt.* 22 (1975) 79–87. doi:10.1007/978-3-642-90857-6_8.
- [104] B. AXS, TOPAS V4.2: General profile and structure analysis software for powder diffraction data, Karlsruhe, Germany, 2009.
- [105] R.E. Dinnebier, S.J.L. Billinge, Principles of powder diffraction, in: R.E. Dinnebier, S.J.L. Billinge (Eds.), *Powder Diffr. Theory Pract.*, The Royal Society of Chemistry Cambridge, UK, 2008.
- [106] S.P. Thompson, J.E. Parker, J. Potter, T.P. Hill, A. Birt, T.M. Cobb, F. Yuan, C.C. Tang, Beamline I11 at Diamond: A new instrument for high resolution powder diffraction, *Rev. Sci. Instrum.* 80 (2009). doi:10.1063/1.3167217.
- [107] S.P. Thompson, J.E. Parker, J. Marchal, J. Potter, A. Birt, F. Yuan, R.D. Fearn, A.R. Lennie, S.R. Street, C.C. Tang, Fast X-ray powder diffraction on I11 at Diamond, *J. Synchrotron Radiat.* 18 (2011) 637–648. doi:10.1107/s0909049511013641.
- [108] C.A. Murray, J. Potter, S.J. Day, A.R. Baker, S.P. Thompson, J. Kelly, C.G. Morris, S. Yang, C.C. Tang, New synchrotron powder diffraction facility for long-duration experiments, *J. Appl. Crystallogr.* 50 (2017) 172–183. doi:10.1107/s1600576716019750.
- [109] R. Snellings, A. Salze, K.L. Scrivener, Use of X-ray diffraction to quantify amorphous supplementary cementitious materials in anhydrous and hydrated blended cements, *Cem. Concr. Res.* 64 (2014) 89–98. doi:10.1016/j.cemconres.2014.06.011.
- [110] G.R. Heal, Thermogravimetry and Derivative Thermogravimetry, in: P.J. Hains (Ed.), *Princ. Therm. Anal. Calorim.*, The Royal Society of Chemistry, Cambridge, UK, n.d.: pp. 10–54. doi:10.1039/9781847551764-00010.
- [111] K.L. Scrivener, Backscattered electron imaging of cementitious microstructures: Understanding and quantification, *Cem. Concr. Compos.* 26 (2004) 935–945. doi:10.1016/j.cemconcomp.2004.02.029.
- [112] W. Zhou, Z.L. Wang, *Scanning Microscopy for Nanotechnology*, Springer New York, New York, NY, 2007. doi:10.1007/978-0-387-39620-0.
- [113] B. Walkley, J.L. Provis, Solid-state nuclear magnetic resonance spectroscopy of cements, *Mater. Today Adv.* 1 (2019) 1–42. doi:10.1016/j.mtadv.2019.100007.
- [114] K.J. Mackenzie, M.E. Smith, *Multinuclear Solid-State NMR of Inorganic Materials*, Elsevier Science Ltd, Oxford, UK, 2002.
- [115] S.A. Bernal, R. San Nicolas, R.J. Myers, R. Mejia de Gutierrez, F. Puertas, J.S.J. van Deventer, J.L. Provis, MgO content of slag controls phase evolution and structural changes induced by accelerated carbonation in alkali-activated binders, *Cem. Concr. Res.* 57 (2014) 33–43. doi:10.1016/j.cemconres.2013.12.003.
- [116] R.J. Myers, S.A. Bernal, J.D. Gehman, J.S.J. Van Deventer, J.L. Provis, The role of al in cross-linking of alkali-Activated slag cements, *J. Am. Ceram. Soc.* 98 (2015) 996–1004. doi:10.1111/jace.13360.
- [117] S.A. Bernal, J.L. Provis, B. Walkley, R. San, J.D. Gehman, D.G. Brice, A.R. Kilcullen, P. Duxson, J.S.J. Van Deventer, Gel nanostructure in alkali-activated binders based on slag and fly ash, and effects of accelerated carbonation, *Cem. Concr. Res.* 53 (2013) 127–144.

doi:10.1016/j.cemconres.2013.06.007.

- [118] D. Massiot, F. Fayon, M. Capron, I. King, S. Le Calvé, B. Alonso, J.O. Durand, B. Bujoli, Z. Gan, G. Hoatson, Modelling one- and two-dimensional solid-state NMR spectra, *Magn. Reson. Chem.* 40 (2002) 70–76. doi:10.1002/mrc.984.
- [119] B. Lothenbach, D. Rentsch, E. Wieland, Hydration of a silica fume blended low-alkali shotcrete cement, *Phys. Chem. Earth.* 70–71 (2014) 3–16. doi:10.1016/j.pce.2013.09.007.
- [120] I.G. Richardson, Model structures for C-(A)-S-H(I), *Acta Crystallogr. Sect. B Struct. Sci. Cryst. Eng. Mater.* 70 (2014) 903–923. doi:10.1107/s2052520614021982.
- [121] F. Moro, H. Böhni, Ink-bottle effect in mercury intrusion porosimetry of cement-based materials, *J. Colloid Interface Sci.* 246 (2002) 135–149. doi:10.1006/jcis.2001.7962.
- [122] S. Diamond, Mercury porosimetry: an inappropriate method for the measurement of pore size distributions in cement-based material, *Cem. Concr. Res.* 30 (2000) 1517–1525. doi:10.1016/S0008-8846(00)00370-7.
- [123] S. Brunauer, P.H. Emmett, E. Teller, Adsorption of Gases in Multimolecular Layers, *J. Am. Chem. Soc.* 60 (1938) 309–319. doi:10.1021/ja01269a023.
- [124] E.P. Barrett, L.G. Joyner, P.P. Halenda, The Determination of Pore Volume and Area Distributions in Porous Substances. I. Computations from Nitrogen Isotherms, *J. Am. Chem. Soc.* 73 (1951) 373–380. doi:10.1021/ja01145a126.
- [125] M.A.B. Promentilla, T. Sugiyama, T. Hitomi, N. Takeda, Quantification of tortuosity in hardened cement pastes using synchrotron-based X-ray computed microtomography, *Cem. Concr. Res.* 39 (2009) 548–557. doi:10.1016/j.cemconres.2009.03.005.
- [126] T. Sugiyama, M.A.B. Promentilla, T. Hitomi, N. Takeda, Application of synchrotron microtomography for pore structure characterization of deteriorated cementitious materials due to leaching, *Cem. Concr. Res.* 40 (2010) 1265–1270. doi:10.1016/j.cemconres.2009.10.009.
- [127] T. Sugiyama, T. Hitomi, K. Kajiwara, Nondestructive Integrated CT-XRD Method for Research on Hydrated Cement System, in: *Proc. 4th Int. Conf. Durab. Concr. Struct.*, Purdue University Libraries Scholarly Publishing Services, 2014: pp. 298–303. doi:10.5703/1288284315415.
- [128] D.P. Bentz, S. Mizell, S. Satterfield, J. Devaney, W. George, P. Ketcham, J. Graham, J. Porterfield, D. Quenard, F. Vallee, H. Sallee, E. Boller, J. Baruchel, The Visible Cement Data Set, *J. Res. Natl. Inst. Stand. Technol.* 107 (2002) 137. doi:10.6028/jres.107.013.
- [129] P.J.M. Monteiro, A.P. Kirchheim, S. Chae, P. Fischer, A.A. MacDowell, E. Schaible, H.R. Wenk, Characterizing the nano and micro structure of concrete to improve its durability, *Cem. Concr. Compos.* 31 (2009) 577–584. doi:10.1016/j.cemconcomp.2008.12.007.
- [130] E.N. Landis, D.T. Keane, X-ray microtomography, *Mater. Charact.* 61 (2010) 1305–1316. doi:10.1016/j.matchar.2010.09.012.
- [131] S. Diamond, E. Landis, Microstructural features of a mortar as seen by computed microtomography, *Mater. Struct.* 40 (2007) 989–993. doi:10.1617/s11527-006-9194-9.
- [132] R. Brooks, G. Dichiro, Beam hardening in X-ray reconstructive tomography, *Phys. Med. Biol.* (1976) 390–398.
- [133] S.J. Hill, *Inductively Coupled Plasma Spectrometry and its Applications*, Blackwell Publishing Ltd, Oxford, UK, 2006. doi:10.1002/9780470988794.
- [134] S.J. Norris, Improve your ICP-OES Performance by using an Internal Standard, CRM Solut. (n.d.). <https://www.armi.com/blog/how-an-internal-standard-can-improve-your-icp-oes-performance> (accessed May 15, 2019).

- [135] J.P. Lemmon, Ion Chromatography, in: *Encycl. Mater. Sci. Technol.*, Elsevier, 2001: pp. 4280–4283. doi:10.1016/B0-08-043152-6/00750-6.
- [136] T.F. Scientific, Dionex ICS-1100 Ion Chromatography System Operator's Manual, (2012).
- [137] R.G.W. Vasconcelos, N. Beaudoin, A. Hamilton, N.C. Hyatt, J.L. Provis, C.L. Corkhill, Characterisation of a high pH cement backfill for the geological disposal of nuclear waste: The Nirex Reference Vault Backfill, 89 (2018) 180–189. doi:10.1016/j.apgeochem.2017.11.007.
- [138] K.L. Scrivener, P. Juilland, P.J.M. Monteiro, Advances in understanding hydration of Portland cement, *Cem. Concr. Res.* (2015). doi:10.1016/j.cemconres.2015.05.025.
- [139] I.G. Richardson, The calcium silicate hydrates, *Cem. Concr. Res.* 38 (2008) 137–158. doi:10.1016/j.cemconres.2007.11.005.
- [140] I.G. Richardson, L. Black, J. Skibsted, R.J. Kirkpatrick, Characterisation of cement hydrate phases by TEM, NMR and Raman spectroscopy, *Adv. Cem. Res.* 22 (2010) 233–248. doi:10.1680/adcr.2010.22.4.233.
- [141] B. Lothenbach, G. Le Saout, E. Gallucci, K. Scrivener, Influence of limestone on the hydration of Portland cements, *Cem. Concr. Res.* 38 (2008) 848–860. doi:10.1016/j.cemconres.2008.01.002.
- [142] M.T. Palou, E. Kuzielova, M. Zemlicka, M. Boha, R. Novotny, The effect of curing temperature on the hydration of binary Portland cement, *J. Therm. Anal. Calorim.* 125 (2016) 1301–1310. doi:10.1007/s10973-016-5395-9.
- [143] F. Lin, C. Meyer, Hydration kinetics modeling of Portland cement considering the effects of curing temperature and applied pressure, *Cem. Concr. Res.* 39 (2009) 255–265. doi:10.1016/j.cemconres.2009.01.014.
- [144] J.. Escalante-García, J.. Sharp, Effect of temperature on the hydration of the main clinker phases in portland cements: part i, neat cements, *Cem. Concr. Res.* 28 (1998) 1245–1257. doi:10.1016/S0008-8846(98)00115-X.
- [145] M. Zajac, A. Rossberg, G. Le Saout, B. Lothenbach, Influence of limestone and anhydrite on the hydration of Portland cements, *Cem. Concr. Compos.* 46 (2014) 99–108. doi:10.1016/j.cemconcomp.2013.11.007.
- [146] K. De Weerd, M. Ben Haha, G. Le Saout, K.O. Kjellsen, H. Justnes, B. Lothenbach, Hydration mechanisms of ternary Portland cements containing limestone powder and fly ash, *Cem. Concr. Res.* 41 (2011) 279–291. doi:10.1016/j.cemconres.2010.11.014.
- [147] T. Matschei, B. Lothenbach, F.P. Glasser, The AFm phase in Portland cement, *Cem. Concr. Res.* 37 (2007) 118–130. doi:10.1016/j.cemconres.2006.10.010.
- [148] R.J. Myers, E.L. Hôpital, J.L. Provis, B. Lothenbach, Effect of temperature and aluminium on calcium (aluminosilicate) hydrate chemistry under equilibrium conditions, *Cem. Concr. Res.* 68 (2015) 83–93. doi:10.1016/j.cemconres.2014.10.015.
- [149] T.T.H. Bach, C.C.D. Coumes, I. Pochard, C. Mercier, B. Revel, A. Nonat, Influence of temperature on the hydration products of low pH cements, *Cem. Concr. Res.* 42 (2012) 805–817. doi:10.1016/j.cemconres.2012.03.009.
- [150] P.W. Brown, J. V. Bothe, The stability of ettringite, *Adv. Cem. Res.* 5 (2012) 47–63. doi:10.1680/adcr.1993.5.18.47.
- [151] Y.N. Chan, G.F. Peng, M. Anson, Residual strength and pore structure of high-strength concrete and normal strength concrete after exposure to high temperatures, *Cem. Concr. Compos.* 21 (1999) 23–27. doi:10.1016/S0958-9465(98)00034-1.

- [152] J. Komonen, V. Penttala, Effect of High Temperature on the Pore Structure and Strength of Granulated Blastfurnace Slag Modified Cement Paste, 11th Int. Congr. Chem. Cem. (2003) 925–934.
- [153] J.M. Galíndez, J. Molinero, Assessment of the long-term stability of cementitious barriers of radioactive waste repositories by using digital-image-based microstructure generation and reactive transport modelling, *Cem. Concr. Res.* 40 (2010) 1278–1289. doi:10.1016/j.cemconres.2009.11.006.
- [154] J. Monzó, D. Martínez-Velandia, J. Payá, M. V. Borrachero, Effect of sonication on the reactivity of silica fume in Portland cement mortars, *Adv. Cem. Res.* 23 (2011) 23–31. doi:10.1680/adcr.8.00027.
- [155] E.C. Arvaniti, M.C.G. Juenger, S. a. Bernal, J. Duchesne, L. Courard, S. Leroy, J.L. Provis, A. Klemm, N. De Belie, Determination of particle size, surface area, and shape of supplementary cementitious materials by different techniques, *Mater. Struct.* 48 (2014) 3687–3701. doi:10.1617/s11527-014-0431-3.
- [156] B. Klemczak, M. Batog, Heat of hydration of low-clinker cements: Part I. Semi-adiabatic and isothermal tests at different temperature, *J. Therm. Anal. Calorim.* 123 (2016) 1351–1360. doi:10.1007/s10973-015-4782-y.
- [157] A. Korpa, T. Kowald, R. Trettin, Hydration behaviour, structure and morphology of hydration phases in advanced cement-based systems containing micro and nanoscale pozzolanic additives, *Cem. Concr. Res.* 38 (2008) 955–962. doi:10.1016/j.cemconres.2008.02.010.
- [158] B.W. Langan, K. Weng, M.A. Ward, Effect of silica fume and fly ash on heat of hydration of Portland cement, *Cem. Concr. Res.* 32 (2002) 1045–1051. doi:10.1016/S0008-8846(02)00742-1.
- [159] P. Siler, J. Kratky, N. De Beli, Isothermal and solution calorimetry to assess the effect of superplasticizers and mineral admixtures on cement hydration, in: *J. Therm. Anal. Calorim.*, 2012: pp. 313–320. doi:10.1007/s10973-011-1479-8.
- [160] T. Bach, C. Cau-Dit-Coumes, I. Pochard, A. Nonat, Retention of alkalis by hydrated low-pH cements designed for underground radioactive waste repositories, in: 13th Int. Congr. Chem. Cem., 2011: pp. 1–7.
- [161] I.G. Richardson, S. Li, Composition and structure of an 18-year-old 5M KOH-activated ground granulated blast-furnace slag paste, *Constr. Build. Mater.* 168 (2018) 404–411. doi:10.1016/j.conbuildmat.2018.02.034.
- [162] D.P. Prentice, S.A. Bernal, M. Bankhead, M. Hayes, J.L. Provis, Phase evolution of slag-rich cementitious grouts for immobilisation of nuclear wastes, *Adv. Cem. Res.* 30 (2018) 345–360. doi:10.1680/jadcr.17.00198.
- [163] R.J. Myers, S.A. Bernal, J.L. Provis, A thermodynamic model for C-(N-)A-S-H gel: CNASH_{ss}. Derivation and validation, *Cem. Concr. Res.* 66 (2014) 27–47. doi:10.1016/j.cemconres.2014.07.005.
- [164] M.D. Andersen, H.J. Jakobsen, J. Skibsted, Incorporation of Aluminum in the Calcium Silicate Hydrate (C–S–H) of Hydrated Portland Cements: A High-Field 27 Al and 29 Si MAS NMR Investigation, *Inorg. Chem.* 42 (2003) 2280–2287. doi:10.1021/ic020607b.
- [165] J.I. Escalante-García, J.H. Sharp, Effect of temperature on the hydration of the main clinker phases in portland cements: part ii, blended cements, *Cem. Concr. Res.* 28 (1998) 1259–1274. doi:10.1016/S0008-8846(98)00107-0.
- [166] W. Ma, D. Sample, R. Martin, P. Brown, Calorimetric Study of Cement Blends Containing Fly Ash, Silica Fume, and Slag at Elevated Temperatures, *Cem. Concr. Aggregates.* 16 (1994) 93.

doi:10.1520/CCA10285J.

- [167] D.P. Prentice, B. Walkley, S.A. Bernal, M. Bankhead, M. Hayes, J.L. Provis, Thermodynamic modelling of BFS-PC cements under temperature conditions relevant to the geological disposal of nuclear wastes, *Cem. Concr. Res.* 119 (2019) 21–35. doi:10.1016/j.cemconres.2019.02.005.
- [168] B. Lothenbach, F. Winnefeld, Thermodynamic modelling of the hydration of Portland cement, *Cem. Concr. Res.* 36 (2006) 209–226. doi:10.1016/j.cemconres.2005.03.001.
- [169] J.W. Bullard, H.M. Jennings, R.A. Livingston, A. Nonat, G.W. Scherer, J.S. Schweitzer, K.L. Scrivener, J.J. Thomas, Mechanisms of cement hydration, *Cem. Concr. Res.* 41 (2011) 1208–1223. doi:10.1016/j.cemconres.2010.09.011.
- [170] K.L. Scrivener, A. Nonat, Hydration of cementitious materials, present and future, *Cem. Concr. Res.* 41 (2011) 651–665. doi:10.1016/j.cemconres.2011.03.026.
- [171] C. Cau Dit Coumes, S. Courtois, S. Peysson, J. Ambroise, J. Pera, Calcium sulfoaluminate cement blended with OPC: A potential binder to encapsulate low-level radioactive slurries of complex chemistry, *Cem. Concr. Res.* 39 (2009) 740–747. doi:10.1016/j.cemconres.2009.05.016.
- [172] N. Mobasher, H. Kinoshita, S.A. Bernal, C.A. Sharrard, Ba(OH)₂ – blast furnace slag composite binders for encapsulation of sulphate bearing nuclear waste, *Adv. Appl. Ceram.* 113 (2014) 460–465. doi:10.1179/1743676114y.0000000148.
- [173] M.L.D. Gougar, B.E. Scheetz, D.M. Roy, Ettringite and C-S-H portland cement phases for waste ion immobilization: A review, *Waste Manag.* 16 (1996) 295–303. doi:10.1016/S0956-053X(96)00072-4.
- [174] K.L. Scrivener, T. Füllmann, E. Gallucci, G. Walenta, E. Bermejo, Quantitative study of Portland cement hydration by X-ray diffraction/Rietveld analysis and independent methods, *Cem. Concr. Res.* 34 (2004) 1541–1547. doi:10.1016/j.cemconres.2004.04.014.
- [175] E.M. Gartner, J.F. Young, D.A. Damidot, I. Jawed, Hydration of Portland Cement, in: P.B. J. Bensted (Ed.), *Struct. Perform. Cem.*, 2nd ed., CRC Press, 2001.
- [176] M.C. Schlegel, A. Sarfraz, U. Müller, U. Panne, F. Emmerling, First seconds in a building's life-in situ synchrotron X-ray diffraction study of cement hydration on the millisecond timescale, *Angew. Chemie - Int. Ed.* 51 (2012) 4993–4996. doi:10.1002/anie.201200993.
- [177] K. De Weerdt, M. Ben Haha, G. Le Saout, K.O. Kjellsen, H. Justnes, B. Lothenbach, Hydration mechanisms of ternary Portland cements containing limestone powder and fly ash, *Cem. Concr. Res.* 41 (2011) 279–291. doi:10.1016/j.cemconres.2010.11.014.
- [178] T. Matschei, B. Lothenbach, F.P. Glasser, The role of calcium carbonate in cement hydration, *Cem. Concr. Res.* 37 (2007) 551–558. doi:10.1016/j.cemconres.2006.10.013.
- [179] V.L. Bonavetti, V.F. Rahhal, E.F. Irassar, Studies on the carboaluminate formation in limestone filler-blended cements, *Cem. Concr. Res.* 31 (2001) 853–859. doi:10.1016/S0008-8846(01)00491-4.
- [180] K. De Weerdt, H. Justnes, The effect of sea water on the phase assemblage of hydrated cement paste, *Cem. Concr. Compos.* 55 (2015) 215–222. doi:10.1016/j.cemconcomp.2014.09.006.
- [181] E.M.J. Berodier, Impact of the Supplementary Cementitious Materials on the kinetics and microstructural development of cement hydration, 2015. doi:10.5075/epfl-thesis-6417.
- [182] B. Lothenbach, G. Le Saout, M. Ben Haha, R. Figi, E. Wieland, Hydration of a low-alkali CEM III/B-SiO₂ cement (LAC), *Cem. Concr. Res.* 42 (2012) 410–423. doi:10.1016/j.cemconres.2011.11.008.

- [183] F. Deschner, F. Winnefeld, B. Lothenbach, S. Seufert, P. Schwesig, S. Dittrich, F. Goetz-Neunhoeffer, J. Neubauer, Hydration of Portland cement with high replacement by siliceous fly ash, *Cem. Concr. Res.* 42 (2012) 1389–1400. doi:10.1016/j.cemconres.2012.06.009.
- [184] I. Pane, W. Hansen, Investigation of blended cement hydration by isothermal calorimetry and thermal analysis, *Cem. Concr. Res.* 35 (2005) 1155–1164. doi:10.1016/j.cemconres.2004.10.027.
- [185] M.C.G. Juenger, R. Siddique, Recent advances in understanding the role of supplementary cementitious materials in concrete, *Cem. Concr. Res.* 78 (2015) 71–80. doi:10.1016/j.cemconres.2015.03.018.
- [186] J. Duchesne, M.A. Bérubé, Long-term effectiveness of supplementary cementing materials against alkali-silica reaction, *Cem. Concr. Res.* 31 (2001) 1057–1063. doi:10.1016/S0008-8846(01)00538-5.
- [187] I.G. Richardson, The importance of proper crystal-chemical and geometrical reasoning demonstrated using layered single and double hydroxides, *Acta Crystallogr. Sect. B Struct. Sci.* 69 (2013) 150–162. doi:10.1107/S0108768113003765.
- [188] X. Ke, S.A. Bernal, J.L. Provis, Controlling the reaction kinetics of sodium carbonate-activated slag cements using calcined layered double hydroxides, *Cem. Concr. Res.* 81 (2016) 24–37. doi:10.1016/j.cemconres.2015.11.012.
- [189] D.M. Roy, G.M. Idorn, Hydration, Structure, and Properties of Blast Furnace Slag Cements, Mortars, and Concrete, *ACI J. Proc.* 79 (1983) 445–457. doi:10.14359/10919.
- [190] I.G. Richardson, Nature of the hydration products in hardened cement pastes, *Cem. Concr. Compos.* 22 (2000) 97–113. doi:10.1016/S0958-9465(99)00036-0.
- [191] S.A. Stronach, F.P. Glasser, Modelling the impact of abundant geochemical components on phase stability and solubility of the CaO—SiO₂—H₂O system at 25°C: Na⁺, K⁺, SO₄²⁻, Cl⁻ and CO₃²⁻, *Adv. Cem. Res.* 9 (1997) 167–181. doi:10.1680/adcr.1997.9.36.167.
- [192] N.C. Collier, Transition and decomposition temperatures of cement phases - a collection of thermal analysis data, *Ceram. - Silikaty.* 60 (2016) 338–343. doi:10.13168/cs.2016.0050.
- [193] R.J. Myers, S.A. Bernal, R. San Nicolas, J.L. Provis, Generalized structural description of calcium-sodium aluminosilicate hydrate gels: The cross-linked substituted tobermorite model, *Langmuir.* 29 (2013) 5294–5306. doi:10.1021/la4000473.
- [194] Q.T. Phung, Effects of Carbonation and Calcium Leaching on Microstructure and Transport Properties of Cement Pastes, 2015. PhD thesis; <http://hdl.handle.net/1854/LU-6913935>.
- [195] A.C. Müller, Characterization of porosity & C-S-H in cement pastes by 1 H NMR, 2014. PhD thesis; doi:10.5075/epfl-thesis-6339.
- [196] K. Haga, S. Sutou, M. Hironaga, S. Tanaka, S. Nagasaki, Effects of porosity on leaching of Ca from hardened ordinary Portland cement paste, *Cem. Concr. Res.* 35 (2005) 1764–1775. doi:10.1016/j.cemconres.2004.06.034.
- [197] A. Dauzères, P. Le Bescop, C. Cau-Dit-Coumes, F. Brunet, X. Bourbon, J. Timonen, M. Voutilainen, L. Chomat, P. Sardini, On the physico-chemical evolution of low-pH and CEM I cement pastes interacting with Callovo-Oxfordian pore water under its in situ CO₂ partial pressure, *Cem. Concr. Res.* 58 (2014) 76–88. doi:10.1016/j.cemconres.2014.01.010.
- [198] M.D. Andersen, H.J. Jakobsen, J. Skibsted, A new aluminium-hydrate species in hydrated Portland cements characterized by 27 Al and 29 Si MAS NMR spectroscopy, *Cem. Concr. Res.* 36 (2006) 3–17. doi:10.1016/j.cemconres.2005.04.010.
- [199] U.H. Jakobsen, K. De Weerd, M.R. Geiker, Elemental zonation in marine concrete, *Cem.*

Concr. Res. 85 (2016) 12–27. doi:10.1016/j.cemconres.2016.02.006.

- [200] T.U. Mohammed, H. Hamada, T. Yamaji, Concrete after 30 years of exposure - Part 1: Mineralogy, microstructures, and interfaces, *ACI Mater. J.* 101 (2004).
- [201] C. Gallé, H. Peycelon, P. Le Bescop, Effect of an accelerated chemical degradation on water permeability and pore structure of cementbased materials, *Adv. Cem. Res.* 16 (2004) 105–114. doi:10.1680/adcr.2004.16.3.105.
- [202] P. Faucon, F. Adenot, M. Jorda, R. Cabrillac, Behaviour of crystallised phases of Portland cement upon water attack, *Mater. Struct.* 30 (1997) 480–485. doi:10.1007/BF02524776.
- [203] G.M.N. Baston, M.M. Cowper, T. a. Marshall, Sorption properties of aged cements, *Mineral. Mag.* 76 (2012) 3411–3423. doi:10.1180/minmag.2012.076.8.54.
- [204] K. De Weerd, H. Justnes, M.R. Geiker, Changes in the phase assemblage of concrete exposed to sea water, *Cem. Concr. Compos.* 47 (2014) 53–63. doi:10.1016/j.cemconcomp.2013.09.015.
- [205] J.C. Wilson, S. Benbow, R. Metcalfe, Reactive transport modelling of a cement backfill for radioactive waste disposal, *Cem. Concr. Res.* 111 (2018) 81–93. doi:10.1016/j.cemconres.2018.06.007.
- [206] M. Balonis, B. Lothenbach, G. Le, F.P. Glasser, Impact of chloride on the mineralogy of hydrated Portland cement systems, *Cem. Concr. Res.* 40 (2010) 1009–1022. doi:10.1016/j.cemconres.2010.03.002.
- [207] K. De Weerd, D. Orsáková, M.R. Geiker, The impact of sulphate and magnesium on chloride binding in Portland cement paste, *Cem. Concr. Res.* 65 (2014) 30–40. doi:10.1016/j.cemconres.2014.07.007.
- [208] H.F. Taylor, C. Famy, K. Scrivener, Delayed ettringite formation, *Cem. Concr. Res.* 31 (2001) 683–693. doi:10.1016/S0008-8846(01)00466-5.
- [209] A. Jenni, U. Mäder, C. Lerouge, S. Gaboreau, B. Schwyn, In situ interaction between different concretes and Opalinus Clay, *Phys. Chem. Earth.* 70–71 (2014) 71–83. doi:10.1016/j.pce.2013.11.004.
- [210] J.M. Oh, S.H. Hwang, J.H. Choy, The effect of synthetic conditions on tailoring the size of hydroxalite particles, *Solid State Ionics.* 151 (2002) 285–291. doi:10.1016/S0167-2738(02)00725-7.
- [211] E. Bernard, B. Lothenbach, C. Cau-Dit-Coumes, C. Chlique, A. Dauzères, I. Pochard, Magnesium and calcium silicate hydrates, Part I: Investigation of the possible magnesium incorporation in calcium silicate hydrate (C-S-H) and of the calcium in magnesium silicate hydrate (M-S-H), *Appl. Geochemistry.* 89 (2018) 229–242. doi:10.1016/j.apgeochem.2017.12.005.
- [212] E. Bernard, A. Dauzères, B. Lothenbach, Magnesium and calcium silicate hydrates, Part II: Mg-exchange at the interface “low-pH” cement and magnesium environment studied in a C-S-H and M-S-H model system, *Appl. Geochemistry.* 89 (2018) 210–218. doi:10.1016/j.apgeochem.2017.12.006.
- [213] A. Dauzères, G. Achiedo, D. Nied, E. Bernard, S. Alahrache, B. Lothenbach, Magnesium perturbation in low-pH concretes placed in clayey environment - Solid characterizations and modeling, *Cem. Concr. Res.* 79 (2016) 137–150. doi:10.1016/j.cemconres.2015.09.002.
- [214] N.R. Buenfeld, J.B. Newman, The development and stability of surface layers on concrete exposed to sea-water, *Cem. Concr. Res.* 16 (1986) 721–732. doi:10.1016/0008-8846(86)90046-3.
- [215] A. Dauzères, P. Le Bescop, P. Sardini, C.C. Dit, Physico-chemical investigation of

clayey/cement-based materials interaction in the context of geological waste disposal: Experimental approach and results, *Cem. Concr. Res.* 40 (2010) 1327–1340. doi:10.1016/j.cemconres.2010.03.015.

- [216] P.W. Brown, A. Doerr, Chemical changes in concrete due to the ingress of aggressive species, *Cem. Concr. Res.* 30 (2000) 411–418. doi:10.1016/S0008-8846(99)00266-5.
- [217] F. Massazza, Pozzolana and Pozzolanic Cements, in: P. Hewlett (Ed.), *Lea's Chem. Cem. Concr.*, 4th ed., Elsevier Science & Technology Books, 1997: pp. 471–635.
- [218] J.A. Chudek, G. Hunter, M.R. Jones, S.N. Scrimgeour, P.C. Hewlett, A.B. Kudryavtsev, Aluminum-27 solid state NMR spectroscopic studies of chloride binding in Portland cement and blends, *J. Mater. Sci.* 35 (2000) 4275–4288. doi:10.1023/A:1004824100029.
- [219] V. Papadakis, S. Tsimas, Supplementary cementing materials in concrete. Part I: efficiency and design, *Cem. Concr. Res.* 32 (2002) 1525–1532. doi:10.1016/S0008-8846(02)00827-X.
- [220] T.W. Hicks, T.D. Baldwin, P.J. Hooker, P.J. Richardson, N.A. Chapman, I.G. McKinley, F.B. Neall, Concepts for the Geological Disposal of Intermediate-Level Radioactive Waste, 44 (2008) 1–66.
- [221] S.W. Swanton, T.G. Heath, A. Clacher, Leaching behaviour of low Ca:Si ratio CaO–SiO₂–H₂O systems, *Cem. Concr. Res.* 88 (2016) 82–95. doi:10.1016/j.cemconres.2016.06.001.
- [222] B. Lothenbach, T. Matschei, G. Möschner, F.P. Glasser, Thermodynamic modelling of the effect of temperature on the hydration and porosity of Portland cement, *Cem. Concr. Res.* 38 (2008) 1–18. doi:10.1016/j.cemconres.2007.08.017.
- [223] D.L. Kantro, Influence of water reducing admixtures on properties of cement paste - A Miniature Slump Test., *Cem. Concr. Aggregates.* 2 (1980) 95–102.
- [224] T. Chappex, K.L. Scrivener, The effect of aluminum in solution on the dissolution of amorphous silica and its relation to cementitious systems, *J. Am. Ceram. Soc.* 96 (2013) 592–597. doi:10.1111/jace.12098.
- [225] T. Chappex, K.L. Scrivener, The influence of aluminium on the dissolution of amorphous silica and its relation to alkali silica reaction, *Cem. Concr. Res.* 42 (2012) 1645–1649. doi:10.1016/j.cemconres.2012.09.009.
- [226] R.K. Iler, The Effect of Particle Size on the Solubility of Amorphous Silica in Water, *J. Phys. Chem.* 43 (1973) 399–408. doi:10.1021/j150557a024.
- [227] M. Onofrei, M. Gray, L. Roe, Cement Based Grouts - Longevity Laboratory Studies: Leaching Behaviour, SKB Tech. Rep. SKB-TR91-33. (1991).
- [228] C.M. Jantzen, Radioactive Waste-Portland Cement Systems: II, Leaching Characteristics, *J. Am. Ceram. Soc.* 67 (1984) 674–676. doi:10.1111/j.1151-2916.1984.tb19681.x.